INTER

International Network on Timber Engineering Research

INTER - International Network on Timber Engineering Research

2014 the International Network on Timber Engineering Research (INTER) was founded.

Scope

Presentation, discussion and documentation of research results in timber engineering and development of application rules for timber design codes or standards related to timber engineering.

Approach

Annual meetings in different countries/places hosted by meeting participants

Presentation and discussion of papers

Peer review of the abstracts before the meeting and of the papers during the meeting

Decision of the acceptance of the abstracts before the meeting by a well-defined review process

Decision of the acceptance of the papers for the proceedings during the meeting

Publication of the papers and the discussion in proceedings

Rules

All decisions including the appointment of the chairperson or the location of annual meetings are made by the participants attending a meeting.

Membership

Persons contributing to or being interested in research related to timber engineering.

INTER PROCEEDINGS MEETING FIFTY-FOUR 2021

MEETING FIFTY-FOUR

ONLINE MEETING

AUGUST 2021

INTER

International Network on Timber Engineering Research

Proceedings

Meeting 54

16 - 19 August 2021

Online Meeting

Edited by Rainer Görlacher

Table of Contents

1 List of participants

AUSTRALIA
K Crews   UTS & UQ

AUSTRIA
R Brandner   Graz University of Technology
M Burtscher
P Dietsch   University of Innsbruck
A Fadai   Vienna University of Technology
D Glasner   Graz University of Technology
M Gstettner   Graz University of Technology
G Hochreiner   Vienna University of Technology
J Lapere   Stora Enso Wood Products GmbH, Brand
M Lukacevic   Vienna University of Technology
R Maderebner   University of Innsbruck
U Mahlknecht   Graz University of Technology
A Malagic   Graz University of Technology
A Ringhofer   Graz University of Technology
R Sieder   Graz University of Technology
S Zimmer   Graz University of Technology

CANADA
G Doudak   University of Ottawa, Gatineau
L Gispert   StructureCraft, Abbotsford
T Heal   ISL Engineering, Whitehorse
F Lam   University of British Columbia, Vancouver
S Malek   University of Victoria, Victoria
S Shen   StructureCraft, Abbotsford
T Tannert   UNBC. Prince George
L Treder   StructureCraft, Abbotsford

CHINA
X Zheng   Tongji Univerisity

ESTONIA
A Just   Tallinn University of Technology
K N Mäger   Tallinn University of Technology
E Tuhkanen   Tallinn University of Technology

FRANCE
C Allemand   CSTB, Marne La Vallee
C Montero   CNRS - Université de Montpellier
A Narcy   CSTB, Marne La Vallee

GERMANY
S Aicher   MPA University Stuttgart
S Aurand   Karlsruhe Institute of Technology (KIT)
H J Blaß   Karlsruhe Institute of Technology (KIT)
L Buchholz   University fo Stuttgart
G D Arenzo   University of Kassel
S Egner   Karlsruhe Institute of Technology (KIT)
S Glattacker   Karlsruhe Institute of Technology (KIT)
R Görlacher   Karlsruhe Institute of Technology (KIT)
A Kovryga   Technical University of Munich
E Kuck   Karlsruhe Institute of Technology (KIT)
U Kuhlmann   University fo Stuttgart
S Mönch   University of Stuttgart
C Sandhaas   Karlsruhe Institute of Technology (KIT)
M Schenk   Technical University of Munich
S Schwendner   University of Kassel
K Simon   MPA University Stuttgart
M Steilner   Karlsruhe Institute of Technology (KIT)
C Tapia Camu   MPA University of Stuttgart
J Töpler   University of Stuttgart
M Vedovelli   Karlsruhe Institute of Technology (KIT)
M Westermayr   Technical University of Munich
L Windeck   Karlsruhe Institute of Technology (KIT)
S Winter   Technical University of Munich

ITALY
D Casagrande   Istituto per la Bioeconomi, San Michele
Y De Santis   Università degli Studi dell'Aquila
M Fragiacomo   Università degli Studi de l'Aquila
R Scotta   University of Padova
A Polastri   CNR - IBE, Dambel

JAPAN
K Kobayashi   Shizuoka University
T Nagashima   Sumitomo Forestry CO.,LTD., Tsukuba
T Tsuchimoto   Building Research Institute, Tsukuba

NEW ZEALAND
J Brown   University of Canterbury
W Dong   University of Canterbury
P Quenneville   The University of Auckland

NORWAY
R Tomasi   Norwegian University of Life Science
E Usher   Norwegian University of Life Science

SPAIN
J M Cabrero   Universidad de Navarra, Pamplona
M Yurrita   Universidad de Navarra, Pamplona

SWEDEN
T Bader   Linnaeus University, Vaxjö
D Caprio   Chalmers Technical University
H Danielsson   Lund University
R Jockwer   Chalmers Technical University
R Lemaitre   Linnaeus University, Vaxjö
M Schweigler   Linnaeus University. Vaxjö
E Serrano   Lund University

SWITZERLAND
T Ehrhart   ETH Zurich
R Fahrni   ETH Zürich
A Frangi   ETH Zurich
S Franke   University of applied sciences BFH, Biel
M Kleinhenz   ETH Zürich
P Palma   EMPA, Duebendorf
S Schilling   ETH Zürich
C Sigrist   University of applied sciences BFH, Biel
R Steiger   EMPA, Duebendorf

THE NETHERLANDS
G Ravenshorst   Delft University of Technology

TURKEY
A Ceccotti   Bogazici University, Istanbul
O A Sisman   Istanbul Technical University

UNITED KINGDOM
I Abeysekera   Arup. London
A Lawrence   Arup, London
A Przystup   University of Edinburgh
T Reynolds   University of Edinburgh
E Toumpanaki   University of Bristol

USA
S Breneman   WoodWorks - Wood Products Council
G Montgomery   Timberlab, Greenville
B Yeh   APA - The Engineered Wood Association, Tacoma

2 Minutes of the Meeting

by F Lam, Canada

CHAIRMAN'S INTRODUCTION

P Dietsch welcomed the delegates to the 8th International Network of Timber Engineering Research (INTER) which was held as an on-line meeting because of the Covid-19 pandemic. He thanked the participants of this meeting for participating in spite of time zone challenges. In total 96 participants from 18 countries registered for this INTER meeting. He also thanked Karlsruhe Institute of Technology KIT for hosting of this meeting.

This is the 54th meeting of the group including the series of former CIB-W18 meetings. By moving to an Online-meeting, INTER could continue its tradition of yearly meetings to discuss research results related to timber structures with the aim of transferring them into practical applications.

The chair introduced all the participants.

Twenty-three papers were accepted for this meeting with 38 submitted abstracts. This includes 7 accepted but withdrawn papers from last year's meeting. 21 of the accepted papers will be presented as 2 papers were withdrawn. The papers were selected based on a review process for the abstracts with 4 acceptance criteria (state of the art, originality, assumed content, and relation to standards or codes). 17 members acted as reviewers and each abstract was reviewed by at least 8 reviewers. Full papers were requested to be submitted one month before the meeting to facilitate distribution to the participants prior to the meeting. The Chair thanked all authors of abstracts and papers as well as all reviewers for their work.

The presentations were limited to 20 minutes each, allowing time for meaningful discussions after each presentation. The Chair asked the presenters to conclude the presentation with a general proposal or statements concerning impact of the research results on existing or future potential applications and development in codes and standards.

The topics covered in this meeting were: Timber Columns (1) Stress for Solid Timber (1) Timber Joints and Fasteners (10) Laminated Members (6) Structural Stability (1) Fire (2). Numbers in parentheses are the number of papers presented in each topic based on initial allocation.

Notes were not presented in this meeting due to the time limitation of 4 hours meeting time each day, which was necessary to best accommodate for the time zone differences.

The Chair encouraged the tradition of active questions and discussion processes for our meeting and reviewed the rules and guidelines for web-based participation for presentations and the question/discussion process.

He invited all authors to amend their papers according to the comments and recommendations received before submit the final paper for the proceedings. Finalized papers must be sent to Rainer Görlacher at the latest end of September this year.

Information from other organizations

P Dietsch provided the following information on European standardization:

CEN/TC 250/SC 5 Design of timber structures: The revision of Eurocode 5 is in full effect. Project Teams 4 "Fire" and 5 "Connections" have finalized their work, Project Team 6 "Bridges" is in its last weeks of finalization.

Eurocode 5 part 1-1 is in the process of being compiled and will go to informal enquiry in October/November this year. The same holds for Eurocode 5 part 1-2 "fire". Eurocode 5 part 2 "bridges" will go into informal enquiry in April/May next year. Then a lot of administrative work at CEN starts, before the formal enquiries will happen in 2023, followed by formal vote in 2025.

The Chairman of SC 5, S Winter, will provide (upon request) a copy of WCTE paper on the current status of Eurocode 5.

CEN/TC 124 Timber structures: The European work on product standards in CEN/TC 124 has slowed down quite a bit due to the unclear situation, namely that the European Commission has stopped citing new or revised hEN candidates in the Official Journal of the European Union. This situation will presumably persist for many years, until a new edition of the Construction Products Regulation (CPR) has been developed or the CPR-Acquis (system of related legal documents) has been changed. The possible workaround to remove new product standards from the hEN-list and publish without Annex ZA is questioned by producers. It is unclear if the signal to the European Commission, namely the possibility to install an alternative system for international approval, outweighs a possible tendency to renationalisation.

M Fragiacomo provided updates on SC8 Earthquake resistance design of structures, as they are working towards provisions for new buildings, existing buildings and timber bridges.

TIMBER COLUMNS

54 - 2 - 1   Buckling of Slender Timber Beam-Columns under Combined Loading,
        Including Creep - I K Abeysekera, I Feltham, A Lawrence

Presented by I K Abeysekera

H Blass asked about the possibility to check imperfections as there can be both material and geometric imperfections in a column. I K Abeysekera said that as long as good grading practice is available material imperfection would average out. H Blass commented that one would not know the ratio of the influence between the two types of imperfections and engineers on site will not be able to check the material imperfections as they are random. H Blass further commented that this approach seems to be deterministic and this would be important especially for creep where low stress ratios would be typically encountered and their findings indicated that creep would not be a problem for slender columns. I K Abeysekera agreed that the approach is deterministic.

G Hochreiner stated that there is no validation in this paper which requires experimental data on creep curve. I K Abeysekera said that the results were based on a logarithmic shaped creep curve as referenced in the STEP book. G Hochreiner stated that this is not considered in Eurocode 5 and it is also referenced to strength and not displacement. P Dietsch suggested further discussion on this topic in a breakout room.

S Aicher said this approach is only valid for monotonically applied loads. Varying vertical loads would result in deformation rebound and creep recovery is a complicated process and not considered in total. IK Abeysekera said the current approach is conservative. The consideration of varying load and creep recovery would be too complicated for code considerations.

S Aicher commented that economic impact analysis on the approach is needed. P Dietsch suggested adding such information as a short appendix for the paper.

P Dietsch commented that stress utilization needs to reach a certain level before creep becomes important. This fact is implicitly covered in the German National Annex. I K Abeysekera agreed that this could be considered in the approach.

M Fragiacomo commented that the limit of load level for creep for high strength engineered wood products might be an issue. He received clarification that the quasi permanent load combination should be used.

A Frangi said most of the loads on the column are non-permanent and he was not sure whether a direct addition of the effects of the permanent and non-permanent loads would be appropriate. In addition he is not sure about the need to solve

differential equations. IK Akeysekera said solutions to the differential equations are provided.

U Kuhlmann commented that one of the outcome of their work on lateral torsional buckling is that creep does not affect stability. A simple approach with a reduction factor to modify stiffness may be more practical and should be attempted. I K Abeysekera agreed.

STRESSES FOR SOLID TIMBER

54 - 6 - 1   A New Probabilistic Approach to Model the Tensile Properties of Split
                  Spruce Boards and its Application in Engineered Timber Products -
                  R Sieder, R Brandner

Presented by R Sieder

H Blass commented that this approach considered resawn or split glulam and asked about application of the approach to consider CLT especially the consideration of finger joints. R Sieder said that the influence of finger joint strength was modeled based on TKAR. H Blass said that in CLT part of the board may have finger joint and part of the board may not have finger joint. R Sieder responded that the model can consider such case.

C Tapia asked what is the benefit of having an intermediate zone in the model. R Sieder said that the influence with and without intermediate zone has not been studied and agreed the influence might be minor. C Tapia said that TKAR values were used to represent finger joints but the actual tensile strength of finger joints are commonly measured. He asked why not work directly with finger joint strength data. R Sieder said this may be done later.

E Ussher asked about MOE values and the situation where reaction wood might be involved. He also asked about the boundary conditions. R Sieder said that MOE as influenced by the resawing process was considered minimal. The timber considered may have reaction wood in it. Also four-point bending with simple supports was considered.

R Brandner added that flat finger joints were considered in the study and discussed with C Tapia that variation of finger joint properties was already considered with the approach.

A Frangi commented that in fire situation there might be an issue with the slender split beam exposed on three sides to fire load. R Sieder stated that no special considerations would be needed.

M Westermayer questioned about need of consideration of fiber deviation in the model. R Sieder stated that fiber deviation was not explicitly considered in the model

and might consider this with additional strength reduction. R Sieder clarified that clear zone length was randomly treated and not fixed at say 150 mm.

P Dietsch suggested adding the table from last two slides to the paper.

C Tapia asked what type of distribution of strength along the board was found. R Sieder said not quite lognormal distribution as tail fittings were not perfect.

TIMBER JOINTS AND FASTENERS

54 - 7 - 1   Steel Properties of Self-Tapping Screws - C Sandhaas, H Blass

Presented by C Sandhaas

A Ringhofer agreed with the conclusions. He commented that torsional moment capacity might be influenced by hardness distribution within the cross section. He also noted that the approach is conservative and asked about allowing more flexibility to adopt higher values based on testing. C Sandhaas agreed that this might be possible. She also confirmed that the screws were produced by European companies but may be produced outside Europe.

M Fragiacomo commented that design for seismic consideration might be problematic especially for over strength factor consideration in capacity based design as there was a large spread between the design values and the upper values. H Blass commented that it would not be a good idea to use screws in dissipative zones for seismic design and agreed that larger over strength factors might be needed.

I K Abeysekera asked about combined axial and bending action with reduced yield moment. C Sandhaas said that this was investigated by H Blass in INTER 2017. IK Abeysekera asked whether it would be possible for manufacturers to limit the COV of their products for seismic zones. C Sandhaas and A Ringhofer responded that the COV for one screw type and one producer would be low. R Brandner said that this would be true within one batch but there would be higher variation between batches. C Sandhaas agreed and commented that this type of issue also exists for steel dowels for seismic design.

54 - 7 - 2   Self-tapping Timber Screws Subjected to Combined Axial and Lateral
                     Loading - A Ringhofer, M Burtscher, M Gstettner, R Sieder

Presented by A Ringhofer

H Blass commented that Bejtka in 2006 performed embedment tests with axial loads. A Ringhofer said the work was referenced in the paper but they could not explain the

difference in findings. It could be due to the smaller size of specimens compared to those used in the current study.

H Blass commented that the "pure" shear load would have axial load due to rope effect. As such higher axial loads in the screw exist, he asked how would one consider this in design. A Ringhofer agreed and stated that this has to be considered via M+V interaction.

R Jockwer asked if one would apply both the axial load and the rope effect in design. A Ringhofer responded that the information as shown in the graphs in the paper is based on test results so both effects exist. Modifying the Eurocode design model based on M+V interaction would solve the problem.

P Dietsch commented that the printed version of the paper will be in B+W so coloured figures will not be available. He noted that Kser values were low compared to Eurocode 5. He asked if this is caused during the drilling, e.g. cutting of fibers, and that such large differences should be considered. A Ringhofer stated that drilling effect should have increased the stiffness via densification of the wood by the screws. For example, with predrilling withdrawal stiffness would decrease compared to non-predrilled cases.

S Shen asked whether these factors could be applied to non-smooth shank nails. A Ringhofer stated that in principle this analogy should be applicable.

A Frangi asked about group effect and if the information would be applicable for groups of connectors. A Ringhofer stated that a limited number of tests with one screw length was done showing similar trend.

54 - 7 - 3   Rigid Glulam Joints with Glued-in Rods Subjected to Axial and Lateral Force Action - S Aicher, K Simon

Presented by S Aicher

P Dietsch commented that the shear force capacity for cases with loading close to the edge might be more a perpendicular to grain situation. S Aicher agreed as one moved more away from the loaded edge one would get more load transfer via compression perpendicular to grain and conversely as one moved closer to the loaded edge one would get more load transfer via tension perpendicular to grain.

R Jockwer stated that the lateral load carrying capacity in the Eurocode draft is supposed to refer to the fastener capacity and not related to timber splitting with the assumption of loading far away from the loaded edge. S Aicher was not sure about the necessity to verify the tension strength perpendicular to grain capacity of the timber. It is more important to make the process more transparent to designers. S Aicher also agreed that one could overcome the problem via reinforcement.

However it is not intended for reinforcement to be used all the time especially if there are many joints for consideration. One should understand how the joint works.

R Jockwer asked about interaction. He questioned whether one is sure about using the quadratic based interaction in the long term if cracks exists. S Aicher said it is important that we find a good solution if we want to utilize most of the axial capacity and find an option to deal with the lateral force. S Aicher said they do not yet have the final answer.

T Tannert commented the reverse loading situation is important and asked if the results would be different under reverse loading. S Aicher responded that the results for reverse loading were not provided in this paper because of limited length of paper. He said that the same load in the opposite side could be achieved and the cracks do not harm the situation too much. However reverse cyclic loading with increasing amplitude may be a problem under many cycles. T Tannert asked whether work is available for screwing rods into side grain. S Aicher responded that this was not planned as insertion into the end grain is more relevant.

E Serrano commented about the test set up in terms of distance to the loaded edge via a point load. E Serrano and S Aicher discussed about the influence of test method in relation to actual load application. S Aicher further said looking at the stress plots they did not notice too much axial forces.

P Dietsch commented that adding reinforcement in this setting can provide a robust solution.

54 - 7 - 4   Slip Modulus Formulas for Timber-to-Timber Inclined Screw Connections – Comparison with other Simplified Models - Y De Santis, M Fragiacomo

Presented by Y De Santis

R Brandner questioned the R^2 value being negative and greater than one. Y De Santis will provide definition of R2. R Brandner later acknowledged in chat that R^2 value outside the range of (0, 1) is possible without using real data.

H Blass commented that the comparison with Eurocode 5 formulation for inclined screws is meaningless as it does not deal with inclined screws. This should be removed from the paper.

W Dong stated that in Girhammer's work embedment test approach was considered to be similar to the compression test approach and deemed to be unsuitable for the model. Y De Santis said that embedment test results provided local deformability information of the timber to allow avoiding the need to experimentally evaluate withdrawal stiffness.

W Dong commented that using the two springs approach for the parallel and perpendicular to grain directions may result in discrepancy in boundary cases of withdrawal test results perpendicular to grain and embedment test results. Y De Santis agreed.

R Tomasi agreed that there may be issues at the extreme say at 0 or 90 degree. He asked about friction in the shear plane. Y De Santis said that model is valid but has an issue with the 90 degree case which is not a realistic situation. Friction was not considered in the model because they observed in some experimental sets say with cross configuration and in some inclined screw configurations, friction did not seem to be present. R Tomasi and Y De Santis discussed the consideration of double stiffness model and single stiffness model for various cases.

A Ringhofer received clarification that angle = 0 degree implies pure shear load.

P Dietsch suggested possible amendments of the paper to be considered based on the comments and discussion.

54 - 7 - 5   Connections with Inclined Screws and Increased Shear Plane Friction - S Aurand, H J Blaß

Presented by S Aurand

R Jockwer asked about lower residual coefficient of friction after slip in the pyramid pattern and asked about ductility. S Aurand said the behaviour is ductile in general. He did not observe failure of the pyramid pattern and did not observe any clear drop of friction forces.

P Dietsch commented that the large pyramids might reduce risk of influence of large moisture changes. He asked if there is interest to study influence of changing moisture content. S Aurand replied that moisture issue is not part of the project and it may be considered in the future.

P Dietsch asked which is the optimal solution based on production, performance and sustainability issues. S Aurand replied that milled pyramids are work intensive to produce; nevertheless, replacing aluminium with a more environmentally friendly option is a good solution.

I K Abeysekera and S Aurand discussed DVM availability in the market. DVM is used in other industrial applications and can be milled.

C Sigrist commented on the competitiveness of aluminium connections with respect to its advantages. H Blass responded that the aluminium connections have disadvantages say with respect to mounting etc. The system overcomes these issues.

A Frangi and P Palma commented that DVM and aluminium connections were considered from the fire performance perspective. Replacing the aluminium connections with DVM is a good idea for fire performance. S Aurand agreed.

S Aicher commented that dovetail aluminium connectors allowed small uptake of normal forces and asked if such issues have been considered. S Aurand stated during the development of prototypes, tests were done with other loading conditions. For example, they did not observe any issue with moment but this paper only deals with friction.

E Ussher asked about ductility as timber connections typically rely on the metal to provide ductility. He asked whether shrinkage could be an issue. A Aurand replied that wood also has ductility from the compression. H Blass also replied that DVM do not shrink nor swell as they are saturated with resin.

O Sisman asked about which failure modes are more ductile and asked about using this in vertical joint. For CLT walls, S Aurand said the screw withdrawal and wood failure with perpendicular orientation seemed to be more ductile. H Blass replied that his connector was not intended to provide ductility for seismic applications and load slip graphs are available in the paper.

P Dietsch commented that page limit being exceeded in the paper. He would be open to discuss the current limit with INTER but a set limit will be more strictly enforced in the future.

54 - 7 - 6   Minimum Geometric and Execution Requirements for Axially Loaded Groups of Screws in Hardwood - U Mahlknecht, R Brandner, A Ringhofer

Presented by U Mahlknecht

M Westermayr commented about n_{eff} of 1 with respect to screw failure. As variation between manufacturers seemed too high, with some manufacturer having COV of 5%, careful consideration of material used would be needed as knot and growth defect could have affected the results. U Mahlknecht agreed in general. The beech material is of high quality and the birch has bit more growth defects. M Westermayr commented that his own work indicated material quality could affect the direction of the drilling.

W Dong asked about the small spacing and what type of equipment was used to drill the holes with tight screw spacing that can avoid contact of the screws. U Mahlknecht agreed that this could depend on the drilling equipment. They did not encounter screw contact with 600 screws installed. U Mahlknecht clarified that predrilling was done stepwise to the total insertion step. 70 mm was drilled first with

a fixed machine and the rest with a manual drill to allow more consistent angle at the beginning. W Dong commented that on site installation might be an issue.

G Ravenshorst asked if there is any relationship with density, e.g. how would this work with say high density material of say 1000 kg/m^3. U Mahlknecht responded that their dataset did not have a large density range. With the available screws of 8 mm at 10d screw tensile failures were encountered for material at 550 kg/m^3. In higher density cases tensile capacity of the screws would govern.

R Brandner commented that predrilling and not on-site installation are advised. R Brandner tested Eucalyptus LVL. The results seemed to show more brittle behaviour with splitting failures. The conclusions in this paper only relate to the products tested in the paper.

I K Abeysekera asked about the distinction between ductile and brittle failure mode and why withdrawal failure was identified as ductile. U Mahlknecht responded that ductile in the sense of comparison to splitting failure and not in the sense of seismic applications. Also there is a possibility of formation of plastic hinges with slender screws.

54 - 7 - 7   Beam-on-Foundation Modelling as an Alternative Design Method for Timber Joints with Dowel-Type Fasteners – Part 4: Joints Subjected to In-Plane Loading - R Lemaître, J-F Bocquet, M Schweigler, T K Bader

Presented by R Lemaître

This paper was already presented in 2020. By request of the authors it was not published in 2020. Discussion of 2020:
P Quenneville asked why the evaluation of Kser started from origin and was not started from the post cyclic zone. R Lemaître said that there was no initial gaps/clearance in the connection between the steel plate and timber.

P Gronquist asked if the BoF approach was compared with other models and compared the difference between timber and steel. R Lemaître said no this was not done.

E Serrano asked about consideration of coupled and uncoupled springs to model connector behaviour.   R Lemaître responded that uncoupled springs were used because comparisons with test results showed good agreement for the embedment behaviour. However the path of the dowel movements between simulations and test results were different. Perhaps coupled springs should be considered.

C Sigrist asked about the power function in the proposal and whether it was possible to determine the power from the model. R Lemaître responded that it was possible by regression approach of the test data one could fit the BoF approach to get the power parameter.

C Sigrist commented that models that can consider axially loaded connectors and Ku would also be needed. R Lemaître responded that past work on 2-D BoF presented in INTER could deal with axially loaded connections. Ku could be estimated from the current approach.

G Hochreiner asked whether out-of-plane bending behaviour could be predicted. R Lemaître responded that this BoF model could work in principle but more work would be needed as the coefficients of the stiffness matrix would need more consideration and input.

in 2021 R Lemaître provided a rationale to accommodate a revision to the paper on a similar subject because coupled springs instead of two uncoupled springs are needed based on observed failure modes.

54 - 7 - 8   Beam-on-Foundation Modeling as an Alternative Design Method for Timber Joints with Dowel-Type Fasteners – Part 3: Second Order Theory Effects for Considering the Rope Effect - M Schweigler, M Vedovelli, R Lemaître, J-F Bocquet, C Sandhaas, T K Bader

Presented by M Schweigler and M Vedovelli

R Jockwer asked if the 0.25 factor to account for rope effect in the current Eurocode 5 is correct. M Schweigler responded that the 0.25 factor can account for the friction in shear mode; therefore, it is a good factor. R Jockwer commented that maybe this factor accounted for more than just the friction.

G Hochreiner asked what would be the plan to account for the gap and friction. M Schweigler said one should not replace EYM. But using this approach would require more parameters to be defined in the standard. G Hochreiner also asked about the impact of elasticity perpendicular to grain, the size of side member, and the size of the washer. M Schweigler said these issues should be investigated in future work.

P Palma questioned on modelling with springs based on embedment tests and asked why not calibrate the model with single fastener tests. M Schweigler said there are many parameters to be considered in a single fastener test which could mask the embedment properties.

E Tuhkanen asked about the friction between the steel plate and timber member as in real connections movement might not be allowed. M Schweigler said only one fastener was considered in this study. With multiple fasteners the modelling approach of R Lemaître would be more realistic which would also work with slotted in steel plate.

S Aicher asked about the density and compressive stiffness of the side member required to activate the friction force. M Schweigler agreed that modelling of spring stiffness k is a challenge.

S Franke agreed with the findings of 20% value as proposed.

54 - 7 - 9   Stiffness of Steel-Timber Dowel Connections – Experimental and Numerical Research - U Kuhlmann J Gauß

Presented by J Gauß

J M Cabrero asked about the details of the embedment test and received explanation of the position of the reinforcement. J Gauß said that small steel plates were used to load the specimen in tension. J M Cabrero and J Gauß discussed the possible reasons of why lower stiffness was measured for some of the reinforced cases as close position of the reinforcements could have densified some wood material leading to lower stiffness.

H Blass received clarification that with reinforcement stiffness decrease was observed but ultimate load was increased. Also the stiffness was based on absolute not relative load.

F Lam received clarification that full hole tests used in the embedment tests did not result in bending of the dowel.

S Aicher and J Gauß discussed the range of the observed stiffness information in terms of fitting of the model curve to the data. J Gauß said some values are 50% to 100% higher than the lowest values. The COV of the embedment test might be around 40% and the COV of the tensile test might be around 25%. Also embedment test results with only the undisturbed specimens might be unrealistic.

A Frangi commented that the reasoning behind group effect as explained was difficult to understand. He suggested not to include group effect for K_{ser} as only having a single connector would be unrealistic. J Gauß said that the hole tolerance limit has large scatter and agreed it would be easier to provide an overall stiffness reduction. A Frangi commented that $d^{1.7}$ is in the Swiss code.

T Tannert asked about the sensitivity of the data to the variability of steel. J Gauß said steel variability did not affect K_{ser} but affected load capacity. T Tannert asked about extending the work to multiple steel plate connections. J Gauß said the beam on foundation model should be applicable for multiple steel plate connections.

54 - 7 - 10 New Analytical Model for Plug Shear of Timber Connections with Small Diameter Dowel-Type Fasteners in the Parallel-to-Grain Direction - M Yurrita, J M Cabrero

Presented by M Yurrita

H Blass said that over 600 tests from others were used for your model. Other models typically only used their own test data for model calibration. Was this model checked with its own data using a calibration set and a verification set? M Yurrita responded that the modelling process did not involve calibration.

C Sigrist questioned why thickness of steel plate was not considered. M Yurrita said that in case of small diameter fasteners there was no difference between thick and thin steel plates (~3% difference only). C Sigrist pondered whether one would get plug shear failure mode in timber to timber connections.

H Hochreiner questioned what would happen for unsymmetrically loaded connections. M Yurrita said that this could be studied in future. H Hochreiner said one would also have moments in such cases.

C Sandhaas asked about background of K_T and K_v. M Yurrita said these are similar factors in Eurocode 5 and they are calibration factors from former models.

54 - 7 - 11 Connection of Timber Foundation Piles to Concrete Extension Piles - G Ravenshorst, J van Dalen, M Mirra, R Steiger, J-W van de Kuilen

Presented by G Ravenshorst

H Blass commented that this is similar to the case of timber column clamped in concrete foundation where design rules are available and shear is a major design consideration. G Ravenshorst replied that shear did not seem to govern in this case as it would depend on the length of the socket.

U Khulmann commented that such stability cases are also important for steel structures where Eurocode 3 part 5 has a lot of information.

E Ussher asked whether there was any influence on point of fixity of the pile and whether the soil parameters would be site specific. G Ravenshorst replied at the final position of the pile, there would be no influence at point of fixity at the pile tip. Also the soil parameters are depth dependent but in general applicable for Dutch conditions of peat and sandy soil.

P Dietsch asked about the background of the limit of 500 mm below water level and why was k_{def}=1 which would be ½ of the value for service class 3 in code. G Ravenshorst replied that the limit of 500 mm was based on practical experience as a

safe limit. k_{def} = 2 might be based on dry/wet cycle and in this study the piles would be under constant wet state. P Dietsch further commented that the creep in the parallel to grain direction might be lower.

LAMINATED MEMBERS

54 - 12 - 1 Mechanical Properties of European Beech Glulam after 32 Years in a
Service Class 2 Environment - T Ehrhart, P Grönquist, S Schilling, R Steiger,
A Frangi

Presented by P Grönquist

P Dietsch supported the shear test set up conclusions. He did not agree with the proposal to split up service class into A and B as the newly proposed approach in Eurocode 5 implicitly also deals with the issue. P Grönquist replied splitting up service class into A and B would be more appropriate for modifying the current standard.

R Brandner asked about the distribution of compressive stress and received clarification that there was no reinforcement used in the support. He commented that the difference between edgewise and depth-wise shear strength results might be due to annual ring orientation effect. He asked whether there was any difference in G for these orientations. P Grönquist replied that the G data was not included in the paper and would look into the issue.

R Brandner commented that some of the mean strength values reported in the text and the table are different. P Grönquist replied that he would look into the issue and the difference might be deal to reporting of maximum likelihood censored data.

R Brandner asked why stop the tests in some cases. P Grönquist replied that probably results of few pretests without failure were reported. They would still be okay because the actual strength would be higher and use of censored data is appropriate.

T Ehrhart added that there was no reinforcement at the support but 8 mm screws were used to fix the support. He agreed that difference in annual ring orientation between flatwise and depth-wise orientation resulted in the difference in the shear strength. The paper will be amended to consider the comment on service class.

G Ravenshorst asked what was the moisture content of the member on site and why not conduct the test at this moisture content. P Grönquist replied that moisture content of the member on site would be between 12 to 20% and the testing was done at 9% MC.

S Malek asked about the difference in shear failure pattern between the edgewise and flatwise orientation. T Ehrhart replied the failures involved the gluelines but they were not clear glueline failures. They could not do more checks as the specimens were accidentally disposed.

S Aicher commented that it is well known that edgewise shear strength is higher than flatwise shear strength in softwood. He doubted that the failures were caused by glueline failures. This could have easily been checked if the specimens were still available. He commented that statements such as "appears to have lower strength" should not be used in the paper. P Grönquist agreed.

54 - 12 - 2 Influence of the Moisture Content on the Compressive Strength and Modulus of Elasticity Parallel to the Grain of Engineered Hardwood Products - T Ehrhart, R Steiger, A Frangi

Presented by T Ehrhart

P Dietsch agreed to differentiate K_{mod} between bending and compression from a scientific point of view but stressed that this issue should also be viewed from a design perspective point of view, think of e.g. members under combined loads. He asked how to ensure not having moisture distribution within the cross section. T Ehrhart said this was not checked but the specimens were conditioned in a constant climate chamber until weight change was acceptable.

R Brandner agreed about differentiating K_{mod}. He commented that wood drying/wetting has hysteresis behaviour. Since the study focused in the absorption phase there might be a 2 to 3% difference from the desorption phase. T Ehrhart said the hardwood product was typically glued at 9% MC, the product would always start from the absorption phase and change in MC would be slow; therefore, desorption would be unlikely. R Brandner said in bridges application absorption followed by desorption might happen. All agreed that there is no solution now.

T Reynolds and T Ehrhart discussed using oven dried method and climate chamber method to achieve target moisture.

C Sigrist commented that there is a lot of work needed for EN408 with the introduction of these new products. The third draft of the standard will be released soon and he encouraged comments and suggestions from the colleagues.

S Aicher agreed different K_{mod} for SC1 and SC2. He commented that there are some European technical documents on downgrading compression strength of hardwood (oak, chestnut etc.) with a single factor due to moisture effect. T Ehrhart will look into these documents.

54 - 12 - 3 Imperfections of Slender Glulam Beams - U Kuhlmann, J Töpler

Presented by J Töpler

P Dietsch commented that the differences to other studies on the topic could be due to the consideration of members in finished buildings (i.e. including dead weight). He said imperfection depends on construction quality, which could vary due to different level of experience, and pondered whether and how to take this into account in future version EC5. J Töpler agreed that the assembly process has the highest influence. It would be an important topic for the next generation of EC5 to provide guidance.

E Ussher asked whether the model was calibrated prior to application. J Töpler said the model was calibrated and verified and the information was presented in WCTE 2021.

G Hochreiner stated that imperfections should be defined independent of the structural model. J Töpler replied this is a topic for discussion in term of approaches. G Hochreiner received clarification that the stiffness of the brace elements was based on values from cited paper. They discussed the influence of local and global effects where global effects might be more dominant.

S Aicher also commented that imperfection also depended on the stiffness in the minor axis. J Töpler said there did not seem to be a big difference in the horizontal axis and this might be the case for the unbraced system.

H Danielsson received clarification on the numerical modeling of the compression behaviour as nonlinearly ideal elastoplastic.

54 - 12 - 4 Probabilistic Description of the Mechanical Properties of Glued Laminated Timber Made from Softwood - S Schilling, P Palma, R Steiger, A Frangi

Presented by S Schilling

C Tapia commented that he is not convinced with size effect consideration of parameters within the Weibull distribution. Only the scale parameter could be modified and the shape parameter related to COV should not be modified. C Tapia also noted that the power law is also related to the Weibull distribution. S Schilling responded that for perfectly brittle material COV would be a material constant. As wood is not a perfectly brittle material changing COV would be okay.

C Tapia stated that modelling compressive strength with normal distribution might be more appropriate compared to lognormal distribution. Also truncation can be used to avoid possible encountering of negative strengths. S Schilling agreed.

R Brandner commented that lognormal distribution for compressive strength perpendicular to grain might be better. Also power law in general can be used and it is not necessarily tied to Weibull theory.

R Brandner asked about the possible physic of material properties with changes in length. S Schilling said accumulation of weak zone might be the issue. R Brandner said lognormal distributions fit better than Weibull distribution in many cases and assuming Weibull distribution might affect results of reliability analysis. He also commented that parameter distribution model by size is messy.

F Lam agreed with most of the comments of C Tapia and R Brandner. He commented he is uncomfortable with having distribution parameters on distribution parameters especially for shape parameter when working with size dependent properties. Canadian test data on glulam beams showed that variability of bending strength did not seem to be size dependent. He said estimation of reliability index (beta) is influenced by the choice of probability distribution but fitting to the lower tails of the strength properties distributions is most important. Also Beta is a relative not absolute value and we just need to be consistent with the approach.

54 - 12 - 5   Load-bearing Capacity and Fracture Behaviour of Notched Cross Laminated Timber Plates - A Malagic, M Augustin, G Silly, A Thiel, G Schickhofer

Presented by M Malagic

P Dietsch received clarification that in the paper it is possible to have a linear interpolation of the proposed K_{mod} as a function of m so that K_{mod} is not discontinuous. The use of the term K_{mod} should be reconsidered to avoid misinterpretation. P Dietsch commented that tension strength perpendicular to grain and rolling shear strength seemed too high. A Malagic responded that analysis assumed volume dependency of these strength properties hence higher values.

H Blass asked about the use of notch beam support $K_n = 4,5$. He said this value is for LVL beams loaded edgewise and asked for justification for their use for CLT as a plate. A Malagic said this is the state of the art in design consideration. H Blass disagreed and commented that this factor cannot be used for CLT.

E Serrano and A Malagic discussed the similarity of the semi rigid approach to a previous paper with different choice of coupling. E Serrano received clarification that comparison of different capacity in units of k_n was based on width of the member used in the experimental program of 600 mm. E Serrano commented that assumed semi infinite length as being a possible severe assumption. A Malagic responded that the transition zone was small and therefore not a limiting factor.

54 - 12 - 6 Characterization of Rolling and Longitudinal Shear Creep for Cross
              Laminated Timber Panels - C Allemand, A Lebée, M Manthey, G Forêt

Presented by C Allemand

T Tannert commented that in a CLT the rolling shear having low stiffness would attract lower loads and questioned the level of load considered in the experiment. C Allemand responded that in the rolling shear direction similar load level was guided by the load level for the longitudinal shear direction which was around 40%, based on past research. T Tannert said different load levels should be considered for rolling shear creep studies.

M Schweigler asked about sealing the specimens and possible influence to deflection measurements. C Allemand replied that sealing did not have any mechanical influence and did not affect the deflection measurements.

P Dietsch asked if there were comparisons with known test configurations to check the proposed test setup. C Allemand replied that other configurations were not tried. P Dietsch said that test configuration in EN789 or EN408 could be tried.

M Fragiacomo questioned about the environmental conditions and asked if the experiment focused on pure shear. C Allemand said there was no consideration of mechano-sorptive effects. M Fragiacomo commented that k_{def} in the Eurocode is referenced with some kind of mechano-sorptive consideration and not sure direct comparisons can be made.

G Hochreiner questioned whether the shear load level would lead to stable or unstable creep. C Allemand provided information on the load level and not sure whether the creep is stable or unstable as the load period is only 8 months. G Hochreiner commented that creep test standards for wood based panels exist for N. America and Europe and asked why they were considered. C Allemand said that she will check these out. P Dietsch commented that load level seemed to be high and could lead to exponential creep.

STRUCTURAL STABILITY

54 - 15 -1   A Proposal for Capacity Design of Multi-Storey CLT Buildings -
             D Casagrande, G Doudak, M Masroor

Presented by D Casagrande

J Brown commented that considering building level and hierarchy of ductility class, overstrength of connection might be overly penalizing. He asked if one would put in an overstrength factor cap. D Casagrande replied that a cap is considered for ductility level 2 and the cap for ductility level 3 should not be applied.

J Brown asked about diaphragm and whether it would be considered as the capacity of whole system. D Casagrande replied that it is important and should be considered. How to provide a simple equation is difficult. G Doudak commented that the influence of the diaphragm was not incorporated in the model. The behaviour of the diaphragm was lumped as non-dissipative element in the paper.

T Tannert asked if the vertical joint resistance needs overstrength factors. D Casagrande replied no as vertical joints should be as close as possible to the design limit. T Tannert asked about the coupled uplift and shear resistance of shear connectors and the uplift resistance might limit the rocking action when overstrength factors are adopted. D Casagrande said that their contribution into the rocking strength of the system was accounted for with the assumption that the shear connectors did not yield.

T Tannert commented that if all the connectors were assumed to have similar yielding mechanism, would this approach work with using different types of connectors having different yield mechanism in a building. D Casagrande replied that this approach should be applied to traditional connection systems and should use similar connections in a building.

R Jockwer asked how to choose overstrength factor percentile for other dissipative connections and limited ductility connections. D Casagrande replied that these should be less than the 95 percentile for the non-dissipative case but these cases are left open for now for further consideration. Running probabilistic analysis on the failure of buildings is needed.

O Sisman asked how to consider joint of perpendicular walls and would they be considered as dissipative or non-dissipative cases. He commented that introduction of level 2 and level 3 might be difficult for young practicing engineers to learn. He suggested that combining levels 2 and 3 into a single level would be easier and should be considered. D Casagrande said combining levels 2 and 3 into a single level could be considered. D Casagrande also replied that the connection of perpendicular

wall should be considered as non-dissipative connection. More studies on brittle failure mode vs more ductile failure mode should be considered.

M Fragiacomo commented that the proposal would go into the evaluation process soon so receiving timely feedback and suggestions would be important. Eurocode sets the three ductility classes and they cannot be changed. Properties of steel and its scatter would be a concern for overstrength factor. One might need to provide upper limit to their yield strength in future standard.

FIRE

54 - 16 -1   Temperature-Dependent Thermal Properties for Cross-Laminated Timber
               Exposed to Standard Fire - M Kleinhenz, A Just, A Frangi

Presented by M Kleinhenz

S Winter commented the study only looked for the resistance with minimum insulation. He questioned why 300 °C as failure criterion was used and that seemed to be high for PU adhesives. He also asked physical explanations for the thermal properties considered. M Kleinhenz said that in this INTER paper only resistance was considered and not EI and would deal with other issues in future work. The 300 °C was chosen based on previous furnace test results (observation of fall off) and will confirm with own small scale fire tests when equipment becomes available. M Kleinhenz replied about the physical explanation as C_p having two peaks. The first peak corresponded with water going out. As energy was needed for pyrolysis to turn the timber into charcoal, it makes physical sense to have the second peak. S Winter commented that water wave / moisture movement condensation might be the physical reason.

G Montgomery questioned why one laminar without cross layer was considered in slide 7. M Kleinhenz said the member was assumed to be able to still take a load but this might not be realistic. G Montgomery asked whether this could be seen in the fire test. M Kleinhenz said it was not possible to see this with the flaring up. G Montgomery said it would be more likely to fall off when the second layer fell off.

G Montgomery asked why specimen C with no drywall layer was more variable. M Kleinhenz said more small scale fire tests would be done for these boxes. G Montgomery received confirmation that the loading applied were typical live and dead loads.

G Montgomery asked if Eurocode accounts for the fall off from the glue bond. M Kleinhenz replied that it would be included in future Eurocode with step model.

S Aicher commented on the case of CLT and GLT working as a T Beam with or without insulation. He said the main problem would be the bond between the GLT beam and the CLT plate where temperature dependency of the PU adhesive would play a major role. The 300 °C would not be appropriate for the PU adhesive where 180 °C to 230 °C would be more appropriate. M Kleinhenz agreed about the lower temperature in general but the 300 °C adopted in the project would be correct. The glueline was not considered in design as rigid connections under fire. Image results showed that at 300 °C the glueline would still be intact. S Aicher said that the size of the beam is important here in term of fire performance of the bondline. He also said that ETA of these T Beam products does not allow rigid connection consideration. A Frangi added that the width of the beam was very important here and 300 °C was well established based on falling off observed in tests.

B J Yeh commented that in N. America char layer falling off issues was tightened by adhesive requirements. He asked how to verify assumptions at the moment of char layer falling off. M Kleinhenz said the model assumed that all elements reaching 300°C were omitted and the model agreed well with results. B J Yeh asked what temperature would be assumed at the fresh layer at the moment of falling off. M Kleinhenz said an instantaneous temperature jump was assumed.

G Ravenhorst received confirmation that there was one test per cross section. He asked about result repeatability with only one test. M Kleinhenz said the model agreed well with results except one case and would like to redo this configuration when equipment becomes available.

54 - 16 - 2 Reliability Improvements of the Fire Design for the Revision of Eurocode 5
         - R Fahrni, A Frangi

Presented by A Frangi

F Lam commented about the calculation of z_i for the reliability analysis where the cross sectional geometry of the residual cross section would be used together with the original beam strength distribution to characterize the random resistance. He received confirmation that the parameters needed to establish the residual cross sectional geometry were not considered as stochastic. A Frangi said that it did not matter because this was a code calibration process against a past approach.

P Parma commented that only beam datasets were used for the calibration and asked if the conclusion would change if one considered columns. A Frangi replied that they would not expect any difference with columns as this was a code calibration process. There were discussions that it would be interesting to extend the dataset to other elements and load conditions. Also stability issues could be important.

F Hochreiner and A Frangi discussed the use of zero strength layer as calibration parameter with only one value. G Hochreiner commented that calculation of internal forces was based on original cross section but stress evaluation was based on residual cross section therefore there would be inconsistencies.

ANY OTHER BUSINESS

4th International Conference on Timber Bridges will be held in May 2022. https://www.bfh.ch/en/news/events/ictb-2021/

Cost Action CA20139 Holistic design of taller timber buildings has been launched.

https://www.cost.eu/cost-action/holistic-design-of-taller-timber-buildings/

VENUE AND PROGRAMME FOR NEXT MEETING

S Aicher and S Winter invited the participants to the 2022 INTER meeting in Bad Aibling Germany.

Co-host: TU Munich and MPA University of Stuttgart.

Date: August 21, 2022 Sunday (Welcome/Greetings) to August 25, 2022 Thursday (Closing)

Venue: B&O Parkhotel Bad Aibling.

Possible Venue for future meetings:

2023 Biel, Switzerland

2024 Shanghai, China

2025 Padua, Italy

2026 Turkey

CLOSE

The Chair thanked the group for their support, participation and attendance of this web-based INTER meeting. He thanked the presenters and participants for their contributions. KIT and their team (H Blass, R Görlacher and C Sandhaas) were thanked for hosting the event. He thanked R Görlacher for work for INTER throughout the year. He also thanked Frank Lam for accepting the added challenge for of taking the minutes and notes for the questions and discussions in this format.

3 INTER Papers, Online Meeting 2021

Buckling of slender timber beam-columns under combined loading, including creep

Ishan K Abeysekera, Specialist Technology and Research, Arup, UK

Ian Feltham, Specialist Technology and Research, Arup, UK

Andrew Lawrence, Specialist Technology and Research, Arup, UK

Keywords: Buckling, Non-linear, Timber, Creep, Beam-columns, LTB

1 Introduction

There is increasing interest in timber structures in the world today as architects, engineers and clients consider timber alongside more traditional materials to help realise their buildings. In addition the timber industry is going through a period of step change where larger and increasingly more ambitious buildings are being designed in timber.

Whilst the manufacture of timber elements is now commonplace, analysis of such elements when subjected to combined loading scenarios whilst accounting for creep can be quite complex.

It is important that engineers have a safe rational way of checking timber beam-columns accounting for slenderness effects, imperfections and creep.

2 Column subjected to axial load only

The simplest case of practical significance is that of an initially imperfect column subjected to an axial load. For such a case the peak value of a sine shaped bow imperfection about the weak axis is δ_0. The total peak nonlinear deflection and peak nonlinear moment in such a column are given by:

$$\delta_{\text{tot}} = \delta_0 \left(\frac{1}{1 - \frac{N}{N_z}} \right) \tag{1}$$

$$M_z{}^{\text{NL}} = N \delta_0 \left(\frac{1}{1 - \frac{N}{N_z}} \right) \tag{2}$$

In the above N_z is the Euler critical load and N is the applied axial load.

In the above we see that the linear moment $N\delta_0$ and the initial imperfection are amplified by the term within brackets. Hence, we see that the column section must be checked for both axial load and nonlinear moment. Since the linear moment and therefore also the nonlinear moment depend on the initial imperfection δ_0, the importance of using a conservative and verifiable initial imperfection value is clear.

3 Behaviour of a column subjected to axial load and biaxial bending

3.1 Coupled equations of equilibrium for a column pin and fork supported at both ends

Slender timber elements are often not only subjected to axial load but also biaxial bending. For a very general case there may be bow imperfections about both axes as well as twist imperfection.

For such a beam-column the imperfections will have the following effects:

- Twist imperfection will result in M_y moment having a component about the z axis and M_z moment having a component about the y axis.
- Axial force acting on the initial twisted shape will give rise to torsion.
- Moments acting on the imperfect bowed shape will result in torsion.
- Axial force acting on the bow imperfections will give rise to moments.

If the beam-column is slender then linear torsion and moments mentioned above will be amplified to give nonlinear moments and torsion.

In order to obtain expressions for the nonlinear elastic deflections and twist of the beam-column the equations for the flexural equilibrium and torsional equilibrium for a slender imperfect element under combined axial load and uniform moments about both axes are given and solved below. These equations are an extension of the equations found in Timoshenko and Gere (1961).

Weak z-axis flexural equilibrium:

$$EI_z \frac{d^4y}{dx^4} + N \frac{d^2(y+y_0)}{dx^2} + M_y \frac{d^2(\phi+\phi_0)}{dx^2} = -1.27 \frac{d^2M_z}{dx^2} \tag{3}$$

Strong y-axis flexural equilibrium:

$$EI_y \frac{d^4z}{dx^4} + N \frac{d^2(z+z_0)}{dx^2} - M_z \frac{d^2(\phi+\phi_0)}{dx^2} = -1.27 \frac{d^2M_y}{dx^2} \tag{4}$$

Torsional equilibrium:

$$Ni^2 \frac{d^2(\phi+\phi_0)}{dx^2} - GJ \frac{d^2\phi}{dx^2} + M_y \frac{d^2(y+y_0)}{dx^2} - M_z \frac{d^2(z+z_0)}{dx^2} = 0 \tag{5}$$

In the above equations, i is the torsional radius of gyration, E is the elastic modulus, J is the torsion constant, I_z and I_y are second moments of area about the z and y axes respectively.

The sign convention is as shown in Figure 1 below. Moment about an axis that causes deflection in the positive direction of the axis perpendicular is taken as positive. Twist resulting in rotation of the x,y,z triax to the x*,y*,z* triax is taken as positive (anti-clockwise positive).
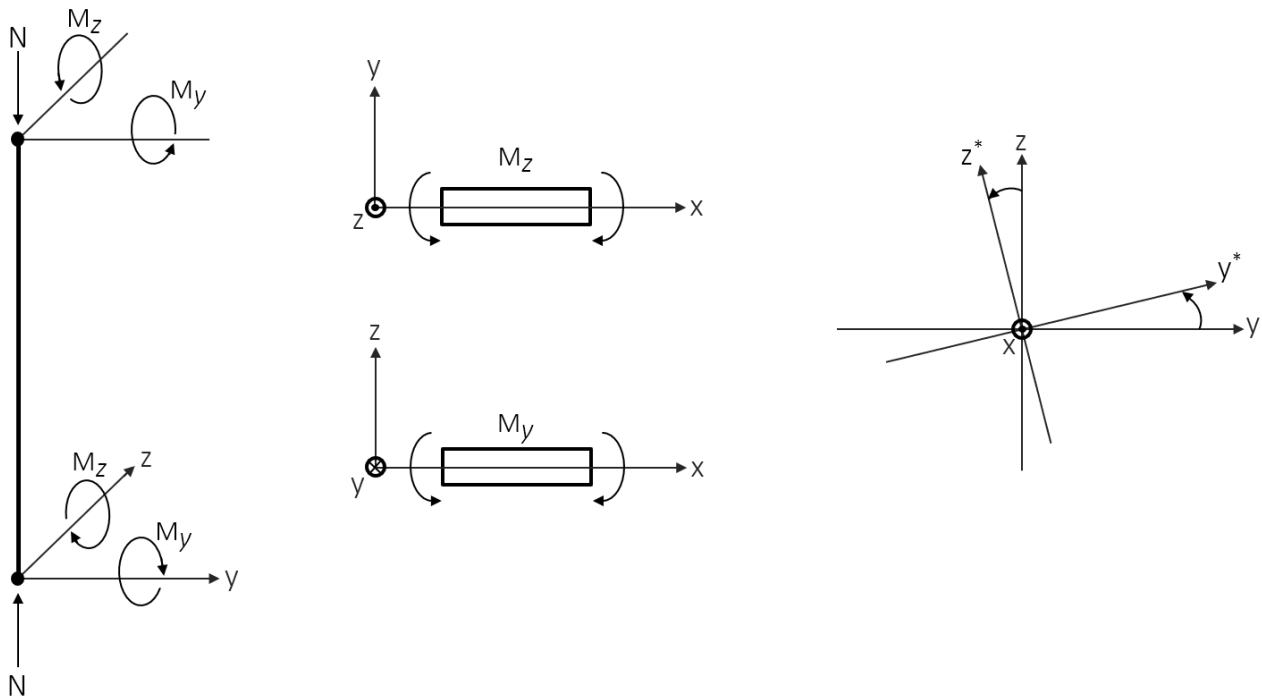
Figure 3.1. Sign convention used to set up the equations of equilibrium.

In setting up and solving the above set of equations, the following is assumed :

- The beam is pin supported at both ends.
- The beam is fork supported against torsion at both ends.
- Warping has been neglected and section symmetry is assumed. Since timber sections are generally solid and symmetric these assumptions are reasonable.
- Imperfections y_0, z_0, and ϕ_0 vary sinusoidally along the length (see Table 1)
- Elastic displacements y,z, and ϕ vary sinusoidally along the length (See Table 1).
- The applied uniform moments M_z and M_y are also assumed to be sinusoidal (terms on the RHS) to aid the solution of the set of equations. Hence the uniform applied moments on the RHS of the equations are multiplied by 1.27, this being the Fourier coefficient of the first term of a Fourier series expansion of a uniform moment (see Table 2 below). At low levels of loading or slenderness this is slightly conservative but as load levels and nonlinear effects increase, the equation above tends to the exact solution.

Table 1. Imperfection and elastic deflected shapes

	Initial imperfection	Elastic deflected shape
Weak axis (about z axis)	$y_0(x)=\delta_0 sin\left(\dfrac{n\pi x}{l}\right)$	$y(x)=\delta^{nl} sin\left(\dfrac{n\pi x}{l}\right)$
Weak axis (about y axis)	$z_0(x)=\mu_0 sin\left(\dfrac{n\pi x}{l}\right)$	$z(x)=\mu^{nl} sin\left(\dfrac{n\pi x}{l}\right)$
Twist (anticlockwise about x axis)	$\phi_0(x)=\theta_0 sin\left(\dfrac{n\pi x}{l}\right)$	$\phi(x)=\theta^{nl} sin\left(\dfrac{n\pi x}{l}\right)$

* Table note : n is the number of half sine waves in the imperfection shape or elastic deformation shape.

Table 2. Approximation of applied constant moment to first term of Fourier series approximation

Applied constant moment	Fourier series approximation
$M_z(x)=M_z$ for all x	$M_z(x)=1.27M_z \sin\left(\frac{n\pi x}{l}\right)$
$M_y(x)=M_y$ for all x	$M_y(x)=1.27M_y \sin\left(\frac{n\pi x}{l}\right)$

* Table note : n=1

Substituting the imperfections and elastic deformations into equations 3,4 and 5, taking n as equal to 1 yields:

$$\begin{bmatrix} N_z-N & 0 & -M_y \\ 0 & N_y-N & M_z \\ -M_y & M_z & i^2(N_T-N) \end{bmatrix} \begin{Bmatrix} \delta^{nl} \\ \mu^{nl} \\ \theta^{nl} \end{Bmatrix} = \begin{Bmatrix} 1.27M_z+N\delta_0+M_y\theta_0 \\ 1.27M_y+N\mu_0-M_z\theta_0 \\ M_y\delta_0-M_z\mu_0+Ni^2\theta_0 \end{Bmatrix} \tag{6}$$

Where:

$$i=\sqrt{\frac{I_z+I_y}{A}} \tag{7}$$

$$N_z=\frac{EI_z\pi^2}{l^2} \tag{8}$$

$$N_y=\frac{EI_y\pi^2}{l^2} \tag{9}$$

$$N_T=\frac{GJ}{i^2} \tag{10}$$

In the above N_z and N_y are the Euler critical loads about the relevant axis and N_T is the torsional critical load.

Noting that the above matrix representation of the equations is of the form $\overline{K}\,\overline{\Delta}=\overline{F}$ it can be seen that (as expected) the stiffness matrix $\overline{K}$ has a material part which includes terms N_z, N_y, N_T, which is diagonal and a geometric part which is made up of terms relating to the applied forces and axial moments N, M_y, M_z which are not diagonal and result in coupling of the equations. It can also be seen that the geometric stiffness is reduced by compression and increased by tension. It can be further observed that for the given sign convention positive strong axis moment reduces the geometric stiffness whilst weak axis moment increases the geometric stiffness.

The beneficial effect of tension and effect of reversal of M_y and M_z can be easily accounted for by multiplying the relevant force or moment by -1.

Solving for nonlinear displacements and twists yields:

$$\delta^{nl}=\frac{[i^2\overline{N_y}\,\overline{N_T}-M_z{}^2]F_1-M_zM_yF_2+M_y\overline{N_y}F_3}{i^2\overline{N_T}\,\overline{N_y}\,\overline{N_z}-M_z{}^2\overline{N_z}-M_y{}^2\overline{N_y}} \tag{11}$$

$$\mu^{nl}=\frac{[i^2\,\overline{N_z}\,\overline{N_T}-M_y{}^2]F_2-M_zM_yF_1-M_z\overline{N_z}F_3}{i^2\overline{N_T}\,\overline{N_y}\,\overline{N_z}-M_z{}^2\overline{N_z}-M_y{}^2\overline{N_y}} \tag{12}$$

$$\theta^{nl}=\frac{M_y\overline{N_y}F_1-M_z\overline{N_z}F_2+\overline{N_y}\,\overline{N_z}F_3}{i^2\overline{N_T}\,\overline{N_y}\,\overline{N_z}-M_z{}^2\overline{N_z}-M_y{}^2\overline{N_y}} \tag{13}$$

Where:

$$\overline{N_y} = N_y - N \tag{14}$$

$$\overline{N_z} = N_z - N \tag{15}$$

$$\overline{N_T} = N_T - N \tag{16}$$

$$F_1 = N\delta_0 + M_y\theta_0 + 1.27M_z \tag{17}$$

$$F_2 = N\mu_0 - M_z\theta_0 + 1.27M_y \tag{18}$$

$$F_3 = M_y\delta_0 - M_z\mu_0 + Ni^2\theta_0 \tag{19}$$

For the given displacement shapes in Table 1, the magnitudes of the nonlinear moments and torsion can be found as follows:

$$M_z^{NL} = EI_z \frac{d^2y}{dx^2} = EI_z \left(\frac{\pi}{l}\right)^2 \delta^{nl} \sin\left(\frac{\pi x}{l}\right) = N_z \delta^{nl} \sin\left(\frac{\pi x}{l}\right) \tag{20}$$

$$M_y^{NL} = EI_y \frac{d^2z}{dx^2} = EI_y \left(\frac{\pi}{l}\right)^2 \mu^{nl} \sin\left(\frac{\pi x}{l}\right) = N_y \mu^{nl} \sin\left(\frac{\pi x}{l}\right) \tag{21}$$

$$T^{NL} = GJ \frac{d\phi}{dx} = \frac{\pi}{l} GJ\theta^{nl} \cos\left(\frac{\pi x}{l}\right) \tag{22}$$

3.2   Section checks

To check the element for nonlinear effects the following section checks need to be carried out.

Where axial load is compressive the following should be checked:

$$\left(\frac{N_{c,0,d}}{A\, f_{c,0,d}}\right)^p + \max\left\{\frac{M_{y,d}^{nl}}{W_y\, f_{m,d}} + k_{red} \frac{M_{z,d}^{nl}}{W_z\, f_{m,d}} ; k_{red} \frac{M_{y,d}^{nl}}{W_y\, f_{m,d}} + \frac{M_{z,d}^{nl}}{W_z\, f_{m,d}}\right\} \leq 1 \tag{23}$$

Where A is the section area and W_y and W_z are the elastic section moduli about the y and z axes respectively. $N_{c,0,d}$ is the design compressive force and $M_{y,d}$ and $M_{z,d}$ are the design moments. $f_{,c,0,d}$ and $f_{m,d}$ are the design parallel to grain compressive and bending strengths. EN1995-1-1 recommends a value for the statistical factor k_{red} of 0.7 for rectangular sections and 1 for all other sections.

The power P may be taken as 2 for softwood rectangular sections where investigations into the combined axial and bending utilisation show a nonlinear interaction between bending and axial utilisation (for all other cases it should be taken as 1). It is a conservative way of accounting for the apparent increase in bending strength due to applied axial load. An explanation for this increase is given by Buchanan 1984. This nonlinear interaction between bending and axial utilisation is explained by the fact that bending failure of characteristic strength timber sections is governed by failure on the tension face and the fact that the applied axial load supresses this tension failure.

Where axial load is tensile the following should be checked:

$$\frac{N_{t,0,d}}{A\, f_{t,0,d}} + \max\left\{\frac{|M_{y,d}^{nl}|}{W_y\, f_{m,d}} + k_{red} \frac{|M_{z,d}^{nl}|}{W_z\, f_{m,d}} ; k_{red} \frac{|M_{y,d}^{nl}|}{W_y\, f_{m,d}} + \frac{|M_{z,d}^{nl}|}{W_z\, f_{m,d}}\right\} \leq 1 \tag{24}$$

In the above equation $f_{t,0,d}$ is the parallel to grain tensile strength.

Section checks for combined torsion and shear checks should also be carried out as per EN1995-1-1. The nonlinear shears can be calculated by differentiating equations 20 and 21. However, for a slender element this check is unlikely to govern.

For most timber elements the applied strong axis moment will be *approximately* equal to the nonlinear moment about the strong axis moment. In these cases the engineer need only calculated the nonlinear moment about the weak axis.

3.3   Critical Stability of a beam-column

The element will be critically stable when the determinant of stiffness matrix $\overline{K}$ is 0. Hence the element will be critically stable when the equation below is satisfied:

$$i^2\left(N_y\text{-}N\right)\left(N_T\text{-}N\right)\left(N_z\text{-}N\right)\text{-}M_z{}^2\left(N_z\text{-}N\right)\text{-}M_y{}^2\left(N_y\text{-}N\right)=0 \tag{25}$$

The above equation (25) can be used to calculate the critical strong axis moment $M_{y,crit}$ accounting for the effects of applied axial load and weak axis moment:

$$M_{y,crit}=\sqrt{i^2\left(N_T\text{-}N\right)\left(N_z\text{-}N\right)-\frac{M_z{}^2\left(N_z\text{-}N\right)}{\left(N_y\text{-}N\right)}} \tag{26}$$

The second term in equation 26 above can often be neglected since N_y is normally many times greater than N_z.

Where no axial load or weak axis moment is present equation 26 simplifies to the well-known expression for critical moment:

$$M_{y,crit}=\sqrt{i^2N_TN_z} \tag{28}$$

3.4   Reduction of the general equations in section 3.1 for simpler loading cases

3.4.1 In-plane buckling

For the case of axial force and moment about the weak (z) axis only, substituting M_z and N into equation 11 and substituting into 20 yields the following equation for the peak nonlinear moment:

$$M_z{}^{NL}= N_z\delta^{nl}=\left(\frac{1}{1-\frac{N}{N_z}}\right)\left(N\delta_0+1.27M_z\right) \tag{29}$$

The above is the well-known expression for in-plane buckling. If M_z is set to zero, this reduces to the standard equation 2 in section 2. For in-plane buckling about the strong (y) axis a similar expression can be obtained after accounting for change in sign of the moment.

Equation 29 can be improved by rewriting it in the following form:

$$M_z{}^{NL}=\left(\frac{1}{1-\frac{N}{N_z}}\right)\left[N\delta_0+\left(1+\frac{N}{N_z}\omega\right)M_z\right] \tag{30}$$

Here the term $\left(1+\frac{N}{N_z}\omega\right)$ is the Fourier coefficient of the first term of the Fourier series of the moment shape. Hence the above expression can be used for a variety of applied moment shapes. The factor ω is sometimes referred to as the Dischinger factor.

3.4.2 Lateral Torsional Buckling

For the case where there is strong axis moment and axial force substituting only N and M_y into equation 11, and then substituting into equation 20 yields the following equation for the peak weak (z) axis moment:

$$M_z^{NL}=N_z\delta^{nl}= N_z\left[\frac{[i^2N(N_T-N)+M_y^2]\delta_0+i^2N_TM_y\theta_0}{i^2(N_T-N)(N_z-N)-M_y^2}\right] \tag{31}$$

3.5   Column fixed and fork supported at one end only (i.e. a cantilever)

From symmetry equations 3, 4 and 5 can easily be solved for a cantilever. The main difference this makes to the elastic deflected shape and imperfections is that the number of half sine waves n is taken as being equal to 0.5.

This results in exactly the same solutions given in equations 11,12 and 13 provided that critical loads N_z and N_y are defined as follows.

$$N_z=\frac{EI_z\pi^2}{(2l)^2} \tag{32}$$

$$N_y=\frac{EI_y\pi^2}{(2l)^2} \tag{33}$$

As expected, the flexural critical loads are the well-known expression for Euler critical load for a beam fixed at one end and free at the other. The torsional critical load remains the same since it is not dependent on the length of the member and only on the section shape/size and the shear modulus.

4 Imperfections

As with any engineering design, it is important that what is assumed in the calculations is practically achievable in the factory and on site. Hence it is important that:

- Conservative estimates of imperfections are made during the design phase.
- From an execution standpoint, that the engineer is able to check that the imperfections on site match what was assumed in design.

Imperfections of timber beam-columns can be subdivided into 2 types:

- Material imperfections which occur on the local section level.
- Geometric (bow/twist) imperfections which are global occurring along a length.

Material imperfections occur due to knots, shrinkage, splits etc. On the level of the section these can result in the loads being applied asymmetric to the effective section. However, on the global level of a whole beam of engineered timber there will be an averaging of section imperfections. Hence the global effect that material

imperfections have will be negligible. The effect that material imperfections have on the section strength are already accounted for by the grading.

Geometric bow, and twist imperfections are what are of primary importance in the design of beam-columns as they give rise to linear moments and twist that are amplified by slenderness effects. Bow in the strong axis is generally negligible for timber elements. Hence it is the weak axis bow and twist imperfections about the axis of the beam that are of significance for timber beam-column. EN1995-1-1 Section 10.2 (1) gives bow limits of 1/300 for solid timber and 1/500 glue laminated timber and LVL. No limits on twist imperfection are given. It is unclear whether the reason for this is the fact that twist imperfections are small and of no consequence or the fact that twist imperfection is more difficult to measure than bow imperfection. This is currently being reviewed by WG3/SG1 of CEN TC 250/SC5.

The comparative calculations in Appendix 1 (Tables 4 and 5) show that for the same column, imperfections assumed by the kc method vary with design case (load duration and fire) and also with the element slenderness. This is clearly inconsistent with reality as imperfection will be a set value.

The results in Appendix 1 show that in some cases the kc method assumes an imperfection larger than 1/500 suggested in Section 10 of EN1995-1-1 and in other cases assumes a value much smaller than 1/500 (which is unconservative).

This is clearly inconsistent with reality as the imperfection will be a set value.

Work by Kuhlmann and Töpler on insitu timber elements show that bow imperfections can range from as large as 1/400 to as small as 1/7000 with 87% of the measured bow imperfections being less than 1/1000. This highlights the variability of imperfections and the fact that imperfections might be larger or smaller than assumed by the calculation methods assumed in the Eurocode 5.

Where imperfections assumed by the kc method are smaller than reality the design will be unconservative and where the imperfections assumed by the kc method are larger than reality the design will overly conservative and uneconomic.

4.1 Creep of an axially loaded imperfect slender column subject to axial load only

Timber is a material that is prone to creep. Therefore, creep can have a significant impact on the final capacity of a column. Taking again the simple case discussed in section 2, we can see that the effect of creep is to increase the final deflection. Bazant & Cedolin (1990) show that for an initially imperfect column under axial load subject to creep the final deflection is:

$$\delta^{nl} = \delta_0 \left(\frac{1}{1 - \frac{N}{N_{Z,inf}}} \right) \tag{34}$$

Where:

$$N_{z,inf} = \frac{EI_z \pi^2}{l^2(1+k_{def})} \tag{35}$$

The above result assumes a standard solid Kelvin type model for creep. Whilst more sophisticated models exist several references including Timber Engineering STEP 1 & work by Ranta-Maunus & Kortesema show creep curves for timber that can reasonably be approximated by the standard Kelvin model. Hence equations 34 and 35 may be used for timber columns.

To consider the effect of creep it is useful to consider the beam-column in figure 2.1. When an axial load N is applied to the imperfect element in Figure 2.1 with initial imperfection δ_0, the element instantly takes the shape δ_{inst}^{nl}. Over time as the timber creeps, the element takes the shape δ_{inf}^{nl}. If after all the creep has taken place the load N is removed, the element will rebound to the creep amplified imperfection shape δ_{0+c} and not δ_0. If the axial load is then reapplied the element will once again instantly take the shape δ_{inf}^{nl}. If we think of an imperfection as being the unstressed shape that causes no stress in the section, it is clear that the effect of creep has been to increase the magnitude of the imperfection from δ_0 to δ_{0+c}.
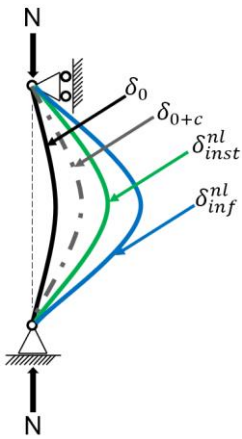
Figure 2.1. Imperfect slender column prone to creep

In general, all load cases can occur after creep has taken place. For example, on a timber structure the peak wind load may occur after 20 years when creep has already taken place. Hence all load cases should be checked using instantaneous values of Young's modulus E and the creep amplified imperfection. It should however be noted that by definition for long term loading this is the same as carrying out a check with the long-term Young's modulus and initial imperfection.

4.2 Calculation of creep amplified imperfections

4.2.1 Creep amplified imperfection for in-plane buckling

From the preceding discussion is clear that the following expression should hold:

$$(N\delta_0 + M_z)\left(\frac{1}{1-\frac{N}{N_{z,inf}}}\right) = (N\delta_{0+c} + M_z)\left(\frac{1}{1-\frac{N}{N_z}}\right) \tag{36}$$

Rearranging yields the following expression for the creep amplified imperfection:

$$\delta_{0+C}=\left(\frac{1-N/N_z}{1-N/N_{z,inf}}\right)\delta_0+\frac{M}{N}\left(\frac{1-N/N_z}{1-N/N_{z,inf}}-1\right) \tag{37}$$

In calculating the creep amplified imperfection, the SLS quasi-permanent load combination should be used. Where the axial force is tensile the minimum of δ_{0+c} and δ_0 should be used.

4.2.2 Creep amplified imperfections for the general case including LTB

For the general case involving combined loading presented in section 3, instead of a single imperfection there is a set of initial imperfection fields $\delta_0(x)$, $\mu_0(x)$, $\theta_0(x)$. From these it is necessary to calculate a set of creep amplified imperfection fields $\delta_{0+c}(x)$, $\mu_{0+c}(x)$, $\theta_{0+c}(x)$. Solving this rigorously using the same methods used by Bazant and Cedolin (1990) becomes mathematically unwieldy and would be difficult to solve without the use of a computer. As an alternative the following conservative method for calculating a creep amplified set of imperfections is proposed.

Maximum weak axis creep amplified imperfection:

$$\delta_{0+c}=\max\left\{\left(\delta_0+\delta_{inf}^{nl}-\delta_{inst}^{nl}\right);\delta_0\right\} \tag{38}$$

Maximum strong axis creep amplified imperfection:

$$\mu_{0+c}=\max\left\{\left(\mu_0+\mu_{inf}^{nl}-\mu_{inst}^{nl}\right);\mu_0\right\} \tag{39}$$

Maximum twist creep amplified imperfection:

$$\theta_{0+c}=\max\left\{\left(\theta_0+\theta_{inf}^{nl}-\theta_{inst}^{nl}\right);\theta_0\right\} \tag{40}$$

In the above all nonlinear deflections with the subscript 'inst' are calculated with instantaneous Young's and shear moduli and all nonlinear deflections with the subscript 'inf' are calculated with the long-term Young's and shear moduli.

As in the previous case when calculating creep amplified imperfections the quasi-permanent SLS combination of loads should be used.

5 Serviceability

Since equations 11,12 and 13 give nonlinear displacements they can easily be used to check serviceability limit states as well as ultimate limit states. Serviceability limit states should generally checked for the quasi-permanent load case accounting for creep. The following equations should be used to calculate final deformations:

$$\delta_{tot}=\delta_0+\delta_{inf}^{nl} \tag{41}$$

$$\mu_{tot}=\mu_0+\mu_{inf}^{nl} \tag{42}$$

$$\theta_{tot}=\theta_0+\theta_{inf}^{nl} \tag{43}$$

6 Existing provisions for buckling under combined loading in EN 1995-1-1

EN1995-1-1 currently gives one procedure for the verification of columns subjected to compression and bending (Clause 6.3.2(3)):

$$\frac{\sigma_{c,0,d}}{k_{c,y}f_{c,0,d}} + \frac{\sigma_{m,y,d}}{f_{m,y,d}} + k_m \frac{\sigma_{m,z,d}}{f_{m,z,d}} \leq 1 \tag{44}$$

$$\frac{\sigma_{c,0,d}}{k_{c,z}f_{c,0,d}} + k_m \frac{\sigma_{m,y,d}}{f_{m,y,d}} + \frac{\sigma_{m,z,d}}{f_{m,z,d}} \leq 1 \tag{45}$$

and another for beams subjected to bending about the strong axis and compression (Clause 6.3.3(5)) :

$$\left(\frac{\sigma_{m,d}}{k_{crit}f_{m,d}}\right)^2 + \frac{\sigma_{c,0,d}}{k_{c,z}f_{c,0,d}} \leq 1$$

Since a column subjected to compression and bending and a beam subjected to bending and compression are mechanically the same, the two equations given in EN1995 should be the same, but they are not. Overall the existing equations have the following shortcomings:

- As noted, the current code provides one set of equations for columns with bending and axial load, and another set of equations for beams with compression. However, they give different answers.
- The effect of creep is not included.
- Imperfections are key to calculating nonlinear deformations and moments. Despite Section 10 EN 1995-1-1 specifically giving limits on bow imperfections of 1/300 for solid timber sections and 1/500 for glulam, the values assumed in the buckling equations in the current code are different and often smaller (See Tables 4 and 5 in Appendix 1).
- In addition there is no visibility for the user about what imperfections are actually being assumed in the equations and therefore it is impossible for the user to check whether what has been built matches the assumptions in the calculations.
- The common case of combined strong axis bending and tension in elements subject LTB is not covered.
- Both equations are mechanically incorrect and can be overly conservative in some cases and unconservative in others. (See comparison of utilisation ratios given by kc method and nonlinear calculations given in Tables 6 and 7 of Appendix 1). This could lead unsafe design in some cases and uneconomic design in other cases.
- There is no method to check SLS cases to see if the combined imperfections and amplified deflections are acceptable from a point of view of appearance etc.

7 Conclusions

This paper provides engineers with a practical and rational method to check timber beam-columns based on mechanics. The methods given in this paper have the following advantages:

- The methods are simple to use – the input forces and moments for the equations are simply the 1st order moments and forces that would normally be extracted from a linear static hand or FE analysis.
- They lends themselves to hand calculation and therefore easy to spreadsheet.
- They are short (only 3-4 pages, see Appendix 2).
- The mechanics of the problem is not hidden from the user; the equations will therefore aid understanding and reduce mistakes.
- They are mechanically correct and therefore give a robust basis for dealing with combined loading of slender elements.
- In combined loading cases the beneficial effects of tension can be included.
- The second order methods presented allow for direct input of imperfections.
- The assumptions made in the design phase can be matched to what is achievable on site.
- The effect of creep is included.
- Since the method is based on mechanics, serviceability checks can easily be carried out.

Appendix 1 – Example numerical comparison of the Nonlinear and kc methods for GL 24 beams with an initial bow subject to axial load only

The 2 methods compared in this appendix are:

- The nonlinear calculation methods presented in this paper.
- The kc method currently in EN 1995-1-1

Unless stated otherwise the section and material property are as follows:

Table 3. Section and material properties used in example calculations

Breadth (mm)	Depth (mm)	E (N/mm^2)	$f_{m,k}$ (N/mm^2)	$f_{c,k}$ (N/mm^2)
250	700	9600	24	24

For time dependent load cases, the design strength is calculated as follows with $\gamma_m =$1.25 and k_{mod} specified in Table 3.1 for service class 1.

For the fire case design strength is calculated from the following equation with $\gamma_m =$1, $k_{mod} = 1$, and $k_{fi} = 1.15$ as per EN 1995 − 2

Calculations are carried out for 2 different lengths and relative slendernesses λ_{rel}. It is assumed that the elements are pin connected top and bottom.

A1.1 Calculation of imperfections assumed in the kc method

The initial imperfection is in-built into the kc method and varies from case to case. A comparison can be made with the non-linear equations to work out what imperfection the kc method is assuming in different cases:

1. Calculate the axial force required to get a utilisation of 1 using the kc method
2. For the axial force calculated in step 1 by trial and error find the assumed initial imperfection required to give a utilisation of 1 using the nonlinear equations.

Imperfections are calculated using the method above for all time dependent cases and fire cases.

Table 4. Example Column 1 : λ_{rel} = 0.69 , Length = 3000 mm

Design case	Design Axial load (kN)	Imperfection divided by length (e/L)	Calculated imperfection divided by value of imperfection Section 10 of EN1995 (e/L=0.002)
Fire (E =9600)	4333	0.00088	0.44
Fire (E =k_{fi}9600)	4389	0.0008	0.4
Instantaneous	3316	0.0087	0.55
Short term	2713	0.0097	0.61
Medium term	2412	0.01	0.64
Long term	1809	0.011	0.71

Table 5. Example Column 2 : λ_{rel} = 1.03 , Length = 4500 mm

Design case	Design Axial load (kN)	Imperfection divided by length (e/L)	Calculated imperfection divided by value in Section 10 of EN1995 (e/L=0.002)
Fire (E =9600)	3432	0.00049	0.25
Fire (E =k_fi9600)	3693	0.00061	0.31
Instantaneous	2626	0.0044	0.83
Short term	2148	0.0063	1.17
Medium term	1910	0.0072	1.34
Long term	1432	0.0090	1.68

A1.2 Calculation of imperfections assumed in the kc method

Here a comparison is made between columns with a utilisation of unity in the kc method, against the same columns checked using the nonlinear method assuming an imperfection 1/500 times length as stated in EN 1995.

Table 6. Example Column 1 : λ_{rel} = 0.69 , Length = 3000 mm

Design case	Design Axial load (kN)	Utilisation kc	Utilisation Nonlinear
Fire (E =9600)	4333	1	1.16
Fire (E =k_fi9600)	4389	1	1.15
Instantaneous	3316	1	1.10
Short term	2713	1	1.08
Medium term	2412	1	1.07
Long term	1809	1	1.05

Table 7. Example Column 2 : λ_{rel} = 1.03 , Length = 4500 mm

Design case	Design Axial load (kN)	Utilisation kc	Utilisation Nonlinear
Fire (E =9600)	3432	1	2.39
Fire (E =k_fi9600)	3693	1	1.84
Instantaneous	2626	1	1.10
Short term	2148	1	0.93
Medium term	1910	1	0.88
Long term	1432	1	0.82

It should be noted that if the effect of creep were considered in the above comparison the nonlinear utilisation ratios would increase. Hence creep would result in even more unconservative results where the kc method is unconservative. Where kc method overly conservative the level of over conservatism will reduce (or even lead to the kc method becoming unconservative in these cases as well).

Appendix 2 – Potential codification of the checks in this paper

The methods and checks in this paper can be readily codified. A proposed version of the codification is shown below. Definition of terms has been left out since terms have already been defined previously. Here δ is replaced with e_y and μ is replaced with e_z. Axial force N is replaced with $N_{c/t,0,d}$.

In-plane buckling

(1) For a member subject to in plane bending and axial force [Formula A.1] should be satisfied:

$$\left(\frac{N_{c,0,d}}{A\,f_{c,0,d}}\right)^{p} + \frac{M_{y/z,d}^{nl}}{W_{y/z}\,f_{m,d}} \le 1 \tag{A.1}$$

(2) The nonlinear deflection should be calculated according to [Formula A.2]:

$$e_{y/z,d}^{nl} = \left[\frac{1}{(N_{y/z}-N_{c,0,d})}\left[N_{c,0,d}e_{0,y/z} + \left(1 + \frac{N_{c,0,d}}{N_{y/z}}\,\omega\right)M_{y/z,d}\right]\right] \tag{A.2}$$

where

(3) The first term of the fourier series approximation of the applied moment shape $1 + \frac{N_{Ed}}{N_{y/z}}\delta$ may be calculated estimating Dischinger factors δ from [Table A.1].

Table A.1 — Dischinger Factors

Constant moment	0,273
Moment due to a point load applied at mid span	-0,189
Moment due to a uniformly distributed load	0,032

(3) The nonlinear moment should be calculated from [Formula A.3]:

$$M_{y/z,d}^{nl} = N_{y/z}e_{y/z,d}^{nl} \tag{A.3}$$

Buckling of members under major axis bending and axial force (compression or tension), subject to lateral torsional buckling

(1) Where the axial load is compressive, cross section should be verified as per [Formula A.4]. When the axial load is tensile the cross section should be verified as per [Formula A.5].

$$\left(\frac{N_{c,0,d}}{A\,f_{c,0,d}}\right)^{p} + \max\left\{\frac{M_{y,d}^{nl}}{W_{y}\,f_{m,d}} + k_{red}\frac{M_{z,d}^{nl}}{W_{z}\,f_{m,d}}; k_{red}\frac{M_{y,d}^{nl}}{W_{y}\,f_{m,d}} + \frac{M_{z,d}^{nl}}{W_{z}\,f_{m,d}}\right\} \le 1 \tag{A.4}$$

$$\frac{N_{t,0,d}}{A\,f_{t,0,d}} + \max\left\{\frac{\left|M_{y,d}^{nl}\right|}{W_{y}\,f_{m,d}} + k_{red}\frac{\left|M_{z,d}^{nl}\right|}{W_{z}\,f_{m,d}}; k_{red}\frac{\left|M_{y,d}^{nl}\right|}{W_{y}\,f_{m,d}} + \frac{\left|M_{z,d}^{nl}\right|}{W_{z}\,f_{m,d}}\right\} \le 1 \tag{A.5}$$

Where

NOTE – It is assumed that the element is stocky about the y-axis and that the initial bow imperfection about the strong y-axis is neglible.

(2) The torsional critical load should be calculated from [Formula A.6]:

$$N_{T} = \frac{GJ}{i^{2}} \tag{A.6}$$

Where the polar radius of gyration is given by the Formula [A.7] below:

$$i = \sqrt{\frac{I_{y}+I_{z}}{A}} \tag{A.7}$$

(4) The nonlinear deflection in the y-direction should be calculated according to [Formula N.8].

$$e_{y,d}^{nl} = \left[\frac{[i^2 N_{c/t,0,d}(N_T - N_{c/t,0,d}) + M_{y,d}^2]e_{0,y} + i^2 N_T M_{y,d}\theta_0}{i^2(N_T - N_{c/t,0,d})(N_z - N_{c/t,0,d}) - M_{y,d}^2}\right]$$ (A.8)

(4) The nonlinear moment about the z-axis due to initial twist, bow imperfection axial force and strong axis moment about y-axis should be calculated according to [Formula A.9]:

$$M_{z,d}^{nl} = N_z e_{y,d}^{nl}$$ (A.9)

(4) The nonlinear twist deformation may be calculated according to [Formula A.10]:

$$\theta^{nl} = \frac{M_{y,d}(N_{c/t,0,d}e_{0,y} + M_{y,d}\theta_0) + (N_z - N_{c/t,0,d})(M_{y,d}e_{0,y} + i^2 N_{c/t,0,d}\theta_0)}{i^2(N_T - N_{c/t,0,d})(N_z - N_{c/t,0,d}) - M_{y,d}^2}$$ (A.10)

Buckling of members which are slender about both axes, under biaxial bending and axial force (compression or tension), subject to combined lateral torsional buckling and strong axis buckling

(1) Where the axial load is compressive cross-section should be verified as per [Formula A.11]. When the axial load is tensile the cross-section should be verified as per [Formula A.12].

$$\left(\frac{N_{c,0,d}}{A f_{c,0,d}}\right)^p + \max\left\{\frac{M_{y,d}^{nl}}{W_y f_{m,d}} + k_{red}\frac{M_{z,d}^{nl}}{W_z f_{m,d}}; k_{red}\frac{M_{y,d}^{nl}}{W_y f_{m,d}} + \frac{M_{z,d}^{nl}}{W_z f_{m,d}}\right\} \leq 1$$ (A.11)

$$\frac{N_{t,0,d}}{A f_{t,0,d}} + \max\left\{\frac{|M_{y,d}^{nl}|}{W_y f_{m,d}} + k_{red}\frac{|M_{z,d}^{nl}|}{W_z f_{m,d}}; k_{red}\frac{|M_{y,d}^{nl}|}{W_y f_{m,d}} + \frac{|M_{z,d}^{nl}|}{W_z f_{m,d}}\right\} \leq 1$$ (A.12)

(2) The nonlinear y-direction, z-direction and twist deformations should be calculated as per [Formulae A.13, A.14 and A.15] respectively below.

$$e_{y,d}^{nl} = \frac{[i^2\overline{N_y}\,\overline{N_T} - M_{z,d}^2]F_1 - M_{z,d}M_{y,d}F_2 + M_{y,d}\overline{N_y}F_3}{i^2\overline{N_T}\,\overline{N_y}\,\overline{N_z} - M_z^2\overline{N_z} - M_y^2\overline{N_y}}$$ (A.13)

$$e_{z,d}^{nl} = \frac{[i^2\overline{N_z}\,\overline{N_T} - M_{y,d}^2]F_2 - M_{z,d}M_{y,d}F_1 - M_{z,d}\overline{N_z}F_3}{i^2\overline{N_T}\,\overline{N_y}\,\overline{N_z} - M_z^2\overline{N_z} - M_y^2\overline{N_y}}$$ (A.14)

$$\theta^{nl} = \frac{M_{y,d}\overline{N_y}F_1 - M_{z,d}\overline{N_z}F_2 + \overline{N_y}\,\overline{N_z}F_3}{i^2\overline{N_T}\,\overline{N_y}\,\overline{N_z} - M_z^2\overline{N_z} - M_y^2\overline{N_y}}$$ (A.15)

with

$$\overline{N_y} = N_y - N_{c/t,0,d}$$ (A.16)

$$\overline{N_z} = N_z - N_{c/t,0,d}$$ (A.17)

$$\overline{N_T} = N_T - N_{c/t,0,d}$$ (A.18)

$$F_1 = N_{c/t,0,d}e_{0,y} + M_{y,d}\theta_0 + 1.27 M_{z,d}$$ (A.19)

$$F_2 = N_{c/t,0,d}e_{0,z} - M_{z,d}\theta_0 + 1.27 M_{y,d}$$ (A.20)

$$F_3 = M_{y,d}e_{0,y} - M_{z,d}e_{0,z} + i^2 N_{c/t,0,d}\theta_0$$ (A.21)

(3) The nonlinear moments about the x and y-axis should be calculated from [Formulae A.22 and A.23], respectively

$$M_{z,d}^{nl} = N_z e_{y,d}^{nl} \tag{A.22}$$

$$M_{y,d}^{nl} = N_y e_{z,d}^{nl} \tag{A.23}$$

NOTE – The nonlinear torsion induced in the beam-column can be calculated from the nonlinear twist deformation using standard theory.

Creep-buckling

(1) The effect of creep should be verified by carrying out verifications in [A.3, A.4 and A.5] considering a creep amplified set of imperfections for all load combinations.

(2) When inplane buckling is being considered, [Formula A.24] should be used to estimate the creep amplified bow imperfection

$$e_{0+C,y/z} = min\left\{\Omega_c e_{0,y/z} + \frac{M_{y/z,Quasi,SLS}}{N_{c,0,Quasi,SLS}}(\Omega_c - 1); e_{0,y/z}\right\} \tag{A.24}$$

with

$$\Omega_c = \frac{1 - N_{c,0,Quasi,SLS}/N_{y/z}}{1 - N_{c,0,Quasi,SLS}(1+k_{def})/N_{y/z}} \tag{A.25}$$

(3) When out of plane (torsional) buckling is being considered the formulae [A.26],[A.27] and [A.28] below should be used to calculate the creep amplified set of imperfections.

$$e_{0+C,y} = max\left\{(e_{0,y} + e_{y,inf,Quasi,SLS}^{nl} - e_{y,inst,Quasi,SLS}^{nl}) ; e_{0,y}\right\} \tag{A.26}$$

$$e_{0+C,z} = max\left\{(e_{0,z} + e_{z,inf,Quasi,SLS}^{nl} - e_{z,inst,Quasi,SLS}^{nl}) ; e_{0,z}\right\} \tag{A.27}$$

$$\theta_{0+c} = max\left\{\left(\theta_0 + \theta_{inf,Quasi,SLS}^{nl} - \theta_{inst,Quasi,SLS}^{nl}\right) ; \theta_0\right\} \tag{A.28}$$

References

Timoshenko, S & Gere, J (1961): Theory of Elastic Stability. McGraw-Hill Book Company

Buchanan, A, H (1984): Strength Model and Design Methods for Bending and Axial Load Interaction in Timber Members. Thesis submitted in partial fulfilment of the requirements for the degree of doctor of philosophy. University of British Columbia.

Kuhlmann, U and Töpler, J (2021): Imperfection of Slender Glulam Beams. INTER 54-12-03. Online Meeting

Bazant, Z and Cedolin, L (2010): Stability of Structures – Elastic, Inelastic, Fracture and Damage Theories. World Scientific Publishing Co Pte Ltd.

Edited by Blass, H, J. Aune,P. Choo, B,S. Gorlacher, R. Griffiths, D, R. Hilson, B, O. Racher, P and Steck, G. (1994): Timber Engineering STEP 1. EUROFORTECH

Ranta-Maunus, A & Kortesmaa, M (2000): Creep of timber during eight years in natural environments. WCTE2000 Conference, Whistler, CA.

Eurocode 5 (2004): Design of timber structures - Part 1-1: General and rules for buildings. CEN. (EN 1995-1-1).

52

DISCUSSION

The papers was presented by I K Abeysekera

H Blass asked about the possibility to check imperfections as there can be both material and geometric imperfections in a column. I K Abeysekera said that as long as good grading practice is available material imperfection would average out. H Blass commented that one would not know the ratio of the influence between the two types of imperfections and engineers on site will not be able to check the material imperfections as they are random. H Blass further commented that this approach seems to be deterministic and this would be important especially for creep where low stress ratios would be typically encountered and their findings indicated that creep would not be a problem for slender columns. I K Abeysekera agreed that the approach is deterministic.

G Hochreiner stated that there is no validation in this paper which requires experimental data on creep curve. I K Abeysekera said that the results were based on a logarithmic shaped creep curve as referenced in the STEP book. G Hochreiner stated that this is not considered in Eurocode 5 and it is also referenced to strength and not displacement. P Dietsch suggested further discussion on this topic in a breakout room.

S Aicher said this approach is only valid for monotonically applied loads. Varying vertical loads would result in deformation rebound and creep recovery is a complicated process and not considered in total. IK Abeysekera said the current approach is conservative. The consideration of varying load and creep recovery would be too complicated for code considerations. S Aicher commented that economic impact analysis on the approach is needed. P Dietsch suggested adding such information as a short appendix for the paper.

P Dietsch commented that stress utilization needs to reach a certain level before creep becomes important. This fact is implicitly covered in the German National Annex. I K Abeysekera agreed that this could be considered in the approach.

M Fragiacomo commented that the limit of load level for creep for high strength engineered wood products might be an issue. He received clarification that the quasi permanent load combination should be used.

A Frangi said most of the loads on the column are non-permanent and he was not sure whether a direct addition of the effects of the permanent and non-permanent loads would be appropriate. In addition he is not sure about the need to solve differential equations. IK Akeysekera said solutions to the differential equations are provided. U Kuhlmann commented that one of the outcome of their work on lateral torsional buckling is that creep does not affect stability. A simple approach with a reduction factor to modify stiffness may be more practical and should be attempted. I K Abeysekera agreed.

A new probabilistic approach to model the tensile properties of split spruce boards and its application in engineered timber products

Raimund Sieder [1], Reinhard Brandner
Institute of Timber Engineering and Wood Technology, Graz University of Technology, Graz, Austria; [1] corresponding author; raimund.sieder@tugraz.at

1   Introduction

Timber is a naturally grown material featuring large uncertainties in its properties. These uncertainties can be identified on the scales of species, growth regions, individual trees as well as between and within timber members. By using timber as base material for structural products additional scales need to be considered, e.g. the production as well as the producers (Fink et al. 2018). To assign timber to a specific set of properties it needs to be graded. Thereby, only some properties are directly and some indirectly controlled by the grading process, whereas the most of them are assigned based on probabilistic models (Köhler 2007). Eigenfrequency or ultrasonic runtime together with density measurements are well predictors for the elastic modulus of elasticity parallel to the grain, characterising timber on average basis, and meanwhile basis of most grading machines. The modulus of elasticity itself is well correlated with the strength properties parallel to the grain, in particular tension and bending strength, which are additionally determined by local, morphological characteristics in timber, in particular knots, which are found to occur in some regularity (e.g. Ehlbeck et al. 1985, Isakson 1999). With focus on the scale of timber, in particular of boards, the uncertainty in corresponding properties can be separated in uncertainties (i) between (variation of average properties) and (ii) within boards (variation of local properties). This can be well represented by a so-called two-level hierarchical model, which has been already successfully used in previous investigations (e.g. Källsner et al. 1994, Ditlevsen et al. 1998, Köhler 2007, Fink 2014, Frese 2016, Brandner 2018).

Strength and elastic properties of structural timber products, such as glued laminated timber (glulam; GLT) and cross laminated timber (CLT), are preferable regulated by so-called "load bearing models" on the basis of the tensile properties parallel to the grain of the base material boards and finger joints. These load bearing models are developed on the basis of experimental investigations but also probabilistic numerical simulations (e.g. Ehlbeck et al. 1985, Colling 1990, Fink 2014, Frese 2016). In linear, unidirectionally layered timber products such as glulam, these models aim on characterising their serial, sub-parallel structure, represented by lamellas further separated in board segments and finger joints, two dimensional, i.e. variation of local characteristics like knots in width and thickness are not considered. The basis of these models is that the boards as base material is strength graded and that their cross-section, to which the strength grading refers, is fully retained in the product manufactured from it. In certain applications, e.g. rim boards or generally for rather small, slender beams, it is considered advantageous to split the structural timber products, like resawn glulam. As a result of this process, however, the strength grading carried out on the base material in full cross section loses its validity after the boards are split and/or the cross section got significantly reduced, which is because of altered natural growth characteristics in the residual cross sections. This also has a corresponding influence on the input parameters necessary for the load-bearing models and/or the relationships contained therein. EN 14081-1 (2019), for example, limits the allowable reduction of cross sections after grading without losing the assigned strength grade by ≤ 5 mm and ≤ 10 mm, respectively, below and above widths of 100 mm. Figure 1 shows the effect of splitting as influence on the distribution and magnitude of macroscopic flaws along the board, represented here by knots, exemplarily for a board split in width into three equally wide pieces. The red marked areas describe the weak zones (WZ) within the board, usually repre-
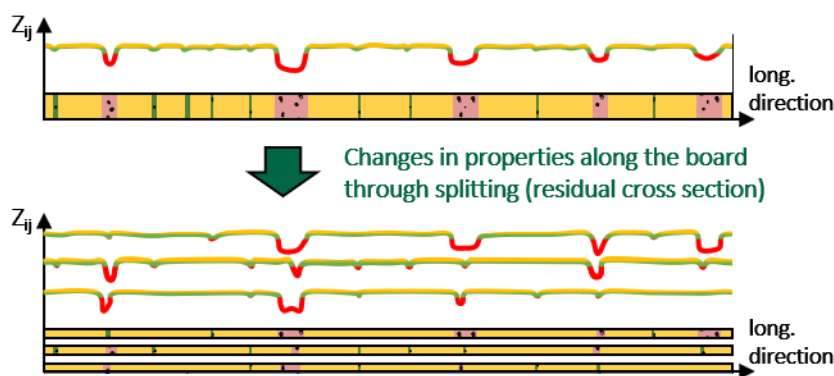
Figure 1. Changes in properties along a single graded board (top) when split lengthwise in three pieces (bottom)

sented by large knots or knot clusters, and the green zones are usually represented by smaller intermediate knot zones (IZ), mirroring also the natural growth structure of branches in trees, whereas the yellow zones in-between represent timber free of knots. Consequently, the more heterogeneous the base material the higher the expected impact of splitting on the properties of the residual pieces and vice versa, i.e. the effect of splitting on the properties of the base material is expected to be higher for lower timber strength classes and negligible for the highest strength classes represented by a widely homogeneous material.

The current European product standard for glulam (EN 14080 2013) provides regulations for resawn glulam beams. Following them, one possible approach is to consider the splitting process during the grading of the boards by setting higher requirements on knot indicators or by grading virtually split boards. Alternatively, the characteristic bending strength of resawn glulam, $f_{m,s,k}$, can be calculated as function of the characteristic bending strength of glulam in full cross section, $f_{m,g,k}$, the tensile strength of the boards, $f_{t,0,l,k}$, and the number of cuts; see Eq. (1). This equation is applicable for 18 MPa $\leq f_{t,0,l,k} \leq$ 30 MPa and under compliance with certain geometric boundary conditions; it also contains an adaptation for the mean modulus of elasticity parallel to the grain of resawn glulam, $E_{0,s,mean}$, based on $E_{0,g,mean}$, the mean modulus of elasticity parallel to the grain of glulam in full cross section.

$$f_{m,s,k} = f_{m,g,k} - \frac{96}{f_{t,0,l,k} - 6} + \begin{cases} 4 & \text{for 1 cut} \\ 0 & \text{for 2 cuts} \end{cases} \qquad E_{0,s,mean} = E_{0,g,mean} - 500 \qquad (1)$$

In order to estimate the load bearing capacity of split glulam, built up of boards of lower strength classes, e.g. T14 according to EN 338 (2016), probabilistic numerical models for boards and thereof build up glulam are developed which consider the impact of splitting of boards lengthwise on their mechanical properties after they had been graded in full cross section as well as on the resawn glulam beams. Apart from the work based on bending properties of boards of Viguier et al. (2014) in which a probabilistic model for the characterisation of resawn glulam beams is presented, there are no further numerical nor probabilistic investigations known to the authors, in particular no probabilistic models based on the tensile properties of boards, which allow characterising resawn glulam. Furthermore, the probabilistic board model, as basis for the probabilistic numerical glulam model presented hereafter, represents timber differently to previous models: (i) by classifying board sections explicitly in weak zones (WZ), i.e. knot clusters, intermediate knot zones (IZ) and knot free zones (CW), (ii) by treating lengths of and distances between these zones random and not by a fixed increment, and (iii) by incorporating also effects of width and splitting of boards in the modelling of geometric and knot parameters and their statistical moments.

2 Probabilistic Board Model

2.1 Board database

For the validation of assumed distribution models, estimation of parameters and main statistics for physical and geometric variables of the probabilistic board model, two board databases were analysed, namely from the project "INTELLIWOOD" (Schickhofer and Augustin 2001) and the project "separate" (Kastner et al. 2011). The databases contain knot data (position and dimension), other technological parameters, like annual ring width or radial distance to pith, and physical properties {$E_{DYN,F}$; ρ_{12}; $E_{t,0,l}$; $f_{t,0,l}$} from more than 1,000 timber boards from Norway spruce (*Picea abies*), of provenience Central Europe (see Table 1).

Table 1. Test data – overview of main- & sub-series, nominal grading classes, quantity and dimensions (from Schickhofer and Augustin 2001 & Kastner et al. 2011)

DB		main- & sub-series	assigned class	quantity [-] all	cen[1]	width w_b [mm]	thickness t_b [mm]	length l_b [mm]
Schickhofer and Augustin (2001)	I-CH	_1:semi:m	na[2]	62	52	150	45	4,450
		_1:semi:s		62	45			
		_1:semi:ss		61	46		29	
	II-AT	_1:vis	S10	45	39	150	35	3,200 ÷ 4,000
		_2:vis	S13	45	33			
		_3:mach	MS13	45	40			
		_4:mach	MS17	41	33			
		_5:mach	MS13	16	14	230		
		_6:mach	MS17	14	8			
	III-AT	_1:vis	S10	45	38	110		
		_2:vis	S13	45	34			
		_3:mach	MS10	45	44			
		_4:mach	MS13	45	39			
		_5:mach	MS17	44	40			
Kastner et al (2011)	seperate	I	rej.	5	0	170	45	4,000
		II	L25	383	33			
		III	L36	151	14			
		Σ =		1,154	552			

[1] datasets with all data present (ρ, $E_{t,0,l}$, $f_{t,0,l}$), number of weak zones $\#_{WZ} > 1$

[2] no strength class assigned

Based on the dynamic modulus of elasticity, as indicating grading property, the boards were divided into two groups, GI and GII, which can be allocated to the strength classes T14 and T24 according to EN 338 (2016). The probabilistic board model is based on the knot data from all boards allocated to both groups. The mechanical properties ($f_{t,0,l}$ & $E_{t,0,loc,12}$) are available only for subset of these boards, which are listed in Table 2.

Table 2. Mechanical properties of groups GI & GII

groups	GI (T14)		GII (T24)	
	$f_{t,0,l}$	$E_{t,0,loc,12}$	$f_{t,0,l}$	$E_{t,0,loc,12}$
#	320		160	
mean	28.4	11,394	39.7	13,540
COV [%]	31 %	16 %	25 %	16 %
5% quantile (emp)	15.5	8,954	24.2	9,194

2.2 Model specifications

The probabilistic board model aims on a generic representation of the distribution and magnitude of global and local growth characteristics in structural timber. Hereby, the focus is on softwood species, in particular, because of its dominance and availability of data, on boards of Norway spruce (*Picea abies*) as base material for structural timber products like glulam and CLT. As mentioned earlier, such products are usually

characterised by means of the tensile properties parallel to grain of its base material boards and finger joints. As the tensile properties are highly influenced by knots and knot clusters, the probabilistic model aims to realistically represent these local growth characteristics and treats them as surrogates for others. In analogy to the typical hierarchical structure of branches in trees, boards in longitudinal direction are further separated in weak zones (WZ), intermediate knot zones (IZ) and knot free zones (CW). The geometric parameters are shown in Figure 2.
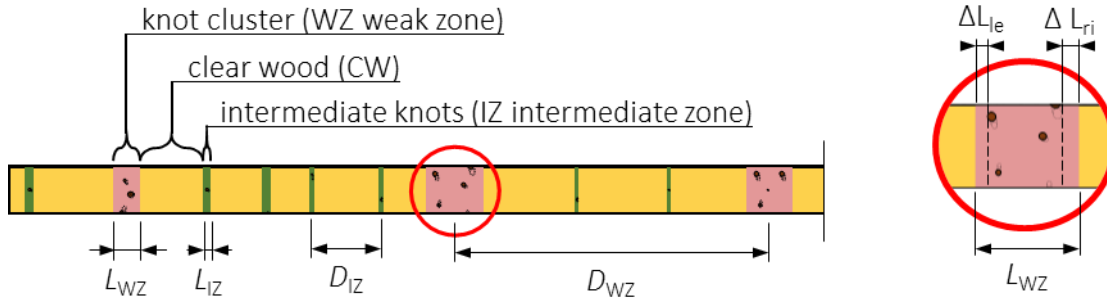

Figure 2.   Definition of geometric parametes (left); detail of knot zone length (right)

In most probabilistic approaches the length of WZ (L_{WZ}) is kept constant with $L_{WZ} = 150$ mm and only the distance in-between weak zones (D_{WZ}) varies discretely. Knots or knot clusters under a certain $tKAR$ (tension/total Knot Area Ratio) threshold are usually neglected and no differentiation is made in WZ and IZ (e.g. Ehlbeck 1985, Fink 2014, Frese 2016). In contrast to these previous studies but similar to the investigations from Brandner (2018), the lengths of the weak and intermediate knot zones (L_{WZ} and L_{IZ}) as well as the distances in-between (D_{WZ} and D_{IZ}) are modelled as continuous variables and the occurrence of weak and intermediate zones is represented by two interlaced alternating renewal (AR) processes. Hereby, the length of knot zones (see Figure 2, right) is defined by the outer distance of knots or knot cluster plus an additional length taking the fibre deviation into account. Olsson et al. (2019) stated that local fibre distortions in the vicinity of knots decay after a distance in longitudinal direction of approximately 1.5 times the adjacent knot diameter. Based on this investigation and the assumption of a gradual decrease of the fibre distortions, the additional length was fixed with 1.0 times the diameter of the knot at the margin of the knot zone. As the length of knot zones is kept random, for the distinction between WZ and IZ no fixed value is possible; instead, the product $L_{WZ} \cdot tKAR_{WZ}$, as measure for the "knot intensity", was introduced and products of $L_{WZ} \cdot tKAR_{WZ} \geq 2.0$ were regarded as weak zones. Figure 3 shows the principle of the employed two-level hierarchical model as well as the definition of the corresponding equi-correlation. This hierarchical model, which describes local properties Z_{ij} of a specific board segment i in board j as sum from the average property Y_j of board j and the local deviation from this average property X_{ij}, can be directly inferred from the hierarchical material structure of timber as natural material. It allows to separate the total variation σ_Z^2 in (i) the variation between the individual boards, σ_Y^2, and (ii) the variation within a single board, σ_X^2; see Ditlevsen et al. (1998).
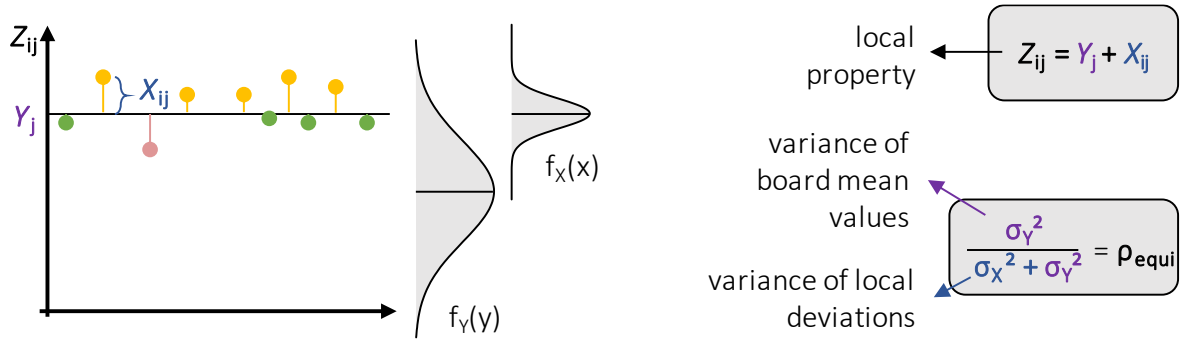
Figure 3. Two-level hierachical model (left); as well as the definition of its components (right)

This approach, wherever applicable, was further applied to characterise the physical properties and geometrical parameters. In total there are six random variables $X = \{L_{WZ}; L_{IZ}; D_{WZ}; D_{IZ}; tKAR_{WZ}; tKAR_{IZ}\}$ necessary to describe the position, extend and magnitude of knot zones. Each variable is characterised by a representative distribution model, selected based on physical constraints and correspondence to data, its distribution parameters and correlation to other variables. The lengths of knot zones, L_{WZ} and L_{IZ}, are described by a lognormal distribution. Similar to Fink (2013), the distances between knot zones, D_{WZ} and D_{IZ}, are assumed to be gamma distributed. For the measures for the magnitudes of knot zones, $tKAR_{WZ}$ and $tKAR_{IZ}$, which are by default restricted to the interval [0, 1], a beta distribution is chosen.

Because of mixed distribution models, the correlation structure between the geometric parameters is modelled by means of a Gaussian copula. For the six geometric parameters there are in total 15 pairwise combinations necessary to fully describe all correlations between these parameters. The calculation of this common correlation matrix may, however, lead to a non-positive semidefinite matrix which would be invalid for a correlation matrix and thus needs to be adjusted to a positive semidefinite matrix following the methodology e.g. in Rebonato and Jäckel (2011).

The statistics and parameters for all these variables were determined from the datasets as described earlier in Section 2.1. In order to describe the dependency of these six geometric parameters from resawing, the change in geometric parameters from splitting all boards virtually in width direction into {2; 3; 5; 8} equally wide pieces is analysed.

Figure 4. Expected (average) functional relationships of L_{WZ} (left) and $tKAR_{WZ}$ (right)

Figure 4 shows exemplarily the expected (average) functional relationships for the variables L_{WZ} and $tKAR_{WZ}$. To describe the variables of residual cross sections, the separation ratio η_s, as ratio between the residual and the original board width, is introduced.
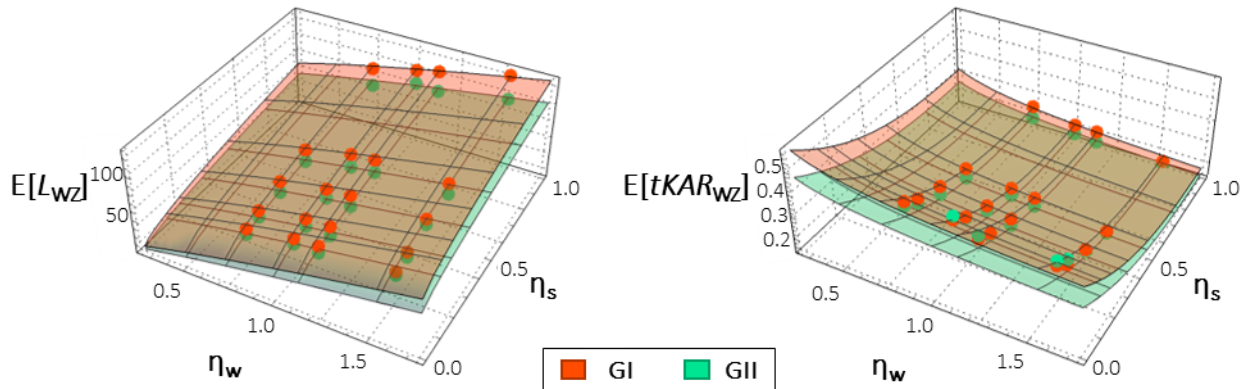
The regression models to describe all variables in dependency of board width ratio, $\eta_w = w_b / 150$, and the separation ratio, η_s, are given in Eq. (2). The individual parameters to describe the expected values, E[X], the coefficients of variation, COV[X], and the equi-correlation coefficients, $\rho_{equi}[X]$, are listed in Table 3. The parameters to model the correlation between the variables, $\rho[X_i, X_{i+1}]$, are summarised in Table 4.

$$Y[X] = \left[\beta_{00} + \beta_{10} \cdot (\tilde{\eta}_w)^{\beta_{11}} + \beta_{20} \cdot (\tilde{\eta}_s)^{\beta_{21}} + \varepsilon \right] \cdot Ref_{GI/GII} \qquad (2)$$

with
β_i .... regression coefficients [–]
$\tilde{\eta}_w$ .... board width ratio factor [–]; $\tilde{\eta}_w = \{\eta_w; 1-\eta_w\}$, with $\eta_w = w_b/150$; see Table 3 & Table 4
$\tilde{\eta}_s$ .... separation ratio factor [–]; $\tilde{\eta}_s = \{\eta_s; 1-\eta_s\}$, with $\eta_s = w_{residual}/w_b$; see Table 3 & Table 4
w_b .... board width [mm]
$w_{residual}$ ..... residual board width [mm]
ε .... error term; $\varepsilon \sim ND(0; \sigma_\varepsilon)$ [–]
$Ref_{GI/GII}$ ..... reference value [mm / % / –]

Table 3. *Parameters for the description of the expected values, coefficients of variation and equi-correlation coefficients for all six geometric variables and reference values for GI and GII*

		β_{00}	β_{10}	β_{11}	β_{20}	β_{21}	σ_ε	$\tilde{\eta}_w$	$\tilde{\eta}_s$	Ref_{GI}	Ref_{GII}
L_{WZ}	E[X]	–	0.40	0.60	0.60	0.60	0.036		η_s	100	80
	COV[X]	1.00	–	–	–	–	0.053			50 %	40 %
	$\rho_{equi}[X]$	1.00	-	-	–	–	0.053			0.10	0.16
$tKAR_{WZ}$	E[X]	-	1.00	-0.35	1.60	2.90	0.165		$1-\eta_s$	0.21	0.16
	COV[X]	1.00	–	–	–	–	0.075			50 %	40 %
	$\rho_{equi}[X]$	1.00	–	–	–	–	0.075			0.14	0.17
D_{WZ}	E[X]	0.95	–	–	0.60	2.10	0.115			500	600
	COV[X]	1.00	–	–	0.40	1.70	0.048			50 %	50 %
	$\rho_{equi}[X]$	1.00	–	–	0.40	1.70	0.048	η_w		0.20	0.10
L_{IZ}	E[X]	1.00	–	–	0.15	1.00	0.106			25	
	COV[X]	0.95	–	–	0.35	1.00	0.114		$1-\eta_s$	45 %	
	$\rho_{equi}[X]$	0.95	–	–	0.35	1.00	0.114			0.09	
$tKAR_{IZ}$	E[X]	1.00	–	–	1.30	1.90	0.156			0.04	
	COV[X]	1.00	–	–	0.50	1.00	0.069			65 %	
	$\rho_{equi}[X]$	1.00	–	–	0.50	1.00	0.069			0.10	
D_{IZ}	E[X]	1.05	–	–	2.35	2.05	0.507			100	135
	COV[X]	1.00	–	–	–	–	0.046		$1-\eta_s$	95 %	95 %
	$\rho_{equi}[X]$	1.00	–	–	–	–	0.046			0.17	0.17

Table 4. *Parameters for correlation functions and reference values for GI and GII*

	β_{00}	β_{10}	β_{11}	β_{20}	β_{21}	σ_ε	$\tilde{\eta}_w$	$\tilde{\eta}_s$	Ref_{GI}	Ref_{GII}
$L_{WZ} - tKAR_{WZ}$	1.00	–	–	0.50	2.00	0.128			0.65	
$L_{WZ} - D_{WZ}$	0.90	–	–	–	–	1.329	$1-\eta_w$	$1-\eta_s$	0.04	
$L_{WZ} - L_{IZ}$	1.00	2.80	1.00	–	–	2.445			0.05	
$L_{WZ} - tKAR_{IZ}$	0.25	–	–	–	–	4.064			-0.03	

	β_{00}	β_{10}	β_{11}	β_{20}	β_{21}	σ_ε	$\tilde{\eta}_w$	$\tilde{\eta}_s$	Ref_{GI}	Ref_{GII}
$L_{WZ} - D_{IZ}$	1.00	–	–	-1.00	4.00	0.485				-0.20
$tKAR_{WZ} - D_{WZ}$	0.85	2.80	1.00	–	–	3.536				0.03
$tKAR_{WZ} - L_{IZ}$	1.00	–	–	–	–	2.646				0.04
$tKAR_{WZ} - tKAR_{IZ}$	1.00	–	–	–	–	11.97				0.01
$tKAR_{WZ} - D_{IZ}$	1.00	–	–	-1.25	1.00	0.170				-0.20
$D_{WZ} - L_{IZ}$	1.00	–	–	–	–	2.080	$1-\eta_w$	$1-\eta_s$		0.04
$D_{WZ} - tKAR_{IZ}$	1.00	–	–	–	–	1.991				0.06
$D_{WZ} - D_{IZ}$	1.00	–	–	–	–	0.239				0.40
$L_{IZ} - tKAR_{IZ}$	1.00	–	–	-1.10	1.00	0.197				0.45
$L_{IZ} - D_{IZ}$	1.00	–	–	–	–	0.382				0.25
$tKAR_{IZ} - D_{IZ}$	1.00	–	–	-0.80	1.00	0.307				0.30

2.3 Board generation process

Figure 5 shows the board generation process by means of the probabilistic board model presented in previous Section 2.2.
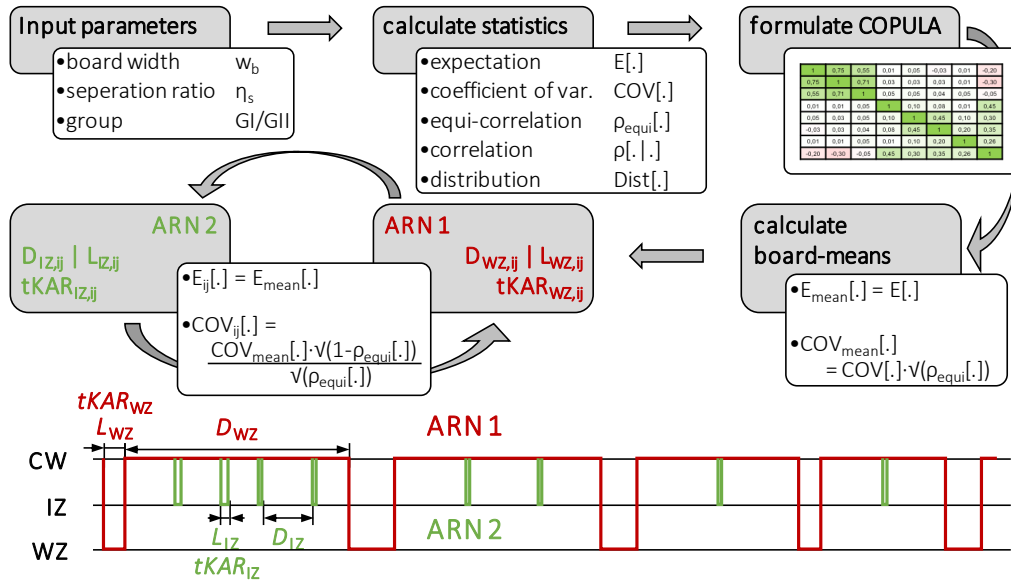
Figure 5. Board generation process (top); two interlaced alternating renewal processes (bottom)

At first and based on the input parameters, the board width, the separation ratio and the strength class as well as the main statistics and parameters of the marginal distributions are calculated. In the next step, the six-dimensional copula is formulated and a random vector Y_j with the correlated mean values for the six geometric parameters for a specific board is generated. Following this, local deviations X_{ij} from the board mean values are calculated for L_{WZ}, $tKAR_{WZ}$ and D_{WZ} for the first alternating renewal process (ARN 1). The positioning and characterisation of the intermediate knot zones within the distance to the next WZ follows in subprocess ARN 2. ARN 1 and ARN 2 are repeated until a board of predefined overlength is fully characterised. To ensure sufficient randomness already at the beginning of the virtually generated boards, as the board generation process always starts with a weak zone, much longer boards than required are created, the first four meters are discarded and a board of predefined length is randomly cut out from the remaining overlength.

2.4 Board mechanical properties

For the allocation of mechanical properties to individual board sections, i.e. the local tensile parallel to grain properties, the regression models from Fink (2013), as given in Eq. (3), apply. The model parameters are summarised in Table 5.

Table 5. Parameters of regression models in Eq. (3) for Y = {$f_{t,0,ij}$; $E_{t,0,ij}$} in [MPa]; from Fink (2013)

	β_0	β_1	β_2	σ_ε
$f_{t,0,ij}$	2.96	$8.50 \cdot 10^{-5}$	-2.22	0.20
$E_{t,0,ij}$	8.41	$7.69 \cdot 10^{-5}$	$-9.02 \cdot 10^{-5}$	0.10

$$\ln(Y) = \beta_0 + \beta_1 \cdot E_{dyn,F} + \beta_2 \cdot tKAR + \varepsilon \quad (3)$$

Similar to Fink (2013), between the error terms of the strength and the modulus of elasticity a correlation of $\rho = 0.8$ was assumed. In-line with the findings in Colling (1990) and the two-level hierarchical model, the error term was separated into two parts. The separation for the error terms of the strength and the modulus of elasticity was done by means of equi-correlation coefficients which were set to account for the different homogeneities in knot and knot-free zones with $\rho_{equi,WZ} = 0.45$, $\rho_{equi,IZ} = 0.70$ and $\rho_{equi,CW} = 0.90$.

The main statistics for the dynamic modulus of elasticity based on eigenfrequency, $E_{dyn,F}$, as indicating property for strength in the grading process and for the average board potential in the virtual board generation process, see Eq. (4), are shown in Table 6. The comparison of $E_{dyn,F}$ from boards before and after lengthwise splitting based on data from Kastner et al (2011) and additional tests (see Section 2.5.2) shows that the mean value approximately remains the same, i.e. independent from the splitting process, whereas the variation increases with decreasing separation ratio; see Eq. (4).

Table 6. Parameters for the dynamic modulus of elasticity in [MPa]

	GI	GII
$E_{dyn,F,mean}$	11,500	14,000
COV[$E_{dyn,F,ref}$]	13.0 %	13.0 %

$$COV[E_{dyn,F}] = COV[E_{dyn,F,ref}] \cdot \eta_s^{-1/4} \quad (4)$$

2.5 Validation of the probabilistic board model

2.5.1 Boards with full cross section

The validation of the probabilistic board model is done by comparing main statistics as well as various influences of geometric parameters, i.e. width and length effects, as calculated from simulated data with data from the literature. Therefore, for each width w_b = {100; 150; 200; 250} mm 10^4 timber boards were virtually generated. The main statistics of the tensile strength determined from these boards, considering a test length acc. to EN 408 (2012) of nine-times the width, are summarised in Table 7. In both groups the mean values are almost constant, i.e. independent of w_b. However, because of decreasing variation with increasing width, slightly increasing characteristic tensile strengths are observed.

In both groups the average module of elasticity in tension parallel to grain is 500 MPa lower than expected for the assignable strength classes T14 and T24 acc. to

EN 338 (2016). A similar outcome is reported in Fink (2013) whose models were applied also here for allocation of mechanical properties to board segments. Table 8 summarises the main statistics of the tensile strength parallel to grain of 150 mm wide boards at different lengths for both groups GI and GII. As expected, decreasing tensile strengths with increasing length are observed.

Table 7. Tensile strength $f_{t,0,l}$ in [MPa] of 10^4 sim. boards for each width, with length $l_{free} = 9 \cdot w_b$

group	GI (T14)				GII (T24)			
board width [mm]	100	150	200	250	100	150	200	250
min	4.24	5.59	5.27	4.53	10.2	11.9	12.9	13.4
max	76.6	72.9	77.8	76.2	131.5	107.3	125.0	114.0
mean	27.6	27.5	27.7	27.5	40.6	40.2	40.4	40.1
COV [%]	34.2	31.8	30.2	29.8	30.2	27.6	27.0	26.5
$X_{05,LN}$	14.5	15.2	15.8	15.8	23.7	24.7	25.2	25.2

Table 8. Tensile strength $f_{t,0,l}$ in [MPa] of 10^4 simulated boards for each length, with width 150 mm

group	GI (T14)				GII (T24)			
board length [mm]	900	1,350	2,000	4,000	900	1,350	2,000	4,000
mean	29.9	27.5	25.5	22.8	42.8	40.2	38.5	35.1
COV [%]	31.8	31.8	31.3	31.1	28.6	27.6	27.8	27.2
$X_{05,LN}$	16.5 (1.087)[1]	15.2 (1.0)[1]	14.0 (0.941)[1]	12.4 (0.845)[1]	25.8 (1.046)[1]	24.3 (1.0)[1]	23.5 (0.957)[1]	21.5 (0.880)[1]

[1] ratio to strength at reference length $9 \cdot w_b = 1,350$ mm

By means of power regression models, usually applied in timber engineering for the description of length and more generally size effects in timber (e.g. EN 14080 2013; EN 1995-1-1 2014), based on the characteristic tensile strength values for group GI a power coefficient of $k_{l,05} = 0.16$ and for group GII of $k_{l,05} = 0.11$ is found. Fink (2014) found a comparable dependency on length with $k_{l,05} = 0.15$ for L25 and $k_{l,05} = 0.10$ for L40. Brandner (2014) calculated power coefficients in dependency on the variation of the tensile strength of the boards. He reported $k_{l,05} = 0.13$ and $k_{l,05} = 0.21$, respectively, for a $COV[f_{t,0,b}] = 25 \pm 5$ % and $COV[f_{t,0,b}] = 35 \pm 5$ %. To conclude, with respect to the variation in herein simulated boards, the length effects are within a plausible range as found from the literature.

2.5.2 Boards in split condition

For validation of the probabilistic board model also in respect to its prediction quality for lengthwise split boards after they had been graded in full cross section, again a comparison between simulated and test data from literature and from additionally conducted test series is made. For the simulated data different board widths w_b = {100; 150; 200; 250} mm and lengths l_b = {2,000; 4,000} mm were generated, each with 10^4 realisations, which were afterwards virtually split lengthwise considering the separation ratios η_s = {1; 1/2; 1/3}. Figure 6 shows the results as main statistics of the tensile strength relative to that of simulated boards with full cross section, i.e. η_s = 1. With respect to the properties of the full cross section, the mean value is decreasing and the

variation in tensile strength is increasing with decreasing residual width, i.e. η_s. This effect is more distinctive within the lower strength class GI. Viguier et al. (2014) investigated the influence of splitting boards lengthwise on the bending strength. Comparing the char. bending strength at full cross section with that at η_s = {1/2; 1/3}, for strength class C24 acc. to EN 338 (2016) reductions to 78 % and 57 % and for strength class C40 to 83 % and 75 % were found. Within the current investigations for the tensile strength similar reductions are observed.
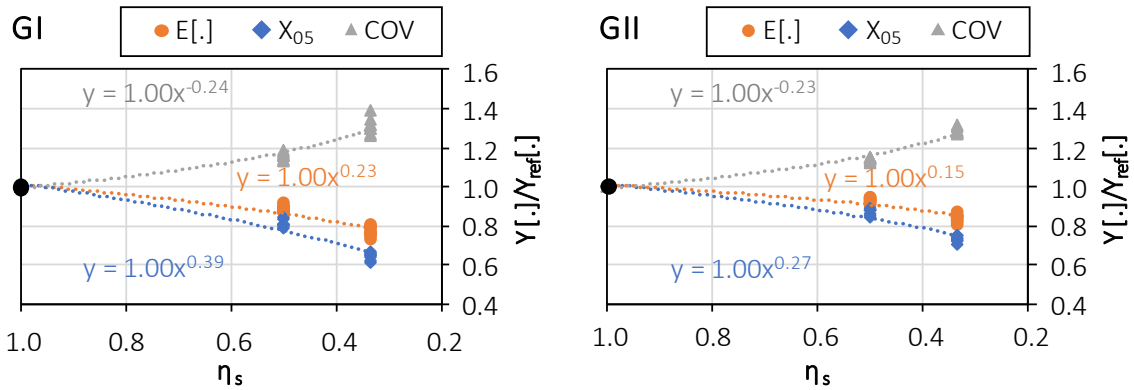

Figure 6. Influence of lengthwise splitting on main statistics Y = {$E[X]$; X_{05}; $COV[X]$} of the tensile strength parallel to the grain ($X = f_{t,0,l}$) relative to full cross section properties of virtually generated boards for GI (left) and GII (right)

Results from tensile tests conducted on unsplit and split boards from Kastner et al. (2011) (strength class T14.5 acc. to EN 338 2016) are shown in Table 9 and a comparison with the model prediction is shown in Figure 7. Overall, the same tendencies in test and simulated data are observed, i.e. with decreasing separation ratio a decrease in the mean and 5 % quantile values as well as an increase in variation.

Table 9. Results of tensile tests parallel to grain on boards for different seperation ratios from Kastner et al. (2011)

η_s	1[2]	1/2[3]
#	49	196
min	12.3	7.4
max	40.4	42.7
mean	23.8 (1.0)[1]	22.1 (0.93)[1]
COV [%]	25.5 (1.0)[1]	28.4 (1.11)[1]
$X_{05,emp}$	15.4 (1.0)[1]	13.1 (0.84)[1]

Figure 7. Model predictions (dashed lines) vs. main statistics Y = {$E[X]$; X_{05}; $COV[X]$} of test results ($X = f_{t,0,l}$) from Kastner et al. (2011) with 95 % CI

[1] relative to board properties at full width

[2] $E_{t,0,loc,12,mean}$ = 11,200 MPa (COV = 8.8 %) | $\rho_{12,mean}$ = 433 kg/m³ (COV =7.5 %)

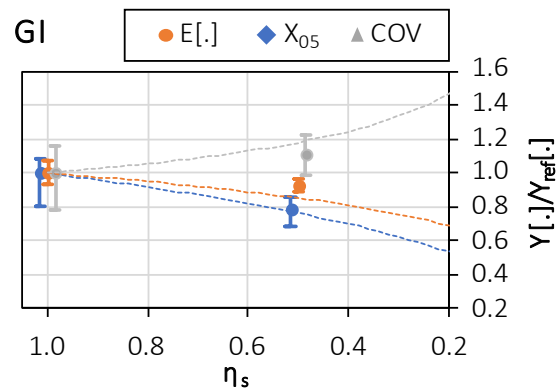[3] $E_{t,0,loc,12,mean}$ = 10,900 MPa (COV = 9.1 %) | $\rho_{12,mean}$ = 431 kg/m³ (COV = 8.1 %)

To further validate the model, an additional test series on boards of Norway spruce of dimensions 165 x 30 x 4,000 mm³ of nominal strength class T14+ acc. to EN 338 (2016)

was carried out. In total 108 boards were delivered. Half of them were tested in tension parallel to grain in full width, half of them were split lengthwise to η_s = {1/3; 2/3} and also tested in tension; free span for both series 3,180 mm. In addition to the tensile properties, the density, the dynamic modulus of elasticity (eigenfrequency) as well as the positions and dimensions of knots were recorded for both split and unsplit boards, for the first group also at unsplit condition.

The test results are shown in Table 10 and compared to the model predictions in Figure 8. The model outcomes show comparable tendencies as the test results. Overall, the mean values of the tensile strength are decreasing, the variation is increasing and therefore, the 5 % quantiles are decreasing with decreasing separation ratios. An increase in the variation of the modulus of elasticity was also observed within the simulated boards. The reduction of the mean modulus of elasticity as found from current tests was neither detected in Kastner et al. (2011) nor from the simulated boards.

Table 10. Results of tensile tests parallel to grain conducted on boards at different seperation ratios

η_s	1[2]	2/3[3]	1/3[4]
#	54	54	54
min	14.8	6.1	4.0
max	71.6	73.8	69.0
mean	41.5 (1.0)[1]	37.4 (0.90)[1]	34.2 (0.83)[1]
COV [%]	40.6 (1.0)[1]	46.5 (1.15)[1]	52.8 (1.30)[1]
$X_{05,emp}$	18.7 (1.0)[1]	12.4 (0.68)[1]	9.1 (0.39)[1]

Figure 8. Model predictions (dashed lines) vs. main statistics Y = {$E[X]$; X_{05}; $COV[X]$} of test results ($X = f_{t,0,l}$) relativ to full-board properties with 95 % CI

[1] relative to full-board properties
[2] $E_{t,0,loc,12,mean}$ = 14,000 MPa (COV = 18.6 %) | $\rho_{12,mean}$ = 458 kg/m³ (COV = 8.7 %)
[3] $E_{t,0,loc,12,mean}$ = 13,100 MPa (COV = 16.8 %) | $\rho_{12,mean}$ = 451 kg/m³ (COV = 8.2 %)
[4] $E_{t,0,loc,12,mean}$ = 12,600 MPa (COV = 21.8 %) | $\rho_{12,mean}$ = 453 kg/m³ (COV = 11.9 %)

Some comments on current tests: although T14+ acc. to EN 338 (2016) was ordered, the material appears to be composed of two groups of strength classes with a significant number of boards belonging to much higher strength grades, which is visible in the statistics, in particular in the unexpected high variation. Since the model for split boards was developed for material featuring a common variation COV[$f_{t,0,l}$] $\cong$ 30 %, discrepancies between data from simulations and tests have to be expected. Although the possibilities for validating the probabilistic model for split boards is limited due to the small number of experimental investigations and the uncertainties accompanying them, an additional, second-level validation is possible by test data from resawn glulam beams; see Section 4.
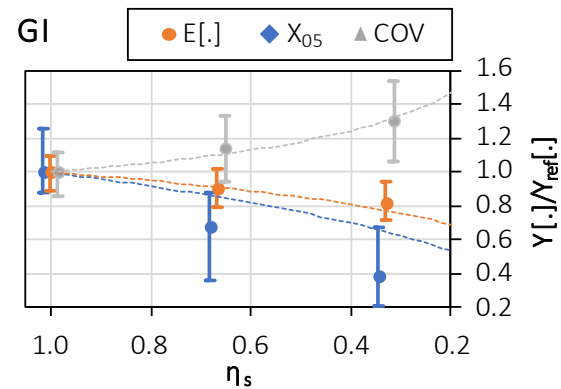
2.6 Probabilistic characterisation of finger joints

Glulam beams are commonly composed of lamellas which themselves consist of boards and board segments which are lengthwise jointed via finger joints. The properties of finger joints, their overall mechanical potential, depend on the properties of the two boards that are joined by them. In addition, also the execution conditions, the machinery and many other production parameters play a major role too but these are assumed to be controlled sufficiently and not considered further. Following the regulations in e.g. EN 14080 (2013), finger joints have to be placed in zones free of knots, which has to be considered also in modelling. Regarding the assignment of mechanical properties, the approach in Fink (2014) is to use a specific *tKAR*-value in combination with the strength model for the WZ. Based on tests $tKAR_{FJ} = 0.20$ was proposed. Following that, the tensile strength of finger joints is defined as the minimum of weak zones in both boards calculated with $tKAR_{FJ} = 0.20$. The modulus of elasticity is approximated as the average value of the module of elasticity from clear wood zones of both boards; see Eq. (5).

$$f_{t,FJ} = \text{Min}\left[f_{t,FJ,i}; f_{t,FJ,i+1}\right] \qquad E_{t,FJ} = \frac{1}{2} \cdot \left[E_{t,CW,i}; E_{t,CW,i+1}\right] \qquad (5)$$

In particular in respect to split boards, edge effects at finger joints are not considered, i.e. flat finger joint profiles (flanges running parallel to the board's side face) are assumed. The length of the finger joints was assumed with 20 mm.

3 Probabilistic Numerical Glulam Beam Model

3.1 Principles of the probabilistic numerical model

In order to examine the load bearing behaviour of virtually generated glulam beams by means of four-point-bending tests in accordance with EN 408 (2012) a stochastic finite-element model was developed within the FE software package Ansys®. All necessary geometric parameters and material properties are provided by individual input-files. Figure 9 shows exemplarily one glulam beam ($h_g = 280$ mm) consisting of seven layers, its elements and distribution of local material properties.
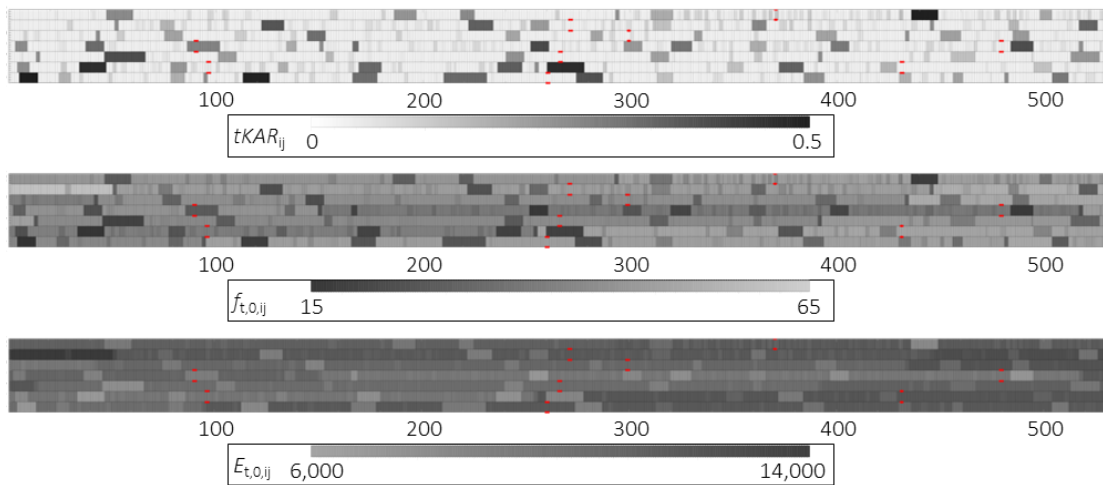

Figure 9.   Representation of glulam beams in FE-analysis, exemplarily demonstrated for one glulam beam of depth of 280 mm (finger joints marked in red)

In order to represent timber boards and also shorter knot zones more realistically, the element size in beam length direction (x-axis), i.e. the increment in longitudinal direction, was set to l_e = 10 mm. In direction of the beam depth (z-axis) one element per layer was used. In respect to the standard lamella thickness commonly used in Europe, the increment in depth direction was set to h_e = 40 mm.

3.2 Beam generation and simulation process

The glulam generation and FE-simulation process is schematically shown in Figure 10.
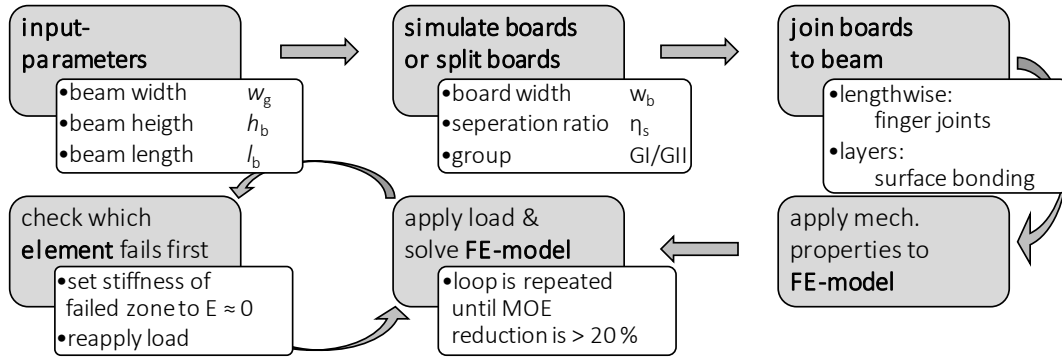

Figure 10. Glulam beam generation and simulation process

At first, the input parameters of the glulam beam, such as depth, width and length, are defined and therefore required boards generated. In the next step, the boards are joined lengthwise via finger joints. Hereby, the finger joints are placed in knot free zones (CW) as close to the board ends as possible, thus mirroring current industrial glulam production lines. Thereby generated lamellas are then built up in layers to glulam beams of predefined dimensions and the total set of mechanical properties passed to the FE-program Ansys®. The glue line in surface bonding is not modelled separately; a rigid composite action between the lamellas is assumed. Similar to Fink (2013) the differences regarding the loading direction (tension/compression) with respect to stiffness is not considered. In Ansys®, a load of fixed magnitude, F_{test}, is applied and the resulting stresses are calculated. Based on the mean tensile stress in each element, their degree of utilisation in tension is calculated. Then, the stiffness of the zone (WZ, IZ, CW or FJ) within the beam containing the FE-element with the highest utilisation ratio in tension is set to zero. This process is repeated until the global MOE is reduced by more than 20 %. For each load step, the maximal load $F_{max,i}$ for the glulam beam is calculated based on the utilisation ratios in tension parallel to grain of each element.

$$F_{max,i} = F_{test}/\eta_{f_{t,0,max,i}} \qquad F_{ult} = \text{Max}[F_{max,i}] \qquad M_{ult} = (F_{ult}/2)\cdot 6\cdot h_g \qquad f_{m,g} = M_{ult}/W_y \qquad (6)$$

The bending strength $f_{m,g}$ of the glulam beam is derived from the ultimate load F_{ult} of all load cycles assuming linear-elastic material behaviour; see Eq. (6).

3.3 Validation of the probabilistic numerical beam model

For validation of the probabilistic numerical beam model for each dimension 10^3 glulam beams with a width of w_g = 150 mm and different depths h_g = {280; 600; 900} were simulated. The length of the used boards was fixed with l_b = 4.0 m. Therefore, the characteristic tensile strengths of the simulated boards with a reference length of $l_{B,ef}$ = 2 m

(see EN 1194 1999) are $f_{t,0,l,k}$ = 14.0 MPa for GI and $f_{t,0,l,k}$ = 23.5 MPa for GII. The results of the simulated glulam beams in bending are summarized in Table 11 and Table 12. The mean bending strength and the variation is decreasing with increasing beam depth. The reduction in the characteristic bending strength corresponds with the size effect k_h in EN 14080 (2013) as well as with the depth effect as proposed in Frese (2008). The characteristic bending strength of 21.2 MPa for the GLT beams built up with boards from GI is below the value for GL24 acc. to EN 14080 (2013), also the MOE is slightly underestimated. Similar results regarding strength and MOE are reported in Fink (2014). One reason might be a lower $COV[f_{t,0,l}] \approx 31\ \%$ (and 30 % in Fink 2014) than frequently found in other studies. For the effect of homogenisation of material properties not only the characteristic strength but also the variation is of utmost importance (see Brandner & Schickhofer 2008 and Brandner & Schickhofer 2010). Blaß et al. (2008), for example, simulated glulam beams of GL24 based on boards with $COV[f_{t,0,l}] \approx 40\ \%$ and reached the stipulated bending strength. The characteristic bending strength of $f_{m,g,k,ref}$ = 29.9 MPa for glulam beams simulated with boards of the higher strength class GII (T24) are well in-line with the load bearing model given in EN 14080 (2013) which implicitly considers less variation in the tensile properties of boards with increasing strength class. Overall, the results of the probabilistic beam model are within a plausible range as found in the literature.

Table 11. Results for the bending strength ($f_{m,g}$) of 10^3 simulated glulam beams of width w_g = 150 mm; base material GI (T14) & GII (T24)

h_g [mm]	$f_{m,g}$ [MPa] | *GI (T14)*			$f_{m,g}$ [MPa] | *GII (T24)*		
	280	600	920	280	600	920
mean	32.0	26.5	24.5	44.9	37.1	34.3
COV [%]	18.7	13.0	11.0	17.4	12.6	10.0
$X_{05,LN}$	23.0 (1.08)[1]	21.2 (1.00)[1]	20.2 (0.96)[1]	33.3 (1.11)[1]	29.9 (1.00)[1]	28.9 (0.97)
k_h = (h/600)$^{0.14}$	1.11	1.00	0.94	1.11	1.00	0.94
k_h Frese (2008)	1.09	1.00	0.94	1.09	1.00	0.94

[1] related to reference depth of $h_{g,ref}$ = 600 mm

Table 12. Results for the MOE ($E_{m,0,g}$) of 10^3 simulated glulam beams of width w_g = 150 mm; base material GI (T14) & GII (T24)

h_g [mm]	$E_{m,0,g}$ [MPa] | *GI (T14)*			$E_{m,0,g}$ [MPa] | *GII (T24)*		
	280	600	920	280	600	920
mean	10,450	10,450	10,450	12,950	12,950	13,000
COV [%]	7.05	4.65	3.63	7.88	5.33	4.08

4 Resawn Glulam Beams

4.1 Glulam in split condition

In order to analyse the influence of splitting glulam beams on the properties of the remaining cross sections, the probabilistic model for lengthwise split boards, presented in Section 2, is combined with the probabilistic numerical model for glulam

beams in Section 3. Therefore, glulam beams were simulated featuring different widths, depths, degrees of separation (one or two cuts, i.e. η_s = 1/2 or 1/3) and board strength classes. The results of all simulated parameter combinations (10^3 for each combination) are summarised in Table 13.

Table 13. Results of the bending strength ($f_{m,g}$) of simulated glulam beams in full & split condition; 10^3 realisations each

w_g	h_g	group	$f_{m,g,mean}$ [MPa]			COV[$f_{m,g}$] [%]			$f_{m,g,05,LN}$ [MPa]		
			full	1 cut	2 cuts	full	1 cut	2 cuts	full	1 cut	2 cuts
100			30.4	29.4 (0.97)[1]	–	19.5	22.1 (1.13)[1]	– –	21.5	19.5 (0.91)[1]	–
150	280	GI (T14)	32.0	30.5 (0.95)[1]	29.3 (0.92)[1]	18.7	20.9 (1.12)[1]	24.1 (1.29)[1]	23.0	20.9 (0.91)[1]	18.5 (0.81)[1]
200			33.3	31.5 (0.95)[1]	30.1 (0.91)[1]	18.5	19.8 (1.07)[1]	22.4 (1.21)[1]	24.1	22.1 (0.91)[1]	20.2 (0.84)[1]
150	600		26.5	24.9 (0.94)[1]	23.3 (0.88)[1]	13.0	14.2 (1.09)[1]	15.2 (1.17)[1]	21.2	19.5 (0.92)[1]	17.8 (0.84)[1]
150	280	GII (T24)	44.9	43.8 (0.98)[1]	41.8 (0.93)[1]	17.4	18.3 (1.05)[1]	21.3 (1.22)[1]	33.3	32.0 (0.96)[1]	28.9 (0.87)[1]
150	600		37.1	36.2 (0.98)[1]	34.5 (0.93)[1]	12.6	13.1 (1.03)[1]	13.5 (1.07)[1]	29.9	28.9 (0.97)[1]	27.4 (0.92)[1]

[1] related to the properties at full cross section, i.e. before splitting

In-line with Viguier et al. (2014) and Crocetti (2009) also here in $E_{m,0,g,mean}$ no reduction due to the splitting was observed. The influence from resawing glulam beams on the main statistics of the bending strength relative to them of glulam in full cross section (η_s = 1) is shown in Figure 11. With respect to the properties at full cross section, with decreasing separation ratio η_s the mean bending strength values are decreasing and the corresponding variations are increasing. This effect is more pronounced in the lower glulam strength class, i.e. glulam of board material with higher variation.
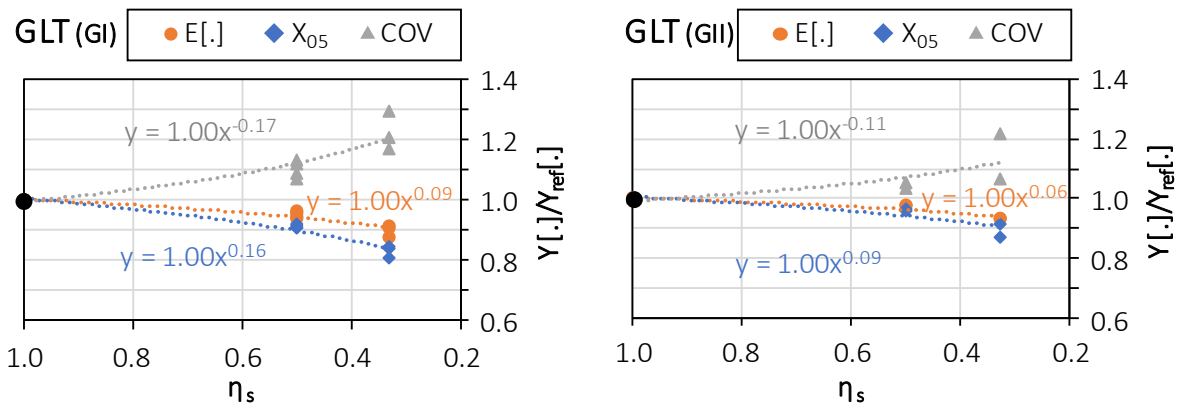
Figure 11. Influence of splitting on the main statistics Y = {$E[X]$; X_{05}; $COV[X]$} of the bending strength (X = $f_{m,g}$) relative to unsplit properties of virtually tested glulam beams with base material GI (left) and GII (right)

4.2 Comparison with previous investigations

There are only a few experimental investigations on the mechanical properties of re-sawn glulam beams known to the authors. These investigations mostly comprise only

a limited number of tests per series (n ≤ 20) which commonly leads to large uncertainties in relative comparisons between properties of split and unsplit glulam beams and thus to apparently not consistent results. Figure 12 shows the test results of various experimental investigations as reported in Kastner et al. (2011), Crocetti (2009), Cleason (2003) and Viguier et al. (2014) in comparison to the model predictions from Section 4.1.

(A) Kastner et al. (2011) – GL24
        170x160 | 80x160 mm² (# 35 full | # 78 1-cut)
(B) Crocetti (2009) – GL30
        90x180 | 40x180 mm² (# 16 full | # 16 1-cut)
(C) Cleason (2003) – GL30
        90x225 | 40x225 mm² (# 16 full | # 16 1-cut)
(D) Viguier et al. (2014) – GL24
        170x400 | 80x400 mm² (# 16 full | # 16 1-cut)
(E) Viguier et al. (2014) – GL28
        170x400 | 80x400 mm² (# 16 full | # 16 1-cut)
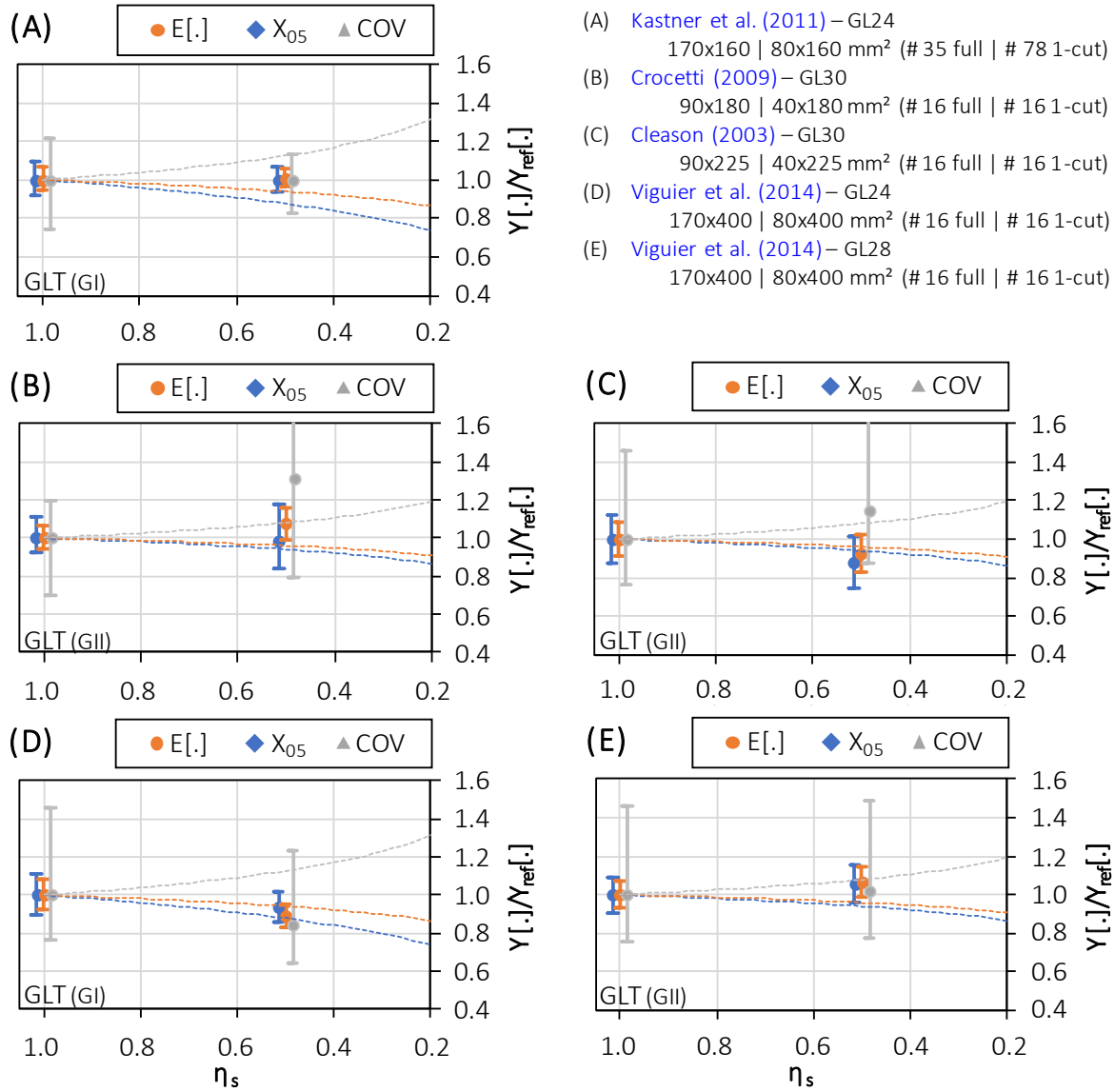
Figure 12. Relative values (split vs. unsplit glulam bending strength; $X = f_{m,g}$) based on model predictions (dashed lines; GI or GII) and main statistics $Y = \{E[X]; X_{05}; COV[X]\}$ of test results from literature together with 95 % confidence intervals; glulam strength class, dimensions and number of tests per series (top rigth)

Overall, the previously described tendencies, decreasing mean and 5 % quantile values and increasing variations due to the splitting process, are to a majority consistent with experimental investigations found in literature. However, there are also two investigations (Kastner et a. 2011 and GL28 in Viguier et al. 2014) which conclude no influence from splitting on bending strength statistics. Experimental investigations with two cuts ($\eta_s = 1/3$) are not known to the authors.

4.3 Modelling the properties of resawn glulam beams

4.3.1 Model based on properties of split boards

Figure 13. *Results of sim. bending strength (h*ref *= 600 mm) vs. model EN 14080 (2013) based on tensile strength of full & split boards with l*B,ref *= 2 m*

One possible approach to characterise the mechanical properties of resawn glulam is via the tensile strength of the lengthwise split boards. For a better comparability between the board properties a reference length of $l_{B,ref}$ = 2 m, as it was anchored in EN 1194 (1999), is applied. Figure 13 shows the characteristic bending strength of all 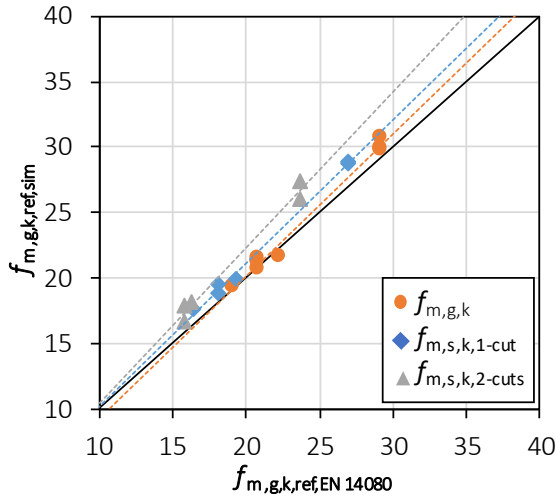simulated glulam beams (see Table 13) corrected to the reference depth h_{ref} = 600 mm acc. to EN 14080 (2013) vs. the characteristic bending strength estimated via the load bearing model as anchored in EN 14080 (2013). The bending strength of the resawn glulam beams is slightly underestimated by the load bearing model. One disadvantage of this approach is, that the tensile strength of the split boards is required as input parameter. For two strength classes, models which account for the influence on the tensile properties of lengthwise split boards are already presented in Section 2.5.2.

4.3.2 Model based on full cross section beam properties
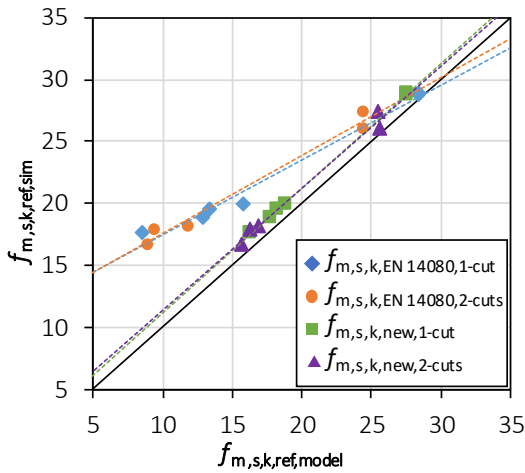
Figure 14. *Results of sim. bending strength for split glulam beams (h*ref *= 600 mm) vs. model in Eq. (1) & new model Eq. (7)*

The second approach is to derive the bending strength of resawn glulam from the bending strength of the unsplit glulam beams and the tensile strength of the used boards. Figure 14 shows a comparison between the bending strength of the simulated resawn glulam beams and the stipulated formula in EN 14080 (2013) as well as the new proposed Eq. (7):

$$f_{m,s,k,new} = f_{m,g,k} - \frac{40}{f_{t,0,l,k} - 6} - \begin{cases} 1 & \text{for 1 cut} \\ 3 & \text{for 2 cuts} \end{cases} \quad (7)$$

Eq. (1) from EN 14080 (2013) is based on experimental results from testing glulam of higher strength classes (see Crocetti 2009, Cleason 2003) which might be the reason for observed larger deviations at lower strength classes. The new proposed Eq. (7) covers also the influence on the bending strength for resawn glulam manufactured from lower strength classes; intentionally, it still gives slightly conservative estimates but features widely a constant bias.

5   Conclusions

The herein presented probabilistic board model allows not only to represent timber boards in respect to its global and local growth characteristics and tension parallel to grain properties longitudinally but also to quantify the impact of lengthwise splitting on the residual cross section's properties. This is in particular of relevance for boards graded and classified in full cross section according to EN 14081-1 (2019) but which are afterwards and in subsequent production processes regularly or arbitrarily reduced in their width to an extend larger than currently allowed in EN 14081-1 (2019). These possibilities are also a prerequisite for the characterisation of unidirectionally and orthogonally layered timber products featuring to a certain amount such in width arbitrarily reduced boards, as it is the focus in the ongoing FFG BRIDGE research project "flex_GLT-CLT-beams" (No. 877111). Based on this probabilistic board model a probabilistic numerical glulam beam model was set up, successfully validated and applied for quantification of the effect of resawing on the bending properties of glulam beams. The current simulations (i) show the possibility to quantify also resawn glulam built up of boards from lower strength classes, (ii) rate the model in EN 14080 (2013) as conservative for low and suitable for high glulam strength classes, and (iii) served as basis for the new model in Eq. (7). A comparison between the resulting bending strength of resawn glulam according to current regulations (EN 14080 2013) and the new proposed model (Eq. 7) is shown in Table 14.

Table 14.   Comparison between the resulting bending strength in [MPa] of resawn glulam acc. to current regulations in EN 14080 (2013) and new model in Eq. (7)

glulam strength class	board strength class	EN 14080 (2013)		new model Eq. (7)	
		1 cut	2 cuts	1 cut	2 cuts
GL24h	T14	16.0[1]	12.0[1]	21.0	19.0
GL28h	T18	24.0	20.0	25.3	23.3
GL32h	T24	30.7	26.7	29.7	27.7

[1]   not allowed acc. to EN 14080 (2013)

6   Acknowledgements

7   References

Blaß HJ, Frese M, Glos P, Denzler JK, Linsenmann P, Ranta-Maunus A (2008). Zuverlässigkeit von Fichten-Brettschichtholz mit modifiziertem Aufbau. Karlsruher Berichte zum Ingenieurholzbau. Universitätsverlag Karlsruhe.

Brandner R, Schickhofer G (2008). Glued laminated timber in bending: new aspects concern-ing modelling. Wood Science and Technology, 42(5):401–425.

Brandner R, Schickhofer G (2010) Glued laminated timber in bending: Thoughts, experiments, models and verification. 11th World Conference on Timber Engineering.

Brandner R (2014) Length effects of tensile strength in timber members with and without joints. Materials and Joints in Timber Structures, RILEM Bookseries 9.

Brandner R (2018) Stochastic Modelling in Timber Engineering. Habilitation. TU Graz.

Burger N (1998) Einfluß der Holzabmessungen auf die Festigkeit von Schnittholz unter Zugbeanspruchung in Faserrichtung. PhD thesis. TU Münschen.

Colling F (1990) Tragfähigkeit von Biegeträgern aus Brettschichtholz in Abhängigkeit von den festigkeitsrelevanten Einflussgrößen. PhD thesis. Universität Fridericiana.

Cleason T (2003) Hallfasthet hos "klycbalkar". SP RISE Sweden.

Crocetti R (2009) Strength of split glulam beams. SP RISE Sweden.

Ditlevsen O, Källsner B (1998) System effects influencing the bending strength of timber beams. IFIP. 8th WG 7.5. Krakow. Poland.

Ehlbeck J, Colling F, Gorlacher R (1985) Einfluß keilgezinkter Lamellen auf die Biegefestigkeit von Brettschichtholzträgern Eingangsdaten für das Rechenmodel. Eur J Wood Prod 43(8): 369–373.

EN 338 (2016) Structural timber – Strength classes. CEN.

EN 408 (2012) Structural timber – Structural timber and glue laminated timber —Determination of some physical and mechanical properties CEN.

EN 1194 (1999) Timber structures – Flued laminated timber – Strength classes and determination of characteristic values. CEN

EN 1995-1-1 (2014) Eurocode 5: Design of timber structures – Part 1-1: General – Common rules and rules for buildings. CEN.

EN 14080 (2013) Timber structures – Glued laminated timber and glued solid timber – Requirements timber – Strength classes. CEN.

EN 14081-1 (2019) Timber structures – Strength graded structural timber with rectangular cross section – Part 1: General requirements. CEN.

Fink G, Frangi A, Kohler J (2013) Modelling the bending strength of glued laminated timber - considering the natural growth characteristics of timber. CIB-W18/46-12-1

Fink G (2014) Influence of varying material properties on the load-bearing capacity of glued laminated timber. PhD thesis. ETH Zurich.

Fink G, Köhler J, Brandner R (2018) Application of European design principles to cross laminated timber. Engineering Structures Volume 171: 934–943.

Frese M, Blass H (2008) Bending strength of spruce glulam new models for the characteristic bending strength. CIB-W18/41-12-2.

Frese M (2016) Computergestützte Verfahren zur pragmatischen Beurteilung der Tragwiderstände von Brettschichtholz: Zusammenfassung exemplarischer Simulationsstudien. Habilitation. Karlsruher Institut für Technologie.

Isaksson T (1999) Modelling the variability of bending strength in structural timber. PhD thesis. Lund Institute of Technology.

Källsner B, Ditlevsen O (1994) Lengthwise bending strength variation of structural timber. IUFRO S 5.02 – Timber Engineering.

Kastner E, Schickhofer G, Brander R, Unterwieser H (2011) Untersuchung der Auswirkung des längsweisen Auftrennens auf das mechanische Potenzial von Brettschichtholzlamellen und daraus aufgebauten Brettschichtholzträgern, hinsichtlich ihrer Festigkeit und Steifigkeit. Forschungsbericht, holz.bau forschungs gmbh.

Köhler J (2007) Reliability of timber structures. PhD thesis. ETH Zurich.

Olsson A, Briggert A, Oscarsson J (2019): Increased yield of finger jointed structural timber by accounting for grain orientation utilizing the tracheid effect. Eur J Wood Prod 77: 1063–1077.

Rebonato R, Jäckel P (2011): The most general methodology to create valid correlation matrix for risk management and option pricing purposes. SSRN Journal.

Schickhofer G, Augustin M (2001) Project INTELLIWOOD working package 3: 'Strength correspondence' – final report. Report LR 9808/4, Lignum Research.

Viguier J, Bocquet J, Dopeux J, Bléron L, Dubois F, Aubert S (2014) Strength grading of split glulam beams. CIB-W18/47-5-1.

DISCUSSION

The papers was presented by R Sieder

H Blass commented that this approach considered resawn or split glulam and asked about application of the approach to consider CLT especially the consideration of finger joints. R Sieder said that the influence of finger joint strength was modeled based on TKAR. H Blass said that in CLT part of the board may have finger joint and part of the board may not have finger joint. R Sieder responded that the model can consider such case.

C Tapia asked what is the benefit of having an intermediate zone in the model. R Sieder said that the influence with and without intermediate zone has not been studied and agreed the influence might be minor. C Tapia said that TKAR values were used to represent finger joints but the actual tensile strength of finger joints are commonly measured. He asked why not work directly with finger joint strength data. R Sieder said this may be done later.

E Ussher asked about MOE values and the situation where reaction wood might be involved. He also asked about the boundary conditions. R Sieder said that MOE as influenced by the resawing process was considered minimal. The timber considered may have reaction wood in it. Also four-point bending with simple supports was considered.

R Brandner added that flat finger joints were considered in the study and discussed with C Tapia that variation of finger joint properties was already considered with the approach.

A Frangi commented that in fire situation there might be an issue with the slender split beam exposed on three sides to fire load. R Sieder stated that no special considerations would be needed.

M Westermayer questioned about need of consideration of fiber deviation in the model. R Sieder stated that fiber deviation was not explicitly considered in the model and might consider this with additional strength reduction. R Sieder clarified that clear zone length was randomly treated and not fixed at say 150 mm.

P Dietsch suggested adding the table from last two slides to the paper.

C Tapia asked what type of distribution of strength along the board was found. R Sieder said not quite lognormal distribution as tail fittings were not perfect.

Steel properties of self-tapping screws

Carmen Sandhaas, Karlsruhe Institute of Technology

Hans Joachim Blass, Karlsruhe Institute of Technology

1 Introduction

In general, the European Yield Model is used to design joints with laterally loaded screws, where the tensile capacity F_t and the yield moment M_y are necessary input parameters when it comes to steel properties. The speed of screw development is so immense that the current Eurocode 5 (2010) does not include bespoke rules for self-tapping screws, with the exception of few specific rules concerning axially loaded screws. Indeed, in order to design joints with screws, most input parameters (e.g. F_t, M_y) must be taken from technical documentation of the screws. In Europe, self-tapping screws can be certified in accordance with EN 14592 (2012) or through a European Technical Assessment (ETA) based on an EAD (2019). The steel properties to be determined in the framework of certification testing are M_y, F_t and the ultimate torsional moment M_{tor}.

The aim of this contribution is to analyse design equations regarding the parameters tensile capacity F_t and yield moment M_y that would eliminate the need to consult technical documentation of individual screw producers. An extensive database comprising more than 10000 test results carried out for certification purposes was analysed. Potential benefits are more robust design models covering a large range of screws, reduced testing and simplified design equations. More specifically, this contribution investigates in a first step the influence of different parameters such as the type of steel or screw on steel properties. Then, two approaches are examined that aim at facilitating testing. The yield moment M_y for instance is not easy to determine experimentally and results depend strongly on their interpretation and on the precise test setup (see section 4.2). The possibility to abandon these tests seems appealing. Proposals are made how M_y could be calculated in future, based on either tensile strength or ultimate torsional moment.

2 State of the art

Self-tapping timber screws are one of the most important fastener typologies in modern timber engineering. Due to their good performance, ease of application and versatile ranges of use, the advent of modern timber screws is one of the primary factors for the advent of many modern engineered timber structures. Screws are often designed to accommodate specific purposes, such as screws optimised for specific timber products (Brandner, 2019) or screws with variable thread geometries to pre-stress timber (Steilner, 2014). Furthermore, screws are an effective means to reinforce against tensile failures perpendicular to the grain (Bejtka and Blaß, 2005), shear (Dietsch, 2012) or as reinforcement of beam supports (Bejtka and Blaß, 2006). Consequently, the variety of modern self-tapping screws in terms of their geometrical and steel properties is enormous, ranging from fully threaded screws over screws with a partial thread or two threaded parts over the screw length to many different head, tip and thread shapes. Concerning steel properties, most screws are made of carbon steel and are hardened. These screws are usually galvanised to protect them against corrosion. Also stainless steel screws are widely applied, where, differently to nails (Sandhaas and Görlacher, 2017), the steel properties differ considerably to those of carbon steel screws because the latter are generally hardened. However, also martensitic stainless steel is used where higher steel properties come with the cost of lesser resistance against corrosion. Ringhofer (Ringhofer, 2017) gives a comprehensive and clear overview of these manifold screw types and explains thoroughly the effect of production processes and geometric and material choices on the screw performance.

As stated in the introduction, in current certification practice, the three steel properties M_y, F_t and M_{tor} are tested in accordance with EN 14592 or EAD 130118-01-0603, where both refer to the respective testing standards (EN 1383, 2016; EN 409, 2009; EN ISO 10666, 2010). The evaluated values on the characteristic level are then declared in technical documents. In the current version of Eurocode 5, design rules exist for "smooth shank screws, where the outer thread diameter is equal to the shank diameter" (8.7.1 (2)), and where reference is made to the rules for bolts (for screws with d > 6 mm; 8.7.1 (4)) and nails (for screws with $d \leq 6$ mm; 8.7.1 (5)). These screws however are screws with a standardised thread, which generally are different to self-tapping screws. Self-tapping screws are cold-formed, mostly hardened and their outer thread diameter is larger than the shank diameter. Generally, confusion exists if rules for bolts and nails apply also to self-tapping screws with a partial thread (fully threaded screws are not covered). Such rules encompass for instance Eq. (1), with which the characteristic yield moment $M_{y,Rk}$ in Nmm of nails and bolts can be calculated:

$$M_{y,Rk} = 0.3 \cdot f_{u,k} \cdot d^{2.6} \tag{1}$$

where $f_{u,k}$ = 600 MPa for nails (corresponds to minimum tensile strength of wire) / characteristic tensile strength of bolt in MPa; d = nominal diameter in mm.

3 Database

The database consists of in total 10419 tests taken from 86 reports. Screws from 32 different producers were considered and the tests were carried out between 2010 and 2019, in accordance with the certification rules valid at the time of testing. Due to the large variability, a rough classification as shown in Figure 1 on the left was used to create subgroups of screws. Partially threaded screws constituted 69% of the database; fully threaded screws 19%, screws with two threaded parts and with a high-low thread 6% each and only 1% were TCC screws. The geometrical properties given in Figure 1 on the right are also recorded in the database. In total, screws with 26 different nominal diameters ranging from 2.5 mm to 14 mm were tested, where diameters of 5, 6 and 8 mm were the most frequent with about 15% each. The ratio between inner and outer thread diameter was between 0.55 and 0.76. Concerning the types of steel, for 33% of all data, the test reports did not explicitly state the types of steel of the screws, which means, with near-certain probability, that these screws were made from carbon steel and hardened. Therefore, these 33% were assigned to carbon steel screws, which then accounted for 72% of the database. 27% were stainless steel screws, 30 screws (0.3%) were hot-dip galvanised and 50 screws (0.5%) were made from unhardened carbon steel. No further information about steel grades was usually given, e.g. if austenitic or martensitic steels were used. The number of tests per parameter is given in Table 1. Concerning the individual parameters, the tensile capacity F_t and the torsional moment M_{tor} are measured maximum values. The given yield moment M_y is the value at a measured deformation angle of 45° or the reached maximum bending angle before rupture of the screws. It has to be pointed out here that issues around test execution and interpretation of results lead to uncertainties about the measured values (see section 4.2).
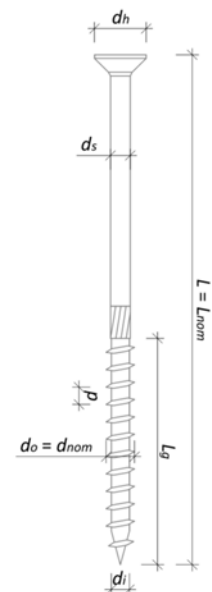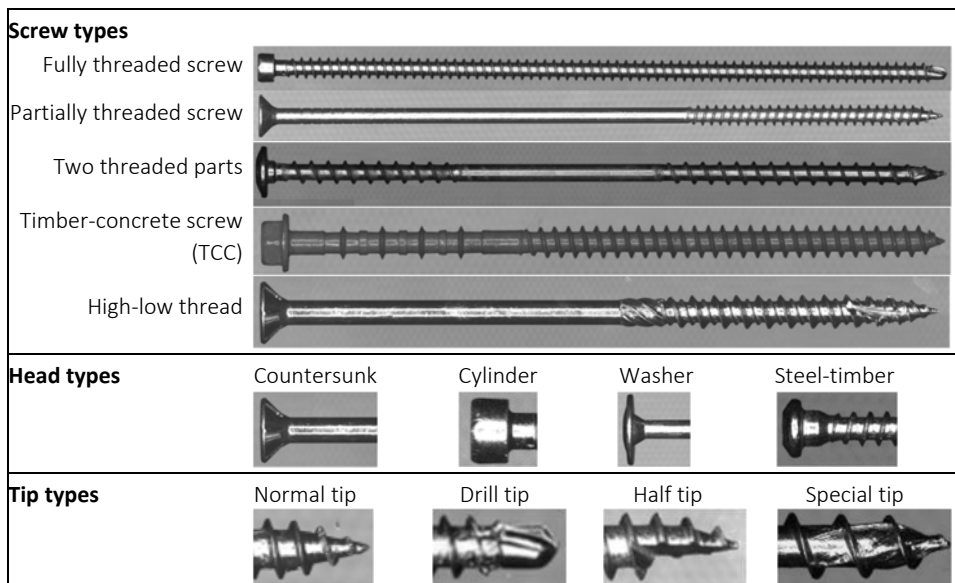

Figure 1.   *Left: Classification of screws. Right: Geometrical properties with d_h = head diameter, d_s = diameter of smooth shank, d_o = outer thread diameter = nominal diameter d_{nom}, d_i = inner thread diameter, p = pitch, L = length = nominal length L_{nom}, L_g = length of threaded part.*

Table 1.   Composition of database, F_t in kN, M_y and M_{tor} in Nm.

	Tensile capacity F_t	Yield moment M_y	Torsional moment capacity M_{tor}
No. of tests	3851	2921	3647
Of which stainless steel	1085	756	1015
Of which hdg[*]	10	10	10
Of which unhardened[#]	50	50	50

[*] hdg = hot-dip galvanised; [#] = only screws made of carbon steel

4 Analysis and discussion

4.1 General

Usually, 10 tests per steel property were carried out using the same screw, i.e. from one batch. The steel properties can be analysed individually, which means that individual test results can be considered, e.g. to evaluate if the shank ribs have an influence on the tensile capacity of partially threaded screws (they have not). Furthermore, steel properties can be compared within test series, e.g. to investigate the relationship between M_y and M_{tor}. For the latter case, only mean values can be used, as there is no direct relationship between individual test values. For instance, M_{tor} cannot be measured on the very screw that was used to determine M_y. Therefore, experimental values contained in the database are grouped although screw parameters may be different, notably length and head type.

As stated before, most screws are made of carbon steel and are hardened. Only about a third of the database contains test results of stainless steel screws, where martensitic stainless steel screws can be hardened contrary to screws made of austenitic stainless steel. Work hardening effects will take place when rolling the thread and consequently, screws with smaller inner diameters (and hence relatively larger nominal diameters) may "benefit" more from work hardening. Subsequent hardening of screws, a process that includes a heat treatment, may reverse the effect of work hardening, but it will lead to higher properties. This heat treatment may again affect screws with smaller diameters more than thicker screws, leading to higher properties of screws with decreasing nominal diameters. In other words, the steel strength is not necessarily homogeneous over the cross-section. In EN ISO 10666 (2010), developed for screws in steel structures, this is considered because e.g. core and surface hardness need to be determined. Also the screw length may influence the steel properties, as the rolling of a long thread may lead to more notches, which in turn lead to reduced properties.

Hence, as a first step, influence factors on the steel properties are investigated. First, the influence of the **type of steel** is assessed. For this, test values must be converted in strength values in order to allow for comparison. The conversion in strength is done as shown in Eqs. (2) to (4), with d_i = measured inner thread diameter in mm. The consideration of d_i, however, does not lead to true strength values. As shown in Ringhofer (2017), the stressed area to consider when transforming capacity into

strength is not circular in the case of screws. Moreover, possible notches, especially in the threaded part or in the transition area between thread and smooth shank of partially threaded screws, are not considered.

"Yield strength σ_{My}" in MPa: $\sigma_{My} = \dfrac{6 \cdot M_y}{d_i^3}$ (2)

"Tensile strength f_t" in MPa: $f_t = \dfrac{4 \cdot F_t}{\pi \cdot d_i^2}$ (3)

"Torsional strength f_{tor}" in MPa: $\sigma_{tor} = \sqrt{3} \cdot \dfrac{M_{tor}}{Z_{tor,pl}} = \sqrt{3} \cdot \dfrac{M_{tor}}{\pi \cdot d_i^3 / 12}$ (4)

In Eq. (3), $Z_{tor,pl}$ is the full plastic polar section modulus of a round section in mm^3 and factor $\sqrt{3}$ accounts for the ratio between tensile and shear strength.

The converted strength values are shown in Figure 2. The "yield strength" (top) and the "torsional strength" (bottom) are similar, whereas both are higher than the "tensile strength" (centre). Different stress states during testing may lead to this. For instance, during a test to determine M_y and M_{tor}, the outer fibres are first stressed whereas during a tensile test, the whole cross-section is stressed. As the hardening procedure is not influencing the whole cross-section evenly, the outer fibres with higher strength may lead to a higher "yield/torsional strength". During a tensile test instead, the whole cross-section with hardened outer fibres and less-hardened inner fibres is activated, leading to lower tensile strength values of hardened screws. When looking at stainless steel screws, two distinct groups can be identified. Obviously, screws made from martensitic stainless steel can reach strength values similar to those made from carbon steel.

Apart from the type of steel, also the **screw type** may influence the steel properties. The following observations made during testing are the reason behind this hypothesis:

- Tensile tests: Screws usually fail in the threaded part with the smallest stressed area (inner diameter). Unhardened stainless steel screws however may also fail in the smooth shank although the diameter of shank is greater than inner diameter. This leads to smaller tensile capacities of partially threaded screws in comparison to fully threaded screws (of the same group). An explanation is that work hardening effects do not occur in the smooth shank of stainless steel screws.

- Yield moment tests: The weakest section of partially threaded screws usually is in the area of the last thread directly adjacent to the smooth shank (the "transition" area). This may be due to local stress concentrations. Within the same group, partially threaded screws may hence have lower yield moments in comparison to fully threaded screws.

- Often, fully threaded screws have higher steel properties than partially threaded screws, as the latter are less hardened.
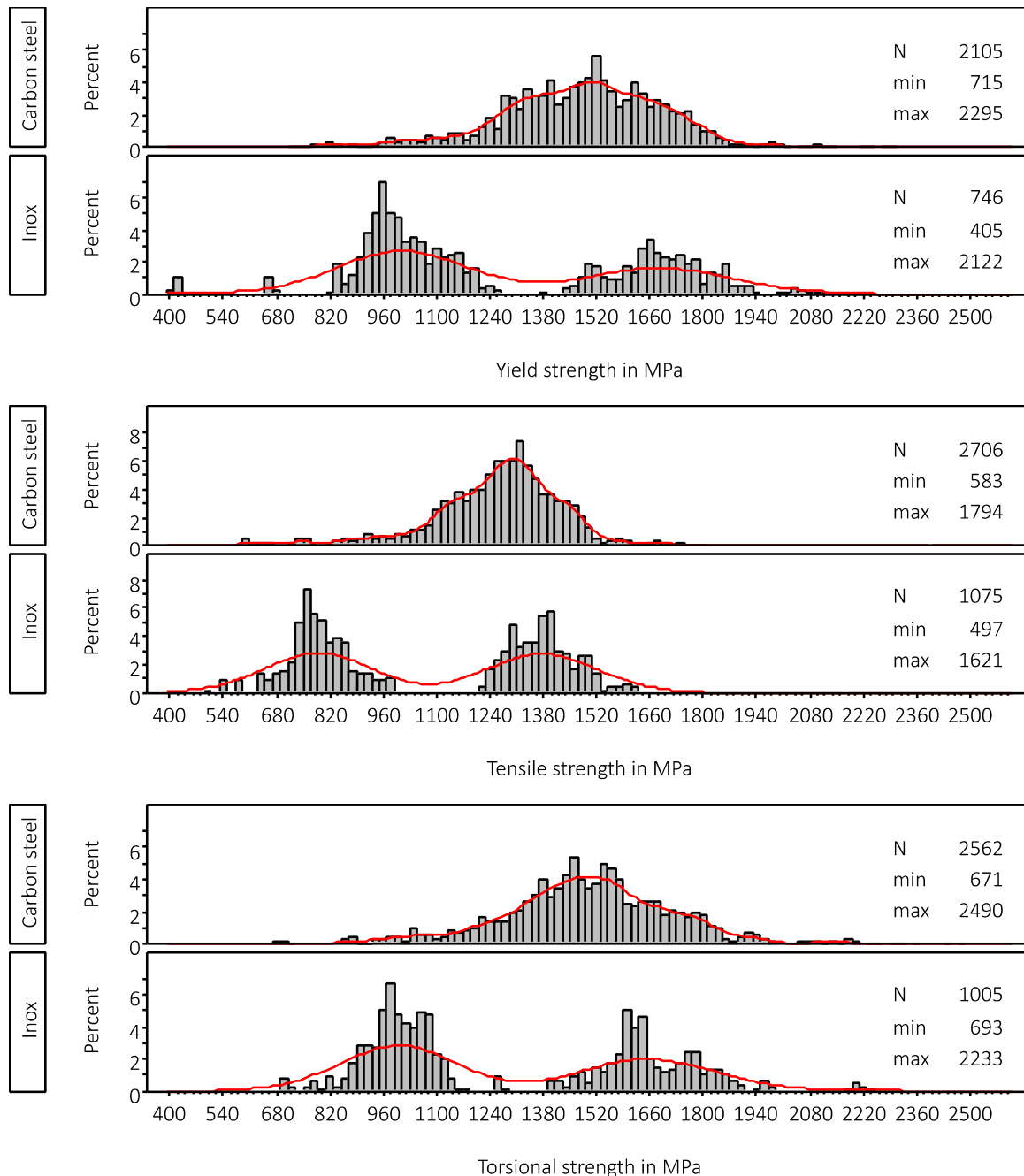
Figure 2. *Histograms of strength values per type of steel. Results for hdg and unhardened screws are not shown and only results for screws with recorded inner diameter d_i are shown.*

Figure 3 shows all three steel properties versus the nominal diameter. Nearly 90% of all screw types were partially threaded and fully threaded screws. The black and red lines in Figure 3 are the quadratic regression lines for partially threaded screws (the red line) and for fully threaded screws (the black line). Considering that the regression for nominal diameters larger than 12 mm is not reliable (few test results and no results for partially threaded screws, i.e. the regression line for partially threaded screws is not correct for large diameters), the two lines do not differ significantly. Therefore, on the level of individual test results, no difference between screw types can be found. In Figure 2 and in Figure 3, the significant scatter of steel properties within the whole population of screws is obvious, which will impact on the quality of design rules.
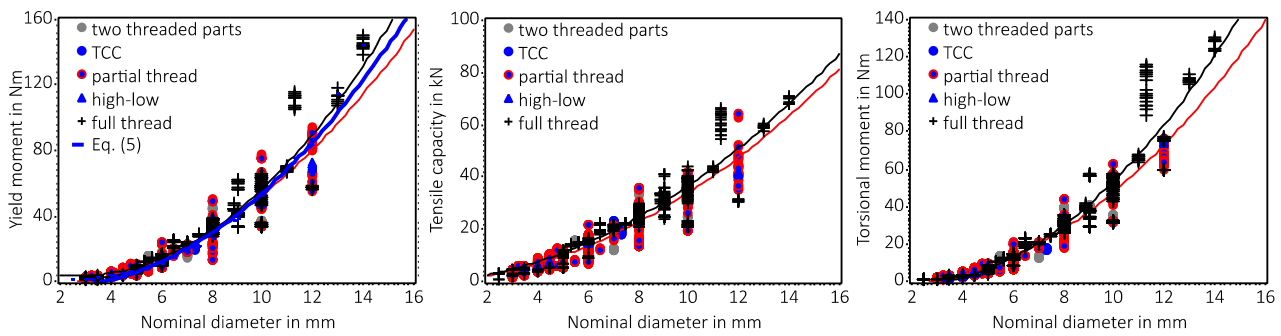
Figure 3. *Properties versus d_{nom}, identified by screw type (hdg and unhardened screws not shown). From left to right : M_y (69.3% partial thread, 17.5% full thread), F_t (70.4% partial thread, 17.4% full thread), M_{tor} (66.6% partial thread, 20.5% full thread). The black and red lines are the quadratic regression lines (forced through zero) for partially threaded (red) and fully threaded (black) screws.*

To conclude this general section, it can be said that the type of steel influences the steel properties, where yield and torsional strength have very similar values. Moreover, it should be taken into account that two distinct groups of stainless steel screws exist in case any simplified equations based on tensile strength values are used. This is proposed in the current draft for the new Eurocode (CEN/TC 250/SC 5/WG 5 N148, 2020), but only a single value of 500 MPa is given as characteristic tensile strength for stainless steel screws. Finally, no clear influence of the screw type can be seen and scatter of steel properties within the whole population of screws is significant. This is in stark contrast to the scatter within the single test series determining M_y, F_t and M_{tor}, where coefficients of variation larger than 0.05 were observed only in 3.5% of the series.

4.2   Challenges to determine M_y

Before pursuing two approaches aimed at calculating M_y instead of executing tests, challenges around the experimental determination of yield moments and their implication for derived characteristic values are discussed. Lack of clarity in testing standards is indeed hampering proper analysis of test data. Both EN 14592 and EAD 130118-01-0603 refer to EN 409 as testing standard, where four-point bending tests are described, with the free length L_2 between the two load insertion points ranging between d and $3 \cdot d$. As L_2 has a significant influence on the obtained M_y-values, this range is too large. Furthermore, in EN 409, the test location along the screw axis is not specified. Especially for partially threaded screws, the exact definition of this location is necessary in order to determine M_y in the weakest section. It is not clearly stated that the screw must be allowed to move horizontally, so that there is scope to find the weakest section. Moreover, EN 409 prescribes different bending angles for different fastener types and timber products, leading to different bending angles for different wood densities. Meanwhile, the EAD states that the yield moment "is the value at the plastic bending angle $\alpha = 45/d^{0.7}$ degrees", whereas neither EN 409 nor EN 14592 mention the word "plastic". This however is crucial, as most test setups measure the

global bending angle, whereas only the plastic (not elastic) bending angle should be considered. Steilner and Blass (2014) addressed this issue and proposed a solution to determine the plastic bending angle. Different laboratories therefore most certainly determine different M_y-values for the same screws, with significant implications for characteristic values. In view of these issues and as said in section 3, M_y-data contained in the database is raw data and no adjustments neither in accordance to Steilner and Blass nor Blass et al. (2000) were made. However, machine slip is still included in all results contained in this database, as the used test setup measures the bending angle directly through the rotation of the machine. This is less of an issue because the registered value for M_y is very close to the plateau value, where only a very slight increase in yield moment with increasing bending angle is observed. It is this dependency on the bending angle which makes a clear and unequivocal definition of M_y impossible.

4.3   Calculation of the yield moment using tensile strength

Eq. (5) in Figure 3 on the left shows the mechanics-based full plastic bending moment M_{mech} for a circular section calculated as follows:

$$M_{mech} = \frac{1}{6} \cdot 1200\,\mathrm{MPa} \cdot \left(0.64 \cdot d_{nom}\right)^3 \tag{5}$$

where 1200 MPa = mean tensile strength of all screws (mean of 3846 individual values, COV = 21%), calculated using the inner diameter d_i, see Eq. (2); 0.64 = mean ratio of d_i/d_{nom}, i.e. d_i is on average 64% of d_{nom} (mean of 27282 individual values, COV = 5.6%).

Giving a first look at Figure 3 on the left, the comparison of Eq. (5) with experimental values for M_y seems to pave the way for a calculation of M_y using tensile strength values, similar to Eq. (1). Therefore, two nonlinear regression analyses based on mean values were carried out, using the format of Eq. (1) with the prefactor and the exponent as regression variables α and β. The process was iterative, eliminating all outliers with studentised residuals larger than |3|. Different independent variables were used, varying the considered diameter between inner diameter d_i and nominal diameter d_{nom}. The results are given in Table 2, where the lower indices indicate the considered diameter when calculating the tensile strength in analogy to Eq. (3). The regression results do not differ much among themselves and are close to the mechanics-based equation that has a prefactor of 1/6 and an exponent of 3. More pragmatic, but less mechanically correct is model B, as nominal diameters of screws are known to engineers in practice. Model C is further simplified by forcing the exponent to be equal to three.

Figure 4 on the left shows the results of the more pragmatic model B as the ratio of experimental over expected values in order to better identify differences, seeing that the high $R^2 = 0.999$ would not allow to see these differences if the values are plotted versus each other. Data for higher nominal diameters are scarce and the ratio scatters more for smaller diameters, where more data is available. The mean value of the ratio

is 0.99 (COV = 6.7%) and the observed 5th percentile is 0.89. A last step to obtain design rules is to derive characteristic values. One option is to correct model B by a factor of 0.89 and replace the mean tensile strength with its characteristic value. By doing so, it is implicitly assumed that the scatter of M_y and f_t is the same, which is reasonable seeing that both are steel properties.

Table 2.   Results of nonlinear regressions based on mean values. The outliers concern mostly screws with $d_{nom} \geq 8$ mm.

Model	No of test series	Regression variables		R^2	Outliers
		α	β		
A $M_{y,mean} = \alpha \cdot f_{t,di,mean} \cdot d_i^{\beta}$	256	0.188	3.019	0.999	27
B $M_{y,mean} = \alpha \cdot f_{t,dnom,mean} \cdot d_{nom}^{\beta}$	239	0.149	2.911	0.999	44
C $M_{y,mean} = \alpha \cdot f_{t,dnom,mean} \cdot d_{nom}^{3}$	238	0.123	–	0.998	45
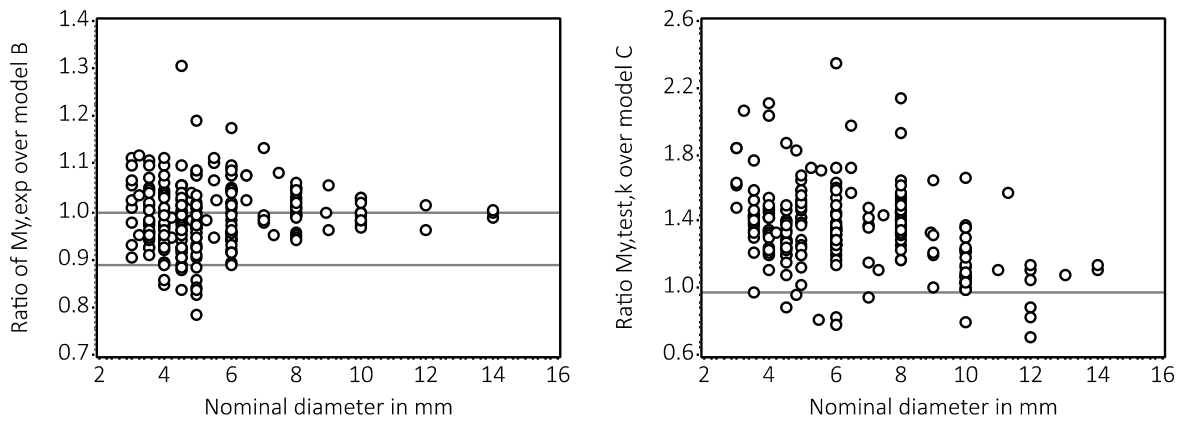
Figure 4.   Left: Ratio of mean experimental value of M_y over expected value of model B. The horizontal line at 0.89 indicates the observed 5th percentile. Right: Ratio of characteristic values over $M_{y,k} = 0.123 \cdot 365$ MPa $\cdot d_{nom}^3$. Only test results for hardened screws made of carbon steel are shown. The horizontal line at 0.98 indicates the observed 5th percentile

However, if the aim of any possible design rule is to make consultation of declarations of performance of individual screw producers superfluous, then a general characteristic value for the tensile strength valid for all screws of a certain type of steel is needed. For instance, 365 MPa, which is the observed 5th percentile of the tensile strength $f_{t,dnom,k}$ of hardened screws made of carbon steel, calculated considering the nominal diameter, can be chosen as characteristic value for the tensile strength. Now, model C is chosen to check regression results, and $f_{t,dnom,k}$ = 365 MPa is inserted instead of $f_{t,dnom,mean}$. The result is shown in Figure 4 on the right, where it is compared with characteristic values determined in accordance with EN 14358 (2016) and where only hardened screws made of carbon steel were considered. The mean value of the shown ratio

is 1.35 (COV = 19%) and the observed 5th percentile is 0.98. Therefore, the chosen value for $f_{t,dnom,k}$ = 365 MPa allows for a calculation of $M_{y,k}$. It must be remembered here that the considered M_y-values were not adjusted in terms of bending angles, see section 4.2. However, such an adjustment leads to even lower M_y-values and hence to an even more punishing situation for many screws.

To conclude, design equations of manifold shapes are possible, but all of them can reproduce only a conservative value for $M_{y,k}$, if the whole population of self-tapping screws is considered. The two main decisions to be taken by code writers are which and how many strength values should be considered (e.g. based on which diameter and for how many subgroups). Finally, the database must be extended with data for larger diameters, as any design equation derived does not hold for diameters larger than ca. $10 - 12$ mm, which gets particularly important if exponential approaches are chosen.

4.4   Comparison between M_y and M_{tor}

As concluded in section 4.1, yield and torsional strength give very similar values which leads to the obvious idea of comparing M_y and M_{tor} directly. This would be straightforward approach without any need of geometrical data. Tests to determine M_{tor} are much easier to execute than tests to determine M_y, and inaccuracies as discussed in section 4.2 are less likely to occur. Above all, M_{tor} is determined independently of any deformation; it is the maximum moment measured before the screw breaks. The torsional moment is not needed for design; the test is carried out to make sure that screws can be driven in without breaking.

In total, mean values of 270 series contained in the database can be compared, as only for these series both M_y (2646 individual values) and M_{tor} (2670 individual values) were determined. If M_{tor} is directly compared to M_y, the torsional moment tends to be slightly lower. Indeed, a direct comparison between yield and torsional moment cannot be done from a mechanical point of view, as a bending test leads to normal stresses in the screw, and a torsional test to shear stresses (see also Eq. (4)). Furthermore, not only the "stress type" is different, but also the section moduli differ. As a consequence, M_{tor} was corrected in accordance with Eq. (6). Figure 5 on the left shows the comparison between mean values of M_y and $M_{tor,corr}$, revealing a promising relationship (M_y-values not adjusted). Differences between both values scatter around ±20%, where 117 series had higher and 153 series lower M_y-values than $M_{tor,corr}$.

$$M_{tor,corr} = \sqrt{3} \cdot M_{tor} \cdot \frac{Z_{pl}}{Z_{tor,pl}} = \sqrt{3} \cdot M_{tor} \cdot \frac{d^3/6}{\pi \cdot d^3/12} = \sqrt{3} \cdot M_{tor} \cdot \frac{2}{\pi} \approx 1.1 \cdot M_{tor} \tag{6}$$

where √3 = correction factor: $\tau = f_y/\sqrt{3}$; Z_{pl} = full plastic section modulus of a circular section in mm^3; $Z_{tor,pl}$ = full plastic polar section modulus of a circular section in mm^3
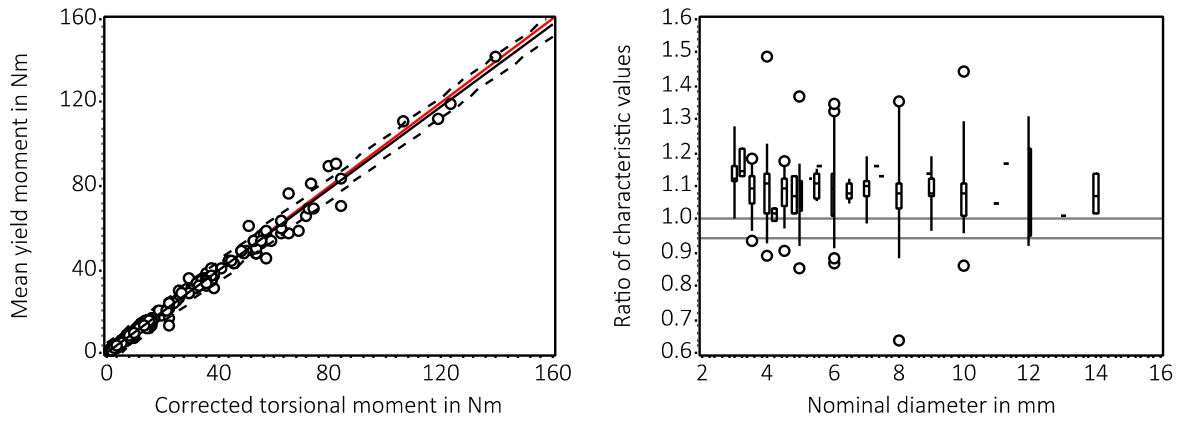
Figure 5. Left: Yield moment versus corrected torsional moment. Mean values of 270 test series. Red line is bisect line, black line is linear regression line, dotted lines are 95% confidence intervals. Right: Boxplot of ratios of characteristic yield moments divided by characteristic torsional moments, which were calculated in accordance with EN 14358 (2016) using **uncorrected** M_{tor}-values. 5th and 95th percentiles are specified.

Concerning a possible calculation of the characteristic yield moment based on the characteristic torsional moment, the two characteristic values could be compared directly, where 5% of the $M_{y,k}$-values can be lower than the $M_{tor,k}$-values. Therefore, the factor of 1.1 given in Eq. (6) is not applied, and uncorrected M_{tor}-values were used to calculate 5th percentiles in accordance with EN 14358 and based on a lognormal distribution. Analogously, 5th percentiles for M_y were calculated for each of the available 270 series. Figure 5 on the right shows a boxplot of the ratio of characteristic values, $M_{y,k}$ divided by $M_{tor,k}$, versus the nominal diameter. The observed 5th percentile is 0.94. This means that an additional conversion factor of 0.94 is needed. Eq. (7) shows a possible equation to calculate $M_{y,k}$ based on $M_{tor,k}$:

$$M_{y,k} = 0.94 \cdot M_{tor,k} \tag{7}$$

Simply eliminating tests to determine the yield moment is not constructive however. The ability of screws to bend without rupture cannot be validated with torsional tests. Current commonly accepted design practice asks for sufficient ductility of joints and hence sufficient elongation of screws. Independently of any possible changes in methodology, the findings of this section allow for plausibility checks, as a comparison of M_y- and M_{tor}-values can help to identify erroneous values.

5 Conclusions and outlook

A large database comprising in total 10419 individual tests evaluating the tensile capacity, the yield and the torsional moment of a large variety of self-tapping screws was analysed. In general, about 10 tests per steel property were carried out per screw type. The observed coefficient of variation within the single test series is max. 5% as can be expected when dealing with steel properties. Between test series however, for instance considering screws with a nominal diameter of 8 mm, observed coefficients of variation were approx. 12% for carbon steel screws and approx. 28% for stainless steel

screws. Consequently, the derivation of general equations valid for the whole screw population comes with the cost of conservative values for certain screws, which will be problematic in seismic design. Particularly screws made of stainless steel should be divided in austenitic and martensitic in order to differentiate between these two different types of stainless steel. Nevertheless, using the database, general design equations to determine the characteristic yield moment valid for a large range of screws can be derived. These general equations can be based on tensile or torsional test results, where the drawback of tensile tests is that capacities are determined whereas strength values are needed. For this, it must be decided if tensile capacities are transferred into tensile strength values using inner or nominal diameters. As a pragmatic approach, it is recommended to use nominal diameters, as these are known to practitioners. Considering inner diameters and a circular section is mechanically more precise, albeit not fully (Ringhofer, 2017), and there is no scope to simulate a mechanical preciseness although the test results show a persistent large scatter.

The database lacks data for screws with nominal diameters larger than 10 mm. This gap should be filled, particularly considering that exponential approaches are best suited to predict the yield moment. Concerning the experimental determination of the yield moment, EN 409 should be reviewed, extended with precise guidelines e.g. concerning the free testing length, and it should only be used to show that screws have enough deformation capability before breaking. If this is not wished for, then also precise information concerning the definition and measurement of the bending angle should be included. Finally, a decision must be taken at which bending angle the yield moment shall be determined and how to deal with the higher yield moment in the smooth shank area of partially threaded screws.

6 Acknowledgements

7 References

Bejtka I, Blaß HJ (2005) Self-tapping screws as reinforcements in connections with dowel-type fasteners. Paper 38-7-4. *CIB-W18 Meeting 38*, Karlsruhe, Germany.

Bejtka I, Blaß HJ (2006) Self-tapping screws as reinforcements in beam supports. Paper 39-7-2. *CIB-W18 Meeting 39*, Florence, Italy.

Blaß HJ, Bienhaus A, Krämer V (2000) Effective bending capacity of dowel-type fasteners. Paper 33-7-5. *CIB-W18 Meeting 33*, Delft, The Netherlands.

Brandner R (2019) Properties of axially loaded self-tapping screws with focus on application in hardwood. *Wood Material Science and Engineering* **14**(5):254-268. doi:10.1080/17480272.2019.1635204.

Dietsch P (2012) *Einsatz und Berechnung von Schubverstärkungen für Brettschichtholzbauteile*. Dissertation, Technische Universität München.

EN ISO 10666 (2010) *Drilling screws with tapping screw thread – Mechanical and functional properties.* Comité Européen de Normalisation (CEN), Brussels, Belgium.

EN 1995 1-1 (2010) *Eurocode 5. Design of timber structures – Part 1-1: General – Common rules and rules for buildings.* Comité Européen de Normalisation (CEN), Brussels, Belgium.

Ringhofer A (2017) *Axially loaded self-tapping screws in solid timber and laminated timber products*. Dissertation, Graz University of Technology.

Sandhaas C, Görlacher R (2017) Nailed joints: Investigation on parameters for Johansen model. Paper 50-7-3, pp. 95-109. *INTER Meeting 50*, Kyoto, Japan.

CEN/TC 250/SC 5/WG 5 N148 (2020) *SC5.T5 Third draft of chapter connections, prEN 1995-1-1, for commenting.* Comité Européen de Normalisation (CEN), Brussels, Belgium.

EAD 130118-01-0603 (2019) *Screws and threaded rods for use in timber constructions.* European Assessment document, EOTA, Brussels, Belgium.

Steilner M (2014) Pre-stressing of wood with full thread screws. *COST Action FP1004 Conference on Experimental Research with Timber*, Prague, Czech Republic.

Steilner M, Blaß HJ (2014) *A method to determine the plastic bending angle of dowel-type fasteners*. In: Aicher S, Reinhardt H W, Garrecht H (eds) RILEM bookseries. Materials and joints in timber structures. Recent developments in technology. Stuttgart, Germany, pp. 603-613.

EN 14358 (2016) *Timber structures – Calculation and verification of characteristic values.* Comité Européen de Normalisation (CEN), Brussels, Belgium.

EN 14592 (2012) *Timber structures – Dowel-type fasteners – Requirements.* Comité Européen de Normalisation (CEN), Brussels, Belgium.

EN 409 (2009) *Timber structures – Test methods – Determination of the yield moment of dowel type fasteners.* Comité Européen de Normalisation (CEN), Brussels, Belgium; Belgium.

EN 1383 (2016) *Timber structures – Test methods – Pull through resistance of timber fasteners.* Comité Européen de Normalisation (CEN), Brussels, Belgium.

DISCUSSION

The papers was presented by C Sandhaas

A Ringhofer agreed with the conclusions. He commented that torsional moment capacity might be influenced by hardness distribution within the cross section. He also noted that the approach is conservative and asked about allowing more flexibility to adopt higher values based on testing. C Sandhaas agreed that this might be possible. She also confirmed that the screws were produced by European companies but may be produced outside Europe.

M Fragiacomo commented that design for seismic consideration might be problematic especially for over strength factor consideration in capacity based design as there was a large spread between the design values and the upper values. H Blass commented that it would not be a good idea to use screws in dissipative zones for seismic design and agreed that larger over strength factors might be needed.

I K Abeysekera asked about combined axial and bending action with reduced yield moment. C Sandhaas said that this was investigated by H Blass in INTER 2017. IK Abeysekera asked whether it would be possible for manufacturers to limit the COV of their products for seismic zones. C Sandhaas and A Ringhofer responded that the COV for one screw type and one producer would be low. R Brandner said that this would be true within one batch but there would be higher variation between batches. C Sandhaas agreed and commented that this type of issue also exists for steel dowels for seismic design.

Self-tapping Timber Screws Subjected to Combined Axial and Lateral Loading

Andreas Ringhofer[*)+)], Markus Burtscher[*)+)], Raimund Sieder[*)], Michael Gstettner[*)]

[*)] Institute of Timber Engineering and Wood Technology | Graz University of Technology | andreas.ringhofer@tugraz.at | [+)] Joint first authorship

Keywords: withdrawal strength; embedment strength; load interaction; rope effect; axial and lateral stiffness; empirical approach; Johansen theory; European Yield Model (EYM);

1   Introduction

Besides their simple and economic application without pre-drilling, modern self-tapping timber screws feature a high performance when loaded in axial direction. This circumstance has been influencing timber engineering for approx. 25 years now and led to various different joint types and reinforcement measures. Both application fields usually consist of screws, which are installed parallel or at least inclined to the load direction to achieve this high resistance and stiffness due to axial loadbearing. In practical application, there are, however, specific requirements and boundary conditions of joint detailing, secondary loading scenarios or stress combinations in possible crack zones, which imped this idea of 'pure' axial loading.

Concentrating on screwed joints, especially system solutions for linear or laminar timber elements usually consist of one or more steel(metal)-to-timber connection(s), which are exposed to loads, acting in more than one direction as a consequence of the versatile application field. This leads to a combined loading of the screws (bending, shear and tension) and the timber member's local area surrounding them (withdrawal, embedment). According to the European design standard Eurocode 5 (EN 1995-1-1 2014) – and similar in several European Technical Assessments of such system connectors – this load interaction has to be verified by Equation (1):

$$\left(\frac{F_{ax,Ed}}{F_{ax,Rd}}\right)^a + \left(\frac{F_{v,Ed}}{F_{v,Rd}}\right)^b \leq 1,\tag{1}$$

with $a = b = 2$ and $F_{ax,Ed}$ & $F_{v,Ed}$ as the design axial and lateral loads and $F_{ax,Rd}$ & $F_{v,Rd}$ as the corresponding resistances; the related characteristic values are given in Equations (2) and (3) for a connection with $n = 1$ screw ($F_{ax,Rk}$ for axial tension):

$F_{ax,Rk} = f_{ax,k} \cdot d \cdot l_{ef}$ (with the screw's steel tensile capacity as upper limit), and (2)

$$
F_{v,Rk} = \min \begin{cases}
f_{h,1,k} \cdot t_1 \cdot d & \text{(c)} \\[2ex]
f_{h,1,k} \cdot t_1 \cdot d \cdot \left[\sqrt{2 + \dfrac{4 \cdot M_{y,Rk}}{f_{h,1,k} \cdot d \cdot t_1^2}} - 1 \right] + \mu \cdot F_{ax,Rk} & \text{(d)}, \\[2ex]
2.3 \cdot \sqrt{M_{y,Rk} \cdot f_{h,1,k} \cdot d} + \mu \cdot F_{ax,Rk} & \text{(e)}
\end{cases}
\qquad (3)
$$

with d as the (nominal) outer thread diameter of the screw, l_{ef} and t_1 as the effective inserted thread length and the total inserted screw length in the timber member, $f_{ax,k}$ and $f_{h,1,k}$ as the characteristic withdrawal and embedment strengths of the timber member under the given conditions, $M_{y,Rk}$ as the characteristic yield moment of the screw and μ (= 0.25) as friction coefficient, representing the axial resistance's share on $F_{v,Rk}$ in form of the so-called 'rope effect', c. f. Bejtka and Blaß (2002).

Thereby, the term ($F_{v,Ed}$ / $F_{v,Rd}$) already covers the verification of all shear loads, possibly acting in different directions but parallel to the timber surface, i. a. by a specific embedment strength for the given condition. Thus, the effect of three-dimensional combined loading can be transformed to a two-dimensional problem as it is illustrated in Figure 1.1.
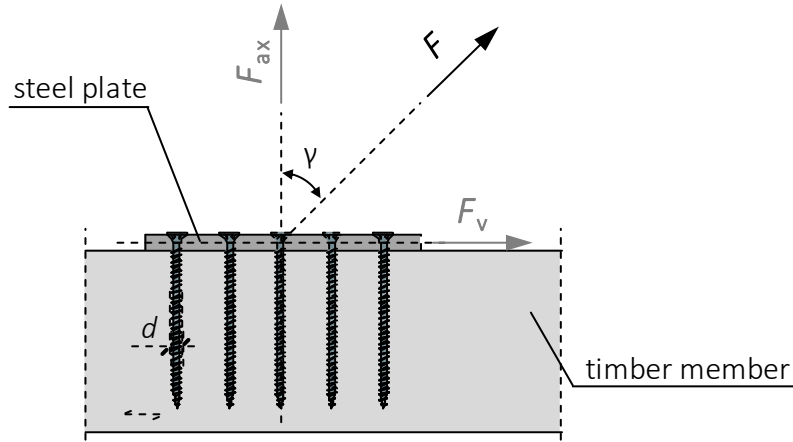
Figure 1.1. Steel-to-timber connection with self-tapping screws subjected to combined axial and lateral loading

Equation (1) for self-tapping screws is equal to the regulation for profiled nails, where it has been adopted from. In contrast, for nails with a smooth shank a linear interaction ($a = b = 1$) has to be applied. Both, the linear and the quadratic interaction for different types of nails are the conclusions of a comprehensive study made by Ehlbeck and Siebert (1984), which has been generally confirmed by McLain and Carroll (1989) and Reyer and Linzer (1993). While the behaviour of smooth and profiled nails under combined loading was investigated quite comprehensively at that time, comparable studies with self-tapping timber screws are missing. Thus, extracted topics, which were investigated by Blaß et al. (2006) (restriction to failure mode (c) according to Equation 3) and Laggner et al. (2016) (restriction to one parameter configuration and failure mode

(e) according to Equation 3) are worth to be highlighted. Even though they chose a completely different experimental approach, both outcomes conclude (Blaß et al. 2006) and quantitatively show respectively (Laggner et al. 2016, $a = b = 2.43$ on mean value level) that the quadratic approach in the current version of Eurocode 5 appears as too conservative.

Besides the need of simplification, the absence of e. g. a comprehensive experimental investigation is probably the reason why the format of Equation 1 does not consider differences due to a variation of strength-influencing parameters (load-to-grain and axis-to-grain angle, screw geometry, timber density and product, etc.) or – more fundamental – due to the matter if a timber (withdrawal, embedment) or screw (tension, bending) failure (or a mixture of both) is given.

To verify the validity of Equation (1) for self-tapping screws, i. e. to check if the approach is too conservative or if certain parameters change the notation of Equation (1), an experimental campaign was carried out in the frame of a recently finished research project at Graz University of Technology. An overview of this programme as well as the developed test configuration are presented in Section 2, while Section 3 comprises the discussion of gained test results and their application to verify theoretical models. As the content of Section 3 had to be limited to some extent, the interested reader is kindly referred to the extended version, which is given in Burtscher (2021).

2 Materials and Methods

2.1 Overview

An overview of the experimental programme, which was carried out by Burtscher (2021), is given in Table 1. Following the principle aim of this study, the most relevant parameter is the share of the axial (F_{ax}) and the lateral load component (F_v) on the combined load F_{test}. As a consequence of the applied test configuration, c. f. Section 2.3.1, this solely depends on γ as load-to-surface angle (= angle between the load direction and the surface normal), see Figure 1.1 and Equation (4),

$$F_{ax} = F_{test} \cdot \cos(\gamma), \text{ and } F_v = F_{test} \cdot \sin(\gamma), \tag{4}$$

and was varied between pure axial ($\gamma = 0\,°$) and pure lateral loading ($\gamma = 90\,°$) in form of two intermediate steps $\gamma = \{30, 60\}\,°$. Taking timber's orthotropic behaviour into account, the load-to-grain angle α and the axis-to-grain angle ε (here: $\varepsilon = 90\,° - \alpha$) were varied as well. In addition, an impact of the certain failure mode (timber vs. steel, or both) on the load interaction was assumed. Thus, the mentioned variations were executed with screws of four different insertion lengths t_1 (or slenderness $\lambda = t_1 / d$). Note: Due to a linear relationship between the effective inserted thread length l_{ef} and the withdrawal capacity R_{ax} (see e. g. Ringhofer 2017), only one screw length was tested in case of pure axial loading.

In order to not overextend the scope of the programme and due to a comparatively time-consuming and cost-intensive test execution, further parameters, possibly influencing the load interaction as well, such as the (nominal) screw diameter, the timber product, the timber density ρ and the moisture content u (c. f. Section 2.2), the connection type (c. f. Section 2.3), etc. had to be excluded from a selective variation.

Table 1. Overview of the test parameters and their range

parameter			range		
			axial loading	lateral loading	combined loading
d	[mm]		8	8	8
t_1	[mm]		105	40, 105, 165, 225	40, 105, 165, 225
$\lambda \approx$	[-]		13	5, 13, 21, 28	5, 13, 21, 28
l_{ef}	[mm]		$t_1 - 1.17\, d^*$	$t_1 - 1.17\, d^*$	$t_1 - 1.17\, d^*$
ε	[°]		0, 30, 60, 90	0, 30, 60, 90	0, 30, 60, 90
α	[°]		-	0, 30, 60, 90	0, 30, 60, 90
γ	[°]		0	90	30, 60
no. of tests	[-]		48	190	369

* tip-correction according to Pirnbacher et al. (2009) for $t_1 \neq 40$ mm

2.2 Materials

2.2.1 Timber

Due to its status as a reference material in fastener testing (c. f. EAD 130118-01-0603 2019) and its widespread use in timber engineering, it was decided to execute the test programme with solid timber (ST) made of Norway spruce (*Picea Abies*) in strength class C24 according to EN 338 (2016) with a nominal average density $\rho_{12} = 420$ kg/m³ (referred to $u = 12$ %). The 12 m³ of raw material was manually graded at the sawmill and went through a technical drying ($u_{target} \approx 10 \div 11$ %) before further processing took place. Thereby, the principle of matched sampling was applied to achieve a comparable density distribution for all single test series. The final dimensions of the test specimens followed most of the requirements according to EN 1382 (2016) and EN 383 (2007) and are given in Table 2.

Table 2. Dimensions of test specimens in dependence of the type of loading and axis-to-grain angle

dimension		axial loading	lateral loading		combined loading
			$\varepsilon = 0\,°$	$\varepsilon > 0\,°$	
length L	[mm]	190	280	370	280
width B	[mm]	115 or 135		115 or 135	115 or 135
height H^*	[-]	280		110 to 280	110 to 280

* parallel to the screw axis and in dependence of t_1

2.2.2 Self-tapping screws

In principle, one $d = 8$ mm, fully threaded screw type with three different lengths (120 mm, 180 mm, 240 mm), a countersunk head and a half-tip, and made by the holder of ETA-12/0373 (2020), was applied for the tests. As both properties serve as

input parameters for theoretical modelling, the steel tensile capacity f_{tens} (n = 6 per length) and the yield moment M_y (n = 15 for 120 mm and 180 mm, n = 10 for 240 mm) were determined according to EN 14592 (2012) and EN 409 (2009) prior to the main test series.

2.3   Methods

2.3.1   Test configuration and test execution

The test configuration, applied for the axial, lateral and combined loading tests of steel-to-timber connections with n = 1 self-tapping screw (t_{plate} = 15 mm → thick steel plate acc. to Eurocode 5) is schematically illustrated in Figure 2.1. The circular shape with a discrete variability of the load-to-surface angle $\Delta\gamma$ = 15 ° bases on the configuration by Munse and Cox (1956), who investigated the mechanical behaviour of rivet joints under combined loading. However, the given problem demanded many modifications of their original idea, which shall be discussed in brief:

The present test set-up consists of two 'steel wheels' (Pos. 2), which are rigidly connected with the test machine (LIGNUM-UNI-275, universal testing device, Zwick GmbH & Co. KG) via the two wheel supports (Pos. 1). The steel plate (Pos. 3), which connects both 'steel wheels', not only serves as a bracing of the test set-up but also – together with the L-brackets (Pos. 4) – as a support for the specimen holder. The test specimen, which is prepared outside the test rig, consists of the timber specimen itself (Pos. 6), the tested screw and the steel plate (Pos. 7). To mount the specimen within the test rig and to transfer axial tensile loads the steel adapters (Pos. 5) are fixed to the timber via self-tapping screws. The whole assembled test specimen (Pos. 5, 6 & 7) is then slit into the rig. The forces are transferred via contact pressure between Pos. 4 and 5.

| Pos. 8 upper wheel |
| Pos. 7 steel plate |
| Pos. 6 timber specimen |
| Pos. 5 steel adapters |
| Pos. 4 L-bracket |
| Pos. 3 steel plate |
| Pos. 2 steel wheel |
| Pos. 1 wheel support |
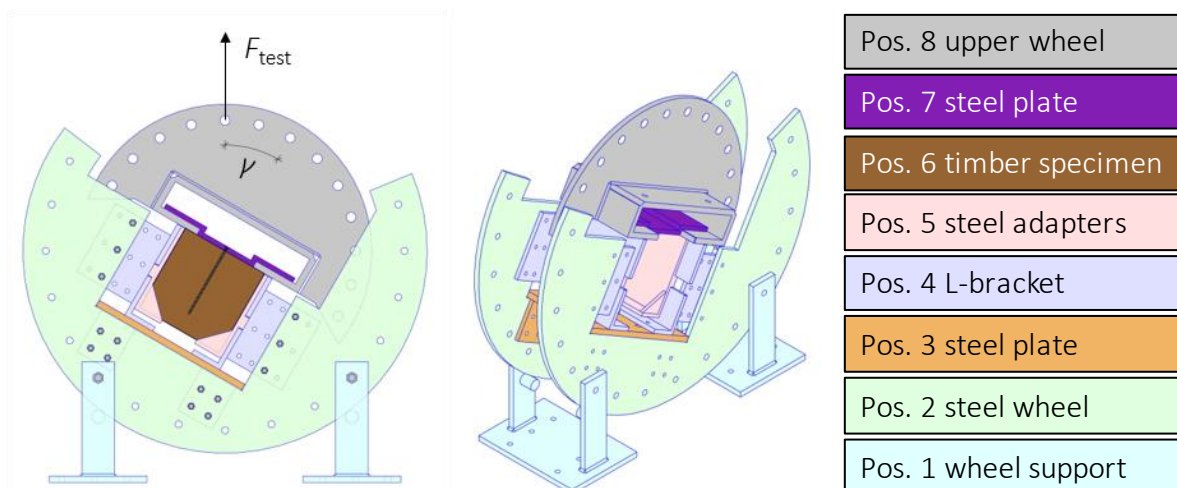
Figure 2.1. Test configuration with the single components in different colouring

The displacement-controlled force application takes place via a vertical movement of the upper 'steel wheel' (Pos. 8), which is connected to the test machine with a bolt. The specific shape of the upper steel wheel's centre bases on an idea of Jockwer et al. (2014) and shall enable also the testing of timber-to-timber connections with $t_1 \leq 90$ mm in future.

The present tests were conducted with a F_{10} / F_{40}-hysteresis loop. The determination of force-displacement relationships for the two main load directions parallel ($\gamma = 90\,°$) and perpendicular to the specimen surface ($\gamma = 0\,°$) demanded the installation of one (axial loading) to three (combined loading; rotation of the steel plate with respect to the timber surface) LVDTs on each side of the timber specimen, c. f. Figure 2.2.

Figure 2.2. Applied devices for way measurement in case of axial (left), lateral (middle) and combined loading (right)

2.3.2 Post-processing

Note: The following is restricted to the test results discussed in Section 3. More details are given in Burtscher (2021). The axial and lateral force components F_{ax} and F_v were determined according to Equation (4) for each applied load-to-surface angle γ. In accordance to EN 26891 (1991), F_{test} was defined as force maximum up to a (global) displacement of $w \leq 15$ mm.

With regard to the deformations w_{ax} and w_v, the rotation of the steel plate with respect to the timber surface disabled a direct adoption of the measurements in the related directions. Thus, Equation (5) was derived, which describes the line vector S ($w_{v,cor} | w_{ax,cor}$) of the screw head during the load test (see also Figure 2.3):

$$S = \begin{bmatrix} w_{v,cor} \\ w_{ax,cor} \end{bmatrix} = \begin{bmatrix} \dfrac{-\Delta w_a \cdot \left(w_1^2 - w_1 \cdot w_2 + \Delta w_a \cdot w_3\right)}{\Delta w_a^2 + \left(w_1 - w_2\right)^2} \\ \dfrac{\Delta w_a \cdot \left(\Delta w_a \cdot w_1 + \left(w_2 - w_1\right)\cdot w_3\right)}{\Delta w_a^2 + \left(w_1 - w_2\right)^2} \end{bmatrix} + \begin{bmatrix} w_{AS} \cdot \left(1 + \dfrac{\left(w_1 - w_2\right)}{\Delta w_a^2}\right)^{-1/2} \\ \dfrac{w_{AS} \cdot \left(w_1 - w_2\right)}{\Delta w_a} \cdot \left(1 + \dfrac{\left(w_1 - w_2\right)}{\Delta w_a^2}\right)^{-1/2} \end{bmatrix} \quad (5)$$

With

    Δw_a .... distance between the vertical LVDTs perp. to the screw axis

    w_1 .... measured $w_{ax,1}$ of the vertical LVDT close to the screw axis + $t_1/2$

    w_2 .... measured $w_{ax,2}$ of the vertical LVDT at $\Delta w_a + w_1$

w_3 ……. measured w_v of the horizontal LVDT + w_{AS}

w_{AS} ……. distance between the steel plate's centre and the brass
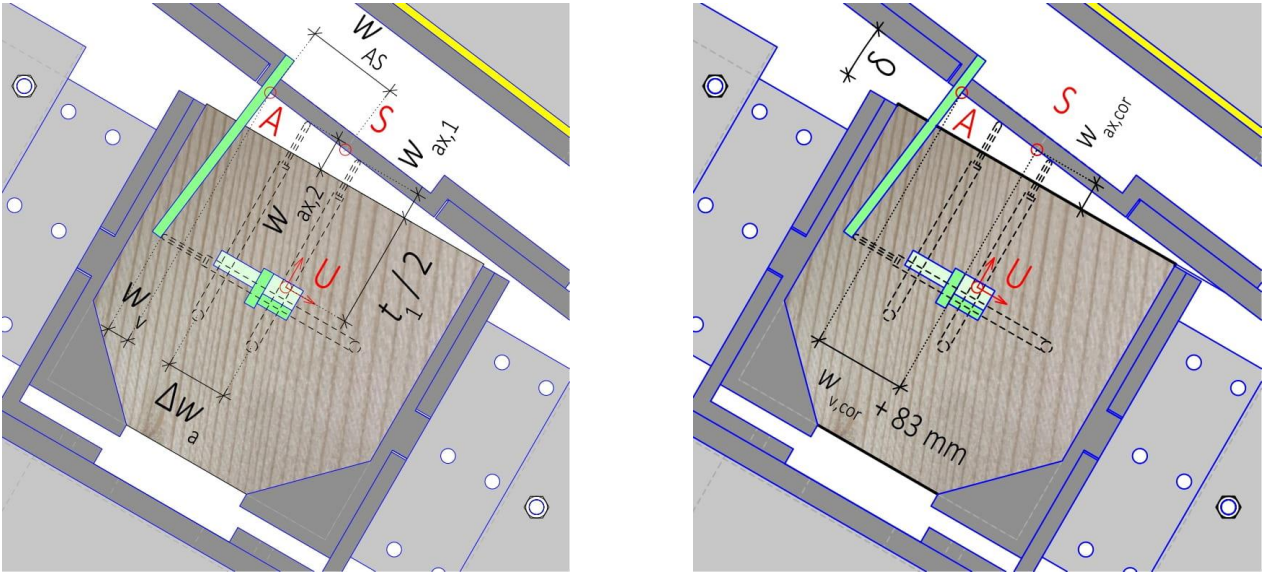
Figure 2.3. Relevant deformation parameters (left: input parameter; right: results of Equation 5)

With the corrected displacements $w_{ax,cor}$ and $w_{v,cor}$ according to Equation (5) the stiffness properties $K_{ser,ax}$ and $K_{ser,v}$ were determined by means of regression analysis in the linear-elastic part of the force-displacement-relationships. Thereby, the unloading and reloading phase of the hysteresis loop were ignored. The final extreme value treatment was done according to Tukey's criteria for statistical outliers (values outside the inter-quartil-range (IQR) ± 1.5-times the IQR) on logarithmised data sets and by means of box-plots.

3   Results and Discussion

3.1   General overview

The main statistics for the moisture content u, the density ρ_{12} and the maximum load per test (up to w = 15 mm), F_{test} are given in Table 3. As a basis of the discussion in Section 3.2, both, the observed failure mode (FM_{test}) and the failure mode predicted by the theoretical approach (FM_{pred}, minimum of (c), (d), (e) in Equation 3) are included as well. Concentrating on the physical timber properties, there are comparable homogeneous moisture contents u_{mean} and densities $\rho_{12,mean}$ for all test series. The maximum deviation to the overall average density of 427 kg/m³ is approx. 4.5 %. In contrast is the timber densities' dispersion; here, significantly different values for CV[ρ_{12}], varying between 1.6 % and 9.5 %, can be observed, which is predominately caused by the comparatively few number per test series. Nevertheless, the relations of the average moisture contents and densities between the test series allow a comparison of test results without any further adjustments.

Table 3. Main statistics of all test series, including the observed and predicted failure modes (FM)

	ID	n	ε	α	γ	λ	u_{mean}	$\rho_{12,mean}$	CV[ρ_{12}]	$F_{test,mean}$	CV[F_{test}]	FM_{pred}	FM_{test}
	[-]	[-]	[°]	[°]	[°]	[-]	[%]	[kg/m³]	[%]	[kN]	[%]	[-]	[-]
axial	15	9	90	-	0	13	9.5	428	3.0	15.7	5.6	-	-
	16	12	30	-	0	13	10.3	425	4.8	12.3	11.9	-	-
	17	12	60	-	0	13	10.3	422	5.7	14.9	12.5	-	-
	18	8	0	-	0	13	10.4	425	1.8	8.7	20.3	-	-
combined	19	11	90	0	30	5	8.2	421	7.1	5.2	7.1	d	c
	20	11	90	0	30	13	8.8	416	5.4	13.2	8.9	e	e
	21	11	90	0	30	21	8.7	424	4.5	20.1	7.3	e	e
	22	10	90	0	30	28	8.8	443	4.7	21.1	2.0	e	d
	23	9	30	60	30	5	8.4	413	3.8	3.5	7.0	c	c
	24	11	30	60	30	13	8.7	413	5.1	7.9	12.5	e	e
	25	11	30	60	30	21	9.5	428	5.4	13.6	11.8	e	e
	26	9	30	60	30	28	9.3	425	1.7	19.2	4.7	e	4d, 5e
	27	11	60	30	30	5	8.4	418	6.1	4.2	12.9	d	c
	28	13	60	30	30	13	8.7	435	7.8	11.5	13.5	e	e
	29	11	60	30	30	21	9.8	442	5.3	19.3	11.8	e	4d, 6e
	30	13	60	30	30	28	8.7	434	4.2	21.0	1.6	e	d
	31	9	0	90	30	5	8.3	408	2.7	2.4	11.2	c	c
	32	9	0	90	30	13	8.6	417	4.3	4.3	16.3	e	c
	33	6	0	90	30	21	9.8	421	3.8	8.6	7.7	e	e
	34	10	0	90	30	28	8.9	417	2.7	11.6	22.6	e	6c, 4e
	35	9	90	0	60	5	9.4	424	3.2	5.8	9.8	d	d
	36	10	90	0	60	13	10.0	432	2.0	12.0	4.5	e	e
	37	11	90	0	60	21	9.6	429	6.3	17.2	6.1	e	2d, 9e
	38	12	90	0	60	28	9.4	424	6.7	17.2	2.4	e	e
	39	9	30	60	60	5	9.4	412	4.0	3.6	7.9	c	d
	40	11	30	60	60	13	9.3	418	3.5	7.0	10.1	e	e
	41	12	30	60	60	21	9.9	417	4.7	10.5	16.9	e	e
	42	9	30	60	60	28	10.0	430	6.3	15.3	5.9	e	4d, 5e
	43	11	60	30	60	5	9.4	416	7.2	4.7	18.0	d	d
	44	11	60	30	60	13	9.7	422	3.2	9.9	7.6	e	e
	45	11	60	30	60	21	9.6	436	3.1	15.6	7.0	e	e
	46	10	60	30	60	28	10.0	440	3.1	17.2	5.1	e	1c, 8d, 1e
	47	11	0	90	60	5	9.1	420	4.9	3.0	11.8	c	d
	48	9	0	90	60	13	9.7	416	2.1	4.6	10.9	e	e
	49	11	0	90	60	21	10.0	439	5.4	5.6	18.7	e	e
	50	9	0	90	60	28	9.7	423	5.1	8.6	19.9	e	e
lateral	51	10	90	0	90	5	9.9	447	9.5	7.0	5.5	d	e
	52	12	90	0	90	13	10.4	429	6.0	11.7	11.9	e	e
	53	13	90	0	90	21	10.1	438	6.5	13.1	9.5	e	d
	54	10	90	0	90	28	10.2	427	4.9	14.6	5.7	e	d
	55	12	30	60	90	5	9.8	420	5.1	3.7	11.1	c	d
	56	10	30	60	90	13	9.8	426	3.3	7.1	9.2	e	d
	57	12	30	60	90	21	9.7	440	4.1	9.7	6.6	e	e
	58	11	30	60	90	28	10.5	442	3.6	11.1	7.4	e	9d, 1e
	59	11	60	30	90	5	10.0	440	5.6	5.9	10.4	d	d
	60	10	60	30	90	13	10.3	430	4.2	10.3	13.1	e	e
	61	12	60	30	90	21	10.6	432	4.7	12.4	11.8	e	e
	62	11	60	30	90	28	9.7	442	5.1	13.4	10.5	e	d
	63	12	0	90	90	5	9.9	426	4.1	2.8	6.3	c	d
	64	9	0	90	90	13	9.9	417	1.6	4.8	12.0	e	e
	65	8	0	90	90	21	9.4	427	1.6	6.0	14.7	e	e
	66	10	0	90	90	28	9.9	424	6.8	7.7	14.4	e	e

3.2   Pure lateral loading

As a by-product of the experimental campaign regarding the load interaction there are 16 test series (ID 51 to 66 in Table 3) with steel-to-timber connections, exposed to pure lateral loading ($\gamma = 90$ °). The results are used to verify the related content of Eurocode 5 in terms of resistance (EYM) and stiffness.

3.2.1   Resistance

The theoretical approach (EYM) to be verified by the experimental results is given in Equation (3). As the European Yield Model serves as a design equation, it inherently takes the different safety factors for steel and timber failure into account. The comparison of single test results with model predictions does not need this modification of the mechanical model behind. Thus, the pre-factor 2.3 of failure mode (e) in Equation (3) was reset to 2.0. The origin of the further model input parameters is discussed in brief:

As a modified form is frequently provided in ETAs of self-tapping screws (c. f. ETA-12/0373 2020 for instance) and recent investigations prove that it is appropriate for the screw type, which was used in the present tests, as well (Gstettner 2019), the empirical approach from Blaß et al. (2006) was applied to determine the embedment strength $f_{h,1}$ of each test specimen, see:

$$f_{h,1} = \frac{0.022 \cdot \rho_{12}^{1.24} \cdot d^{-0.3}}{2.5 \cdot \cos^2 \varepsilon + \sin^2 \varepsilon}. \tag{6}$$

Worth mentioning, nominal values for d and ε and the measured density ρ_{12} were used. In case of the yield moment, a doubtful rotation measurement disabled the consideration of the experimentally determined M_y. As alternative, the mechanical approach by Ringhofer and Schickhofer (2019), which bases on the screw's tensile capacity f_{tens}, was applied (note: M_y as $M_{z,pl,pred}$; bending about the screw's weaker z-axis). The axial resistance F_{ax} was determined by means of Equation (2) with the screw's steel tensile capacity as upper limit. Thereby, the withdrawal parameter f_{ax} was gained from the axial load tests for the specific insertion angle ε. Friction was considered by $\mu = 0.25$. Worth mentioning, the Eurocode 5 regulation for the upper limit of the 'rope effect' $\mu \cdot F_{ax} \leq F_v$ (without $\mu \cdot F_{ax}$) was ignored.

Figure 3.1 compares the gained test results with the predicted values according to (modified) Equation (3). Concentrating on the left scatterplot, wherein the resistance $F_{v,pred}$ was calculated as a minimum of failure modes (c) to (e), a fairly good agreement between $F_{v,test}$ and $F_{v,pred}$ is given. This is in fact interestingly since only the half of the observed failure modes FM_{test} coincides with the ones with minimum resistance (FM_{pred}). These deviations between FM_{test} and FM_{pred} especially occur for configurations with low and high λ and for perpendicular-to-grain insertion rather than for parallel-to-grain insertion, c. f. Table 3. The deviating failure modes for configurations with low insertion lengths (small λ) do not lead to a remarkable difference between $F_{v,test}$

and $F_{v,pred}$. This is shown in Figure 3.1 (right), wherein $F_{v,pred}$ was calculated with FM_{test}, and can be explained by the fact, that $F_{v,pred}$ of test series with $\lambda = 5$ is frequently located in the transition between failure modes (c) and (d) or (d) and (e).

In case of $\lambda \approx \{21, 28\}$ and $\varepsilon > 0\,°$, the situation is completely different in form of a significant overestimation of test results. The reason therefore is seen in the behaviour of FM_{test} in dependence of λ: For the change of $\lambda = 5 \rightarrow 13$ (21) the expected increase in the order of FM_{test} is given, which means that the number of plastic hinges along the inserted screw thread increases from 0 to 1 and from 1 to 2 respectively. For the change of $\lambda = 13$ (21) $\rightarrow 21$ (28), now a decrease of the number of plastic hinges from 2 to 1 can be observed. It is worth mentioning that this one plastic hinge was always located at the transition between steel plate and timber specimen and that screw (steel) failure occurred for the related test series.

In fact, this contradicts the theory behind the EYM and is probably caused by the applied fastener type. Self-tapping screws have a high tensile strength ($\approx 1{,}200$ MPa) but a comparatively low ductility (Ringhofer and Schickhofer 2019). Given a long insertion length, a high axial loadbearing capacity F_{ax} leads to a dominant share of the 'rope effect' on F_v. Unfortunately, this goes along with an interaction of high tensile (due to F_{ax}), bending and shear (due to F_v) stresses in the area of the plastic hinge. Further taking a comparatively low plastic reserve of the screw into account, it is assumed that the steel failure must occur before a second plastic hinge can be formed, i. e. the failure mode (d) has not reached its upper limit of resistance yet.
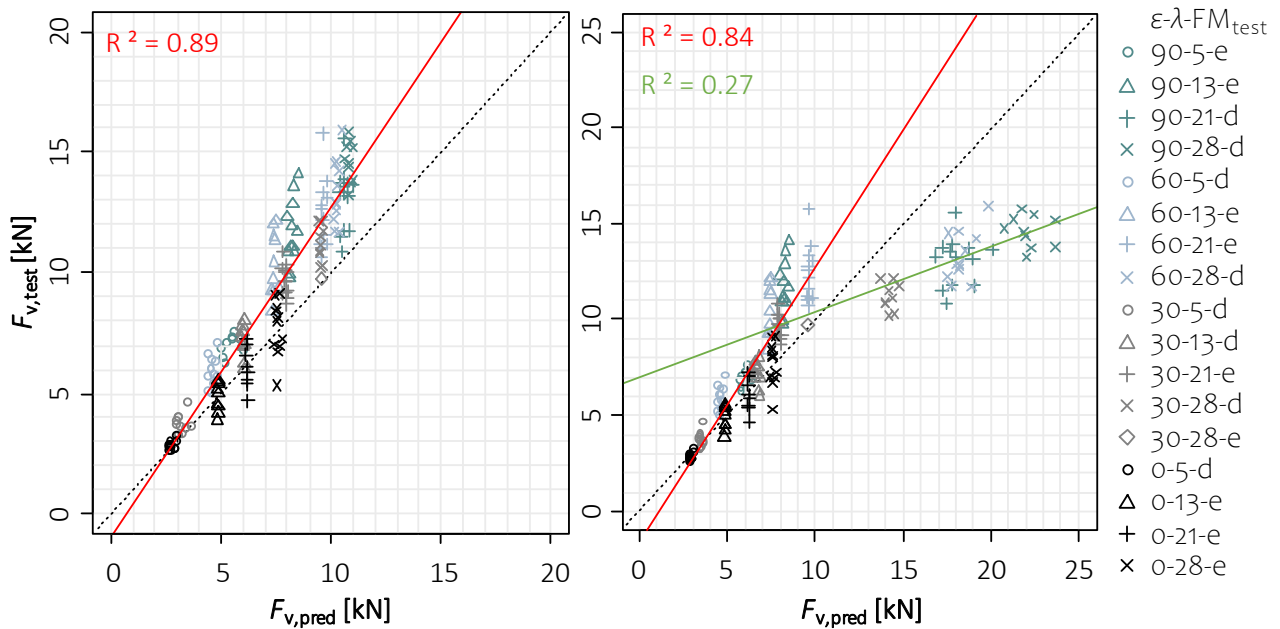

Figure 3.1. Test results vs. model predictions (left: $F_{v,pred}$ for FM_{pred}; right: $F_{v,pred}$ for FM_{test})

3.2.2 Stiffness

Besides resistance, Eurocode 5 also provides a theoretical approach to determine the stiffness $K_{ser,v}$ of laterally loaded steel-to-timber joints with self-tapping screws (Equation 7), which shall be verified in the frame of this subsection.

$$K_{ser,v,EC5} = 2 \cdot \frac{\rho_{12}^{1.5} \cdot d}{23} \cdot \qquad (7)$$

As there is a remarkable deviation in the parameter treatment, it was decided to consider the approaches given in SIA 265 (2012) to determine $K_{ser,v}$ of laterally loaded dowels (Equation 8) and nails (Equation 9) for the present comparison as well:

$$K_{ser,v,SIA,SD} = 6(3) \cdot \rho_{12,k}^{0.5} \cdot d_{ef}^{1.7}, \text{ and} \qquad (8)$$

$$K_{ser,v,SIA,NA} = 120(60) \cdot d_{ef}^{1.7}, \qquad (9)$$

for parallel-to-grain (perpendicular-to-grain in brackets) loading and with $d_{ef} = 1.1 \cdot d_s$ (shank diameter). The comparison between experimentally determined values and the ones calculated with Equation (7) to (9) is given in Table 4. Note: for the majority of tests of two series (ID 59 and 63) a doubtful horizontal displacement measurement had to be observed. Thus, both series were excluded from stiffness data assessment.

In fact, a significant overestimation of the measured stiffness is given for all applied models but especially for Equation (7) according to Eurocode 5 with a maximum difference $\Delta_{EC5} = 4,561 \%$. While the magnitude of $\{\Delta_{EC5}, \Delta_{SIA}\}$ remains as an open question (which is possibly influenced by the method to determine $K_{ser,v}$, c. f. Section 2.3.2), its variability can be explained by the non-consideration of t_1, ε (Equations 7 to 9) and α (Equation 7) in the theoretical approaches, while a related impact can be observed for the test results.

Table 4 Comparison of experimentally and empirically determined lateral stiffness $K_{ser,v}$

ID	n	$K_{ser,v,mean}$	CV[$K_{ser,v}$]	$K_{ser,v,EC5}$	Δ_{EC5}	$K_{ser,v,SIA,SD}$	$\Delta_{SIA,SD}$	$K_{ser,v,SIA,NA}$	$\Delta_{SIA,NA}$
[-]	[-]	[kN/mm]	[%]	[kN/mm]	[%]	[kN/mm]	[%]	[kN/mm]	[%]
51	8	1.07	20.7	6.57	614	2.46	230	2.33	218
52	7	1.18	19.5	6.18	524	2.41	204	2.33	197
53	12	1.26	24.6	6.38	506	2.44	194	2.33	185
54	11	1.50	17.4	6.14	409	2.40	160	2.33	155
55	11	0.43	19.9	6.00	1,395	1.59	370	1.55	360
56	10	0.55	22.2	6.12	1,113	1.60	291	1.55	282
57	11	0.79	15.6	6.42	813	1.63	206	1.55	196
58	12	0.89	18.0	6.46	726	1.63	183	1.55	174
60	6	0.84	21.0	6.21	739	2.01	239	1.94	231
61	10	0.98	10.5	6.25	638	2.02	206	1.94	198
62	8	1.17	14.0	6.46	552	2.04	174	1.94	166
64	10	0.38	17.2	5.93	4,561	1.19	313	1.16	305
65	9	0.45	17.3	6.14	1,364	1.20	267	1.16	258
66	6	0.58	4.5	6.07	1,047	1.20	207	1.16	200

3.3   Combined Loading

The test results of steel-to-timber connections with self-tapping screws (n = 1), subjected to combined axial and lateral loading, are shown in Figure 3.2 in dependence of the insertion length t_1 (or slenderness λ) and the axis-to-grain angle ε. For a better understanding of the impact of load interaction, several lines as the outcomes of Equation (1) are illustrated as well. Thereby, their colour represents the related insertion length t_1 (or slenderness λ), while the line type depends on the size of a = b = {1.0, 1.5, 2.0} as varied model parameters. As the focus of this comparison is on the load interaction itself (γ = {30, 60} °), the limit resistances F_v (γ = 90 °) and F_{ax} (γ = 0 °) were either adopted from the test results ($F_{v,test,i}$) or again determined by means of Equation (2) ($F_{ax,test,i}$), c. f. Section 3.2.1.
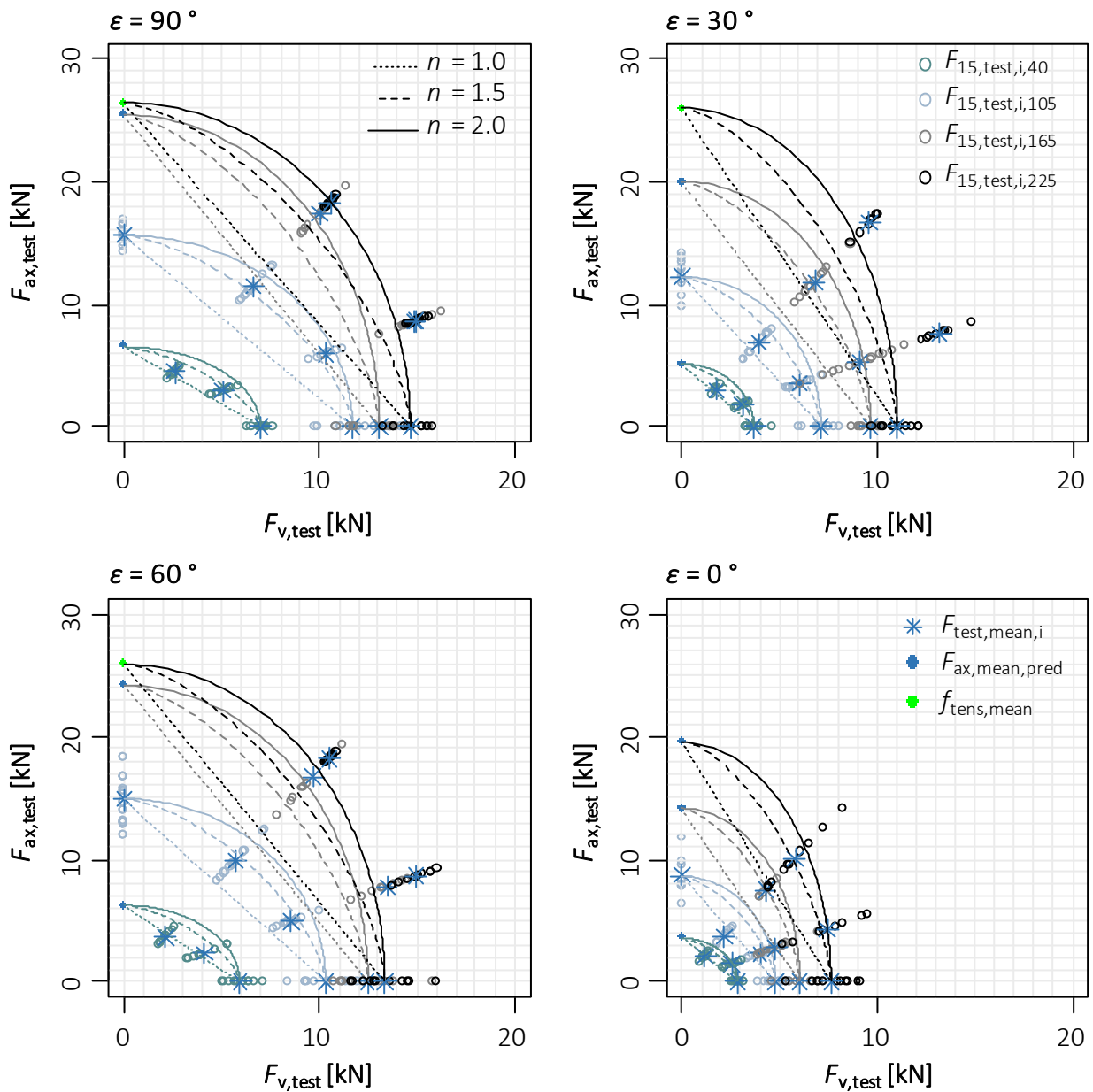

Figure 3.2. Test results and model comparison for combined loading in dependence of the inserted screw length t_1 and the axis-to-grain angle ε

With regard to the comparison between test results and the outcomes of Equation (1), the following is worth being discussed:

First, an increasing slenderness λ coincides with increasing a and b as best model fit of the test results. While the results of test series with $\lambda = 5$ (and partially 13) are well described by power values of $1.0 \div 1.5$, the ones of test series with $\lambda \approx 21$ and 28 need power values of $1.5 \div 2.0$ and even more than 2.0 for a good agreement. This is well in line with the findings made by Laggner et al. (2016) for a $d = 6$ mm screw with $\lambda \approx 25$ but in a clear contrast to the ones made by Blaß et al. (2006) for small λ, c. f. Section 1.

Second, apart from the parallel-to-grain insertion ($\varepsilon = 0$ °) this is irrespective of both load-to-grain and axis-to-grain angels α and ε. In case of $\varepsilon = 0$ ° however, a sudden and brittle splitting failure of several timber specimens, exposed to combined axial and lateral loading, had to be observed. This phenomenon, which took place at much higher end-grain and edge distances than the minimum ones given in Eurocode 5, decreased the related resistances and consequently the best fitting power values {a, b} by far. Interestingly, this only occurred for combined loading of screws in timber's end grain, while in case of pure axial or pure lateral loading, the expected failure modes (withdrawal, bending, embedment) were observed.

4   Summary and Conclusion

The versatile application field of system connectors with self-tapping screws, secondary loading scenarios on screwed connections in general or stress combinations in possible crack zones of screw reinforcements cause additional lateral loads on self-tapping screws, which are intended for pure axial loading. In such cases, current design codes provide a quadratic load interaction for verification.

This regulation for self-tapping screws was adapted from profiled nails and does not have an own broad experimental basis. Thus, it was decided to carry out a comprehensive test programme related. It focused on the impact of selected parameters such as the load-to-surface angle (representing the share of F_{ax} and F_v), the load-to-grain and axis-to-grain angles (representing timber's orthotropic characteristics) and the screw's insertion length (or slenderness) on the behaviour of steel-to-timber connections with $n = 1$ self-tapping screw, which are subjected to combined axial and lateral loading. The present paper is a summary of these efforts made by Burtscher (2021) and especially concentrates on the methodology applied for test execution and the gained results. With regard to the latter, the following main conclusions are drawn:

On the face of it, the results of laterally loaded screws are quite closely located to predictions by the EYM – if the missing agreement between assumed (minimum of (c) to (e)) and observed failure modes is ignored. Looking deeper into this, especially the resistance of screwed connections with high t_1 (or λ) is significantly overestimated by the EYM if the observed failure mode is considered instead. Interestingly, the latter is characterised by a decrease of the number of plastic hinges if compared to configurations with smaller t_1. The interaction of normal (bending, tensile) and shear stresses at the

transition between steel plate and timber member (= plastic region) in combination with the self-tapping screw as a high-strength but low-ductile steel product is regarded as the reason for this phenomenon. The extension of the EYM, taking the MNV-interaction in case of hardwood joints or high-strength fasteners into account (as indicated in Blaß et al. 2017), is seen as a mandatory task for code development.

With regard to the stiffness $K_{ser,v}$ of laterally loaded screws, the magnitude of the test results has to be internally checked once more. Nevertheless, they clearly point out that the currently provided theoretical models do not consider parameters with a significant impact on the size of $K_{ser,v}$, i. e. t_1, and both angles α and ε.

For self-tapping screws subjected to combined axial and lateral loading, two main outcomes are worth being highlighted: first, a clear, positive relationship between the insertion length t_1 (λ) and the power values $\{a, b\}$ according to Equation (1) is given. Although there is a smooth transition between failure mode and the size of $\{a, b\}$, under the premise 'ease-of-use' a reasonable (simplified) approach for a related modification of Equation (1) could be $a = b = \{1.0, 1.5, 2.0\}$ for failure modes $\{c, d, e\}$ according to Eurocode 5. And second, with the present test configuration, several timber splitting failures were observed for combined loaded self-tapping screws, inserted in timber's end grain. Thus, an investigation of end-grain joints with axially loaded self-tapping screws regarding an unplanned transmission of additional lateral loads is strongly recommended.

5   References

Bejtka, I; Blaß, HJ (2002): Joints with inclined screws. In: Proceedings of the 35th CIB W18 Meeting, Kyoto (Japan), Paper CIB-W18/35-75-5.

Blaß, HJ; Bejtka, I; Uibel, T (2006): Tragfähigkeit von Verbindungen mit selbstbohrenden Holzschrauben mit Vollgewinde. No. 4 in ‚Karlsruher Berichte zum Ingenieurholzbau', University of Karlsruhe. (in German)

Blaß, HJ; Sandhaas, C; Meyer, N (2017): Steel-to-timber connections: Failure of laterally loaded dowel-type fasteners. In: Proceedings of the 4th INTER Meeting, Kyoto (Japan), Paper INTER/50-07-1.

Burtscher, M (2021): Experimentelle Untersuchung des Tragverhaltens mehrachsig beanspruchter Holzschrauben. Master's Thesis, Graz University of Technology. (in German)

Ehlbeck, J; Siebert, W (1984): Tragverhalten von Nagelverbindungen bei gleichzeitiger Beanspruchung auf Abscheren und Ausziehen. Research report, University of Karlsruhe. (in German)

EN 1995-1-1:2004 + AC:2006 + A1:2008 + A2:2014 (2014): Eurocode 5: Design of timber structures – Part 1-1: General – Common rules and rules for buildings. CEN.

EAD 130118-01-0603 (2019): Screws and threaded rods for use in timber constuctions.

EN 338 (2016): Structural timber – Strength classes.

EN 1382 (2016): Timber structures – Test Methods – Withdrawal capacity of timber fasteners.

EN 383 (2007): Timber structures – Test methods – Determination of embedment strength and bedding values for pin-shaped fasteners.

ETA-12/0373 (2020), Schmid Schrauben Hainfeld GmbH: Schmid screws RAPID, STAR-DRIVE and SP, European Technical Assessment, OIB. (in German)

EN 14592 (2017): Timber structures – Dowel-type fasteners – Requirements.

EN 409 (2009): Timber structures – Test methods – Determinatioin oft he yield moment of dowel type fasteners.

EN 26891 (1999): Timber structures – Joints mad with mechanical fasteners – General principles for the determination of strength and deformation characteris-tics.

Gstettner, M (2019): Experimentelle Untersuchung des Tragverhaltens lateral beanspruchter, selbstbohrender Holzschrauben. Master's Thesis, Graz University of Technology. (in German)

Jockwer, R; Steiger, R; Frangi, A (2014): Design model for inclined screws under varying load to grain angles. In: Proceedings of the 1st INTER Meeting, Bath (United Kingdom). Paper INTER/47-7-5.

Laggner, TM; Flatscher, G; Schickhofer, G (2016): Combined loading of self-tapping screws. In: Proceedings of the 14th World Conference on Timber Engineering WCTE2016, Vienna (Austria).

McLain, TE; Carroll, JD (1990): Combined load capacity of threaded fastener – wood connections. Journal of Structural Engineering 116(9), 2419-2432.

Munse, WH; Cox, HL (1956): The Static Strength of Rivets Subjected to combined Tension and Shear. Research report, University of Illinois. Engineering Experiment Station Bulletin No. 437.

Pirnbacher, G; Brandner, R; Schickhofer, G (2009): Base parameters of self-tapping screws. In: Proceedings of the 42nd CIB W18 Meeting, Dübendorf (Switzerland). Paper CIB-W18/42-7-1.

Reyer, E; Linzner, P (1993): Tragfähigkeit von Hirnholznägeln und Hirnholzschrauben unter Ausziehbelastung, Abscherbelastung und kombinierter Belastung zur Herstellung rationeller Holzverbindungen. Reserach report, Ruhr-university of Bochum. (in German)

Ringhofer, A (2017): Axially Loaded Self-Tapping Screws in Solid Timber and Laminated Timber Products. In: Schickhofer, G; Brandner, R (eds.) Timber Engineering & Technology, TET 5, Verlag der Technischen Universität Graz.

Ringhofer, A; Schickhofer, G (2019): Product Characteristics of Self-Tapping Timber Screws. In: Proceedings of the 6th INTER Meeting, Tacoma (USA), Paper INTER/52-7-1.

SIA 265 (2012): Timber structures. (in German)

6   Acknowledgement

DISCUSSION

The papers was presented by A Ringhofer

H Blass commented that Bejtka in 2006 performed embedment tests with axial loads. A Ringhofer said the work was referenced in the paper but they could not explain the difference in findings. It could be due to the smaller size of specimens compared to those used in the current study.

H Blass commented that the "pure" shear load would have axial load due to rope effect. As such higher axial loads in the screw exist, he asked how would one consider this in design. A Ringhofer agreed and stated that this has to be considered via M+V interaction.

R Jockwer asked if one would apply both the axial load and the rope effect in design. A Ringhofer responded that the information as shown in the graphs in the paper is based on test results so both effects exist. Modifying the Eurocode design model based on M+V interaction would solve the problem.

P Dietsch commented that the printed version of the paper will be in B+W so coloured figures will not be available. He noted that Kser values were low compared to Eurocode 5. He asked if this is caused during the drilling, e.g. cutting of fibers, and that such large differences should be considered. A Ringhofer stated that drilling effect should have increased the stiffness via densification of the wood by the screws. For example, with predrilling withdrawal stiffness would decrease compared to non-predrilled cases.

S Shen asked whether these factors could be applied to non-smooth shank nails. A Ringhofer stated that in principle this analogy should be applicable.

A Frangi asked about group effect and if the information would be applicable for groups of connectors. A Ringhofer stated that a limited number of tests with one screw length was done showing similar trend.

Rigid Glulam Joints with Glued-in Rods subjected to Axial and Lateral Force Action

Simon Aicher and Kai Simon

Materials Testing Institute, Department of Timber Constructions, University of Stuttgart

1   Introduction

Glued-in steel rods in glulam (GLT) oriented parallel or slightly inclined to grain direction allow for the transfer of high axial loads hereby enabling rigid joints to either timber members or massive concrete or steel abutments/members. The latter connections, termed integral joints and regarded here in first instance allow for economic timber solutions for clamped columns and members e.g. of bridge superstructures. In each mentioned application, with regard to a high moment transfer, the rods are placed at the minimum permissible distances to the bending tension and compression edges of the GLT beam/column. In all cases of reversed loading the rod edge distances must be equal. Especially for plate-type bridge deck beams made from block-glued GLT with a larger edge aspect ratio where the tension and compression loaded rods are placed oppositely at the narrow cross-section side a closest possible edge distance is indispensable in order to establish a sufficiently high internal lever arm. Regarding the transfer of shear forces in the joint by lateral rod forces, however short rod distances to the loaded edge are detrimental as the evolving stresses perpendicular to grain direction lead to premature splitting and consequently low lateral resistance. The shear force capacity can be significantly increased by reinforcements, e.g. by self-tapping screws arranged orthogonal to the rod and member axis, not regarded in this paper (see below).

Irrespective of the high structural potential of moment rigid glulam or CLT joints especially for clamped columns, floors and bridge superstructure (plate-type) beams this construction technology is not widely used so far. This is due to several reasons, mainly: More demanding labour experience for bonding operations, as e.g. compared to manufacture of today's prevailing mechanical joints, more strict regulatory restrictions and rather little research and field experience in such joints. In order to establish a broader

knowledge base beyond exclusive uni-axial or lateral force tests, hereby comprising known, standardized and new calculation approaches an extensive research program is currently conducted at MPA, Department of Timber Constructions, within the frame of the excellence cluster INTCDC (Integrative Computational Design and Construction for Architecture) at Stuttgart University. The research program covers monotonic, reversed and cyclic loading of unreinforced and differently reinforced joints based on glued-in rods. This paper reports in a first contribution on unreversed ramp-load behaviour and design of unreinforced glued-in rod joints.

2 Review of literature known experimental results

The presented literature review is by far not exhaustive and may unintentionally omit important contributions on the short and long-term mechanical behaviour of joints with steel rods glued-in parallel to grain and subjected to either pure axial or almost pure lateral rod forces. Pioneering work on glued-in rods has been performed by *Edlund* (1975), *Riberholt* (1977; 1988), *Möhler and Hemmer* (1981), *Johansson et al.* (1996). In the follow-up contributions were reported by *Aicher et al.* (1999), *Gustafsson et al.* (2001) and *Blaß and Laskewitz* (2001). The duration of load effect was reported by *Aicher and Dill-Langer* (2001). On the theoretical side the works by Gustafsson and Serrano have provided most fundamental input for axially loaded rods. Noteworthy later research was published i.a. by *Steiger et al.* (2006), *Dietsch* (2012), *Jockwer* (2014) and *Dietsch and Brandner* (2015).

Regarding the bond line shear resistance of axially loaded rods glued-in parallel to grain a comprehensive compilation of published data has been given by *Aicher and Stapf* (2017) and is shown in Figure 1(a) for experimental tests with spruce. The pronounced bond line shear strength decrease with increasing bond line length is evident and reflected in national standards (e.g. DIN EN 1995-1-1 / NA (2013)), Technical approvals (e.g. Z-9.1-705 (2017)) and the final draft *Connections* of the new EC5-1-1 (2021).

Concerning the lateral capacity of rods glued-in parallel to grain much less research work is found in literature. Most important are the contributions by *Riberholt* (1986), *Möhler and Hemmer* (1981) and *Blaß and Laskewitz* (2001). The results of these investigations are compiled in Figure 1(b) altogether with some existent or proposed design approaches. The most important feature of the lateral capacity characteristics of a rod glued-in parallel to grain is its pronounced increase with rising distance from the loaded beam edge, $a_{2,t}$ (normalized: $\alpha = a_{2,t}/h$, with h = beam height). This sensible mechanical behaviour is very well described by a design approach by *Blaß and Laskewitz* (2001) based on the solution from *Ehlbeck and Görlacher* (1983) for a mechanical joint loaded perpendicular to the grain. It is further evident from Fig. 1(b) that the present German design approach (DIN EN 1995-1-1 / NA, 2013) and alike the present proposal for the new EC5-1-1 *Connections* (2021) do not take into consideration the aspect of variable edge distances at all and aim at the lowest capacity, being related to edge-close rods.
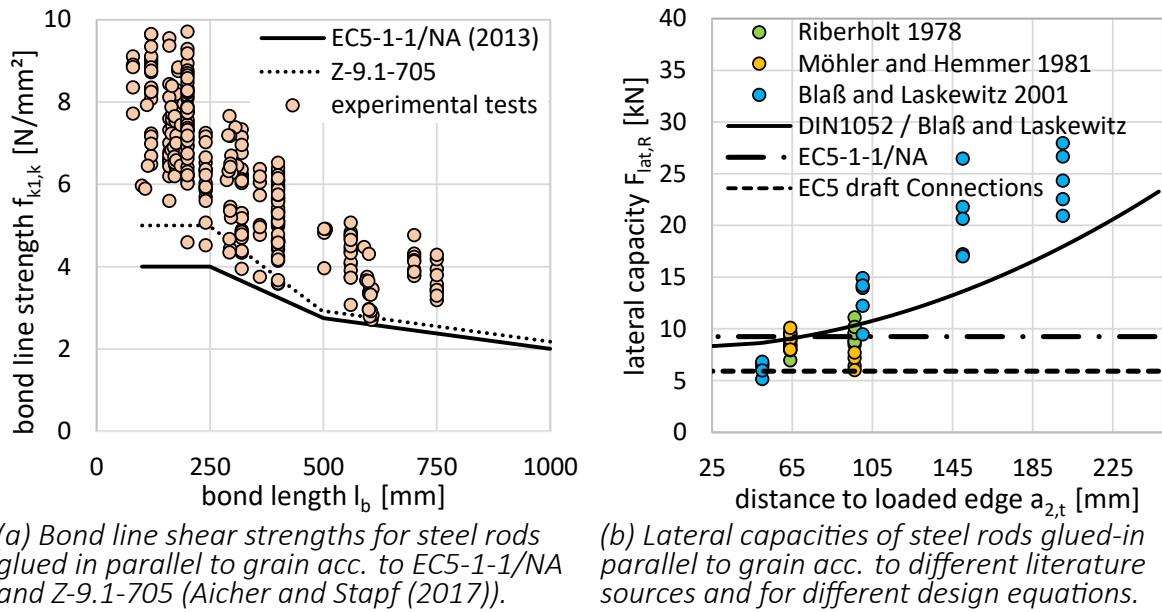
(a) Bond line shear strengths for steel rods glued in parallel to grain acc. to EC5-1-1/NA and Z-9.1-705 (Aicher and Stapf (2017)).

(b) Lateral capacities of steel rods glued-in parallel to grain acc. to different literature sources and for different design equations.

Figure 1

3 Review of design approaches

In the following the design approaches for steel rods glued-in parallel to grain and loaded axially and / or laterally according to DIN EN 1995-1-1 / NA (2013), the draft *Connections* of EC5-1-1 (2021) and the lateral capacity design according to DIN 1052 (2004) and *Blaß and Laskewitz* (2001) are specified and compared.

3.1 Design approach acc. to DIN EN 1995-1-1 / NA (2013)

3.1.1 Axial load capacity

The axial load-carrying capacity is given by

$$F_{ax,Rk} = min\left\{f_{y,k} \cdot A_{ef}; \quad \pi \cdot d \cdot l_b \cdot f_{k1,k}\right\} \tag{1}$$

where $f_{y,k}$ is the characteristic yield strength of the rod, A_{ef} is the nominal stress area of the steel rod, $l_b = l_{ad}$ is the glued-in length of the rod, d is the nominal diameter of the rod and $f_{k1,k}$ is the characteristic bond line shear strength given in table NA.12 of DIN EN 1995-1-1 / NA (2013) which is graphically shown in Figure 1(a), too. The graph also shows the bond line shear strength related to service class 1 for the specific adhesive (Z-9.1-705, 2017) used in the experiments reported here, where a higher bond-line strength is permissible.

3.1.2 Lateral load capacity

For lateral loading the design rules refer to sections 8.2 and 8.5 of EN 1995-1-1 (2010) were the design for laterally loaded steel bolts is described. For rigid connections between timber and steel or concrete, e.g. a clamped column, the design rules for steel-to-timber

connections with dowel-type fasteners apply. These specifications differ whether it is a connection to a thin or a thick steel plate (thin: thickness of steel plate ≤ 0.5·d; thick: thickness ≥ d and hole tolerance < 0.1·d; at 0.5 · d to d a linear interpolation applies). The equations for the load-carrying capacities according to section 8.2.3 of EN 1995-1-1 (2010) are

$$
F_{lat,Rk,thin} = min \begin{cases} \text{(a): } 0,4 \cdot f_{h,k} \cdot t_1 \cdot d \\ \text{(b): } 1,15 \cdot \sqrt{2 \cdot M_{y,Rk} \cdot f_{h,k} \cdot d} \end{cases} \tag{2}
$$

$$
F_{lat,Rk,thick} = min \begin{cases} \text{(a): } f_{h,k} \cdot t_1 \cdot d \\ \text{(b): } f_{h,k} \cdot t_1 \cdot d \cdot \left[\sqrt{2 + \frac{4M_{y,Rk}}{f_{h,k}\cdot d\cdot t_1^2}} - 1 \right] \\ \text{(c): } 2,3\sqrt{M_{y,Rk} \cdot f_{h,k} \cdot d} \end{cases} \tag{3}
$$

where $F_{lat,Rk}$ is the characteristic load-carrying capacity per shear plane and fastener, t_1 is the smaller value of either the thickness of the timber or the penetration depth (in mm), d is fastener diameter (in mm), $M_{y,Rk}$ is the characteristic fastener yield moment (in Nmm) and $f_{h,k}$ is the characteristic embedment strength of the timber (in N/mm^2). The embedment strength $f_{h,k}$ for rods bonded in parallel to the grain and loaded perpendicular to grain is

$$
f_{h,0,90,k} = 0,125 \cdot 0,082 \cdot (1 - 0,01 \cdot d) \cdot \rho_k \tag{4}
$$

where ρ_k is the characteristic timber density (in kg/m^3). The yield moment of the steel rod is

$$
M_{y,Rk} = 0.3 \cdot f_{u,k} \cdot d^{2,6} \tag{5}
$$

where $f_{u,k}$ is the characteristic tensile strength (in N/mm^2).

3.1.3   Interaction of lateral and acial capacities

For combined lateral and axial loads, acting on glued-in rods a quadratic interaction is specified:

$$
\left(\frac{F_{lat,Ed}}{F_{lat,Rd}}\right)^n + \left(\frac{F_{ax,Ed}}{F_{ax,Rd}}\right)^n \leq 1,0 \quad \text{with n = 2.} \tag{6}
$$

3.1.4   Constructive detailing

Table 1 gives the relevant constructive detailing specifications regarding minimum spacing and edge distances as well as minimum glued-in rod length.

Table 1. Minimum spacings, edge distances and glued-in length of glued-in rods parallel to grain.

	a_2	$a_{2,c}$	$a_{2,t}$
axial loading	5d	2,5d	-
lateral loading	5d	2,5d	4d

$$l_{b,min} = max\left\{0.5 \cdot d^2;\ 10 \cdot d\right\}$$

3.2 Design acc. to Final draft *Connections* for EC5-1-1

3.2.1 Axial load capacity

The design rules for the axial resistance are similar to those given in DIN EN 1995-1-1 / NA (2013) but are appended by further equations. The characteristic resistance is given by the minimum of the bond-line resistance $F_{ax,b,Rk}$ and the resistance of the glued-in rod $F_{ax,rod,Rk}$ as

$$F_{ax,b,Rk} = min\left\{\pi \cdot d \cdot l_{b,ef} \cdot f_{k1,k};\quad E_s \cdot A_s \cdot \varepsilon_{u,timber}\right\} \tag{7}$$

$$F_{ax,rod,Rk} = min\left\{f_{y,k} \cdot A_{ef};\quad 0.9 \cdot f_{u,k} \cdot A_{ef}\right\} \tag{8}$$

where d is the nominal diameter of the bonded-in rod (in mm), $l_{b,ef}$ is the effective rod anchorage length given as $l_{b,ef} = min\left\{l_b;\ 40 \cdot d;\ 1000\ mm\right\}$ (in mm), where l_b is the geometric anchorage length (in mm), $f_{k1,k}$ is the characteristic bond-line strength (in N/mm^2) (same in DIN EN 1995-1-1 / NA (2013) shown in Fig. 1(a)), E_s is the modulus of elasticity of the steel grade of the rod (in N/mm^2), A_s is the nominal stress area for the ribbed rods acc. to EN ISO 898-1 (2013) (in mm^2), $\varepsilon_{u,timber}$ is the failure strain of the timber parallel to grain, given as 2,4 ‰ for softwood, $f_{y,k}$ is the characteristic yield strength of the rod (in N/mm^2) and $f_{u,k}$ is the characteristic ultimate tensile strength of the rod (in N/mm^2).

3.2.2 Lateral load capacity

The characteristic value of the lateral load-carrying capacity $F_{lat,k}$ is specified by

$$F_{lat,Rk} = min\begin{cases} \text{(a): } d \cdot f_{h,k}\left(\sqrt{(l_b + 2 \cdot e)^2 + l_b^2} - l_b - 2e\right) \\ \text{(b): } d \cdot f_{h,k} \cdot \left(\sqrt{e^2 + \frac{2M_{y,k}}{f_{h,k}\cdot d}} - e\right) \end{cases} \tag{9}$$

whereby Eq. 9(a) represents the pure embedment resistance. The equation can be reduced to 9(c): $F_{lat,Rk} = 0.41 \cdot d \cdot f_{h,k} \cdot l_b$ and then coincides for the case of e = 0 with the pure embedment solution of Eq. 2(a), with $t_1 = l_b$.

Eq. 9(b) can be reduced to 9(d): $F_{lat,Rk} = 1.41 \cdot \sqrt{M_{y,k} \cdot f_{h,k} \cdot d}$ which is comparable to Eqs. 2(b) and 3(c). Equation 9(b) has been first derived by *Riberholt* (1988).

3.2.3   Interaction of lateral and axial capacities

A rather conservative linear interaction of lateral and axial capacities is proposed, i.e. Eq. 6 now with n = 1.

3.2.4   Constructive detailing

The spacings and edge distances for glued-in rods parallel to the grain are similar as given in DIN EN 1995-1-1 / NA (2013), see Table 1.

3.3   Lateral force design acc. to Blaß and Laskewitz (2001)

Based on the sensible perception that the lateral load-carrying capacity of a steel rod glued-in parallel to grain in the end grain face represents a tensile perpendicular to grain strength issue, *Blaß and Laskewitz* (2001) have modified an equation given firstly in the former DIN 1052 (2004) and presently in DIN EN 1995-1-1 / NA (2013) for lateral connections where $h_e/h \leq 0.7$ (see below). Said original resistance equation is based on work of *Möhler and Lautenschläger* (1978), *Möhler and Siebert* (1980) and *Ehlbeck and Görlacher* (1983). In order to adjust the equation to the end grain bonded rod situation, very plausible a multiplier of 0.5 was introduced as the tensile perpendicular to grain resistance is exclusively one-sided at the location of the embedded rod. Further, the distance a_r specifying in the original equation the maximum distance of the mechanical fasteners in one row parallel to grain was modified to account for an effective embedment length of the rod (see below). The modified lateral resistance equation reads

$$F_{90,k} = k_s \cdot k_r \cdot \left(6.5 + \frac{18 \cdot h_e^2}{h^2}\right) \cdot \left(t_{ef} \cdot h\right)^{0.8} \cdot f_{t,90,k} \cdot 0.5 \tag{10}$$

where $k_s = max\,\{1;\ 0.7 + 1.4\,a_r/h\}$, a_r is the distance from the end grain face to the plastic hinge of the rod (in mm), $k_r = n/\left(\sum_{i=1}^{n}(\frac{h_1}{h_i})^2\right)$, n is the number of rods, h_i is distance of rod i from the lower edge (in mm), h_e is the distance between the fastener group and the loaded edge (here $a_{2,t}$, (in mm)), h is the height of the beam (in mm), $t_{ef} = min\,\{b;\ 6 \cdot d\}$ is the effective width where b = width of the timber beam (in mm) and $f_{t,90,k}$ is the characteristic value of the tensile strength perpendicular to the grain (in N/mm^2). (Note: for the experimental configurations described below, the parameters of Eq. 10 result in: $a_r = 137mm$, $k_s = 1.38$ and $k_r = 1$.)

3.4 Comparison of the design approaches

The specified design approaches are compared for the specifically investigated connection configurations consisting of a glulam (GL 30h) with width of 80 mm and a depth of 280 mm, one glued-in metrically threaded steel rod with diameter d = 16 mm ($f_{y,k}$ = 640 N/mm²) and bond length $l_{b,ef}$ = 320 mm and a placement of the rod with edge distances of either $a_{2,t}$ = 64 mm or 216 mm, i.e. α_1 = 0.23 and α_2 = 0.77. The specified edge distances apply either to single rods or to pairs of rods necessary to create the moment resistance (see Fig. 2). The eccentricity is e = 5 mm. The characteristic embedment strength of the GLT (ρ_k = 430 kg/m³) acc. to Eq. 4 is $f_{h,0,90,k}$ = 3.7 N/mm², the characteristic yield moment of the steel rod according to Eq. 5 is $M_{y,k}$ = 324.3 Nm and the characteristic bond line shear strength is $f_{k1,k}$ = 3.65 N/mm² acc. to DIN EN 1995-1-1 / NA (2013), compare Figure 1(a).

The axial rod capacity results equally for all specified design approaches in $F_{ax,k}$ = 58.7 kN. The lateral rod capacity is independent of α in case of both, DIN EN 1995-1-1 / NA (2013) and the draft *Connections* of EC5-1-1 (2021). The respective capacities amount to $F_{lat,k,EC5/NA}$ = 9.2 kN in case of a thick steel plate (Eq. 3(a)), applying here (note: $F_{lat,k,EC5/NA}$ = 7.1 kN for a thin steel plate, Eq. 2(b)) and $F_{lat,k,draftEC5}$ = 5.7 kN (Eq. 9(b)), respectively. In case of the *Blaß and Laskewitz* (2001) approach, the respective characteristic lateral capacities are $F_{lat,k(\alpha_1=0.23)}$ = 7.8 kN and $F_{lat,k(\alpha_2=0.77)}$ = 18.0 kN (Eq. 10). Significant differences between the respective design approaches can be noted for the lateral force capacities. The new Eurocode draft delivers an almost 40 % lower capacity as compared to the present DIN EN 1995-1-1 / NA (2013) application document whereas the Blaß and Laskewitz (2001) solutions are, depending on edge distances α_i, minimally 37 % and maximally 315 % higher as compared to the value specified by the draft *Connections* of EC5-1-1 (2021).

4 Experimental investigations

The experimental investigations aimed especially to verify the interaction behaviour of axial and lateral resistances of glued-in rods connections. For this, three principally different test set-ups were chosen being *i)* pure axially loaded rods, *ii)* shear force tests with very small / negligible moment interaction and *iii)* cantilever tests with a moment and shear force rigid clamped end. All tests were performed with steel rods with metric thread with a nominal diameter of d = 16 mm and strength class 8.8 acc. to EN ISO 898-1 (2013); hence the characteristic yield strength is $f_{y,k}$ = 640 N/mm² and the nominal stress area is A_s = 157 mm².

The geometric glued-in length l_b was throughout 320 mm (20 · d). The timber was homogenous spruce glulam of the strength class GL 30h acc. to EN 14080 (2013) with a depth of h = 280 mm and two different widths of 80 mm and 160 mm. The adhesive used for the bonding of the steel rods was a special two-component epoxy resin (EP
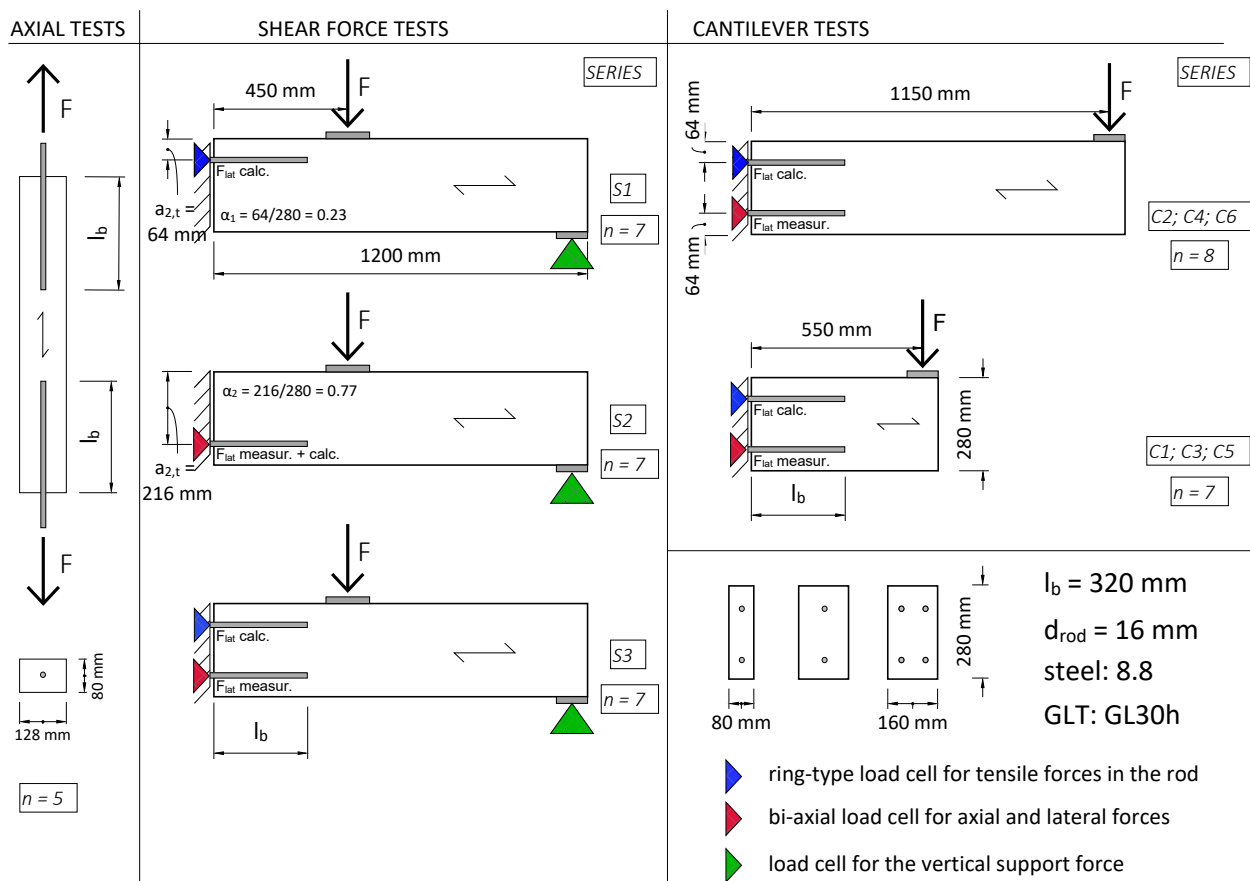
Figure 2. Investigated test configurations: axial tests, shear force tests, cantilever tests and cross-sections.

32 S with hardener B 22 TS, company WEVO Chemie), conforming to German National Technical Approval (Z-9.1-705, 2017). The bonding parameters were chosen acc. to the National Technical Approval and the drill hole diameter was d_{drill} = 20 mm.

4.1   Test configurations and procedure

The tests with the axially loaded rods were performed with glulam pieces of a length of 850 mm with two oppositely glued-in rods. The number of tests was rather low (n = 5) as these tests merely served to verify the characteristic design values given in the mentioned standard specifications. It should be mentioned that the rods were not fixed by hinges to the test machine but gripped rigidly. This cramping leads to minor end moments and hence to somewhat reduced capacities as compared to a both-sided hinged fixation to the test machine due to inevitable deviations of the rods from the specimen axis of the manufacturing (bonding) process.

The test configurations for the determination of the shear force capacity were performed with beam specimens simply supported at one end and with glued-in steel rods placed oppositely at two different α-values (α_1 = 0.23 and α_2 = 0.77) with either one or two rods along beam height and along beam width (see Fig. 2).

The tests with the moment and shear force rigid joints were performed with cantilever type specimens and loaded by a single vertical force. Two significantly different global

Table 2. Compilation of test program for ramp-load tests.

type and designation of test		GLT length	GLT width (No. of rods in width)	position of rod along beam height ($\alpha = a_{2,t}/h$)	n	specimen designation
		[cm]	[mm]	α_1 = 0,23 $\|\|$ α_2 = 0,77		
shear force tests	S1	120	80 (1)	near (α_1) far (α_2) near + far ($\alpha_1 + \alpha_2$)	3 3 3	S_{near}_80_1_01- 03 S_{far}_80_1_01 − 03 S_{n+f}_80_1_01 − 03
	S2	120	160 (1)	near (α_1) far (α_2) near + far ($\alpha_1 + \alpha_2$)	2 2 2	S_{near}_160_1_01- 02 S_{far}_160_1_01 − 02 S_{n+f}_160_1_01 − 02
	S3	120	160 (2)	near (α_1) far (α_2) near + far ($\alpha_1 + \alpha_2$)	2 2 2	S_{near}_160_2_01- 02 S_{far}_160_2_01 − 02 S_{n+f}_160_2_01 − 02
cantilever tests	C1 C2	60 120	80 (1)	near + far ($\alpha_1 + \alpha_2$)	4 5	C_{short}_80_1_01 − 04 C_{long}_80_1_01 − 05
	C3 C4	60 120	160 (1)	near + far ($\alpha_1 + \alpha_2$)	- 2	- C_{long}_160_1_01 − 02
	C5 C6	60 120	160 (2)	near + far ($\alpha_1 + \alpha_2$)	3 3	C_{short}_160_2_01 − 03 C_{long}_160_2_01 − 03

moment / shear force ratios of M/V = 0,55 and M/V = 1,15 were realized by lever arm lengths of 550 mm and 1150 mm. Figure 2 illustrates the test set-up and Table 2 gives a compilation of the test program.

Special attention was paid to the measurement of the axial and lateral forces of the rods, whereby the axial and shear forces of the rod of the bending compression side were measured by a special bi-axial load cell. In case of two parallelly arranged compression rods the resultant forces of both rods were measured. At the bending tension edge of the specimen due to spacing restrictions exclusively the axial rod forces could be measured by ring-type load cells. As a consequence, the lateral shear force of the tension rod(s) was determined from the difference of the applied vertical force, i.e. from the global shear force minus the experimentally measured shear force of the compression rods. For the mounting of the load cells a special steel frame was constructed. Displacements were measured by LVDT´s at several locations: *i)* at the force application point (cantilever end deflection). Secondly *ii)* and most important the axial deformations at the clamped end were measured to compute the rotational stiffness. Thirdly *iii)* the deformations along depth were measured at the clamped end in order to detect the cracking parallel to grain in the area of the tension rods.

The loading of the specimens was throughout performed monotonic. The cantilever tests were performed displacement controlled whereas the beam shear force tests, done at a different test machine, were performed quasi force controlled. Further experimental details are given in Aicher and Simon (2021).
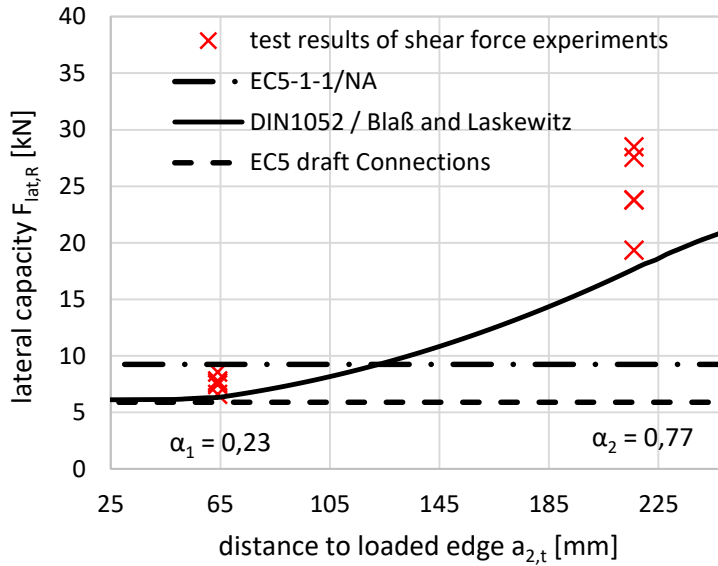
Figure 3. Test results of shear force experiments with rods at two significantly different edge distances $\alpha_i = a_{2,t}/h$.

4.2 Test results

4.2.1 Axial loading

The mean value of the ultimate axial force amounted to $F_{ax,u,mean}$ = 83.1 ± 5.1 kN (COV = 6.1%) resulting in a mean bond line shear strength of $f_{k1,mean}$ = 5.16 ± 0.32 N/mm². The minimum values were 76.4 kN and 4.75 N/mm², respectively. Assuming a larger COV of e.g. 15%, the characteristic value of the population would be $F_{ax,u,k}$ = 62.6 kN. This conservatively derived characteristic value is well in the range proposed by the above design equations (Chap. 3.4: $F_{ax,k}$ = 58.7 kN).

4.2.2 Lateral force loading

The results of the lateral force loading are depicted in Figure 3 altogether with the results from above discussed design equations for the characteristic values. Following only the results for the narrow beams with width b = 80 mm (test series S1) and beams with width b = 160 mm and two rods per width (test series S3) are regarded. The mentioned test series forwarded very plausibly significantly lower values as compared to test series S2 with one rod in a width of b = 160 mm.

The mean and minimum failure loads for the shear force tests with α_1 = 0.23, also termed "near" configuration, were $V_{u,near,mean}$ = 7.6 kN and $V_{u,near,min}$ = 6.6 kN, respectively. The mean and minimum failure loads for the shear force tests with α_2 = 0.77, also termed "far" configuration, were $V_{u,far,mean}$ = 24.6 kN and $V_{u,far,min}$ = 19.3 kN, respectively.

The minimum shear force value for α_1 = 0.23 conforms rather well (+ 16 %) with the characteristic value acc. to the Final draft *Connections* for the new EC5-1-1 (2021). Contrary hereto the minimum value for α_2 = 0.77 exceeds the characteristic value of the design proposal by a factor of 3.3. Overall the test results are highly in line with the results from the proposal by Blaß and Laskewitz (2001).
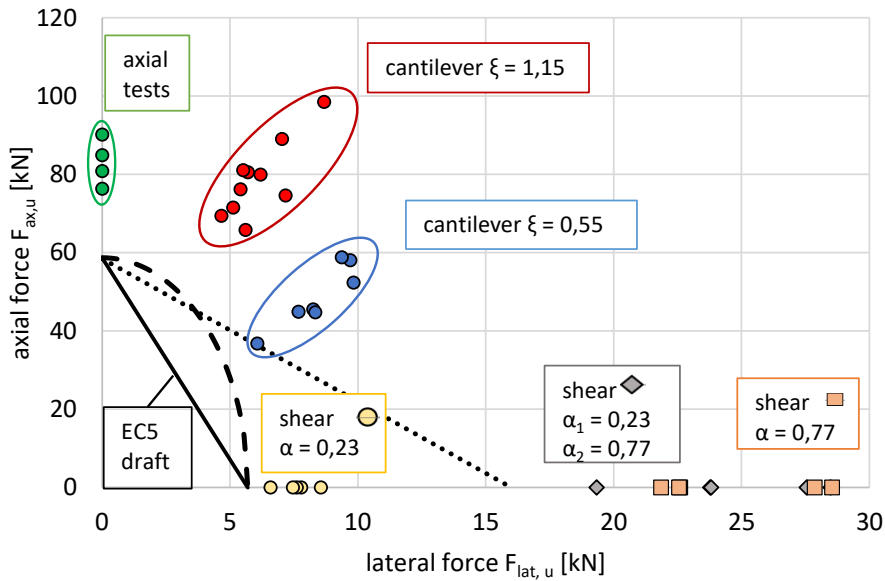
Figure 4. Force interaction results of cantilever tests with different M/V = ξ ratios; also given are the results for pure axial and lateral rod loading

4.2.3   Moment and shear force loadings of cantilevers

Tables 3 and 4 contain the primary test results being the cantilever shear forces and maximum moments at first cracking and at ultimate load. In case of the beams with width b = 160 mm and two rods arranged parallelly along width (test series C5 and C6) the test results are also given for half width of the beam in order to enable an immediate comparison with the test results for the beams with b = 80 mm (test series C1 and C2). In all cases a rather low / moderate scatter of the test results has to be stated.

Table 5 specifies the measured axial and lateral forces of the cantilever type specimens with beam width of b = 80 mm. With regard to page limitation the results for the specimens with b = 160 mm are given in a research report (Aicher and Simon (2021)).

In three of the four test series with an effective beam width of 80 mm per rod (series C1, C2, C5 and C6) a significant difference between the shear force at first crack and ultimate load had to be stated, whereby $V_u/V_c \approx 1.3$.

With regard to the measured lateral and axial forces the following aspects are note-worthy:

- The measured axial rod forces at the tension and compression side coincide through-out very well. This is true for the elastic state up to the first crack and also up to ultimate load.

- The distribution of the lateral forces between the bending tension rod close to the loaded edge (α_1 = 0.23) and the remote rod with α_2 = 0,77 is extremely uneven. This is true for the elastic state end even more for the ultimate load range after first crack formation at the bending tension rod. In the elastic state the lateral force at

the rod close to the loaded edge is very roughly half of the force value at the remote rod and partly much less. At the initial and fully cracked state the lateral force is plausibly entirely carried by the remote rod and the shear force of the rod close to the bending tension edge is pointing at the opposite direction. There is some indication from first tests with reversed loading of the connections with a different activation of the biaxial load cell in a modified test set-up that the quantitative differences of the lateral force distribution is somewhat less expressed as lined out, but qualitatively the above stated results are supported by these tests as well.

Figure 4 depicts the experimentally obtained interaction of the combined M/V cantilever tests results altogether with the uni-axial and pure lateral force tests results. Further the linear interaction line according to the draft *Connections* of EC5-1-1 (2021) is given. It is evident that the draft proposed linear interaction is by far too conservative and that a quadratic combination of axial and lateral rod resistances as specified presently in DIN EN 1995-1-1 / NA (2013) is more justified, see Fig. 4. For cantilevers, e.g. clamped columns, where throughout a minimum of two rods at the opposite edges is necessary tp create a moment resistance the dotted linear interaction relationship in Fig. 4 could considered for a design proposal. Note, the pure shear force (test) results depicted as yellow circles in Fig. 4 represent a rather rare realistic construction situation, meaning that the results of the double rod shear configurations depicted as grey rhombuses seem more approperate.

Table 3. Beam section forces at 1st crack and at failure of cantilever specimens with beam width b = 80 mm.

specimen configuration (M / F_{lat} ratio) [test designation]	No.	beam shear force		beam moment	
		at 1st crack	at failure	at 1st crack	at failure
		V_c	V_u	M_c	M_u
		[kN]	[kN]	[kNm]	[kNm]
cant_s_80_1 (0,55) [C1]	_01	16,11	16,52	8,9	9,1
	_02	12,79	19,66	7,0	10,8
	_03	12,35	19,42	6,8	10,7
	_04	13,93	16,67	7,7	9,2
	mean	**13,8**	**18,1**	**7,6**	**9,9**
	± std	**± 1,5**	**± 1,5**	**± 0,8**	**± 0,8**
cant_l_80_1 (1,15) [C2]	_01	11,9	14,4	13,7	16,6
	_02	6,2	11,2	7,1	12,9
	_03	9,9	11,2	11,4	12,9
	_04	11,2	17,4	12,9	20,0
	_05	7,7	10,4	8,9	12,0
	mean	**9,4**	**12,9**	**10,8**	**14,9**
	± std	**± 2,1**	**± 2,6**	**± 2,5**	**± 3,0**

Table 4. Beam section forces at 1st crack and at failure of cantilever specimens with beam width b = 160 mm.

specimen configuration (M / F_{lat} ratio) [test designation]	No.	beam shear force V = F		beam moment M = F x l_{cant}	
		at 1st crack	at failure	at 1st crack	at failure
		V_c [kN]	V_u [kN]	M_c [kNm]	M_u [kNm]
cant_s_160_2 (0,55) [C5]	_01	29,2	37,5	16,1	20,6
	_02	24,8	30,7	13,6	16,9
	_03	17,3	24,3	9,5	13,4
	mean	**23,8**	**30,8**	**13,1**	**17,0**
	± std	**± 4,9**	**± 5,4**	**± 2,7**	**± 3,0**
	results for the half width b/2 = 80 mm:				
	_01	14,6	18,8	8,0	10,3
	_02	12,4	15,4	6,8	8,4
	_03	8,7	12,2	4,8	6,7
	mean	**11,9**	**15,4**	**6,5**	**8,5**
	± std	**± 2,5**	**± 2,7**	**± 1,4**	**± 1,5**
cant_l_160_2 (1,15) [C6]	_01	27,6	28,2	31,7	32,4
	_02	18	18,6	20,7	21,4
	_03	24,2	24,8	27,8	28,5
	mean	**23,3**	**23,9**	**26,8**	**27,4**
	± std	**± 4,0**	**± 4,0**	**± 4,6**	**± 4,6**
	results for the half width b/2 = 80 mm:				
	_01	13,8	14,1	15,9	16,2
	_02	9,0	9,3	10,4	10,7
	_03	12,1	12,4	13,9	14,3
	mean	**11,6**	**11,9**	**13,4**	**13,7**
	± std	**± 2,0**	**± 2,0**	**± 2,3**	**± 2,3**
cant_l_160_1 (1,15) [C4]	_01		10,2		11,7
	_02		11		12,7
	mean		**10,6**		**12,2**
	± std		**± 0,4**		**± 0,5**

Table 5. Measured axial and lateral rod forces of cantilever type specimens (beam width b = 80 mm) with two different M/F_{lat} ratios of 0,55 and 1,15.

specimen configuration [test designation]	No.	measured[1] rod forces [kN]							
		1st crack				ultimate load			
		shear forces		axial forces		shear forces		axial forces	
		$V_{1,c}$ [kN]	$V_{2,c}$ [kN]	$F_{ax,1,c}$ [kN]	$F_{ax,2,c}$ [kN]	$V_{1,u}$ [kN]	$V_{2,u}$ [kN]	$F_{ax,1,u}$ [kN]	$F_{ax,2,u}$ [kN]
cant_s_80_1 (0,55) [C1]	_01	4,5	11,6	45,5	-46,9	-1,5	18	45,5	-42,9
	_02	4,5	8,3	41,8	-39,3	-4,9	24,6	52,4	-48,7
	_03	3,9	8,5	38,4	-38,6	4,8	14,7	58,1	-59
	_04	0,3	13,6	26,7	-39,4	-4	20,6	29,5	-44,8
	mean	**4,3**	**9,5**	**41,9**	**-41,6**	**-0,5**	**19,1**	**52,0**	**-50,2**
	± std	**± 0,3**	**± 1,5**	**± 2,9**	**± 3,8**	**± 4,0**	**± 4,1**	**± 5,2**	**± 6,7**
cant_l_80_1 (1,15) [C2]	_01	-5,5	17,3	53,3	-67,3	-9,8	24,1	67,6	-81,7
	_02	-1,3	7,7	38,6	-28,9	-8,3	19,6	64,6	-67,1
	_03	4,6	8,3	70,2	-72,8	0	11,4	80,6	-80,4
	_04	-4	15,2	55,6	-66,7	-9	26,4	93,8	-103,2
	_05	3,2	4,4	50,2	-56,9	2,2	8,6	72,3	-80,1
	mean	**-0,6**	**10,6**	**53,6**	**-58,5**	**-5,0**	**18,0**	**75,8**	**-82,5**
	± std	**± 3,9**	**± 4,9**	**± 10,2**	**± 15,7**	**± 5,0**	**± 7,0**	**± 10,5**	**± 11,6**

1) $V_{1,c/u} = V_{c/u} - V_{2,c/u}$

5   Conclusions

The performed investigations with unreinforced connections with steel rods glued-in parallel to grain revealed especially two aspects:

- The lateral force distribution on rods in one row with different distances to the loaded edge is not uniform and depends pronouncedly on the distance to the loaded edge. The difference in the load sharing exists in the fully elastic state and increases in plausible manner significantly close / after initial crack formation occurring at the rod closer to the loaded edge. In the performed experiments the shear force at the remote rod was throughout well two times higher as compared to the rod closer to the loaded edge. This extreme difference could be somewhat biased, especially in the elastic state, by the specifically realized rod force measurement configuration with the bi-axial load cell. Nevertheless, first results with reversed loading and a modified clamping device supported the significant difference in the lateral force distribution at comparable magnitude. The uneven lateral force distribution, being in line with former results by *Blaß and Laskewitz* (2001) is not reflected in the present design proposal in the draft *Connections* of EC5-1-1 (2021). According to the performed investigations the proposal recommends overly conservative values for lateral rod resistances being exclusively correct for very close edge distances.

- The cantilever tests with different moment / shear force ratios at the moment rigid joints revealed in conjunction with the pure axial and shear force tests, that the linear interaction of axial and lateral rod force resistances specified in the present design proposal in the draft *Connections* of EC5-1-1 (2021) is by far too conservative. A quadratic interaction as proposed presently in the German National Application document to EC5 (DIN EN 1995-1-1 / NA, 2013) seems more appropriate and preferable for competitive timber construction solutions.

6   Acknowledgements

7   References

Aicher, S., M. Wolf, and P. Gustafsson (1999). "Load displacement and bond strength of glued-in rods in timber influenced by adhesive, wood density, rod slenderness and diameter." In: *First RILEM Symposium on Timber Engineering*.

Aicher, S. and G. Dill-Langer (Sept. 2001). "Influence of moisture, temperature and load duration on performance of glued-in rods." In: *RILEM Proc. 22, RILEM Publications SARL, France*.

Aicher, S. and G. Stapf (Dec. 2017). "Glued-in Rods – state-of-the-art- Influencing parameters, test results, approvals, adhesive standardization, design and execution rules." In: *IHF2017 Garmisch-Partenkirchen*, pp. 193–208.

Blaß, H.-J. and B. Laskewitz (2001). *Glued-in Rods for Timber Structures – Effect of distance between rods and between rods and timber edge on the axial strength*. Tech. rep. Versuchsanstalt für Stahl, Holz und Steine, Abteilung Ingenieurholzbau, Universität Fridericiana, Karlsruhe, Germany.

Dietsch, P. (2012). "Design and application of shear reinforcements for glued-laminated timber beams; in German." Dissertation. München: Technische Universität München.

Dietsch, P. and R. Brandner (Oct. 2015). "Self-tapping screws and threaded rods as reinforcement for structural timber elements – A state-of-the-art report." In: *Construction and Building Materials* 97, pp. 78–89.

DIN 1052 (2004). *Design of timber structures - General rules and rules for buildings*. Berlin, Germany: German Institute for Standardization.

DIN EN 1995-1-1 / NA (2013). *Nationally determined parameters – Eurocode 5: Design of timber structures – Part 1-1: General – Common rules and rules for buildings*. Brussels, Belgium: European Committee for Standardization.

EC5-1-1 (2021). *Eurocode 5: Design of timber structures – Part 1-1: Chapt. Connections (FINAL DRAFT version 30-04-2021).* Brussels, Belgium: CEN/TC 250/SC 5/WG 5 "Connections and fasteners".

Edlund, G. (1975). *I limträ inlimmad skruv (Glued-in rods in glulam)*. Tech. rep. SFTFI Svenska Träforskninginst, Stockholm.

Ehlbeck, J. and R. Görlacher (1983). *Tragverhalten von Queranschlüssen mittels Stahlformteilen, insbesondere Balkenschuhen, im Holzbau*. Forschungsbericht No. 1041. Stuttgart: IRB-Verl.

EN 14080 (2013). *Timber Structures – Glued laminated timber and glued solid timber – Requirements*. Brussels, Belgium: European Committee for Standardization.

EN 1995-1-1 (2010). *Design of timber structures – Part 1-1: General – Common rules and rules for buildings*. Brussels, Belgium: European Committee for Standardization.

EN ISO 898-1 (2013). *Mechanical properties of fasteners made of carbon steel and alloy steel –Part 1: Bolts, screws and studs with specified property classes – Coarse thread and fine pitch threads*. Brussels, Belgium: European Committee for Standardization.

Gustafsson, P., E. Serrano, S. Aicher, and C. Johansson (Sept. 2001). "A strength design equation for glued-in rods." In: *RILEM Proc. 22, RILEM Publications SARL, France*, pp. 323–332.

Jockwer, R. (2014). "Structural behaviour of glued laminated timber beams with unreinforced and reinforced notches." PhD thesis. ETH Zurich.

Johansson, C.-J., E. Serrano, P. Gustaffson, and B. Enquist (1996). "Axial strength of glued-in bolts. Calculation model based on nonlinear frature mechanics- A preliminary study." In: *International Council for Building Research, Studies and Documentation, Working Commission W18A Timber Structures, Meeting 28., Kopenhagen.*

Möhler, K. and K. Hemmer (1981). *Versuche mit eingeleimten Gewindestangen: Forschungsarbeit*. Karlsruhe: Universität, Lehrstuhl für Ingenieurholzbau und Baukonstruktionen.

Möhler, K. and R. Lautenschläger (1978). *Großflächige Queranschlüsse bei Brettschichtholz*. Forschungsbericht. Stuttgart: Informationszentrum Raum und Bau.

Möhler, K. and W. Siebert (1980). *Ausbildung von Queranschlüssen bei angehängten Lasten an Brettschichtträger oder Vollholzbalken*. Karlsruhe: Lehrstuhl für Ingenieurholzbau und Baukonstruktion, Universität Karlsruhe (TH).

Riberholt, H. (1977). *Bolte indlimet i limtrae*. ABK. ab. [Lyngby]: ABK.

– (1986). *Glued bolts in glulam*. Serie R, No 210. [Lyngby]: Department of Structural Engineering, Technical University of Denmark.

– (1988). "Glued bolts in glulam- Proposals for CIB Code." In: *International Council for Building Research, Studies and Documentation, Working Commission W18A Timber Structures, Meeting 21., Parksville.*

Steiger, R., E. Gehri, and R. Widmann (2006). "Materials and Structures, Springer." In: chap. Pull-out strength of axially loaded steel rods bonded in glulam parallel to the grain, pp. 69–78.

Z-9.1-705 (24.05. 2017). *2K-EP-Adhesive WEVO special resin EP 32 S with WEVO hardener B 22 TS for bonding-in steel rods in timber construction materials*. gültig bis 26.11.2021. WEVO-CHEMIE GmbH, Schönbergstraße 14, 73760 Ostfildern-Kemnat, DIBt, Berlin.

DISCUSSION

The papers was presented by S Aicher

P Dietsch commented that the shear force capacity for cases with loading close to the edge might be more a perpendicular to grain situation. S Aicher agreed as one moved more away from the loaded edge one would get more load transfer via compression perpendicular to grain and conversely as one moved closer to the loaded edge one would get more load transfer via tension perpendicular to grain.

R Jockwer stated that the lateral load carrying capacity in the Eurocode draft is supposed to refer to the fastener capacity and not related to timber splitting with the assumption of loading far away from the loaded edge. S Aicher was not sure about the necessity to verify the tension strength perpendicular to grain capacity of the timber. It is more important to make the process more transparent to designers. S Aicher also agreed that one could overcome the problem via reinforcement. However it is not intended for reinforcement to be used all the time especially if there are many joints for consideration. One should understand how the joint works.

R Jockwer asked about interaction. He questioned whether one is sure about using the quadratic based interaction in the long term if cracks exists. S Aicher said it is important that we find a good solution if we want to utilize most of the axial capacity and find an option to deal with the lateral force. S Aicher said they do not yet have the final answer.

T Tannert commented the reverse loading situation is important and asked if the results would be different under reverse loading. S Aicher responded that the results for reverse loading were not provided in this paper because of limited length of paper. He said that the same load in the opposite side could be achieved and the cracks do not harm the situation too much. However reverse cyclic loading with increasing amplitude may be a problem under many cycles. T Tannert asked whether work is available for screwing rods into side grain. S Aicher responded that this was not planned as insertion into the end grain is more relevant.

E Serrano commented about the test set up in terms of distance to the loaded edge via a point load. E Serrano and S Aicher discussed about the influence of test method in relation to actual load application. S Aicher further said looking at the stress plots they did not notice too much axial forces.

P Dietsch commented that adding reinforcement in this setting can provide a robust solution.

Slip modulus formulas for timber-to-timber inclined screw connections – Comparison with other simplified models

Yuri De Santis, Department of Civil, Building-Construction and Environmental Engineering, University of L'Aquila, 67100 L'Aquila, Italy

Massimo Fragiacomo, Department of Civil, Building-Construction and Environmental Engineering, University of L'Aquila, 67100 L'Aquila, Italy

Keywords: timber joints, inclined screws, slip modulus, beam on elastic foundation, Eurocode 5

1 Introduction

Joints made with dowel-type fasteners are among the most commonly used types of connections in timber engineering. In particular the self-tapping screws, thanks to the speed and ease of installation and the possibility of arranging them in various geometric configurations, are well suited for use in composite floors and beams. The high values of withdrawal stiffness of the screws and the possibility of arranging them inclined with respect to the sliding plane lead to connections with high slip modulus and consequently high performance of the composite element in terms of strength and stiffness.

According to the current *Eurocode 5* (2004) the slip modulus k_{ser} per shear plane per fastener under service load for joints made with dowel-type fasteners is related to the mean density ρ_m (2) and the diameter d by (1).

$$K_{ser,EC5} = \rho_m^{1.5} d/23 \tag{1}$$

$$\rho_m = \sqrt{\rho_{m,1}\rho_{m,2}} \tag{2}$$

The current formulation lacks parameters such as the length of penetration of the screw into the timber members and the angle of inclination with respect to the sliding plane which numerous studies have shown to be closely related to the slip modulus of connections with inclined screws, e.g. *Tomasi et al.*(2010), *Girhammar et al.*(2017) and *Blass & Steige* (2018).

According to the formulation (3) proposed by *Tomasi et al.*(2010), the sliding modulus of a joint with inclined screw can be determined starting from the lateral stiffness defined for the orthogonal screws in *Eurocode 5* (2004) $K_\perp$ (1) where the effective screw diameter is used $d_{ef}=1.1d_{core}$ and the withdrawal stiffness $K_\parallel$ calculated using experimentally derived interpolation laws, e.g. *Blass et al.*(2006), *Ringhofer et al.*(2015), and *Blass & Steige* (2018). The authors suggest the expression given in the technical approval of the SFS-Intec WT-T screws (4) for the calculation of $K_\parallel$ where s_g is the embedment length of the threaded segment of the screw, and d is the outer diameter of the screws thread (*Allgemeine baufsichliche Zulassung*, 2006).

$$k_{ser,Tom}=K_\perp \cos\vartheta\,(\cos\vartheta-\mu\sin\vartheta)+K_\parallel \sin\vartheta\,(\sin\vartheta+\mu\cos\vartheta) \tag{3}$$

$$K_\parallel=30s_g d \tag{4}$$

An analytical formulation for the calculation of withdrawal stiffness that still requires a regression analysis on the experimental results, was proposed by *Stamatopoulos et al.*(2016). An alternative approach to the problem was proposed by *Girhammar et al.*(2017), in this case the formulation (5) for the slip modulus was derived from an analytical model that considers the screw as a rigid body on elastic springs.

$$k_{ser,Gir}=\frac{1}{2}K_{h,1}d_h l_1 \frac{2-\frac{s_1}{x_1}}{1+\frac{x_2}{x_1}}\cos\vartheta\,(\cos\vartheta-\mu\sin\vartheta)+ \tag{5}$$

$$+K_{ax,eff,1}\pi d_{ax}l_{thr,1}\frac{1}{1+(1/\beta_{ax})(l_{thr,1}/l_{thr,2})}\sin\vartheta\,(\sin\vartheta+\mu\cos\vartheta)$$

Where the embedment stiffness of the timber per unit area $K_{h,1}$ must be determined experimentally via embedment test and effective axial withdrawal stiffness per unit area $K_{ax,eff,1}$ can be determined from (4). The authors, to account for the flexibility and extensibility of the screw in approximate manner, suggest expressions of corrective coefficients to be applied to $K_{h,1}$ and $K_{ax,eff,1}$ depending on the geometry and mechanical properties of the system.

The final draft revision of the connections chapter of Eurocode 5 (*Revision of Eurocode 5*, 2021) suggests the formulation (6) analogous to the one proposed by *Tomasi et al.*(2010) (3). The mean slip modulus per fastener in lateral direction $K_{ser,v}$ is given by (1) and should be reduced by 50% for connection members loaded perpendicular to grain. As discussed by *Tomasi et al.*(2010), from a theorical point of view, the withdrawal contribution $K_{ser,ax}$ should be determined by considering the simultaneous pull-out of the two threaded portions of the screw from both timber members (DSM: Double-Stiffness-Model) and therefore $K_{ser,ax}$ of (6) is the resulting withdrawal stiffness of two springs placed in series each of stiffness calculated according to the experimentally derived interpolation law (7) found by *Blass H.J. & Steige Y.* (2018) where d is the outer diameter of the screws thread. The same authors, due to a better correspondence between their experimental results and model predictions, sug-

gest to consider only the withdrawal stiffness of the portion of the screw inserted in the member on the head side (SSM: Single-Stiffness-Model). In this work DSM is considered for the EC5 proposal, while SSM is considered for Tomasi et al. model.

$$k_{ser,EC5P}=K_{ser,v} \cos \vartheta \, (\cos \vartheta - \mu \sin \vartheta) + K_{ser,ax} \sin \vartheta \, (\sin \vartheta + \mu \cos \vartheta) \qquad (6)$$

$$K_{ser,ax}=2d^{0.6} l_w^{0.6} \rho_m^{0.9} \qquad (7)$$

The aim of the work presented herein is to propose simplified but more accurate formulas to predict the sliding modulus starting from the geometric characteristics and timber member densities of the connection. These formulas, based on an analytical model taking into account the timber anisotropy and the axial and flexural stiffness of the screws, are then compared with current literature proposals. A modification of the new formulation proposed in the revision of EN 1995-1-1 is then suggested.

2 Proposed formulas derivation

The model used for the derivation of the proposed simplified formulas consist of a beam on two layers of continuous elastic springs, one parallel and the other perpendicular to the sliding plane. The beam on elastic foundation model has been previously applied by *Symons et al.*(2010) and *Di Nino et al.*(2020) for the slip modulus prediction of timber-concrete connections. The model has been extended to the case of timber-timber connections.
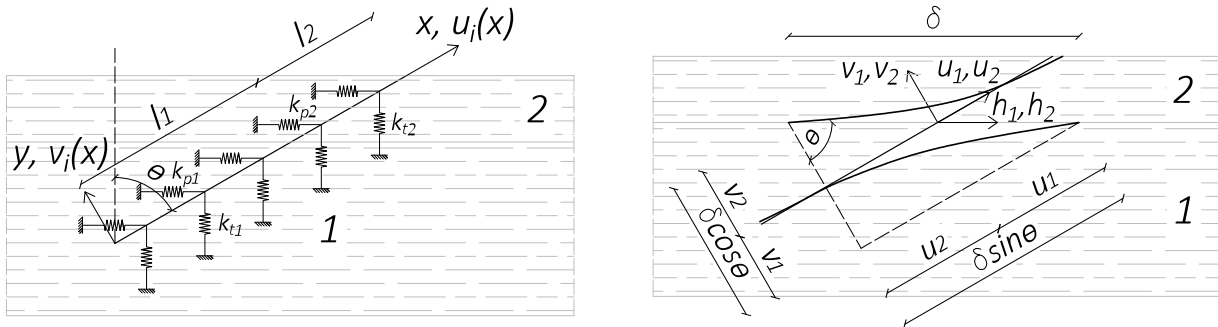

Figure 1 Analytical model representation. (a) Division into domains; (b) Initial and deformed configuration of the beam representing the screw

By assuming small strains and small displacements and by adopting linear kinematics, the elastic problem of an inclined beam on elastic foundation is governed by Eqs. (8) for the *i*-th domain. $u_i(x)$ and $v_i(x)$ denote the displacement of fields in axial and transverse direction respectively for the *i*-th domain, ϑ is the angle between the normal of the sliding plane and the fastener (Figure 1) and K_{xxi}, K_{xyi}, K_{yxi}, K_{yyi} are defined by Eqs. (9).

$$K_{xx_i}(\vartheta)u_i(x)+K_{xy_i}(\vartheta)v_i(x)-EAu_i''(x)=0$$

$$K_{yx_i}(\vartheta)u_i(x)+K_{yy_i}(\vartheta)\,v_i(x)+EIv_i''''(x)=0 \tag{8}$$

$$K_{xx_i}(\vartheta)= \cos\vartheta\sin\vartheta\,(k_{t_i}\cos\vartheta+k_{p_i}\sin\vartheta\,)$$

$$K_{yyi}(\vartheta)=k_{p_i}\cos^3\vartheta+k_{t_i}\sin^3\vartheta$$

$$K_{xy_i}(\vartheta)= \cos\vartheta\sin\vartheta\,(-k_{p_i}\cos\vartheta+k_{p_i}\sin\vartheta\,)$$

$$K_{yx_i}(\vartheta)=K_{xy_i}(\vartheta) \tag{9}$$

EA and EI represent the axial and flexural stiffness of the beam respectively. E is the elastic modulus of the steel, A is the section area and I is the second moment of area. It should be noted that due to the complex geometry of the screws whose central section is often of reduced crossed section due to the lack of thread, it is not easy to identify the diameters to be used for the calculation of the axial and bending stiffness. Preliminary studies have shown a good correspondence with the experimental results when the external diameter of the thread is adopted for the axial stiffness calculation, while the internal diameter of the thread is adopted for the bending stiffness calculation ($A = \pi\phi^2/4$ and $I = \pi\phi_{inn}^4/64$).

k_{pi} and k_{ti} in Eqs. (9) represent the stiffnesses of the two layers of springs (Figure 1). The stiffness of the springs parallel to the sliding plane can be determined starting from the experimental foundation modulus deriving from embedment tests carried out parallel to the grain: $k_{pi}=Kf_0\phi$. On the basis of the results of embedment tests performed in the orthogonal direction with respect to the grain and as also done in by *Symons et al.*(2010) and *Di Nino et al.*(2020), perpendicular spring stiffness can be taken as $k_{ti}= \beta k_{pi}$ with $\beta= 0.5$. Interpolation laws Eq. (10) for sawn timber (ST), glued laminated timber (GL) and cross laminated timber (CLT) and Eq. (11) for laminated veneer lumber (LVL), parallel strand lumber (PSL), laminated strand lumber (LSL) and plywood (PLY) was found based on thirty-eight embedment tests results. The interpolated data come from the following experimental campaigns (Figure 2): *Gattesco* (1998)*, Gattesco and Toffolo* (2004)*, Santos et al.*(2010)*, Karagiannis et al.*(2016)*, Tuhkanen et al.*(2018)*, Franke et al.*(2014)*, Lederer et al.*(2016)*, Schweigler et al.*(2016)*, Hwang et al.*(2002)*, Lemaitre et al.*(2019) and *Schweigler et al.*(2019).

$$K_{f0}(\rho,\phi)=-147.8+\frac{30.9\,\rho^{0.46}}{\phi^{0.32}} \tag{10}$$

$$K_{f0}(\rho,\phi)=-62.3+\frac{0.0282\,\rho^{1.41}}{\phi^{0.23}} \tag{11}$$
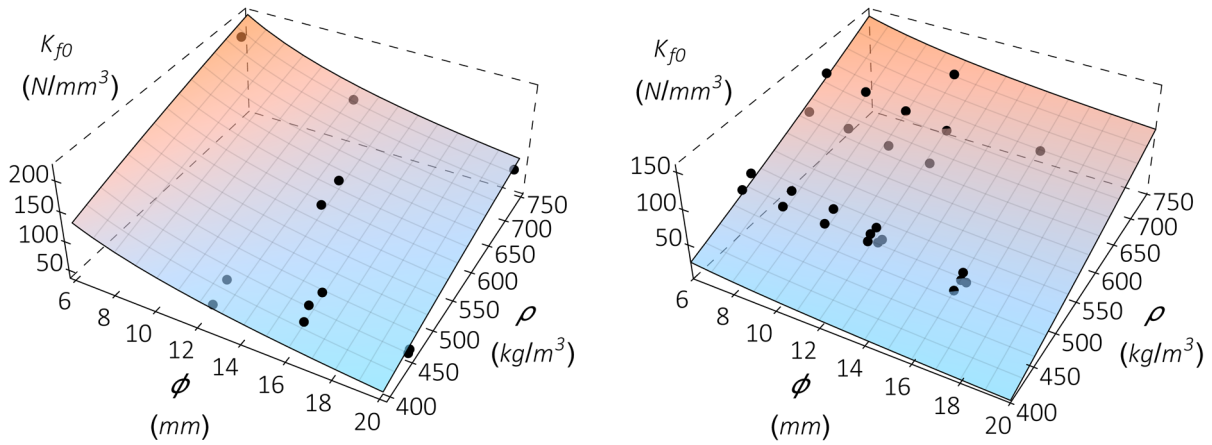
Figure 2 Experimental data and interpolating functions of the foundation modulus for (a) ST, GL and XLAM and (b) LVL, PSL, LSL and PLY.

The slip modulus of the connection is given by the ratio between the component parallel to the sliding plane of the internal forces of the beam and the internal distortion δ (*Figure 1*).

$$k_{ser,An} = \frac{N_1 \sin(\vartheta) - T_1 \cos(\vartheta)}{\delta} = \frac{EA\, u_1'(l_1) \sin(\vartheta)}{\delta} + \frac{EI\, v_1'''(l_1) \cos(\vartheta)}{\delta} \tag{12}$$

The boundary conditions of described model are expressed by Eqs. (13).

$$EA\, u_1'(0) = 0$$

$$EI\, v_1''(0) = 0$$

$$-EI\, v_1'''(0) = 0 \tag{13.1}$$

$$EA\, u_1'(l_1) = EA\, u_2'(l_1)$$

$$EI\, v_1''(l_1) = EI\, v_2''(l_1)$$

$$-EI\, v_1'''(l_1) = -EI\, v_2'''(l_1)$$

$$u_1(l_1) - \delta \sin \vartheta = u_2(l_1)$$

$$v_1(l_1) + \delta \cos \vartheta = v_2(l_1)$$

$$v_1'(l_1) = v_2'(l_1) \tag{13.2}$$

$$EA\, u_2'(l_1 + l_2) = 0$$

$$EI\, v_2''(l_1 + l_2) = 0$$

$$-EI\, v_2'''(l_1 + l_2) = 0 \tag{13.3}$$

The exact solution of the analytical model was interpolated by means of the Eqs. (14) ($\vartheta=0°$ and $\vartheta=15°$) and (15) ($\vartheta \geq 30°$) whose coefficients for various screw inclinations are contained in *Table 1*.
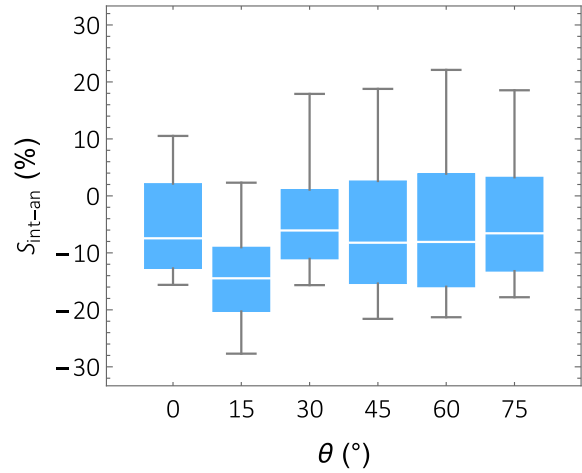
$$k_{ser,Int}= dd(\rho_1^{aa}\, l_1^{bb} + \rho_2^{aa}\, l_2^{bb})\, \phi^{cc} \tag{14}$$

$$k_{ser,Int}= \frac{dd\, \phi^{cc}}{\dfrac{1}{\rho_1^{aa}\, l_1^{bb}} + \dfrac{1}{\rho_2^{aa}\, l_2^{bb}}} \tag{15}$$

Table 1. Coefficient of interpolating formulas.

ϑ (°)	aa	bb	cc	dd
0	1.04	0.056	1.11	0.18
15*	1.04	0.056	1.11	0.18
30	1.07	0.51	0.76	0.31
45	1.07	0.68	0.65	0.29
60	1.09	0.77	0.58	0.23
75	1.14	0.86	0.47	0.095

* The formula found for orthogonal screws is used.

Figure 3 Figure 4 Maximum, 95th percentiles, median, 5th percentiles and minimum values of the scatters between interpolating formulas and exact solution for 3000 configurations.

The formulas has been tested for random configurations of diameters ϕ 6÷18 mm, ρ 400÷750 kg/m^3, l 50÷200 mm excepts for Eqs. *(14)* for which l was limited to the interval 60÷150 mm. The scatters between the exact solution of the analytical model and simplified interpolating law are given in Figure 3.

3   Experimental verification

The slip modulus of joints made with mechanical connections can be experimentally evaluated according to the procedure described in *UNI EN 26891* (1991). The push-out test consists of a partial loading and unloading cycle followed by a second phase carried out in displacement control that ends with the reaching of ultimate load or of a sliding of 15 mm. The slip modulus is given by the slope of the secant to the first load branch of the force-slip curve for the points corresponding to 40% and 10% of the estimated maximum load (Eq. (16)).

$$k_{ser,Exp}= \frac{0.4F_{est}-0.1F_{est}}{v_{0.4}-v_{0.1}} \tag{16}$$

The reliability of the proposed model and simplified formulas was quantified and compared with the reliability of other formulations based on the results of extensive

experimental push-out test programmes. The push-out tests taken as reference were performed on connection specimens with double threaded screws and fully treaded screws placed in shear-tension or crossed configurations (Table 2).

The external thread diameter ϕ assumed in the calculations is shown in Table 2. In the case of double-threaded screws, ϕ corresponds to the average value of the two threaded sections. The inner thread diameter has been assumed: $\phi_{inn}=0.66\phi$.

The anchorage lengths used in the calculation of the withdrawal stiffness were obtained subtracting from the penetration lengths *(l₁ and l₂)* of Table 2 the tip length *(l_p=1.1\phi)* and, in the case of double threaded screws, the length of the central smooth section.

The friction coefficients considered for the inclined screws in shear-tension and for the crossed-screws configurations are $\mu=0.25$ and $\mu=0$ respectively.

In the models in which withdrawal from only one of the two members is assumed, this were considered to happen in the screw-head side (*Tomasi et al.*, 2010).

Table 2. Experimental setups description for reference experimental data.

Authors	Member 1	Member 2	ϕ (mm)	ρ_1 (kg/m³)	ρ_2 (kg/m³)	l_1 (mm)	l_2 (mm)	Screw type and layout	ϑ (°)
Schiro G. et al. (2018)	Beech LVL	CLT	8.3	796	465	69	81	Dt	45
	Spruce solid C24	Beech LVL GL70	8.3	460	846	91	71	Dt I	45
	Spruce solid C24	CLT	8.3	460	465	69	81	Dt	45
	Spruce solid C24	CLT	8.6	460	465	81	81	Dt I	45
Wang F. et al. (2019)	Douglas Fir LVL	Douglas Fir LVL	5.3	560	560	39	61	Tt	45
	Douglas Fir LVL	Douglas Fir LVL	5.3	560	560	50	50	Tt	30
	Douglas Fir LVL	Douglas Fir LVL	5.3	560	560	55	45	Tt	15
	Douglas Fir LVL	Douglas Fir LVL	5.3	560	560	57	43	Tt	0
Ringhofer A. (2016)	Spruce solid T24		8.0	408	408	113	113	Tt	45
			8.0	410	408	130	130	Tt	60
Jacquier N. (2014)	Spruce GL32	CLT C24	6.5	456	471	75	85	Dt	45
	Spruce GL32	CLT C24	8.2	462	459	75	85	Dt	45
Blaß H.J. et al. (2018)	Spruce solid T28		8.0	409	409	113	113	Tt	45
			8.0	412	412	130	130	Tt	60
			8.0	412	412	113	113	Tt X	45
			8.0	407	407	130	130	Tt X	60
			8.0	421	421	130	130	Tt	60
			8.0	427	427	130	130	Tt X	60
			8.0	475	475	113	113	Tt	45
			8.0	438	438	130	130	Tt	60

	8.0	482	482	113	113	Tt X	45
	8.0	456	456	130	130	Tt X	60
	6.0	424	424	85	85	Tt	45
	6.0	416	416	85	85	Tt X	45
	10.0	411	411	141	141	Tt	45
	10.0	414	414	141	141	Tt X	45
	8.0	426	426	130	130	Tt	30
	8.0	424	424	130	130	Tt X	30
	8.0	433	433	130	130	Tt	50
	8.0	429	429	130	130	Tt X	50
	8.0	428	428	130	130	Tt	60
	8.0	426	426	130	130	Tt	70
	8.0	430	430	130	130	Tt X	70
	8.0	442	442	40	40	Tt	45
	8.0	417	417	40	40	Tt X	45
	8.0	420	420	80	80	Tt	45
	8.0	434	434	80	80	Tt X	45
	8.0	443	443	113	113	Tt	45
	8.0	455	455	113	113	Tt X	45
	8.0	413	413	160	160	Tt	45
	8.0	427	427	160	160	Tt X	45
	8.0	433	433	200	200	Tt	45
	8.0	446	446	200	200	Tt X	45
	8.6	426	426	79	141	Dt	45
	8.6	426	426	105	115	Dt	30
Tomasi R. et al. (2010) Spruce GL24h	8.6	426	426	86	104	Dt	15
	8.6	426	426	90	100	Dt	0
	8.6	426	426	79	141	Dt X	45
	8.6	426	426	105	115	Dt X	30
	8.6	426	426	86	104	Dt X	15

* Tt: total thread screws, Dt: double thread screw, X: crossed screws, I: interlayer.

The slip modulus values predicted by the proposed analytical model have a good correspondence with the experimental results, both in terms of determination coefficient (Table 3) and in terms of percentage deviations (Figure 5). The slight tendency of the model to underestimate the predicted values could result from neglecting the friction on the sliding plane. The analytical model proposed by *Girhammar et al.*(2017) is characterized by a distribution of percentage deviations similar to that of the proposed model.

Although the coefficient of determination of the proposed simplified formulas is the same of that of the model of the final draft revision of Eurocode 5, proposed formu-

las have a lower 95th percentile and a lower maximum value of the percentage deviations as well as a 50th percentile closer to zero. The Tomasi et al. model strongly overestimate the slip modulus in the vast majority of cases.
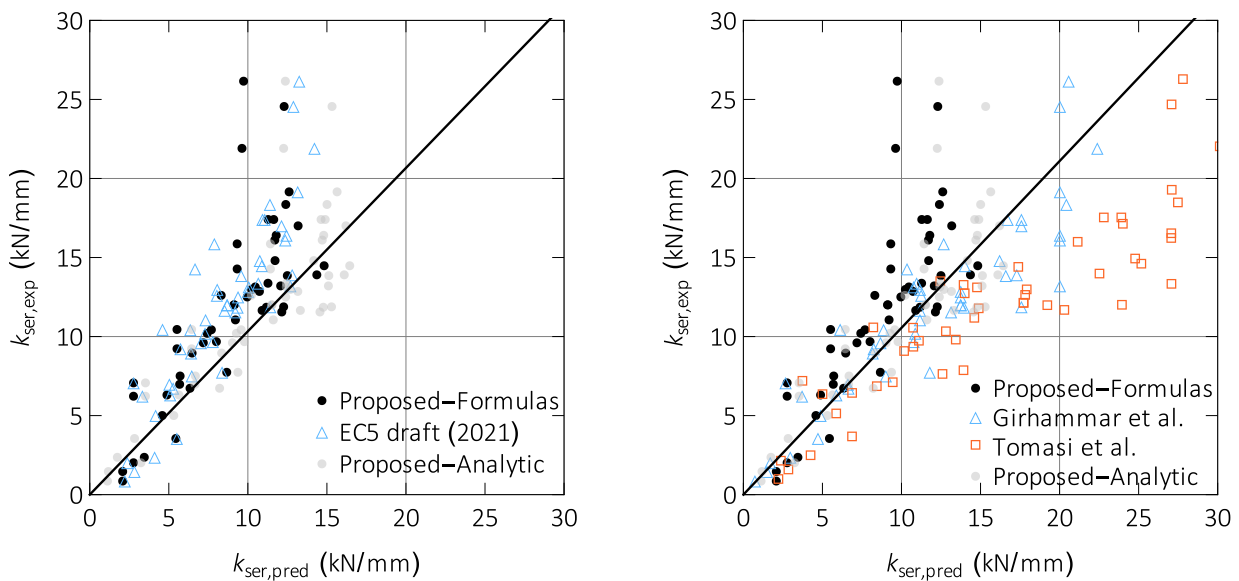

Figure 4 The observed slip modulus versus the estimated slip modulus

Table 3. Coefficient of determination.

Models	Proposed-Analytic	Proposed-Formulas	EC5 draft (2021)	Girhammar et al.	Tomasi et al.
R^2	0.62	0.28	0.28	0.79	-0.29
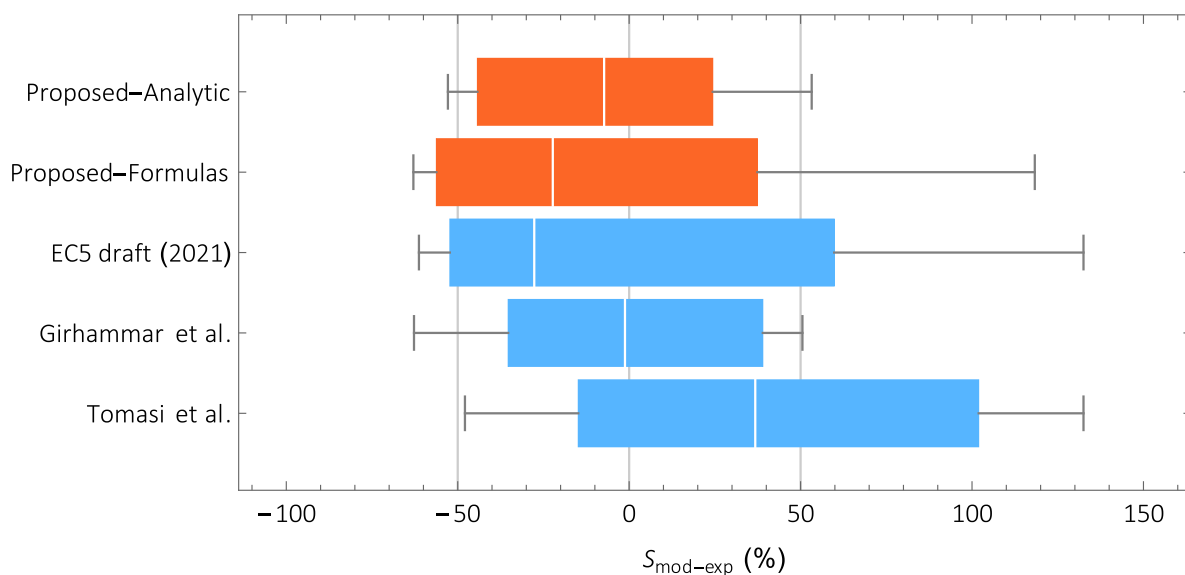
Figure 5 Maximum, 95th percentiles, median, 5th percentiles and minimum values of the scatters between models and experimental slip modulus.

4   Comparison with other models through parametric studies

The qualitative and quantitative differences between the proposed analytical model and simplified formulas and the other models from literature including the new formulation in the revised EN 1995-1-1 have been studied by varying each of the significant parameters of the system such as the inclination of the screw, the diameter of the screw, the lengths of penetration and the densities of the members.

The first parametric study was performed with the aim of investigating the dependence of the slip modulus on the screw diameter (Figure 6). A symmetrical connection was considered, i.e., with member density $\rho_1=\rho_2=430$ kg/m^3 and penetration lengths $l_1=l_2=100$ mm. It is worth noting that the dependence of the slip modulus on the screw diameter is very similar between the proposed formulas and the model of *Revision of Eurocode 5* (2021). The predicted slip modulus of all other models increases, for increasing diameter, much faster than the slip modus predicted by proposed formulas and analytical model. It is also noted that the proposed formulas return values in good agreement with those of the current EC5 for orthogonal screws of diameters up to 12 mm.
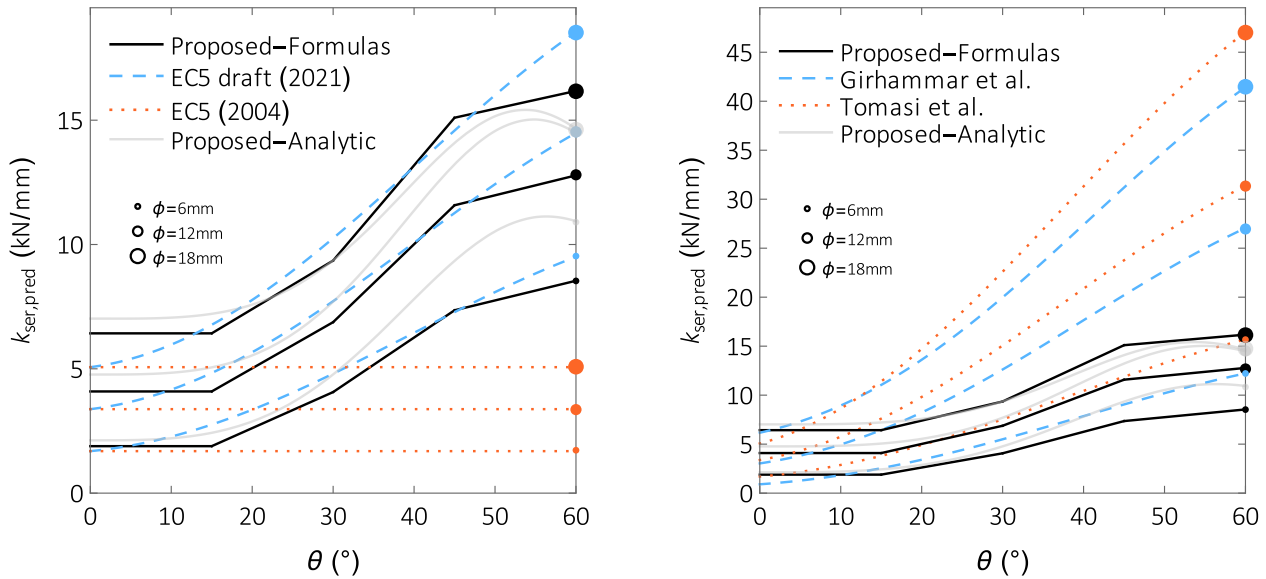

Figure 6 Models predictions for varying diameters (6, 12 and 18 mm). (a) Comparison of proposed formulas and model with standards proposal and current standard; (b) Comparison of proposed simplified formulas with exact solution of analytical model and other models.

The second parametric study aims to highlight how the expected values of the slip modulus vary when the penetration lengths in the timber members on the screw head side or tip side are doubled (Figure 7). The analyzed configuration is characterized by $\rho_1=\rho_2=430$ kg/m^3 and $\phi=8$ mm. According to the proposed model and the model of *Revision of Eurocode 5* (2021), the sliding modulus increases by the same amount by doubling the length of penetration in one or the other member. According

to the Tomasi et al. model the slip modulus increases only when the penetration length on the head side member is increased. In the Girhammar et al. model, the greatest increase is obtained by doubling the length of penetration into the member on the screw head side for which a halved withdrawal stiffness is assumed as suggested by the author.
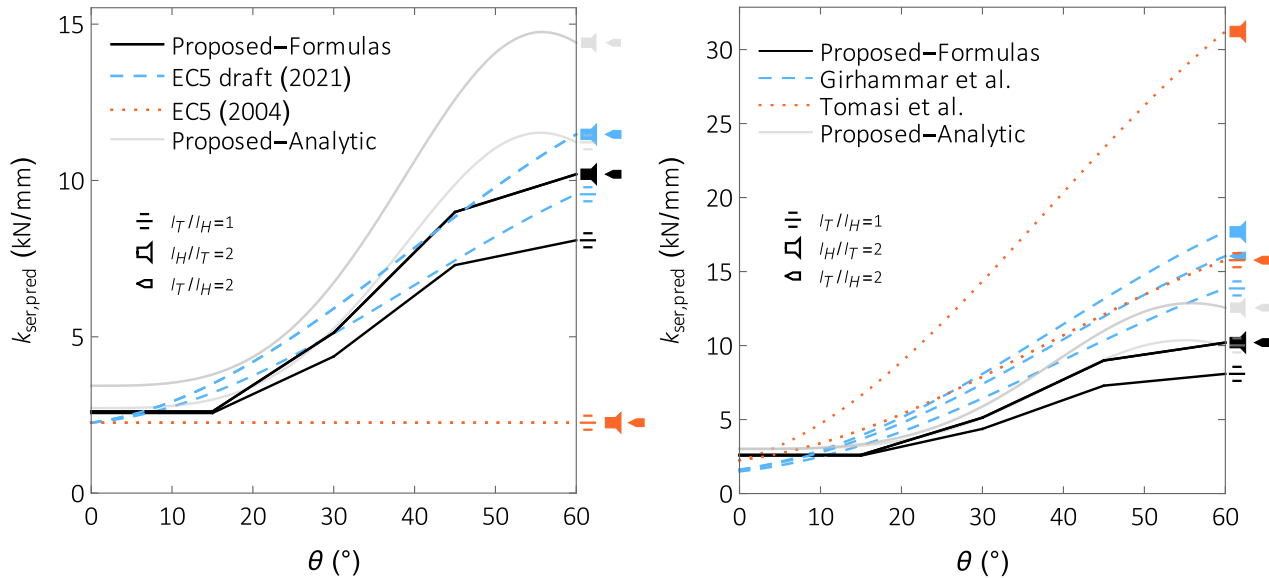

Figure 7 Models predictions for varying length penetration ($l_T= l_H$=75 mm, l_T=75 mm and l_H=150 mm and l_T=150 mm and l_H=75 mm). (a) Comparison of proposed formulas and model with standards proposal and current standard; (b) Comparison of proposed simplified formulas with exact solution of analytical model and other models.

The third parametric study aims to highlight how the expected values of the slip modulus vary when the density of the timber members on the screw head side or tip side are doubled (Figure 8). The analyzed configuration is characterized by $l_1=l_2$=100 mm and ϕ=8 mm. According to the proposed model and to the model of *Revision of Eurocode 5* (2021), the sliding modulus increases by the same amount by doubling the density of one or the other member. According to the Tomasi et al. model, the density affects only the lateral contribution, therefore doubling the density of any timber member produces the same limited increase of the slip modulus. In the Girhammar et al. model, as presented and applied by the author, the dependence of the slip modulus on density is not explicit, as the author considers experimentally derived embedment and withdrawal stiffnesses.
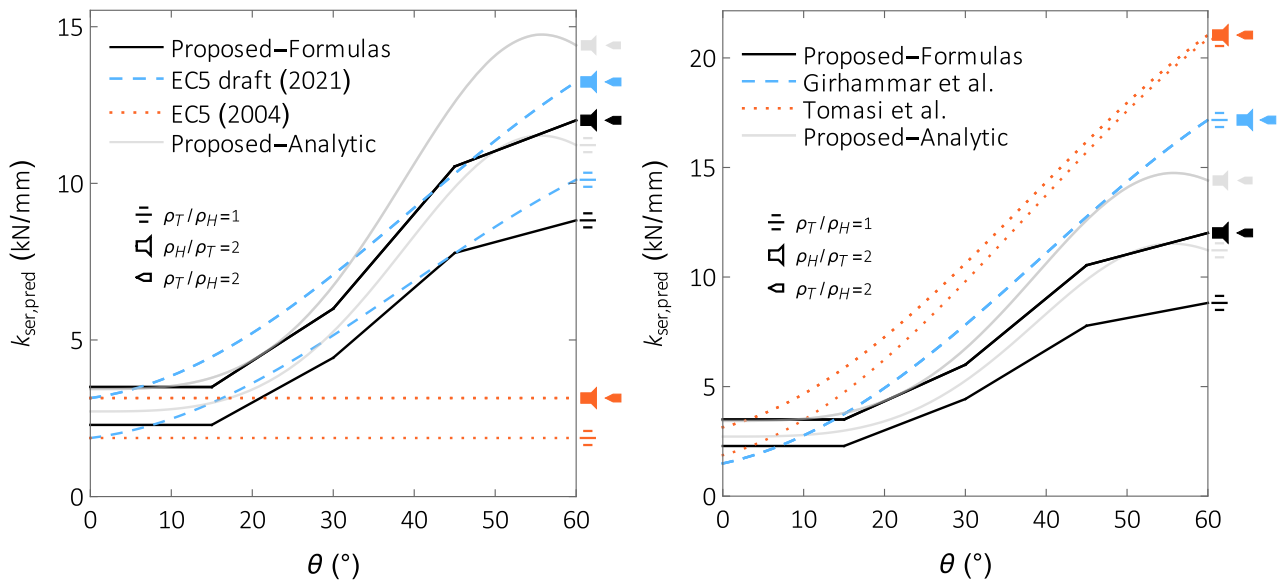
Figure 8 Models predictions for varying member densities ($\rho_1 = \rho_2 = 380$ kg/m³, $\rho_1 = 380$ kg/m³ and $\rho_2 = 760$ kg/m³ and $\rho_1 = 760$ kg/m³ and $\rho_2 = 380$ kg/m³). (a) Comparison of proposed formulas and model with standards proposal and current standard; (b) Comparison of proposed simplified formulas with exact solution of analytical model and other models.

5   Conclusions

The derived analytical model for calculating the slip modulus of screw connections proved effective. The proposed model allows to consider the effective flexural and axial stiffness of the screw, the orthotropic behavior of the timber and the geometric and mechanical characteristics of the connection.

The interpolation functions found for the foundation elastic modulus make the model completely predictive without the need to perform withdrawal tests. Therefore, the model allows to predict the sliding modulus when the external diameter of the thread, the density of the members, the penetration lengths and the angle of inclination are known.

The reliability of the proposed analytical model is similar to that of Girhammar et al. model, but both, due to their complexity, cannot be directly implemented in standards. Simplified formulas have been obtained from the proposed analytical model. Although the expression proposed in the revision drafts of Eurocode 5 (2021) for withdrawal stiffness was derived by interpolation of the results of withdrawal tests performed on specimens with the same screws and timber as many of the push-out tests taken as a reference for the validation of the models (*Blass & Steige*, 2018), the proposed simplified formulas are more accurate than the model of *Revision of Eurocode 5* (2021).

The proposed model allows to consider the withdrawal of the screw from both members resulting more accurate than Tomasi et al. model for those configurations in which the withdrawal stiffness of the tip-side cannot be considered infinitely greater

than that on the head-side, i.e. those cases in which the density and/or the length of penetration on the tip side are significantly lower than those on the head-side.

The proposed approach may be proposed for implementation in the revised EN 1995-1-1. Furthermore, an extension of this formula could also be proposed in an Annex of EN 1995-1-1 for the prediction of the slip modulus of connections with an interlayer.

6   References

Eurocode 5 (2004): Design of timber structures - Part 1-1: General and rules for buildings. CEN. (EN 1995-1-1).

Tomasi R., Crosatti A., Piazza M. (2010): Theoretical and experimental analysis of timber-to-timber joints connected with inclined screws. Constr. Build. Mater. 24, 1560–1571.

Girhammar U.A., Jacquier N., Källsner B. (2017): Stiffness model for inclined screws in shear-tension mode in timber-to-timber joints. Eng. Struct. 136, 580–595.

Blass H.J. & Steige Y. (2018): Steifigkeit axial beanspruchter Vollgewindeschrauben. KIT Scientific Publicing, Karlsruhe.

Blass H.J., Bejtka I., Uibel T. (2006): Trägfähigkeit von Verbindung mit selbst bohrenden Holzschrauben mit Vollgewinde. Karlsruher Berichte zum Ingenieurholzbau.

Ringhofer A., Brandner R., Schickhofer G. (2015): A Universal Approach for Withdrawal Properties of Self-Tapping Screws in Solid Timber and Laminated Timber Products. INTER, Sibenik (Croatia).

Allgemeine baufsichliche Zulassung (2006): SFS Befestiger WT-T-6,5, WT-T-8,2

und WR-T-8,9 als Holzverbindungsmittel. Deutsches Institut für Bautechnik (DIBt),

Z-9.1-472, Berlin (Germany).

Stamatopoulos H., Malo K. (2016): Withdrawal Stiffness of Threaded Rods Embedded in Timber Elements. Constr. Build. Mater. 116, 263–72.

Revision of Eurocode 5 (2021): Final draft revision of chapter connections. CEN/TC 250/SC 5 N 1339. (prEN 1995-1-1).

Symons D., Persaud R., Stanislaus H. (2010): Slip modulus of inclined screws in timber–concrete floors. Proc Instit Civ Engineers – Struct Build 163(4), 245–55.

Di Nino S., Gregori A., Fragiacomo M. (2020): Experimental and numerical investigations on timber-concrete connections with inclined screws. Eng. Struct. 209.

Gattesco N. (1998): Strength and local deformability of wood beneath bolted connectors. J. Struct. Eng. 124(2), 195–202.

Gattesco N., Toffolo I. (2004): Experimental study on multiple-bolt steel-to-timber tension joints. Mater. Struct. Constr. 37(2), 129–38.

Santos C.L., De Jesus A.M.P., Morais J.J.L., Lousada J.L.P.C. (2010): A Comparison Between the EN 383 and ASTM D5764 Test Methods for Dowel-Bearing Strength Assessment of Wood: Experimental and Numerical Investigations. Strain 46, 159-174.

Karagiannis V., Málaga-Chuquitaype C., Elghazouli AY. (2016): Modified foundation modelling of dowel embedment in glulam connections. Constr. Build. Mater.102, 1168–1179.

Tuhkanen E., Mölder J., Schickhofer G. (2018): Influence of number of layers on embedment strength of dowel-type connections for glulam and cross-laminated timber. Eng. Struct. 176, 361–368.

Franke S., Magnière N. (2014): The Embedment Failure of European Beech Compared to Spruce Wood and Standards. In: Aicher S., Reinhardt HW, Garrecht H (eds) Mater. Struct. Constr. RILEM Bookseries, vol 9. Dordrecht: Springer; 221-229.

Lederer W., Bader T.K., Muszyński L., Eberhardsteiner J. (2016): Exploring a Multimodal Experimental Approach to Investigation of Local Embedment Behaviour of Wood under Steel Dowels. Strain 52, 531-547.

Lederer W., Bader T.K., Unger G., Eberhardsteiner J. (2016): Influence of different types of reinforcements on the embedment behavior of steel dowels in wood. Eur. J. Wood Prod. 74, 793–807.

Schweigler M., Bader T.K., Hochreiner G., Unger G., Eberhardsteiner E. (2016): Load-to-grain angle dependence of the embedment behavior of dowel-type fasteners in laminated veneer lumber. Constr. Build. Mater. 126, 1020–1033.

Hwang K., Komatsu K. (2002): Bearing properties of engineered wood products I: effects of dowel diameter and loading direction. J. Wood Sci. 48, 295-301.

Schweigler M., Bader T.K., Bocquet J.F., Lemaitre R., Sandhaas C. (2019): Database of embedment parameters from soft and hardwoods. Linnaeus University, Växjö, Sweden.

UNI EN 26891 (1991): Timber structure – Joints made with mechanical fasteners – General principles for the determination of strength and deformation characteristic. CEN.

Schiro G., Giongo I., Sebastian W., Riccadonna D., Piazza M. (2018): Testing of timber-to-timber screw-connections in hybrid configurations. Constr. Build. Mater. 171, 170–186.

Wang F., Wang X., Cai W., Chang C., Que Z. (2019): Effect of Inclined Self-tapping Screws Connecting Laminated Veneer Lumber on the Shear Resistance. BioResources 14(2), 4006-4021.

Ringhofer A. (2016): Stiffness Properties of Axially Loaded Self-Tapping Screws. COST-STSM-FP1402-536 30283, Graz.

Jacquier N., Girhammar U.A. (2014): Tests on glulam–CLT shear connections with double-sided punched metal plate fasteners and inclined screws. Constr. Build. Mater. 72, 444–457.

DISCUSSION

The papers was presented by Y De Santis

R Brandner questioned the R^2 value being negative and greater than one. Y De Santis will provide definition of R2. R Brandner later acknowledged in chat that R^2 value outside the range of (0, 1) is possible without using real data.

H Blass commented that the comparison with Eurocode 5 formulation for inclined screws is meaningless as it does not deal with inclined screws. This should be removed from the paper.

W Dong stated that in Girhammer's work embedment test approach was considered to be similar to the compression test approach and deemed to be unsuitable for the model. Y De Santis said that embedment test results provided local deformability information of the timber to allow avoiding the need to experimentally evaluate withdrawal stiffness.

W Dong commented that using the two springs approach for the parallel and perpendicular to grain directions may result in discrepancy in boundary cases of withdrawal test results perpendicular to grain and embedment test results. Y De Santis agreed.

R Tomasi agreed that there may be issues at the extreme say at 0 or 90 degree. He asked about friction in the shear plane. Y De Santis said that model is valid but has an issue with the 90 degree case which is not a realistic situation. Friction was not considered in the model because they observed in some experimental sets say with cross configuration and in some inclined screw configurations, friction did not seem to be present. R Tomasi and Y De Santis discussed the consideration of double stiffness model and single stiffness model for various cases.

A Ringhofer received clarification that angle = 0 degree implies pure shear load.

P Dietsch suggested possible amendments of the paper to be considered based on the comments and discussion.

Connections with inclined screws and increased shear plane friction

Simon Aurand, Hans Joachim Blass

Karlsruhe Institute of Technology (KIT), Timber Structures and Building Construction

1   Introduction

Joist to header connectors are widely available in different shapes and sizes. One of the most common types resembles dovetail connections, where two parts slide into each other to enable load transfer (Figure 1a). Usually, aluminium is used for the connectors. One scope of the here presented project was to replace the aluminium with densified veneer wood (DVW). The connectors are mostly fastened with self-tapping and fully threaded screws, which are often inclined by 45° to the connector plane. In such connections with inclined screws, the load parallel to the shear plane is mainly transferred by axial screw loading, see *Bejtka & Blass (*2002). Due to equilibrium conditions, a compressive force results perpendicular to the shear plane. This compressive force leads to frictional resistance*,* which depends on the size of the compressive force and the coefficient of friction μ. For connections with inclined screws, this additional load-carrying capacity can be taken into account by default, although the screws are loaded in tension. This is the difference to connections under combined lateral and tensile load, where the load increase due to friction, i.e. the rope effect, cannot be applied. Another scope of the project was to utilize the frictional resistance, which depends on the size of the compressive force and the coefficient of friction (COF). Therefore, two possibilities can be examined: (i) increasing the compressive force by designing the connection to reach the tensile capacity of the screws and (ii) increasing the COF by treating the surface adequately. The latter was done in this study.

To increase the load-carrying capacity due to surface treatment, first an extensive literature review was accomplished. This was followed by own tests to modify the surface and determine the COF and hence the optimal modification. Following this, push-out tests with connectors made of the afore mentioned DVW were performed. Finally, an analytical model for the load-carrying capacity was derived.
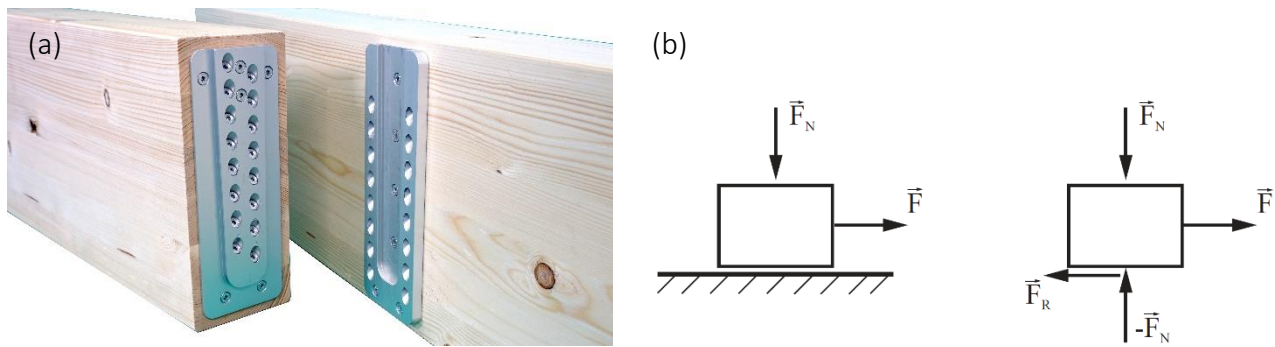
Figure 1. (a) Aluminium dove tail connector. (b) A body stressed by normal and tangential forces and the force equilibrium with the reaction force F_N and the friction force F_R (Popov (2015)).

2 Friction – Literature review

2.1 Introduction

The COF is defined as the dimensionless ratio of the friction force F_R between two bodies to the normal force F_N perpendicular to the contact area between these bodies (Figure 1b). The static COF μ_{stat} corresponds to the maximum friction force that must be overcome to initiate relative displacement between two bodies.

In the literature, many different values for the static COF for wood on wood as well as steel on wood can be found. Table 1 gives an overview of the publications having determined the COF for wood on wood or wood on steel. Also given is the number of values, which were taken from the literature. This number is not necessarily equal to the performed tests. For example, *Stošié (*1959) performed 9000 tests in total, however, only ten values can be extracted from his two-page article. In most of the research listed in Table 1 many parameters were varied, such as the contact pressure between the specimens (normal force F_N), the sliding speed, the surface roughness, the angle between the grain direction of the wood specimens and the sliding direction, as well as the moisture content. The following sections examine a possible correlation between the COF and the respective parameter.

The values in Table 1 and from Figure 3 through to Figure 9 are all taken from the literature and do not include test results from chapter 4.

2.2 Test setup

The most common test setups can be seen in Figure 2. Setup (a) with the inclined plane is very easy to use. The normal force is applied with weights and the plane is inclined just until the specimen starts sliding. However, due to the constantly changing contact pressure depending on the angle, the inclined plane is not suitable to determine the COF reliably (*Stošié (*1959)). Because of its simple design, the horizontal plane (b) was the most used test setup. This setup allows the evaluation of parameters such as contact pressure and sliding speed. Test setup (e) is similar to the horizontal plane with the only difference using a vertical cylinder to apply the normal force. The rotating plane in setup (c) was mostly used for tests with wood sliding on steel. An effective setup for higher contact pressure but without having to use a second cylinder is setup

(d) with pre-stressed rods. However, the size of the specimen is much larger than for the other tests and also the time to assemble the specimen takes longer. The last setup (f) for shear tests with inclined screws is not primarily used for determination of the COF, but the COF can be back calculated (*Blass & Steige (*2018)).
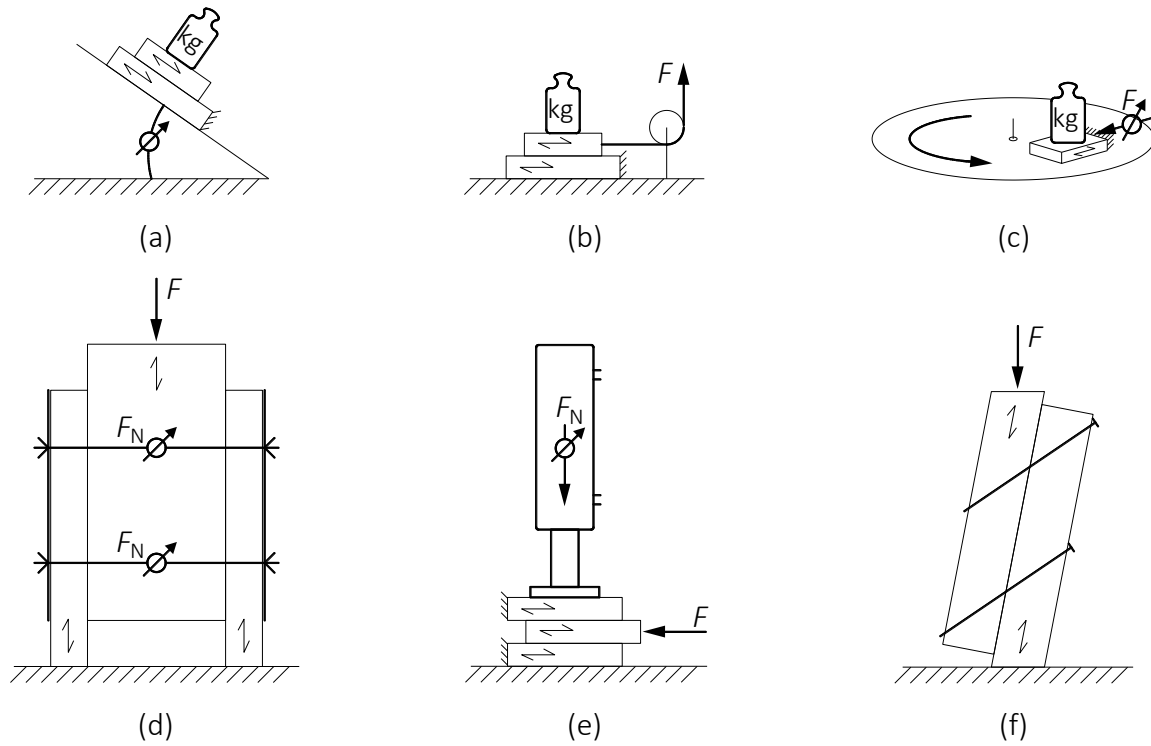

Figure 2. Test setups to determine the coefficient of friction: a) inclined plane b) horizontal plane, c) rotating plane d) pre-stressed rods e) two hydraulic cylinders f) shear tests with inclined screws.

2.3   Contact pressure

Figure 3 shows the influence of the contact pressure on the static COF. The recorded pressures ranged from 0.0001-1.0 N/mm² for tests with wood on wood and from 0.0069-30 N/mm² for tests with steel or aluminium on wood. The logarithmic trend line shows firstly an increase of the COF with rising contact pressure and later a horizontal convergence. For the tests with steel / aluminium on wood, no correlation between the COF and the contact pressure can be observed.
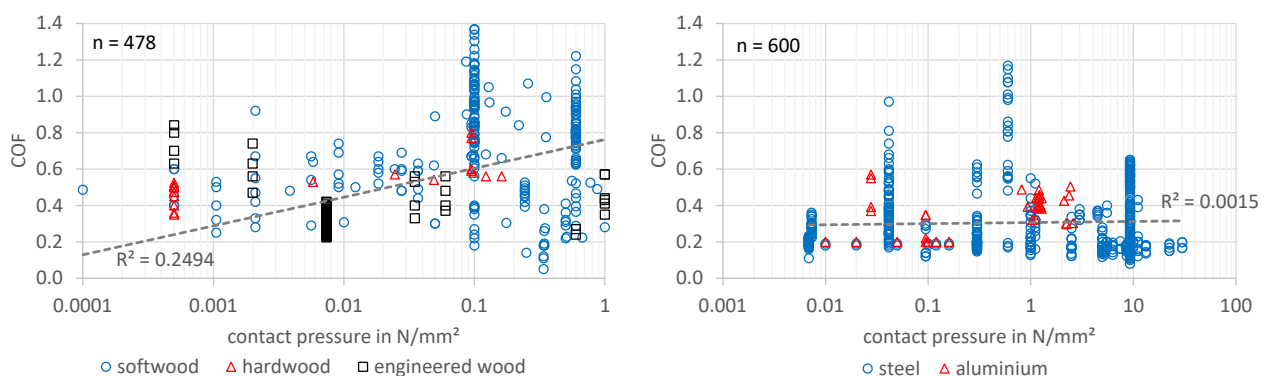

Figure 3. COF versus contact pressure for wood on wood (left) and steel on wood (right).

Table 1. Reviewed literature and respective number of friction coefficients found in the literature (this list is not intended to be exhaustive). Values of μ_{stat} only for MC < 20%.

Publication	Total no. of tests resp. no. of series	μ_{stat}	Total no. of tests resp. no. of series	μ_{stat}
SOFTWOOD	ON SOFTWOOD		ON STEEL / ALUMINIUM	
Aira et al. (2014)	9	0.05-0.38	-	-
Atack & Tabor (1958)	-	-	2	0.50-0.60 [1]
Blass & Steige (2018)	79	0.02-1.03	-	-
Claus et al. (2018)	19	0.14-0.89	-	-
Crespo et al. (2011)	10	0.39-0.53	-	-
Gaber (1940)	41	0.17-0.92	-	-
Garcia (2012)	-	-	4	0.39-0.57
Gorst et al. (2003)	45	0.30-0.80	159	0.30-0.70
Guan et al. (1983)	-	-	58	0.17-0.38
Koch (2011)	6	0.37-0.66	-	-
Koubek & Dedicova (2014)	-	-	108	0.10-0.90
Lemoine et al. (1970)	-	-	48	0.10-0.57
McKenzie & Karpovich (1968)	6	0.45-0.60	47	0.11-0.65
Meng et al. (2008)	-	-	24	0.23-0.36
Möhler & Herröder (1979)	132	0.29-1.37	20	0.55-1.15
Möhler & Maier (1969)	16	0.22-1.19	-	-
Murase (1984)	10	0.60-0.68	30	0.18-0.20
Niemz & Sonderegger (2017)	1	0.34	-	-
Park et al. (2011)	20	0.44-0.74	-	-
Schmidt (2018)	-	-	18	0.22-0.63
Seki et al. (2013)	-	-	30	0.12-0.39
Stošié (1959)	5	0.30-0.49	-	-
Xu et al. (2014)	5	0.40-0.60	-	-
	sum = 404	mean = 0.48	sum = 548	mean = 0.34
HARDWOOD	ON HARDWOOD		ON STEEL / ALUMINIUM	
Gorst et al. (2003)	18	0.40-0.60	99	0.30-0.70
Guan et al. (1983)	-	-	14	0.20-0.30
McKenzie & Karpovich (1968)	-	-	105	0.08-0.64
Murase (1984)	10	0.53-0.60	-	-
Niemz & Sonderegger (2017)	4	0.28-0.46	-	-
Stošié (1959)	3	0.30-0.31	-	-
Xu et al. (2014)	10	0.35-0.53	-	-
	sum = 45	mean = 0.49	sum = 218	mean = 0.41
ENGINEERED WOOD	ON SOFTWOOD / HARDWOOD		ON STEEL / ALUMINIUM	
Bejo et al. (2000)	16	0.33-0.84	-	-
Gorst et al. (2003)	207	0.10-0.60	210	0.10-0.70
Koubek & Dedicova (2014)	-	-	70	0.12-0.63
Meng et al. (2008)	192	0.23-0.42	-	-
Niemz & Sonderegger (2017)	72	0.12-0.59	-	-
Steiger et al. (2018)	8	0.24-0.57	-	-
	sum = 495	mean = 0.30	sum = 280	mean = 0.25

1) MC > 20%

2.4 Sliding speed

The recorded sliding speeds ranged from 1-3300 mm/min for tests with wood on wood and from 1-2640000 mm/min (= 44 m/s) for tests with steel / aluminium on wood. Figure 4 shows an increase at the beginning with increasing sliding speed and later a horizontal convergence.
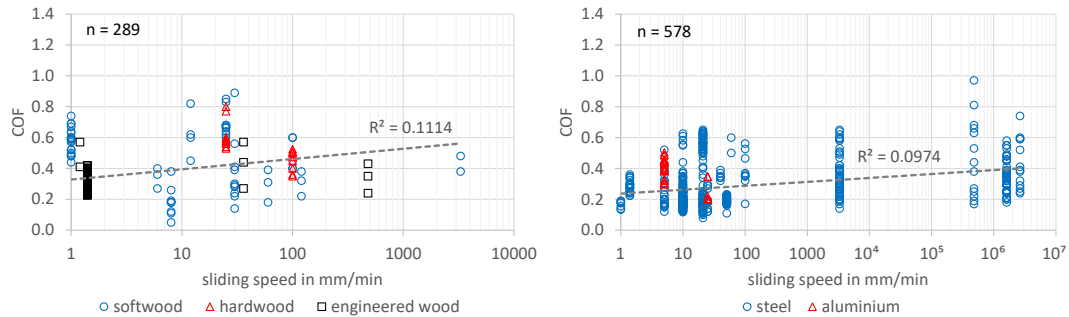

Figure 4. COF versus sliding speed for wood on wood (left) and steel on wood (right).

2.5 Density

Figure 5 shows no correlation between the COF and the density of the wood specimens. In general, there were very few results for tests with hardwood (*n* = 119) of which for only 20 specimens the density was recorded.
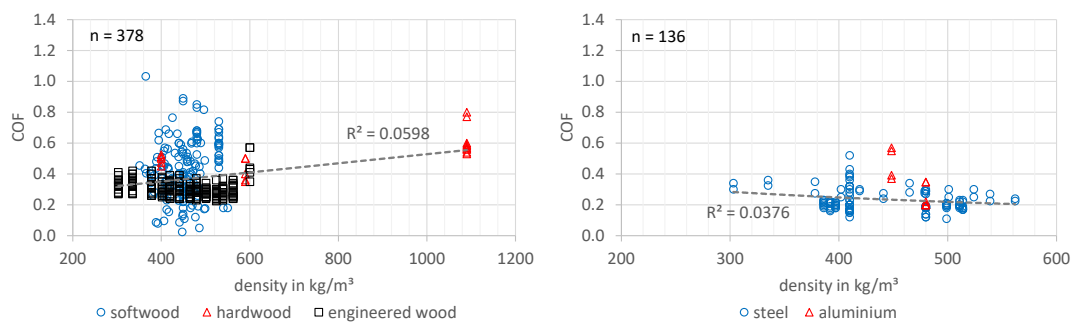

Figure 5. COF versus density for wood on wood (left) and steel on wood (right).

2.6 Moisture content

The moisture content was the only parameter, which was given for almost all tests. The moisture content of the wood specimens has the most distinct influence on the static COF (Figure 6). Especially for the tests with wood on wood, a moisture content greater than 20% led to a notable increase of the COF. The tests with steel / aluminium on wood were mostly independent of the moisture content of the wood.
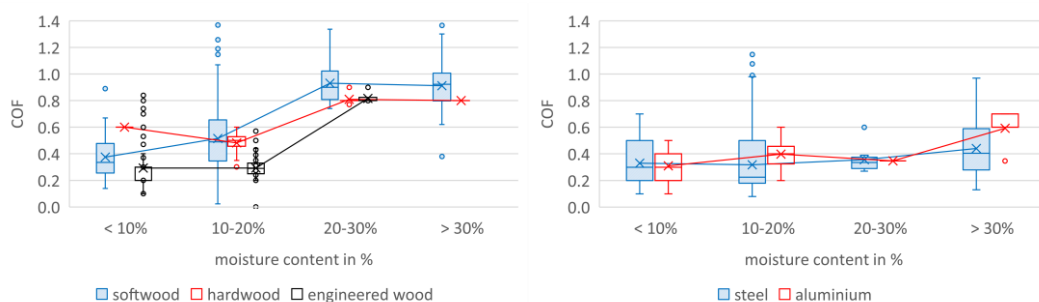

Figure 6. COF versus moisture content for wood on wood (left) and steel on wood (right).

2.7 Surface roughness

As expected, the surface roughness of the tested specimens had the highest influence on the COF. Figure 7 shows a box plot with three different surfaces for wood on wood (left) and four different surfaces for steel on wood (right). Treated surfaces were for example formwork panels. The classification "normal steel" was used when no other surface quality was explicitly mentioned.
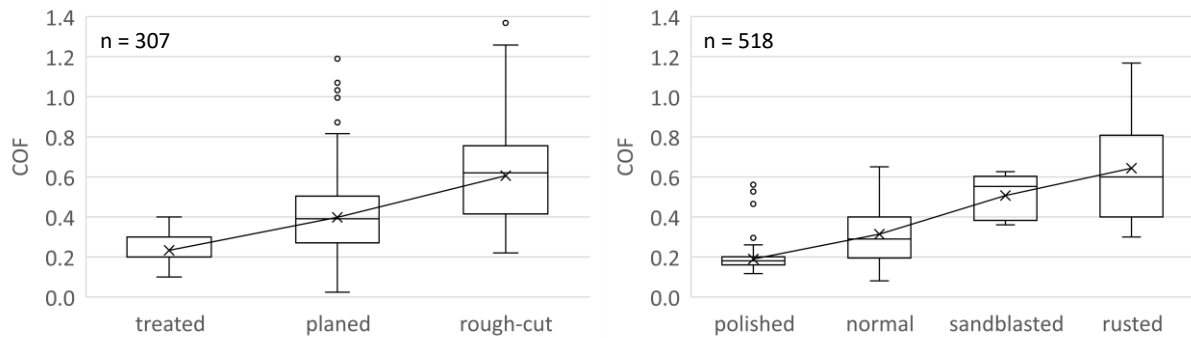

Figure 7. The effect of the surface roughness on the static COF for wood (left) and steel (right).

2.8 Grain direction

In many tests the orientation of the grain with regard to the sliding direction was varied, with the different orientations being parallel (grain direction of the specimens parallel to each other), perpendicular (one specimen rotated by 90°) and end grain (end grain sliding on end grain). In some publications further angles were examined, but for the sake of clarity only the three main directions parallel, perpendicular and end grain were considered in Figure 8. The difference in the COF for parallel and perpendicular was marginal, and it can be stated, that the grain direction had close to no influence on the COF. Only exception were the tests with end grain on end grain and steel on end grain, respectively.
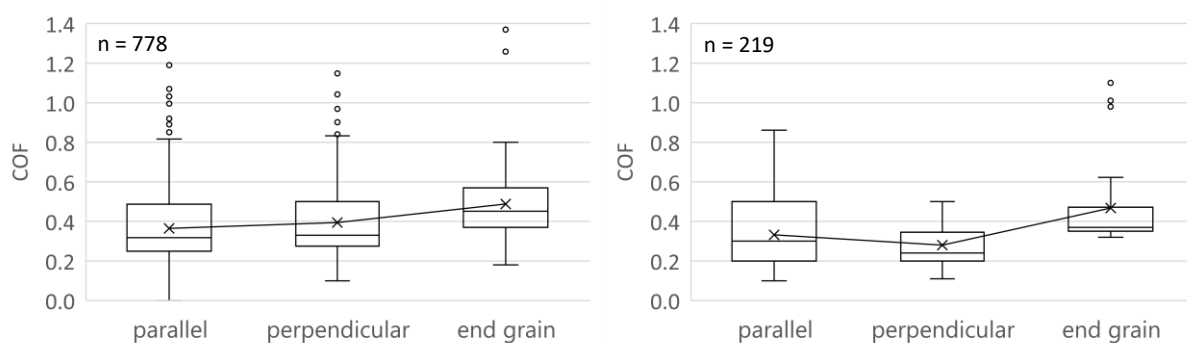

Figure 8. The effect of the grain direction of the surface on the static COF for wood on wood (left) and steel on wood (right).

2.9 Scatter of the COF

As it is evident by now, the values of the COF vary to a large extent for the same tested surfaces and parameters. To highlight the scatter, Figure 9 shows an exemplary plot for the COF of softwood on softwood, hardwood on hardwood, engineered wood on either softwood or hardwood, as well as steel and aluminium on softwood. The sliding

direction for all tests was parallel to the grain of the wood specimens. The moisture content was ≤ 20% and the wood surface was planed. Taking the COF for softwood as an example: the minimum is 0.02 and the maximum is 1.19, resulting in a coefficient of variation of 50%. For hardwood and aluminium the scatter is smaller, however the number of tests is equally lower.
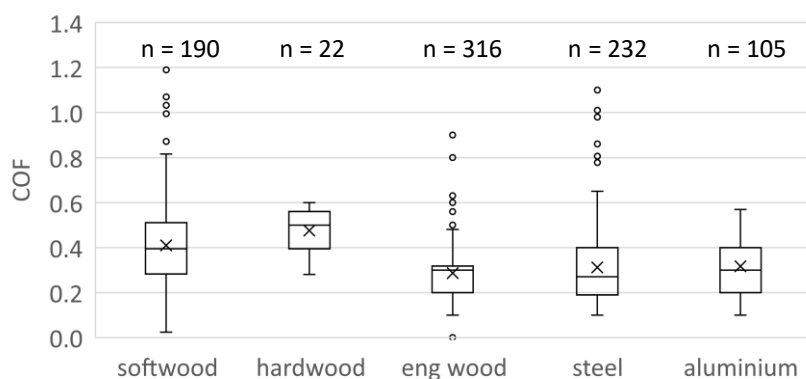

Figure 9. Scatter of the static COF (sliding direction = parallel, MC ≤ 20%, surface = planed where applicable).

3 Surface modification

For the connectors to reach high load-carrying capacities and stiffnesses the friction between connector and timber part should be increased. Therefore, various surface modifications have been investigated experimentally to increase the COF. In tests, the COF for each modified surface was determined and characteristic values were calculated as 5th-percentile values. As mentioned before, DVW was used for the specimens with sizes of 110 x 150 mm. The results are given in Table 2.

3.1 Sanded

The top layer of the test specimen was sanded using a belt sander and sandpaper with P40 grit. The sanding was carried out perpendicular to the fibre direction of the top layer and therefore perpendicular to the sliding direction during the friction tests. A noticeable structuring was visible.

3.2 Sandblasted

Each test specimen was sandblasted manually on both sides. As a result, slightly different surfaces appeared on each side and on each test specimen. During the sandblasting, it was observed that the earlywood of the veneers was removed and only the latewood remained. This resulted in a structuring along the grain direction of the cover veneers and thus parallel to sliding direction.

3.3 Brushed

Both surfaces of the test specimen were brushed with a braided steel wire pot brush. A clear structuring of the surface was visible, but the roughness was hardly noticeable. In preliminary tests, only a very low COF was determined and therefore this type of surface treatment was not further pursued.

3.4 Coated

Two different bonding agents were used: firstly, a pasty two-component adhesive and secondly, an epoxy resin adhesive tape. The test specimens were coated either with quartz sand with a grain size of 0-2 mm or with grit with a grain size of 2-4 mm. Additionally, the specimens of one series were coated with skateboard griptape.

3.4.1 Two-component adhesive (2K SE-polymer)

A two-component epoxy resin was used. The surfaces of the test specimens were sand-blasted before the adhesive was applied. A 0.5 mm thick adhesive layer was chosen for coating with quartz sand (Figure 10) and a 1.0 mm thick adhesive layer for coating with grit. The test specimens were pressed manually into the respective aggregate. The specimens cured at room temperature for one week, according to the manufacturer's instructions.

Figure 10. Coated surface with 2K epoxy resin and quartz sand 0-2 mm.

3.4.2 Epoxy adhesive tape (EpoxyTape)

Epoxy resin adhesive tapes with an adhesive layer thickness of 1.0 mm and 0.1 mm were used. The tapes were applied at room temperature and then cured in the oven at a temperature of 130°C for 45 min. For both thicknesses of adhesive tape, only the quartz sand was chosen and pressed with a constant pressure of 2 N/mm² for two minutes.

3.4.3 Griptape

A commercially available griptape for the top of skateboards for better grip was used. The grain of the griptape was significantly finer than that of the quartz sand and resembled sandpaper. The processing of the grip tape was significantly easier as it already combined adhesive tape and aggregate.

3.5 Milled

Different patterns were examined by using different milling tools on a CNC milling machine, such as a chamfer cutter for longitudinally and transversely arranged grooves or a cartridge mill for circular grooves

3.5.1 Pyramid pattern

Girardon (2014) developed form-fitting and rigid connections with milled surfaces. Based on his studies, parallel grooves with the same depth were milled into the top layer of the test specimens using a chamfer cutter. The test specimens were then rotated by 90° and again parallel grooves were milled into the top layer resulting in small

pyramids. Test specimens with 0.5 mm, 1.0 mm, 1.5 mm and 2.0 mm deep grooves were produced. Figure 11a shows an example of a test specimen with pyramids 1.5 mm deep.

3.5.2 Circular grooves

Circular grooves with multiple intersections were milled 1.0 mm deep into the top layer of the DVW (Figure 11b). As a result, pyramid-like shapes remained at the edge of the test specimen while elongated grooves with a spacing of about 1.5 mm remained in the middle of the test specimen.

3.5.3 Scale pattern

Using a simple end mill that was inclined by 5°, longitudinal and transverse grooves were milled 1 mm deep into the surface, similar to the pyramid pattern (Figure 11c). This created a scale pattern. Again, preliminary tests resulted in a low COF and therefore this pattern was not further examined.

3.5.4 Embossed pattern

The pyramid pattern was milled into a steel plate. The steel plate was then pressed into the surface of the DVW. The pyramid tips penetrated about 1.0 mm into the top layer and a surface embossed with the impression of the pyramid pattern was created (Figure 11d).
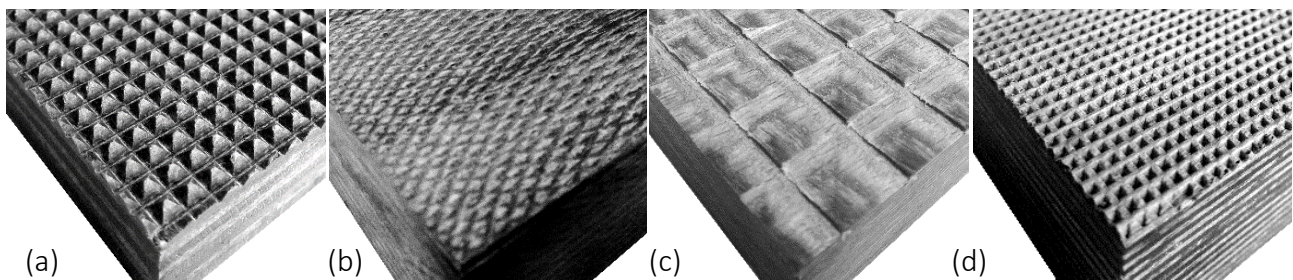

(a)   (b)   (c)   (d)

Figure 11. Milled surfaces: (a)pyramid pattern(b)circular grooves(c)scale pattern(d)embossed surface.

3.6 Sheet metals

Additionally to the tests with DVW and modified surfaces, some tests with different sheet metals were performed. On the one hand a chequer plate was used, which is normally applied for e.g. anti-slip flooring (Figure 12a), on the other hand sheets with perforated round holes were used. Type 1 had a clear-cut round hole (e.g. steel scaffold planks, Figure 12b) while for type 2 the excess material led to small, sharp hooks (similar to a kitchen grater, Figure 12c).
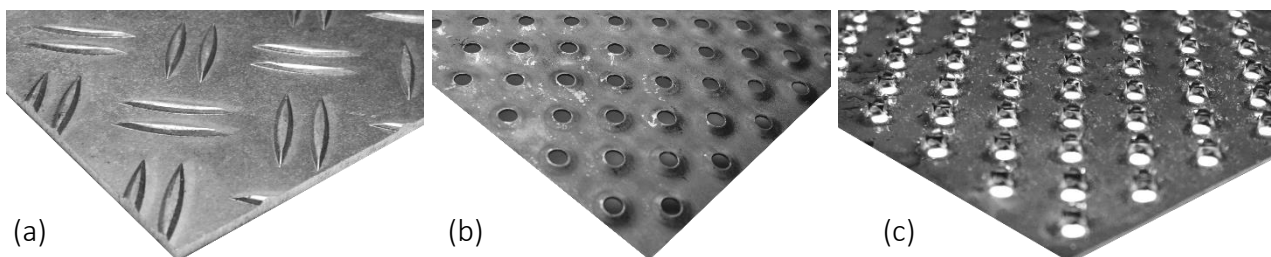

(a)   (b)   (c)

Figure 12. Sheet metals: (a) chequer plate (b) perforated sheet metal 1 (c) perforated sheet metal 2.

4 Tests to determine the COF

4.1 Test setup

The test setup is shown in Figure 13. The normal force F_N perpendicular to the friction surface was applied with a threaded rod and a spindle. F_N was measured continuously during the tests with a load cell. Spruce/fir with a mean density of $\rho = 420$ kg/m³ was used for the softwood, which was stored in a standard climate 20/65 and had an average moisture content of $u = 12\%$. The surfaces were free of knots larger than 5 mm and without adhesive joints. The tangential force F parallel to the friction surface was applied using a universal testing machine. The entire test sequence was displacement controlled up to a displacement of 15 mm.
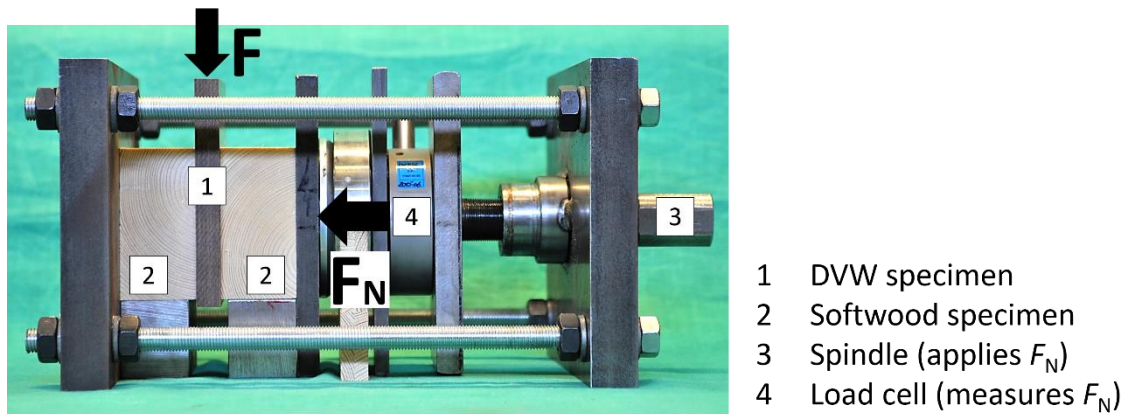

1	DVW specimen
2	Softwood specimen
3	Spindle (applies F_N)
4	Load cell (measures F_N)

Figure 13. Test setup for friction tests.

For the tests, it was distinguished between face grain parallel and perpendicular to the sliding direction as well as end grain of the softwood. The different test configurations are highlighted in Figure 14. For the tests, side members with a similar density were chosen.
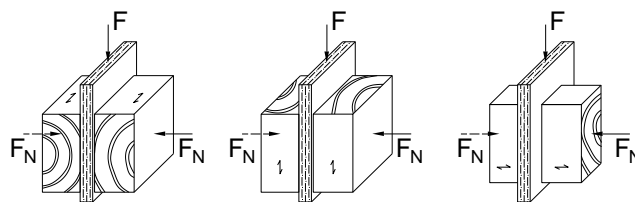

Figure 14. Grain and sliding direction.

4.2 Results

At the beginning, the parameters contact pressure and sliding speed were varied, in order to confirm the established trends from the literature review. The contact pressure was varied between 1, 2.5 and 6 N/mm². The sliding speed was varied between 1, 5 and 10 mm/min, to fill the gaps in the range found in the literature. No correlation between the COF and the two varied parameters was visible (Figure 15). Based on these results, the following tests were conducted with a contact pressure of 2.5 N/mm², corresponding to the characteristic compressive strength perpendicular to

the grain of softwood. The sliding speed was set at 5 mm/min, because then a pronounced peak with the onset of sliding followed by subsequent continuous sliding was observed.
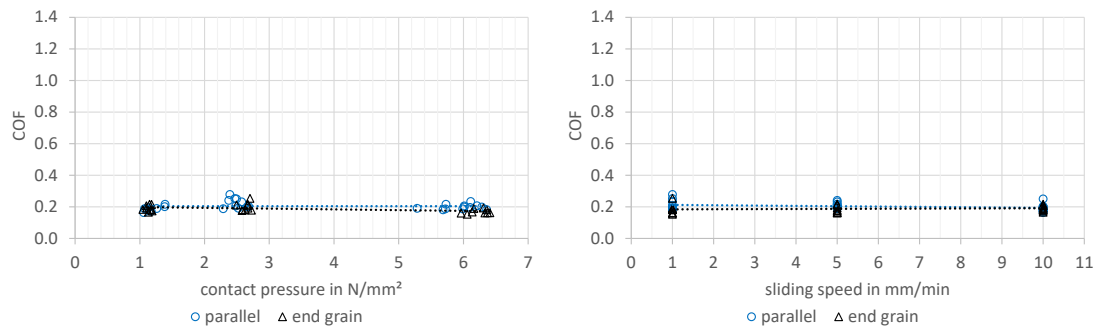

Figure 15. COF versus contact pressure (left) and sliding speed (right).

4.2.1 Untreated surface, aluminium, sanded, and sandblasted surfaces

In order to create reference values and to quantify the effect of subsequent surface treatments, a first series of tests was carried out with smooth, untreated DVW. In addition, tests were performed with anodised aluminium, as found in most system connectors. On average, a COF for the smooth surface of $\mu = 0.20$ and for aluminium of $\mu = 0.38$ was determined. For the sanded and sandblasted surfaces the determined values were already significantly higher with $\mu = 0.56$ and $\mu = 0.49$, respectively.

4.2.2 Coated surfaces

For the test specimens with the two-component adhesive, adhesive failure of the coating was observed. The glue and aggregate came off the DVW almost completely. This observation was independent of the grain size of the coating (Figure 16 left). Due to the failure of the adhesive, only a lower limit for the COF was determined. This was $\mu = 0.64$ for coating with quartz sand and $\mu = 0.61$ for coating with grit.

Figure 16. Coated test specimens: 2K adhesive and grit (left) and griptape (right).

Adhesive failure also occurred when coating with epoxy tape with a layer thickness of 0.1 mm. However, only a few spots of the epoxy tape came off the DVW. During the tests with the epoxy tape with a thickness of 1.0 mm cohesive failure occurred and the aggregate stuck to the softwood. Overall, the results showed significantly higher friction coefficients than with the pasty epoxy resin and were on average $\mu = 0.82$ for the thin and $\mu = 0.74$ for the thick epoxy tape. For the tests with griptape, again no exact COF was determined due to the lack of adhesion of the griptape to the DVW (Figure 16 right). The average COF was $\mu = 0.24$, which is only slightly higher than for untreated DVW.

4.2.3 Milled surfaces

For all four examined pyramid patterns the results for the COF were significantly higher than for the surface treatments shown so far with $\mu = 0.82$ (0.5 mm), $\mu = 0.89$ (1.0 mm), $\mu = 1.06$ (1.5 mm) and $\mu = 1.15$ (2.0 mm). The larger the pyramids the deeper they pressed into the softwood and the higher the COF determined. For the tests with the circular pattern and the scale pattern, the mean values were calculated to $\mu = 0.89$ and $\mu = 0.66$. The tests with the embossed pattern lead to a COF of $\mu = 0.79$.

4.2.4 Sheet metals

On average, the COF for the chequer plate was $\mu = 0.74$ and therefore considerably higher than the COF for a normal steel or aluminium surface. The tests with the perforated sheet type 1 resulted with an even higher COF of $\mu = 0.98$, mainly because the surface with the small punched holes interlocked better with the softwood than the rather big texture of the chequer plate. For the tests with the perforated sheet type 2 only a lower limit of the COF was determined with $\mu = 0.82$. Because of the sharp hooks and the high interlocking, the tensile strength of the very thin sheets was reached.

4.3 Characteristic values

The characteristic values were calculated based on EN 14358. For the 5th-percentile a global coefficient of variation COV_g was calculated based on all friction tests according to EN 14545. A total of $n = 467$ friction tests were performed and the COV_g was calculated to 0.10, resulting in $k_s(n) = 1.76$.

Table 2. Values for the static COF (mean and characteristic).

Surface	COF								
	face grain ⊥			face grain ‖			end grain		
	mean	char.	n	mean	char.	n	mean	char.	n
Untreated	0.20	0.17	31	-	-		0.19	0.16	27
Sanded	0.56	0.47	6	-	-		0.47	0.40	6
Sandblasted	0.49	0.41	6	-	-		0.47	0.40	6
Coated with 2K-epoxy + quartz sand	0.64	0.54	3	-	-		0.54	0.46	3
Coated with 2K-epoxy + grit	0.61	0.52	3	-	-		0.69	0.58	3
Coated with EpoxyTape (0.1 mm)	0.82	0.69	3	-	-		0.97	0.82	3
Coated with EpoxyTape (1.0 mm)	0.74	0.63	3	-	-		0.82	0.69	3
Coated with Griptape	0.24	0.20	3	-	-		0.32	0.27	4
Milled 0.5 mm pyramid pattern	0.84	0.71	40	0.82	0.69	10	0.82	0.69	30
Milled 1.0 mm pyramid pattern	0.94	0.79	15	0.88	0.74	20	0.80	0.68	10
Milled 1.5 mm pyramid pattern	1.06	0.90	20	1.03	0.87	19	1.06	0.90	18
Milled 2.0 mm pyramid pattern	1.15	0.97	12	-	-		-	-	
Milled circular grooves	0.89	0.75	14	0.78	0.66	20	0.82	0.69	13
Milled scale pattern	0.66	0.56	7	0.55	0.46	2	-	-	
Embossed pattern	0.79	0.67	30	0.67	0.57	10	0.71	0.60	21
Aluminium	0.38	0.32	12	-	-		0.43	0.36	12
Chequer plate	0.74	0.63	6	0.85	0.72	6	-	-	
Perforated sheet type 1	0.98	0.83	2	0.78	0.66	2	-	-	
Perforated sheet type 2	0.83	0.70	3	-	-		-	-	

5 Tests with inclined screws

5.1 Test setup and execution

To validate the impact of the higher COF on the load-carrying capacity, push-out tests with inclined screws were performed. Connector plates made of densified veneer wood with modified surfaces were fastened to softwood with fully threaded screws. The screws were inclined by 45°. The experimental setup is shown in Figure 17. The test specimens were loaded with a universal testing machine. The relative displacement of each connection was measured on the front and back of the test specimens. The test procedure and the evaluation were based on EN 26891. Both the ultimate test load $F_{V,test}$ and the stiffness k_s per connector were determined. The stiffness was determined in the range between 10% and 40% of the ultimate load in the linear-elastic range.
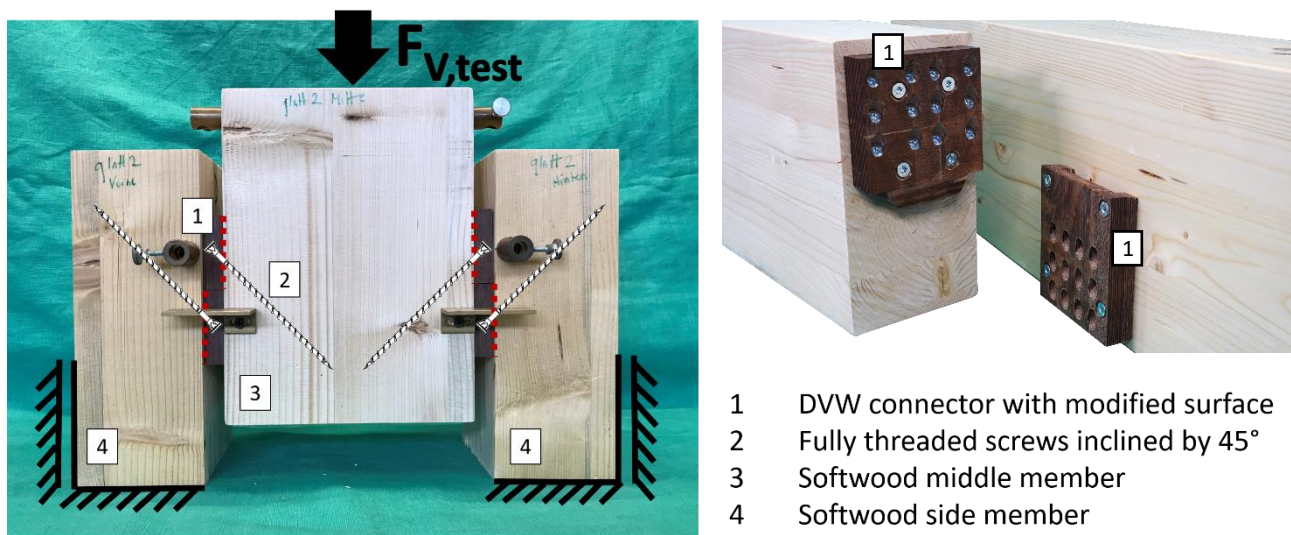

1	DVW connector with modified surface
2	Fully threaded screws inclined by 45°
3	Softwood middle member
4	Softwood side member

Figure 17. Test setup for push out tests with connectors with modified surfaces and inclined screws.

Table 3 summarises the tested configurations. The given number of screws is per shear plane. The series differ in the type of surface treatment, the number of screws, and the type of screws. In a first series (S1), most of the previously introduced surfaces were tested. In series 2 (S2) the screw arrangement was varied. In series 3 (S3) longer screws were used to validate the analytical model. In series 4 (S4) 15 screws were used per connector to investigate the influence of the number of screws. In series 5 (S5) the same connectors were tested with longer screws. Lastly, in series 6 (S6) and 7 (S7) two connector prototypes were tested to compare to conventional system connectors made of aluminium. For more details on the tests with the DVW connectors see *Aurand & Blass (*2021).

5.2 Results

Table 3 shows the ultimate loads and corresponding stiffnesses for all surfaces examined. The ultimate loads were determined independently of the displacement. The results show a significant increase in the load-carrying capacity of the connection for any

type of surface modification. The only exception to this are the tests with griptape. The mean value of the ultimate load of the tests with untreated surface was $F_{V,test}$ = 40.5 kN per connector. Maximum loads of around 53 kN were determined for the different pyramid patterns, which implies a capacity increase of over 30% (albeit the different displacements). Load-displacement plots for all series are shown in Figure 18. Within the different series, the specimens differ in their surface treatment. For the sake of clarity, only two curves are labelled exemplarily.
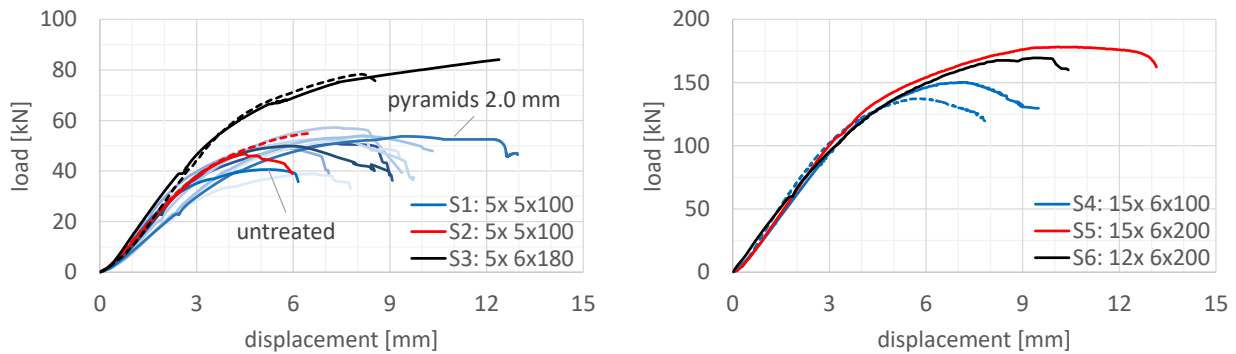

Figure 18. Load-displacement plots (averaged curves) for all tests of series 1, 2 and 3 (left) and series 4, 5 and 6 (right).

It is noteworthy that with greater pyramid size a higher COF was reached and thus a higher load-carrying capacity. However, the greater pyramid sizes led to lower stiffnesses. In general, it can be stated that higher stiffnesses were reached with less protruding surfaces (see also series 4). This might be because with the flat surfaces immediately full contact between the surfaces was reached, whereas the rougher surfaces needed some initial displacement to interlock.

The observed failure modes for series 1-4 were either a tensile failure of one or more screws in the shear plane or a withdrawal of the screws from the softwood members. For the series 5-7, with significantly higher ultimate loads, also compressive failure of the connector plates was observed. Furthermore, large displacements of the connectors were observed for these series. After opening the test specimens, clearly visible plastic hinges close to the shear plane were noticed (Figure 19). Another failure mode for series 6 and especially series 7 was compressive failure perpendicular to the grain of the timber members. Because of the large number of screws on the relatively small area, high contact pressure perpendicular to the grain occurred under the connector plates.
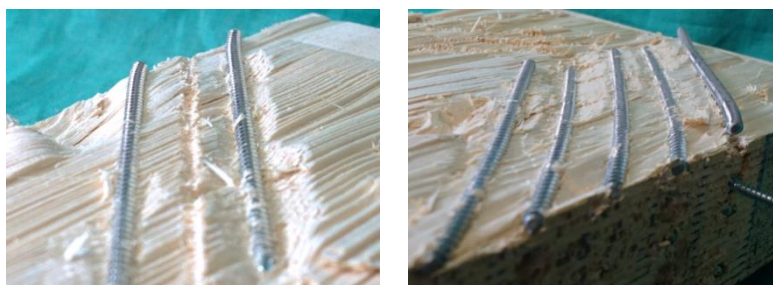

Figure 19. Plastic deformation of screws 6x200 (left) and 8x300 (right).

Table 3. Ultimate loads and stiffnesses and corresponding density (mean values).

	Surface	No. of tests	No. of screws	Screws [mm]	Density [kg/m³]	$F_{V,test}$ [kN]	k_s [kN/mm]
S1	Untreated	3	5	5x100	468	40.5 ± 0.8	16.7 ± 0.9
S1	Sanded	3	5	5x100	473	50.3 ± 1.6	16.3 ± 2.9
S1	Sandblasted	3	5	5x100	477	50.6 ± 1.7	17.9 ± 2.5
S1	EpoxyTape 0.1 mm + sand	3	5	5x100	465	57.8 ± 1.2	13.6 ± 0.7
S1	EpoxyTape 1.0 mm + sand	3	5	5x100	480	52.3 ± 2.3	11.4 ± 0.7
S1	Griptape	3	5	5x100	486	39.0 ± 2.1	11.4 ± 0.9
S1	Pyramid pattern 1.0 mm	3	5	5x100	440	52.9 ± 4.0	15.6 ± 0.8
S1	Pyramid pattern 1.5 mm	3	5	5x100	446	53.4 ± 1.3	12.2 ± 0.7
S1	Pyramid pattern 2.0 mm	3	5	5x100	438	52.8 ± 2.1	11.0 ± 1.0
S1	Circular grooves	3	5	5x100	477	49.9 ± 0.2	14.7 ± 1.4
S2	Pyramid pattern 1.0 mm	5	5	5x100	455	49.1 ± 3.8	14.1 ± 2.5
S2	Pyramid pattern 1.5 mm	5	5	5x100	461	47.8 ± 5.4	15.0 ± 3.2
S3	Pyramid pattern 0.5 mm	5	5	6x180	445	84.5 ± 5.3	17.8 ± 1.2
S3	Circular grooves	5	5	6x180	464	80.0 ± 2.0	17.7 ± 1.8
S4	Pyramid pattern 0.5 mm	5	15	6x100	453	153 ± 3.9	34.0 ± 3.5
S4	Embossed pattern	5	15	6x100	444	140 ± 2.9	42.6 ± 9.0
S5	Embossed pattern	3	15	6x200	429	185 ± 11	37.4 ± 3.8
S6	Pyramid pattern 0.5 mm	2	12	6x200	476	173 ± 8.5	33.3 ± 2.4
S7	Pyramid pattern 1.0 mm	3	20	8x300	440	496 ± 4.9	80.1 ± 4.3

5.3   Analytical model for load-carrying capacity

The analytical model to calculate the load-carrying capacity is based on equation (1). Contrary to Eurocode 5, the effective number of axially loaded screws is set to $n_{ef} = n$.

$$F_{V,exp} = n_{ef} \cdot F_{ax} \cdot (\cos\alpha + \mu\sin\alpha) \qquad (1)$$

The withdrawal capacity F_{ax} is calculated with equation (2) given by *Blass et al. (*2006):

$$F_{ax} = \frac{0.6 \cdot \sqrt{d} \cdot \ell_{ef}^{0.9} \cdot \rho^{0.8}}{1.2 \cdot \cos^2\alpha + \sin^2\alpha} \qquad [N] \qquad (2)$$

For the first tests with five screws $\ell = 100$ mm (series 1 and 2) the model predicts the ultimate load quite well. The mean ratio of test load to expected load $F_{V,test}/F_{V,exp}$ is 1.0. For the tests with 15 screws $\ell = 100$ mm (series 4) the mean ratio is 1.1. However, for the tests with longer screws, which were designed to exceed the tensile capacity, the model's prediction of the load-carrying capacity is too high, see the blue markers in Figure 20. However, it was observed during the tests, that the test load is reached at quite large deformations. Therefore, the friction tests were re-evaluated to match the displacements in the shear plane. The adjusted COF μ_{adj} (i.e. the COF evaluated at the same displacement as was reached in the corresponding push-out tests) is between 80 and 90% of the static COF. The expected load calculated with the adjusted COF is closer

to the test load. However, the model still overestimates the load-carrying capacity, especially for the tests with longer screw lengths (red markers in Figure 20).

On closer examination, plastic hinges in the screws were observed, due to the large deformations (see Figure 19). This led to the assumption of bending moment-normal force-shear force (MNV) interaction. To check for MNV interaction, equation (3) is appropriate, which was presented by *Blass et al. (*2017). As long as the interaction relationship according to equation (3) is maintained, the design equations according to Eurocode 5 can be used. If the conditions are not met, the properties of the dowel-type fastener must be reduced accordingly.

$$\frac{M}{M_y} + \left(\frac{N}{f_{tens}} + \frac{V}{f_{shear}}\right)^2 = 1 \tag{3}$$

With the normal force N in the screw and the allocation of area of the screw's circular cross-section, the simultaneously acting moment M can be calculated. If these values are put into equation (3) together with the yield moment M_y and the tensile strength f_{tens}, the utilisation rates for series 6 and 7 are greater than 1.0. The shear force is here neglected: on the one hand, the screws are almost exclusively subjected to tensile load due to the inclined arrangement and on the other hand, the plastic hinges are very close to the shear plane, due to the clamping effect in the DVW. Thus, according to equation (3), it has also been analytically proven that not the entire cross-section of the screw is available for the tensile load. It is therefore suggested to reduce the tensile capacity of the screws. If the ratio of the actually existing normal force N to the maximum possible normal force F_{tens} is evaluated, a mean value of 0.9 results. The average ratio of test load to the expected load with the adjusted COF and the reduced tensile strength is 1.04 ± 0.1 and the coefficient of determination has also increased significantly to $R^2 = 0.98$ (green markers in Figure 20).

To simplify the model, the dynamic COF (μ_{dyn}) instead of the static COF was used in equation (1), where the dynamic COF was calculated as the ratio of the friction force during sliding to the applied normal force. The mean values for the dynamic COF for the different surfaces are distinctively smaller and were as low as 50% of its static counterparts. The mean ratio of $F_{V,test}$ to $F_{V,exp}$ is now significantly higher than 1.0, especially for the tests with short screws, where tensile failure was not decisive (black markers in Figure 20). Table 4 shows the progress of the mean ratio of test load to expected load for the different COF: static, adjusted and dynamic.

Table 4. Ratio of test load to expected load for different COF (mean values).

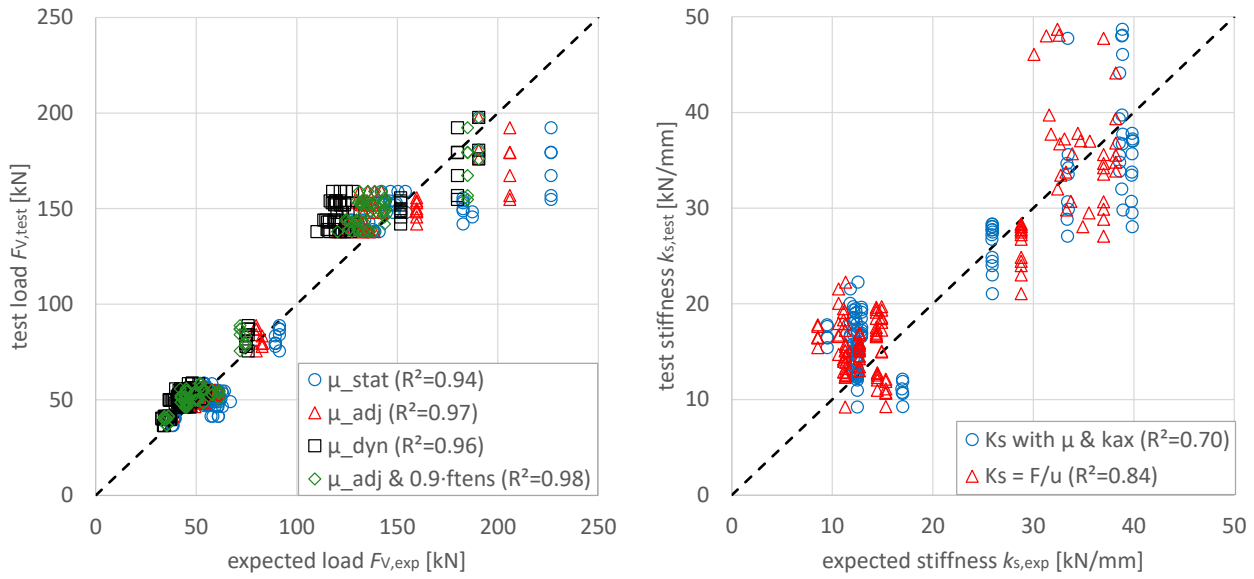| COF	Series 1	Series 2	Series 3	Series 4	Series 5	Series 6	Series 7
μ_{stat}	1.02	0.87	0.91	1.05	0.97	0.76	0.91
μ_{adj}	1.00	1.07	1.01	1.11	0.97	0.83	0.94
μ_{dyn}	1.18	1.13	1.09	1.22	0.97	0.95	0.95
$\mu_{adj} + 0.9 \cdot f_{tens}$	1.05	1.10	1.12	1.11	0.97	0.93	0.97

Figure 20. Test versus model for load-carrying capacity (left) and stiffness (right) of inclined screws.

Further failure modes discussed in chapter 5.2 also have to be considered, i.e. compressive failure perpendicular to the grain of the timber members as well as the load-carrying capacity of the connector itself. Thus, the capacity of the connection with inclined screws and increased shear plane friction results in the minimum of equation (4):

$$F_{V,inclined} = \min \begin{cases} n \cdot F_{ax} \cdot (\mu_{adj} \cdot \sin\alpha + \cos\alpha) \\ n \cdot 0.9 \cdot F_{tens} \cdot (\mu_{adj} \cdot \sin\alpha + \cos\alpha) \\ F_{V,connector} \\ A_{c,90,header} \cdot f_{c,90,header} \cdot k_{c,90,header} \cdot \left(\mu_{adj} + \dfrac{1}{\tan\alpha} \right) \end{cases} \quad (4)$$

Where

n		number of screws
F_{ax}		withdrawal capacity of the screws
F_{tens}		tensile capacity of the screws
μ_{adj}		adjusted coefficient of friction
α		angle of the inclined screws towards the connector plane
$F_{V,connector}$		load-carrying capacity of the connector (i.e. compressive strength depending on material)
$A_{c,90,header}$		effective contact area of header loaded perpendicular to grain
$f_{c,90,header}$		compressive strength perpendicular to grain of the header
$k_{c,90,header}$		coefficient for compression perpendicular to grain

5.4 Analytical model for stiffness

To estimate the stiffness for connections with inclined screws taking the friction into account, *Blass & Steige (*2018) derived equation (5), where $k_{ax,1}$ and $k_{ax,2}$ are the stiffnesses of the screw in the two connected parts, depending on the respective penetration depths.

$$K_{\text{inclined}} = n \cdot \frac{\cos^2 \alpha \cdot (1 + \mu \cdot \tan \alpha)}{\dfrac{1}{k_{ax,1}} + \dfrac{1}{k_{ax,2}}}$$

(5)

where n number of inclined screws

        k_{ax} axial stiffness of the screws

        μ coefficient of friction

        α angle of the inclined screws towards the shear plane

The axial stiffness can be calculated with equation (6), proposed by *Blass & Steige (*2018). The equation is derived analytically and based on 290 tests with varying parameters.

$$k_{ax} = 0.48 \cdot d^{0.4} \cdot \ell_{ef}^{0.4} \cdot \rho_m^{0.3} \qquad \text{[kN/mm]}$$

(6)

For the two parts $k_{ax,1}$ and $k_{ax,2}$ of the total stiffness of the screw, different penetration lengths have to be considered. Equation (6) can be used to determine $k_{ax,1}$, the stiffness of the part in the softwood. However, using the same equation for calculating the axial stiffness of the part of the screw in the connector leads to too high stiffnesses and the overall stiffness of the connection K_{inclined} is overestimated. This is because the screw sits only loosely in the connector with some hole clearance. That is why it is suggested to use a calibrated value of 3.5 kN/mm for $k_{ax,2}$. The good fit of the model shows with the ratio of test stiffness to expected stiffness ranging from 0.65 to 1.76 and a mean value of 1.07 (blue markers in Figure 20). Alternatively, and analogous to ETAs for system connectors, the stiffness can be calculated by dividing the estimated load-carrying capacity by a fixed displacement u. For the tests with screws ℓ = 100 mm a displacement of u = 4 mm is suitable, while for the tests with screws ℓ > 100 mm a displacement of u = 5 mm is suitable (red markers in Figure 20). The ratio ranges here from 0.72 to 1.95 with a mean value of 1.17.

6   Conclusions, relation to EC 5 and outlook

The following conclusions can be drawn from the study:

- The scatter of experimentally determined friction coefficients for wood on wood is rather high, independent of the test setup and the chosen parameters.
- Based on a mean COF of 0.48 for softwood on softwood from the literature, the value of a characteristic μ = 0.25 as given in Eurocode 5 seems quite reasonable.

- The tests to determine the COF of the different surfaces showed that higher than usual COF can be obtained with easy to accomplish surface treatments. All examined surfaces led to higher COF than aluminium, which is mostly used for system connectors (only exception being the tests with griptape).
- In case coating as surface treatment is applied, the optimal solution would be a thin adhesive layer for better bonding and a small grain size for high COF
- The tests with the milled pyramid pattern showed high static COF for larger pyramids and high stiffnesses for smaller pyramids. Therefore, if a high stiffness is needed, small protruding surfaces should be chosen. And if a high load-carrying capacity is needed, surfaces with larger protruding surfaces should be chosen.
- The tests with the sheet metals showed significantly higher COF than tests with normal steel (see literature review). This shows the potential for such surface treatments for all kinds of connectors made of steel/metal, e.g. joist hangers, angle brackets, hold-downs, etc.
- The tests with inclined screws and simple connectors proved the applicability of the examined surfaces in an assembly situation. An effective interaction of treated surface and inclined screws could be established.
- The push-out tests furthermore revealed additional failure modes which should be considered for connections with inclined screws: (i) a reduction of the tensile capacity of the screws due to bending moment-normal force interaction and (ii) compressive failure perpendicular to the grain of the timber parts underneath the connector plate.

The load-carrying capacity for connections with inclined screws (45°) and a COF of $\mu = 0.25$ as given in Eurocode 5 results in $F_V = 1.25 \cdot F_{ax} / \sqrt{2}$, according to equation (1). If a milled surface with a pyramid pattern with a characteristic COF of $\mu_{stat} = 0.79$ is chosen, the load-carrying capacity for the same connection is more than 40% higher. Conversely, this also means, that fewer fasteners are needed in order to reach the same load-carrying capacity as before.

As mentioned before, series 6 and 7 were tests with prototype connectors. A comparison of the characteristic load-carrying capacity of currently available system connectors, with similar dimensions as the specimens in series 6 and 7, shows a significant increase in load-carrying capacity for connectors with treated surface and inclined screws. This is confirmed to a great extent by the ultimate load per screw (see Table 5).

To further simplify the evaluation of the COF it should be considered to use either the static or dynamic COF, instead of the adjusted COF. Because of the much lower dynamic COF, a reduction of the tensile strength of the screws would no longer be necessary. With a mean ratio of test load to expected load of 1.15 the correlation between tests and model is quite good ($R^2 = 0.96$). However, for all cases where the tensile capacity is not decisive, the use of the dynamic COF would largely underestimate the load-carrying capacity. Alternatively, if the static COF is used in the model, the tensile

strength of the screws should be reduced to 75%, for an adequate fit of the model. Here the mean ratio of test to model is 1.16 and the coefficient of determination R^2 = 0.98. However, now the model would overestimate the cases with short screws, where the withdrawal capacity is decisive.

Table 5. Comparison of characteristic load-carrying capacities and customary system connectors.

Connector	Width [mm]	Height [mm]	Depth [mm]	Screw type [mm]	No. of screws	$F_{V,k}$[1] [kN]	Load per screw [kN]
Series 6	110	220	25	6x200	24	154[2]	6.4
Pitzl HVP 88425	120	250	15+15	8x200	20	93.3	4.7
Sherpa XL 55	140	250	16+16	8x200	18	81.9	4.6
Series 7	140	558	50	8x300	40	330[2]	8.3
Pitzl HVP 88555	140	550	15+15	8x300	56	395	7.1
Sherpa XXL 280	140	570	16+16	8x200[3]	54	349	6.5

1) for glulam GL 24h

2) 5th-percentile according to EN 14358 with $k_s(n)$ = 2.1

3) max. allowed screw length according to ETA-12/0067

7   References

Aira JR, Arriaga F, Íñiguez-González G, Crespo J (2014) Static and kinetic friction coefficients of Scots pine (Pinus sylvestris L.), parallel and perpendicular to grain direction. In: Materiales de Construcción 64 (315).

Atack D, Tabor D (1958) The friction of wood. In: Proceedings of the Royal Society of London. Series A. Mathematical and Physical Sciences 246 (1247), S. 539–555.

Aurand S, Blass HJ (2021) Verbinder aus Kunstharzpressholz – Versuche mit ersten Prototypen für Traglasten bis 500 kN. In: Bautechnik 98 (S1), S. 40–50.

Bejo L, Lang EM, Fodor T (2000) Friction coefficients of wood-based structural composites. In: Forest products journal 50 (3), S. 39–43.

Bejtka I, Blass HJ (2002) Joints with Inclined Screws. Paper 35-7-4. CIB W18 - Meeting 35. Kyoto, Japan, 2002.

Blass HJ, Bejtka I and Uibel T (2006) Tragfähigkeit von Verbindungen mit selbstbohrenden Holzschrauben mit Vollgewinde. Karlsruher Berichte zum Ingenieurholzbau, Bd. 4. Universitätsverlag Karlsruhe.

Blass HJ, Sandhaas C, Meyer N (2017) Steel-to-timber connections: Failure of laterally loaded dowel-type fasteners. Paper 50-7-1. In: Proceedings of the INTER Meeting 50, 28.-31. Aug. 2017. Kyoto, Japan.

Blass HJ and Steige Y (2018) Steifigkeit axial beanspruchter Vollgewindeschrauben. Karlsruher Berichte zum Ingenieurholzbau, Bd. 34. KIT Scientific Publishing. Karlsruhe.

Claus T, Seim W, Liese J (2018) Friction under cyclic loading. World Conference on Timber Engineering WCTE. Seoul, Korea, 2018.

Crespo J, Regueira R, Soilán A, Díez MR, Guaita M (2011) Desarrollo de metodología para la determinación de los coeficientes de fricción estático y dinámico de diferentes especies de madera. CIMAD 11 – 1º Congresso Ibero-LatinoAmericano da Madeira na Construção. Coimbra, Portugal, 6/7/2011.

Gaber E (1940) Versuche über die Reibung von Nadelholz. In: Holz als Roh- und Werkstoff 3 (4), S. 119–122.

Garcia A (2012) Untersuchungen zum Tragverhalten von beschichteten HVP-Verbindern. Bachelorarbeit. Karlsruher Institut für Technologie (KIT) - Holzbau und Baukonstruktionen (Unveröffentlicht).

Girardon S (2014) Amélioration des performances mécaniques des assemblages bois sur bois vissés par préparation des interfaces: Application à la réalisation d'éléments de structure. Dissertation. Université de Lorraine - École Doctorale RP2E.

Gorst N, Williamson SJ, Pallett PF, Clark LA (2003) Friction in temporary works: Research report 071. Hg. v. University of Birmingham.

Guan N, Thunell B, Lyth K (1983) On the Friction Between Steel and Some Common Swedish Wood Species. In: Holz als Roh- und Werkstoff 41 (2), S. 55–60.

Koch H (2011) Untersuchungen zum Last-Verformungsverhalten historischer Holztragwerke - Der abgestirnte Zapfen. Schriftenreihe Bauwerkserhaltung und Holzbau, Bd. 5. Kassel Univ. Press. Kassel.

Koubek R, Dedicova K (2014) Friction of wood on steel. Master's Thesis. Linnaeus University - Faculty of Technology.

Lemoine TJ, McMillin CW, Manwiller FG (1970) Wood Variables Affecting the Friction Coefficient of Spruce Pine on Steel. In: Wood Science 2 (3), S. 144–148.

McKenzie WM, Karpovich H (1968) The Frictional Behaviour of Wood. In: Wood Science and Technology 2 (2), S. 139–152.

Meng Q, Hirai T, Koizumi A (2008) Frictional Coefficients between Timber and Some Structural Sheet Materials. In: Journal of the Japan Wood Research Society 54 (5), S. 281–288.

Möhler K, Herröder W (1979) Obere und untere Reibbeiwerte von sägerauhem Fichtenholz. In: Holz als Roh- und Werkstoff 37 (1), S. 27–32.

Möhler K, Maier G (1969) Der Reibbeiwert bei Fichtenholz im Hinblick auf die Wirksamkeit reibschlüssiger Holzverbindungen. In: Holz als Roh- und Werkstoff 27 (8), S. 303–307.

Murase Y (1984) Friction of Wood Sliding on Various Materials. In: Journal of the Faculty of Agriculture, Kyushu University 28 (4), S. 147–160.

Niemz P and Sonderegger W (2017) Holzphysik: Physik des Holzes und der Holzwerkstoffe. Carl Hanser Verlag. München.

Park C-Y, Kim C-K, Kim H-K, Lee J-J (2011) Evaluation of Friction Properties According to Normal Force and Direction of Wood Grain in Real Contact Area. In: Journal of the Korean Wood Science and Technology 39 (5), S. 437–443.

Popov VL (2015) Kontaktmechanik und Reibung: Von der Nanotribologie bis zur Erdbebendynamik:3. Aufl. Springer Vieweg. Berlin, Heidelberg.

Schmidt T (2018) Kontaktverbindungen für aussteifende Scheiben aus Brettsperrholz. Karlsruher Berichte zum Ingenieurholzbau, Bd. 33. KIT Scientific Publishing.

Seki M, Sugimoto H, Miki T, Kanayama K, Furuta Y (2013) Wood friction characteristics during exposure to high pressure: influence of wood/metal tool surface finishing conditions. In: Journal of Wood Science 59 (1), S. 10–16.

Steiger R, Fink G, Nerbano S, Hack E, Beyer K (2018) Experimental investigation of friction stresses between adjacent panels made of Oriented Strand Board (OSB) and between OSB panels and glued laminated timber (GLT) frame members. In: Materials and Structures 51 (1), S. 123.

Stošié DZ (1959) Untersuchungen über den statischen Reibungskoeffizienten des Holzes. In: Holz als Roh- und Werkstoff 17 (3), S. 86–87.

Xu M, Li L, Wang M, Luo B (2014) Effects of Surface Roughness and Wood Grain on the Friction Coefficient of Wooden Materials for Wood–Wood Frictional Pair. In: Tribology Transactions 57 (5), S. 871–878.

EN 14358:2016 Timber structures - Calculation and verification of characteristic values.

EN 14545:2008 Timber structures - Connectors - Requirements.

EN 26891:1991 Timber structures; Joints made with mechanical fasteners; General principle for the determination of strength and deformation characteristics (ISO 6891:1983).

DISCUSSION

The papers was presented by S Aurand

R Jockwer asked about lower residual coefficient of friction after slip in the pyramid pattern and asked about ductility. S Aurand said the behaviour is ductile in general. He did not observe failure of the pyramid pattern and did not observe any clear drop of friction forces.

P Dietsch commented that the large pyramids might reduce risk of influence of large moisture changes. He asked if there is interest to study influence of changing moisture content. S Aurand replied that moisture issue is not part of the project and it may be considered in the future.

P Dietsch asked which is the optimal solution based on production, performance and sustainability issues. S Aurand replied that milled pyramids are work intensive to produce; nevertheless, replacing aluminium with a more environmentally friendly option is a good solution.

I K Abeysekera and S Aurand discussed DVM availability in the market. DVM is used in other industrial applications and can be milled.

C Sigrist commented on the competitiveness of aluminium connections with respect to its advantages. H Blass responded that the aluminium connections have disadvantages say with respect to mounting etc. The system overcomes these issues.

A Frangi and P Palma commented that DVM and aluminium connections were considered from the fire performance perspective. Replacing the aluminium connections with DVM is a good idea for fire performance. S Aurand agreed.

S Aicher commented that dovetail aluminium connectors allowed small uptake of normal forces and asked if such issues have been considered. S Aurand stated during the development of prototypes, tests were done with other loading conditions. For example, they did not observe any issue with moment but this paper only deals with friction.E Ussher asked about ductility as timber connections typically rely on the metal to provide ductility. He asked whether shrinkage could be an issue. A Aurand replied that wood also has ductility from the compression. H Blass also replied that DVM do not shrink nor swell as they are saturated with resin.

O Sisman asked about which failure modes are more ductile and asked about using this in vertical joint. For CLT walls, S Aurand said the screw withdrawal and wood failure with perpendicular orientation seemed to be more ductile. H Blass replied that his connector was not intended to provide ductility for seismic applications and load slip graphs are available in the paper.

P Dietsch commented that page limit being exceeded in the paper. He would be open to discuss the current limit with INTER but a set limit will be more strictly enforced in the future.

Minimum Geometric and Execution Requirements for Axially Loaded Groups of Screws in Hardwood

Ursula Mahlknecht[1)*)], Reinhard Brandner[1)], Andreas Ringhofer[1)]

[1)] Institute of Timber Engineering and Wood Technology, Graz University of Technology, Graz, Austria, [*)]u.mahlknecht@tugraz.at

1 Introduction

Societal demand on sustainable buildings motivates timber as construction material. Actually, deciduous tree species (hardwoods) play a minor role in timber engineering despite their considerably increasing harvest stock, not only in Europe. The substitution of softwood by new hardwood products for structural purposes is needed and under development. Consequently, rules for execution and design of joints established for softwood must be adapted as well. With focus on the dowel-type fastener self-tapping timber screw, applications in hardwood usually coincide with distinctively higher insertion moments but also higher capacities and stiffnesses. In respect to the insertion moment, EAD 130118-00-0603:2016 forces a ratio of ≥ 1.5 between the characteristic (5 %) torque of the screw and the mean value of maximum insertion moment (along the maximum inserted length). This demand remarkably restricts deep insertion of self-tapping screws in dense hardwood products. So, for common screw types applied in hardwood pre-drilling is required (e.g. ETA-12/0114:2017, ETA-11/0190:2018, ETA-11/0027:2019, ETA-12/0062:2019, ETA-12/0197:2019), at least at longer penetration length and/or for larger diameters (e.g. ETA-11/0030:2019, ETA-12/0063:2019, ETA-19/0175:2020, ETA-19/0553:2020, ETA-20/0558:2020). Recently, self-tapping screws explicitly for applications in hardwood became available: apart from screw type RAPID®hardwood, regulated in ETA-12/0373:2020, also other screw types are approved for applications without pre-drilling, e.g. in beech-LVL according to EN 14374:2005 and/or ETA-14/0354:2018 (e.g. ETA-11/0030:2019, ETA-11/0190:2018 and ETA-20/0558:2020).

With a look on the global scale, screws applied in hardwood are commonly laterally loaded, e.g. Draft Malaysian Standard:2017, or, in its real high capacity vantage, axially loaded, as it is common in Europe. Design standards like EN 1995-1-1:2014 (EC 5) or SIA 265:2012 as well as diverse European Technical Approvals/Assessments (ETAs) provide regulations separately for both lateral and axial loading whereas for the latter a tighter group design is allowed.

With focus on joints of axially loaded screws, classification can be made in respect to the angles between the screw axis and the grain, α, and between the screw axis and the loading direction, γ; see Figure 1. In case of $\alpha = \gamma$, the outer (steel) members take off when screws are loaded, enabling a free (unrestricted) surface deformation of the timber member. For joints with inclined screws and $\alpha \neq \gamma$, between inner and outer members friction is activated which restricts the surface deformation. Blaß et al. (2006) classify such joints as being primary axially loaded for $\alpha \leq 45°$. Krenn (2017) propose to consider lateral loading at $\alpha \geq 60°$ and Gehri (2010) defines $\alpha \leq 60°$ as brittle and $60° < \alpha \leq 75°$ as ductile. Due to the increasing risk of splitting in conjunction with an increasing share of lateral load, joints of inclined screws with $\alpha > 45°$ are seen as critical and regulations for laterally loaded screws should be considered as well.

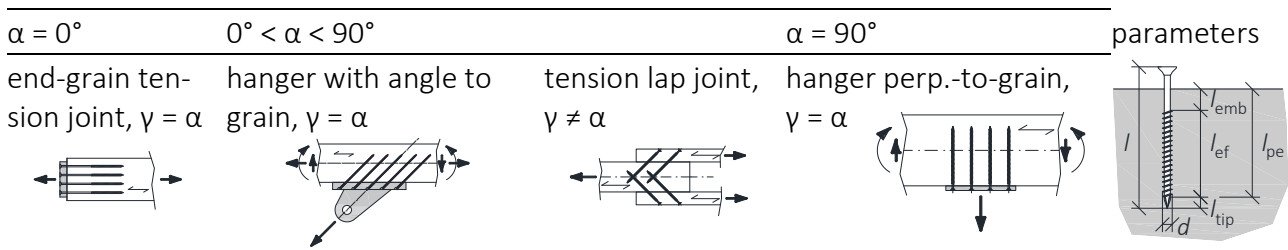| $\alpha = 0°$	$0° < \alpha < 90°$		$\alpha = 90°$	parameters
end-grain tension joint, $\gamma = \alpha$	hanger with angle to grain, $\gamma = \alpha$	tension lap joint, $\gamma \neq \alpha$	hanger perp.-to-grain, $\gamma = \alpha$	

Figure 1.   (left) overview of joints with primary axially loaded groups of screws classified in respect to the thread-grain angle α and the load-grain angle γ; (right) main parameters.

The stress distribution of the joint is influenced by the joint type, angles (α, γ), member dimensions and group arrangement, determined by minimum edge and end distances, $a_{1,CG}$ and $a_{2,CG}$, spacing parallel and perpendicular-to-grain, a_1 and a_2, member thickness t and point-side penetration length l_{pe} as sum of embedment length l_{emb} and effective thread length l_{ef}. The all are key parameters for the overall behaviour of the joint, e.g. the resistance, stiffness, ductility and failure mode. In respect to edge and end distances care has to be taken as some ETAs, in contrast to EC 5, provide explicit regulations for purely axial loading, which leads to the fact, that member ends and edges are treated unloaded, i.e. $a_{1,CG} = a_{3,c}$ and $a_{2,CG} = a_{4,c}$.

There is a number of different joint failure modes which are further differentiated in (i) failure modes sufficiently determined by single fastener properties in conjunction with the effective number of screws in the group, n_{ef}, usually referred to as ductile failure modes (what is considered questionable in the case of axially loaded screws), e.g. withdrawal, steel tension, head pull-through and buckling, and (ii) failure modes which cannot be derived from the individual screw parameters alone and which are frequently described as brittle joint failure modes, e.g. failure of the net cross section, splitting as well as row, plug and block shear; see e.g. Mahlknecht & Brandner (2019).

In respect to (i), models for calculating the withdrawal strength, f_{ax}, or capacity F_{ax} of screws applied in hardwood, are provided in e.g. Hübner (2013), Brandner et al. (2019) and Westermayr & van de Kuilen (2019; 2020), and values for the characteristic capacity of screws in tension, $f_{tens,k}$, are given in ETAs. Consequently, for a specific joint design the selection of the effective thread length, l_{ef}, decides the failure mode in group (i) Thereby, for hardwood species steel failure can be expected already at shorter l_{ef} than for softwood. Consequently, the preferred screw tension failure mode, associated also with much lower uncertainties, is easier to achieve. However, apart from better prediction there is no further benefit in the design, e.g. by a lower partial safety factor γ_M, i.e. EC 5 does not differentiate between joint types nor failure modes. However, for a number of applications much higher ratios of l_{ef} / d are required, e.g. in hangers ($l_{pe} / H \geq 0.7$), in tension lap joints (required overlap between opposite screws in the member center) and for reinforcements. As also the insertion moment increases with increasing l_{ef} and density, pre-drilling and/or the use of partially-threaded screws might be advantageous, also in respect to ductility.

More generally spoken, European standards like EC 5 or SIA 265:2012 provide a framework with minimum geometric and execution requirements as well as design procedures for most but not all of the possible failure modes but request to verify all of them at ultimate limit state (ULS). There is widely convergence between these two standards. Differences are only given in respect to spacing perpendicular-to-grain and requirements for pre-drilling of screws used in hardwood. As already mentioned before, there are a number of ETAs which also regulate the application of screws in hardwood. Their design and execution rules partly go beyond code regulations, e.g. in case of axially loaded screws by allowing shorter minimum spacing parallel and perpendicular-to-grain $\{a_1; a_2; a_{3,c}; a_{4,c}\} \geq \{5; 2.5; 5; 3\}$ as long as $a_1 \cdot a_2 = 25\ d^2$.

Although the characteristic properties of single screws were tailored for hardwoods, this is usually not the case for the geometric minimum requirements. Actually, the minimum spacing, distances and member thicknesses in ETAs have to be (partly) determined according to EAD 130118-01-0603:2016 by evaluating crack surfaces after conducting insertion tests perpendicular-to-grain. This procedure, so far not tailored for hardwood, should secure a reliable joint execution, but misses a direct relationship to the performance of screws when loaded. However, both insertion and loading generate stresses perpendicular-to-grain provoking local cracking as initiator of most failure modes, in particular of type (ii). Consequently, a set of minimum geometric requirements able to limit cracks has the potential to control also the failure modes.

Looking more specific to the different joint types and current regulations it is found that EC 5 limits the application of axially loaded screws to $\alpha \geq 30°$, whereas SIA 265:2012 and diverse ETAs even allow the execution of end-grain joints. Further, EC 5, SIA 265:2012 and all mentioned ETAs demand for all groups of screws which are

also axially loaded $n_{ef} = n^{0.9}$. However, in case of $30° \leq \alpha \leq 60°$ and $\alpha \neq \gamma$ some ETAs allow $n_{ef} = \max\{n^{0.9}; 0.9\,n\}$, partly with n as number of screws in a row parallel-to-grain and partly with n as the entire number of screws in a commonly acting group.

The efficiency of joints is usually discussed by means of utilisation ratios η, commonly defined as ratio between the resistances of joint and timber member at its gross cross section. In end-grain joints the number of fasteners in a group is limited by the member's cross section and the capacity of screws in tension. Any brittle failure mode of group (ii) further limits the overall capacity; see e.g. Obermair (2014), Grabner & Ringhofer (2014), Koppauer (2017), Eckerstorfer (2017), Meyer & Blaß (2018), Westermayer & van der Kuilen (2019), Brandner (2019), Franke et al. (2019) and Meyer (2021). Consequently, to optimise the capacity in end-grain joints, a tight joint design with minimised spacing and edge distance and a maximised steel capacity by preventing brittle failure modes are needed, latter due to additional minimum geometric and execution conditions and/or reinforcements.

For such a tight joint design in hardwood, Koppauer (2017) outlines the necessity of pre-drilling; to achieve failure modes (i) in beech glulam he recommends $a_2 = a_{2,CG} = 3\,d$ in conjunction with $l_{emb} \geq 8.3\,d$; see also Brandner (2019). The positive effect of l_{emb} was already earlier reported in Grabner & Ringhofer (2014) and confirmed later in Westermayer & van der Kuilen (2019) and Meyer (2021) who demonstrated a reduced risk for splitting at $l_{emb} \geq 5\,d$ by testing joints in glulam of birch, beech and beech-LVL.

In contrast, investigations on axially loaded screw joints in hardwood with $\alpha = 90°$, e.g. hangers, or inclined screws, e.g. tension lap joints, the number of previous are rather limited. Schiro et al. (2018), for example, conducted shear-compression tests on lap joints with four inclined screws on each side ($d = 10$ mm; $\alpha = 45°$; $a_1 = 7\,d$) and with beech-LVL ($t = 40$ mm; ETA-14/0354:2018) as outer members. Although partially threaded, the thread length in conjunction with the head pull-through resistance of screws in combination with washers were sufficient to observe screw tension failure.

Considering all this previous information as summary of current state-of-knowledge and state-of-the-art, there are still a number of open or insufficiently elaborated questions from execution to design even for these relatively simple joints of primary axially-loaded screws in hardwood, which motivates the publication presented here. Based on a number of comprehensive investigations conducted on single screws and screwed joints in hardwood products over the last years, the aim is to summarise and conclude what is available for execution and design of joints.

2 Materials and Methods

2.1 Materials

Further reported data origin from tests, which were conducted on two diffuse porous hardwood species, namely beech (*Fagus sylvatica*; BE) and birch (*Betula pendula*; BI). The selection of these two species was motivated by their availability, i.e. stock volume in Central and Northern Europe, and their suitability to be used for structural purposes.

The raw material of birch from Hasslacher Norica Timber in Sachsenburg (A) had a thickness of 42 mm and featured facultative heart wood in most of the planks. The beech sideboards from Pollmeier Furnierwerkstoffe GmbH in Creuzburg (D) with thicknesses 52, 63 and 78 mm were graded as superior quality, featured no facultative heart wood and was widely free of any local growth characteristics like knots or checks. To build up specimen of required dimensions, after conditioning the raw material at 20°C / 65 % rel. hum. for a couple of months, side-face gluing of boards was performed in institutional own laboratory by means of a two-component melamine adhesive (DYNEA; adhesive prefere 4546; hardener prefere 5022). Apart from thereby produced glulam specimen also beech-LVL according to ETA-14/0354:2018 was used.

Two types of screws were tested: the RAPID®hardwood (ETA-12/0373:2017), a self-tapping, partially-threaded screw, with nominal diameter d = 8 mm and total screw / thread length of 400 / 100 mm and of 396 / 300 mm (α = 90°), 240 / 100 mm (α = 90° and 0°), and of 160 / 100 (α = 45°). The second type was ASSYplus (ETA-11/0190:2018), a fully threaded, self-tapping screw with d = 10 mm and total length of 400 mm. Note: the second type was solely applied for α = 0° and screw tension failure as target failure mode.

2.2 Methods

2.2.1 General settings

The investigations cover a wide range of joint types, from end-grain joints with $\alpha = \gamma = 0°$ to hangers loaded perpendicular-to-grain with $\alpha = \gamma = 90°$, both allowing free surface deformation, as well as tension lap-joints with inclined screws (α = 45°; γ = 0°). For these tension lap-joints failure behaviour and corresponding geometric parameters can be partly transferred from other tests by applying trigonometrical relations, thus, one focus in these investigations was rather on the loaded end distance $a_{1,CG}$.

The overall targets of all these investigations were (1) to check the applicability of minimum geometric requirements, in particular a_1, a_2, l_{ef} and l_{emb}, as currently anchored in EC 5 and diverse ETAs or even of further reduced settings, also for joints in hardwood, (2) to identify corresponding failure modes and relations between different settings of these geometric parameters, as well as (3) to find feasible/practicable geometric and execution requirements to reach the target or at least easy to handle failure modes (i), i.e. withdrawal and screw tension failure.

Apart from geometric parameters also the group size n and arrangement of screws in groups were varied to an extend that was possible with regard to the test equipment and the maximum capacities of used facilities. Equal loading of all screws in the group was realised by applying a torque, i.e. by pre-tensioning the screws. In case of steel-to-timber joints (α = 0° and 90°) thick steel-plates were applied which allowed to limit the maximum deformation differences between two farthermost screws in the group to a minimum (< 0.1 mm). Furthermore, in the same groups pure loading in tension was realised by bi-directional hinge chains on both ends of the specimen.

The applied test procedure followed the regulations in EN 26891:1991. In case of timber failure modes, the crack pattern was analysed in detail, e.g. by cutting the specimen after testing at specific positions, and the information obtained from this compared with the information from the load-deformation diagram.

To have adequate reference withdrawal properties for evaluation of the group performance also single screw tests according to EN 1382:1999 were performed; this by means of a push-pull test setup for α = 45° and 90° series and a pull-pull test setup for series α = 0°. The tension capacity of the partially threaded screw type 8 × 396 / 300 was determined from six tension tests according to EN 1383:2016.

The joint performance was evaluated in comparison to the performance of the single fasteners, among others based on the effective number of commonly acting screws, n_{ef}, as ratio between group resistance F_{max} and the withdrawal or steel capacity of single screws, F_{ax} or f_{tens}, multiplied by n. To have the best estimators for statistics of the performance of single joints, in test series with α = 0° realised as pull-pull setup with two identical joints on both member ends, representing a serial system of two components, the Maximum Likelihood Estimation technique for right censored data (MLErc) was applied; see Benjamin & Cornell (1970). Thereby lognormal distributed strengths were assumed. In case of timber failure modes, dependency between the timber properties at both specimen ends was considered; because of the high timber quality at the joints by a correlation coefficient of 0.7, see Brandner et al. (2015) and Brandner (2018). MLErc was also applied to estimate statistics for specific failure modes in series featuring mixed failures. For a better comparison of the lot of test series despite observed density variations, the test data is multiplied with the factor $(\rho_{ref,species,mean} / \rho_i)^{1.6}$ according to Brandner (2019) with $\rho_{ref,BI,mean}$ = 590 kg/m³, $\rho_{ref,BE,mean}$ = 730 kg/m³ and $\rho_{ref,BB,mean}$ = 780 kg/m³.

2.2.2 End-grain joints ($\alpha = \gamma = 0°$)

The investigations on end-grain joints are separated in two groups: the first group of new test series represents a follow up from the works of Koppauer (2017) and Eckerstorfer (2017) who tested beech glulam and LVL; see also Brandner (2019). The applicability of their findings and suggestions, e.g. $l_{emb} \geq 10\,d$, $a_2 = a_{2,CG} \geq 3\,d$ for beech glulam and $a_{2,paral-to-layer} = a_{2,CG} \geq 3\,d$ together with $a_{2,perp-to-layer} \geq 4\,d$ for beech-LVL, was checked also for birch glulam by applying the same settings as in the previous works.

In the second group of test series, aiming on increasing the efficiency of end-grain joints and based on previous works of Obermair (2014) and Grabner & Ringhofer (2014), end-grain joints of up to n = 12 fully-threaded screws of d = 10 mm were investigated in birch and beech glulam with l_{ef} to provoke screw tension failure in combination with a tight spacing a_2 = 2.1 d and l_{emb} = 10 d.

In both groups all screws were applied pre-drilled, with a pre-drill diameter along the total l_{ef} of d_{PD} = 6 and 7 mm and along l_{emb} of $d_{lemb,PD}$ = 8.5 and 10 mm, respectively, for d = 8 and 10 mm screws. The test setups are schematically shown in Figure 2 (a) & (b)

and the test series together with their main parameters are listed in Table 1. Further details are provided in Schweiger (2021) and Oboril (2021).

2.2.3 Hangers loaded perpendicular-to-grain (α = γ = 90°)

The representation of girders as classical hangers loaded perpendicular-to-grain under realistic conditions would request a span of at least six times the member depth; this to allow load spreading and to avoid influences from supports. Variation of parameters would consequence resource intense research. Hence, Mahlknecht & Brandner (2019) suggest a test setup with near supports to reduce the demand on material. So for a first group of series hangers with cross section $B \times H$ and support distance $L_{sup-dist}$ are tested in the configuration with near supports (90n). The aim was to check a number of geometric parameters and their influence on the performance of the joints and corresponding failure modes. With the target to obtain failure modes withdrawal and/or screw tension failure in the group, tests at various spacing a_1 and a_2 and penetration length were conducted on beech boards and glulam. Thereby, also the failure modes associated with minimum spacing according to diverse ETAs, with $\{a_1; a_2\} / d = \{5; 5\}$, and, due to available testing facilities, spacing close to diverse ETAs (spacing cETA), with $\{a_1; a_2\} / d = \{7.5; 2.5\}$ and $a_1 \cdot a_2 = 19 \, d^2$, were investigated. This group of test series comprised also tests in beech boards with three screws arranged in one row and screwed through the boards, with spacing $a_1 = 5 \, d$; here, the specimen thickness $t = 49$ mm does not fulfil the required minimum member thickness t_{min}. Found minimum spacing for withdrawal failure from tests in beech as well as spacing cETA are additionally reviewed also for birch glulam and beech-LVL, the latter with insertion of screws perpendicular to the veneers (radially).

In the second group of test series an adapted test setup for single span girders made of beech glulam and LVL as well as birch glulam (90d) was applied and only a limited number of parameters varied. For a comparison with outcomes from tests with near supports again the spacing cETA together with $l_{ef} = 7 \, d$ or $l_{ef} = 10 \, d$ were tested. To fulfil the required ratio between penetration length and member depth of $l_{pe} / H \geq 0.7$, the embedment of screws was necessary. All screws were inserted with pre-drilling solely of l_{emb} with $d_{emb,DP} = 8.5$ mm.

Both setups are schematically shown in Figure 2 (c) & (d) and the series together with their main parameters listed in Table 1. More details are provided in Luef (2020).

2.2.4 Timber-to-timber tension lap joints with single row of screws (α = 45°; γ = 0°)

Given the available resources for tests on timber and screws, symmetric timber-to-timber tension lap joints with one single row of three screws on each side and overlapping screw tips in the center, as proposed by Krenn (2017), were investigated. The inner members consisted of structural timber of beech or birch with cross section 60 x 80 mm² whereas the outer members were made of beech-LVL (BauBuche Q; Z-9.1-838:2018). The partially-threaded screws were inserted at α = 45° to the grain and additionally with β = 7° out of plane in order to avoid contact problems with opposite

screws in the center. To increase the resistance against head pull-through and for a more controlled loading washer (d_{outer} = 50 mm; d_{inner} = 16 mm; t = 6 mm) and an angle washer 45° according to ETA-11/0190:2018 were applied. The aim was to check the applicability of $a_1 = a_{3,t} = 5\,d$. As a consequence of available member, screw and washer dimensions, required overlapping, $a_{2,CG}$ and target failure mode withdrawal, for the inner members the following setting applied: $l_{emb} + l_{ef} = 1.5\,d + 9\,d$. The screws were inserted non-pre-drilled solely at the length of l_{emb} = 12 mm with $d_{emb,PD}$ = 10 mm. The test setup is schematically shown in Figure 2 (e), the test series and their main parameters are listed in Table 1. Further details are provided in Mahlknecht et al. (2021) and Schweiger (2021).
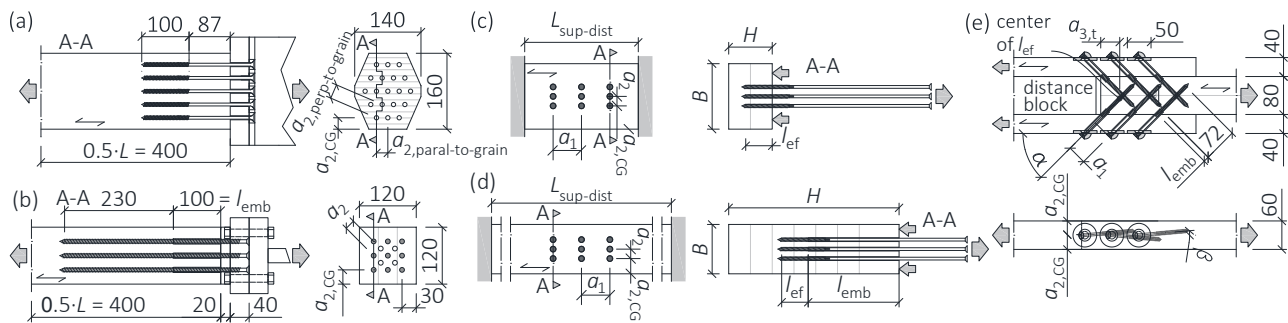

Figure 2. Schematic overview of joints tested in end-grain with traget failure mode (a) withdrawal and (b) screw tension; hanger loaded perpendicular-to-grain with (c) near and (d) distant supports, and (e) tension lap joints.

Table 1. Test series on axially loaded (groups of) screws with α = 0°, 45° and 90°

α [°]	species/product	n	0°: $(a_2/a_{2,CG})$ / d; 90°: (a_1/a_2) / d; 45°: $(a_1/a_{1,t})$ / d	$(l_{emb} + l_{ef})$ / d	BxH [mm²]	0°: L [mm]; 90°: $L_{sup\text{-}dist}$ [mm]	no. of tests	$\rho_{12,mean}$ [kg/m³] (CoV[ρ_{12}] [%])	u_{mean} [%]	comment
	BE			3.0+11.5	80x78	300	21	725(6.3)	9.4	struct. timber (BE,
0	BI	1	-	6.0+11.5	80x125	420	20	589(6.3)	10.3	BI)
	BB			8.0+10.0	140x78	450	16	772(2.4)	7.3	
0	BE	19	3.0/3.0	8.3+11.5	152x132	800	6	749(8.0)	8.1	2-lay. glulam, ETA,[2)]
0	BI	19	3.0/3.0	10.0+11.5	152x132	800	6	630(3.0)	9.4	glulam, ETA
0	BB	19	3.0-4.0/3.0	10.0+11.5	140x160	800	6	789(2.2)	6.2	ETA, a_2 differs for layer orientation
0	BI	12	2.1/3.0	10.0+23.0[1)]	120x120	400	4	606(6.0)	11.3	glulam, cETA
0	BE	12	2.1/2.6	10.0+18.0[1)]	112x112	700	2	749(-)	10.9	2-lay. glulam, cETA
	BE			0+6.1	160x49	160	20	729(6.4)	10.7	struct. timber (BI,
90	BI	1	-	0+5.4	160x43	160	20	589(5.4)	10.7	BE)
	BB			0+7.3	160x58	160	20	788(2.1)	8.4	
	BE			4.0+9.0	160x104	160	20	732(5.3)	9.2	2-lay. glulam (BE,
90	BI	1	-	6.0+7.0	160x104	160	20	604(6.1)	9.6	BI)
	BB			6.0+7.0	160x104	160	20	777(2.6)	6.0	
90n	BE	3	5.0/-	0+6.1	160x49	160	5	738(7.3)	10.6	struct. timber, cETA
90n	BE	9	5.0/7.5	0+6.1	180x138	180	2	693(-)	10.1	glulam, ETA

	BE			0+7.0	138x92		6	742(7.3)	10.9	EC5
90n	BI	9	7.0/5.0	0+7.0	200x120	210	6	617(6.5)	10.8	
	BB			0+7.0	192x160		2	805(-)	7.3	
90n	BB	9	7.5/7.5	0+7.0	185x160	240	2	817(-)	7.3	
90n	BB	4	10.0/10.0	0+7.0	185x160	240	4	817(-)	7.1	
90n	BE	9	5.0/5.0	0+7.0	138x138	180	6	675(4.7)	10.6	ETA
90n	BE	9	5.0/5.0	4.0+6.0	183x138	240	6	737(4.7)	10.4	ETA
	BE				138x92		6	735(5.2)	10.7	cETA
90n	BI	9	7.5/2.5	0+7.0	182x126	240	6	591(5.0)	11.1	
	BB				185x160		4	822(0.7)	7.4	
90n	BE	6	7.5/2.5	0+12.0	138x138	180	6	693(4.7)	10.3	cETA
90n	BE	6	7.0/2.5	0+15.0[1]	138x138	210	5	708(5.7)	10.2	cETA
			5.0/3.5			180	6	713(5.0)	10.5	
	BE			24.0+7.0	104x360	2200	3	757(-)	11.1	cETA
90d	BI	9	7.5/2.5				3	596(-)	10.8	
	BB						3	812(-)	5.8	
90d	BE	9	7.5/2.5	24.0+7.0	144x360	2200	3	750(-)	11.1	cETA
	BI						3	637(-)	11.0	
90d	BB	9	7.5/2.5	24.0+7.0	160x360	2200	3	794(-)	6.2	cETA
90d	BB	6	10.0/2.5	3.0+10.0	150x160	800	6	807(1.4)	6.7	ETA
90d	BI	6	10.0/2.5	6.0+10.0	160x178	800	8	612(1.0)	10.8	ETA
45	BE	1	-	10.8	65x100	160	17	733(6.1)	9.5	struct. timber
	BI			10.8	80x100	134	18	610(5.7)	10.7	
45	BE	3+3	5.0/5.0	1.5+9.0	80x60	1000	6	696(5.8)	10.0	struct. timber, cETA
45	BI	3+3	5.0/5.0	1.5+9.0	80x60	1200	6	594(5.5)	10.7	glulam, cETA

90n … near support; 90d … distant support; BB … beech-LVL acc. to ETA-14/0354:2018; BE … beech; BI … birch; spacing and distances close to diverse ETAs (cETA), acc. to diverse ETAs (ETA) and acc. to EC 5 (EC5); [1] threaded length to provoke screw tension failure; [2] data of Eckerstorfer (2017)

3 Results and Discussion

Statistics of density ρ_{12} and moisture content u are already listed in Table 1.

3.1 Analysis of observed failure modes

In the group of failure modes (i), withdrawal failure mode (W) could be identified after the screw channel had been opened and even in unclear overall joint behaviour by shearing off of the fibers along l_{ef}. Initial cracking close to the surface caused by screw insertion was observed in test series 90n on joints without thread embedment ($l_{emb} = 0$) as well as in corresponding single screw tests. These cracks further propagated during axial loading. No initial cracking was observed in any of the single fastener and joint tests with $l_{emb} > 0$. In case of screw tension failure (S), also group (i), all or almost all screws of the group failed within their free length.

The classification of failure modes in group (ii), brittle failure modes, was done by analysing cracks in cross cuts made at specific positions at the joint. In series 90n and 90d the most frequent observed failure mode was block shear (B) and/or a combination of block shear with tension perpendicular-to-grain (BP). In case of (B), cracks propagating in-grain (rolling shear) where visible in length along the outer rows of screws delimiting

the group and in depth corresponding to l_{ef}. In series 90d, with l_{emb} = 24 d, cracks in-grain were observed solely in depth of l_{ef} and not over l_{emb}. In joints within series 90n featuring a_2 = 5 d a similar crack was additionally observed at the middle row. In addition to the cracks corresponding to rolling shear failure, in case of (B) there was also a crack at the bottom of the group of screws, in depth of the screw tips (in glulam of beech and birch at $l_{emb} + l_{ef}$ and in beech-LVL at approximately 2 mm above l_{pe}) and in width limited by the width of the group of screws, caused by the local exceedance of the tension perpendicular-to-grain resistance; see Figure 3 (B).

In case of failure mode (BP), the tension perpendicular-to-grain crack at the plane of screw tips runs across the entire width of the specimen; see Figure 3 (BP). In some cases during testing internal cracking, although not visible from the outside, was acoustically perceptible and also detectable by short load drops in load-deformation curves. The intermediate maximum load recorded at such short load drops is further referred to load at first failure, F_{1st}. However, formation of tension perpendicular-to-grain and rolling shear cracks usually occurred at the maximum (ultimate) resistance, F_{max}. The tension perpendicular-to-grain failure mode (P) was characterized by a tension perpendicular-to-grain crack across the entire width of the specimen; see Figure 3 (P). As failure modes (P) and (BP) are clearly distinguishable, (BP) was further interpreted as block shear failure, followed by propagation of tension perpendicular-to-grain cracks.
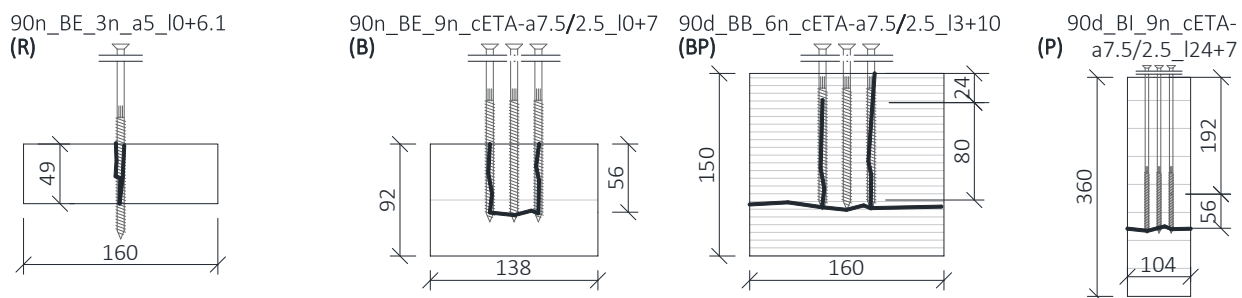
Figure 3.   Observed failure modes (ii): (R) row shear, (B) block shear, (BP) block shear combined with tension perpendicular-to-grain, and (P) tension perpendicular-to-grain

In series 90d_BB_n9_cETA_l24+7_B160 another limit case between withdrawal and block shear failure (WB) mode was observed. Although the crack pattern indicates block shear failure, the course in load deformation curve and overall resistance indicate withdrawal failure. At one test of series 90n_BE_n9_cETA_l0+7 with block shear failure tension perpendicular-to-grain crack partially followed the glue line, failure (K). Finally, in series 90n_BE_n3_a5_l0+6.1 row shear (R) was observed; see Figure 3 (R). Only one specimen of the tested end-grain joints failed by splitting (SP). The ultimate load of this specimen was higher than that of the remaining specimen of this series which all failed in withdrawal.

3.2   Analysis of series with screw tension failure

In herein tested joints, screw tension failure already occurred at $l_{ef} \geq 15\ d$. The parameters and main statistics of the corresponding test series are summarised in Table 2

and Figure 4. Neither for glulam of birch nor beech splitting failure was observed although even rather tight group arrangements were tested, e.g. $a_2 = 2.1\ d$ in combination with $l_{emb} = 10\ d$ at $\alpha = \gamma = 0°$ and $a_1 \cdot a_2 = 17.5\ d^2$ at $\alpha = \gamma = 90°$. Common action of screws and balanced loading is indicated as all screws of the group failed in tension, which consequences in a high $n_{ef,mean} \geq 0.99\ n$ (note: because of the limited number of tests per series $n_{ef,05}$ is omitted). To be able to calculate $n_{ef,mean}$, the reference value for the average screw tension capacity of end-grain joints, $F_{tens,mean} = 35.9$ kN, was back calculated from the characteristic tension capacity as given in ETA-11/0190:2018 by assuming a coefficient of variation (CoV) of 5 % and by following the rules in EN 14358:2016.

A high effective number of screws was reported also in Grabner & Ringhofer (2014) ($\{a_2;\ a_{2,CG};\ l_{emb}\} / d = \{2.1;\ 3;\ 5\}$; $n = 13$; birch-LVL; $n_{ef,mean} \geq 0.92\ n$), Westermayer & van der Kuilen (2019) ($\{a_2;\ a_{2,CG};\ l_{emb}\} / d = \{2;\ 1.5;\ 6.4\}$ $n = 9$; glulam of beech; not all screws of the group failed) and Meyer (2021) ($\{a_2;\ a_{2,CG};\ l_{emb}\} / d = \{2.5;\ 1.5;\ 5\}$; $n = 4$; beech-LVL; failure of all screws). The reason for $n_{ef} < n$ in these reports is seen in splitting failures as observed in some of the tests. Gehri (2010) proposes for ash glulam, based on $\{a_2;\ a_{2,CG}\} / d = \{4;\ 2.8\}$ and $n = 8$, $n_{ef} \geq 0.85\ n$, even for joints without thread embedment. Concluding, present results confirm the positive effect of $l_{emb} \geq 10\ d$ as proposed by Brandner (2019) to reach failure mode (i) and n_{ef} close to n.

In series 90n screw tension failure occurred within the rolled thread which features much fewer surface discontinuities than the starting thread produced by means of flat die rollers, that part of the thread which usually determines the tensile capacity of screws, see Ringhofer (2017). Consequently, the capacity observed from joint tests is 4 % higher than $F_{max,n=1,mean} = 36.5$ kN (CoV[$F_{max,n=1}$] = 0.6 %), which is in-line with results from screw tension tests explicitly conducted on both parts of the thread; see e.g. Ringhofer & Schickhofer (2019).

Table 2.   Series with screw tension failure at $\alpha = \gamma = 0°$ and $90°$

series name containing characteristic identification parameters	no. of tests & failure mode	mode (i)/(ii)	$F_{max,MLErc\text{-}eq,mean}$ [kN] (CoV[F_{max}] [%])	$\tau_{ax,mean} / n$ [MPa]	$n_{ef,mean}$
0_BI_n12_cETA_l10+23	4S	(i)	427(0.8)	-	1.00
0_BE_n12_cETA_l10+18	2S	(i)	425(-)	-	0.99
90n_BE_n6_cETA-a7/2.5_l0+15	5S 1W	(i)	228(0.3)	-	1.04
90n_BE_n6_cETA-a5/3.5_l0+15	6S	(i)	227(0.9)		1.04

W… withdrawal, S… screw tension failure

Figure 4.   Load per screw vs. test series

In assessing the efficiency of tested end-grain joints for glulam of birch via the utilisation ratio, in lack of tensile tests on tested timber specimen the characteristic tension
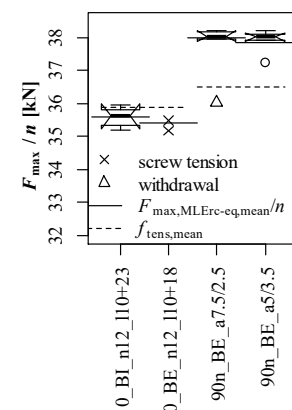
parallel-to-grain strength $f_{t,0,k}$ was assumed with 30 MPa according to data of Obermair (2014). Consequently, for series 0_BI_n12_cETA_l10+23 the utilisation ratio was estimated with $\eta_{05,gross}$ = 0.98. Westermayer & van der Kuilen (2019) report of achieving a high efficiency for target screw tension failure with $\eta_{mean} \geq 0.80$ for joints in glulam of beech built up of rather low quality boards.

3.3 Analysis of series featuring timber failure modes

As in a number of test series more than one timber failure mode was observed, in the following all series featuring primary timber failures are presented and discussed together; see Table 3, Figure 5 and Figure 6. To be able to trace the data and observations in a very compact format, the following information is provided: failure mode and corresponding number of tests, statistics of ultimate load $F_{max,mean}$ / n per screw and CoV[F_{max}], average load $F_{1st,mean}$ / n per screw and corresponding number of tests, mean value, $\tau_{ax,ref,mean}$, CoV[τ_{ax}] and 5 %-quantile, $\tau_{ax,ref,05}$, of the axial shear stress per screw at ultimate load, adjusted to reference density, according to Eq. (1) for $\alpha = \gamma = 90°$ and 0° and according to Eq. (2) for $\alpha = 45°$ | $\gamma = 0°$ (assumed friction coefficient $\mu = 0.25$), as well as the effective number of screws based on mean values, $n_{ef,mean}$, and 5 %-quantiles, $n_{ef,05}$. Thereby, joints with pre-drilled embedment length, $l_{emb} > 0$, are referenced to single data tested with $l_{emb} = 6\,d$ for beech-LVL and glulam of birch and $4\,d$ for glulam of beech, whereas joints without thread embedment ($l_{emb} = 0$) are referenced to corresponding single screw tests. In Figure 5 and Figure 6 the horizontal dashed lines represent the 5 %-quantile of single screw withdrawal resistance whereas the dotted lines additionally consider the regulations for n_{ef} according to EC 5 by multiplying these 5 %-quantiles with the factor $k_{nef} = n^{0.9}$ / n.

$$\tau_{ax,i} = F_{max,i} \cdot (\rho_{ref,species} / \rho_i)^{1.6} / (n_i \cdot d_i \cdot l_{ef} \cdot \pi) \tag{1}$$

$$\tau_{ax,i} = F_{max,i} \cdot (\rho_{ref,species} / \rho_i)^{1.6} / (n_i \cdot d_i \cdot l_{ef} \cdot \pi \cdot (\cos\alpha + \mu \cdot \sin\alpha)) \tag{2}$$

In series featuring mainly withdrawal failures, $\tau_{ax,MLErc,mean}$ and CoV[$\tau_{ax,MLErc}$] are estimated from MLErc analysis and further used to discuss n_{ef} for the withdrawal failure mode, i.e. values of tests failing in modes others than withdrawal are treated as right-censored. In series featuring mainly failure modes of group (ii), $\tau_{ax,mean}$, CoV[τ_{ax}] and n_{ef} are calculated by considering all tests per series; thus calculated n_{ef} only serves for comparison of load levels.

Table 3. Test series featuring primary timber failure modes

series names including main parameters	no. of tests & failure mode	mode (i)/(ii)	$F_{max,mean}$ / n [kN] (CoV[F_{max}] [%])	no. of tests with $F_{1st,mean}$ / n [kN]	$\tau_{ax,mean}$ [MPa] (CoV[τ_{ax}] [%])	$n_{ef,mean}$ / n	$\tau_{ax,ref,05}$ [MPa]	$n_{ef,05}$ / n
0_BE_n1_l3+11.5	21W		28.7(16.3) | -		12.6(9.4)		10.8	
0_BI_n1_l6+11.5	20W	(i)	15.3(11.6) | -		6.7(10.1)	-	5.6	-
0_BB_n1_l8+10	16W		26.4(9.5) | -		12.9(7.4)		11.4	

0_BE_n19 (Eckerstorfer 2017)	6W	(i)	26.1(15.2)[1] | -	10.4(6.1)	0.83	9.4[1]	0.87
0_BI_n19_ETA-a3/3_l10+11.5	6W	(i)	15.5(4.6)[1] | -	6.1(3.3)[1]	0.91	5.8[1]	1.04
0_BB_n19_ETA-a3-4/3_l10+11.5	5W 1SP	(i)	24.7(3.1)[1,2] | -	10.7(3.1)[1]	0.83	10.2[1]	0.89
90_BE_n1_l0+6.1	21W		17.8(13.1)	14.5(7.4)		12.8	
90_BI_n1_l0+5.4	20W	(i)	10.3(12.1)	9.6(6.0)	-	8.7	-
90_BB_n1_l0+7.3	20W		22.3(5.8)	15.0(5.6)		13.7	
90_BE_n1_l4+9	20W		29.5(7.5)	16.2(5.3)		14.9	
90_BI_n1_l6+7	20W	(i)	14.9(13.9)	10.2(5.3)	-	9.3	-
90_BB_n1_l6+7	20W		25.4(6.7)	18.1(5.1)		16.7	
90n_BE_n3_a5_l0+6.1	5R	(ii)	14.9(9.6)	11.9(3.8)	0.82	11.2	0.88
90n_BE_n9_ETA-a5/7.5_l0+6.1	2W	(i)	19.6(-)	15.2(-)	1.05	-	-
90n_BE_n9_EC5-a7/5_l0+7	5W 1B	(i)	21.3(13.9)[2]	14.8(7.9)[3]	1.02	13.2[3]	1.03
90n_BI_n9_EC5-a7/5_l0+7	5W 1B	(i)	15.2(12.6)[2]	10.1(3.5)[3]	1.04	9.5[3]	1.09
90n_BB_n9_EC5-a7/5_l0+7	2B	(ii)	17.9(-)	12.1(-)	0.81	-	-
90n_BB_n9_a7.5/7.5_l0+7	2B	(ii)	19.1(-) | $_1$16.2	12.6(-)	0.84	-	-
90n_BB_n4_a10/10_l0+7	4W	(i)	23.5(3.2) | $_1$18.2	15.5(3.5)	1.03	14.7	1.07
90n_BE_n9_ETA-a5/5_l0+7	1W 5B	(ii)	18.9(10.0)	15.2(5.3)[2]	1.05	13.9	1.09
90n_BE_n9_ETA-a5/5_l4+7	1W 5B	(ii)	24.6(9.2) | $_5$21.0	17.1(4.7)[2]	1.18	15.9	1.07
90n_BE_n9_cETA-a7.5/2.5_l0+7	5B+1K	(ii)	18.3(9.2)[2] | $_5$21.0	12.9(8.9)	0.89	11.1	0.87
90n_BI_n9_cETA-a7.5/2.5_l0+7	6B	(ii)	10.7(11.0) | $_4$9.6	7.6(12.3)	0.79	6.1	0.70
90n_BB_n9_cETA-a7.5/2.5_l0+7	4B	(ii)	12.7(5.7) | $_4$11.9	8.2(5.6)	0.55	7.5	0.56
90n_BE_n6_cETA-a7.5/2.5_l0+12	3W 3B	(ii)	31.0(7.4)[2] | $_{12}$29.8	14.1(13.0)[2]	0.97	11.4	0.89
90d_BE_n9_cETA_l24+7_B104	3W	(i)	24.6(-)	16.5(-)	1.02	-	-
90d_BE_n9_cETA_l24+7_B144	3W	(i)	22.8(-)	15.5(-)	0.96	-	-
90d_BI_n9_cETA_l24+7_B104	2W 1P	(ii)	16.9(-)[2]	11.8(-)[2]	1.11	-	-
90d_BI_n9_cETA_l24+7_B144	3W	(i)	20.4(-)	12.8(-)	1.21	-	-
90d_BB_n9_cETA_l24+7_B104	3BP	(ii)	20.5(-) | $_3$19.3	13.7(-)	0.76	-	-
90d_BB_n9_cETA_l24+7_B160	3WB	(i)	27.4(-) | $_2$20.9	19.0(-)	1.05	-	-
90d_BB_n6_ETA5_l3+10	6BP	(ii)	28.6(3.4)	13.5(3.8)	0.75	12.6	0.75
90d_BI_n6_ETA_l6+10	8W	(i)	23.3(4.3)	10.9(4.1)	1.03	10.2	1.10
45_BE_n1_l0+10.8	15W 2S	(i)	34.5(18.0)[3]	15.6(4.2)[3]	-	14.6[3]	-
45_BI_n1_l0+10.8	18W	(i)	24.2(12.9	10.0(9.3)	-	8.6	-
45_BE_n3+3_ETA-a5/5_l1.5+9	6W	(i)	21.0(23.5)[1]	13.1(5.8)[1,4]	0.84	11.9[1,4]	0.82
45_BI_n3+3_ETA-a5/5_l1.5+9	6W	(i)	13.0(9.1)[1]	8.2(12.2)[1,4]	0.82	6.6[1,4]	0.77

W … withdrawal; SP … splitting; R … row shear; B … block shear; K … block shear combined with partially failed glue line; P … tension perp.-to-grain; BP … block shear combined with tension perp.-to-grain crack; WP … withdrawal combined with block shear cracks; 1) via MLErc assuming equi-correlated and lognormal data; 2) mean value over all failure modes; 3) via MLErc assuming lognormal data; 4) determined with Eq. (2)

Overall, the behaviour of joints tested in glulam of beech and birch is quite similar, which allows a common discussion of their results. The behaviour of joints tested in beech-LVL, however, partially differs and needs to be discussed separately. A safe application in beech and birch glulam following the regulations in diverse ETAs and EC 5 can be concluded. In contrast, for beech-LVL according to ETA-14/0354:2018 the application of self-tapping screws is seen critically; pre-drilling might significantly reduce initial cracking.
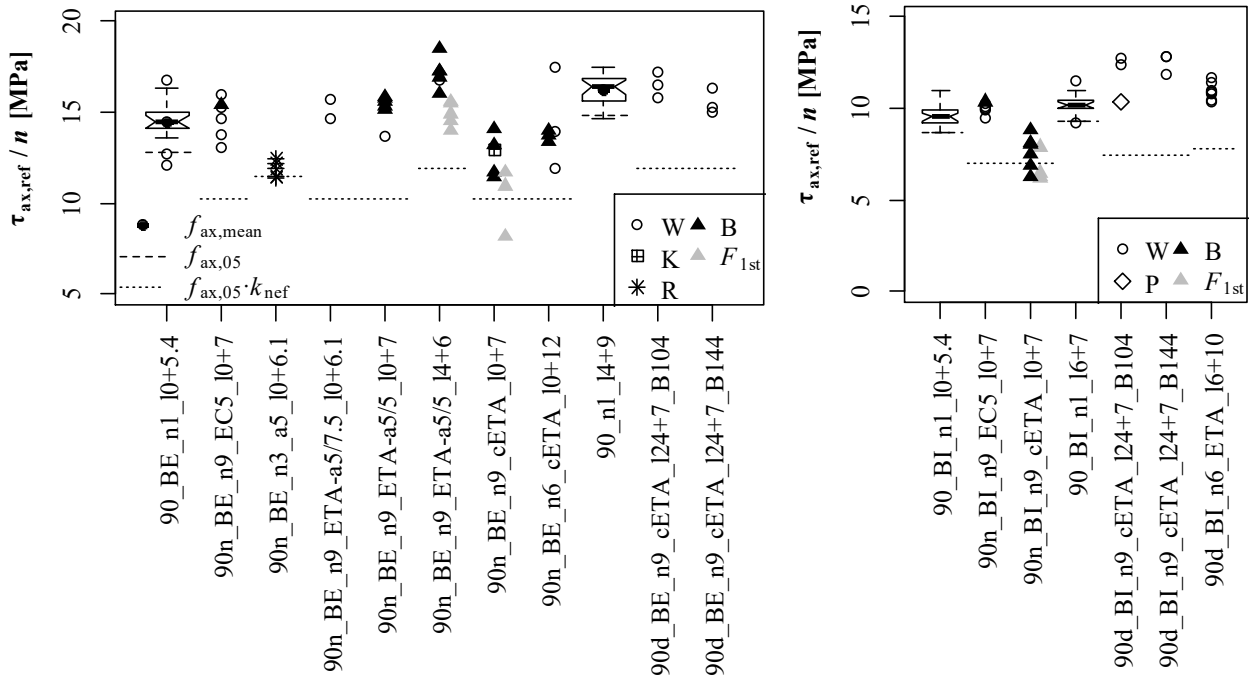
Figure 5.   Test results at α = 90° of series featuring mainly timber failure modes: (left) beech BE and (right) birch BI
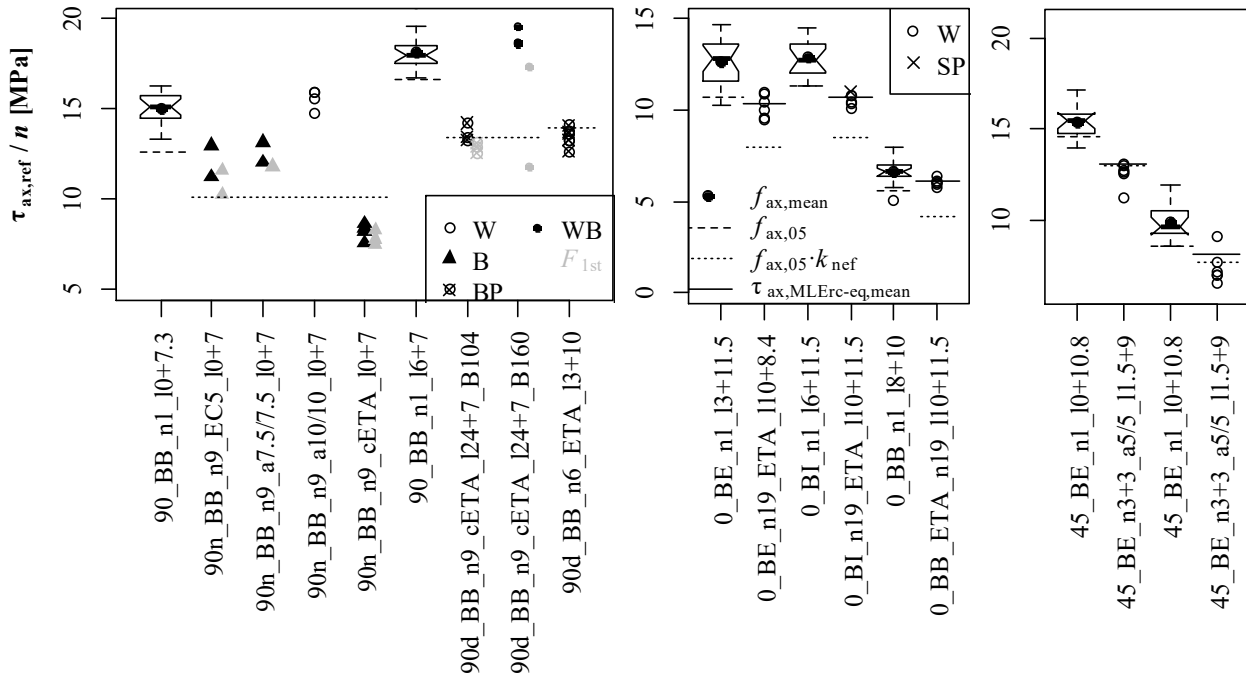

Figure 6.   Test results of series featuring mainly timber failure modes: (left) α = 90°, beech-LVL BB; (middle) α = 0°, beech glulam BE, birch glulam BI, beech-LVL BB; (right) single rows of screws at α = 45° in beech glulam BE

3.3.1   Hangers loaded perpendicular-to-grain (α = γ = 90°)

Initial cracking close to the surface, as observed in single tests at α = 90° and l_{emb} = 0, has a negative impact on the withdrawal capacity because of unintended reduction of l_{ef}. Thread embedment can prevent initial cracking and help to maintain l_{ef} as intended, as especially demonstrated by tests in beech-LVL featuring l_{emb} = 6 d. Apart from l_{emb} > 0, the capacity of screwed joints can be further improved by anchoring screws in a number of layers activating a system effect as observed for beech and birch single

tests with l_{emb} = 4 d and 6 d, respectively. E. g. Ringhofer et al. (2015) report a system factor, as multiplication factor for the withdrawal capacity determined from testing screws in structural timber of Norway spruce (single layer), of $k_{sys,mean}$ = 1.05 already for anchoring in two layers.

Partly, intermediate load peaks identified as first failures were observed. In case of e.g. 90n_BI_n9_cETA_l0+7, the resistances at first failures are comparable with the ultimate loads, see Figure 5. In contrast, e.g. in 90d_BB_n9_cETA_l24+7 both resistances are clearly different, see Figure 6. First failures as consequence of partial failures, i.e. cracking, is seen critical in respect to the long-term behaviour, and the potential for crack propagation, e.g. due to cyclic variation in climate conditions. Therefore, it is suggested to consider F_{1st} rather than F_{max} at the resistance level for the design in ultimate limit states.

One interesting aspect is also apparent comparing series 90n_BE_3n_a5_l0+6.1 (t = 6.1 d) with 90n_BE_9n_ETA-a5/7.5_l0+6.1. Although both series feature comparable group arrangements, with a_1 = 5 d and l_{ef} = 6.1 d, specimen in the first series failed in row shear, featuring capacities even below $f_{ax,05} \cdot k_{nef}$ (see Figure 5), whereas in the latter series withdrawal was observed. Differences in specimen's stiffnesses are seen as one reason. Furthermore, specimen in the first series also fall short of t_{min} = 12 d according to ETA-12/0373:2017.

Although test series with a_1 = a_2 = 5 d fulfil the minimum spacing requirements according to diverse ETAs, in series 90n_BE_n9_ETA-a5/5_l0+7 block shear failure as predominant failure mode occurred; however, at ultimate loads exceeding the estimated average withdrawal capacity, i.e. $n_{ef,mean}$ = 1.05. Overall, the capacities of series 90n_BE_n9_ETA-a5/5_l4+7, featuring l_{emb} = 4 d, exceed the one of previous series but values at first failures are comparable. In comparison to series 90n_n9_cETA_l0+7 (l_{ef} = 7 d) with group arrangement cETA $\{a_1; a_2\} / d$ = {7.5; 2.5} and although the group arrangements are similar, even higher resistances are achieved in series 90n_n6_cETA_l0+12 (l_{ef} = 12 d), with close supports, and 90d_n9_cETA_l24+7 $\{l_{emb}; l_{ef}\} / d$ = {24; 7}, tested as single span girder; in the last series differing stress distributions might have an influence as well. The influence of close vs. distant supports is even more evident when comparing failure modes and capacities for specimen of beech-LVL featuring $\{a_1; a_2\} / d$ = {7.5; 2.5} or rather {10; 2.5}; 90n_BB_n9 _cETA_l24-7, 90d_BB_n9_cETA_l24-7 and 90d_BB_n6_ETA_l3-10. These comparisons underline that in addition to minimum spacing requirements also the third dimension, i.e. in direction of the thread axis, need to be regulated as well. Apart from that, tension perp.-to-grain failures in series 90d_BI_n9_cETA_l24+7 alert not to use the combination of $\{a_2; a_{2,CG}\} / d$ = {2.5; 4} although currently allowed in some ETAs.

In joints tested in beech and birch glulam which fulfil the spacing according to EC 5 the target failure mode withdrawal was observed in series 90n. However, joints tested in beech-LVL at α = 90°, spacing according to EC 5 and near supports failed in block shear;

withdrawal was only observed in a group of n = 4 screws and $a_1 = a_2 = 10\ d$. Independent of the timber product, for series which predominately failed in withdrawal show $n_{ef,mean} \geq 0.96\ n$. Based on 5 %-quantiles even $n_{ef,05} \geq 1.03\ n$ can be concluded; this is because of a reduced variation in withdrawal capacities of groups of screws in comparison to tests on single screws and due to laboratory conditions.

Finally, all joint configurations tested in glulam of birch and beech featuring spacing and distances according to diverse ETAs or EC 5 or cETA fulfilling $l_{pe}\ /\ h \geq 0.7$, achieve resistances above the withdrawal capacity of single screws times k_{nef}, with $n_{ef} = n^{0.9}$ according to EC 5 and diverse ETAs, at least under laboratory conditions. For beech-LVL the current regulations are judged as being not sufficient to relay on safe side with $F_{ax,k} \cdot n_{ef}$. As alternative, the arrangement of the screws with preferable wider spacing than according to EC 5 or, effective length for screw tension failure as easily to reach within the high density of beech-LVL or corresponding verification of failure modes (ii) are suggested.

3.3.2 Timber-to-timber tension lap joints with single row of screws (α = 45°; γ = 0°)

In tests on timber-to-timber tension lap joints with spacing and end distance $a_1 = a_{1,t} = 5\ d$, withdrawal failure was observed for both birch and beech structural timber. Consequently, although diverse ETAs allow $a_{1,c} = 5\ d$ only for cases of pure axial loading, the same minimum end-distance proofed to be sufficient also for the tested tension lap joints.

In contrast to hangers loaded perpendicular-to-grain, n_{ef} according to Eq. (2) applying a rather conservative value $\mu = 0.25$ is found with $n_{ef,05} \geq 0.77\ n$, which is below current design regulations in diverse ETAs and EC 5. Reasons for this low value are not completely clarified yet. Possible reasons are a slight loss of contact by the system deformations influencing the effective thread embedment or by the used distance block, see Figure 2, possibly causing a reduced friction activation. Nevertheless, current findings are in contrast to literature, e.g. tension lap joints with outer steel plates (e.g. Krenn 2017) and timber-to-timber joints (e.g. Blaß et al. 2006) who both report $n_{ef}\ /\ n$ close to one.

3.3.3 End-grain joints (α = γ = 0°)

In regard to end-grain joints, all tests conducted with screws applied pre-drilled, with $l_{emb} = 10\ d$ and $a_2 = a_{2,CG} = 3\ d$ for beech and birch glulam and $a_{2,paral-to-layer} = a_{2,CG} \geq 3\ d$ together with $a_{2,perp-to-layer} \geq 4\ d$ for beech-LVL are assigned to withdrawal failure with $n_{ef,mean} \geq 0.83\ n$. Overall, the regulation for the effective number of screws in the group, $n_{ef} = n^{0.9}$ from EC 5, gives results on the safe side for end-grain joints.

4 Conclusions

Limited experience on joints in hardwood in contrast to the variety of deciduous timber species necessitates regulations to endeavour well controllable failure modes of type (i). Apart from adequate minimum spacing and distances, thereby, the effective length

and thread embedment length, as geometric parameters in the third dimension, need to be regulated as well. To be able to insert self-tapping screws in hardwood sufficiently deep even without pre-drilling, special screws with sufficient torsional strength are required; meanwhile some screw types especially developed for hardwood are available, further developments can be expected. However, for some joint types, e.g. end-grain joints, which require an extremely tight group arrangement to achieve acceptable degrees of utilisation, predrilled application, which allows smaller spacing and distances by about half (e.g. Brandner 2019), is seen as advantageous, with predrilling diameter equal or close to the thread core diameter. In particular for this type of joints but also more generally, partially threaded screws might be advantageous as well; on the one hand to easily achieve sufficient insertion depth and thread embedment to prevent failure modes (ii), on the other hand to provide some additional deformation capacity before reaching the ultimate load which also leads to better load distribution. In this respect, for herein presented steel to-timber joints equal loading of all commonly acting screws in a group is seen as prerequisite for safe joints featuring reliable utilisation ratios and high effective number of screws. Therefore, the application of torque, to secure a tight fit and equal loading of each screw in the group, in case of $\alpha = \gamma$ in conjunction with thick outer steel plates, which allow only minimal differential deformations between screws, are required as well.

More specifically, for glulam of beech and birch and self-tapping application of screws, failure modes (i) can be achieved with minimum spacing and distances according to EC 5. To attain the same failure modes under the same conditions in beech-LVL according to ETA-14/0354:2018 or EN 14374:2005, much larger spacing and distances, predrilling and/or effective length for screw tension failure are recommended. In case of cross joints in hangers which are under pure axial load ($\alpha = \gamma$ and $30° \leq \alpha \leq 90°$; see Figure 1), $l_{pe} / H \geq 0.7$ is recommended.

In case of end-grain joints and pre-drilled application, again failure modes (i) can be reached reliably with spacing and distances $a_2 = a_{2,CG} = 3\,d$ for beech and birch glulam and $a_{2,\text{paral-to-layer}} = a_{2,CG} \geq 3\,d$ and $a_{2,\text{perp-to-layer}} \geq 4\,d$ for beech-LVL, all in combination with $l_{emb} = 10\,d$. For an even higher efficiency within beech and birch glulam $a_2 = a_{2,CG} > 2\,d$ with $l_{emb} = 10\,d$ and target screw tension failure is possible. However, as indicated from comparison of test data in Westermayer & van der Kuilen (2019) with tests reported in Brandner (2019), a severe negative impact of additional moments in planed pure axially-loaded end-grain joints cannot be excluded. Thus, a combination of stiff and high capacity screwed end-grain joints with ductile site-joints arranged in a chain and designed according to overstrength principles and/or screws featuring a ductile shaft are considered advantageous. Furthermore, for pre-drilling over lengths of $\geq 25\,d$, as required for such end-grain joints, adequate drilling equipment is indispensable; otherwise and to prevent contact between screws and/or lateral exit from timber members, larger, uneconomic spacing and distances would be necessary.

Tighter spacing and distances according to diverse ETAs, with $\{a_1; a_2; a_{3,c}; a_{4,c}\}$ = {5; 2.5; 5; 3} and as long as $a_1 \cdot a_2 \geq 25\ d^2$, are also possible for glulam made of beech and birch, as long as the joints are designed to fail by screw tension failure and are under pure axial load. This concerns hangers loaded perpendicular-to-grain ($\alpha = \gamma$ and $30° \leq \alpha \leq 90°$); a similar behaviour is expected also for steel-to-timber tension lap joints ($\alpha \neq \gamma$ and $30° \leq \alpha \leq 45°$), although latter were not part of experimental investigations. Note: although withdrawal failure was shown with a small distance for loaded end, $a_{1,CG}$, as a consequence of geometrical requirements (e.g. to avoid protruding screws) $a_{1,CG} \geq 10\ d$ is recommended.

If all these requirements are fulfilled, i.e. failure modes (i) are attained, the regulations for the effective number of screws according to EC 5 and diverse ETAs lead to conservative estimates for the joint capacity. Otherwise, the verification of all failure modes, (i) and (ii), is inevitable. Actually, verification models for axially loaded groups of screws considering row shear, tension perpendicular-to-grain and block shear failure are under discussion, see Blaß et al. (2019) and Mahlknecht & Brandner (2019).

5   Acknowledgements

6   References

Benjamin JR, Cornell CA (1970) Probability, statistics and decisions in civil engineering. Mc Graw-Hill Book 1070 Company.

Blaß HJ, Bejtka I, Uibel I (2006): Tragfähigkeit von Verbindungen mit selbstbohrenden Holzschrauben mit Vollgewinde (in German). Karlsruher Berichte, Band 4, Universitätsverlag Karlsruhe.

Blaß JH, Flaig M, Meyer N (2019) Row shear and block shear failure of connections with axially loaded screws. 6th INTER Meeting, Tacoma, USA.

Brandner R, Bratulic K, Ringhofer A (2015) Serial correlation of withdrawal properties from axially loaded self-tapping screws. 12th ICASP12, Vancouver, (Canada).

Brandner R (2018) Stochastic Modelling in Timber Engineering. Habilitation, Graz University of Technology, Austria.

Brandner R (2019): Properties of axially loaded self-tapping screws with focus on application in hardwood. Wood Mater Sci Eng 14(5):254-268.

Brandner R, Ringhofer A, Reichinger T (2019) Performance of axially-loaded self-tapping screws in hardwood: Properties and design. Eng Struct 188, 677-699.

Draft Malaysian Standard:2017 MTIB15TC2006R1 – Code of practice for structural use of timber – Part 5: timber joints. ICS: 91.080.20 – Department of standards Malaysia

EAD 130118-01-0603 (2019): Screws and threaded rods for use in timber constructions. EOTA.

Eckerstorfer B (2017): Gruppenversuche in Hartlaubholz (Buche) (in German). Master project, Graz University of Technology, Austria.

EN 1382:1999 Timber structures – Test methods – Withdrawal capacity of timber fasteners. CEN

EN 1383:2016 Timber structures – Test methods – Pull through resistance of timber fasteners. CEN

EN 14374:2005 Holzbauwerke – Furnierschichtholz (LVL) – Anforderungen. CEN.

EN 14358:2016 Holzbauwerke – Berechnung und Kontrolle charakteristischer Werte. CEN.

EN 26891:1991 Timber structures – Joints made with mechanical fasteners. CEN.

ETA-11/0027:2019 fischer Power-Fast Schrauben und fischer Holzbauschrauben (fischerwerke GmbH & Co. KG). ETA-Danmark A/S

ETA-11/0030:2019 Screws and threaded rods for use in timber constructions: Rotho Blaas Self-tapping screws and threaded rods (Rotho Blaas s.r.l). ETA-Danmark A/S.

ETA-11/0190:2018 Self-tapping screws for use in timber constructions: Würth self-tapping screws (Adolf Würth GmbH & Co. KG). DIBt.

ETA-12/0062:2019 Self-tapping screws for use in timber constructions: SFS Selbstbohrende Schrauben WR (SFS intec AG). DIBt.

ETA-12/0063:2019 SFS Selbstbohrende Schrauben WT (SFS intec AG). DIBt.

ETA-12/0114:2017 Self-tapping screws for use in timber constructions: SPAX screws (SPAX International GmbH & Co. KG). ETA-Danmark A/S.

ETA-12/0373:2017 Self-tapping screws for use in timber constructions: Schmid Schrauben RAPID®, STARDRIVE and SP (Schmid Schrauben Hainfeld GmbH). OIB.

ETA-19/0175:2020 Self-tapping screws for use in timber constructions: Fischer Power-Fast II (fischerwerke GmbH & Co. KG). ETA-Danmark A/S.

ETA-12/0197:2019 Self-tapping screws for use in timber constructions: SWG "Timtec-", "Timtec Isotec-" and "Timbtec plus VG" (SWG Schraubenwerk Gaisbach GmbH). ETA-Danmark A/S.

ETA-14/0354:2018 Glued laminated timber made of hardwood – structural laminated veneer lumber made of beech: Beam BauBuche GL75, OIB.

ETA-19/0553:2020 HECO-TOPIX-plus, HECO-TOPIX-plus-T und HECO-TOPIX-plus-CC Schrauben (HECO-Schrauben GmbH & Co. KG), ETA-Danmark A/S.

ETA-20/0558:2020 GoFix MS II, GoFix S+, GoFix X+, GoFix TS / ZS and GoFix SH (SIHGA GmbH). ETA-Danmark A/S.

Eurocode 5:2014 – EN 1995-1-1:2004 +AC:2006 +A1:2008 +A2:2014 Design of timber structures – Part 1-1: General – Common rules and rules for buildings. CEN.

Franke S, Franke B, Heubuch S, Frangi A, Jockwer R (2019): Anschlüsse in Buchenholz (in German). Forschungsbericht, Schweizerische Eidgenossenschaft, BAFU, ETH Zürich, Empa, Berner Fachhochschule, Biel, Switzerland.

Gehri E (2010): Schraubenverbindungen für Laubholzkonstruktionen (in German). 16. IHF, Garmisch-Partenkirchen, Germany.

Grabner M, Ringhofer A (2014): Untersuchung zum Tragverhalten von leistungsfähigen Hirnholzanschlüssen in Laubholz (in German). 20. IHF, Garmisch-Partenkirchen, Germany.

Hübner U (2013): Mechanische Kenngrößen von Buchen-, Eschen- und Robinienholz für lastabtragende Bauteile (in German). Monographic series TU Graz / Timber Engineering & Technology.

Koppauer L (2017): Optimierung von axial beanspruchten Hirnholz-Schraubenverbindungen in Hartlaubholz (in German). Master thesis, Graz University of Technology, Austria.

Krenn H (2017): Die Stahlblech-Holz-Laschenverbindung mit schrägen Schrauben (in German). Monographic Series TU Graz / Timber Engineering & Technology.

Luef M (2020): Untersuchung von rechtwinklig zur Faser eingebrachten, axial beanspruchten Schraubengruppen in Laubholz (in German). Master thesis, Graz University of Technology, Austria.

Mahlknecht U, Brandner R (2019): Block shear failure mechanism of axially-loaded groups of screws. Eng Struct 183, 220-242.

Mahlknecht U, Brandner R, Ringhofer A (2021) Untersuchung an symmetrischen Zuglaschenstößen: Je Seite eine Schraubenreihe unter 45° (in German). Technical report, Graz University of Technology, Austria.

Meyer N, Blass HJ (2018): Connections with glued-in rods in trusses made of beech-LVL. WCTE2018, Seoul, Republic of Korea.

Meyer N (2021): Tragfähigkeit mechanischer und geklebter Verbindungsmittel in Buchenfurnier-schichtholz (in German). Karlsruher Berichte 36, KIT Scientific Publishing.

Obermayr I (2014): Leistungsfähige Hirnholz-Schrauben- und Klebeverbindungen für schlanke Birken-Laubholz-Konstruktionen (in German). Master thesis, Graz University of Technology, Austria.

Oboril M (2021): Dimensionierung und Herstellung eines Hirnholzanschlusses in den Laubholzarten Buche und Birke (in German). Master project, Graz University of Technology, Austria.

Ringhofer A, Brandner R, Schickhofer G (2015): A universal approach for withdrawal properties of self-tapping screws in solid timber and laminated timber products. 2nd INTER Meeting, Sibenik, Croatia.

Ringhofer A (2017): Axially loaded self-tapping screws in solid timber and laminated timber products. Monographic Series TU Graz / Timber Engineering & Technology.

Ringhofer A, Schickhofer G (2019): Product Characteristics of Self-Tapping Timber Screws. 6th INTER Meeting, Tacoma (USA).

Schiro G, Giongo I, Sebastian W, Riccadonna D, Piazza M (2018): Testing of timber-to-timber screw-connections in hybrid configurations. Constr Build Mater 171, 170-186.

Schweiger K (2021): Axial beanspruchte Schraubengruppen in Laubholz – Hirnholzanschluss und geneigt angeordnete Schraubengruppen (in German). Master thesis, Graz University of Technology, Austria.

SIA 265:2012 Holzbau, Schweizerischer Ingenieur- und Architektenverein. SIA.

Westermayr M, van de Kuilen JW (2019): Withdrawal strength of screws and screw groups in European beech (Fagus s.) parallel-to-grain. 6th INTER Meeting, Tacoma, USA.

Westermayr M, van de Kuilen JW (2020): A conceptual model to predict the withdrawal capacity of screws inserted parallel-to-grain in beech, ash and spruce. 7th INTER Meeting, online.

Z-9.1-838:2018 Furnierschichtholz aus Buche zur Ausbildung stabförmiger und flächiger Tragwerke "Platte BauBuche S" und "Platte BauBuche Q". Allgemeine Bauartengenehmigung, DIBt.

DISCUSSION

The papers was presented by U Mahlknecht

M Westermayr commented about n_{eff} of 1 with respect to screw failure. As variation between manufacturers seemed too high, with some manufacturer having COV of 5%, careful consideration of material used would be needed as knot and growth defect could have affected the results. U Mahlknecht agreed in general. The beech material is of high quality and the birch has bit more growth defects. M Westermayr commented that his own work indicated material quality could affect the direction of the drilling.

W Dong asked about the small spacing and what type of equipment was used to drill the holes with tight screw spacing that can avoid contact of the screws. U Mahlknecht agreed that this could depend on the drilling equipment. They did not encounter screw contact with 600 screws installed. U Mahlknecht clarified that predrilling was done stepwise to the total insertion step. 70 mm was drilled first with a fixed machine and the rest with a manual drill to allow more consistent angle at the beginning. W Dong commented that on site installation might be an issue.

G Ravenshorst asked if there is any relationship with density, e.g. how would this work with say high density material of say 1000 kg/m³. U Mahlknecht responded that their dataset did not have a large density range. With the available screws of 8 mm at 10d screw tensile failures were encountered for material at 550 kg/m³. In higher density cases tensile capacity of the screws would govern.

R Brandner commented that predrilling and not on-site installation are advised. R Brandner tested Eucalyptus LVL. The results seemed to show more brittle behaviour with splitting failures. The conclusions in this paper only relate to the products tested in the paper.

I K Abeysekera asked about the distinction between ductile and brittle failure mode and why withdrawal failure was identified as ductile. U Mahlknecht responded that ductile in the sense of comparison to splitting failure and not in the sense of seismic applications. Also there is a possibility of formation of plastic hinges with slender screws.

Beam-on-Foundation Modelling as an Alternative Design Method for Timber Joints with Dowel-Type Fasteners – Part 4: Joints Subjected to In-Plane Loading

Romain Lemaître, Department of Building Technology, Linnaeus University, Växjö, Sweden

Jean-François Bocquet, ENSTIB/LERMaB, University of Lorraine, Épinal, France

Michael Schweigler, Department of Building Technology, Linnaeus University, Växjö, Sweden

Thomas K. Bader, Department of Building Technology, Linnaeus University, Växjö, Sweden

Keywords: dowelled timber connections, numerical modelling, beam-on-foundation, in-plane loading.

1 Introduction

Several different modelling techniques to analyse the mechanical behaviour of the fastener-wood interaction, and thus indirectly to model a dowel-type timber connection, have been developed. However, due to the complex mechanical behaviour of the wood material, no model is capable to satisfactorily analysis the complex stress state and to predict the brittle fracture due to splitting of timber elements around the drilled hole. In addition, most of the advanced material models are based on a complex mathematical formalism, which makes their application in engineering work cumbersome and their integration in a design standard such as Eurocode 5 challenging. Furthermore, their high computing times hinder application in engineering practice (Lemaître, 2020).

This paper continues the work presented in Lemaître et al. (2018, 2019) on strength and stiffness estimation of multiple dowel joints using a Beam-on-Foundation (BoF) model. In the two previous papers, the modelling was inspired by Hirai's work presented in 1983, see Hirai (1983). Even though Lemaître et al. (2018, 2019) were limited to joints subjected to normal force, they showed that numerical modelling can help engineers to fill the gaps of current regulations in Eurocode 5 and to improve the design process. Moreover, the use of engineered wood materials in structures with large

spans and in tall timber buildings increase even more the gap between the engineer's needs and currently available regulations in Eurocode 5. Due to their shapes and sizes, the global mechanical behaviour of large timber structures highly dependents on the stiffness of their connections, which influences eigenmodes and eigenfrequencies, deformation and internal load distribution. In addition, the connections are subjected to more complex loading. For this reason, the BoF model is herein extended to dowelled timber connections subjected to in-plane loading, in the connection shear planes (in-plane bending moment, forces parallel and perpendicular to the neutral axis of the connected timber elements).

Applying a BoF model means to idealize the fastener-wood interaction by non-linear springs. The stiffness of these springs is expressed by mathematical functions, which are empirically determined. Several authors have worked on this type of modelling, see Lemaître (2020) for a review. Previous works however were limited to one-dimensional foundation, which limits the applicability of the model to connections subjected to pure normal or shear loading. The objectives of this paper are to (i) propose techniques to extend this approach to a three-dimensional modelling of the fastener-wood interaction, (ii) show the suitability of the model for estimating the connection stiffness, plastic capacity (no brittle failure can be considered) as well as the load distribution and (iii) highlight the advantages of this type of model for the design of dowelled timber joints in the context of Eurocode 5.

This paper is limited to dowel fasteners. No normal force is considered along the fasteners axis, and thus, neither screwed connections (with inclined or not inclined screws) nor bolted connections were calculated, since the rope effect is not considered.

2 Materials and methods

To simulate the mechanical behaviour of dowel-type timber connections, a three-dimensional finite element model is developed using Cast3M, a French finite element (FE) calculation code[1]. The model integrates the different material behaviours for this type of connection: the elastic behaviour of the components wood and steel (Part 2.2), the elasto-plastic behaviour of the steel fasteners (Part 2.3) and the non-linear behaviour of the fastener-wood interaction (Part 2.4). The general approach to three-dimensional modelling of dowel-type timber connections is illustrated in Figure 1 through a steel-to-timber connection with multiple shear planes and two rows of four dowels. In the following, the modelling approach as well as the behaviour of the materials, governing the behaviour of the connection, are described in detail.
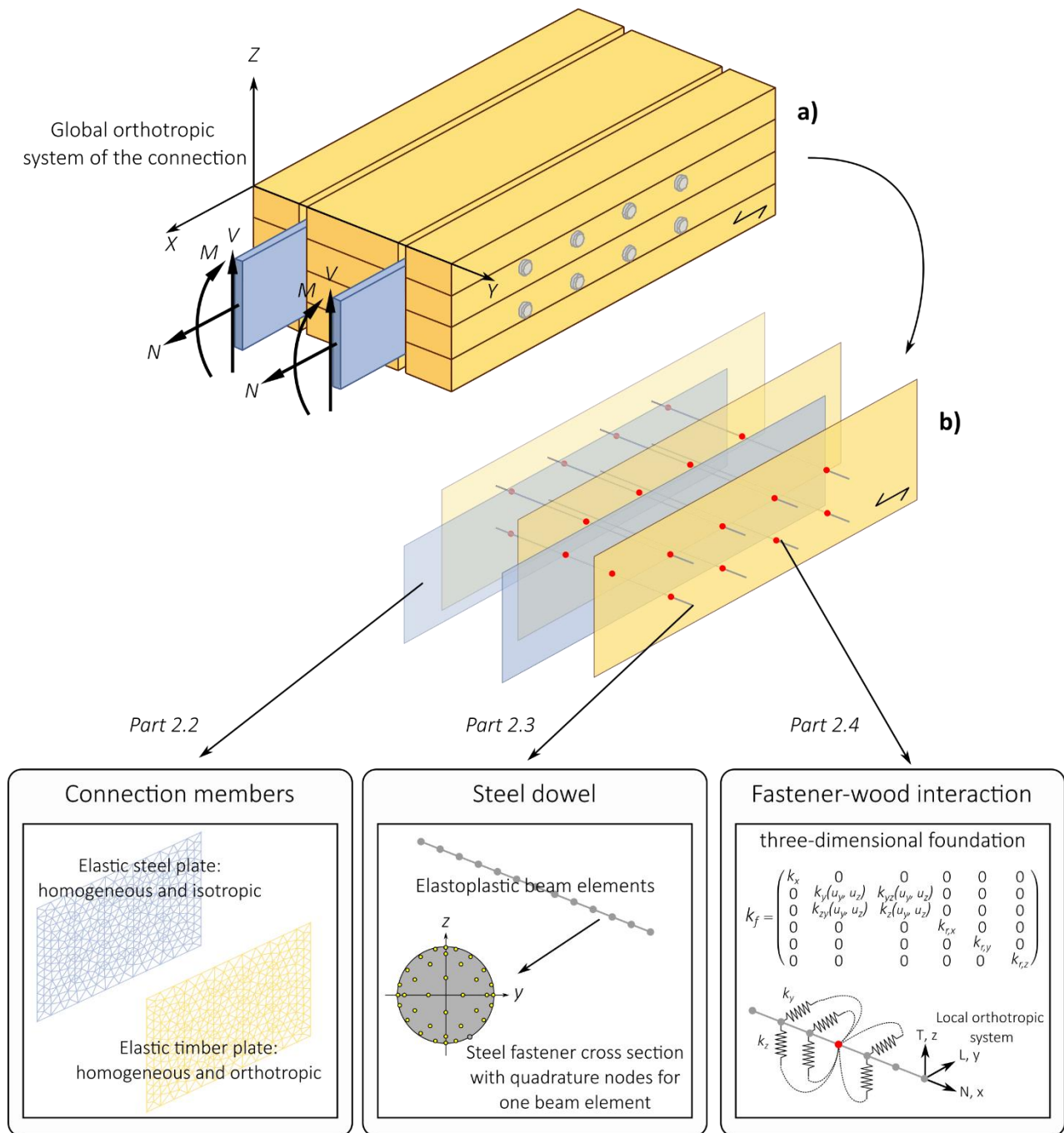
---

[1] http://www-cast3m.cea.fr/index.php

Figure 1. Three-dimensional modeling principle of dowelled timber connections. a) Example on steel-to-timber connection with four shear planes and two rows of fastener. b) FE mesh of the example with timber and steel plates, elasto-plastic beam elements and three-dimensional, non-linear foundation.

2.1 General approach to modelling dowelled timber connections

The numerical calculation of the connection's mechanical behaviour is done incrementally. At each increment n (until the increment number n_{inc}), a linear system is constructed from the elementary stiffness matrices of the different elements of the model: plates, beams, springs (see Figure 1). These elementary stiffness matrices are then assembled to build the global stiffness matrix of the system. The general approach to modelling dowelled timber connections and the pre- and post-processing steps are illustrated in the flowchart in Figure 2.

```
                          ┌─────────┐
                          │  Start  │
                          └─────────┘
                               │
                               ▼
                    ╱─────────────────────╲
                   ╱      Input data        ╲
                  ╱  (geometry, material     ╲
                  ╲      prop., ...)         ╱
                   ╲─────────────────────────╱
                               │
                               ▼
                    ┌─────────────────────┐
                    │  Generate the mesh   │
                    │   of the connection  │
                    └─────────────────────┘
                               │
                               ▼
                    ┌─────────────────────┐
                    │ Define the boundary  │
                    │ conditions and loads │
                    └─────────────────────┘
                               │
                               ▼
                    ┌──────────────────────────┐
                    │ Generate the global       │
                    │ stiffness matrix of the   │
                    │ plates Kᵖˡᵃᵗᵉˢ            │
                    └──────────────────────────┘
```

Generate the global stiffness matrix of the plates K^{plates}

Initialize the vector of displacements $\{U_0\}$

Start the iterations $n \leftarrow 1$

$n \leftarrow n + 1$

$n \le n_{inc}$

Generate the global stiffness matrix of the fasteners $K^{fasteners}(\{U_{n-1}\})$

Generate the global stiffness matrix of the springs $K^{springs}(\{U_{n-1}\})$

Generate the global stiffness matrix of the system $K(\{U_{n-1}\}) = K^{plates} + K^{fasteners} + K^{springs}$

Solve the linear system $\{F_n\} = K(\{U_{n-1}\}) \{U_n\}$

Update the vector of displacements at the spring's nodes

Post-processing

Output files

End

Figure 2. General flowchart for the proposed dowelled timber connection model.

The non-linear behaviour of the fasteners and the fastener-wood interaction is integrated into the model by calculating at each increment new elementary stiffness matrices, k_e. This solution method therefore consists of constructing a solution sequence

$\{U_0\}$, $\{U_1\}$, …, $\{U_n\}$, where $\{U_n\}$ is the vector of displacements at the increment n calculated from the solution $\{U_{n-1}\}$ obtained at the previous increment $n - 1$ by solving the linear system

$$\{F_n\} = K(\{U_{n-1}\}) \{U_n\}, \quad n = \{1, 2, 3, …\} \tag{1}$$

Since the solution $\{U_{n-1}\}$ is known, it is possible to build the elementary stiffness matrices $k_e^{fastener}(\{u_{n-1}\})$ and $k_e^{spring}(\{u_{n-1}\})$, where $k_e^{fastener}(\{u_{n-1}\})$ is the elementary stiffness matrix for a beam element (see Part 2.3); $k_e^{spring}(\{u_{n-1}\})$ is the elementary stiffness matrix for a spring element (see Part 2.4); and $\{u_{n-1}\}$ is the local displacement vector at the element nodes for the $n - 1$ increment.

These elementary stiffness matrices are then assembled with those of the plate elements k_e^{plate} to obtain the global system stiffness matrix $K(\{U_{n-1}\})$. Since the material behaviour constituting the plates is elastic, the matrices need to be calculated only once. This is done before the start of the calculation loop to reduce the computing time.

The calculation method used herein does not include a convergence test, like used at the Newton-Raphson method. The convergence of the results is then linked to the choice of the increment size.

2.2   Elastic behaviour of the components

The mesh of the connection members, which were modelled as plate elements, consists of two-dimensional, triangular, linear elements. The mesh is automatically generated from the plate edges by a Cast3M's subroutine. The mesh density around the nodes $P_0^{i,j}$ linking the plates and the dowels is also controlled to avoid high stress singularities. The definition of nodes $P_0^{i,j}$ is illustrated in Figure 4 in Part 2.4.

For the timber, elastic and orthotropic material behaviour is used. This type of behaviour is defined by four parameters: two moduli of elasticity E_1 and E_2, in the directions parallel and perpendicular to the fibres, respectively (in MPa), a Poisson's ratio v_{12} in the plane of the plate, and a shear modulus G_{12} in the plane of the plate (in MPa). For steel, the material model is elastic and isotropic. It requires only two parameters: a modulus of elasticity E (in MPa) and a Poisson's ratio v. The kinematic plate model chosen is that of Love-Kirchhoff. The Poisson's ratios are taken equal to the average value of v_{LT} and v_{LR}, which are given for softwood in Guitard (1987). The Poisson's ratio v_{12} for laminated veneer lumber with parallel oriented veneers (LVL-S) from spruce wood is assumed equal to the value for glulam.

Material parameters for the timber and steel members, used for the simulations in Part 3, are given in Table 1.

Table 1. Elastic properties of timber and steel members used for FE modelling.

	Timber plate			Steel plate	
	GL24h[*]	GL28h[*]	LVL-S[**]		
E_1 (MPa)	11 500	12 600	13 800	E (MPa)	210 000
E_2 (MPa)	300	300	430	v	0.3
v_{12}	0.41	0.41	0.41		
G_{12} (MPa)	650	650	600		

* Values from EN 14080:2013.
** Values for Kerto-S© (MetsäWood).

2.3 Elasto-plastic behaviour of the steel dowels

Steel dowel fasteners are discretized by one-dimensional linear elements with six degrees of freedom per node. Beam elements based on Euler-Bernoulli beam theory and with a circular cross-section were used. This type of element is characterized by two material parameters, i.e. the modulus of elasticity E and the Poisson's ratio v, as well as by four geometric parameters, namely the cross-sectional area S, the area moments of inertias I_y and I_z around the local axes y and z, respectively, and the polar moment of inertia J.

The elasto-plastic behaviour of the steel dowel is integrated using an own procedure developed in Cast3M. This procedure enables to integrate the elasto-plastic behaviour while keeping one dimensional beam elements. Therefore, the computing time is substantially reduced. The basic idea of this procedure is to integrate for each beam element the evolution of the plastic zone in the cross-section by associating Young's moduli at different support points, see Figure 3. Considering a simple bending case, the plastic zone extends inwards from the outer fibres of the fastener cross-section with a circular segment shape. By a sufficiently larger number of support points and a suitable distribution in the cross-section, the physical phenomenon of plasticity in steel dowels can be modelled (Lemaître 2020).
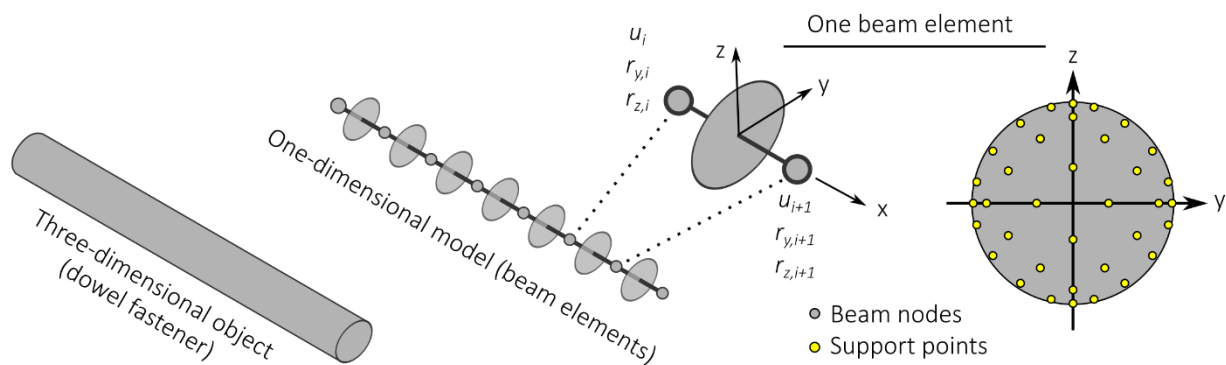
Figure 3. Modelling of the elasto-plastic behaviour of steel dowel fasteners.

The Young's modulus associated at one support point is calculated by first calculating the axial strain ε_{xx} at this position of the cross-section,

$$\varepsilon_{xx}(y, z) = [u_{i+1} - u_i - y\,(r_{z,i+1} - r_{z,i}) + z\,(r_{y,i+1} - r_{y,i})] / L_i \tag{2}$$

where u_{i+1} and u_i are the longitudinal displacements, $r_{z,i+1}$, $r_{z,i}$, $r_{y,i+1}$ and $r_{y,i}$ are the rotations at the nodes of the beam element, L_i is the length of the beam element and (y, z) are the local cross-sectional coordinates of the support point.

If the computed axial strain from Equation (2) is lower than f_y / E, then the Young's modulus associated to the support point is equal to the elastic Young's modulus E_0, else the Young's modulus is equal to the plastic modulus E_t. This test assumes a bilinear behaviour of the fastener under uniaxial tension. E_0 and E_t are the Young's modulus and the plastic modulus of the steel dowel fastener, respectively, both in MPa, and f_y is the yield strength of the fastener (in MPa).

Once the operation described above has been performed for each support point in the cross-section, it is possible to calculate the new equivalent stiffness of one beam element by integration over the cross-section S,

$$(ES)_{eq} = \iint_S E(y,z)\,dS \tag{3.a}$$

$$(EI)_{y,eq} = \iint_S E(y,z)z^2\,dS \tag{3.b}$$

$$(EI)_{z,eq} = \iint_S E(y,z)y^2\,dS \tag{3.c}$$

$$(EI)_{yz,eq} = \iint_S E(y,z)yz\,dS \tag{3.d}$$

The coordinates of the support points are chosen to numerically compute the different Equations (3). In this study, these coordinates are defined by the Gauss-Legendre quadrature rule. A number of 36 points in the cross-section gives a good balance between computing time and relative error compared to the analytical solutions, see Lemaître (2020).

The different equivalent stiffness computed with Equations (3) allow to calculate the effective modulus of elasticity E and the area moments of inertia I_y and I_z (expressed in the principal axes of inertia) of one beam element. From these three parameters, the elementary stiffness matrix $k_e^{fastener}(\{u_{n-1}\})$ is computed. At each increment, the whole operation described above is repeated for each beam element of each steel dowel fastener.

The approach here is limited to the case of asymmetrical bending. In the case of bending with normal force, the calculation of the new centre position of the plasticized cross-section needs to be added. With this extension, the influence of the rope effect on the mechanical behaviour of the dowelled connection could be considered.

2.4 Non-linear behaviour of the fastener-wood and fastener-steel interaction

2.4.1 *Description of the spring elements*

The complexity of local deformation and stress state in wood close to the dowel suggests using a simpler approach to describe the fastener-wood interaction than using continuum modelling approaches. Thus, beam-on-foundation approaches have been developed, where non-linear spring elements are used as contact elements between the nodes of the elasto-plastic beam elements forming the dowels and connection nodes $P_0^{i,j}$ belong to the plates (see Figure 4).
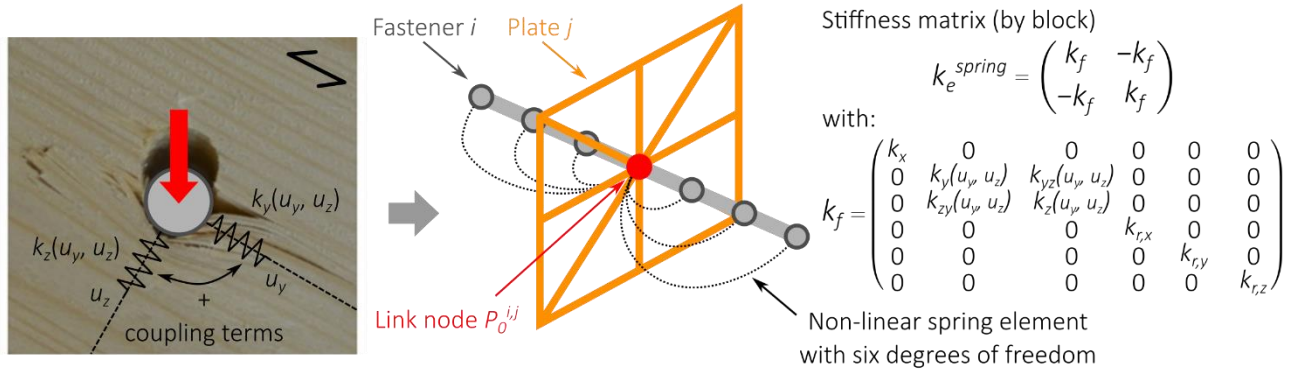
Figure 4. Modelling the fastener-wood interaction with coupled non-linear spring elements.

The orthotropic behaviour of wood is accounted for by using two coupled orthogonal non-linear springs which depend on two orthogonal, local displacements u_y and u_z, respectively in the direction parallel and perpendicular to the grain (see Figure 4). The two springs are defined in the three-dimensional elementary stiffness matrix k_f by four coefficients k_y, k_z, k_{yz} and k_{zy}. The other coefficients k_x, $k_{r,x}$, $k_{r,y}$ and $k_{r,z}$ are constant and independent of the dowel displacement. Thus, the steel dowel is three-dimensionally embedded in the wood.

The discretisation of the embedment behaviour, i.e., the number of spring elements along the dowel, depends on the side member thickness (Hirai 1983). A previous study showed that a minimum distance between spring elements of 0.4d is suggested (Lemaître et al. 2019). This value is used for all simulations presented in this paper.

For the fastener-steel plate interaction, an isotropic and elastic behaviour is considered. Thus, stiffness $k_{y,steel}$ and $k_{z,steel}$ are assumed to be constant, uncoupled and independent of the dowel displacement,

$$k_{y,steel}(u_y, u_z) = k_{z,steel}(u_y, u_z) = \lambda \tag{4.a}$$

$$k_{yz,steel}(u_y, u_z) = k_{zy,steel}(u_y, u_z) = 0 \tag{4.b}$$

Different values of λ included in $\{10^2; 10^3; 10^4\}$ are used and discussed in Part 3.

2.4.2 *Phenomenological embedment surfaces for fastener-wood interaction*

Several parametric equations for the non-linear material behaviour have been proposed in literature. Some of these equations can be applied to the ductile embedment

behaviour of steel dowels in timber, see Schweigler et al. (2018) for a review. In this study, an adaptation of two phenomenological functions is applied to build two surfaces, which described embedment stress parallel and perpendicular to the grain, f_{h0} and f_{h90}, as a function of dowel displacement, u_y and u_z, in the orthotropic coordinate system of timber. In cylindrical coordinates, the parametric equations read as

$$f_{h0}(r, \theta) = (f_{h,inter} + k_{f,pl} \cdot r) \cdot (1 - \exp(-k_{f,el} \cdot r / f_{h,inter})) \cdot (\arctan((a_6 \cdot |\theta| + a_5)^{a4}) + a_2) / (\arctan(a_5^{a4}) + a_2) \quad (5.a)$$

$$f_{h90}(r, \theta) = (f_{h,inter} + k_{f,pl} \cdot r) \cdot (1 - \exp(-k_{f,el} \cdot r / f_{h,inter})) \cdot (\arctan((a_6 \cdot |\pi/2 - \theta| + a_5)^{a4}) + a_2) / (\arctan(a_5^{a4}) + a_2) \quad (5.b)$$

with f_{h0} and f_{h90} as the embedment stress parallel and perpendicular to the grain, respectively, the displacement $r = (u_y^2 + u_z^2)^{1/2}$ and the displacement-to-grain angle $\theta = \arctan(u_z / u_y)$. The parameters a_2, a_4, a_5 and a_6 can be considered as shape parameters which can be fitted from experimental results of load-to-grain embedment tests. The derivatives of Equations (5) with respect to the orthogonal displacements parallel, u_y, and perpendicular to the grain, u_z, yield the coefficients of the elementary stiffness matrix of the springs (see Figure 4).

$$k_y(u_y, u_z) = \partial f_{h,0} / \partial u_y \quad (6.a)$$

$$k_z(u_y, u_z) = \partial f_{h,90} / \partial u_z \quad (6.b)$$

$$k_{yz}(u_y, u_z) = \partial f_{h,0} / \partial u_z \quad (6.c)$$

$$k_{zy}(u_y, u_z) = \partial f_{h,90} / \partial u_y \quad (6.d)$$

Schweigler et al. (2019) compiled a database for embedment properties of different engineered wood products and dowel diameters, for modelling of dowel-type timber connections. Three experimental embedment test series used herein (for simulations presented in Section 3) include two different dowel diameters d (12 and 16 mm), as well as three different materials: spruce and larch glued laminated timber (GLT) and spruce LVL-S. The corresponding embedment parameters for Equations (5) are given in Table 2.

Table 2. Physical and mathematical parameters assigned to the non-linear spring elements.

		$k_{f,el}$ *	$k_{f,pl}$ **	$f_{h,inter}$ ***	a_2	a_4	a_5	a_6
		[N/mm³]	[N/mm³]	[MPa]	[rad]	[-]	[mm]	[-]
GLT (spruce)	0°	25.11	0.07	34.15	$-\pi/2$	5	−2.5	2.5
d = 16 mm	90°	10.18	0.99	14.92	$-\pi/2$	5	−2.5	2.5
GLT (larch)	0°	46.90	−0.67	43.48	$-\pi/2$	5	−2.5	2.5
d = 16 mm	90°	23.81	1.50	19.60	$-\pi/2$	5	−2.5	2.5
LVL-S	0°	27.62	−0.14	35.79	$-\pi/2$	5	−2.5	2.5
d = 12 mm	90°	21.42	1.26	20.42	$-\pi/2$	5	−2.5	2.5

* Elastic foundation modulus.
** Plastic foundation modulus.
*** Embedment stress at the intersection of $k_{f,pl}$ with the stress axis.

3   Results

Four experimental connection test campaigns, previously reported in literature (Bocquet et al. 2012; Bader et al. 2015), are simulated with the BoF approach described in Part 2. In these works, one timber-to-timber (Series 1) and three steel-to-timber connections (Series 2 to 4) were tested. The tested connections in Bocquet et al. (2012) and Bader et al. (2015) were tested with dowel diameters of 16 and 12 mm, respectively. More information on the connection geometries, material properties and experimental programs can be found in Bocquet et al. (2012) and Bader et al. (2015). A schematic sketch of the tested connections can be see in Figure 5.

For each series, the experimental and the numerical global moment-rotation response are compared. This comparison conforms the capability of the model to estimate rotational stiffness as well as bending moment load bearing capacity of dowelled connections. The importance the coupling between the two orthogonal springs for the parallel and perpendicular to the grain embedment behavior, is shown by the comparison with simulations with uncoupled springs.

3.1   Global Moment-Rotation response

Regarding rotational stiffness, differences between numerical and experimental results are given in the Table 3. For each series, a small difference of the rotational stiffness is observed between coupled and uncoupled approach. For steel-to-timber connections (Series 2 to 4), different values of λ are used (see Equation 4) to investigate the influence of the fastener steel-plate interaction on the rotational stiffness, extracted from the numerical simulations. For these series (2 to 4), the rotational stiffness increases with increasing λ. However, for Series 2, the difference with experimental results decreases with decreasing λ while for Series 3 and 4 the difference with experimental results increases with increasing λ. This can be explained by the different deformation measurement and evaluation procedures in the corresponding experimental campaigns. In contrast, only small differences are observed for Series 1 (timber-to-timber connection), which highlights the importance of an accurate definition of the λ value in steel-to-timber connections.

Table 3. Differences between numerical and average experimental rotational stiffness for each series.

	Series 1		Series 2	Series 3	Series 4
Uncoupled	−1.0 %	Uncoupled ($\lambda=10^3$)	+34.0 %	−25.6 %	−29.1 %
Coupled	−3.1 %	Coupled ($\lambda=10^2$)	+10.7 %	−43.2 %	−50.8 %
		Coupled ($\lambda=10^3$)	+33.5 %	−20.1 %	−31.3 %
		Coupled ($\lambda=10^4$)	+34.0 %	−16.2 %	−27.7 %

From Figure 5 it can be seen that, the simulations with uncoupled springs always overestimate the numerical global moment-rotation response with coupled springs which the latter gives good agreement with the experimentally observed slip curves.
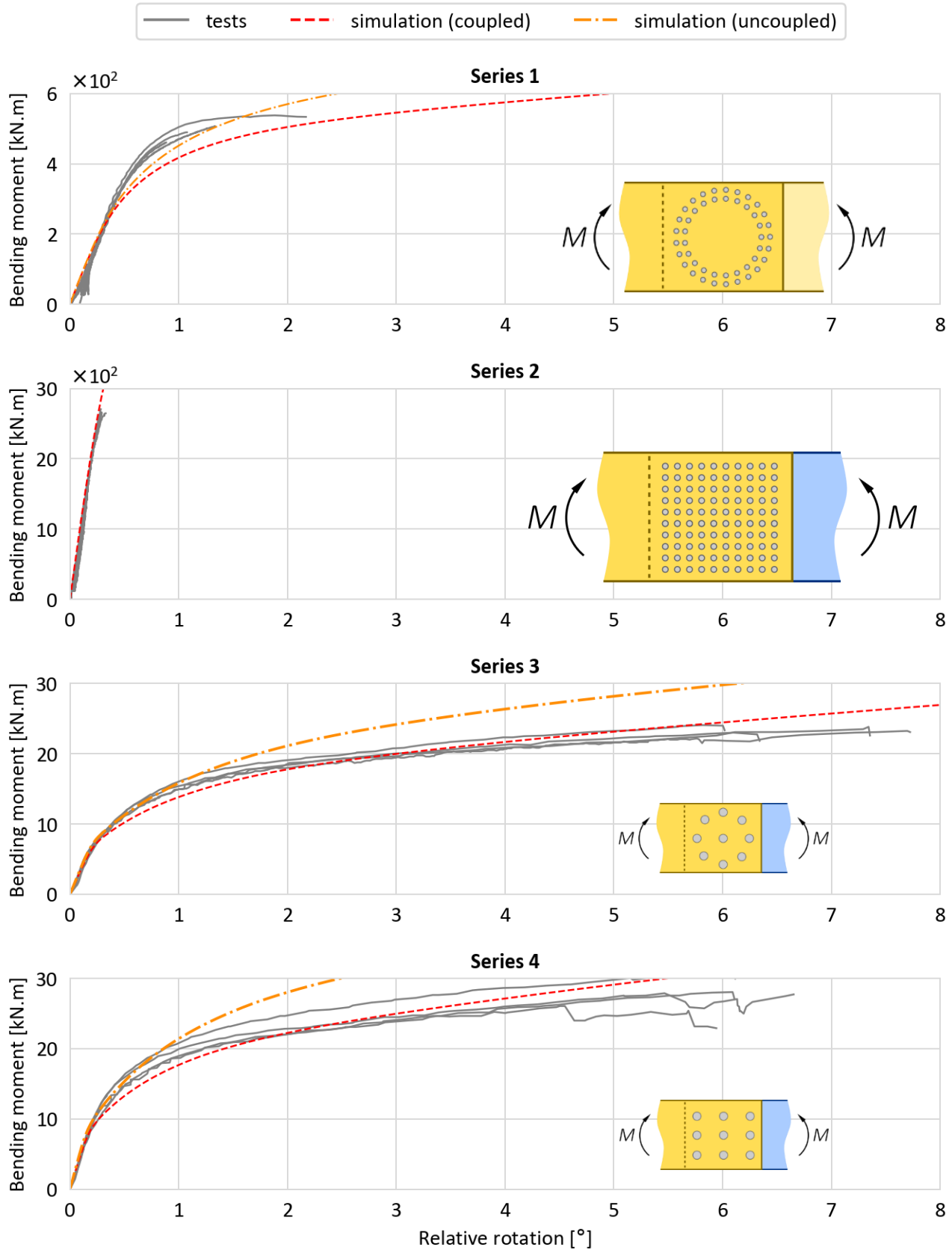
Figure 5. Comparison of experimental moment-rotation curves with simulations. Experimental curves of Series 1 and 2 come from Bocquet et al. (2012). Experimental curves of Series 3 and 4 come from Bader et al. (2015). For Series 2 to 4, a value of $\lambda = 10^3$ is used for the simulations, see Equation (4). The steel properties used for the simulations are: f_y in (400 MPa, 900, 300, 300) and E_t in (1 Gpa, 0, 4, 4) for Series 1, 2, 3 and 4, respectively.

Comparison of the uncoupled/coupled model ($\lambda = 10^3$ for Series 3 and 4) with experiments gives differences in the bending moment of −7.2%/−11.2% (at 0.5°) and −6.8%/−14.0% (at 1°) for Series 1; −2.2%/−11.0% (at 0.5°), +3.0%/−9.7% (at 1°) and +26.9%/+4.7% (at 5°) for Series 3; −0.7%/−14.4% (at 0.5°), +9.1%/−10.0% (at 1°) and +39.6%/+7.1% (at 5°) for Series 4. Since the connection tests in Series 2 showed brittle failure modes, the model was not compared with the experimental data.

3.2   Load distribution

The simulations from Series 3 and 4 are exploited to study differences in the load distribution predicted by the coupled and the uncoupled approach. Figure 6 compares the numerical results for both test series and both modelling approaches. The load observed for the dowels in the connection's corners (numbers 1, 3, 7 and 9) with an uncoupled approach is considerably higher than with a coupled approach. For Series 3 and 4, differences are at 1° relative rotation were as high as +31.9% and +37.0%, and at 5° relative rotation the difference was +48.4% and +50.2%, respectively. Almost no differences are observed for dowels loaded parallel to the grain (numbers 2 and 8) and perpendicular to the grain (numbers 4 and 6). The differences in dowels loaded under an angle to the grain explain why an uncoupled approach is always overestimating the global moment-rotation response.
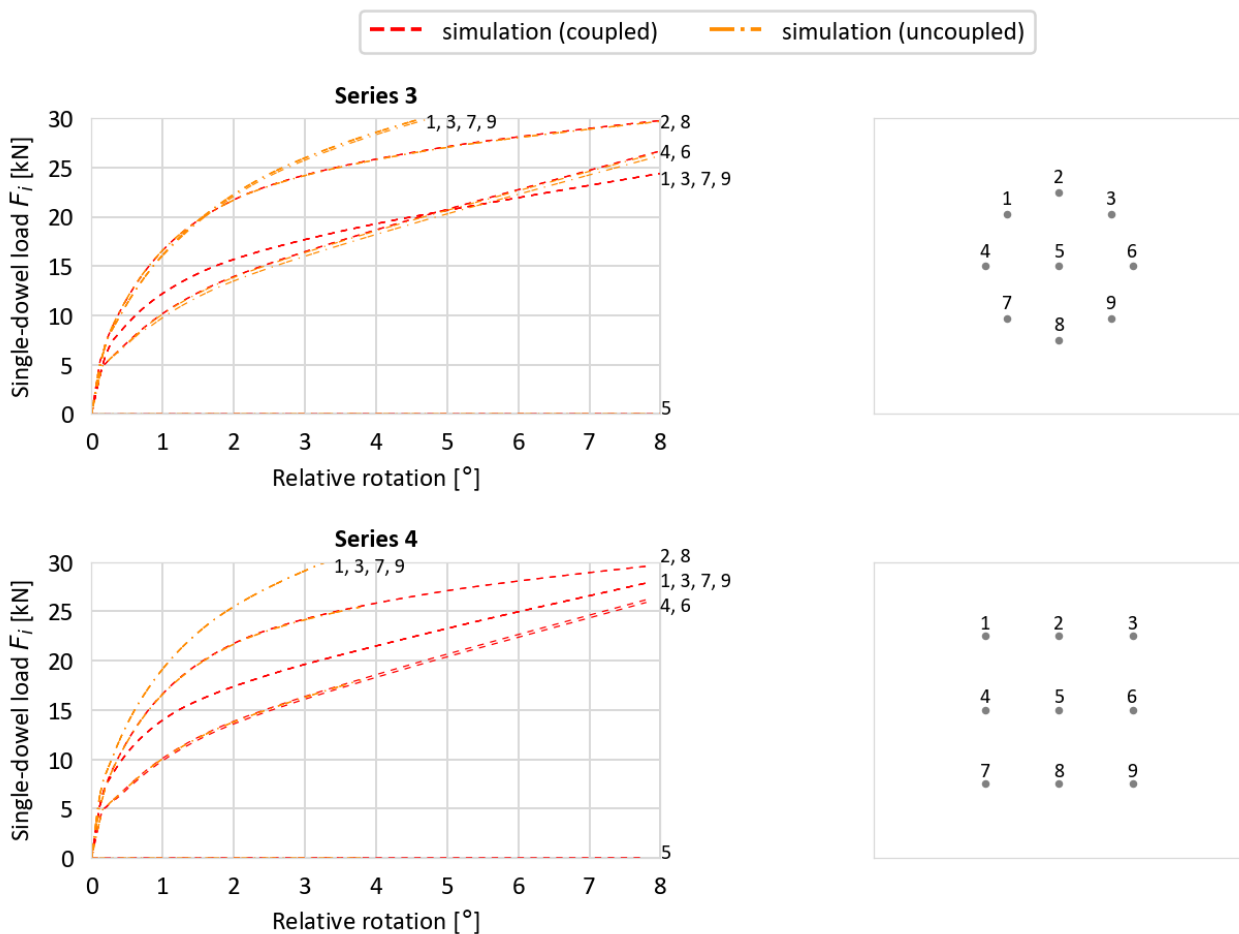
Figure 6. Comparison of single-dowel load between coupled and uncoupled springs for Series 3 and 4.

4   Discussion and conclusion

This paper brings together a certain number of concepts and proposes a numerical method for the design of dowelled timber connections subjected to in-plane loading. It showed that it is possible to simulate the global mechanical behaviour of a connection with a BoF modelling approach using the finite element method. In order to limit the size of the system to be solved, the finite elements used in this three-dimensional model are linear with one-dimensional (beam) and two-dimensional (triangular) plate elements. The main idea of this work is to idealize the fastener-wood interaction by an elasto-plastic beam on non-linear foundation. This pattern is repeated for each dowel and it connects in thickness to the different nodes at the intersection of the two-dimensional timber/steel plate with the elements of the one-dimensional dowel. The timber/steel elements are modelled by two-dimensional plates, with elastic, orthotropic material behaviour for timber and elastic, isotropic behaviour for steel members. To simulate the embedment behaviour of the dowel over the thickness of the wood, the non-linear elastic foundation is composed of two coupled orthogonal springs, one in the direction parallel to the grain and another in the perpendicular direction. This choice of modelling is a way to tackle the difficulties raised by the complex mechanical behaviour of timber under embedment loading of dowels.

The model has been validated with different experimental connection tests: timber-to-timber and steel-to-timber with different fastener arrangements. The experimentally determined moment-rotation curves of the different tests have been compared with simulations. The comparisons showed a good agreement between the experimental and numerical results. The relative error of the rotational stiffness is close to −3% for a timber-to-timber connection with a circular pattern (Series 1). For steel-to-timber connections (Series 2 to 4), the differences vary from +33.5% to −31.3%. The importance of the elastic fastener steel-plate interaction and its influence on the rotational stiffness was shown in the simulations. This interaction needs to be investigated further in order to increase model accuracy for steel-to-timber connections. Moreover, a part of the difference can be explained by the method used to measure of connection member's rotations. The proposed model highlighted the influence of the orthotropic material behaviour of timber members on the load distribution. Simulations showed that with a high shear modulus and neglecting shear deformations in timber, the load in the direction perpendicular to the grain is reduced.

The computing time for the simulated configurations varied from 3 to 30 min, which is suitable for application in engineering practice. A further decrease in computation time can be achieved by optimizing the programming. Thanks to the integration of the model for single fasteners in the model for the group of fasteners, normal force, shear force and bending moment along the fasteners can be evaluated as well. This allows to study failure modes of the steel fastener, typically seen in connections with members of high strength, like hardwood joints. Future works will include new develop-

ments in the proposed BoF modelling. Second order effects can be included for quantifying the influence of the rope effect. Other investigation on the load distribution such as the influence of cracks on wood as well as drilling quality could be considered.

5   References

Bader T. K., Schweigler M., Hochreiner G., Serrano E., Enquist B. and Dorn M. (2015): Dowel deformations in multi-dowel LVL-connections under moment loading. Wood Material Science & Engineering, 10(3):216–231.

Bocquet J.-F., Barthram C. and Pineur A. (2012): L block failure of dowelled connections subject to bending reinforced with threaded rods. CIB-W18 meeting, paper 45-07-03, Växjö, Sweden.

EN 14080 (2013). "Timber structures – Test method – Glued laminated timber and glued solid timber. Requirements." In: European Committee for Standardization (CEN), Brussels, Belgium.

Guitard (1987): Mécanique du matériau bois et composites. Collection Nabla. Cepadues-Éditions, Toulouse, France.

Hirai T. (1983): Nonlinear load-slip relationship of bolted wood-joints with steel side-members II. Application of the generalized theory of a beam on an elastic foundation. Mokuzai Gakkaishi 29(12):839-844.

Lemaître R., Bocquet J. F., Schweigler M., Bader T. K. (2018): Beam-on-foundation modelling as an alternative design method for timber joints with dowel-type fasteners – Part 1: Strength and stiffness per shear plane of single-fastener joints. INTER meeting 51, paper 51-07-13, Tallinn, Estonia.

Lemaître R., Bocquet J. F., Schweigler M., Bader T. K. (2019): Beam-on-foundation modelling as an alternative design method for timber joints with dowel-type fasteners – Part 2: modelling techniques for multiple fastener connections. INTER meeting 52, paper 52-07-09, Tacoma, United-States.

Lemaître (2020): Engineering modelling to design dowel-type timber joints with in-plane loading. PhD thesis. University of Lorraine, France (in french).

Schweigler M., Bader T.K., Hochreiner G., Lemaître R. (2018): Parameterization equations for the nonlinear connection slip applied to the anisotropic behaviour of wood. Composites Part B: Engineering, 142:142-158.

Schweigler M., Bader T. K., Lemaître R., Bocquet J. F., Sandhaas C. (2019): Embedment test analysis and data in the context of phenomenological modeling for dowelled timber joint design. INTER meeting 52, paper 52-07-08, Tacoma, United-States.

DISCUSSION

The papers was presented by R Lemaître

This paper was already presented in 2020. By request of the authors it was not published in 2020. Discussion of 2020:
P Quenneville asked why the evaluation of Kser started from origin and was not started from the post cyclic zone. R Lemaître said that there was no initial gaps/clearance in the connection between the steel plate and timber.

P Gronquist asked if the BoF approach was compared with other models and compared the difference between timber and steel. R Lemaître said no this was not done.

E Serrano asked about consideration of coupled and uncoupled springs to model connector behaviour.   R Lemaître responded that uncoupled springs were used because comparisons with test results showed good agreement for the embedment behaviour. However the path of the dowel movements between simulations and test results were different. Perhaps coupled springs should be considered.

C Sigrist asked about the power function in the proposal and whether it was possible to determine the power from the model. R Lemaître responded that it was possible by regression approach of the test data one could fit the BoF approach to get the power parameter.

C Sigrist commented that models that can consider axially loaded connectors and Ku would also be needed. R Lemaître responded that past work on 2-D BoF presented in INTER could deal with axially loaded connections. Ku could be estimated from the current approach.

G Hochreiner asked whether out-of-plane bending behaviour could be predicted. R Lemaître responded that this BoF model could work in principle but more work would be needed as the coefficients of the stiffness matrix would need more consideration and input.

in 2021 R Lemaître provided a rationale to accommodate a revision to the paper on a similar subject because coupled springs instead of two uncoupled springs are needed based on observed failure modes.

Beam-on-Foundation Modeling as an Alternative Design Method for Timber Joints with Dowel-Type Fasteners – Part 3: Second Order Theory Effects for Considering the Rope Effect

Michael Schweigler[1], Monica Vedovelli[2], Romain Lemaître[1], Jean-François Bocquet[3], Carmen Sandhaas[2], Thomas K. Bader[1]

[1]Department of Building Technology, Linnaeus University, Växjö, Sweden

[2]Karlsruhe Institute of Technology, Germany

[3]ENSTIB/LERMaB, University of Lorraine, Épinal, France

Keywords: dowelled timber joints, rope effect, beam-on-foundation model

1   Introduction

It is well understood that load transfer in joints with laterally loaded dowel-type fasteners is a function of the bending deformation of the fastener and embedment deformation in the wood. This load transfer mechanism was the basis for the derivation of the European Yield Model (EYM). The corresponding equations for the load-bearing capacities, given in Eurocode 5 (EN 1995-1-1, 2004), were derived with equilibrium conditions applied on the undeformed state of the fastener, i.e., based on geometrically linear analysis. Second order theory effects, as a result of equilibrium definition in the deformed state, are however less understood and less investigated. Svensson and Munch-Andersen (2018) derived an analytical model based on mechanical equilibrium in the deformed state of the fastener. However, as for the EYM, compatibility between connection forces and deformations was not considered. Compatibility could be considered by application of a second order theory approach, which would not only allow to consider large deformation effects, but also to include the influence of the rope effect on the connection load-displacement behavior.

As an alternative design method, phenomenological approaches like Beam-on-Foundation (BOF) models have been proposed not only for the prediction of connection capacity but also for the slip modulus and the nonlinear load-displacement behavior (including the deformation) of dowelled connections (Hirai 1983, Sawata and Yasumura 2003, Hochreiner et al. 2013, Bader et al. 2016, Lemaître et al. 2018, 2019,

2021). Validity of the method was proven by good agreement between the EYM and BOF-model predictions for single-fastener joints. The BOF-model gave moreover new insight into stiffness and load distribution in multiple-dowel joints. The model was however not yet fully exploited as regards second order theory effects, which is the content of this paper. The purpose of this paper is to

- define the rope effect and large deformation effects in dowelled connections,
- present a theoretical framework for the local load-displacement behavior of spring elements used in BOF-models,
- validate the proposed method by comparison with novel experiments,
- present parameter studies in order to assess the influence of certain factors.

The aim of this paper is moreover to strengthen the reliability of the method, which has strong potential to be used for the design of connections in advanced timber structures, as well as for the derivation and validation of simplified design rules for design standards. Current Eurocode 5 regulations regarding the rope effect in laterally loaded connections of different fastener types can be validated and adjusted, based on results from this study.

2 Beam-on-foundation model with the rope effect

Beam-on-Foundation (BOF) modeling of dowel-type timber joints relies on beam elements with elasto-plastic material behavior of the steel fastener, which are connected to a discrete number of nonlinear spring elements that represent the embedment behavior of the fastener in wood. A possible withdrawal resistance of the fastener is considered either by nonlinear spring elements, or by friction in the axial direction of the fastener. Coupling between the embedment behavior and the withdrawal behavior is considered in the spring properties. In three-dimensional modeling, three spring elements (two for embedment and one for withdrawal) in orthogonal directions are assigned to each coupling between the beam and the foundation, while only two orthogonal springs are required in case of two-dimensional modeling. A schematic illustration of the BOF-model can be found in Lemaître et al. (2018).

2.1 The rope effect

The expression "rope effect" covers several load transfer effects. These effects can be quantified if a second order theory approach is applied. This also means, that large deformations are required to activate the rope effect. In the following, three different effects being part of the "rope effect" are presented.

2.1.1 Effect 1 - Normal force in the fastener

The normal force in the fastener, N, contributes to the shear resistance, $F_{v,R}$, of a connection, if the fastener axis, or a part of the fastener axis, is inclined in the deformed

state. This is the case for connection failure modes with plastic hinges. The normal force in the fastener, N, might be caused by friction between the fastener and the borehole (Figure 2.1a left), and/or by a mechanical resistance against withdrawal like the thread of a screw or the washers of a bolted connection (Figure 2.1a right). This effect appears also in connections with initially inclined fastener axis, like in connections with inclined screws (Bejtka and Blaß, 2002).

2.1.2   Effect 2 - Friction in the shear plane

The normal force in the fastener, as described in Section 2.1.1, causes in addition to the component parallel to the shear plane, also a compression component perpendicular to the shear plane (Figure 2.1b). If this compression force component is larger than the counteracting force component from the inclined embedment loading (see Figure 2.2), then a resultant compression force acts perpendicular to the shear plane. This compressive force generates frictional forces parallel to the shear plane, which increase the shear resistance, $F_{v,R}$, of the connection (Hilson, 1995). This is the rope effect as considered in the current Eurocode 5, with a friction coefficient of 0.25.

2.1.3   Effect 3 – Straightening of the fastener

Additional embedment forces, and thus an additional connection resistance, $F_{v,R}$, can be activated in some connections with failure modes exhibiting multiple plastic hinges. For example in bolted connections (Figure 2.1c), the washer acts as an anchor, which induces normal forces in the bolt. This normal force causes a straightening of the fastener, which generates additional embedment resistance in the area of the plastic hinge. This effect can also appear in e.g. screwed connections, or doweled connections with steel plates as outer members or multiple shear planes.
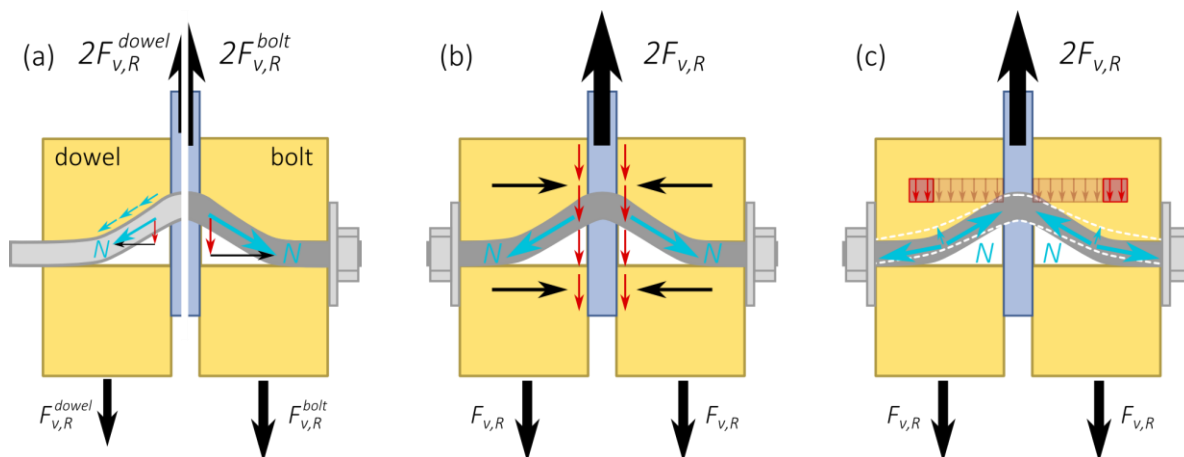
Figure 2.1. Rope effect in dowel and bolt connections. Illustration of effects contributing to an increased $F_{v,R}$ by (a) normal force in the fastener, (b) friction in the shear plane, and (c) straightening of the fastener.

2.2 Large deformation effects

Different spring definitions for embedment and withdrawal behavior of the fastener in BOF-models can be used (Figure 2.2 right). In Definition 1, spring displacements, *CU*, and spring forces, *CTF*, are defined in the undeformed system (first order approach). In Definition 2, *CU* is considered in the undeformed system, and *CTF* in the deformed system, while in Definition 3, both *CU* and *CTF* are considered in the deformed system (second order approaches).

By applying second order theory approaches (Definition 2 and 3), large deformation effects can be considered in BOF-modeling. In these approaches, the withdrawal force, *CTF1*, and the embedment force, *CTF2,* are respectively assumed to be parallel and perpendicular to the deformed state of the fastener. Thus, both components (*CTF1* and *CTF2*) cause force components perpendicular, *F1*, and parallel, *F2*, to the shear plane. Furthermore, the rope effect as described in Section 2.1, can only be considered if second order theory approaches are applied.

In Figure 2.2 the influence of large deformation effects on the overall load-displacement behavior of a steel-to-timber connection is shown. To separate these effects from the rope effect as described in Section 2.1, no withdrawal resistance of the fastener was considered. Reaction forces F_1 appear only if second order theory effects are considered, see Definition 2 and 3 in Figure 2.2. Compared to the first order theory (Definition 1), lead second order approaches to a decreased F_2 (Definition 2 and 3) with increasing u_2. This is a result of the embedment forces acting perpendicular to the deformed, i.e. inclined fastener axis, which divides the embedment force into a component parallel and perpendicular to the shear plane. Thus, with increasing fastener inclination the embedment force share moves from F_2 (parallel to the shear plane) to F_1 (perpendicular to the shear plane).
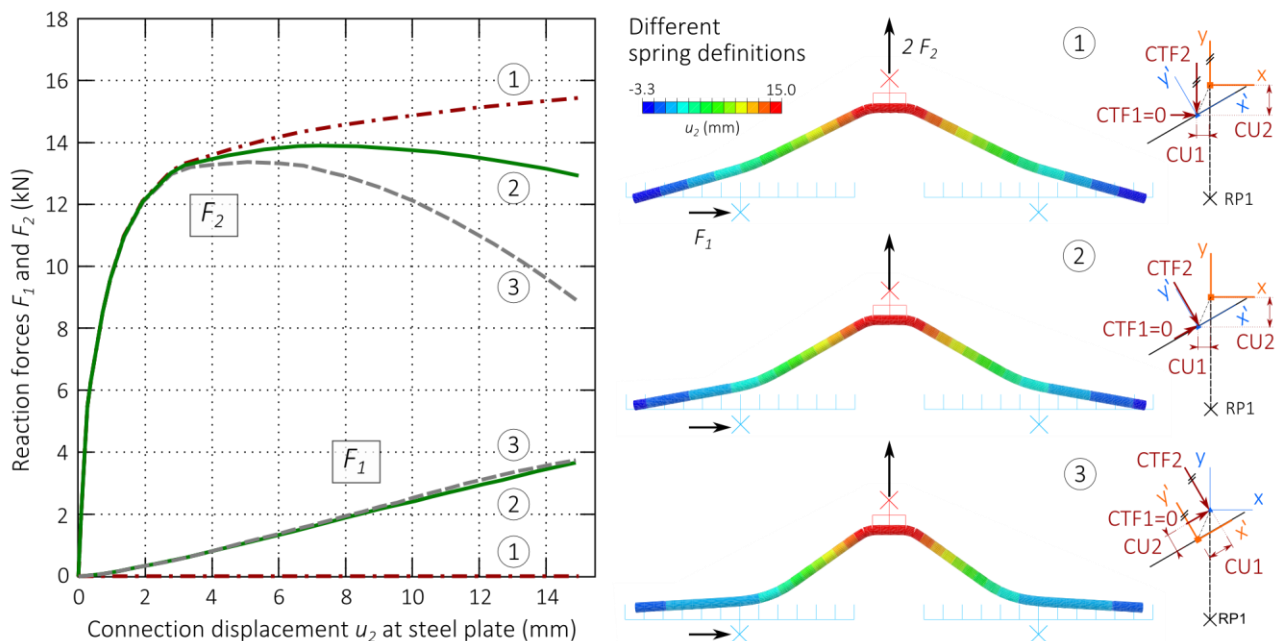
Figure 2.2. BOF-model predictions for a steel-to-timber connection based on first order and second order theory with different definitions of spring properties.

Definition 2 was found to be the most suitable approach when considering large deformation effects in BOF connection models. This approach mimics best experimental investigations and engineering design approaches by using input data definitions in the undeformed state, but still considers second order theory effects by force application in the deformed state. This allows for the use of conventional experimental data as model input, and for comparison with experimental results from connection tests. Thus, Definition 2 is used for the remaining examples in this paper.

3 Validation of the model with novel experiments

To validate the BOF-model with second order theory effects, a novel test set up was developed. In addition to the overall load-displacement behavior, the tensile force in the dowel of a laterally loaded steel-to-timber connection was measured with a strain gauge inserted in the dowel's neutral axis. Thus, this tensile force can be directly compared with the normal force in the beam element of the BOF-model.

In addition to the connection tests, embedment tests, dowel friction tests and dowel tensile have been carried out by using the same material as in the connection tests. Results from these tests serve as input to the BOF-model, and thus allow for a consistent validation of the model.

3.1 Experimental investigations

3.1.1 Connection tests

In order to determine the rope effect, five connection tests were carried out in accordance with EN 26891. Two displacement transducers were attached to the steel plate in order to measure the displacements during the test (see Figure 3.1).

For the timber elements, beech-LVL with cross-layers (LVL Q) and without cross-layers (LVL S) were used. Furthermore, steel plates with steel grade S235, and mild steel dowels with a diameter of 11.99 mm were applied. Connections with slotted-in steel plates as shown in Figure 3.1 were tested. In order to avoid frictional

Figure 3.1. Test setup for shear tests. Left: cross section; top right: axonometric view; bottom left: exploded view.

forces between connection members, a distance t_{gap} of 0.5 mm between these elements was ensured, by gluing two spruce boards with a thickness of 11 mm next to the 10 mm thick slotted-in steel plate (see Figure 3.1).

2.0   40.0   3.0

60.5   11.99

dimensions in mm
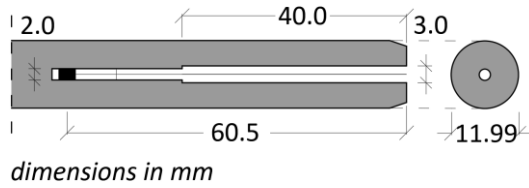
Figure 3.2. Dowels with strain gauge "KFB-3-120-C20-11 N5C2" from Kyowa Electronic Instruments Co., Ltd.

In order to measure the rope effect of the connection, a 64 mm deep hole with a diameter of 2 and 3 mm was drilled into the dowels and a strain gauge was glued in (see Figure 3.1 and Figure 3.2). The strain gauge measured the strain of the dowel in the neutral axis, which allows to calculate normal forces inside the dowel during the test.

During the connection tests, a mean maximum machine load per shear plane F_{max} of 30.9 kN at a displacement w_{Fmax} of 14.2 mm was measured. In all specimens, the dowel formed two plastic hinges per shear plane and sheared off at connection failure. The average maximum normal force in the dowel $F_{max,SG}$ measured with the strain gauges was 3.6 kN.

The slip modulus, K_{ser}, was determined following the principles of EN 26891. However, the yield capacity was used instead of the connection capacity, $F_{v,R}$, for determination of K_{ser}. The yield capacity was defined at a displacement offset of 0.1d, as proposed by Schweigler et al. (2019) for embedment tests. K_{ser}, was then defined as inclination of the line connecting the points on the curve at 10% and 40% of the yield capacity. Results are summarized in Table 3.2 and load-displacement curves are given in Figure 3.6.

3.1.2   Embedment tests

A total of 15 embedment tests were carried out to determine the embedment strength of beech LVL as shown in Figure 3.3. The specimens were obtained from the side members of the connection tests described previously: 12 tests with LVL Q (from specimens 1 to 4), 3 tests with LVL S (from specimen 5). The specimens were not reinforced. The tests were carried out according to EN 383 until a maximum vertical displacement of 15 mm. An overview of the results is given in Table 3.2.
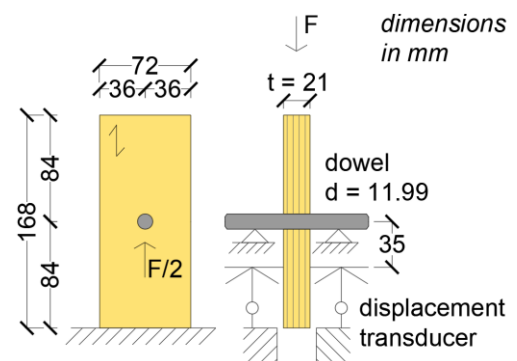
Figure 3.3. Test setup for embedment tests.

3.1.3 Friction tests

Friction between dowel and narrow face of beech LVL was investigated experimentally on five specimens. The test set-up for friction tests in Schmidt (2018) was adopted, see Figure 3.4. The force F is applied axially to the dowel and hence parallel to the friction surface, while the constant force F_N is applied at 90 degrees to the friction surface, so that an embedment pressure σ_N of 2.5 N/mm² acted at the dowel-wood interface. The force F is applied on the dowel up to a dowel displacement of 15 mm and at a speed of 5 mm/min. Static friction corresponds to the maximum force, F_{stat}, necessary to initiate a displacement between dowel and timber members. Dynamic friction corresponds to the average force, F_{dyn}, after the initial force peak, F_{stat}, when dowel and timber members move relative to each other. The static and dynamic friction coefficients, μ, were calculated according to ASTM G115 (Equation (1)) and the results are shown in Table 3.1.
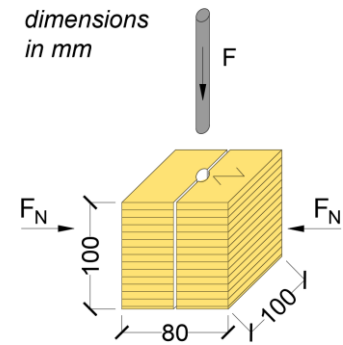
Figure 3.4. Test setup for friction tests.

$$\mu_{stat/dyn} = \frac{F_{stat/dyn}}{2\,F_N} \tag{1}$$

Table 3.1. Results of friction tests.

	μ_{stat}		μ_{dyn}		σ_N	n
mean	CoV	mean	CoV	N/mm²		
0.22	20.6 %	0.15	18.8 %	2.5		5

μ_{stat} = coeff. of static friction; μ_{dyn} = coeff. of dynamic fricion; n = number of specimens

3.1.4 Tensile tests on dowels

In order to define the mechanical properties of the dowels, 10 tensile tests were realized. The tests were carried out according to EN ISO 6892-1 on dowels with no reduction of their cross section (without "dog-bone shape"). An overview of the results can be seen in Figure 3.5.
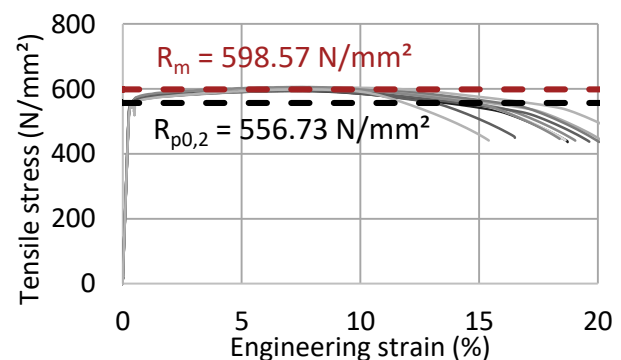
Figure 3.5. Stress-strain curves of tensile tests.

Table 3.2. Results of the shear connection tests and embedment tests.

specimen	mat.	ρ (kg/m³)	u (%)	$f_{h,EN383}$ (N/mm²)	$f_{h,Fmax}$ (N/mm²)	F_{max} (kN)	w_{Fmax} (mm)	$F_{max,SG}$ (kN)	K_{ser} (kN/mm)
1	LVL Q	833	8.8	78.2	87.7	31.20	15.23	4.0	27.9
2	LVL Q	828	8.8	76.1	82.0	31.42	14.48	3.8	25.0
3	LVL Q	833	8.9	73.9	83.1	31.24	14.33	3.0	22.1
4	LVL Q	854	8.5	79.3	89.4	31.36	12.83	4.3	28.4
5	LVL S	806	7.9	67.0	67.0	29.48	14.14	2.9	24.9
mean		831	8.5	74.9	81.8	30.9	14.2	3.6	25.7
CoV		2.1%	4.8%	6.5%	10.8%	2.7%	6.1%	17.2%	10.0%

mat. = material, ρ = density, u = moisture content, SG= strain gauge

3.2 Input for model validation

The connection geometry, i.e. side member thickness, t_1, steel plate thickness, t_{steel}, dowel diameter, d, and gap between connection members, t_{gap}, as well as results from connection component tests (Section 3.1), i.e. embedment tests, friction tests, and dowel tensile tests, were used as input to the BOF-model (Table 3.3).

The non-linear embedment load-displacement curve was defined by the parameterization method presented in Schweigler et al. (2019), using the herein presented approach from Richard and Abbott reading as

$$f_h(u_{emb}) = \frac{(k_{f,el}^{load}-k_{f,pl})\,u_{emb}}{\left[1+\left[\frac{(k_{f,el}^{load}-k_{f,pl})\,u_{emb}}{f_{h,inter}}\right]^a\right]^{1/a}} + k_{f,pl}\,u_{emb}. \tag{2}$$

Corresponding values are presented as mean values in Table 3.3.

Table 3.3. Some BOF input properties for the model validation (mean values).

t_1 (mm)	t_{steel} (mm)	t_{gap} (mm)	d (mm)	$f_{h,inter}$ (N/mm²)	$k_{f,el}^{load}$ (N/mm³)	$k_{f,pl}$ (N/mm³)	a (-)
72	10	0.5	12	70.5	110.8	0.547	3

For the elasto-plastic behavior of the dowel, the mean stress-strain curve from dowel tensile tests presented in Section 3.1.4 was taken. The applied friction between dowel and borehole is based on the findings from the friction tests (see Section 3.1.3). As regards the development of the coefficient of friction, μ_{fast}, with increasing embedment displacement, u_{emb}, and thus with increasing embedment stress, three hypotheses were investigated (see Table 3.4). In Hypotheses $\mathcal{H}1$ *and* $\mathcal{H}2$, the coefficient of friction was assumed to be constant and independent from the

embedment displacement. In Hypothesis $\mathcal{H}3$ a linear increase of the coefficient of friction with increasing embedment displacement was assumed. μ_{fast}= 0.80 at large embedment displacements was found in pretests at Linnaeus University.

Table 3.4. The different hypotheses used to apply the friction between dowel and borehole.

	$\mathcal{H}1$	$\mathcal{H}2$	$\mathcal{H}3$
μ_{fast}	0	0.15	$0.15 + \left(\dfrac{0.80 - 0.15}{15}\right) u_{emb}$

3.3 Engineering design approaches

In addition to the experimental results from connection tests, current connection design approaches are applied for model validation, both in terms of capacity, $F_{v,R}$, and slip modulus, K_{ser}.

For the estimation of $F_{v,R,EYM}$ the European Yield Model (EYM) was used. The mean embedment strength, f_h, as input to the EYM; was calculated by computing Equations (2)) for u_{emb}= 15 mm. For the connection geometry, values given in Table 3.3 were used. The fastener yield moment was calculated by $M_{y,R}= d^3 R_m / 6$, with R_m as the mean value of the experimental dowel tensile strength given in Figure 3.5. The current prefactors given in Eurocode 5 were not applied.The connection slip modulus, $K_{ser,EC5}$, was estimated according to Eurocode 5, with the dowel diameter as given in Table 3.3, and the mean density for beech LVL given in Table 3.2.

3.4 Model validation

Consistent use of materials in experiments, input data for BOF-model and engineering design approaches, as well as consistent use of evaluation methods allow for direct comparison of experiments, BOF model and design approaches. This is done by means of connection load-displacement curves, tensile force in the fastener, connection capacity and slip modulus.

In Figure 3.6a, the shear load, F_2, per side member (shear plane) is plotted over the connection displacement, u_2. In addition, the evolution of the normal force, N, in the dowel with u_2 is illustrated. Thin gray lines represent experiments, while the three thick lines represent the results from the BOF model, corresponding to the three hypotheses for the friction between fastener and borehole. The horizontal red line gives the connection capacity, $F_{v,R,EYM}$, according to the EYM.

From experiments and BOF-model, a pronounced nonlinear, ductile connection behavior can be seen. The BOF-model prediction follows closely the experiments in the quasi-elastic part of the load-displacement curve. However, as soon as yielding of the connection starts, a considerable deviation can be seen. It is also seen, that BOF-curves for the three hypotheses start to deviate, which indicates the importance of the friction between dowel and borehole, which is the only difference in the three

hypotheses. Friction between LVL side member and steel plate was prevented in the BOF-model as it was done for the experiments. One explanation for the deviation between BOF and experiments after yielding could be an even higher friction between dowel and borehole as assumed in the three hypotheses for the BOF-model. Assumption of a linearly increasing friction with the embedment displacement fits best but the relationship might be nonlinear. Additionally, a significant load transfer in fastener direction in the area of largest embedment displacement, i.e. close to the steel plate, could take place. This area is located between the strain gauge and steel plate, and thus does not contribute to an increase of the normal force at the position of the strain gauge.
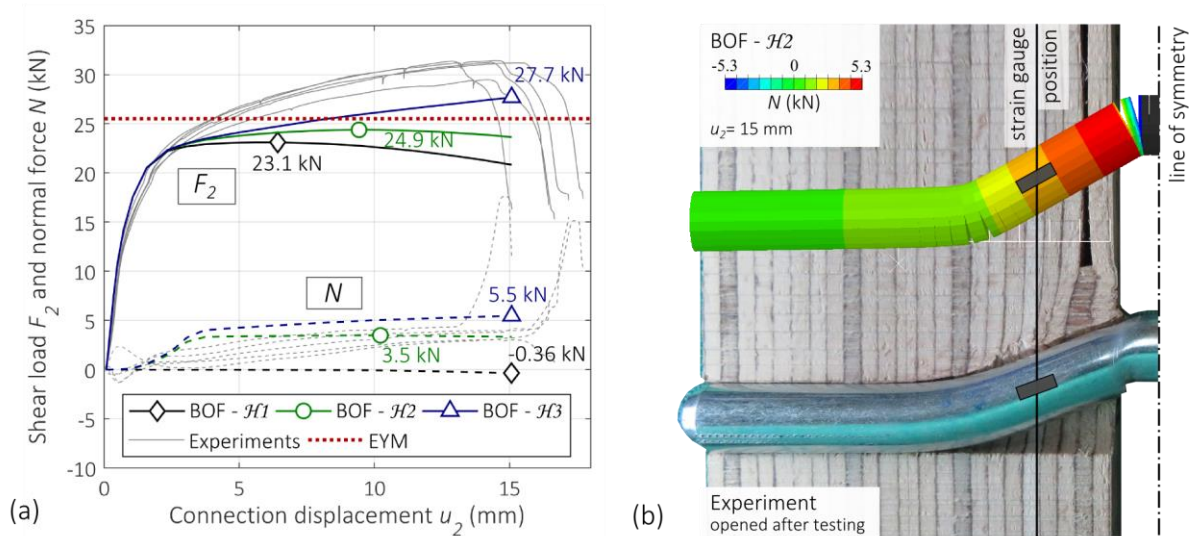
Figure 3.6. Comparison of BOF-model ($\mathcal{H}1$, $\mathcal{H}2$ and $\mathcal{H}3$) with connection tests and EYM; (a) shear load, F_2, per shear plane and normal force, N, in the dowel, plotted over connection displacement, u_2, at the steel plate; (b) deformed state of the dowel for BOF-model ($\mathcal{H}2$) and experiment.

In general, a good correlation of the normal force, N, from experiments and BOF-model $\mathcal{H}2$ and $\mathcal{H}3$ is seen. Nevertheless, BOF-model $\mathcal{H}3$ overestimates N. Beside the aforementioned uncertainty in the assumed friction behavior between dowel and borehole, there are uncertainties in the measured strains from the strain gauge. Even if it was aimed to place the strain gauge exactly in the neutral axis of the dowel, it still might have happened that the measured strains included strains from bending deformations, and thus falsified the calculated normal force. As expected, no significant N builds up if no friction is considered between dowel and borehole ($\mathcal{H}1$).

In Figure 3.6b, the distribution of N along the fastener is illustrated (only half of the connection is illustrated). Considerable normal forces can only be seen in the part between the plastic hinges, since only in this part, significant embedment loads to activate friction exist. It also can be seen that the measured N strongly depends on the position of the strain gauge along the fastener. Compared to the chosen position, an about 50% higher N gets visible next to the steel plate (BOF-model $\mathcal{H}2$). In addition, Figure 3.6b shows the deformed state of the dowel from experiments and BOF. A good agreement of the deformed shape and position of the plastic hinge was found.

Comparing the connection capacity, $F_{v,R}$, the EYM prediction was about 20% lower than the mean value of the experiments (Table 3.5). The BOF-model with no friction ($\mathcal{H}1$) gives about 10% lower capacity as the EYM. This can be explained by the assumption of full plastic embedment behavior in the EYM, which results in an overestimation of the connection capacity. Compared to $\mathcal{H}1$, $\mathcal{H}2$ and $\mathcal{H}3$ lead to 8% and 20% higher capacities, respectively. Nevertheless, experiments still show about 10% higher capacity compared to the BOF-model with ($\mathcal{H}3$). The slip modulus, K_{ser}, shows a very good agreement between experiments, BOF-model and EC5, with deviations of less than 5%.

Table 3.5. Comparison of $F_{v,R}$, $N_{max,SG}$ and K_{ser} from experiments, BOF-model, and EYM/EC5.

	friction	$F_{v,R}$ (kN)	$N_{max,SG}$ (kN)	K_{ser} (kN/mm)
Experiments (mean)	-	30.9	3.6	25.7
BOF	$\mathcal{H}1$	23.1	-0.36	26.9
	$\mathcal{H}2$	24.9	3.5	26.9
	$\mathcal{H}3$	27.7	5.5	26.9
EYM / EC5	-	25.5	0	25.0

4 Parameter study

A parameter study is performed to investigate the influence of material properties, i.e., the fastener withdrawal behavior, as well as friction in the shear plane. Furthermore, the influence of the connection geometry on the rope effect is studied by varying the connection slenderness. Results are expressed as connection capacity, $F_{v,R}$, and slip modulus, K_{ser}, and are compared to the EYM and stiffness estimations by EC5.

The connection used for model validation (see Section 3.1), serves as reference configuration. Hence, a steel-to-beech LVL connection with two shear planes, connected with a steel dowel is used. Friction between side member and steel plate was prevented, if not other stated. In the following, individual parameters are varied to study their effect on the connection behavior.

4.1 Withdrawal behavior

Here the influence of the *Effect 1*, i.e., the normal force in the dowel (see Section 2.1.1), on $F_{v,R}$ and K_{ser} is studied. This is done by variation of the coefficient of friction, μ_{fast}, between dowel and borehole from 0 to 1.0. A constant μ_{fast} over the embedment displacement is assumed, as it was done for $\mathcal{H}1$ and $\mathcal{H}2$.
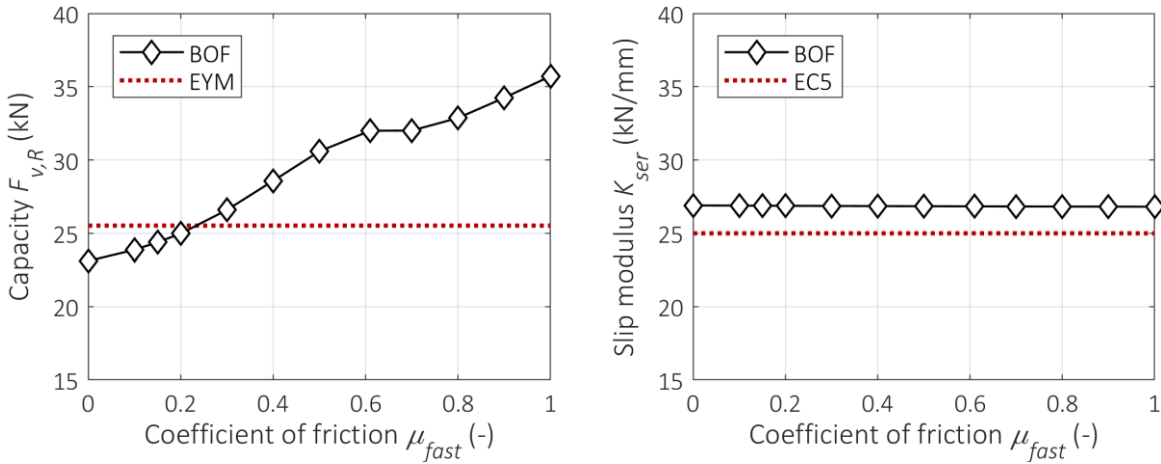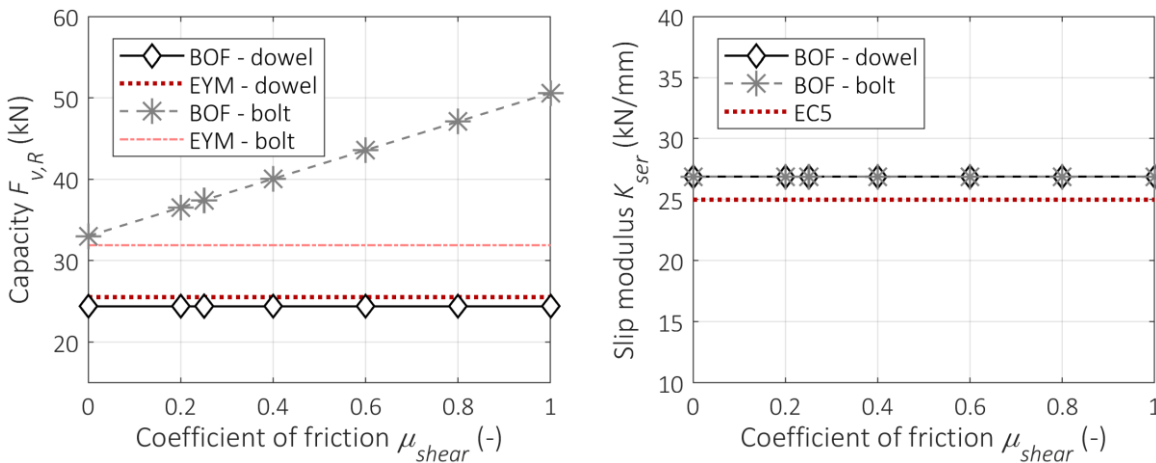
Figure 4.1. Connection capacity, $F_{v,R}$, and slip modulus, K_{ser}, per shear plane depending on the coefficient of friction, μ_{fast}, acting between fastener and borehole.

The connection capacity, $F_{v,R}$, increases considerably by up to 55% with increasing μ_{fast} (Figure 4.1 left). In contrast, the EYM prediction is constant with changing μ_{fast} since it is based on first order theory. Thus, EYM gives up to 40% lower capacity. The increase in capacity is solely based on *Effect 1*, i.e., the additional force component from the normal force in the dowel, acting in direction of the shear plane, since friction in the shear plane is prevented. Nevertheless, it needs to be mentioned, that it can be questioned if $\mu_{fast}= 1.0$ can be achieved in dowel connections, and that the steel dowel might fail due to M/N/V-interaction (Blaß et al., 2017) before the connection capacity at 15 mm displacement is reached.

The slip modulus, K_{ser}, shows to be independent from μ_{fast} (Figure 4.1 right). The same is true for the prediction by EC5, which was about 7% lower than the model prediction. A constant, K_{ser}, is expected, since it is a quasi-elastic property, and thus independent from the rope effect, which is activated at larger connection displacements.

4.2   Friction in the shear plane

In this parameter study, *Effect 2*, i.e., activation of friction in the shear planes (see Section 2.1.2) is investigated. The corresponding coefficient of friction, μ_{shear}, between side members and steel plate is varied from 0 to 1.0. For the friction between fastener and borehole, μ_{fast}, is chosen according to $\mathcal{H}2$ to be constant 0.15. To cover two different connector types, a bolted connection is investigated in addition to the dowel connection, by extending the dowel connection with washers at both ends.

The connection capacity, $F_{v,R}$, is illustrated in Figure 4.2 left. For the dowel connection no influence of μ_{shear} on its capacity was seen. This can be explained by the side members not getting in contact with the steel plate, since the force component from the inclined embedment loading is larger than the counteraction force component from the tensile force, N, in the fastener, which would generate the contact pressure in the shear plane to activate friction. In contrast, for the bolted connection, an increase of $F_{v,R}$ with increasing μ_{shear} by up to 50% is seen. Interestingly, an about 35% higher

capacity of the bolted connection compared to the dowel connection is seen, even if $\mu_{shear}= 0$. This can be explained by the larger normal force in the bolt, which leads to a stronger *Effect 1*. In addition, *Effect 3*, i.e., straightening of the fastener, can be activated for the bolted connection. For the dowel connection a good agreement with the EYM was found, while the BOF bolt model showed 3%-59% higher capacity. As discussed in Section 4.2, $\mu_{shear}= 1.0$ might be questioned, and the connection capacity could be limited by M/N/V-interaction of the fastener, which is not considered in the model. Nevertheless, for $\mu_{shear}= 0.25$, which is the basis for the EYM, a 17% higher capacity was found in the BOF bolt model as for the EYM.

The slip moduli, K_{ser}, of the dowel and bolt connection are identical and constant with μ_{shear}, since the rope effect is activated at larger displacements (Figure 4.2 right). The same is true for K_{ser} calculated according to EC5.

Figure 4.2. Connection capacity ,$F_{v,R}$, and slip modulus, K_{ser}, per shear plane depending on the coefficient of friction, μ_{shear}, acting in the shear planes between connection members.

4.3   Connection slenderness

The influence of the connection slenderness, t_1/d, was investigated. This was done by using the reference connection for hypotheses $\mathcal{H}2$ and $\mathcal{H}3$, by adjusting the side member thickness t_1. As for the model validation, activation of friction in the shear planes was prevented. For a connection with a slotted-in steel plate, three failure modes are possible, namely failure mode (f) no plastic hinge; (g) one plastic hinge at the steel plate, and (h) one plastic hinge in the steel plate and one in each side member (see Figure 4.3).

In Figure 4.3, qualitatively the same trend can be seen for the EYM model and for the BOF-model ($\mathcal{H}2$ and $\mathcal{H}3$). However, development of the first plastic hinge starts earlier than predicted by EYM. For mode (g), a similar nonlinear trend as for the EYM is seen, however with a stronger increase of $F_{v,R}$ with t_1. Highest $F_{v,R}$ is found at the transition from mode (g) to (h), follow by a decreasing $F_{v,R}$ with increasing t_1 for mode (h). This decrease is in contrast to the constant $F_{v,R}$ from EYM, and can be explained by second order theory effects, which are neglected in the EYM. For failure mode (g)

and (h), $F_{v,R}$ from BOF with $\mathcal{H}2$ is underestimated by 5-10%. This can be explained by assuming full plasticity in the EYM, which overestimates $F_{v,R}$. In contrast, the more pronounced rope effect in the BOF-model with $\mathcal{H}3$ results in up to 15% higher $F_{v,R}$.

In failure mode (f), the BOF-model shows a linearly increasing trend of K_{ser} with t_1. Thereafter, K_{ser} is almost constant, with first a slight decrease for mode (g) followed by a slight increase for mode (h) with increasing t_1. The exactly same K_{ser} was found for BOF with $\mathcal{H}2$ and $\mathcal{H}3$, which once more proves its independence from the rope effect. According to EC5, the slip modulus K_{ser} is independent from the side member thickness and thus from the failure mode, which is shown by BOF to be a strong simplification. For mode (f), EYM overestimates K_{ser} by up to 40%, while an underestimation of up to 10% was seen for mode (g) and (h).
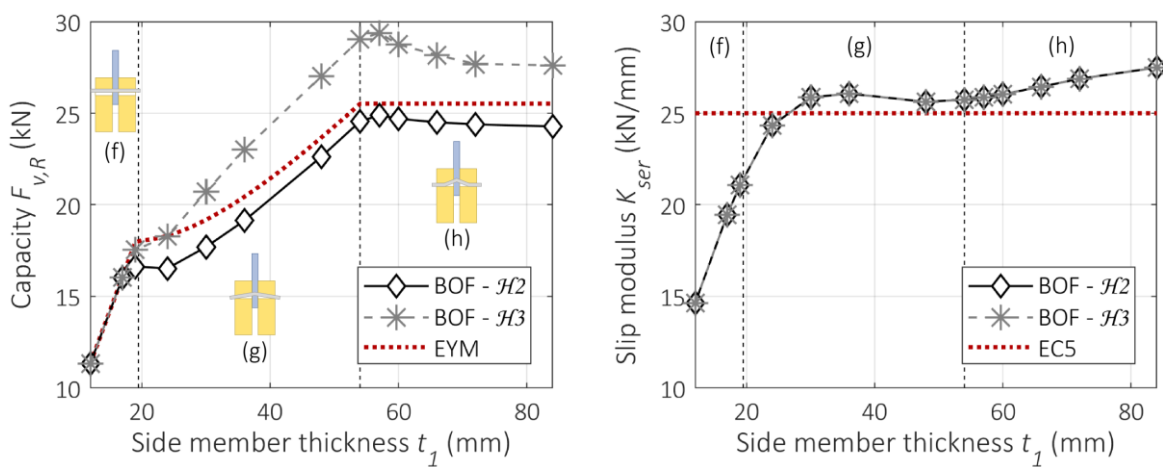
Figure 4.3. Connection capacity ,$F_{v,R}$, and slip modulus, K_{ser}, per shear plane depending on the side member thickness, t_1. Illustration for $\mathcal{H}2$ and $\mathcal{H}3$.

5 Conclusions

Comparing the European Yield Model (EYM) and BOF-model with experimental findings demonstrated the potential of gaining higher connection capacity due to the rope effect in engineering design. In the example presented here, the capacity of the dowelled connection from experiments was about 20% higher as predicted by the EYM. This indicates that also in dowelled connections, a rope effect can be activated and thus could be considered in the design equations of the EYM.

From model validation and parameter study it can be concluded that the rope effect considerably influences the capacity of dowelled and bolted connections. Thus, a revision of the EYM could allow to consider the rope effect also for dowel connections and allow for a higher increase of the connection capacity of bolted connections. However, it was also seen that a displacement of several millimeters is required to activate the rope effect. Especially, to activate friction in the shear planes requires large displacements if a gap between connection members exists for assembly purposes. It was also seen that the slip modulus is not influenced by the rope effect, but

by the connection slenderness, which should be considered in future revisions of design standards.

In this contribution, the importance of the friction between connection members in the shear planes, and of the withdrawal behavior of the fastener was shown. To increase the validity of the BOF-model, considering second order theory effects, more experiments including different connection types are required. Furthermore, it is of highest importance to deepen the understanding for the interaction between embedment stress and withdrawal behavior of dowel-type fasteners, as an essential input to phenomenological approaches, like BOF-models. Taking these steps, we are convinced that this type of models can be a valuable tool for advanced engineering design of connections in timber structures.

6 Acknowledgements

7 References

ASTM G115 – 10 (2018): Standard Guide for Measuring and Reporting Friction Coefficients. ASTM - American Society for Testing Materials.

Bader, T.K., Schweigler, M., Serrano, E., Dorn, M., Enquist, B., and Hochreiner, G. (2016): Integrative experimental characterization and engineering modeling of single-dowel connections in LVL. Construction and Building Materials, 107, 235-246.

Bejtka, I., & H. J. Blaß (2002): Joints with inclined screws. In: Proceedings of CIB-W18/35-7-4, Kyoto, Japan.

Blaß, HJ., Sandhaas, C., Meyer, N. (2017). Steel-to-timber connections: Failure of laterally loaded dowel-type fasteners. In: Proceedings of INTER/50-7-1, Kyoto, Japan.

EN 26891 (1991): Timber Structures - Joints Made with Mechanical Fasteners - General Principles for the Determination of Strength and Deformation Characteristics. CEN, Brussels, Belgium.

EN 383 (2007): Timber structures - Test methods - Determination of embedment strength and foundation values for dowel type fasteners. CEN, Brussels, Belgium.

EN 409 (2009): Timber structures - Test methods - Determination of the yield moment of dowel type fasteners. CEN, Brussels, Belgium.

EN 1995-1-1 (2004): Eurocode 5: Design of timber structures – Part 1-1: General – Common rules and rules for buildings. CEN, Brussels, Belgium.

EN ISO 6892-1 (2019): Metallic materials – Tensile testing – Part 1: Method of test at room temperature. CEN, Brussels, Belgium.

Hilson, B.O (1995): Joints with dowel-type fasteners—Theory, Lecture C3, Timber Engineering, Step 1, STEP/Eurofortech, Centrum Hout, Almere.

Hirai, T. (1983): Nonlinear load-slip relationship of bolted wood-joints with steel side-members II. Mokuzai Gakkaishi 29(12):839-844.

Hochreiner, G., Bader, T.K., de Borst, K., Eberhardsteiner, J. (2013): Stiftförmige Verbindungsmittel im EC5 und baustatische Modellbildung mittels kommerzieller Statiksoftware. Bauingenieur 88:275-289 (in German).

Lemaître, R., Bocquet, J. F., Schweigler, M., & Bader, T. K. (2018): Beam-on-foundation modelling as an alternative design method for timber joints with dowel-type fasteners: Part 1: Strength and stiffness per shear plane of single-fastener joints. In: Proceedings of INTER/51-7-13, Tallinn, Estonia.

Lemaître, R., Bocquet, J. F., Schweigler, M., & Bader, T. K. (2019): Beam-on-Foundation Modelling as an Alternative Design Method for Timber Joints with Dowel-Type Fasteners: Part 2: Modelling Techniques for Multiple Fastener Connections. In: Proceedings of INTER/52-7-9, Tacoma, USA.

Lemaître, R., Bocquet, J. F., Schweigler, M., & Bader, T. K. (2021): Beam-on-Foundation Modelling as an Alternative Design Method for Timber Joints with Dowel-Type Fasteners – Part 2: Modelling Techniques for Multiple Fastener Connections. In: Proceedings of INTER/53-7-4.

Sawata, K., Yasumura, M. (2003): Estimation of yield and ultimate strengths of bolted timber joints by nonlinear analysis and yield theory. Journal of Wood Science 49(5), 383-391.

Schmidt, T. (2018): Kontaktverbindungen für aussteifende Scheiben aus Brettsperrholz (in German). PhD thesis, Karlsruher Institut für Technologie (KIT).

Schweigler, M., Bader, T. K., Bocquet, J. F., Lemaitre, R., Sandhaas, C. (2019): Embedment test analysis and data in the context of phenomenological modeling for dowelled timber joint design. In: Proceedings of INTER/52-7-8, Tacoma, USA.

Svensson, S., & Munch-Andersen, J. (2018): Theory of timber connections with slender dowel type fasteners. Wood Material Science and Engineering, 13(1):7-15.

DISCUSSION

The papers was presented by M Schweigler and M Vedovelli

R Jockwer asked if the 0.25 factor to account for rope effect in the current Eurocode 5 is correct. M Schweigler responded that the 0.25 factor can account for the friction in shear mode; therefore, it is a good factor. R Jockwer commented that maybe this factor accounted for more than just the friction.

G Hochreiner asked what would be the plan to account for the gap and friction. M Schweigler said one should not replace EYM. But using this approach would require more parameters to be defined in the standard. G Hochreiner also asked about the impact of elasticity perpendicular to grain, the size of side member, and the size of the washer. M Schweigler said these issues should be investigated in future work.

P Palma questioned on modelling with springs based on embedment tests and asked why not calibrate the model with single fastener tests. M Schweigler said there are many parameters to be considered in a single fastener test which could mask the embedment properties.

E Tuhkanen asked about the friction between the steel plate and timber member as in real connections movement might not be allowed. M Schweigler said only one fastener was considered in this study. With multiple fasteners the modelling approach of R Lemaître would be more realistic which would also work with slotted in steel plate.

S Aicher asked about the density and compressive stiffness of the side member required to activate the friction force. M Schweigler agreed that modelling of spring stiffness k is a challenge.

S Franke agreed with the findings of 20% value as proposed.

Stiffness of Steel-Timber Dowel Connections – Experimental and Numerical Research

Prof. Dr.-Ing. Ulrike Kuhlmann, Head of Institute

Julius Gauß, M.Sc., Scientific Researcher

Institute of Structural Design, University of Stuttgart, Germany

1 Introduction

Timber construction is gaining more and more importance, also because of the growing public awareness of the building industry's impact on the climate footprint. In order to enable the use of timber construction with its many positive properties in as many areas of application as possible, developments in the design methods have to take place parallel to further developments on the material side. Today the use of computer-based design methods is state of the art and is indispensable, especially in the case of highly indeterminate structures. At first sight, these numerical design methods provide very precise results for the internal forces and the deformations of the structure, but require just as precise input parameters. The stiffness of the cross-sections used and, above all, of the modelled joints have a major influence on the results. Since timber construction

Figure 1.1. Tensile test on steel-timber connection with 2x3 fasteners

with its slender load-bearing members and relatively low cross-sectional stiffness is highly dependent on the correct consideration of the connection stiffness, there is a great need to provide more detailed rules for adequate stiffness assumptions.

Within a former INTER publication (KUHLMANN & GAUß (2019 b)), the possibilities and advantages of the application of the component method in timber construction were pointed out, but also the need of an accurate prediction of the joint load-displacement behaviour. However, several investigations (KUHLMANN & GAUß (2019 a), KUHLMANN & GAUß (2019 b), JOCKWER & JORISSEN (2018), SANDHAAS & VAN DE KUILEN (2017), DORN ET AL. (2013)) showed that the stiffness calculation according to EN 1995-1-1 (2004) is not satisfactory and the revision of rules regarding the connection stiffness consequently is also part of the current work of PT SC5.T5 within the Mandate M/515 of CEN/TC 250. The deviations of the calculated and the experimental stiffness values are caused by the neglect of important influencing parameters like the load-to-grain angle, the slenderness of the fastener or the occurring group effect.

In 2019 the stiffness and the load-carrying capacity of 66 steel-timber dowel connections have been presented in KUHLMANN & GAUß (2019 b). As a result, the deviation of the stiffness of the investigated connections compared with EN 1995-1-1 (2004) has been stated. A further series of 260 tests on steel-timber connections (see Fig. 1.1) were therefore carried out in a current research project, see KUHLMANN & GAUß (2021).

Content of this paper are the results of experimental tests (steel-timber dowel connections, timber embedment tests, steel tensile tests), the results of numerical investigations based on Beam on Foundation (BoF)-models and a discussion of the formulas to determine the connection stiffness given in EN 1995-1-1 (2004).

2 Experimental research

2.1 General

In the scope of the IGF research project No. 20625 N (see KUHLMANN & GAUß (2021)) tests on 260 steel-timber dowel connections and 18 tensile tests of fasteners were conducted. To gain realistic load-displacement curves as input values for the numerical modelling, within a DFG research project (see KUHLMANN ET AL. (2021)) additionally 93 embedment tests on clear and faulty (e.g. cracks, knots) softwood and beech-LVL specimens were carried out. The most important results are listed below, for more detailed information see the related project reports.

2.2 Tensile tests on steel-timber dowel connections

2.2.1 Test programme and setup

In Table 2.1 the experimental programme of the tensile tests on steel-timber dowel connections is shown. Besides the type (dowels, bolts), the diameter (12 mm, 16 mm, 20 mm) and the number of fasteners, the load-to-grain angle α, the type of reinforcement with fully threaded screws, the slenderness of the fastener λ (t / d) and the spacings a_1 and $a_{3,t}$ related to the minimum distances were varied (see Figure 2.1). The standard timber grade was GL 24h, but comparative tests were also carried out on GL 28h and beech-LVL (GL 75h). In consultation with practitioners, the centred reinforcement with fully threaded screws was chosen as the standard case.

Table 2.1. Experimental programme of the component tests

Fastener	Ø [mm]	$n_\perp$ x $n_\parallel$	α	Reinforcement	Timber grade	λ (t)	a_1, $a_{3,t}$
Single (dowel)	12 16 20	1 x 1	0° 30° 60° 90°	Without (1) Centred (2) Close (3)	GL 24h GL 25h GL 75h	1.7 (t_3) 4.5 (t_2) 7.0 (t_1)	1.0
Single (bolt)	12 16 20	1 x 1	0°	Without (1) Centred (2)		7.0 (t_1)	1.0
Group (bolts + dowels)	12 16 20	1 x 3 1 x 5 2 x 3 2 x 5	0°	Centred (2)		7.0 (t_1)	1.0 +25 % + 50 %

Example short name: "SD16 11 0 2" = dowel – Ø = 16 mm – 1x1 – 0° – centred reinforcement (2)

For the tests with the load-to-grain angles 0°, 30° and 60° a symmetrical setup was chosen so that in each case two connections per specimen were tested at the same time. In Figure 2.1 the specimen of the tensile test of a connection with 1x3 fasteners and a centred reinforcement is shown. The measurement devices were placed following the specifications of EN 383 (2007). The application of the load followed the procedure according to EN 26891 (1991). Further information on the geometry and the test setup of the component tests are given in KUHLMANN & GAUß (2021).
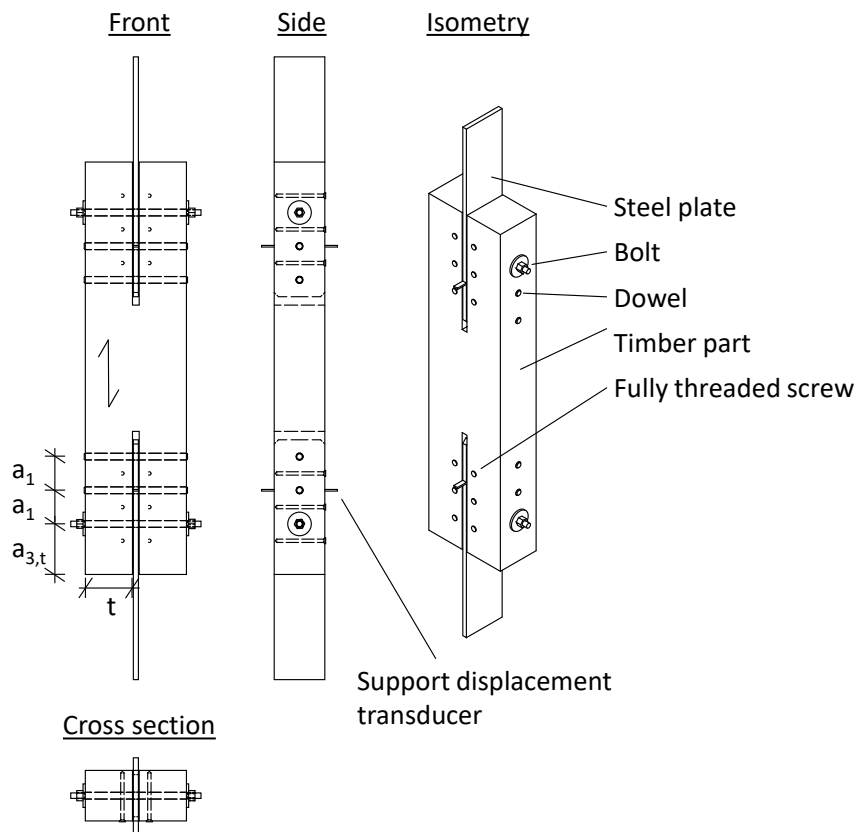
Figure 2.1. Example of a specimen for tensile test parallel to grain with 1x3 fasteners

2.2.2 Test results

The main test results for the initial stiffness K_{ser} and the reloading stiffness K_e are summarised in Table 2.2 to Table 2.4 for the different fastener diameters. They also give a comparison of the mean values to the stiffness according to EN 1995-1-1 (2004), as well as the respective standard deviation (SD) and the coefficient of variation (CV). For a better understanding of the tables, the main characteristics of the individual test series are briefly explained below. The name of the test series is composed as follows:

G-	SD	16	11	0	2	_t2
	Fastener type	Diameter in [mm]	No. of fasteners	Load-to-grain angle	Reinforcement	Additional properties
	SD = dowel / group				1 = without	
	B = bolt		$n_\perp$ x $n_\parallel$		2 = centred	Timber thickness
			11 = 1x1		3 = close	Timber grade
			25 = 2x5			Spacings

Additional properties are for example the timber thickness t (t_2, t_3), the timber grade (GL 28h, GL 75h) or the spacing of fasteners (a_1, $a_{3,t}$). In the standard case, t was dimensioned in such a way that two plastic hinges are formed per shear plane (t_1). The thickness t_2 was chosen so that one plastic hinge is formed, for t_3 the connection should show an embedment failure. Another variant is the spacing of the fasteners. In the standard case, the minimum distance according to EN 1995-1-1 (2004) was used. As variations of the fastener group with 1x5 fasteners (Ø 16 mm) the minimum distance between the fasteners a_1 and the minimum distance to the end grain $a_{3,t}$ were enlarged by 25 % and 50 %. To support the evaluation of test results and to be able to better quantify the influence of the material scattering on the connection stiffness, 3D-computer tomography (3D-CT) scans of the timber parts of 60 connections were carried out before testing. The scans also delivered very interesting results (see KUHLMANN & GAUß (2021)), but are not dealt with further in this paper due to lack of space.

Table 2.2. Initial stiffness K_{ser} and reloading stiffness K_e from tensile tests on steel-timber dowel connections Ø = 12 mm; SD = standard deviation, CV = coefficient of variation

Ø 12 mm	Mean [kN/mm] (K_{test} / K_{EC5})		SD [kN/mm]		CV [%]	
Series	K_{ser}	K_e	K_{ser}	K_e	K_{ser}	K_e
G-SD12 11 0 1	23.5 (131 %)	58.9 (250 %)	4.7	16.7	19.8	28.4
G-SD12 11 0 2	20.2 (112 %)	52.0 (258 %)	5.1	10.2	25.3	19.6
G-SD12 11 0 3	17.8 (99 %)	49.6 (279 %)	1.9	6.9	10.6	13.8
G-SD12 11 0 1_t2	22.4 (124 %)	44.2 (198 %)	4.1	9.0	18.1	20.4
G-SD12 11 0 1_t3	15.3 (85 %)	44.1 (288 %)	2.3	4.3	15.3	9.6
G-SD12 11 90 1	11.3 (63 %)	22.5 (200 %)	1.5	2.5	13.2	11.0
G-SD12 11 90 2	9.4 (53 %)	18.5 (196 %)	2.5	3.5	26.1	19.1
G-SD12 13 0 2	44.5 (83 %)	124.9 (281 %)	6.1	8.6	13.7	6.9
G-SD12 15 0 2	80.6 (90 %)	195.7 (243 %)	12.9	16.1	16.0	8.2
G-B12 11 0 1	21.1 (118 %)	53.2 (252 %)	4.1	10.6	19.2	19.9
G-B12 11 0 2	20.9 (117 %)	54.1 (259 %)	3.3	3.6	15.7	6.7

Table 2.3. Initial stiffness K_{ser} and reloading stiffness K_e from tensile tests on steel-timber dowel connections Ø = 12 mm; SD = standard deviation, CV = coefficient of variation

Ø 16 mm	Mean [kN/mm] (K_{test} / K_{EC5})		SD [kN/mm]		CV [%]	
Series	K_{ser}	K_e	K_{ser}	K_e	K_{ser}	K_e
G-SD16 11 0 1	33.0 (138 %)	57.7 (175 %)	10.9	11.8	33.1	20.4
G-SD16 11 0 2	37.5 (157 %)	68.0 (181 %)	5.3	8.4	14.0	12.4
G-SD16 11 0 3	35.8 (149 %)	70.2 (196 %)	3.6	10.0	9.9	14.3
G-SD16 11 0 1_t2	30.4 (127 %)	48.7 (160 %)	5.0	6.7	16.4	13.8
G-SD16 11 0 1_t3	22.2 (93 %)	57.9 (308 %)	4.4	9.3	19.7	16.0
G-SD16 11 0 2_GL28	34.4 (144 %)	70.9 (206 %)	1.9	8.7	5.6	12.2
G-SD16 11 0 2_GL75	61.7 (98 %)	98.5 (160 %)	17.3	25.6	27.9	26.0
G-SD16 11 30 1	26.4 (110 %)	43.3 (164 %)	3.5	2.1	13.4	4.8
G-SD16 11 30 2	26.7 (111 %)	43.1 (162 %))	2.8	1.9	10.5	4.5
G-SD16 11 60 1	24.2 (101 %)	36.6 (152 %)	2.0	1.5	8.5	4.2
G-SD16 11 60 2	22.3 (93 %)	32.9 (148 %)	3.0	4.3	13.5	13.0
G-SD16 11 90 1	22.4 (94 %)	33.5 (149 %)	1.1	0.9	4.8	2.6
G-SD16 13 0 2	91.3 (127 %)	199.7 (219 %)	10.4	14.4	11.4	7.2
G-SD16 15 0 2	148.4 (124 %)	290.4 (196 %)	28.2	47.8	19.0	16.5
G-SD16 15 0 2_1.25 a1	150.9 (126 %)	326.4 (216 %)	16.1	21.9	10.7	6.7
G-SD16 15 0 2_1.5 a1	169.8 (142 %)	345.7 (204 %)	19.6	55.3	11.6	16.0
G-SD16 15 0 2_1.25 a3	172.4 (144 %)	330.0 (191 %)	23.5	45.2	13.6	13.7
G-SD16 15 0 2_1.5 a3	134.4 (112 %)	282.9 (210 %)	10.7	20.8	8.0	7.3
G-SD16 23 0 2	172.6 (120 %)	323.8 (188 %)	17.4	10.6	10.1	3.3
G-B16 11 0 1	38.3 (160 %)	72.4 (189 %)	6.0	12.4	15.6	17.1
G-B16 11 0 2	40.7 (170 %)	76.4 (187 %)	5.8	12.5	14.3	16.4

Table 2.4. Initial stiffness K_{ser} and reloading stiffness K_e from tensile tests on steel-timber dowel connections Ø = 20 mm; SD = standard deviation. CV = coefficient of variation

Ø 20 mm	Mean [kN/mm] (K_{test} / K_{EC5})		SD [kN/mm]		CV [%]	
Series	K_{ser}	K_e	K_{ser}	K_e	K_{ser}	K_e
G-SD20 11 0 1	62.7 (210 %)	99.2 (158 %)	8.9	12.0	14.2	12.1
G-SD20 11 0 2	56.2 (188 %)	111.0 (197 %)	7.4	25.2	13.1	22.7
G-SD20 11 0 3	58.8 (197 %)	99.6 (169 %)	9.3	22.5	15.7	22.6
G-SD20 11 0 1_t2	57.7 (193 %)	87.5 (152 %)	10.2	16.7	17.7	19.1
G-SD20 11 0 1_t3	55.5 (185 %)	105.8 (191 %)	4.9	11.0	8.8	10.4
G-SD20 11 90 1	32.7 (109 %)	48.1 (147 %)	2.3	4.8	7.1	9.9
G-SD20 11 90 2	32.3 (108 %)	51.2 (159 %)	3.9	9.2	12.2	18.0
G-SD20 13 0 2	145.1 (162 %)	273.1 (188 %)	11.2	25.9	7.7	9.5
G-SD20 15 0 2	255.1 (170 %)	483.9 (190 %)	43.2	58.3	16.9	12.0
G-B20 11 0 1	48.2 (161 %)	94.2 (196 %)	8.4	12.6	17.3	13.4
G-B20 11 0 2	60.3 (202 %)	110.2 (183 %)	11.5	16.4	19.1	14.8

The influence of the individual parameters on the load-displacement behaviour of the connections was evaluated. The most important findings regarding the connection stiffness are summarized in Chapter 4 together with the results of the numerical and analytical investigations. In Figure 2.2 exemplarily the stiffness values K_{ser} and K_e are compared for connections with a fastener diameter of 16 mm and a varying number of fasteners. The solid lines represent the ideal linear correlation between the number of fasteners and the connection stiffness, the dashed lines connect the mean values of the respective series. It can be seen that the

Figure 2.2. Comparison of the stiffnesses K_{ser} and K_e of fastener groups

stiffness per fastener is lower for the fastener groups than for the single fastener. However, there is no significant decrease of the stiffness K_{ser} per fastener with a further increasing number of fasteners, but rather a general reduction for fastener groups compared to the single fastener.

2.3   Tensile tests on dowels and bolts

The dowels and bolts were made from cold-drawn bars (ordered S235JR) with a length of 6 m and then were galvanized. The bolts correspond to longer dowels, which were threaded at both ends. The material properties of the connectors listed in Table 2.5 have been determined by tensile tests on the basis of randomly taken samples. The actually existing tensile strength $f_{u,k}$ (see R_m in Table 2.5) is on average considerably higher than the minimum strength according to the standard for a structural steel S235 acc. EN 1993-1-1 (2005) or for the screw tensile strength 4.6 acc. EN 1993-1-8 (2005). This overstrength coincides with the values determined in other research projects for the material properties of dowels (e.g. BRÜHL (2020), SCHWEIGLER (2018), SANDHAAS (2012)). For the determination of the connection stiffness the tensile strength of the fastener plays a subordinate role, but it is decisive for the load-bearing capacity.

Table 2.5. Mean values of the material properties of fasteners from tensile tests

Diameter [mm]	Yield strength $R_{p\,0.2}$ [N/mm²]	Tensile strength R_m [N/mm²]	MoE [N/mm²]	No. of tests
12	521.4	579.3	212 728	7
16	595.3	623.9	208 250	5
20	593.6	627.4	211 107	6

2.4   Embedment tests

Normally clear samples are used for embedment tests. In real connections, however, it cannot be prevented that there are different material imperfections like knots or cracks in the embedment area of the fasteners. In order to be able to consider the

influence of these imperfections on the embedment behaviour and to ensure comparable boundary conditions between the connection and embedment tests, 93 own embedment tests were carried out on clear and faulty softwood and hardwood specimens within the framework of the Cluster of Excellence "IntCDC" (see KUHLMANN ET AL. (2021)). In addition to the timber grade (GL 24h, GL 75h), the fastener diameter (12 mm, 16 mm, 20 mm) and the load-to-grain angle (0°, 90°) were varied. The deformation measurements were carried out with the optical measuring system ARAMIS. The mean values of the different embedment tests were used as input values for the numerical models and also for the verification and validation of the models. For more detailed information see also KUHLMANN ET AL. (2021).

3 Numerical investigations

3.1 Model description

In order to be able to examine the influence of the various parameters involved in the load-displacement behaviour of dowel-type fasteners, such as the embedment properties of the timber below the fastener, the stress-strain curve of the steel or the geometry of the specimen, a numerical model was developed in RFEM (Dlubal). The numerical model is based on the approach presented by HOCHREINER ET AL. (2013) and expanded by SCHWEIGLER (2018). The load-displacement behaviour of the connection is approximated by means of a non-linearly embedded beam. Figure 3.1 shows a detail of the numerical model and gives an overview of the individual components and node properties. Deviating from the original approach, the modelling of the contact area between the fastener and the steel plate was modified. The occurring deformations of the fastener and the development of the plastic hinges at the edge of the steel plate are considered in detail. The modelling of the embedment behaviour of the timber and the steel plate as well as the material properties of the fasteners were carried out using multilinear approaches. The timber embedment was approximated through 9 individual points, the steel plate embedment and the fasteners material by 12 points.
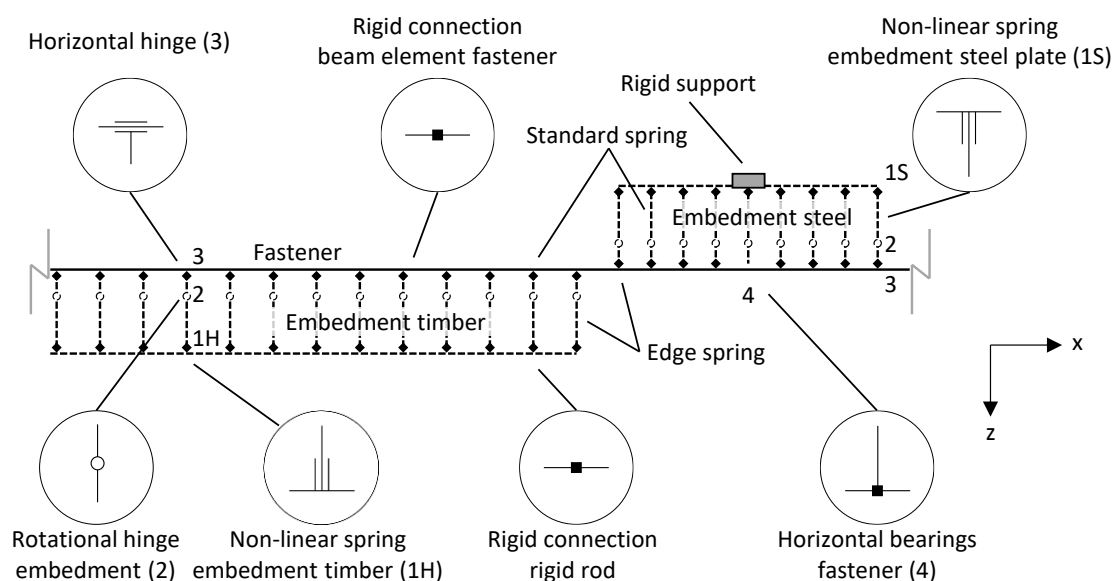
Figure 3.1. Detail of the numerical model and overview of the individual components

The model was verified and validated by the experimental tests (connections and embedment) and a numerical parameter study was carried out on the basis of the validated model.

3.2   Results

The modeling approach based on the non-linearly embedded beam is a good way of predicting the load-displacement behaviour of steel-timber dowel connections. The embedment behaviour of the timber could be verified on the basis of embedment tests carried out. The occuring deformations in the contact area of the steel plate and the fastener has proven to be an important parameter that influences both the connection stiffness and the load-bearing capacity. However, it is not the deformations of the steel plate that is decisive, but the

Figure 3.2. Occuring plastic deformations of the fastener for large bending angles

large plastic deformations of the fastener due to their multi-axial stress state, see Figure 3.2. The material behaviour of the fastener can be described very well by the stress-strain relationship obtained in the tensile tests of the fasteners.

If the input parameters were appropriately selected, the load-displacement behaviour and the stiffness K of the numerical models always showed a very good accordance with the experimental results (see "RFEM" in Figure 3.3). Using averaged input values from the embedment and the tensile tests, it was also possible to predict the connection behaviour under varying geometric boundary conditions (see "Mean"). Therefore, the modeling approach seems to be suitable for predicting the connection stiffness in the context of a numerical parameter study. An
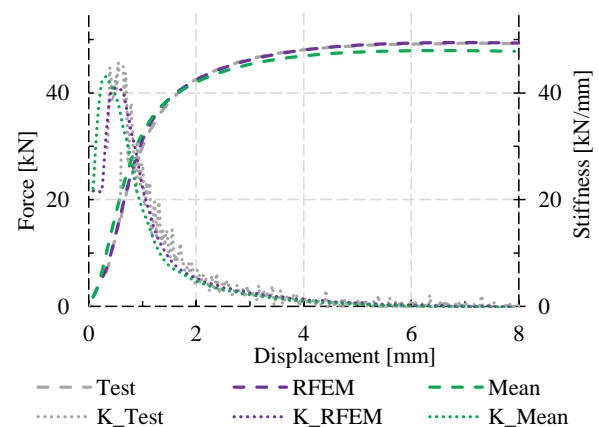
Figure 3.3. Experimental ("Test") and numerical ("RFEM" + "Mean") load-displacement curves and related connection stiffness

important finding of the numerical investigations is that the tolerances in the connection have a greater effect on the connection stiffness than expected. Such tolerances can arise from the scheduled hole tolerance between the fastener and the steel plate, from the initial slip in the embedment of timber or from tolerances in the timber geometry and can hardly be avoided in real connections. The existing tolerances lead to a delayed activation of different embedment areas for the individual fasteners or, in the case of fastener groups, to a stepwise activation of the fasteners. This stepwise activation reduces the maximum stiffness of the connection, as individual areas begin to plasticize before others can develop their full stiffness.

4 Conclusions and suggestions for the determination of the connection stiffness

4.1 General

This chapter summarizes the most important findings from the conducted experimental, numerical and analytical investigations regarding the influencing parameters on the load-displacement behaviour of steel-timber dowel connections. Due to the large scatter of the stiffness values occurring within the individual test series and when comparing it with other research results, it is not meaningful to specify one single value for the connection stiffness within EN 1995-1-1. Rather, it is recommended to specify limit values for minimum, average and maximum expected stiffness values in future versions of the design standards, which are based on the scatter observed in the tests. This procedure would increase the understanding and acceptance of the values given in the standard and enable the planner to use the most unfavourable connection stiffness depending on the design situation. In order to be able to specify the scatter range as realistically as possible, the values should be based on the largest possible data basis. This requires the establishment of a comprehensive database of connection stiffnesses, which, in the ideal case, contains not only the pure stiffness values but also boundary conditions such as the way of deformation measurement, the dimensions of the individual parameters and information on the manufacturing tolerances. As part of the IGF research project, a first step was taken and the stiffness values recorded in this and another research project were included into a database. The extension by further data records and the evaluation of the data can thus take place in the next step. Despite the large spread of the stiffness values, the influence of the individual factors is quantified as well as possible. Based on this, the following suggestions for the calculation of the connection stiffness can be made.

4.2 Embedment properties of timber

The embedment behaviour of the timber has a direct effect on the load-displacement behaviour of the connection. The evaluation of the numerical parameter study has shown that an increase in the elastic embedment stiffness by 20 %, for example, leads to an increase in the maximum stiffness of the connection by 12 %. The initial slip u_0 also has a strong effect on the maximum value of the stiffness due to a delay in reaching the maximum connection stiffness. An initial slip of 0.1 mm leads to a decrease in the maximum connection stiffness of approx. 7 %, a slip of 0.2 mm leads to a decrease of approx. 15 % compared to a connection without an initial slip. The initial slip resulting from the roughness of the borehole surface or from deviations in the borehole geometry from the nominal size thus has a strong effect on the connection stiffness even with relatively small values of u_0. The maximum embedment stress of the timber and the course of the embedment curve in the plastic area, on the other hand, have a strong effect on the load-bearing capacity of the connection, but only have a minor influence on its initial stiffness.

However, due to the numerous material but also geometric imperfections that occur in the timber components, these properties vary widely. By using mean values for the embedment properties from experimental tests, the fundamental load-displacement behaviour of the connection can, however, be predicted relatively precisely. An estimation of the scatter range of the connection stiffness can be made by using minimum and maximum embedment properties. Through the work of SCHWEIGLER & SANDHAAS (2018), numerous experimentally determined embedment values have already been collected and made available in the form of a database, which can be used as input values for the numerical and analytical modelling.

4.3   Fastener diameter d

For the influence of the fastener diameter d, when determining the connection stiffness according to EN 1995-1-1 (2004), a linear relationship between diameter and stiffness is currently assumed. In Table 4.1, various parameters of the different diameters are set in relation to each other. As a comparison, the individual diameters and the respective cross-sectional areas in relation to the fastener Ø 12 mm are given. There is thus a linear relationship between the values of the diameter d and a quadratic relationship between the diameter d and the ratio value for the cross-sectional area. If one compares the ratios of the initial stiffness K_{ser}, it is noticeable that for the timber thickness t_1 (mean value over all reinforcement variants in each case) the ratios of the individual diameters show a quadratic relationship rather than a linear one. For the timber thicknesses t_2 and t_3, the values for the diameter 16 mm lie between the ratios of the linear and the quadratic relationship, for the diameter 20 mm, there is still a quadratic relationship with the diameter. Since the stiffness values for the timber thicknesses t_2 and t_3 are subject to significantly larger geometric imperfections and the sample size is small, these ratio values are, however, subject to greater uncertainties than the values for the timber thickness t_1.

Based on the results of the experimental investigations, it can be stated that the influence of the diameter on the connection stiffness is currently underestimated by EN 1995-1-1 (2004). The approximately quadratic relationship between the fastener diameter and the connection stiffness determined in these investigations should therefore be checked using further existing test results and other fastener diameters. If the relationship is confirmed, the size influence of the diameter could be considered, for example, by introducing an exponent (e.g. $d^{1.9}$) for the diameter in the equation of the stiffness. The specific value of the exponent should be checked with further test data.

Table 4.1. Comparison of the ratios of the diameter, the area and the stiffness values K_{ser} for different timber thicknesses t related to the fastener diameter 12 mm, value = $K_{ser} / K_{ser,12mm}$

Series	Diameter d	Area A	K_{ser} (t_1)	K_{ser} (t_2)	K_{ser} (t_3)
Ø 12 mm	1.0	1.0	1.0	1.0	1.0
Ø 16 mm	1.33	1.78	1.72	1.36	1.45
Ø 20 mm	1.67	2.78	2.89	2.58	3.6

4.4   Load-to-grain angle α

The load-to-grain angle α is currently only considered when determining the load-bearing capacity of a connection and not when determining the connection stiffness. The experimental and numerical investigations with experimentally determined embedment values have shown, however, that with increasing angle α a strong decrease in connection stiffness can be observed. Since load-to-grain angles not equal to 0° in complex structures, such as trusses, are the rule rather than the exception, the load-to-grain angle should be considered, when determining the connection stiffness. Table 4.2 shows the stiffness values determined for the different diameters for the in-

Figure 4.1. Experimental stiffness K_{ser} of dowels Ø 16 mm for different load-to-grain angles α compared to approximations (Hankinson, Linear)

vestigated load-to-grain angles in relation to the stiffness with a load in grain direction. It can be seen that the stiffness for a load perpendicular to the grain direction is approx. 50 % lower than for a load in the grain direction. The value for α = 90° for a diameter of 16 mm is only of limited significance, as it is only made up of the results of three unreinforced connections. For the remaining diameters, at least 10 values each (5x unreinforced and 5x reinforced) could be used. From the values for the angles α = 30° and 60°, a disproportionate large decrease in stiffness with increasing load-to-grain angle can be seen at the beginning. However, as α continues to increase, the rate of decrease in stiffness becomes lower and lower (see Figure 4.1).

Table 4.2. Comparison of the initial stiffness K_{ser} for different load-to-grain angles α in relation to loading parallel to the grain-direction (α = 0°), value = K_{ser} / $K_{ser,0°}$

Series	α = 0°	α = 30°	α = 60°	α = 90°
Ø 12 mm	1.0	-	-	0.51
Ø 16 mm	1.0	0.75	0.63	(0.63)*
Ø 20 mm	1.0	-	-	0.55

* Only a small sample size was available

It is recommended to reduce the initial stiffness for a load-to-grain angle α = 90° compared to a loading parallel to the grain (α = 0°) by 50 %, as is already the case, for example, in the Swiss timber construction standard SIA 265 (2012). For the investigated load-to-grain angles between 0° and 90°, a non-linear relationship between the load-to-grain angle and the stiffness was found. For example, an approach based on the Hankinson equation could be used to determine the intermediate values. For an exponent between 1.5 and 2.0, a relatively good accordance is achieved for the connections examined (see Figure 4.1 with exponent 1.6). However, the test results are subject to a certain degree of uncertainty due to the test setup chosen and the small
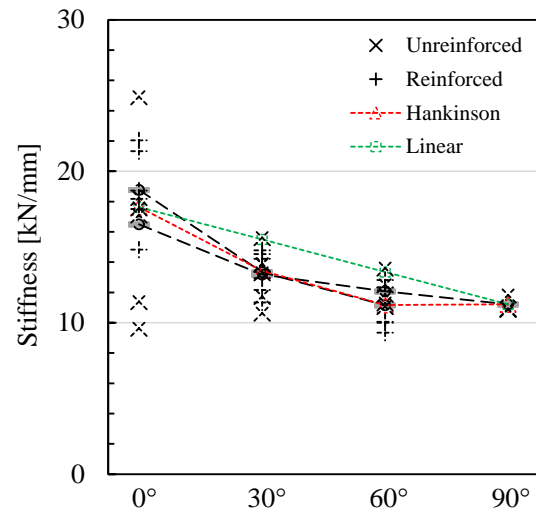
sample size. A comparison with other test results or with numerical results is therefore recommended. Since the scatter of the stiffness values is usually very large, a simplified approach in the form of a linear interpolation between the stiffness values for α = 0° and α = 90° would certainly also be a reasonable approximation that would significantly reduce the effort of determination.

4.5 Number of fasteners

A group effect for the initial stiffness could be determined for all examined diameters (experimental results see Figure 2.2). In Table 4.3, the experimental initial stiffness K_{ser} per fastener is given in relation to the stiffness of a single fastener for the examined diameters. It can be seen that the values all fluctuate around the value 0.8. A clear dependence of the values on the total number of fasteners cannot be seen when considering all diameters. The numerical investigations have shown that the decrease in stiffness per fastener can be explained by a stepwise activation of the individual fasteners within the fastener group. This stepwise activation can mostly be explained by the existing hole tolerance between fastener and steel plate and is therefore subject to a certain scattering depending on its distribution within the connection. The deformation of the timber matrix between the individual fasteners also contributes to an uneven distribution of the forces within the connection, but this proportion is to be assessed as low in relation to the hole tolerance.

Table 4.3. Comparison of the initial stiffness K_{ser} per fastener for a different number of fasteners in relation to the stiffness of a single fastener, value = $K_{ser} / (K_{ser,1x1} \cdot n)$

Series	1x1	1x3	1x5	2x3
Ø 12 mm	1.0	0.72	0.79	-
Ø 16 mm	1.0	0.85	0.83	0.81
Ø 20 mm	1.0	0.82	0.86	-

Due to the complexity of precisely considering the hole tolerance within a fastener group, it is recommended to reduce the stiffness for fastener groups by a fixed value of 0.8, independently of the number of fasteners. The initial slip of the connections examined was usually one third of the maximum possible hole play, i.e. 0.33 mm on average with an oversize of the holes in the slotted plate of 1 mm.

5 Summary

The interaction of the non-linear behaviour of the timber and the fastener is challenging, when predicting the load-displacement behaviour of dowel connections. In chap. 4, the most important influencing factors on the connection stiffness were summarized, considering the experimental, numerical and analytical results, and recommendations were given for consideration in the design. The establishment and evaluation of a comprehensive database is seen as the key for the revision of the values for K_{ser} given in EN 1995-1-1 (2004) as well as for the specification of minimum, mean and maximum values. In addition to the numerous tests on steel-timber dowel connections carried out at the Institute of Structural Design at the University of Stuttgart, further

results from other research projects should also be included to be able to realistically assess the large scattering of stiffness values. However, important adjustments could already be made in the context of the next generation of Eurocode 5. For example, a 50 % reduction of the initial stiffness for a load perpendicular to the grain direction compared to a load parallel to grain direction could easily be included. A reduced stiffness for $\alpha = 90°$ is already considered in the Swiss timber standard SIA 265 (2012) and has already been published several times in various research projects and therefore may be regarded to be state of the art. The reduction of the stiffness per fastener for fastener groups has also been known for a long time (BRÜHL (2020), JORISSEN (1998), SANDHAAS (2012)) and could be considered as a first approach using a general reduction factor (e.g. 0.8). The influence of the diameter is also underestimated according to the results of this research project and should therefore be further evaluated in comparison with other research results. In addition to the respective research reports, a further summary of the overall results is currently being prepared (GAUß (2022)).

6 Acknowledgements

7 References

Bader, T. K. et al. (2016): Experimental characterization of the global and local behavior of multi-dowel LVL-connections under complex loading. In: Materials and Structures, 49, 6.

Bejtka, I. (2005): Verstärkung von Bauteilen aus Holz mit Vollgewindeschrauben. Karlsruhe Institute of Technology, Germany, dissertation.

Bocquet, J.-F. & Lemaître, R. & Bader, T. K. (2018): Design recommendations and example calculations for dowel-type connections with multiple shear forces. In: Design of Connections in Timber Structures – A state-of-the-art report by COST Action FP1402 / WG3.

Brühl, F. (2020): *Ductility in timber structures – possibilities and requirements with regard to dowel type fasteners*. University of Stuttgart, dissertation.

Dorn, M. (2012): Untersuchungen zum Gebrauchstauglichkeitszustand von Dübelverbindungen im Holzbau. TU Vienna, Austria, dissertation.

Dorn, M.; De Borst, K.; Eberhardsteiner, J. (2013): Experiments on dowel-type timber connections. Engineering Structures 47 (2013), pp. 67-80.

EN 383 (2007): Timber Structures – Test methods – Determination of embedment strength and foundation values for dowel type fasteners. CEN, Brussels.

EN 1993-1-1 (2005): Eurocode 3: Design of steel structures - Part-1-1: General rules and rules for buildings. European Committee for Standardization (CEN), Brussels, 2005.

EN 1993-1-8 (2005): Eurocode 3: Design of steel structures - Part-1-8: Design of joints. European Committee for Standardization (CEN), Brussels, with corrections AC:2009.

EN 1995-1-1 (2004): Eurocode 5: Design of timber structures – Part 1-1: General – Common rules and rules for buildings. European Committee for Standardization (CEN), Brussels, with corrections and amendments + AC:2006 and A1:2008.

EN 26891 (1991): Timber Structures – Joints made with mechanical fasteners – General principles for the determination of strength and deformation characteristics. CEN, Brussels.

Jockwer, R. & Jorissen, A. (2018): Stiffness and deformation of connections with dowel-type fasteners. In: Design of Connections in Timber Structures – A state-of-the-art report by COST Action FP1402 / WG3.

Jorissen, A. (1998): Double Shear Timber Connections with Dowel Type Fasteners. Dissertation, TU Delft.

Gauß, J. (2022): Zum Trag- und Verformungsverhalten von Stahl-Holz-Stabdübelverbindungen. Dissertation, in preparation.

Hochreiner, G. et al. (2013): Stiftförmige Verbindungsmittel im EC5 und baustatische Modellbildung mittels kommerzieller Statiksoftware. In: Bauingenieur, 88, pp. 275 – 289.

Kuhlmann, U. & Gauß, J. (2019 a): Optimierung von Anschlüssen im Holzbau zur Verbreitung der ressourcenschonenden Bauweise. Research report, Zukunft Bau (SWD-10.08.18.7-17.12), Institute of Structural Design, University of Stuttgart.

Kuhlmann, U. & Gauß, J. (2019 b): Component Method in Timber Construction – Experimental and Numerical Research. INTER, 52-7-11, Tacoma, Institute of Structural Design, University of Stuttgart.

Kuhlmann, U. & Gauß, J. (2021): Wirtschaftliche Dimensionierung von Holztragwerken durch leistungsfähige Stahl-Holz-Stabdübelverbindungen. IGF research project No. 20625 N (AiF/iVTH), Institute of Structural Design, University of Stuttgart.

Kuhlmann, U.; Gauß, J.; Töpler, J.; Buchholz, L. (2021): Integrated approach of testing and numerical verifications (IATN). Research projekt RP 7, DFG Cluster of Excellence "Integrative Computational Design and Construction for Architecture" (IntCDC), Institute of Structural Design, University of Stuttgart, ongoing.

Sandhaas, C. (2012): Mechanical behavior of timber joints with slotted-in steel plates. TU Delft, dissertation.

Sandhaas, C. & Van de Kuilen, J.-W. G. (2017): Strength and stiffness of timber joints with very high strength steel dowels. Engineering Structures 131 (2017), pp. 394-404.

Schweigler, M. (2018): Nonlinear modelling of reinforced dowel joints in timber structures – a combined experimental-numerical study. Dissertation, Vienna University of Technology.

Schweigler, M. & Sandhaas, C. (2018): Database and parameterization of embedment slip curves. In: Design of Connections in Timber Structures – A state-of-the-art report, COST Action FP1402 / WG3.

Schweigler, M. et al. (2019): Embedment test analysis and data in the context of phenomenological modelling for dowelled timber joint design. INTER / 52-07-8, Tacoma.

SIA 265 (2012): Timber Structures. Zürich, swiss society of engineers and architects.

DISCUSSION

The papers was presented by J Gauß

J M Cabrero asked about the details of the embedment test and received explanation of the position of the reinforcement. J Gauß said that small steel plates were used to load the specimen in tension. J M Cabrero and J Gauß discussed the possible reasons of why lower stiffness was measured for some of the reinforced cases as close position of the reinforcements could have densified some wood material leading to lower stiffness.

H Blass received clarification that with reinforcement stiffness decrease was observed but ultimate load was increased. Also the stiffness was based on absolute not relative load.

F Lam received clarification that full hole tests used in the embedment tests did not result in bending of the dowel.

S Aicher and J Gauß discussed the range of the observed stiffness information in terms of fitting of the model curve to the data. J Gauß said some values are 50% to 100% higher than the lowest values. The COV of the embedment test might be around 40% and the COV of the tensile test might be around 25%. Also embedment test results with only the undisturbed specimens might be unrealistic.

A Frangi commented that the reasoning behind group effect as explained was difficult to understand. He suggested not to include group effect for K_{ser} as only having a single connector would be unrealistic. J Gauß said that the hole tolerance limit has large scatter and agreed it would be easier to provide an overall stiffness reduction. A Frangi commented that $d^{1.7}$ is in the Swiss code.

T Tannert asked about the sensitivity of the data to the variability of steel. J Gauß said steel variability did not affect K_{ser} but affected load capacity. T Tannert asked about extending the work to multiple steel plate connections. J Gauß said the beam on foundation model should be applicable for multiple steel plate connections.

New analytic model for plug shear of timber connections with small diameter dowel-type fasteners in the parallel-to-grain direction

Miguel Yurrita. Wood Chair. Department of Building Construction, Services and Structures. University of Navarra. 31009 Pamplona, Spain. myurrital@alumni.unav.es

José Manuel Cabrero. Wood Chair. Department of Building Construction, Services and Structures. University of Navarra. 31009 Pamplona, Spain. jcabrero@unav.es

1   Introduction

Timber connections with steel dowel-type fasteners are currently the most commonly used type of connection in timber engineering. In the case of structures submitted to low loads, such as housing and low-rise buildings, usually connections with small diameter fasteners such as nails, screws, and rivets, which partially penetrate the timber element, are used. A representative timber-to-steel connection loaded parallel-to-grain with a total of 15 small diameter dowel-type fasteners distributed in 5 columns and 3 rows is depicted in Fig. 1a, while Fig. 1b and Fig. 1c show the side view of the connection before and after the brittle failure, respectively. The geometrical parameters that describe the connection and the used nomenclature within this paper are included in Fig. 1.

Fig. 2 depicts different configurations of a connection with small diameter fasteners, by combining timber members with steel plates (Fig. 2a and Fig. 2b) or only timber elements (Fig. 2c and Fig. 2d). The number of shear planes n_s depends on the total number of elements of the connection: connetions in Fig. 2a and Fig. 2c

(a) Front view *(b) Side view* *(c) Side view after failure*
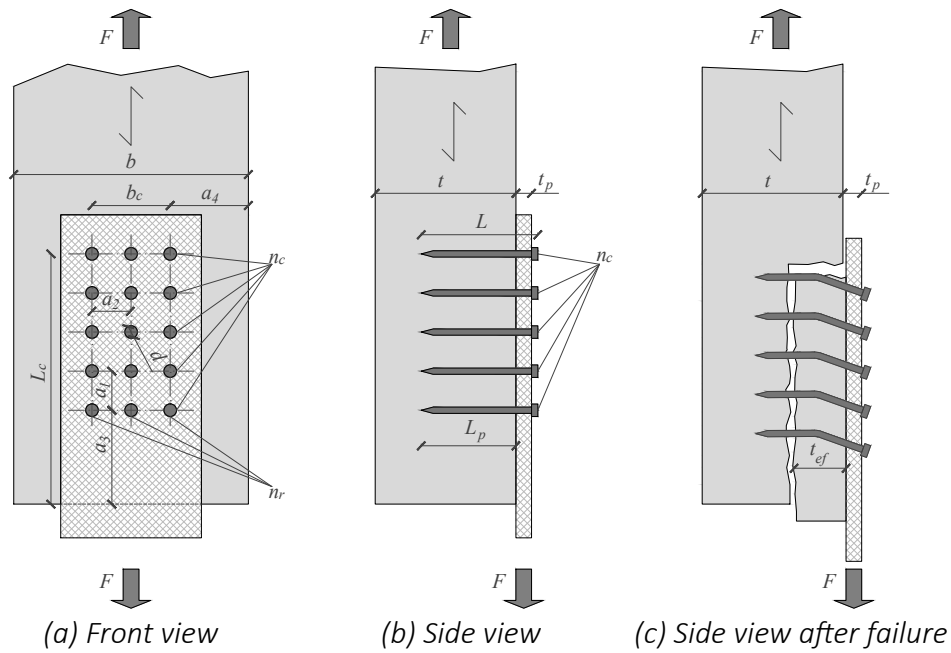
Figure 1. Basic geometry of a generic timber-to-steel connection with small diameter dowel-type fasteners.

have two members and one shear plane, whereas those in Fig. 2b and Fig. 2d have three elements and two shear planes.

A ductile response is desirable in connections, especially in seismic regions. Ductile behaviour relates to the embedment of the wood and the yielding of the fasteners. A brittle behaviour implies a sudden failure of the connection related to the wood fracture. The European Yield Model (EYM) included in most of the standards worldwide considers ductile mechanisms. In contrast, models dealing with brittle failure modes are quite recent, and its inclusion in standards such as the *Eurocode 5* (2004), the *CSA Standard O86-09* (2009) or in the connection chapter of the future version of the New Zealand standard (*Quenneville and Zarnani*, 2017) is still ongoing. Regarding connections with small diameter fasteners, due to the usual high slenderness L_p/d of the fasteners, a pure brittle failure is quite unusual. Instead, a mixed failure (as noticed by *Zarnani and Quenneville* (2014) and *Yurrita, M. and Cabrero, J.M.* (2021)), in which the cracks of the wood are developed after yielding of the fastener has begun, is more probable.

The most relevant brittle failure type of timber connections with small diameter dowel-type fasteners loaded parallel to the grain is plug shear, which is depicted in Fig. 3c. In this failure mode, the wood planes that define the volume of the connection are activated: two lateral shear planes L, a bottom shear plane B and a head tensile plane H. The area $A_{v,L}$ of the L plane is defined by the length of the

(a) wood-steel *(b) steel-wood-steel* *(c) wood-wood* *(d) wood-wood-wood*
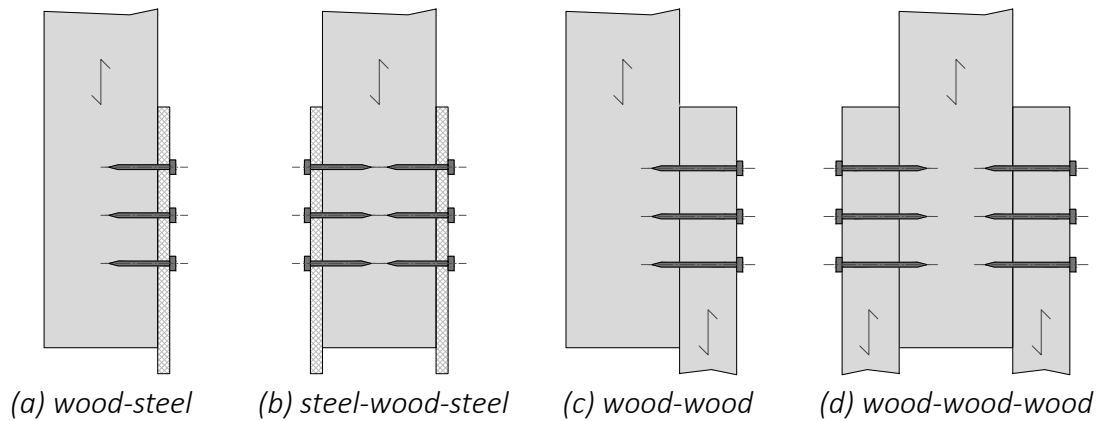
Figure 2. Side view of the possible configurations in connections with partially penetrating small diameter dowel-type fasteners.

(a) Mode A *(b) Mode B* *(c) Mode C*
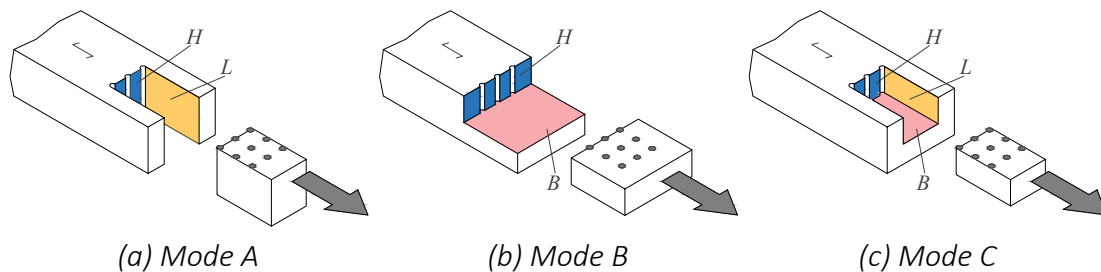
Figure 3. Failure modes including the failure planes (lateral shear L, bottom shear B and head tensile H).

connection L_c and the effective thickness t_{ef} of the timber member. The area $A_{v,B}$ of the B plane is defined by the length of the connection L_c and the width of the connection b_c. Finally, the area $A_{t,H}$ of the H plane is obtained by multiplying the width of the connection b_c by the effective thickness t_{ef}. Fig. 3a and Fig. 3b depict two additional types of plug shear in which one of the described failure planes is not activated: in Mode A (Fig. 3a), the lack of a bottom shear plane expands the lateral shear planes up to the whole timber thickness t (block shear failure); in the case of Mode B (Fig. 3b), the lateral shear planes disappear, leading to a bottom shear plane and including the whole timber width b.

2 Existing proposals

Existing models for brittle failure of timber connections with small diameter fasteners focus on Mode C (plug shear, Fig. 3c), while not all of them considers the two other variants. All of them are conceived as design models which determine the capacity of each of the failure planes. Such capacity is obtained by multiplying the area of each failure plane by the corresponding strength (tensile strength

Table 1. Summary of the existing models for brittle failure in connections with small diameter dowel-type fasteners.

Model	Mode A	Mode B	Mode C
Stahl et al. (2004)	$A_{v,L}f_v + A_{t,H}f_{t,0}$	$A_{v,B}f_v + A_{t,H}f_{t,0}$	$(A_{v,L} + A_{v,B})f_v + A_{t,H}f_{t,0}$
Eurocode 5 (2004)	$\max \begin{cases} 1.5A_{t,H}f_{t,0} \\ 0.7A_{v,L}f_v \end{cases}$	—	$\max \begin{cases} 1.5A_{t,H}f_{t,0} \\ 0.7(A_{v,L} + A_{v,B})f_v \end{cases}$
Kangas and Vesa (1998)	—	—	$A_{v,B}f_v + A_{t,H}f_{t,0}$
Johnsson and Parida (2013)	—	—	$\max \begin{cases} A_{t,H}f_{t,0} \\ A_{v,B}f_v \end{cases}$
Quenneville and Zarnani (2017)	Stiffness approach	Stiffness approach	Stiffness approach

[a] *Stahl et al.* (2004) and *Eurocode 5* (2004) consider L_{net} instead of L_c for L planes.

parallel-to-grain $f_{t,0}$ for the head plane H and shear strength f_v for lateral planes L and bottom plane B). They differ on how the area of the involved failure planes is defined (specially regarding the effective thickness t_{ef}, and considering net or gross values for the length and width of the connection) and on how the load carrying capacities of these failure planes are combined to achieve the total capacity of the connection. A summary of the criteria followed by each model is given in Table 1.

The model from *Stahl et al.* (2004) considers the three previously described failure modes. The load-carrying capacity of each failure mode is defined as the sum of the capacities of the involved failure planes. The effective thickness t_{ef} is equal to the penetration length L_p of the fastener.

Originally, the prenormative version from 1995 of the *Eurocode 5* (2004) did not consider plug shear. In the current version, modes A and C were considered in its informative annex A. The load-carrying capacity is considered as either the maximum among that of the H plane or the sum of the capacities of the L and B planes. The effective thickness t_{ef} depends on the yielding mode of the fastener (none, one or two plastic hinges) derived from the EYM.

The models from *Kangas and Vesa* (1998) and *Johnsson and Parida* (2013) consider only Mode C and define the effective thickness t_{ef} as that corresponding to the yielding mode with two plastic hinges ($t_{ef} = \sqrt{\frac{M_y}{f_{h,0}d}}$). Both of them also described that the failure of L planes was reached prior to the failure of the other planes and, therefore, they discarded them: *Kangas and Vesa* (1998) defines the load-carrying capacity as the sum of the capacities of the H and B planes, while *Johnsson and Parida* (2013) considers only the maximum capacity between the H and B planes.

The model from *Zarnani and Quenneville* (2014), included in the draft of the New Zealand standard (*Quenneville and Zarnani* (2017)) is the most recent and exhaustive model. Originally developed for rivets, it considers the three failure modes.

The load carrying-capacities of the failure planes are combined by means of a stiffness model. In addition, brittle and mixed failure modes are distinguished, and therefore, two different effective thickness (elastic $t_{ef,el}$ and plastic $t_{ef,pl}$) are defined, and the calculation must be applied twice.

3 Proposal of a new model

3.1 General considerations

The proposed model intends to improve the prediction accuracy of the existing ones, which were previously benchmarked (*Cabrero and Yurrita* (2018) and *Yurrita, M. and Cabrero, J.M.* (2021)). Previous works allowed to identify the main parameters related to plug shear. The following model is based on that proposed by *Yurrita and Cabrero* (2020) for connections with large diameter dowel-type fasteners so that they are coherent between them.

The tests performed by *Yurrita, M. and Cabrero, J.M.* (2021) featured both brittle and mixed failure. Therefore, and as done by *Quenneville and Zarnani* (2017), the model considers both brittle and mixed behaviours by means of an elastic effective thickness $t_{ef,el}$ and a plastic effective thickness $t_{ef,pl}$.

As noticed by *Kangas and Vesa* (1998) and *Johnsson and Parida* (2013), *Yurrita, M. and Cabrero, J.M.* (2021) also detected that the *L* planes failed normally before than the *B* and *H* planes, which always collapsed simultaneously. However, since it is not possible to determine that the *L* planes will fail in advance in all the cases, the plug shear capacity F_{plug} is assumed as the maximum between the load-carrying capacity of the *L* planes and the addition of the capacities of the *B* and *H* planes:

$$F_{plug} = \max \begin{cases} k_v A_{v,L} f_v \\ k_t A_{t,H} f_{t,0} + k_v A_{v,B} f_v, \end{cases}$$
(1)

where $A_{v,L}$, $A_{v,B}$ and $A_{t,H}$ are the areas of the *L*, *B* and *H* planes, respectively; f_v and $f_{t,0}$ are the shear and tensile parallel-to-grain strengths of the timber product; k_v and k_t are the shear and tensile factors already considered by *Yurrita and Cabrero* (2020) and defined as $k_v = 0.4 + 1.5\sqrt{\frac{G}{E_0}}$, and $k_t = 0.9 + 1.5\sqrt{\frac{G}{E_0}}$.

3.2 Areas of the failure planes

As in the other existing models, the proposal requires the definition of the areas of the three involved failure planes:

- Head tensile plane, defined by the effective thickness t_{ef} of the timber member and the net width of the connection b_{net}. $A_{t,H} = t_{ef}b_{net}$.

- Lateral shear planes, defined by the effective thickness t_{ef} of the timber member and the gross length L_c of the connection: $A_{v,L} = 2L_ct_{ef}$.

- Bottom shear plane, defined by the net width b_{net} and the gross length L_c of the connection: $A_{v,B} = L_cb_{net}$.

Where $L_c = a_1(n_c - 1) + a_3$, $b_{net} = (a_2 - d)(n_r - 1)$, and t_{ef} is the effective thickness of the timber element, defined as the minimum between the elastic effective thickness $t_{ef,el}$ and the plastic effective thickness $t_{ef,pl}$.

3.3 Effective thickness

The elastic effective thickness $t_{ef,el}$ is obtained by applying the same formula proposed by *Yurrita and Cabrero* (2019) for the case of outer timber elements with thick steel plates (*Görlacher* (1995) and *Yurrita, M. and Cabrero, J.M.* (2021) noticed that there is no difference between thin and thick plates when combined with small diameter fasteners), which are based on a beam on elastic foundation model:

$$t_{ef,el} = \begin{cases} L_p & \text{if } \frac{L_p}{d} \leq 11.5 \\ \max\left(1.95 - \frac{L_p}{12d}; 0.65\right) L_p & \text{if } \frac{L_p}{d} > 11.5 \end{cases} \tag{2}$$

The plastic effective thickness $t_{ef,pl}$, is defined as the distance between the first plastic hinge and the shear plane, plus an extra distance that considers the contact between the timber element and the unyielded part of the fastener. This extra distance depends on whether the connection is assembled with or without predrilling, as the insertion of the fasteners without predrilling leads to additional local perpendicular-to-grain stresses (*Blaß and Uibel* (2009)). In the case of insertion without predrilling, (3) considers this distance as half of the penetration length L_p. In the case of predrilling, the extra distance is obtained by applying (2) (based on a beam on elastic foundation model), but now considering the distance $L_{p,pl}$ (6), in which the distance to the plastic hinge is excluded (4).

$$\text{No pre-drilling: } \quad t_{ef,pl} = \sqrt{\frac{My}{f_{h,0}d}} + \frac{L_p}{2} \tag{3}$$

Pre-drilling:
$$t_{ef,pl} = \sqrt{\frac{My}{f_{h,0}d}} + c_1 \qquad (4)$$

where c_1 is the elastic effective thickness of the fastener after discounting the plastic hinge distance, and it is defined as:

$$c_1 = \begin{cases} L_{p,pl} & \text{if } \frac{L_{p,pl}}{d} \leq 11.5 \\ \max\left(1.95 - \frac{L_{p,pl}}{12d}; 0.65\right) L_{p,pl} & \text{if } \frac{L_{p,pl}}{d} > 11.5 \end{cases} \qquad (5)$$

where $L_{p,pl}$ is defined as:

$$L_{p,pl} = L_p - \sqrt{\frac{My}{f_{h,0}d}}. \qquad (6)$$

3.4 Modes A and B

Modes A and B are indirectly considered by respecting some design limitations.

The limitation regarding Mode A (block shear, Fig. 3a) affects the timber thickness t, which should be enough to ensure that the block shear capacity defined by *Yurrita and Cabrero* (2020) is higher than the plug shear capacity, leading to:

$$t_{min} = \frac{F_{plug} - k_v A_{v,L} f_v}{k_t b_{net} f_{t,0}} \qquad (7)$$

in which the difference between the plug shear capacity and that of the L planes from block shear is divided by the capacity of the block shear H plane.

Mode B (Fig. 3b) is avoided by establishing a minimum distance to the lateral edge a_4, so that the load-carrying capacities of the extra areas of the expanded H and B planes are higher than the load-carrying capacity of the L planes:

$$a_{4,min} = \frac{L_c t_{ef} f_v}{L_c f_v + t_{ef} f_{t,0}} \qquad (8)$$

4 Validation of the new design model

An extensive database of experimental tests has been gathered in order to evaluate and compare the prediction accuracy of the five existing models and the new

proposal. In total, the database gathers 629 single tests distributed in 163 different configurations from 9 test campaigns. A summary of them is given in Table 2.

The validation has been performed in two stages. Firstly, the prediction ability of the studied brittle models is assessed. Therefore, only the tests in which brittle failure was reported were included in this phase. In the second stage, the discrimination ability between ductile and brittle failure modes for each model was evaluated. For this stage, all the tests, including those with a ductile failure, were considered.

4.1   Evaluation of the prediction accuracy of brittle load-carrying capacity

Due to the reduced number of replicates per configuration in most of the test campaigns, the mean level is considered to be more adequate than the characteristic one to establish a proper comparison of the prediction ability of the models with the tested results. The mean material properties have been obtained from the characteristic ones given in standards by means of the model from *Jockwer et al.* (2018), and are used to calculate the theoretical brittle load-carrying capacity of each test configuration according to the four analysed models.

The prediction ability of each model is plotted in Fig. 4, which compares the test results (F_T, abscissas axis) with the theoretical predictions (F_P, ordinates axis). A linear fitting passing through the origin of coordinates is depicted, and its corresponding slope m and coefficient of correlation R^2 are given. A dashed line provides the reference of the ideal slope 1:1.

The model from *Stahl et al.* (2004) (Fig. 4a) is the least accurate, and the only unconservative model (Fig. 4a), even with many results falling out of the shown area. On the other hand, the most conservative one is that from *Quenneville and Zarnani* (2017) (Fig. 4e), with the lowest R^2. The models from *Kangas and Vesa* (1998) (Fig. 4b) and *Johnsson* (2003) (Fig. 4c) get similar performance. Both are slightly conservative, with a lower scatter in comparison to the models above. Regarding the existing models, the closest slope to the ideal value of 1 is reached by the *Eurocode 5* (2004) (Fig. 4d). However, its low R^2 demonstrates a high scatter of the results with many unconservative predictions. The proposal improves the results of the existing models, obtaining both the best slope and coefficient of correlation.

The boxplot depicted in Fig. 5 complements the previous figures by evaluating the ratio between the predicted F_P and the experimental capacities F_T, whose ideal ratio $F_P/F_T = 1$ is given as a reference by a vertical dashed line. Similar results

Table 2. Summary of gathered database of experimental results.

Author	Number of		Joint scheme			Fastener Type			Timber product				Failure mode	
	Config.	Tests	ws	sws	www[a]	Rivet	Screw	Nail	LVL	Glulam	CLT[b]	Solid	Ductile	Brittle
Foschi and Longworth (1975)	10	30	10	-	-	10	-	-	-	10	-	-	2	8
Johnsson (2003)	22	91	22	-	-	-	-	22	-	22	-	-	1	21
Zarnani (2013)	32	102	-	32	-	32	-	-	6	26	-	-	4	28
Zarnani and Quenneville (2014)	8	24	-	8	-	8	-	-	8	-	-	-	2	6
Ottenhaus et al. (2016)	3	9	-	3	-	-	-	3	1	-	2	-	2	1
Choquette (2016)	21	63	-	21	-	12	-	9	-	21	-	-	14	7
Yurrita, M. and Cabrero, J.M. (2021)	34	102	34	-	-	-	17	17	14	20	-	-	-	34
Blaß and Schmid (2002)	9	136	-	-	9	-	-	9	-	-	-	9	9	-
Ballerini (2012)	24	72	-	-	24	-	16	8	-	-	-	24	24	-
Total	163	629	66	64	33	62	33	68	29	99	2	33	58	105
%	-	-	40.5%	39.3%	20.2%	38.0%	20.2%	41.7%	17.8%	60.7%	1.2%	20.2%	35.6%	64.4%

[a] All the www test achieved a ductile behaviour.
[b] Only one layer of the CLT was penetrated by the fasteners.
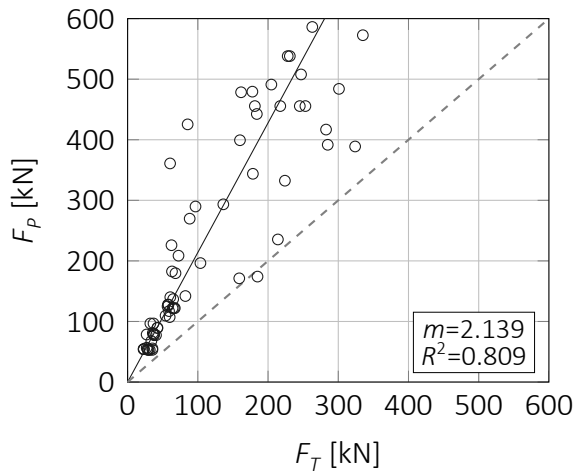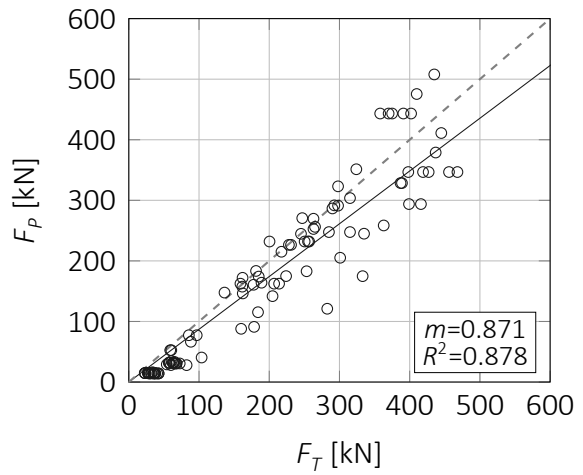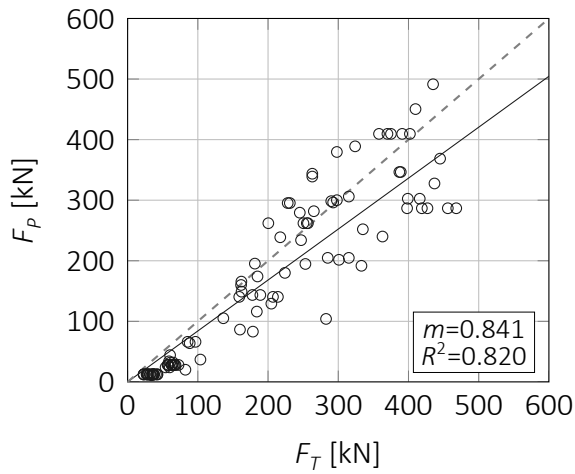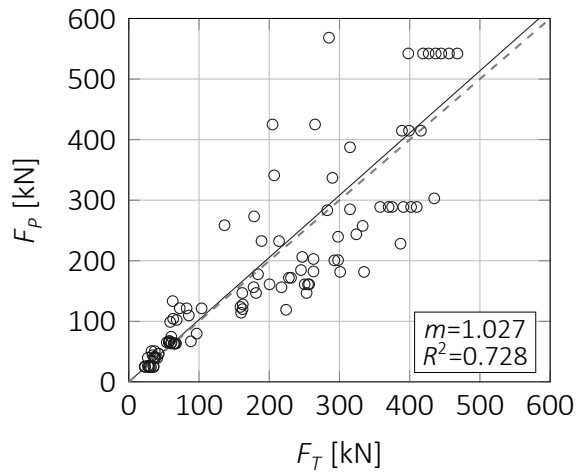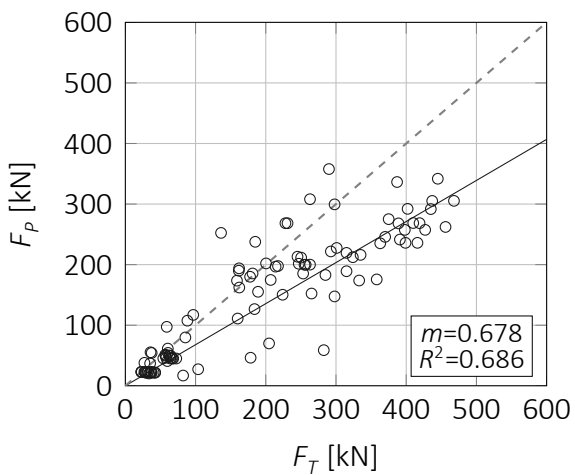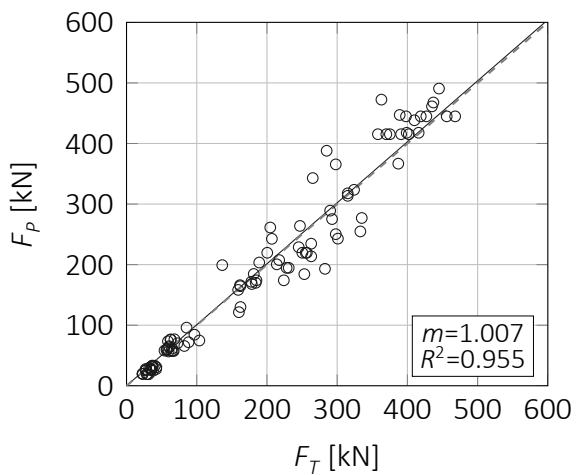
Figure 4. Comparison between the experimental load-carrying capacities F_T and the corresponding theoretical values F_P predicted by the existing models and the proposal.
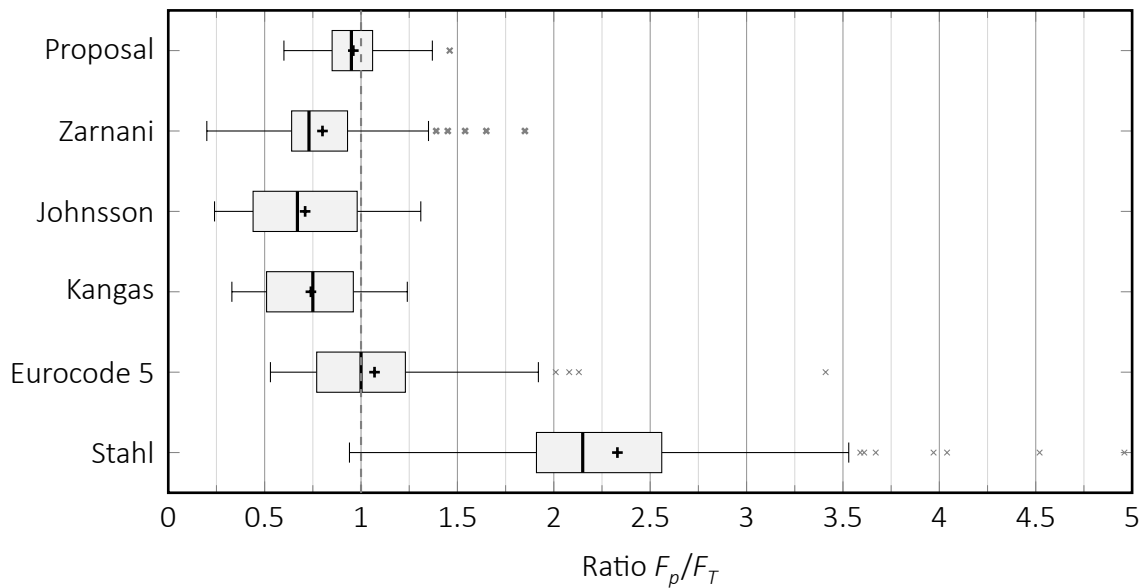
Figure 5. *Boxplot considering the accuracy of the ratio between the predicted failure load-carrying capacity F_P and the tested one F_T.*

Table 3. *Evaluation of the accuracy obtained by the six studied models. The metrics used are the already used and described by Cabrero and Yurrita (2018).*

Model	Q^2	MRE (SD)	m	c	CCC
Stahl et al. (2004)	-3.505	1.241 (0.995)	2.138	0.930	0.464
Eurocode 5 (2004)	0.604	0.306 (0.358)	1.027	0.923	0.838
Kangas and Vesa (1998)	0.840	0.206 (0.217)	0.870	0.956	0.918
Johnsson and Parida (2013)	0.768	0.253 (0.257)	0.840	0.940	0.880
Quenneville and Zarnani (2017)	0.568	0.319 (0.375)	0.676	0.885	0.727
Proposal	0.949	0.116 (0.121)	1.006	0.978	0.976

are obtained. The model of *Stahl et al.* (2004) appears again as the least accurate and most scattered approach. The boxes (representing the 25th to 75th percentile range of the results) from the three conservative models (*Quenneville and Zarnani* (2017), *Kangas and Vesa* (1998) *Johnsson* (2003)) fall below the ideal ratio $F_P/F_T =$ 1, although the case of *Quenneville and Zarnani* (2017) is the only of them with unconservative outliers. Although the median and average values (represented by a thick black line and a cross, respectively) from *Eurocode 5* (2004) are very good, its high scatter is clear, specially the unconservative cases. The proposal obtains the most balanced boxplot.

A statistical analysis considering different metrics is provided in Table 3: the coefficient of determination Q^2 (best values are those closest to 1), the mean root square error *MRE* and its corresponding standard deviation *SD* (lower values are the best ones), the fitting slope *m*, the correlation coefficient *c* (values closer to 1 are the best) and, finally, the concordance correlation coefficient *CCC* (values
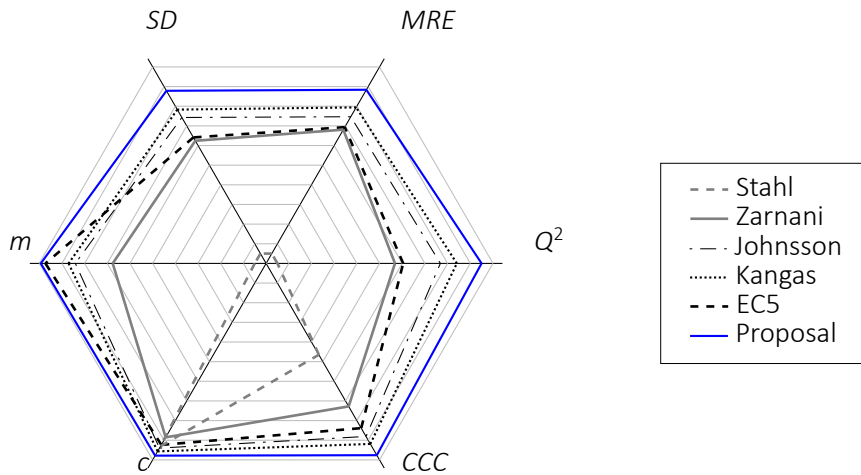
Figure 6. Radar chart of the metrics given in Table 3 for the six studied models, where the metric values are adapted so that the best values correspond to the outer zone of the chart.

close to 1 are the best ones, with a recommended threshold value of 0.85). A detailed description of these metrics can be consulted in *Cabrero and Yurrita* (2018). For a clearer overview, a radar chart (Fig. 6) plots a graphical comparison of the results. The metrics have been adapted so that the best values correspond to the outer zone of the chart.

The statistical analysis confirms the results from the previous analysis. *Stahl et al.* (2004) reaches consistently the worst metrics (with the exception of the correlation coefficient c). *Quenneville and Zarnani* (2017) and *Eurocode 5* (2004) rank in the fifth and fourth position, respectively, excepting the slope m from the *Eurocode 5* (2004), which was already ranked as the second best one. *Kangas and Vesa* (1998) reaches slightly better results than *Johnsson and Parida* (2013), ranking in the second and third position, respectively. They both surpass the recommended threshold value of $CCC = 0.85$. The proposal improves their results and consistently ranks in the the first position in all metrics.

4.2   Discrimination ability between ductile and brittle failure

Apart from the prediction ability of the load-carrying capacity, it is also required to verify the ability of the models to correctly discriminate between ductile and brittle failure modes. For such analysis both the ductile (by means of the EYM) and brittle models are used. The lower predicted value between the ductile and brittle models is considered as the predicted failure mode, which should match to the experimentally observed failure mode. Fig. 7 presents in dark gray the percentage of positive matches (true ductile and true brittle) and in bright gray the errors (false ductile and false brittle).
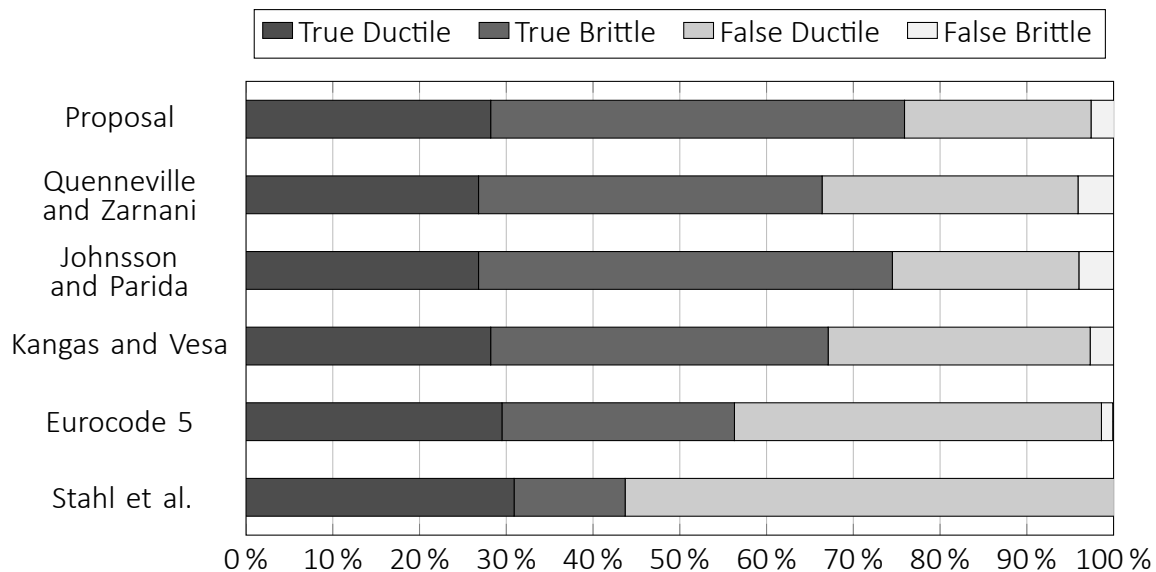
Figure 7. Discrimination ability. Comparison between Stahl et al. (2004), Eurocode 5 (2004), Kangas and Vesa (1998), Johnsson and Parida (2013), Quenneville and Zarnani (2017) and the proposal.

The best discrimination ability is obtained by the proposal (75.8% of correct predictions), closely followed by *Johnsson and Parida* (2013) (74.5%). The models from *Kangas and Vesa* (1998) and *Quenneville and Zarnani* (2017) rank in third and fourth position, with 67.1% and 66.4% of positive matches, respectively. Despite the good average values predicted by the *Eurocode 5* (2004), it only reaches 56.4% of positive matches. Finally, the model from *Stahl et al.* (2004), with only 43.6% of correct predictions obtains the poorest discrimination ability.

5 Conclusions

A safe design of timber connections requires a correct prediction of the brittle failure modes. This work presents a new design model to obtain the brittle load-carrying capacity of connections with small dowel-type diameter fasteners (those partially penetrating the timber member) loaded parallel to grain. The new model is based on the model proposed by *Yurrita and Cabrero* (2020) for the case of large diameter fasteners, and it improves the results of the existing models by a different consideration of several parameters.

An extensive database is used to evaluate and compare the proposal to the existing models. The validation process demonstrates a clear improvement regarding both the accuracy and the discrimination ability between ductile and brittle failure modes.

6   Acknowledgements

7   References

Ballerini, M. (2012). "Experimental investigation on parallel-to-grain wood-to-wood joints with self-tapping screws." In: *Proceedings of the World Conference on Timber Engineering (WCTE)*. Auckland New Zealand, pp. 173–182.

Blaß, H. J. and M. Schmid (2002). *Spaltgefahr von Nadelhölzern*. Tech. rep. Karlsruhe, Germany: Versuchsanstalt für Stahl, Holz und Steine, Karlsruhe University.

Blaß, H. J. and T. Uibel (2009). *Spaltversagen von Holz in Verbindungen - Ein Rechenmodell für die Rissbildung beim Eindrehen von Holzschrauben*. German. Tech. rep. doi:10.5445/KSP/1000009896. Karlsruher Institut für Technologie (KIT). 180 pp.

Cabrero, J. M. and M. Yurrita (2018). "Performance assessment of existing models to predict brittle failure modes of steel-to-timber connections loaded parallel-to-grain with dowel-type fasteners." In: *Engineering Structures* 171. doi:10.1016/j.engstruct. 2018.03.037, 895-910 (INTER version 51–7–12).

Choquette, J. (2016). "Évaluation d 'une nouvelle méthode de calcul des assemblages de bois à l 'aide de connecteurs de petits diamètres." MA thesis. Université Laval, Québec, p. 80.

CSA Standard O86-09 (2009). *Engineering design in wood*. Canadian Standards Association.

Eurocode 5 (2004). *CEN:EN 1995-1-1:2004 - Eurocode 5: Design of timber structures - Part 1-1: General - Common rules and rules for buildings*. Comité Européen de Normalisation (CTN).

Foschi, R. O. and J. Longworth (1975). "Analysis and Design of Griplam Nailed Connections." In: *Journal of the Structural Division* 101. doi:10.1061/JSDEAG.0004232, pp. 2537–2555.

Görlacher, R. (1995). "Load-carrying capacity of steel-to-timber joints with annular ringed shank nails." In: *CIB-W18 Timber Structures, Paper 28–7–3*. Copenhagen, Denmark.

Jockwer, R., G. Fink, and J. Köhler (2018). "Assessment of the failure behaviour and reliability of timber connections with multiple dowel-type fasteners." In: *Engineering Structures* 172. doi:10.1016/j.engstruct.2018.05.081, pp. 76–84.

Johnsson, H. (2003). "Plug shear failure in nailed timber connections: experimental studies." In: *CIB-W18 Timber Structures, Paper 36–7–2*. Colorado, USA.

Johnsson, H. and G. Parida (2013). "Prediction model for the load-carrying capacity of nailed timber joints subjected to plug shear." In: *Materials and Structures* 46.12. doi:10.1617/s11527-013-0030-8, pp. 1973–1985. ISSN: 1359-5997.

Kangas, J. and J. Vesa (1998). "Design on timber capacity in nailed steel-to-timber joints." In: *CIB-W18 Timber Structures, Paper 31–7–4*. Savonlinna, Finland.

Ottenhaus, L.-M., M. Li, T. Smith, and P. Quenneville (2016). "Ductility od dowelled and nailed CLT and LVL connections under monotonic and cyclic loading." In: *Australian Earthquake Engineering Society*. doi:10.1061/(ASCE)ST.1943-541X.0002074. Melbourne, Australia. ISBN: 000000171298.

Quenneville, P. and P. Zarnani (2017). *Proposal for the Connection Chapter of the New Zealand Design of Timber Structures*. Unpublished.

Stahl, D. C., R. W. Wolfe, and M. Begel (2004). "Simplified analysis of timber rivet connections." In: *Journal of Structural Engineering* 130.August. doi:10.1061/(ASCE)0733-9445(2004)130:8(1272), pp. 1272–1279. ISSN: 0733-9445.

Yurrita, M. and J. M. Cabrero (2020). "New design model for brittle failure in the parallel-to-grain direction of timber connections with large diameter fasteners." In: *Engineering Structures* 217. doi:10.1016/j.conbuildmat.2019.04.100, (INTER version 52–7–7).

Yurrita, M. and J. M. Cabrero (2019). "Effective thickness of dowel-type fasteners at the elastic range for steel-to-timber connections under brittle failure mode in the parallel-to-grain direction: a new method based on a beam on elastic foundation." In: *Engineering Structures* 209. doi:10.1016/j.engstruct.2019.109959, (INTER version 52-7–5).

Yurrita, M. and Cabrero, J.M. (2021). "Experimental analysis of plug shear failure in timber connections with small diameter fasteners loaded parallel-to-grain." In: *Engineering Structures* 238. doi:10.1016/j.engstruct.2020.111766, 111766 (INTER version 53-7–6).

Zarnani, P. and P. Quenneville (2014a). "Wood Block Tear-Out Resistance and Failure Modes of Timber Rivet Connections: A Stiffness-Based Approach." In: *Journal of Structural Engineering* 140.2. doi:10.1061/(ASCE)ST.1943-541X.0000840, p. 04013055. ISSN: 0733-9445.

Zarnani, P. (2013). "Load-Carrying Capacity and Failure Mode Analysis of Timber Rivet Connections." PhD thesis. University of Auckland, p. 225.

Zarnani, P. and P. Quenneville (2014b). "Group Tear-Out in Small-Dowel-Type Timber Connections: Brittle and Mixed Failure Modes of Multinail Joints." In: *Journal of Structural Engineering* 141.2. doi:10.1061/(asce)st.1943-541x.0001053, p. 4014110. ISSN: 0733-9445.

DISCUSSION

The papers was presented by M Yurrita

H Blass said that over 600 tests from others were used for your model. Other models typically only used their own test data for model calibration. Was this model checked with its own data using a calibration set and a verification set? M Yurrita responded that the modelling process did not involve calibration.

C Sigrist questioned why thickness of steel plate was not considered. M Yurrita said that in case of small diameter fasteners there was no difference between thick and thin steel plates (~3% difference only). C Sigrist pondered whether one would get plug shear failure mode in timber to timber connections.

H Hochreiner questioned what would happen for unsymmetrically loaded connections. M Yurrita said that this could be studied in future. H Hochreiner said one would also have moments in such cases.

C Sandhaas asked about background of K_T and K_v. M Yurrita said these are similar factors in Eurocode 5 and they are calibration factors from former models.

Connection of timber foundation piles to concrete extension piles

Geert Ravenshorst, Delft University of Technology, Netherlands

Jan van Dalen, Delft University of Technology, Netherlands

Michele Mirra, Delft University of Technology

René Steiger, Swiss Federal Laboratories for Materials and Science & Technology, Switzerland

Jan-Willem van de Kuilen, Delft University of Technology, Netherlands, Technical University of Munich, Germany

1   Introduction

In many regions of the world, timber piles have been used for centuries for the foundation of buildings and bridges. For historical buildings, it is common that masonry foundation walls are placed upon timber piles and cross beams that remain below the water level. With the introduction of concrete foundation beams in the 20th century, the distance between the head of the timber pile and the concrete foundation beam was bridged by concrete extension piles. Originally made in situ, currently only prefabricated extension piles are used. In the Netherlands foundations of houses were widely realized with timber piles until the 1980s (Van de Kuilen, 1995). Currently, timber piles are mostly used for the foundation of industrial buildings like greenhouses. However, the lacking of relevant mechanical properties of timber piles and connections of parts of piles and of piles with pile extensions together with respective design rules, hinder the wider application of timber foundation piles. For the verification, the strength properties of timber piles and the connections have to be specified in standards or determined by tests, but still test data is available only to a very limited extent.

In the future revised version of Eurocode 5, rules for the design of timber foundation piles will be included. The new Clause to prEN 1995-1-1 drafted by the Project Team SC5.T3 (Project team SC5.T3 ,2020) and by CEN/TC 250/SC 5/WG 3 (Working Group CEN/TC 250/SC 5/WG 3, 2021) covers general rules for timber piles, materials (wood

species, grading rules), properties (compressive strength and MOE parallel to the grain in the fibre saturated state, shrinkage, shaft friction), durability, ultimate limit states (axial compression, stability) and execution.

In order to guarantee for sufficient durability throughout the design service life of the foundation, the tops of softwood piles should be permanently located at least 500 mm below the lowest ground water table to be expected at the location of the foundation. If this cannot be met, the timber pile is driven to a level reliably beyond the lowest ground water table and extended by a pile extension made of material exhibiting sufficient durability when exposed to varying ground water levels (Figure 1).

Extension piles are frequently made out of a concrete, either totally out of concrete or with a steel tube on the concrete. In tests in the Netherlands the strength and failure mechanisms of the connection of such a concrete extension pile was investigated, together with the influence of the stiffness of the connection on the overall behaviour of the pile in the soil. This paper presents elements of the draft section for the new EC 5 on timber foundation piles related to this connection and test results on a connection type. The failure mechanisms are analysed and the effect of the found strength and stiffness on the behaviour of the pile in the soil. Specific calculation rules are necessary because with the available rules according to the current version of EN 1995-1-1 [Eurocode 5, 2004)], engineers in practice have concluded that the timber would not fulfil the requirements for strength at the location of the connection.

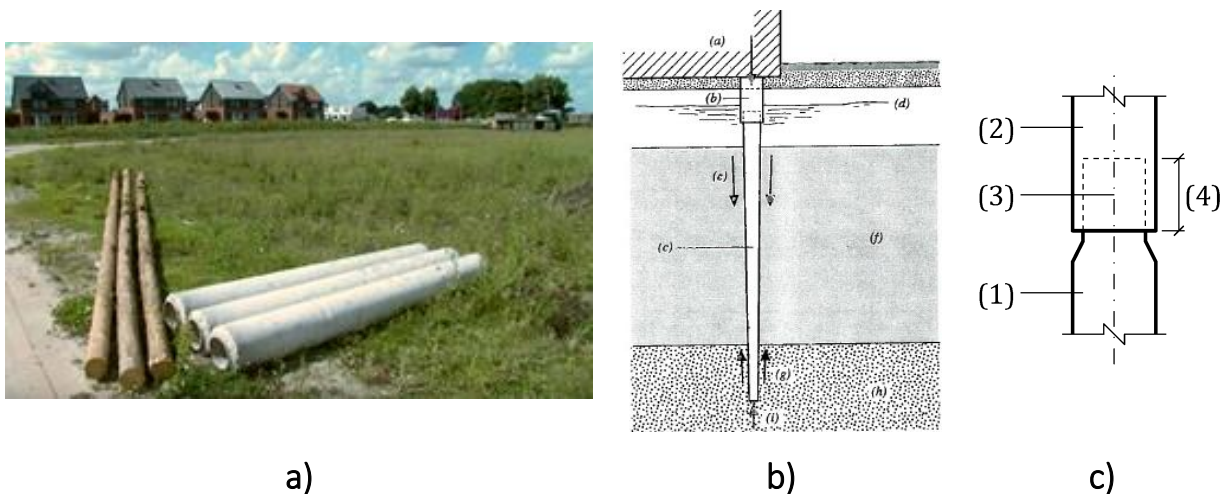a)   b)   c)

*Figure 1 **a)**: Timber piles and concrete extension piles. **b)**: Timber pile with concrete extension pile (b) on top of the timber pile (c). (d) is the ground water level. **c)**: Detail view of the top of the timber pile (1) and the concrete extension pile (2) with a socket (3) of a certain depth (4).*

# 2 New design rules for timber piles in future EC 5

2.1 Introduction

On request by several CEN member states a set of new design rules for timber foundation piles were drafted for inclusion in the future version of EC 5. The scope is on piles, used as foundation for new buildings, subjected to axial compression loading. The objective is to verify the timber pile only; the geotechnical loadbearing capacity has to be determined according to prEN 1997 (Project teams SC7.T4 and SC7.T5, 2019). This standard states that methods used to determine the geotechnical bearing capacity of the piles have to be based on results of in situ load tests or on analytical formulas, of which the validity is priorly demonstrated, using the results of similar load tests. Several National Application Documents supply such analytical formulas in combination with parameters to be used.

One of the main differences with other use of timber in structures is that timber piles under buildings are fully saturated. In the new design rules, this is addressed by applying directly the saturated values for the compressive strength and the MOE determined from test in the verification rules.

2.2 Durability aspects

To fulfil the structural requirements for the entire design service life, special care has to be taken in the design of foundations with timber piles. When piles are used in waterworks or temporary structures where parts are not permanently fully submerged in ground water, durable wood species should be used. However, when piles are used fully submerged under the ground water level during the entire service life, softwood species with a low natural durability like Norway spruce (*picea abies*) can be used without chemical treatment. This is because in that case there is not enough oxygen to activate fungal decay (bacterial decay can also take place under the water level, but this is a much slower process). However, currently in the Netherlands, pine (*pinus sylvestris*) piles are not used for new foundations, because of bad experiences with fungal decay of the sapwood (which has a larger amount for pine than spruce) in situations where the ground water level was temporarily lowered and the pile heads occasionally came above that level.

To guarantee for sufficient durability, it is advised to permanently keep the pile head 500 mm below the lowest ground water level. In that case, a concrete extension pile has to be applied to bridge the gap between pile heads and foundation beams. Types of connections between timber pile and extension pile that are currently used are shown in Figure 2.
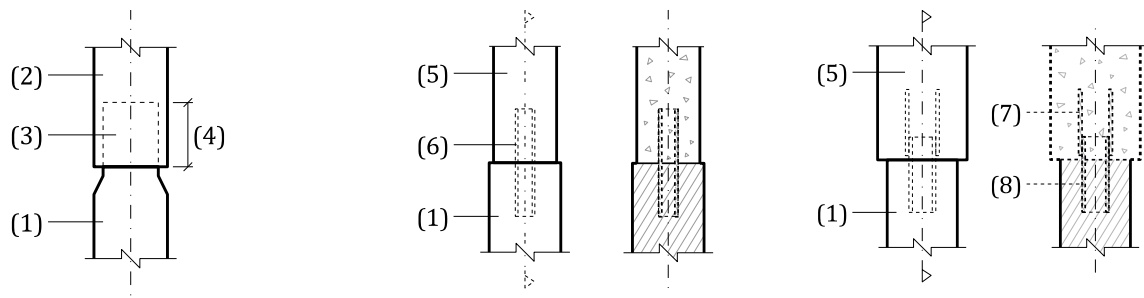
a) Socket-type joint

b) Pen-type joint with steel pen (tube)

c) Pen-type joint with steel cylinder / rebars

Figure 2. Different connection types for concrete extension piles with timber piles. Taken from (Project team SC5.T3 ,2020) and (Working Group CEN/TC 250/SC 5/WG 3, 2021).

The principle of type a) in Figure 2 is that a socket at the end of the concrete extension pile is driven over the pile head, clamping the pile head. A steel ring is placed at the bottom of the socket, allowing the pile head to be oversized and enabling removing of split parts.

For types b) and c) a steel pen (tube) is partly integrated in the concrete extension pile and the part outside the extension pile is driven into the pile head. In this case the diameter of the pen is smaller, so the clamping is provided by a smaller part of the pile.

The extension piles as well as their connections with the timber piles have to be able to resist the actions from the structure. The connection strength and stiffness will have an influence on the stability of the pile. This paper will focus on the resistance against tangential (usually horizontal) loads. prEN 1997 describes that the resistance against horizontal loads has to be determined by taking the interaction between pile and surrounding soil into account, but gives no procedure on how to determine this interaction. It is stated that properties like the strength and stiffness of the piles should be based on the material standards. In this paper, a procedure for timber piles with an extension pile is proposed. This paper will focus on the influence of the connections' strength and stiffness on horizontal loads due to asymmetric soil addition, applied to counter effect the lowering of the ground level caused by settlements.

3 Connection between timber piles and concrete extension piles

3.1 Background of the investigated connection type

The investigated connection between timber the pile and the concrete extension piles is of so called socket type which is frequently used in the Netherlands. However, only one calculation model where the maximum depends on the axial loads, which gives a very low capacity was available (Rensman, 1997).

The motivation for this research was the outcome from practice in the Netherlands where the connection between the timber pile and the concrete extension pile was verified for cases where extra horizontal load on the piles was acting due to asymmetric support by the soil because of settlements and soil additions. In that case, the engineers concluded that the pile would fail at the connection due to a combination of compression parallel to the grain and bending stresses. Thereby the engineers had started from the following assumptions:

- The verification rule for bending and compression according to clause 6.19 of EN 1995-1-1was used.
- A linear elastic and completely stiff behaviour of the connection was assumed.
- For the bending properties, a strength class C18 for the pile was assumed, because for this strength class the characteristic compressive strength was closest to that of strength class C18. (The characteristic compressive strength for softwood foundation piles according to the Dutch NAD is 19.8 N/mm^2, related to a moisture content of 12%)

Based on these assumptions the failure mechanism as shown in the bottom graph of Figure 3 b) develops, leading to brittle failure in the pile just below the connection.

The following considerations can be made regarding this outcome:

- It is questionable if the verification rules for a combination of bending and compression according the current version of EC 5 are applicable. Experimental research on combined compression and bending always involves stability issues, and does not focus on very local stress interactions (Buchanan, A.H., 1984). Anyhow, the verification is mainly governed by the bending part, and therefore the assumption for the bending strength plays an important role.
- When the bending moment capacity of the pile is higher than the flexural capacity due to compression perpendicular to the grain as a result of the force couple transferring the moment from the timber pile to the concrete extension pile, a plastic failure can occur (Figure 3b) top graph). Previous research on small diameter roundwood indicate different relationships for the bending

> strength and compression strength than for sawn timber (Ranta-Maunus, A. (2000).
>
> - The stiffness of the connection can influence the stress distribution in the pile.
> - In Germany there is an approval document for clamping glulam timber columns in a concrete foundation, where the clamping is achieved by casting mortar(DIBt, 2016). However, this approval only covers the use of timber in service class 1 and 2, and it does not give a calculation method to derive the stiffness of the connection. The correction factors to be used for compression perpendicular to the grain and for shear give an indication that higher values for these properties can be expected for confined timber. For compression perpendicular to the grain a value for $k_{c,90}$ of 2.0 is given and a factor $k_{v,c} = 2.4$ for shear in combination with compression perpendicular to the grain is introduced, where the shear strength may be multiplied with. It can be expected that these strength values also increase for the piles investigated in this study in the fully saturated state.

To get more insight in the consideration given above these aspects, a testing program was performed on a socket type extension pile-timber pile connection (type a) according to Figure 2). With the outcomes of the experiments, the stress distribution in the pile regarding its interaction with the soil under horizontal loads is investigated.

Parallel to this investigation, in situ inspection of 7 piles under the foundation under 3 different houses built in the 1980s was carried out (Lobbe, 2019). There the dimensions of the concrete extension pile were confirmed to be equal to those declared by producers. The inspection showed that the pile heads were fully clamped in the concrete extension pile. The piles showed no significant decay.

The outer diameter of the concrete extension pile was 280 mm and the socket had an inner diameter of 180 mm and a depth of 230 mm (distance 4 in Figure 2a).

For the test series, 12 new fresh Norway spruce piles were ordered with a length of 2 meters and a head diameter of 200 mm. The piles were stored in a mist chamber (at 100 % relative humidity of surrounding air) to ensure that the high moisture content of the piles was maintained until they were tested.

3.2   Test set-up

It was decided to use a steel tube of 193.7 mm x 8 mm to simulate the socket of the concrete extension pile. The steel tube has approximately the same stiffness as the concrete socket and it could be reused for all 12 tests. To represent a socket of 230 mm long, a thick steel plate was welded, to transfer the axial load on the pile (see Figure 3a, top figure). The adopted mechanical scheme of the test set-up, enabling to apply a combination of a normal force and a bending moment on the connection, is shown in Figure 3.

In practice, at the end of the socket (which is smaller in diameter than the pile head), a steel ring integrated, to drive the socket over the pile head to provide complete

clamping. In the laboratory, the diameter of the pile head was reduced manually to fit into the socket. For the evaluation of the stresses, the location where the pile head enters the socket is looked at (parameter M_A, in the Figure 3a). There, the diameter was 178 mm.
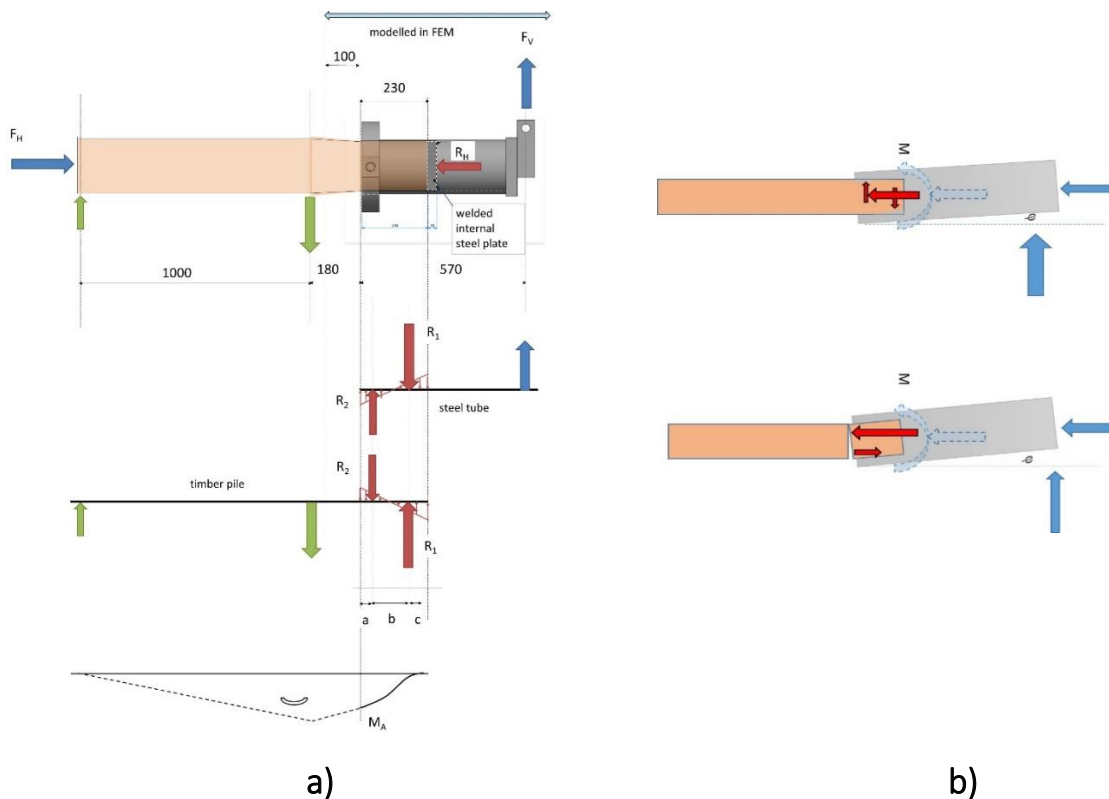

a)   b)

Figure 3 a) Adopted mechanical scheme, with forces on the total system and the steel tube and the timber pile head, assuming the failure mechanism according to the top of figure b). In the bottom of a) a graph with the location of paramter M_A. b) Possible failure mechanisms. Above ductile failure behaviour due to compression perpencidular to the grain, below brittle failure behaviour due to combination of compression and bending parallel to the grain.

After a preliminary test on one specimen, the following loading protocol was adopted:

- At the start of the test an axial force F_H = 50 kN was applied.
- The actuator that measured the vertical load F_V was moved up vertically with a speed of 5 mm/min until a displacement of 50 mm was reached.
- Then the axial force F_H = 50 kN was increased to 170 kN. This force was kept constant for 1 hour, and the change in force F_V due to relaxation was measured.
- After 1 hour, the vertical actuator was moved up with a speed of 5 mm/min until a displacement of 90 mm was reached.
- The vertical displacement of the steel tube was measured at 2 positions spaced 420 mm apart. These measurements were used to determine the rotation angle of the connection, where no bending deformation of the steel tube was assumed.

3.3　　Results

Table 1 shows the material properties of the 12 piles at the time of testing.

Table 1. Material properties of the 12 tested piles.

	Density [kg/m³]	MOE_{dyn}* [N/mm²]	m.c. [%]
Mean value	850	10'100	83
Coefficient of variation (%)	7	14	27

*MOE_{dyn} was calculated with $MOE_{dyn} = 4f^2l^2\rho$, where the first natural frequency f (Hz) was measured with the Brookhuis MTG 960 handheld

Figure 4 shows the measured force F_V (see Figure 3) in the vertical actuator for a typical test result against time (a) and vertical displacement of F_V.

The figure shows an initial linear branch, after which plasticisation occurs. After the axial force is increased to 170 kN and kept constant for an hour, the vertical force relaxes by approximately 1/3. When after an hour the displacement of the vertical actuator is increased again, the actuator force returns to the same level as in the first stage and then full plastic behaviour is visible. After 90 mm vertical displacement the test was stopped.

The mean values for the bending stiffness and the bending moment in the elastic phase are C_{el} = 275 kNm/rad and $M_{A,el}$ = 7.7 kNm, respectively. The mean value for the plastic moment is $M_{A,pl}$ = 12.3 kNm. At that point, for all specimen, a rotation angle of 0.1 rad was reached. The behaviour of the connection can therefore be described with a tri-linear approximation (see Figure 5). The elastic-plastic phase is caused by the softening of the wood subjected to compression perpendicular to the grain.

a)　　　　　　　　　　　　　　　　　　b)
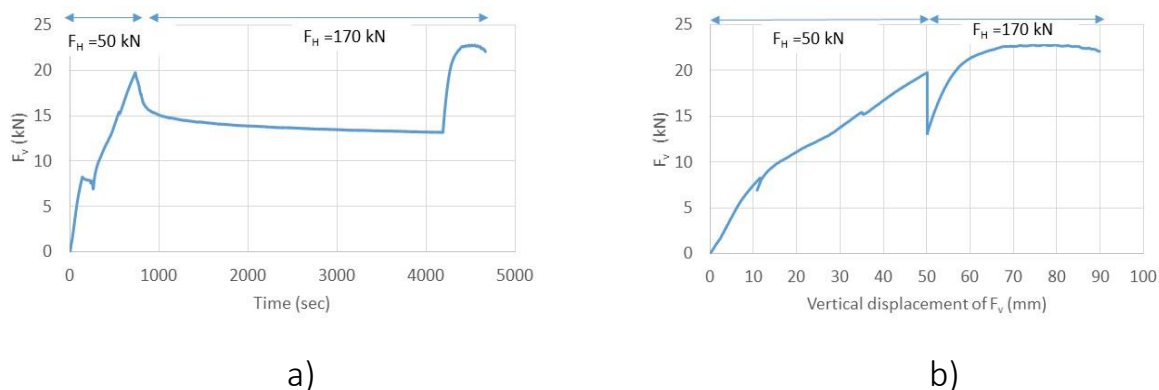
Figure 4 a). Vertical force F_V (see Figure 3a) against time. b) Vertical force F_V (see Figure 3a) against the vertical displacement of F_V (right figure). In both a) and b) the applied axial force in that stage of the test are shown in the top of the figures.
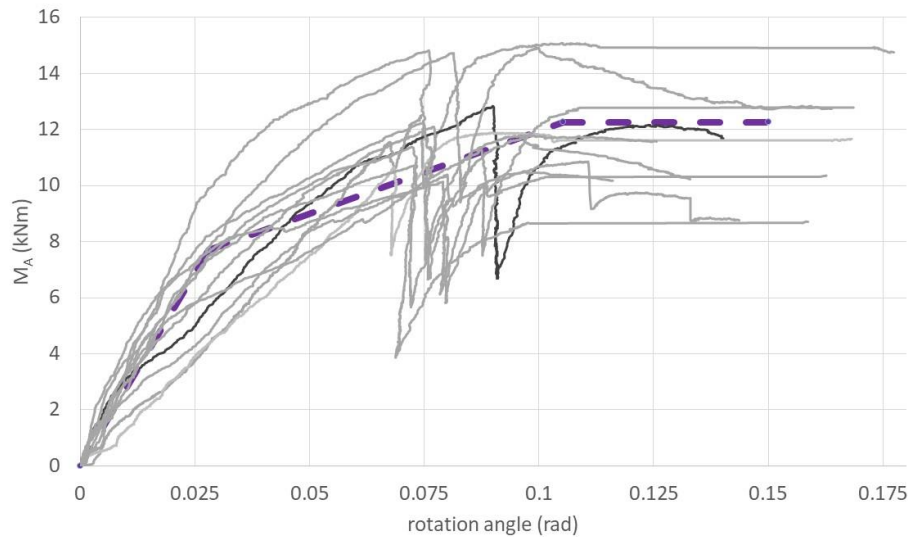
Figure 5. Moment M_A against rotation for all 12 test. The dotted line represents the mean tri-linear representation based on the tests.

The compressive stresses parallel to the grain were 2.7 N/mm^2 in the first phase and 6.9 N/mm^2 in the second phase. The maximum measured bending stresses reached a mean value of 21.9 N/mm^2 (cov = 14.1%). The combination of normal and bending stresses did not cause any (brittle) failure.

It can be concluded that the bending strength of the timber at the connection will not be governing since failure due to compression perpendicular to the grain occurs first. Then plastic deformations can develop.

3.4   Analysis

The compressive strength perpendicular to the grain is a property that is very dependent on the configuration of the material in the structure and the moisture content. Nobel(2014) showed that for the standardised test specimen according to EN 408 the mean compressive strength is reduced by more than 50 % with the m.c. increasing from 12% to 45%, but that for more stocky specimens, this reduction is much less. In the investigated situation the timber pile head is confined by a circular tube. An FEM model was used to investigate the occurring stresses in the elastic phase. Nobel (2014) showed, that the modulus of elasticity (MOE) for compression perpendicular to the grain is much lower at high levels of moisture content (m.c.) for every configuration and for Norway spruce timber could vary between 50 N/mm^2 and 150 N/mm^2. In the FEM model a value of 70 N/mm^2 was used.

The FEM model was programmed in DIANA FEA 10.4 (Ferreira, D and Manie, J, 2020). Timber was modelled with 8-noded linear elastic orthotropic solid elements with a mesh size of 5 mm. For the MOE parallel to the grain a value of 9600 N/mm^2 was adopted, and for the MOE perpendicular to the grain 70 N/mm^2. For the steel tube 8-noded linear elastic isotropic solid elements were used, with a mesh size of 5 mm.

The contact area between steel tube and timber pile in the socket, was modelled with connection elements that could only transfer compressive forces and no tension. Linear elastic behaviour was assumed.

Only a vertical force causing bending moments was applied in the model. The axial compression was not taken into account, because in the experiments no influence of the axial load on the failure mechanism for bending was observed. See Figure 4b, where the loading path does not seem to be influenced by the axial load.

The pile was modelled until 100 mm outside the socket, where it was clamped. The deformations are shown in Figure 6. The model confirms that rotation is governed by the elastic properties compression perpendicular to the grain of the timber.

a)   b)
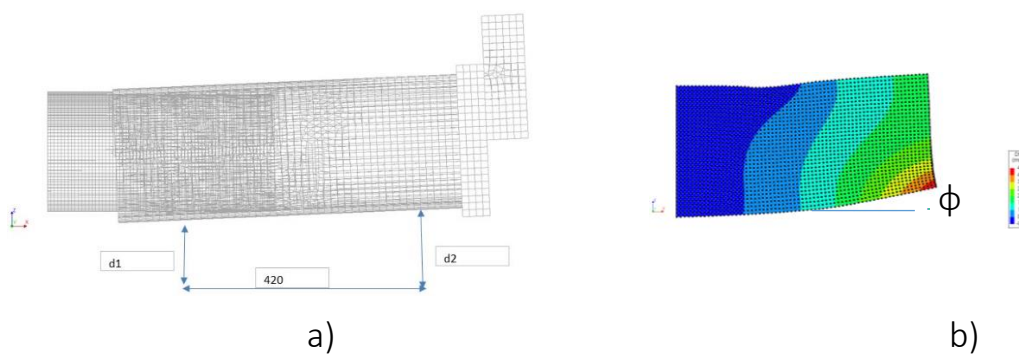
Figure 6. Deformation of the model for a load F_V = 13.7 kN, corresponding to M_A=7.7 kNm. a) Deformation of the timber pile head and the steel tube. b) Deformation of the pile head only.

Figure 7 shows a triangular distribution of compressive stresses perpendicular to the grain at the contact areas at the top and bottom of the timber pile head in the socket. The maximum compressive stress found at the bottom edge was $\sigma_{c,90,max,1}$ = 2.8 N/mm² and at the top edge $\sigma_{c,90,max,2}$ = 2.3 N/mm².

The length of the contact areas can be taken from Figure 7 (for the bottom edge l_1 = 125 mm and for the top edge l_2 = 105 mm). Based on that the forces R_1 and R_2 according to Figure 4 can be calculated with Formula (1):
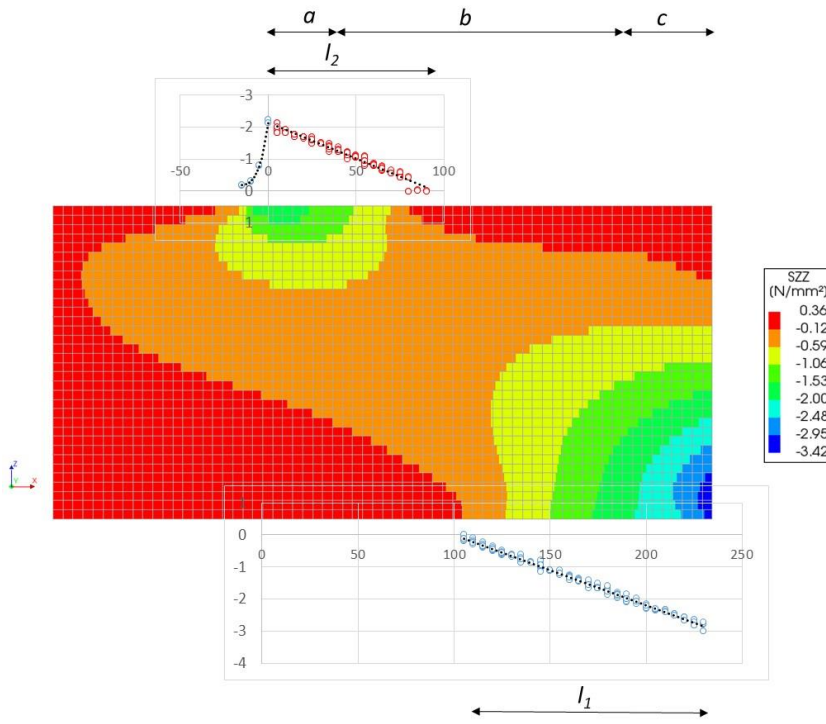
Figure 7. Stress distribution perpendicular to the grain from the FEM model. Top and bottom edge show triangular stress distrubutions for compression perpendicular to the grain where the load couple is intorduced. Dimension a,b and c relate to those defined in Figure 3. l_1 and l_2 are the contact lengths where the forces R_1 and R_2 are introduced (see Figure 3).

$$R_i = 0.5\,\sigma_{c,90,max,i}\,l_i\,D\,d \tag{1}$$

In Formula (1) D is the pile head diameter in mm and d accounts for the irregular stress distribution because of the circular contact area. A value of 1.5 gives values for R_1 and R_2 that are consistent and predicts a moment M_A of 7.7 kNm calculated with Formula (2):

$$M_{A,el} = R_{1,el}(a + b) - R_{2,el}a \tag{2}$$

The calculated moment M_A of 7.7 kNm is similar to the mean elastic moment found in the experiments.

The shear stress found in the FEM model was τ_v = 2.4 N/mm², where a value of 2.9 N/mm² can be calculated according to elastic theory with the value of $R_{1,el}$ determined with equation (1).

When for calculation of the plastic moment the same contact lengths are assumed but instead of a triangular stress distribution assumed a constant value of $f_{c,90,max}$ =2.8 N/mm² both at the top and bottom edge is assumed, the plastic moment can be calculated with Formula (3):

$$M_{A,pl} = R_{1,pl}\left(a + b + c - \frac{l_1}{2}\right) - R_{2,pl}\frac{l_2}{2} \tag{3}$$

With Formula (3) a plastic moment of 11.5 kNm is predicted, which slightly underestimates the mean value of 12.3 kNm found in the experiments.

The shear stress found according to elastic theory with the calculated value of $R_{1,pl}$ is τ_v = 5.8 N/mm². No shear failure occurred.

The rotation of the connection can be determined from the deformation at the bottom egde. The contribution of the steel tube in the deformation can be neglected. The rotation determined by means of the FEM model for $M_{A,el}$ =7.7 kNm was 0.025 rad , close to the mean value of 0.028 rad found in the experiments.
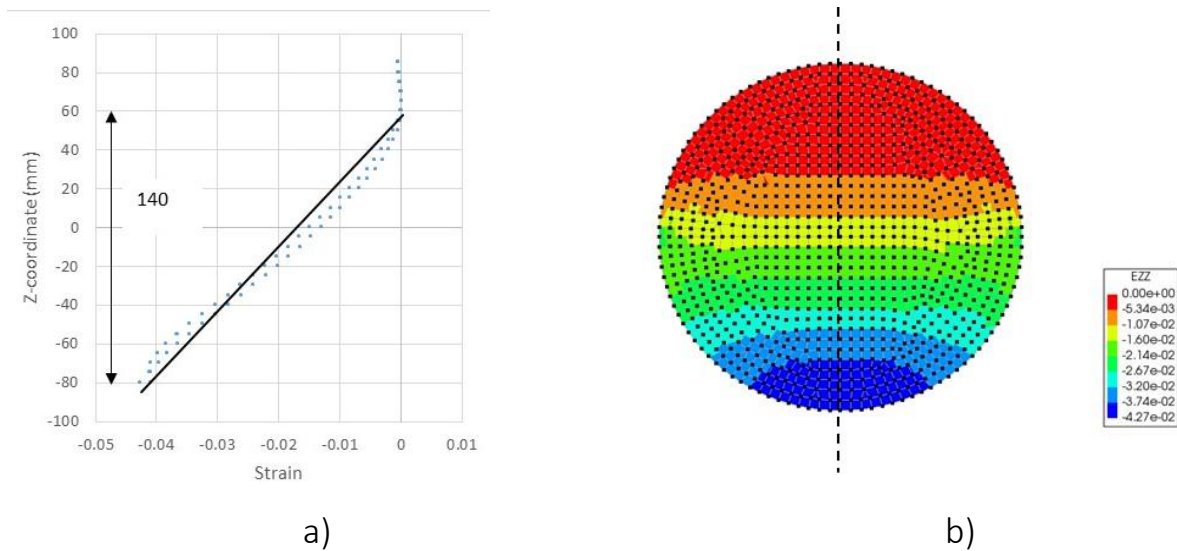

a)   b)

Figure 8. a) Strain distribution perpendicular to the grain over the center line of the cross section of the pile at $\sigma_{c,90,max,1}$.   b)Strain distribution plot over the cross section with the center line indicated

Figure 8 shows the strains over the cross section at the position of $\sigma_{c,90,max,1}$ at the bottom edge. This shows a linear strain decrease from the bottom outside to zero at 140 mm inwards. Over this length, the average strain can be used. The rotation due to the deformation of the pile at the bottom side due to force R_1 can then be calculated with Formula (4):

$$\theta_{el} = 0.5 \; \frac{\sigma_{c,90,max,1}}{MOE_{90}} \; \frac{140}{l_1} \tag{4}$$

This gives a value of 0.022, slightly less than the value of 0.028 found in the experiments.

The results of the FEM analysis was confirmed by hand calculations and underpin that the strength and stiffness of the connection is governed by the strength and stiffness of the timber pile head subjected to compression perpendicular to the grain stresses.

3.5 Material properties for soil modelling

EN 1995-1-1 does not give reduction factors for the MOE for high moisture content for short-term loads. The creep factors given in EN 1995-1-1 only relate to the load duration. For service class 3 this a value of k_{def} = 2 is given. However, the influence of high moisture content and load duration should be accounted for separately. The set of new clauses for the design of timber piles advises to use a value of 80% for the MOE parallel to the grain for saturated piles, compared to the values for service

class 1, if no information about the saturated value is available. Form the study presented in this paper, the saturated value is directly available. A value of $k_{def} = 1$ is proposed for both creep and relaxation. The high value of 2 in the current version of EC 5 (EN 1995-1-1/A1/A2 (2014)) applies to situations with repetitive wetting and drying, which this is not the case for timber piles that are constantly submerged.

In Table 2 the assumptions regarding input to the soil interaction model are listed. Because the main objective is to study which element is governing in case of horizontal loads, mean values are used for both strength and stiffness.

Table 2. Input values for the soil-pile interaction model.

Property	Value
$MOE_{0,mean,sat}$ (N/mm^2)	0.95 $MOE_{dyn,sat,0,mean}$ = 0.95 10'100 = 9'600
$MOE_{0,mean,fin,sat}$ (N/mm^2)	$MOE_{sat,0,mean}$ /(1+1) =4'800
Pile head diameter (mm)	200
Pile length (mm)	10'000
Taper (mm/m)	7.5
Length of concrete extension pile (mm)	1'000
Ground water level	500 mm below the pile head
Ground level	at the top of the concrete extension pile
Connection properties	Trilinear moment – rotation diagram according to Figure 5.
$f_{m,0,mean,sat}$ (N/mm^2)	30*

* In Ranta-Maunus, A. (2000) a ratio of 2 is found between the bending strength and compression strength of small diameter roundwood. The compression strength of roundwood piles in the Dutch NAD were based on compression tests with a mean value of 20 N/mm^2 for saturated pieces. In the table a ratio of 1.5 is used.

4 Mechanical behaviour of a timber pile with a concrete extension piles in the soil

4.1 Strength and stability for vertical loads

The stability of a foundation pile in the soil under axial loading is influenced by the resistance of the soil. Tangential displacement of the pile will lead to reaction stresses in the opposite direction, which stabilises the pile. A new appendix in prEN 1997 gives a method for determining the stability of the pile including that effect. In EN 1993-5 a verification method for buckling of steel foundation piles is given, together with estimations of the buckling lengths of piles in the soil. The new appendix of prEN 1997 might be aligned with this approach. However, both approaches are valid for prismatic piles and therefore the applicability for wooden piles with a varying diameter in combination with concrete extension piles has yet to be demonstrated.

4.2 Strength and stability for horizontal loads

Two kinds of horizontal loads were examined:

1. Horizontal soil displacements, which for example can be the result of differences in ground level on both sides of the foundation pile.
2. Horizontal loads on the head of a vertical foundation pile, for example caused by wind load on a construction.

For both cases 1 and 2, the interaction between pile and surrounding soil can be determined using the model of an elastic beam (the pile) on a plasto-elastic bed (the soil). This kind of model is in engineering practice also used for the calculation of retaining walls.

For some examples the effects have been determined using that method. The calculations were performed with the Dutch Deltares model D-sheetpiling v.19.3. This program allows assigning physical non-linear material properties to the soil and geometric non-linear calculations. The pile properties addressed in 3.5 were used, with the short-term (higher) *MOE* value. The connection between pile and concrete extension is modelled by assuming the average relation between bending moment and rotation as found in the laboratory tests (Figure 5). For reasons of simplicity, the head of the concrete extension (=the connection of the extension with the construction) was in this case assumed at ground level. The soil is represented by the Brich-Hansen reaction model.

Figure 9 gives an overview of the material properties that are used for the modelling. In the modelling, linear behaviour was assigned to both timber pile, concrete exten-

sion pile and the connection of the concrete extension pile with the timber pile. How-ever, the latter was manually iterated until the output for the chosen stiffness coin-cided with a point on the tri-linear moment-rotation diagram.
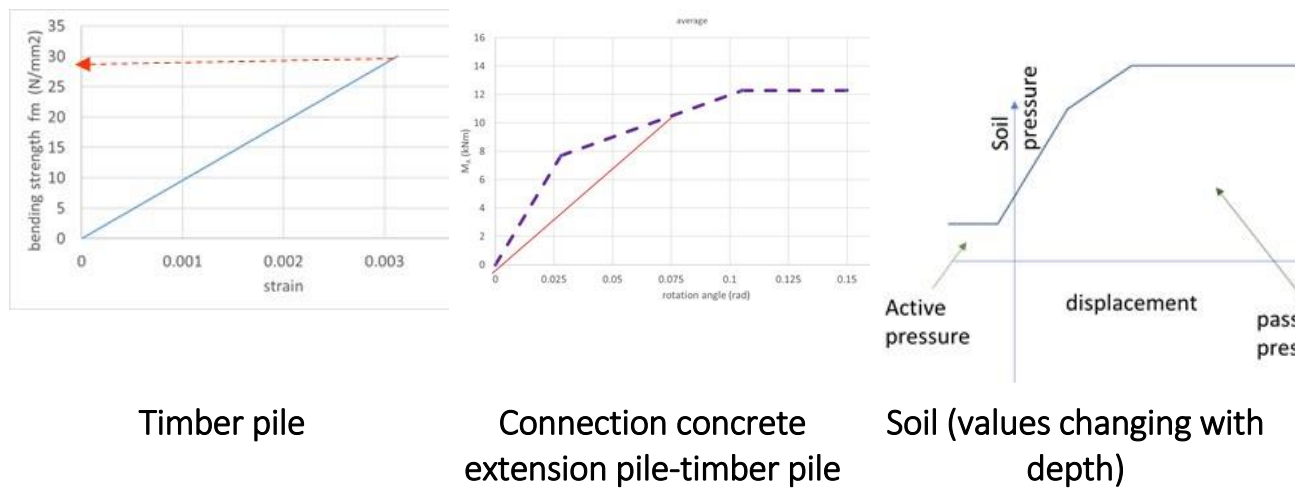

Timber pile   Connection concrete extension pile-timber pile   Soil (values changing with depth)

Figure 9. Material properties used for the different elements in the modelling.

Table 3 gives the soil profiles used in the analyses. Profiles A and B represent subse-quently a lower and upper boundary for the strength and stiffness of the soil. It is de-batable if foundation piles would even be applied in soil profile B.

Table 3. Soil parameters used

soil profile	Soil layer	Top side of the layer	Saturated volu-metric weight [kN/m³]	Stiffness of the soil [kN/m³]	Angle of internal friction / Cohe-sion [deg] / [kN/m²]
A (weak)	Peat	ground level (+1m)	11	1'000	15 / 5
	Sand	-9 m	20	10'000	33 / 0
B (strong)	Sand	ground level (+1m)	20	10'000	33 / 0

Case 1: soil displacements

For this case, the tangential soil displacements are assumed to decrease linearly with depth with the maximum at ground level, as shown in Figure 10. The displacement of the pile head itself is assumed zero, i.e. the situation in which there is no displace-ment of the construction.

Calculations have been made for the case in which the connection between concrete extension and foundation beam is fixed or can rotate freely. In general, the reality is somewhere in between those two extremes.
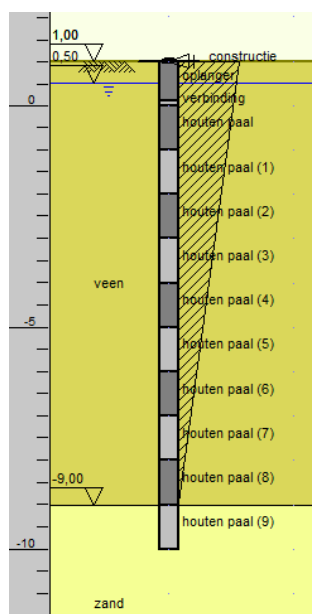

Figure 10. Schematisation of the pile. As indicated, the pile is divided into parts, to account for the difference in cross section. The shaded part indicates the horizontal soil displacement.

In the calculations, the maximum soil displacement at the pile head for which collapse of the pile would occur has been examined.

Table 4. Calculation results for the effect of soil displacements

connection extension and foundation beam	soil profile	Max. soil deformation at ground level near collapse of the pile [mm]	Delimiting mechanism	Max. rotation of the connection pile/extension [rad]
Fixed	A (weak) *)	230	Bending moment deeper in the pile reaches maximum	0.05
	B (strong)	80		0.08
Hinged	A (weak)	250	Max. rotation examined in the lab tests reached **)	0.15
	B (strong)	250		0.15

*) The calculation result for the indicated case is shown in Figure 11.

**) For the 'hinged' cases the maximum rotation of the connection between pile and extension for which the tests were performed is assumed to be the point of collapse.

It can be concluded that the connection between extension and pile could be delimiting in the case there is a hinge between extension and foundation beam. However, this is only reached at an extreme soil deformation of 250 mm.

If the soil deformation is a slow, long-term effect, so that the low long term value for *MOE* (see Table 2) should be used, it is likely that the values found for the maximum soil deformation would be larger.
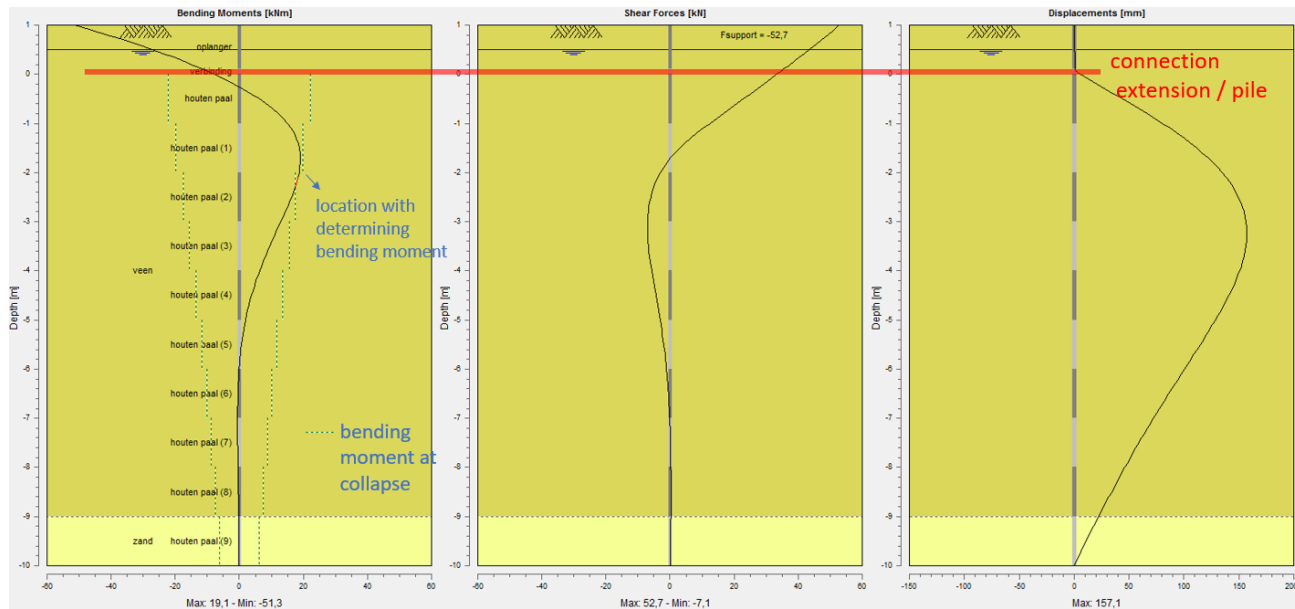

Figure 11. Example of the caculation result of case soil profile A, fixed connection between extension and foundation beam and max. soil displacement of 230 mm.

The procedure used to examine the effects of soil displacements on the foundation pile is well applicable in engineering situations and can be used as an example how the interaction analyses as requested in prEN 1997 can be performed.

Case 2: horizontal loads

For this case, the pile head (head of the extension) is assumed to be able to translate freely, i.e. the situation in which all piles under the construction are loaded equally and respond equally to the horizontal load. Calculations have been made for the case in which the pile head is fixed against rotation or can rotate freely. The maximum applicable pile load at collapse is determined.

Table 5. Calculation results effect of horizontal pile loads

Connection extension and foundation beam	Soil profile	Max. short-term horizontal load on the pile at collapse [kN]	Delimiting mechanism	Rotation of the connection pile/ extension [rad]	Horizontal deformation pile head [mm]
Fixed	A (weak)	53	Bending moment deeper in the pile reaches maximum	0.10	215
	B (strong)	90		0.05	68
Hinged	A (weak)	21.5	Max. bending moment in the connection (12.5 kNm) reached	0.15	200
	B (strong)	21.5		0.15	101

In the case of the fixed connection, the largest values for the horizontal load at collapse were found. This is caused by the fact that the horizontal resistance over a larger part of the pile is mobilised than in the case of a hinge at the pile head. The maximum horizontal force at collapse is for the hinged cases determined by the maximum moment capacity of the connection between pile and extension. Since this moment capacity is strongly time dependant, the results can only be applied for short-term loads. From the tests, it is known that the long term strength of the connection is much lower; a reduction in bending moment in time was observed when the deformation was kept equal. For the fixed cases, the bending moment deeper in the pile was determining for the result, however it would be reasonable to assume that if the bending moment capacity of the connection decreases, it will become determining as well.

5   Conclusions

The set of new clauses to prEN 1995-1-1 on the design of timber foundation piles and on logs to be used as timber foundation piles provides the opportunity of an increase in use of timber for this kind of application. The new clauses describe the verification rules for piles subjected to axial compression and give guidance related to the grading of timber logs, the connection of the timber pile with extension piles and to the evaluation of stability of timber piles.

In this paper, the relationship for one connection type (socket-type) was investigated and a trilinear moment-rotation diagram was determined by means of experiment.

FEM and analytical models confirmed that the material properties for compression perpendicular to the grain are governing for the connections' strength and stiffness properties. This was similar to the behaviour found in the experiment, where ductile behaviour was observed, which can be explained from the plasticization after the compression strength perpendicular was reached. Although because of the specific configuration (confined in a circular tube) the found strength perpendicular to the grain cannot be assigned to other configurations, a good estimation of the stiffness of the connection can be made with FEM models, assuming an MOE_{90} of 70 N/mm^2 for a fully saturated pile. With a conservative assumption for the strength perpendicular to the grain the influence of the connection in a pile-soil model can be investigated also for other configurations than the tested one.

A procedure to study the influence of tangential (usually horizontal) soil displacements on timber piles with concrete extensions piles on top is proposed.

The outcome of a specific situation from practice with high horizontal loads showed that the bending capacity of the timber pile will in most cases be governing and not the investigated socket connection.

6   References

Buchanan, A.H. (1984). Strength model and design methods for bending and axial load interaction in timber members. PhD Thesis, University of British Columbia, Canada.

DIBt, Deutsches Institut fűr Bautechnik (2016), Stűtzen aus Brettschichtholz zur Einspannung durch Verguss in Stahlbetonfundamente. Zulassung Z-9.1-136. (In German).

EN 1993-5 (2007) Eurocode 3 – Design of steel structures – Part 5: Piling. CEN. Brussels.

EN 1995-1-1/A1/A2 (2014) Eurocode 5: Design of timber structures - Part 1-1: General - Common rules and rules for buildings. CEN. Brussels.

Ferreira, D and Manie,J . (2020). DIANA FEA release 10.4. User's manual.

Lobbe, S. (2019) Sandra Lobbe Inspectie & Advies nr.1810188v2, 3 December 2019 (in Dutch).

Nobel, W. (2014). De druksterkte van een kesp loodrecht op de vezel. BsC Thesis, Delft University of Technology, Netherlands (in Dutch).

Project team SC5.T3 (2020) Subtask 5. New Section 14 to EN 1995-1-1: Design rules for foundations with timber piles. Final draft 30-04-2020.
Document CEN/TC 250/SC 5/N 1235 .

Rensman, J.G.(1997). Verbinding betonnen oplangers met houten palen. Technische Houtdocumentatie. Centrum Hout. The Netherlands.

Project teams SC7.T4 and SC7.T5 (2019). PrEN 1997-3 (2019): Geotechnical design- Geotechnical structures. Final draft 2019-11-04

Ranta-Maunus, A. (2000) Bending and compression properties of small diameter round timber. WCTE 2000 Conference, Whistler, Canada.

Van de Kuilen, J.W.G. Bepaling van de karakteristieke druksterkte van houten heipalen. TNO report 94-CON-R0271. Delft. The Netherlands (in Dutch).

Van de Kuilen, J.W.G. (1995) Timber piles. Timber Engineering. STEP 2. Centrum Hout. Almere. The Netherlands.

Working Group CEN/TC 250/SC 5/WG 3. Revised version of New Section 14 to EN 1995-1-1: Design rules for foundations with timber piles. Final draft 30-04-2021. Document CEN/TC 250/SC 5/WG 3/N293.

Manual D-sheetpiling, Deltares November 2019

DISCUSSION

The papers was presented by G Ravenshorst

H Blass commented that this is similar to the case of timber column clamped in concrete foundation where design rules are available and shear is a major design consideration. G Ravenshorst replied that shear did not seem to govern in this case as it would depend on the length of the socket.

U Khulmann commented that such stability cases are also important for steel structures where Eurocode 3 part 5 has a lot of information.

E Ussher asked whether there was any influence on point of fixity of the pile and whether the soil parameters would be site specific. G Ravenshorst replied at the final position of the pile, there would be no influence at point of fixity at the pile tip. Also the soil parameters are depth dependent but in general applicable for Dutch conditions of peat and sandy soil.

P Dietsch asked about the background of the limit of 500 mm below water level and why was k_{def}=1 which would be ½ of the value for service class 3 in code. G Ravenshorst replied that the limit of 500 mm was based on practical experience as a safe limit. k_{def} = 2 might be based on dry/wet cycle and in this study the piles would be under constant wet state. P Dietsch further commented that the creep in the parallel to grain direction might be lower.

Mechanical properties of European beech glulam after 32 years in a service class 2 environment

Thomas Ehrhart[1], Philippe Grönquist[2], Stephan Schilling[2], René Steiger[3], Andrea Frangi[2]

[1] Schnetzer Puskas Ingenieure, Zweierstrasse 100, CH-8003 Zürich, Switzerland

[2] ETH Zürich, Swiss Federal Institute of Technology, Institute of Structural Engineering (IBK), CH-8093 Zürich, Switzerland

[3] Empa, Swiss Federal Laboratories for Materials Science and Technology, Structural Engineering Research Laboratory, CH-8600 Dübendorf, Switzerland

1   Introduction

Wood and engineered wood products are subject to aging processes, i.e., the physical, chemical, and mechanical properties change over time. Whereas aging effects appear to be minimal in favorable climatic conditions [1] even for archaeological structures more than 4400 years old [2], humid environments, contact with liquid water and exposure to UV radiation may have led to a chemical degradation. Consequently, changes with regard to the physical, chemical and mechanical properties may occur [3].

When designing timber structures, the environmental conditions expected at the site where the structure will be built, must be accounted for. In the framework of Eurocode 5 (EN 1995-1-1) [4] this is accomplished by assigning each timber structure to service class (SC) 1, 2, or 3. The mechanical properties are adjusted to specific climatic conditions (temperature and relative humidity of the air) by means of the modification factor k_{mod}. In the next generation of Eurocode 5 [5], a fourth SC will be introduced.

The resistance against decay depends on the actual timber species. EN 335 [6] defines the durability classes (DC) based on the natural durability of solid wood. To assess the durability of timber products within a few hours or days, standardized procedures have been developed, allowing for – or at least aiming at – a simulation of the aging process and its impact on the product properties.
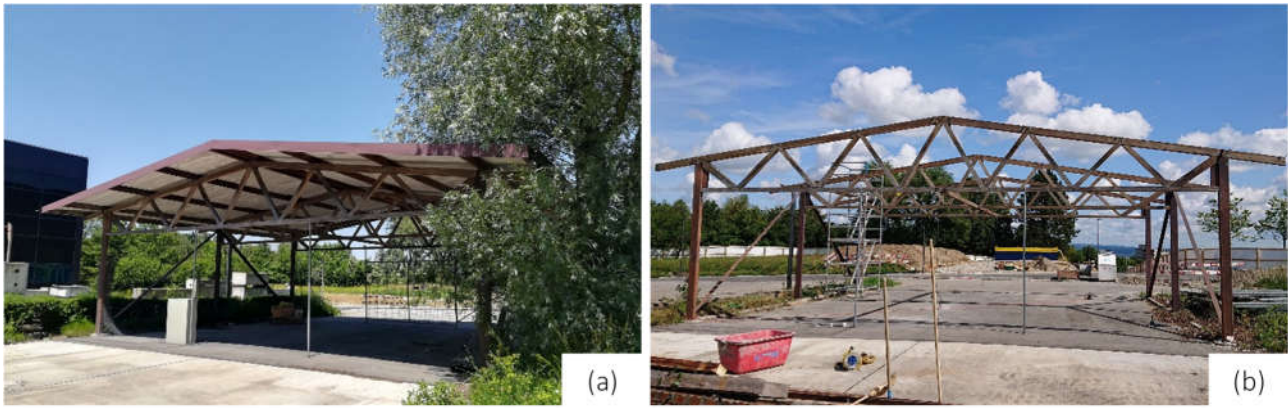
Figure 1: Shed at ETH Zürich (Switzerland) with truss girders made of European beech (Fagus sylvatica L.) glulam erected in 1987 (a) and its disassembling in August 2019 (b).

For example, test methods for verifying the resistance against delamination of bond lines are implemented in the test standard to assess the performance of adhesives for load-bearing timber structures EN 302-2 [7] and in the standard EN 14080 [8] containing the requirements in the production of glued-laminated and glued solid timber.

Several studies have focused on the aging effects on softwoods and the respective influences on the mechanical properties [3]. However, for a long-term use of European beech (*Fagus sylvatica* L.) glulam in SC 2, to the knowledge of the authors, no investigations are available. European beech wood features a comparably low durability and hence, it is assigned to DC5, "not durable". Consequently, this species should only be applied in use class (UC) 1 or (depending on the actual wood product, climatic conditions and cross-sectional dimensions) UC 2 according to EN 335 [6].

This paper presents experimental investigations on beech glulam subjected for 32 years to an environment corresponding to an exposure belonging to SC 2 and UC 2 according to Eurocode 5 (EN 1995-1-1) and EN 335 [6], respectively. Compression and tension tests parallel to the grain as well as shear tests were conducted.

The investigated beech glulam members originate from three truss girders of a shed at ETH Zürich (campus Hönggerberg; 47°24'36.5"N 8°30'24.7"E) (Figure 1). The span of the duopitch roof trusses with raised eaves was 11.9 m and the height varied between 0.72 and 1.64 m (Figure 1). The slope of the roof was 9°. The cross-section dimensions of the bottom chords and the diagonals was 100×100 mm^2. The top chords and the diagonals closest to the supports had a cross section of 100×160 mm^2. Connections between truss members were realized with two slotted-in steel plates ($t = 4$ mm) and steel dowels ($d = 8$ mm) (Figure 2). Light corrosion was visible on the steel plates and dowels (Figure 2). According to [9], beech wood is classified in the corrosion class "gering" (low). Prior to the tests described in the paper, tests on the truss girders were conducted [10]. In these tests, the tensile strength of the steel plates, which was back-calculated from the first truss test where net failure of a pair of steel plates occurred, was found to be $f_{u,test-1} = 360$ MPa. In the subsequent truss tests, the connection limiting the ultimate resistance was reinforced. The tensile strength of the steel dowels (5 tension tests) was $f_{u,mean} = 1131$ MPa (cov = 0.03) [10].
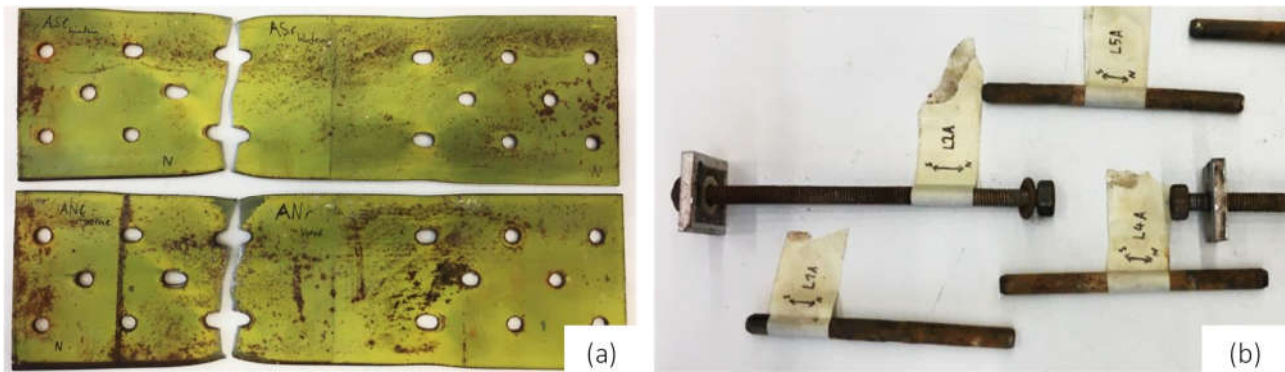
Figure 2: Slotted-in steel plates after testing the first truss (a) and steel dowels (b).

2 Material and Methods

2.1 Beech glulam members

2.1.1 Wood and wood aging effects

In order to investigate possible chemical structural changes, e.g., degradation of the aged beech glulam resulting from exposure to high UV radiation rates and moisture, surface samples and samples cut out in 10 mm depth were collected from the aged beech members. As a reference, samples from fresh beech wood were also investigated. Pieces of 2 mm × 2 mm early-wood samples were analyzed with a Fourier transform infrared (FTIR) spectrometer (Tensor 27, Bruker Optics) equipped with a single bounce diamond ATR element (Platinum ATR). Three spectra were recorded for each sample in the wavelength-range of 350-4000 cm^{-1} and averaged. The spectra were baseline corrected. The wavelength range was cropped to the wood-relevant region (800–1800 cm^{-1}) and normalized by the respective maximum peak.

2.1.2 Adhesives

No information from the producers / designers regarding the adhesive used for face gluing and finger jointing was available. The dark red-brown color of the adhesive bonds indicated either a resorcinol-formaldehyde (RF) or phenol-resorcinol-formaldehyde (PRF) adhesive had been used. Investigations with a FTIR spectrometer revealed a spectrum similar to that of an RF adhesive.

2.1.3 Lamination thickness

The lamination thickness of the bottom chord members and the diagonals was 20 mm. The top chord members and the diagonals closest to the supports had a lamination thickness of 25 mm. This is considerably less compared to glulam made of softwood, where usually laminations of 35 to 45 mm in thickness are used. As reported in [11], thin laminations are favorable with regard to internal stresses resulting from changes in temperature and moisture content. Therefore, glulam members with comparably thin laminations exhibit a higher resistance against delamination. In recent research studies on the application of beech glulam for load-bearing structural elements, thicknesses of laminations were chosen below 30 mm [12]–[14].

2.1.4 Moisture content (at time of testing)

After conducting the tests on the truss girders [10], the trusses were stored in indoor heated climate condition. To determine the moisture content (MC), small segments of the specimens were analyzed directly after testing using the dry-oven method according EN 13183-1 [15]. The average MC was 8.7% (cov = 0.01).

2.2 Environmental situation

Zurich has a temperate oceanic (Cfb) / humid continental climate (Dfb) [16] with warm summers and four distinct seasons. The climate is moderate with no excessive heat, cold or humidity. The temperatures vary (record lows and highs measured in Zurich since 1901) between -24.2°C and 37.7°C.

The average relative humidity lies between approximately 70% (March - July) and 85% (October - January). Figure 3 shows the average daily temperatures measured in Zurich in 2020 and the min. and max. values (daily average) measured since 1864 [17]. Since the shed had a corrugated metal roof, temperatures in summer are assumed to have exceeded the values measured in protected weather stations. Thanks to the big neighboring building, the shed has been protected from intense west wind rain events. No signs of direct weathering (rain or snow) of the truss members have been found.

Overall, the environmental conditions are corresponding to an exposure belonging to SC 2 and UC 2 according to Eurocode 5 (EN 1995-1-1) [4] and EN 335 [6], respectively.

2.2.1 Loading history

During its lifetime, the shed mainly had to withstand snow and wind loads. According to the Swiss standard SIA 261 [19], characteristic snow loads of s_k = 1.2 kN/m^2 have to be considered in the design. Actual record values of daily snowfall were 54 cm in 2006, which corresponds to a load of about 1 kN/m^2 (density after a few hours/days after snowfall: 2 kN/m^3). The reference wind pressure for the site is q_{p0} = 0.9 kN/m^2 [18].
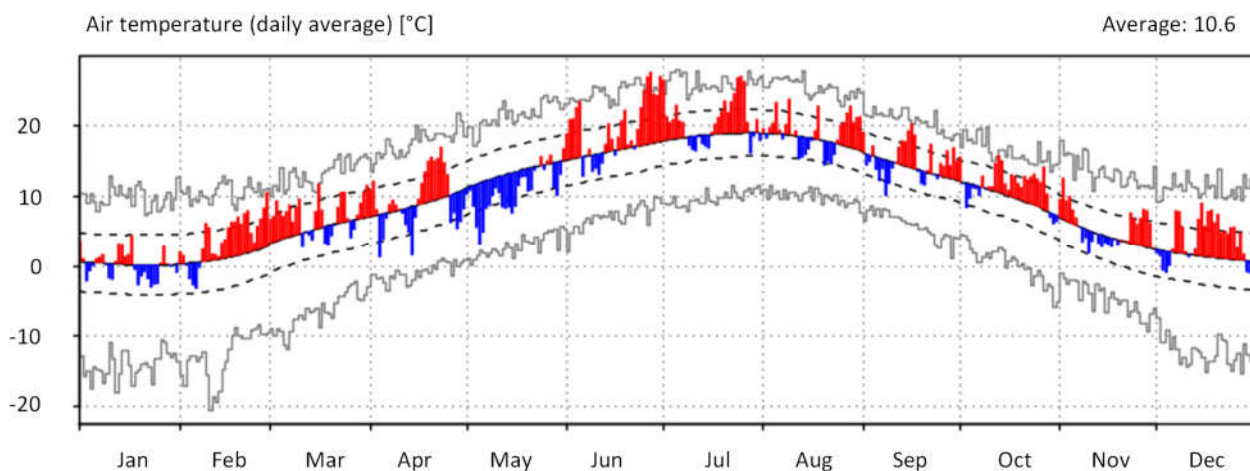

Figure 3: Daily average temperatures in Zurich in 2020 (station Fluntern) and min. and max. values between 1864 and 2018 (grey) [17]. The red and blue bars indicate warmer / colder temperatures in 2020 compared to the average temperatures between 1981-2010.

2.3 Experiments

2.3.1 Compression tests

Compression tests parallel to the grain (n = 12) were carried out in accordance with EN 408 [19] using a hydraulic testing machine of the type Schenck 1600 with a maximum capacity of 1600 kN (Figure 4a). The cross-section dimension of the specimens was 100 × 100 mm^2 and their length was (6 × h) = 600 mm.

The compressive modulus of elasticity (MOE) parallel to the grain was determined in accordance with EN 408 [19] based on measuring the local axial displacement over a length of (4 × h) = 400 mm with two linear variable differential transducers (LVDTs) mounted on two opposite surfaces of the specimens. The tests were conducted displacement controlled with a constant displacement rate of 0.02 mm/s. When reaching 40% of the expected maximum force, the LVDTs were disassembled. The net time until the maximum force was reached was 300 ± 120 s.

2.3.2 Tension tests

Tension tests parallel to the grain (n = 10) were carried out in accordance with EN 408 [19] using a hydraulic testing machine of the type Gehzu 1800 with a maximum capacity of 1800 kN (Figure 4b). The cross-section dimension of the specimens was 100 × 100 mm^2, the free testing length was (12 × h) = 1200 mm and the length of the clamping jaws (clamping pressure: 5.6 MPa) was 520 mm at both ends.

The tensile MOE parallel to the grain was determined in accordance with EN 408 [19] based on measurements of the local horizontal displacement over a length of (5 × h) = 500 mm recorded with two LVDTs mounted on two opposite surfaces of the specimens.
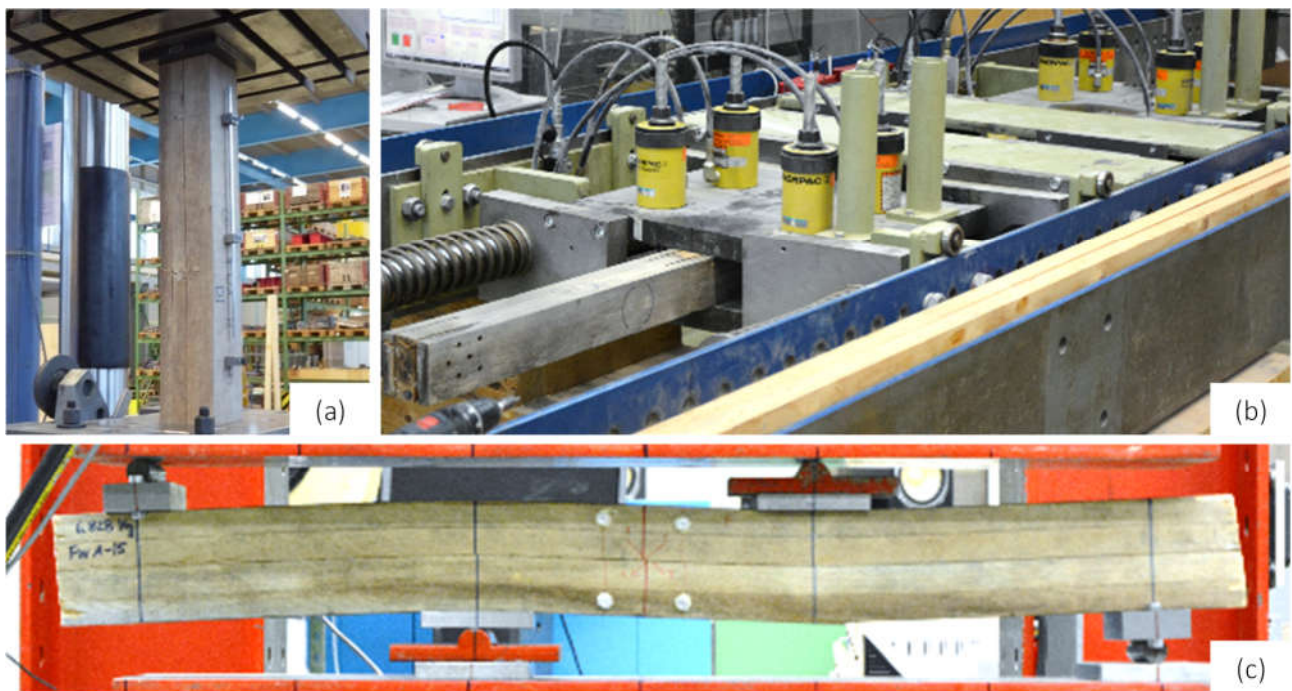

Figure 4: Test setups for compression- (a), tension- (b) and shear tests (c).

Initially, the specimens were subjected to axial tensile forces corresponding to 40% of the expected maximum force and unloaded again. Subsequently, the LVDTs were dis-assembled, and the force was increased until failure occurred after 300 ± 120 s.

2.3.3   Shear tests

Currently, there is no test configuration available in European standards for the deter-mination of the shear strength of glulam beams in full-size. In this study, the asymmet-ric four-point bending test setup (Figure 4c) presented in [20] was applied. It is based on [21] and a similar test setup has been successfully employed for the testing of clear wood samples [22]. The cross-section dimension was 100×100 mm^2 and the total length of the specimens was $(10 \times h) = 1000$ mm. The distance between the load ap-plication points / supports was $(3 \times h) = 300$ mm. Half of in total $(n =)$ 18 specimens were tested with the laminations in flatwise-, the other half with the laminations in edgewise orientation. The shear modulus was determined by analyzing a quadratic shear field in the center of the beams on both sides.

3   Results and discussion

Tab. 1 summarizes the main results of the compression-, tension- and shear tests and contains information on the density of the specimens. The distribution parameters of the strength and stiffness properties were calculated according to EN 14358 [23] as-suming a lognormal distribution [24]. The 5%-fractile value was additionally calculated applying the maximum-likelihood method (MLE) [25]. For density, a normal distribu-tion was assumed [24].

3.1   Density

The average value of density for all specimens was $\rho_{mean,glob} = 687$ kg/m^3 with a mini-mum value of 640 kg/m^3 and maximum value of 727 kg/m^3. The density was very sim-ilar for the compression- ($\rho_{mean,c} = 687$ kg/m^3), tension- ($\rho_{mean,t} = 683$ kg/m^3) and shear test specimens ($\rho_{mean,v} = 688$ kg/m^3). All densities reported refer to their actual mois-ture contents of $u = 8.7 \pm 0.1\%$. A mean value of density of $\rho_{mean,12} = 698$ kg/m^3 results when applying the moisture correction to MC = 12% according to EN 384 [26].

3.2   Compression tests

The mean value of the compressive strength parallel to the grain ($f_{c,0}$) was 64.4 MPa. The variation was very low, i.e., a coefficient of variation (cov) of 0.04 and min. / max. values of 60.9 / 68.2 MPa were found ($f_{c,0,k} = 60.8$ MPa). The mean value of the com-pressive MOE parallel to the grain ($E_{c,0}$) was 15.8 GPa, with min. / max. values of 15.0 / 17.7 GPa (cov = 0.05). The 5%-fractile value was $E_{c,0,05} = 14.7$ GPa.

A rather ductile failure behavior was observed, which can be explained by the local crushing of fibers before reaching the ultimate force. The force-displacement curve was almost linear until a level of 85 to 90% of the ultimate force. While applying the remaining 10 to 15% of the force, 40 to 45% of the total displacements occurred.

Tab. 1: Density and compressive-, tensile- and shear properties of beech glulam after 32 years in a service class 2 environment.

Density	ρ [kg/m³]	n	40	MC during static testing: $u = 8.7 \pm 0.1\%$. [1] Using MLE [25]. [2] According to EN 14358 [23]. [3] Lam. subjected to edgewise bending. [4] Lam. subjected to flatwise bending [5] Right-censored data analysis with 95% confidence level [27]		
		min	640			
		mean	687			
		max	727			
		cov	0.02			
		05 ND[1]	661			
		05 EN[2]	624			

		Strength			**Stiffness**	
Compression ‖ to the grain	$f_{c,0}$ [MPa]	n	12	$E_{c,0}$ [GPa]	n	12
		min	60.9		min	15.0
		mean	64.4		mean	15.8
		max	68.2		max	17.7
		cov	0.04		cov	0.05
		05 LN[1]	60.8		05 LN[1]	14.7
		05 EN[2]	58.2		05 EN[2]	14.2
Tension ‖ to the grain	$f_{t,0}$ [MPa]	n	9	$E_{t,0}$ [GPa]	n	10
		min	35.7		min	14.0
		mean	43.8		mean	15.8
		max	55.5		max	17.2
		cov	0.15		cov	0.06
		05 LN[1]	34.5		05 LN[1]	14.3
		05 EN[2]	31.7		05 EN[2]	13.8
Shear	f_v [MPa]	n	9[3] | 9[4]	G_v [MPa]	n	6[3] | 6[4]
		min	8.5 | 7.5		min	828 | 879
		mean[5]	12.5 | 9.4		mean	925 | 924
		max	14.3 | 13.0		max	1009 | 1041
		cov[5]	0.10 | 0.20		cov	0.07 | 0.06
		05 LN[5]	10.6 | 6.7		05 LN[1]	825 | 840
		05 EN[2]	-		05 EN[2]	-

3.3 Tension tests

The mean value of the tensile strength ($f_{t,0,\text{mean}}$) was 43.8 MPa. Compared to the compressive properties, a larger scatter of results was observed, with min. / max. values of 35.7 / 55.5 MPa (cov = 0.15). One specimen failed in the clamping area, where the cross section was reduced due to the connection in the truss girder (slotted in steel plates). Hence, the respective low (gross) tensile strength of 28.5 MPa was excluded from the data analysis ($n = 9$).

In the tension tests, exclusively brittle failures were observed. In most cases, a combination of failures of one or several finger joints (Figure 5a), wood failure next to knots (Figure 5b) and local fiber deviations (Figure 5c,d) was observed.

The mean value of the tensile MOE parallel to the grain ($E_{t,0}$) was 15.8 GPa, with min. / max. values of 14.0 / 17.2 GPa (cov = 0.06). The 5%-fractile value was $E_{t,0,05} = 14.3$ GPa.
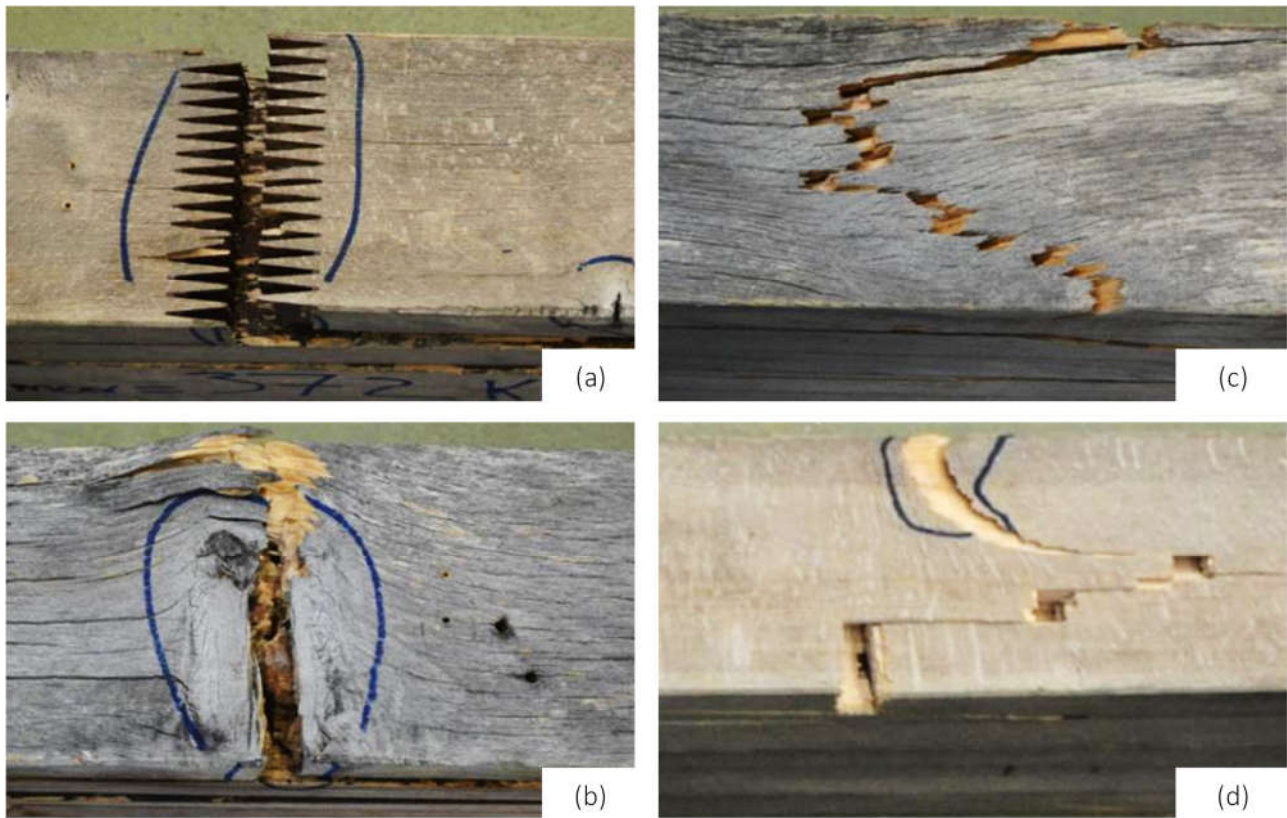
Figure 5: Typical failure pattern of beech glulam specimens subjected to tension tests, i.e. failure of finger joints (a), failure close to knots (b) and failures in areas of local fiber deviation (c,d).

3.4   Shear tests

Undesired failure mechanisms, such as premature bending failure (of finger joints; 1 out of 18 specimens) and compression failure perpendicular to the grain (1 out of 18 specimens), were accounted for by a censored data analysis [27]. Results for specimens tested with the laminations subjected to edgewise- and flatwise bending are shown separately in Tab. 1 (using the pipe "|"symbol). The shear strengths (f_v) determined with the laminations subjected to edgewise bending ($f_{v,mean,edge,CD}$ = 12.5 MPa; cov = 0.10) were higher compared to flatwise bending ($f_{v,mean,flat,CD}$ = 9.4 MPa; cov = 0.20). The scatter was larger for the latter configuration, which can be explained by homogenization effects when testing specimens with the laminations subjected to edgewise bending. The glueline (not stressed in edgewise bending) was involved in the failure of several beams tested with the laminations in flatwise bending (Figure 6). However, no exclusive failures of the glueline were observed, i.e., the failure mainly propagated in the wood. For the shear modulus (G_v), no significant difference between edgewise and flatwise bending was found ($G_{v,mean}$ = 925 | 924 MPa; $G_{v,05}$ = 825 | 840 MPa; Tab. 1).

3.5   Comparison with properties of beech glulam right after production

In order to evaluate the influence of the climate exposure and potential degradation on the mechanical properties, the test results from this study are compared to mechanical properties reported by Ehrhart [20] ($u \approx 9\%$), Westermayr et al. [13] ($u \approx 10\%$) and Aicher & Ohnesorg [28] ($u \approx 11\%$), see Tab. 2. Besides the mean and 5%-fractile values, the test configuration and the dimensions are indicated.
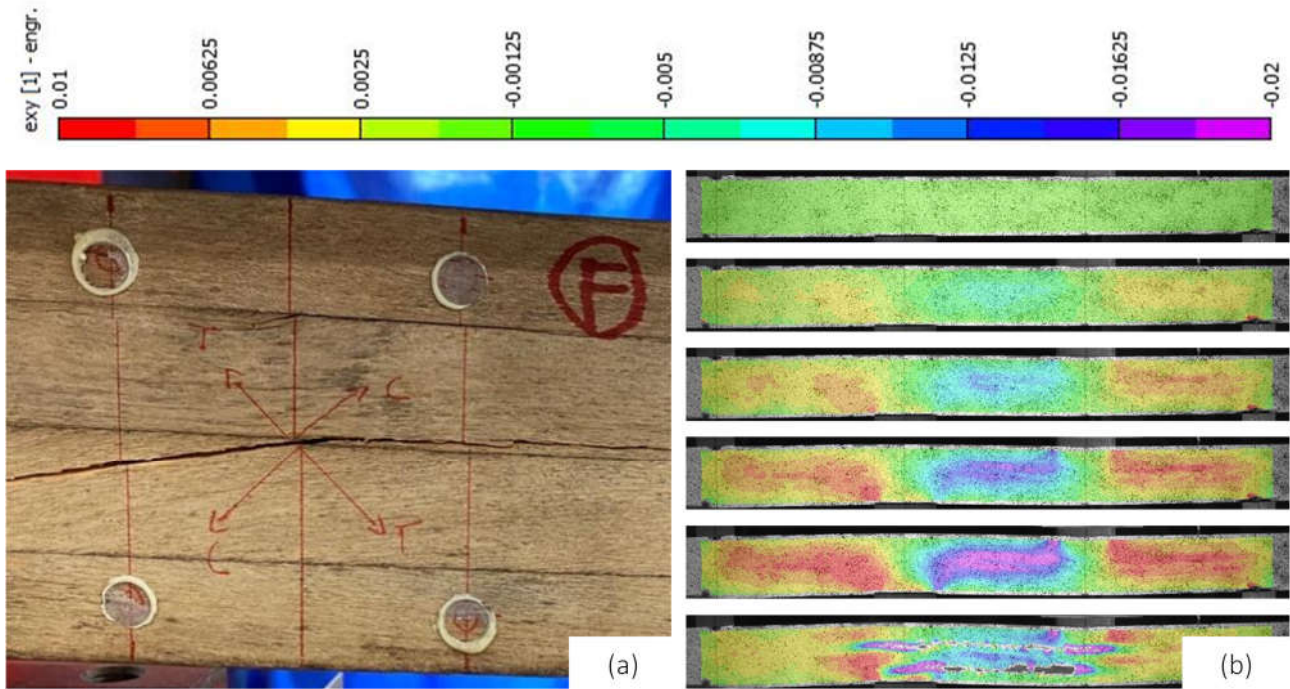
Figure 6: Shear failure pattern of beams tested with the laminations subjected to flatwise bending (a) and evolution of shear strain ε_{xy} during the asymmetric four-point bending tests (b).

Regarding the density, similar mean and 5%-fractile values were found in this study compared to [14] and [13], which means that the mechanical properties determined in this study can be compared with the test results from previous studies.

The compressive strength parallel to the grain of the aged beech glulam ($f_{c,0,mean}$ = 64.4 MPa) is slightly higher than the values reported in [29] for beech glulam of strength class GL 48h (63.8 MPa; + 0.9%; $u \approx 9\%$) right after production. Compressive strengths reported in [13] for low quality beech glulam, i.e., wood featuring fiber deviation, pith, cracks, discoloration as well as knots, are slightly lower (60.5 MPa; + 6.4%; $u \approx 10\%$). Thus, no influence of aging on the compressive strength parallel to the grain could be identified. The same applies for the compressive MOE parallel to the grain.

The tensile strength of the aged beech glulam ($f_{t,0,mean}$ = 43.8 MPa) has been determined on a similar level compared to the strength class GL 40h [20]. Values reported in [13] are about 30% higher. However, in the latter study, specimens without finger joints were tested. Finger joints are often triggering failure and, thus, limit the tensile strength. Again, the MOE (in tension; 15.8 GPa) is on a similar level as for beech glulam of strength class GL 48h (15.5 GPa) right after production [20] and considerably higher than the values reported in [13] (12.9 GPa).

The shear strength of the aged beech glulam with the laminations subjected to edgewise bending was slightly higher, and with the laminations subjected to flatwise bending slightly lower compared to beech glulam (GL 48h) right after production [29]. However, the shear strength of timber is known to be subjected to a size effect [30]–[32] and. Thus, the results of the present study must be adjusted to allow for comparison.

Tab. 2: Comparison of mean and 5%-fractile values of density and compressive-, tensile- and shear strength and stiffness with values for fresh beech glulam right after production.

Property		Aged glulam (This study)	Glulam right after production Ehrhart [20]			Further literature
			GL 40h	GL 48h	GL 55h	
ρ_{mean}	kg/m³	687	693 - 701	697 - 712	708 – 715	690[6]
ρ_{05}	kg/m³	661	669 - 682	706 - 664	693 - 697	-
$f_{c,0,mean}$	MPa	64.4	60.4[1]	63.8[1]	65.8[1]	60.5[5]
$f_{c,0,05}$	MPa	60.8	59.7[1]	62.5[1]	63.7[1]	-
$E_{c,0,mean}$	GPa	15.8	15.1[1]	16.0[1]	17.0[1]	13.3[5]
$E_{c,0,05}$	GPa	14.7	14.4[1]	15.4[1]	16.7[1]	-
$f_{t,0,mean}$	MPa	43.8	43.7[2]	53.3[2]	57.7[2]	57.6[5]
$f_{t,0,05}$	MPa	34.5	36.6[2]	44.3[2]	52.9[2]	-
$E_{t,0,mean}$	GPa	15.8	15.2[2]	15.5[2]	17.0[2]	12.9[5]
$E_{t,0,05}$	GPa	14.3	13.9[2]	14.7[2]	16.3[2]	-
$f_{v,mean}$	MPa	12.5 | 9.4	-	10.8[3]	-	6.1[6]
$f_{v,05}$	MPa	10.6 | 6.7	-	9.0[3]	-	4.3[6]
$G_{v,mean}$	MPa	925 | 924	-	1270[4]	1180[4]	-
$G_{v,05}$	MPa	825 | 840	-	1140[4]	1100[4]	-

[1] Dimensions of test specimens: 200 × 200 × 1200 mm³; $u \approx 9\%$

[2] Dimensions of test specimens: 160 × 75 × 3600 mm³; $u \approx 9\%$

[3] Dimensions of test specimens: 400 × 160 × 3200 mm³ (asymmetric 4P bending test); $u \approx 9\%$

[4] Several different test configurations and specimen dimensions; $u \approx 9\%$

[5] Westermayr et al. [13]: 80 × 80 × 180 / 2320 mm³, homogenous layup; $u \approx 10\%$

[6] Aicher & Ohnesorg [28]: 608 × 120 × 3040 mm³ (symmetric 4P bending test); $u \approx 11\%$

According to [20], the shear strength of beech glulam can be estimated with Equation 1 ($f_{v,mean}$) and Equation 2 ($f_{v,k}$), respectively. For a beam height of 100 mm, estimated shear strengths of $f_{v,mean,est}$ = 13.6 MPa / $f_{v,k,est}$ = 11.0 MPa result.

$$f_{v,mean} = 94 \cdot h^{-0.42} \qquad (1) \qquad\qquad f_{v,k} = 76 \cdot h^{-0.42} \qquad (2)$$

Compared to the results for the beams tested in edgewise- ($f_{v,mean}$ = 12.5 / $f_{v,05}$ = 10.6 MPa) and flatwise bending (9.4 / 6.7 MPa), a small (-9%) and strong (-45%) reduction in shear strength is found.

3.6 Chemical degradation of the beech glulam members

The results of the FTIR analysis are shown in Figure 7 in the form of vertically shifted spectra for sake of comparison. The spectra of the reference samples and of the aged glulam samples cut out at 10 mm depth do not show any apparent differences.

Hence, it can be concluded that the material inside the glulam members remained perfectly intact with respect to chemical structure. However, large degradations in lignin, cellulose, and hemicellulose of the samples collected at the weather-exposed surface of the aged glulam are apparent by comparing the characteristic spectra bands to the reference samples' spectra.
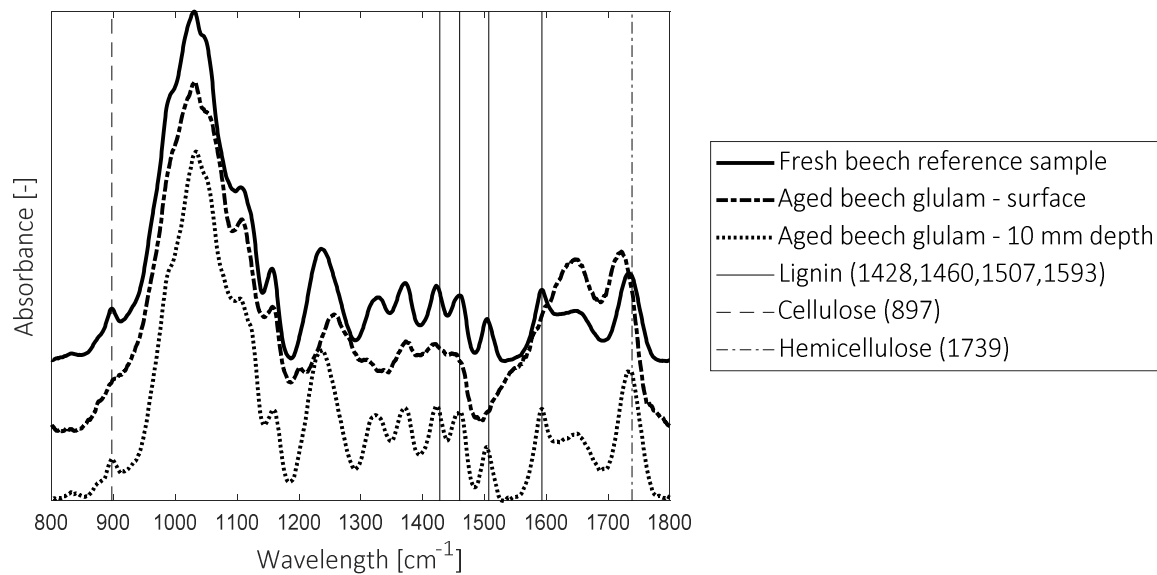
Figure 7: Spectra resulting of the FTIR-analysis. Characteristic band assignments for lignin, cellulose, and hemicellulose are pointed out by the vertical lines following a band-assignment table for hardwood [33].

The zone of surface degradation was identified to be approximately 1 mm deep throughout all aged glulam members. It can be assumed that this 1 mm thick band around the cross section does not significantly reduce the mechanical strength and stiffness properties in the case of the conducted tension, compression, and shear tests.

4   Conclusions

Based on the results presented in this study, the following conclusions can be drawn:

- Beech glulam can be used in service class (SC) 2, if the following prerequisites are met:
    - o The beech glulam members are protected from direct rain and other liquid water sources. According to the next generation of Eurocode 5 (prEN 1995-1-1) [5] and the new definition of service classes, this is the case for service class 2 (*"structures under shelter in non-insulated and unheated conditions"). The use of beech glulam in service class 3 according to the next generation of Eurocode 5 (prEN 1995-1-1) [5] ("exposed to weathering if water will run off"*) and service class 4 (*"structures submerged in soil or water"*) is not recommended.
    - o An appropriate / durable adhesive system is used for finger jointing and face gluing of the laminations.
    - o The lamination thickness is reduced compared to softwood glulam (in this study, the lamination thickness was l_t = 20 - 25 mm).
- No significant influence of aging could be observed regarding the density, the compressive strength and MOE parallel to the grain and the tensile strength and MOE parallel to the grain.

- Although no exclusive failures of the glueline were observed, the shear strength of beams tested with the laminations in flatwise bending was 25% lower compared to beams tested with the laminations subjected to edgewise bending. On the one hand, this can be attributed to homogenization effects in edgewise bending. On the other hand, the glueline is subjected to shear stresses when beams are tested with the laminations in flatwise bending and was involved in several failures.

- The asymmetric four-point bending test was successfully applied for determining the shear strength and modulus. It is recommended to be implemented as an additional reference test configuration in EN 408 [19], at least for applications in research.

- A Fourier transform infrared (FTIR) spectrometer analysis revealed that for the surface (outermost 1 mm) degradations in lignin, cellulose, and hemicellulose occurred. The spectra of the reference samples and of the aged glulam samples cut out at 10 mm depth did not show any differences, meaning that the wood structure was perfectly retained.

- The results of the FTIR analysis and the comparison of the test results with properties of beech glulam tested right after production indicate that aging has no or only a negligible influence on the mechanical properties.

The presented results are considered to be relevant for the standardization of beech (and other hardwood) glulam on a European level in the future product standard prEN 14080-2 [34].

5 Acknowledgement

6 References

[1] Erhardt, D; Mecklenburg, M; Tumosa, C; Olstad, T (1996) New versus old wood: differences and similarities in physical, mechanical, and chemical properties. International council of museums-committee for conservation 11th triennial meeting, pp. 903–910.

[2] Nilsson, T; Daniel, G (1989) Structure and the aging process of dry archaeological wood. Adv. Chem., vol. 225, pp. 67–86.

[3] Kránitz, K; Sonderegger, W; Bues, CT; Niemz, P (2016) Effects of aging on wood: a literature review," Wood Sci. Technol., 50 (1), pp. 7–22.

[4] EN 1995-1-1 (2010) Design of timber structures - Part 1-1: General - Common rules and rules for buildings. CEN.

[5] prEN 1995-1-1 (n.d.) Basis of design and materials. Final draft (22.01.2021). Project team SC5.T3 & SC5/WG10, CEN.

[6] EN 335 (2013) Durability of wood and wood-based products - Use classes: definitions, application to solid wood and wood-based products. CEN.

[7] EN 302-2 (2017) Adhesives for load-bearing timber structures - Test methods - Part 2: Determination of resistance to delamination. CEN.

[8] EN 14080 (2013) Timber structures - Glued laminated timber and glued solid timber - Requirements. CEN.

[9] Informationsdienst Holz (2013) Korrosion metallischer Verbindungsmittel in Holz und Holzwerkstoffen. Internationaler Verein für Technische Holzfragen e.V. iVTH, Braunschweig und Fraunhofer-Institut für Holzforschung - Wilhelm-Klauditz-Institut WKI, Braunschweig, Germany.

[10] Merkel, J (2019) Tragverhalten von Buchenfachwerken nach 30 Jahren in Feuchteklasse 2. Master's Thesis, ETH Zürich, Switzerland.

[11] Frühwald, A; Ressel, JB; Bernasconi, A (2003) Hochwertiges Brettschichtholz aus Buchenholz. Hamburg, Germany.

[12] Studiengemeinschaft Holzleimbau e.V. (2009) Allgemeine bauaufsichtliche Zulassung für BS-Holz aus Buche und BS-Holz Buche-Hybridträger, Z-9.1-679.

[13] Westermayr, M; Stapel, P; Van de Kuilen, JWG (2018) Tensile and compression strength of small cross section beech glulam members. Paper 51-12-2, International Network on Timber Engineering Research - Meeting Fifty-One, pp. 307–322, Tallinn, Estonia.

[14] Ehrhart, T; Steiger, R; Lehmann, M; Frangi, A (2019) European beech (*Fagus sylvatica L.*) glued laminated timber: Lamination strength grading, production and mechanical properties. Eur. J. Wood Wood Prod., vol. 78, pp. 971-984.

[15] EN 13183-1 (2002): Moisture content of a piece of sawn timber - Part 1: Determination by oven dry method. CEN.

[16] Kottek, M; Grieser, J; Beck, C; Rudolf, B; Rubel, F (2006) World map of the Köppen-Geiger climate classification updated. Meteorol. Zeitschrift, 15 (3), pp. 259–263.

[17] Bundesamt für Meteorologie und Klimatologie MeteoSchweiz. Available online: https://www.meteoschweiz.admin.ch.

[18] SIA 261 (2020) Einwirkungen auf Tragwerke.

[19] EN 408 (2012) Timber structures - Structural timber and glued laminated timber - Determination of some physical and mechanical properties. CEN.

[20] Ehrhart, T (2019) European beech glued laminated timber. Doctoral Thesis, ETH Zürich, Switzerland.

[21] Basler, K; Yen, BT; Mueller, JA; Thürlimann, B (1960) Web buckling tests on welded plate girders.

[22] Yoshihara, H; Kubojima, Y (2002) Measurement of the shear modulus of wood by asymmetric four-point bending tests. J. Wood Sci., vol. 48, pp. 14–19.

[23] EN 14358 (2016) Timber structures - Calculation and verification of characteristic values. CEN.

[24] JCSS Probabilistic Model Code (2006) Part 3: Resistance Models.

[25] Fink, G (2014) Influence of varying material properties on the load-bearing capacity of glued laminated timber. Doctoral Thesis, ETH Zürich, Switzerland.

[26] EN 384 (2019) Structural Timber - Determination of characteristic values of mechanical properties and density. CEN.

[27] Steiger, R; Köhler, J (2005) Analysis of censored data - examples in timber engineering research. Paper 38-17-1, CIB W18 - Meeting Thirty-Eight.

[28] Aicher, S; Ohnesorg, D (2011) Shear strength of glued laminated timber made from European beech timber. Eur. J. Wood Wood Prod., vol. 69, pp. 143–154.

[29] Ehrhart, T; Steiger, R; Palma, P; Frangi, A (2018) Mechanical properties of European beech (*Fagus sylvatica L.*) glued laminated timber. Paper 51-12-4, International Network on Timber Engineering Research - Meeting Fifty-One, pp. 343–360, Tallinn, Estonia.

[30] Keenan, FJ (1974) Shear strength of wood beams. For. Prod. J. 24 (9) pp. 63–70.

[31] Foschi, RO; Barrett, JD (1980) Consideration of size effects and longitudinal shear strength for uncracked beams. Paper 13-6-2, CIB W18 - Meeting Thirteen.

[32] Colling, F (1986) Influence of volume and stress distribution on the shear strength and tensile strength perpendicular to grain. Paper 19-12-3 CIB W18 - Meeting Nineteen, Volume 2, pp. 254–276.

[33] Moosavinejad, SM; Madhoushi, M; Vakili, M; Rasouli, D (2019) Evaluation of degradation in chemical compounds of wood in historical buildings using Ft-Ir And Ft-Raman vibrational spectroscopy. Maderas Cienc. y Tecnol., 21 (3), pp. 381–392.

[34] prEN 14080-2 (n.d.) Timber structures - Part 2: Glued laminated timber and glued laminated solid timber made of hardwood - Requirements. CEN.

DISCUSSION

The papers was presented by P Grönquist

P Dietsch supported the shear test set up conclusions. He did not agree with the proposal to split up service class into A and B as the newly proposed approach in Eurocode 5 implicitly also deals with the issue. P Grönquist replied splitting up service class into A and B would be more appropriate for modifying the current standard.

R Brandner asked about the distribution of compressive stress and received clarification that there was no reinforcement used in the support. He commented that the difference between edgewise and depth-wise shear strength results might be due to annual ring orientation effect. He asked whether there was any difference in G for these orientations. P Grönquist replied that the G data was not included in the paper and would look into the issue.

R Brandner commented that some of the mean strength values reported in the text and the table are different. P Grönquist replied that he would look into the issue and the difference might be deal to reporting of maximum likelihood censored data.

R Brandner asked why stop the tests in some cases. P Grönquist replied that probably results of few pretests without failure were reported. They would still be okay because the actual strength would be higher and use of censored data is appropriate.

T Ehrhart added that there was no reinforcement at the support but 8 mm screws were used to fix the support. He agreed that difference in annual ring orientation between flatwise and depth-wise orientation resulted in the difference in the shear strength. The paper will be amended to consider the comment on service class.

G Ravenshorst asked what was the moisture content of the member on site and why not conduct the test at this moisture content. P Grönquist replied that moisture content of the member on site would be between 12 to 20% and the testing was done at 9% MC.

S Malek asked about the difference in shear failure pattern between the edgewise and flatwise orientation. T Ehrhart replied the failures involved the gluelines but they were not clear glueline failures. They could not do more checks as the specimens were accidentally disposed.

S Aicher commented that it is well known that edgewise shear strength is higher than flatwise shear strength in softwood. He doubted that the failures were caused by glueline failures. This could have easily been checked if the specimens were still available. He commented that statements such as "appears to have lower strength" should not be used in the paper. P Grönquist agreed.

Influence of the moisture content on the compressive strength and modulus of elasticity parallel to the grain of engineered hardwood products (EHP)

Thomas Ehrhart, Schnetzer Puskas Ingenieure, CH-8003 Zurich, Switzerland

René Steiger, Empa - Swiss Federal Laboratories for Materials Science and Technology, Structural Engineering Research Laboratory, CH-8600 Duebendorf, Switzerland

Andrea Frangi, ETH Zürich, Swiss Federal Institute of Technology, Institute of Structural Engineering (IBK), CH-8093 Zurich, Switzerland

1   Introduction

The use of hardwoods in timber engineering offers enormous potential from a technical, architectural and climate-political point of view. However, the lack of standardization of engineered hardwood products (EHP) is a major obstacle to their use in practice. Research on engineered hardwood products [1]–[6] and their application in construction has been intensified in the recent years due to the increase in share of hardwoods in European forests [7]–[10]. As knowledge on the production and properties of EHPs increases, the work on prEN 14080-2 [11] – a new European hardwood glulam standard – has been resumed in 2018 by a Task Group within CEN/TC 124/WG 3.

One field of application where EHPs have a great potential are columns [12]. In this context, the compressive strength parallel to the grain ($f_{c,0}$) and the compressive modulus of elasticity ($E_{c,0}$) are the most relevant parameters. The influence of the moisture content (MC) on these properties must be quantified in order to allow for the design of EHPs in service classes (SC) 1 (20°C/65% RH) and 2 (20°C/85% RH) according to Eurocode 5 (EN 1995) [13]. However, respective investigations are currently not available for many EHPs. Furthermore, the validity of the formulae given EN 384 [14] for considering the influence of the MC on $f_{c,0}$ and $E_{c,0}$ has not been verified yet for EHPs.

According to the European Assessment Document EAD 130230-00-0304 [15], the characteristic value of the compressive strength parallel to the grain shall be reduced with a factor of 0.8 in case hardwood glulam is applied in SC 2 or SC 3.

2   Material and Methods

2.1   Material

2.1.1   Wood species

The hardwood species European beech (*Fagus sylvatica* L.; 18.1% of the Swiss wood resources), European ash (*Fraxinus excelsior* L.; 4.1%), European oak (*Quercus robur* L.; 1.9%) and sweet chestnut (*Castanea sativa* Mill.; 1.3%) were investigated in this study [8]. These species were selected due to their large share in Swiss forests. European beech is also the dominating hardwood species in Austria (68% of the hardwood standing stock) and in Germany (60%), whereas European oak has by far the largest share of hardwood standing stock in France (59%) [7]. The standing stock of each of the two species exceeds 1 billion m^3 (solid over bark) in the three mentioned Central European countries. The share of European ash is considerably high in Austria (15%) and Germany (7%), sweet chestnut plays a significant role in France (11%) [7] and Italy. Norway spruce (*Picea abies* (L.) Karst.) has been the most important wood species in Switzerland (43.7% of the Swiss wood resources) and in neighboring countries for many decades and it is still the dominating species for engineered wood products in Central Europe. Hence, Norway spruce was selected as the reference material.

2.1.2   Investigated engineered hardwood products (EHP)

The investigation covered the EHPs glued laminated timber (glulam) made from European beech, European ash, European oak and sweet chestnut (all Swiss grown) and laminated veneer lumber (LVL) made from European beech (Figure 1). Glulam made from Swiss grown Norway spruce served as reference material in this study. In Table 1, the most relevant product properties are summarized. In order to improve the delamination behavior [16] and to assure a homogenization effect, a relatively small lamination thickness of 25 mm (European beech), 31 mm (European oak) and 34 mm (European ash and Norway spruce) was chosen. Laminations used to produce the sweet chestnut glulam were 40 mm thick.

The glulam made of European beech, European ash, Norway spruce (using PUR adhesive for face gluing) and European oak (using PRF adhesive for face gluing) was produced by the company neue Holzbau AG (Lungern, Switzerland). The company Filippi SA (Airolo, Switzerland) produced the sweet chestnut glulam using PUR adhesive. The German company Pollmeier produced the European beech LVL (PRF adhesive).

2.1.3   Strength grading of the raw material

Currently, there is a lack of standardized strength grading rules for hardwoods of high strength classes. Thus, European beech [17] and sweet chestnut [18] were strength graded according to recent investigations.

Figure 1: Five different engineered hardwood products (EHP) and (as the reference material) Norway spruce glulam were investigated.

The European ash boards were strength graded by the company neue Holzbau AG according to internal strength grading rules. To produce the European oak glulam, boards with large knots were excluded but no additional strength grading rules were applied.

Table 1: Summary of relevant product properties of the investigated EHPs.

Species	Product | Strength class	Producer	Adhesive[a]	Lam. thickness [mm]	Strength grading
European beech	Glulam | GL 48h	nH[b]	PUR	25	[17]
	Glulam | GL 40h				
	Glulam | GL 32h				
European ash	Glulam | GL 48h	nH	PUR	34	nH[e]
	Glulam | GL 40h				
European oak	Glulam | ---------	nH	PRF	31	- [f]
Sweet chestnut	Glulam | GL 24h	Filippi SA[c]	PUR	40	[18]
European beech	LVL | GL 75	Pollmeier[d]	PRF	3	-
Norway spruce	Glulam | GL 28h	nH	PUR	34	[19]

[a] Type of adhesive used for face gluing of the laminations. | [b] Neue Holzbau AG, Lungern, CH.
[c] Filippi SA, Airolo, CH. | [d] Pollmeier Massivholz GmbH & Co.KG, Creuzburg, GER.
[e] Internal strength grading criteria developed by the company Neue Holzbau AG.
[f] Besides excluding boards with large knots, no strength grading was applied.

2.2 Methods

2.2.1 Concept

The aim of the study was to determine the influence of the wood MC on the compressive strength and the modulus of elasticity parallel to the grain. In order to exclude (as far as possible) the influence of parameters other than the wood MC, such as the density, the growth ring width or the sawing pattern, the following procedure was chosen for the production of the specimens:

1. Glulam elements with a length of 1100 mm and cross-sectional dimensions of 160 mm × 90 mm were produced. The LVL elements were 2000 mm long and had cross-section dimensions of 80 mm × 80 mm (Figure 2a).
2. Subsequently, the elements were cut into four pieces (quadruplets) with dimensions of 78 × 90 × 468 mm^3 (glulam; Figure 2b,c) and 80 × 80 × 480 mm^3 (LVL). The properties of the quadruplets, such as the density, the growth ring width and the sawing pattern, were almost identical.
3. One "piece of waste" of each element was kept and used for the determination of the initial MC.
4. Finally, each of the four quadruplets was stored in a chamber with different climatic conditions (see section 2.2.2) in terms of temperature and relative humidity of the surrounding air.

Figure 2: In order to receive almost identical specimens (with regard to density, annual ring width, etc.) in all climatic conditions, glulam and LVL elements were labeled (a) and then cut into half in the longitudianl (b) and transversal direction (c).

2.2.2 Climatic conditions: Relative humidity and temperature

After the test specimens had been cut, labelled and measured, they were conditioned in climate chambers or climate cabinets. The climatization aimed at obtaining the broadest possible spectrum of different humidity ranges in order to determine the influence of the wood MC on the compressive strength and the modulus of elasticity parallel to the grain. Table 2 provides an overview on the climatic conditions (temperature in °C and relative humidity in %) and the number of specimens per product and climatic condition. Due to the limited availability of the climate chambers and cabinets, unfortunately, not all products could be stored under the same conditions.

Table 2: Number of specimens per product, strength class and climatic condition.

| | | Temperature [°C] \| Relative humidity [%] | | | | | |
Species	Product	20°|30%	20°|50%	20°|65%	20°|75%	20°|85%	20°|95%
	Glulam | GL 48h	4	4	8	4	-	4
European beech	Glulam | GL 40h	8	8	14	6	-	8
	Glulam | GL 32h	14	14	20	6	-	14
European ash	Glulam | GL 48h	6	6	6	-	6	-
	Glulam | GL 40h	6	6	6	-	6	-
European oak	Glulam | ---------	11	11	11	-	-	11
Sweet chestnut	Glulam | GL 24h	6	6	6	-	-	6
European beech	LVL | GL 75	6	6	6	-	-	6
Norway spruce	Glulam | GL 28h	6	6	6	-	6	-

2.2.3 Compression tests

In total, 300 compression tests parallel to the grain were carried out under displacement controlled loading regime (v_{test} = 0.02 mm/s) on a servo-hydraulic testing machine (Figure 3a) in accordance with EN 408 [20]. The length of the specimens was l_c = 6 × b_{min}, i.e., either 468 mm (glulam) or 480 mm (LVL).

The compressive MOE parallel to the grain was determined based on local vertical displacements over a length of $l_{E,c}$ = 4 × b_{min} recorded with linear variable differential transducers (LVDT) on two opposite sides (Figure 3b). The LVDTs were disassembled at a level of 40% of the expected maximum force. Afterwards, the force was increased until failure occurred or until the resistance dropped by more than 20% (Figure 3c) compared to the maximum force.
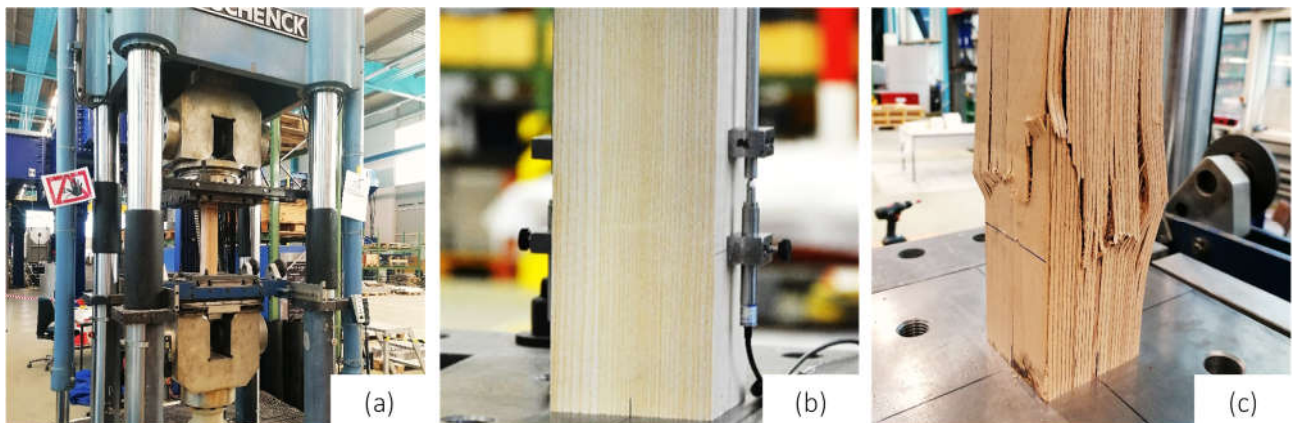

Figure 3: The compression tests were performed on a servo-hydraulic testing machine of type "Schenck 1600" (a). By means of LVDT sensors mounted on two opposite sides of the specimens, the longitudinal displacements were measured and used to determine the MOE parallel to the grain (b). After disasembling the LVDTs, the force was increased displacement-controlled until failure occurred or until the restistance dropped by 20% (c).

The compressive strength parallel to the grain ($f_{c,0}$) was calculated based on the actual cross-section dimensions measured just before the tests ($b_{1,is}$ and $b_{2,is}$) and the maximum force (F_{max}) using Formula 1.

$$f_{c,0} = \frac{F_{max}}{b_{1,is} \cdot b_{2,is}} \qquad (1) \qquad\qquad u\,[\%] = \frac{m_u - m_0}{m_0} \cdot 100\,\% \qquad (2)$$

The compressive modulus of elasticity parallel to the grain ($E_{c,0}$) was calculated based on the actual cross-section dimensions measured just before the tests and a linear regression analysis of the stress-strain curve in a range between $0.1 \times F_{max}$ and $0.4 \times F_{max}$. As requested by the test standard EN 408 [20], the coefficient of determination was higher than 0.99 for all of the 300 tests carried out.

2.2.4 Determination of the moisture content (MC)

The MC (u) of all 300 specimens was determined using the dry oven method according to [21]. Small segments were cut from the centre of the specimens directly (≤ 1.5 h) after the compression test. The MC was calculated using Formula 2, based on the mass of the cut segments before (m_u) and after the drying process (m_0). The latter took between 4 and 6 days.

3 Results and Discussion

3.1.1 Moisture contents resulting from different climatic conditions

Table 3 summarizes the mean values (x) and the standard deviations (s) of the MC determined for the EHPs having been exposed to different climatic conditions. The MC of glulam made from European beech and ash was found to be about 1% lower compared to Norway spruce glulam in all climatic conditions. The absolute values and the trend of the MC being lower for hardwoods compared to softwoods agree well with findings by Schaffrath [22]. The high MC of European beech glulam in climate 20|75 is attributed to the fact that these specimens had been stored in a 20|95 climate initially. Therefore, desorption occurs, which results in higher MC compared to adsorption.

The MC values determined for sweet chestnut were very similar to the ones of Norway spruce and agree well with the values reported in [22] as well as the values specified in EC 5 [13] for SC 1 (20|65 → 12%) and SC 2 (20|85 → 18%).

For European beech LVL, significantly lower MC values have been found compared to the other EHPs and Norway spruce glulam. Mainly, this is due to the production process where very dry veneers are glued together and, subsequently, all MC are considered to represent the adsorption curve. Benthien et al. [23] reported that both the desorption and adsorption curves of beech LVL correspond to those of solid beech wood.

For comparison of the different EHPs and the respective mechanical properties, reference MCs for SC 1 and SC 2 are listed in Table 4. The values are based on the results from this study and on the results reported in [22] and [23].

Table 3: Moisture content (MC) resulting for EHPs exposed to different climatic conditions (mean value ± standard deviation) in this study and values reported in [22] and [23].

x ± s	Temperature [°C] | Relative humidity [%]					
Species	20°|30%	20°|50%	20°|65%	20°|75%	20°|85%	20°|95%
European beech glulam	8.2 ± 0.21	9.6 ± 0.28	10.6 ± 0.34 11.2[1]	14.6 ± 0.39 [2]	- 13.8[1]	16.8 ± 0.46
European ash glulam	8.0 ± 0.11	9.3 ± 0.13	10.1 ± 0.17 11.4[1]	-	13.9 ± 0.33 14.5 [1]	-
European oak glulam	8.9 ± 0.24	9.8 ± 0.19	11.0 ± 0.17 11.2[1]	-	- 13.1[1]	15.9 ± 0.45
Sweet chestnut glulam	8.7 ± 0.33	10.1 ± 0.26	11.5 ± 0.27 -	-	- -	17.5 ± 0.51
European beech LVL	6.1 ± 0.14	7.0 ± 0.19 8.2[2)3)]	8.9 ± 0.22 10.6[3)]	-	- 17.1[3)]	16.9 ± 0.37 22.4[3)]
Norway spruce glulam	8.9 ± 0.15	10.5 ± 0.18	11.7 ± 0.16 12.5[1]	-	16.0 ± 0.23 16.5[1]	-

[1] Values reported in [22]

[2] Desorption curve

[3] Values reported in [23]

The reference MC for European beech, ash, and oak glulam as well as European beech LVL in SC 1 (11%) and SC 2 (15%) can be assigned identically. The reference MC of sweet chestnut and Norway spruce glulam is slightly higher (12% | 17%).

Table 4: Reference moisture contents (u_{ref}) for the EHP in service classes 1 and 2. Exponents ϑ_i for the moisture correction of the compressive strength parallel to the grain (ϑ_1; Formula 3) and for the correction of the MOE parallel to the grain (ϑ_2; Formula 4).

EHP	Reference MC u_{ref} [%]		Exponents ϑ_i	
	SC 1	SC 2	ϑ_1 ($f_{c,0}$)	ϑ_2 ($E_{c,0}$)
European beech glulam	11	15	0.8	0.2
European ash glulam	11	15	0.8	0.2
European oak glulam	11	15	0.6	0.1
Sweet chestnut glulam	12	17	0.6	0.1
Norway spruce glulam	12	17	0.8	0.2
European beech LVL	11	15	0.8	0.2

3.1.2 Density

In order to check the successful implementation of the "quadruplet approach" (see 2.2.1), the density of all 300 specimens was determined just after production, i.e., when all specimens of a certain EHP type still had the same MC. The differences of the mean values of the density between series of a certain EHP, e.g., European beech glulam of strength class GL 40h, were below 3%.

The density of all 300 specimens was determined for a second time just before static testing (after conditioning in the climate chambers) with the specimen having a MC of u based on the actual mass (m_u) and the actual dimensions ($b_{1,u}$; $b_{2,u}$; l_u) (Formula 3). Consequently, the mass (numerator) but also the volume (denominator) increases due to adsorption and swelling effects, respectively.

$$\rho_u = \frac{m_u}{b_{1,u} \cdot b_{2,u} \cdot l_u} \qquad (3) \qquad\qquad f_{c,0,ref} = f_{c,0,u} \cdot \left(\frac{u}{u_{ref}}\right)^{\vartheta_1} \qquad (4)$$

Figure 4 shows plots of density vs. MC for the investigated EHPs and for Norway spruce glulam. The correlation between the parameters is generally low, i.e., the coefficient of determination (R^2) is below 0.05 for all products. However, a positive trend was found for most products. According to EN 384 [14], the density shall be corrected by 0.5% for each percent change in MC. This correction appears to be adequate for the investigated EHPs and Norway spruce glulam. However, for European beech LVL, the swelling effects seem to overcompensate the increase in mass for increasing MC and the correction factor according to EN 384 [14] is recommend not to be applied.

3.1.3 Compressive strength parallel to the grain

Figure 5 shows the compressive strength parallel to the grain plotted against the MC for the investigated EHPs and for Norway spruce. For all products, a strong influence, i.e., a significant decrease of strength for increasing MC, is obvious. For European beech LVL, results from tests at TU Munich (2012) and MPA Stuttgart (2013, 2014) (not publicly available) are included for the sake of comparison.

A power function as described by Formula 4 was found to best describe the relationship between the MC and the compressive strength parallel to the grain. Linear functions – as specified in the current version of EN 384 [14] for the correction of the compressive strength parallel to the grain depending on the MC – either do not allow to cover the ranges of high strengths for low MC or lead to negative strength values for high MC. By means of Formula 4 and applying the exponents ϑ_1 found in the regression analysis of the EHPs and Norway spruce glulam (Figure 5), all data was projected to the reference MC for SC 1 and 2 (Table 4). Subsequently, the 5%-fractile values of the compressive strength parallel to the grain ($f_{c,0,05}$) was calculated according to EN 14358 [24] assuming a lognormal distribution.

Table 5 presents the resulting values of the compressive strength parallel to the grain for SC 1 and 2. The compressive strength of European beech, ash and oak glulam and European beech LVL was up to 45% higher compared to Norway spruce glulam (GL 28h), showing the great potential of EHPs in the production of columns. The strength values found for sweet chestnut were slightly higher than those of Norway spruce glulam, demonstrating its potential for the substitution of softwood glulam.

In good agreement with EAD 130320-00-0304 [15] and SIA 265 [25], where a reduction factor of 0.8 is specified for SC 2 applications of glulam, reduction factors of 0.78 (beech, ash) to 0.83 (sweet chestnut, oak) were found (SC 2/SC 1 ratios of $f_{c,0,k}$ values).
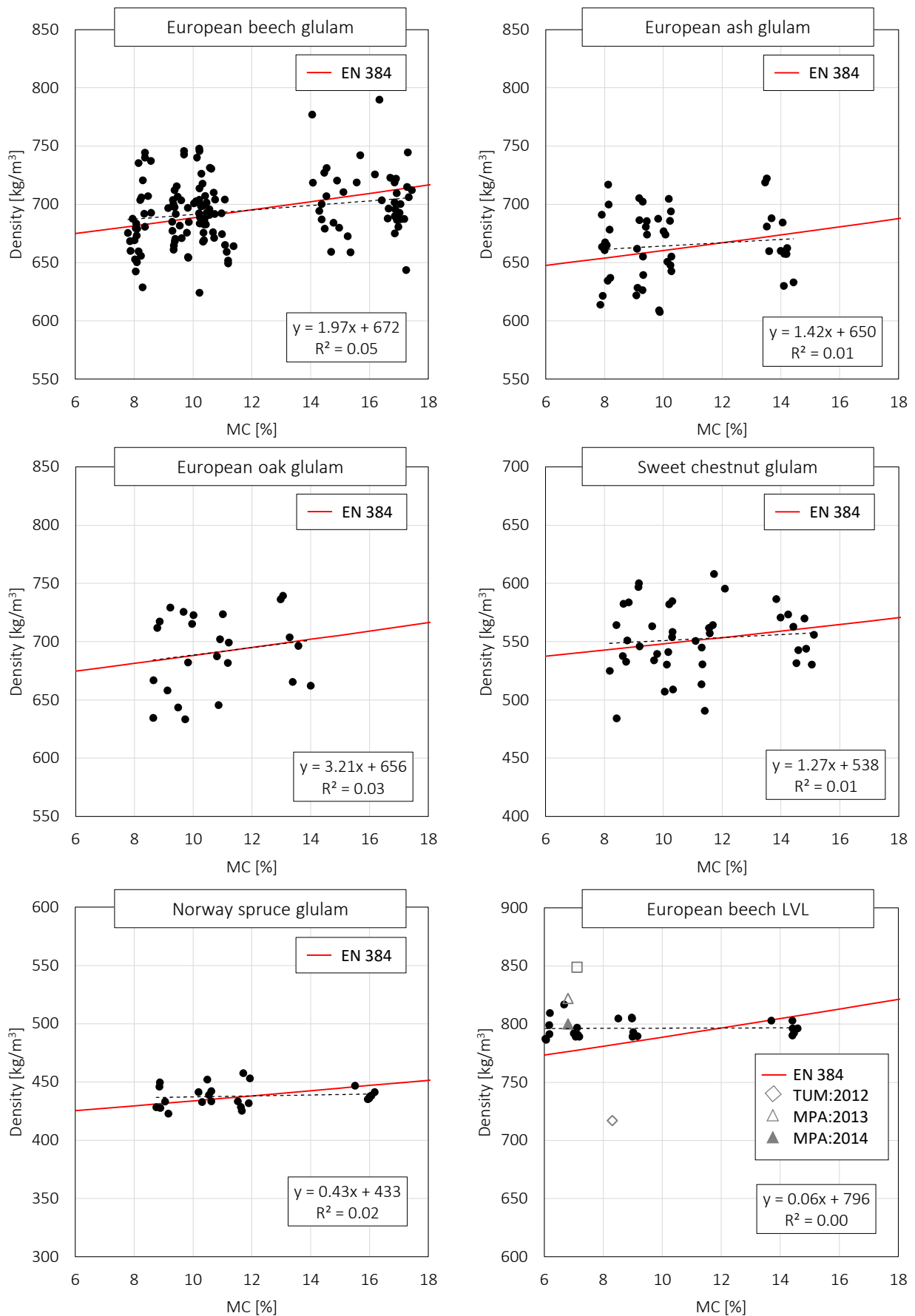
Figure 4: Density vs. moisture content. The functions and the coefficients of determination (R^2) resulting from a linear regression anaylsis are shown. For European beech LVL, results (mean values) from previous studies have been added to the plots.
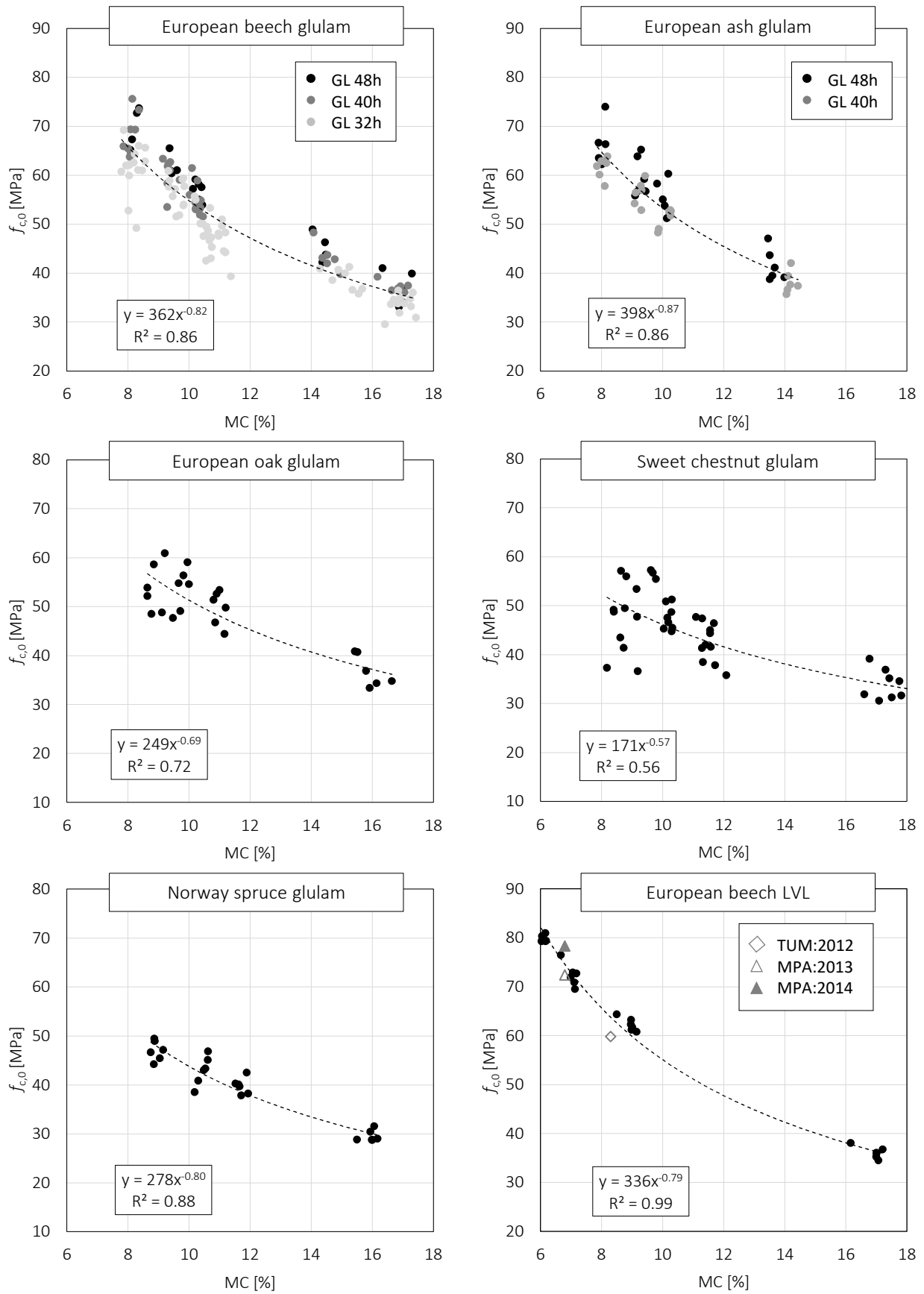
Figure 5: Compressive strength parallel to the grain vs. moisture content. The power functions fitted to the test data and the coefficients of determination (R²) are shown. For European beech LVL, results (mean values) from previous studies have been added to the plots.

Table 5: Compressive strength and MOE parallel to the grain for service classes 1 and 2 (in MPa). All values were calculated according to EN 14358 [24].

		European beech			European ash		European oak	Sweet chestnut	Norway spruce	Beech LVL
		GL 48h	GL 40h	GL 32h	GL 48h	GL 40h	-	GL 24h	GL 28h	GL 75
SC 1 [20 | 65]	$f_{c,0,mean}$	54.3	52.6	48.4	51.1	47.9	48.2	41.8	37.9	51.0
	$f_{c,0,05}$	48.6	48.0	44.1	46.4	43.5	43.7	37.9	34.4	46.4
	$E_{c,0,mean}$	15 600	14 500	13 700	15 200	14 200	11 300	11 800	13 000	14 600
	$E_{c,0,05}$	13 900	13 200	12 500	13 800	12 900	10 200	10 700	11 800	13 200
SC 2 [20 | 85]	$f_{c,0,mean}$	42.4	41.1	37.8	39.8	37.4	40.0	33.9	28.7	39.8
	$f_{c,0,05}$	37.9	37.5	34.4	36.2	33.9	36.3	30.8	26.0	36.2
	$E_{c,0,mean}$	14 700	13 600	12 900	14 300	13 400	10 900	11 400	12 100	13 700
	$E_{c,0,05}$	13 100	12 400	11 700	13 000	12 100	9 900	10 300	11 000	12 400

To make full use of the material's potential and to make use of the wood resources more efficiently, a differentiation between the two SC in the design of hardwood and softwood columns in compression by assigning different k_{mod} values is advised.

According to EN 384 [14], the compressive strength parallel to the grain determined in tests shall be corrected by 3% per percent difference between the actual MC and the reference MC of 12%. Comparison of the correction curve prescribed in EN 384 [14] with results from this study and test results reported in [26] (also referred to in [27]) show that the correction according to EN 384 underestimates the actual influence of the MC on the compressive strength parallel to the grain, i.e., the correction curve defined in EN 384 [14] is "too flat" (Figure 6).

In good agreement with the results of this study, Frese et al. [28] found a much stronger influence of the MC (i.e. about 4.5% per percent change in MC) on the compressive strength of Norway spruce glulam than defined in EN 384 [14].

In testing practice, this leads to an overestimation of the actual compressive strength parallel to the grain for specimens tested with a MC < 12%, and vice versa. For specimen tested with a MC of 8%, the actual compressive strength parallel to the grain at the reference MC of 12% is overestimated by more than 15% if the correction formula given in EN 384 [14] is applied.
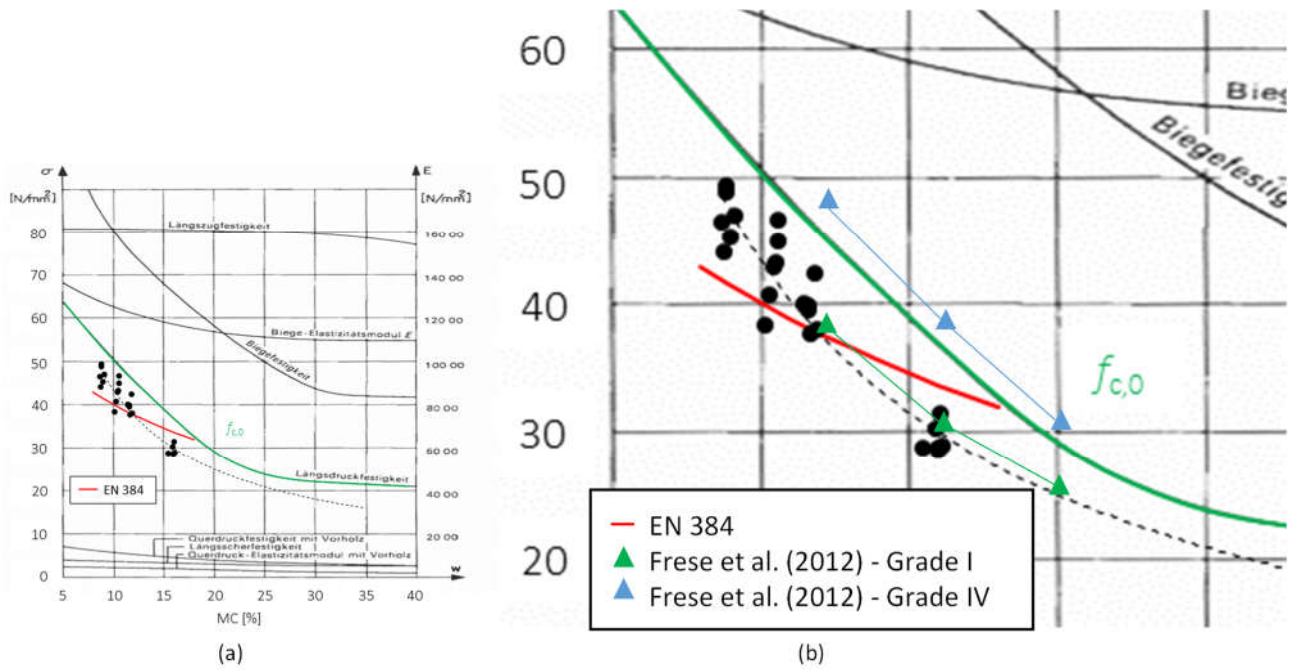
Figure 6: Influence of the moisture content on different mechanical properties of Norway spruce clear wood according to [26] (also referred to in [27]) and test data from this study (GL 28h) and from a study by Frese et al [28].

3.1.4 Compressive MOE parallel to the grain

Figure 7 shows the compressive MOE parallel to the grain plotted against the MC for the investigated EHPs and for Norway spruce. For all products besides European oak glulam, a moderate influence of the MC (between 1.1 and 1.5% per percent MC) was found. This finding agrees well with the formula for the MC correction of the MOE according to EN 384 [14] (1% per percent MC).

The ratio between the MOE parallel to the grain in SC 2 and SC 1 lies between 0.93 (beech, ash and Norway spruce glulam, beech LVL) and 0.96 (oak and sweet chestnut glulam). Hence, applying a reduction factor η_w for SC 2 as done in SIA 265 [25] is confirmed by the experiments carried out in this study, but the respective value of 0.9 is conservative for oak and sweet chestnut glulam. According to Eurocode 5 [13] and EAD 130320-00-0304 [15], no modification / reduction is required for the MOE for any kind of hardwood members used in SC 2.

Again, a power function as described by Formula 5 was determined to describe the relationship between the compressive MOE parallel to the grain and the MC best. By means of Formula 5 and applying the exponents ϑ_2 found in the regression analysis of the EHPs and Norway spruce glulam (Figure 7), all data was projected to the reference MC for SC 1 and 2 (Table 4).

$$E_{c,0,\text{ref}} = E_{c,0,u} \cdot \left(\frac{u}{u_{\text{ref}}} \right)^{\vartheta_2} \tag{5}$$
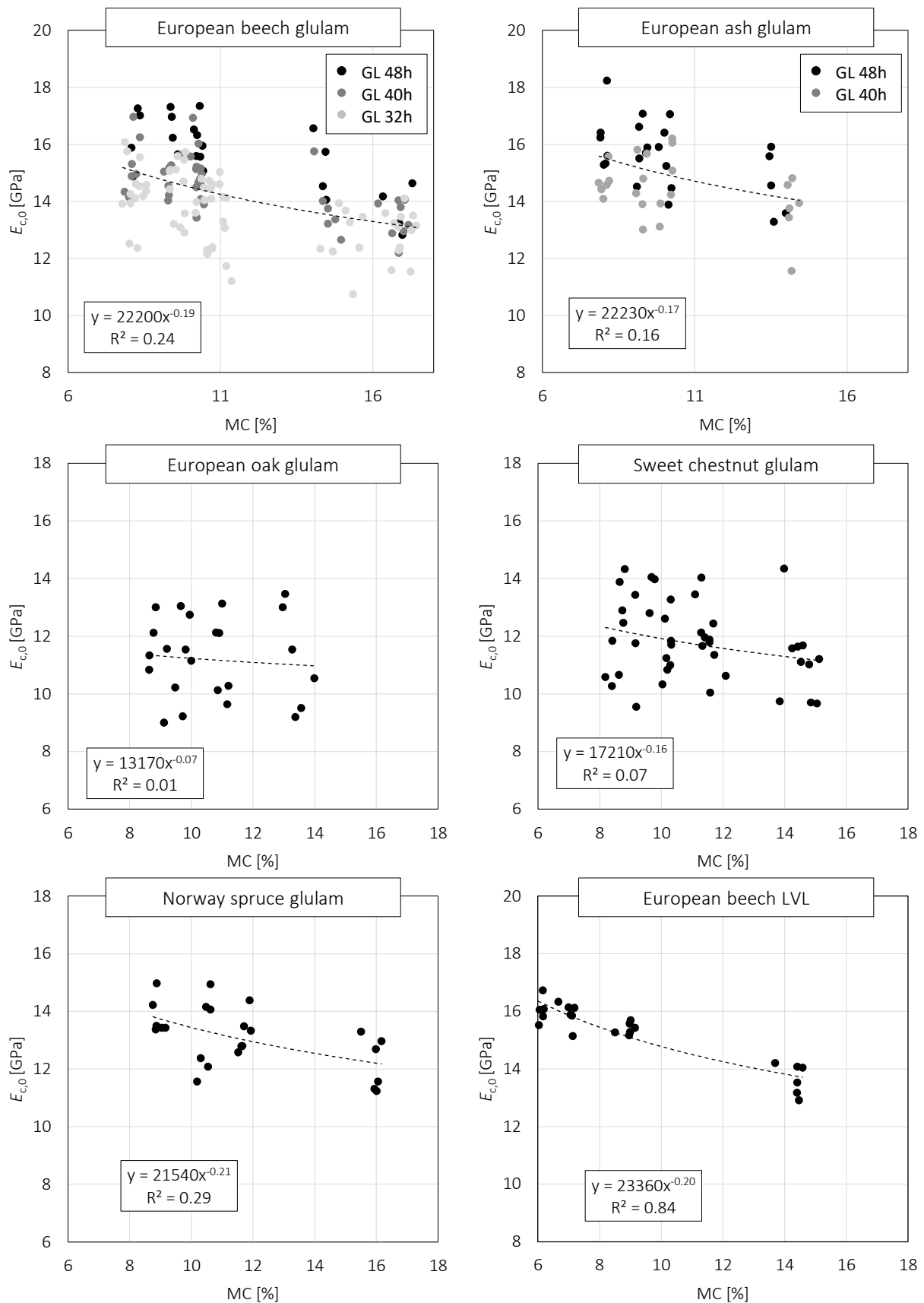
Figure 7: Compressive MOE parallel to the grain vs. moisture content. The power functions fitted to test data and the coefficients of determination (R²) are shown.

3.1.5 Further observations and recommendations

When conditioning the test specimens, it was observed that the definition of constant mass according to EN 408 [20] is not applicable to EHPs, i.e., changes in mass of less than 0.1% within 6h do not necessarily provide that the equilibrium MC has been reached. Therefore, a longer period (about 48h), after which the mass difference shall be checked, should be defined in EN 408.

According to EN 13183-1 [21], the sample for determining the MC using the dry oven method shall be cut from the middle part of the tested specimen. However, even if the specimens have been conditioned according to EN 408 [20], (small) differences in MC exist along the specimens' longitudinal axis. In case of compression tests parallel to the grain, small differences in MC can lead to large differences in strength (about 5% change in strength per percent change in MC; see section 3.1.3). In order to avoid relating strength results to wrong levels of MC, it is recommended to cut the sample for determining the MC as close as possible to the location of failure.

4 Conclusions

Based on the investigation of five glued-laminated engineered hardwood products (EHP) and Norway spruce glulam at moisture contents (MC) between 6 and 17%, the following conclusions regarding the compressive strength and MOE parallel to the grain can be drawn:

- The investigated glued-laminated EHPs show a great potential in the production of columns due to their excellent compression properties.

- For European beech, ash, and oak glulam as well as European beech LVL, up to 45% higher compressive strengths parallel to the grain compared to Norway spruce glulam (GL 28h) were found.

- The compressive strength parallel to the grain of sweet chestnut glulam was slightly higher, and the MOE slightly lower compared to Norway spruce glulam (GL 28h).

- When exposed to the same climatic conditions, different EHPs and Norway spruce glulam have different equilibrium MC. Reference MCs for all investigated EHPs for service class (SC) 1 and 2 according to Eurocode 5 [13] are presented in this paper.

- The formulae specified in EN 384 [14] allow for an appropriate moisture correction of the density and the MOE parallel to the grain.

- The moisture correction according to EN 384 [14] underestimates the influence of the MC on the compressive strength parallel to the grain. A more accurate correction formula is presented in this paper.

- The strength values in SC 1 were found to be up to 30% higher compared to SC 2. This is in good agreement with the reduction factor of 0.8 for members used in SC 2 as defined in EAD 130320-00-0304 [15] and SIA 265 [25].

- The MOE values parallel to the grain in SC 2 were found to be 7% (beech and ash glulam, beech LVL, Norway spruce) and 4% (oak and sweet chestnut glulam) lower compared to SC 1. A reduction of the MOE in SC 2 for the first group of EHP as specified in SIA 265 [25] with $\eta_w = 0.9$ appears to be appropriate.

- To make full use of the material's potential and to make use of the wood resources more efficiently, a differentiation between the SC in the design (k_{mod}) of hardwood as well as softwood columns subjected to compression loading is advised.

5   Acknowledgement

6   References

[1]   Frühwald, A; Ressel, JB; Bernasconi, A (2003) Hochwertiges Brettschichtholz aus Buchenholz. Hamburg, Germany.

[2]   Blaß, HJ; Denzler, J; Frese, M; Glos, P; Linsenmann, P (2005) Biegefestigkeit von Brettschichtholz aus Buche. Karlsruher Berichte zum Ingenieurholzbau - Band 1, Karlsruhe, Germany.

[3]   Ehrhart, T; Steiger, R; Lehmann, M; Frangi, A (2019) European beech glued laminated timber: Lamination strength grading, production and mechanical properties. European Journal of Wood and Wood Products, 78:971-984.

[4]   Kovryga, A; Schlotzhauer, P; Stapel, P; Militz, H (2019) Visual and machine strength grading of European ash and maple for glulam application. Holzforschung.

[5]   Westermayr, M; Stapel, P; Van de Kuilen, JWG (2018) Tensile and compression strength of small cross section beech glulam members. Paper 51-12-2, INTER - Meeting 51, pp.307-322, Tallinn, Estonia.

[6]   Plos, M; Fortuna, B; Straze, A; Turk, G (2018) Visual grading of beech wood - a decision tree approach. WCTE, Seoul, Korea.

[7]   Sauter, UH; Breinig, L (2016) European hardwoods for the building sector: Reality of today - possibilities for tomorrow, WP 1 - Hardwood resources in Europe: Standing stock and resource forecasts. Workshop, Garmisch-Partenkirchen, Germany.

[8]   BAFU (2019) Jahrbuch Wald und Holz 2019. Bern, Switzerland.

[9]   Allgaier-Leuch, B; Streit, K; Brang, P (2017) Der Schweizer Wald im Klimawandel - Welche Entwicklungen kommen auf uns zu?

[10]   Lindner, M (2010) Climate change impacts, adaptive capacity, and vulnerability of European forest ecosystems. Forest Ecology and Management, 259 (4):698-709.

[11]   prEN 14080-2 (n.d.), Timber structures - Part 2: Glued laminated timber and glued laminated solid timber made of hardwood - Requirements. CEN.

[12] Ehrhart, T; Steiger, R; Palma, P; Frangi, A; Gehri, E (2020) Glulam columns made of European beech timber: compressive strength and stiffness parallel to the grain, buckling resistance and adaptation of the effective-length method according to Eurocode 5. Materials and Structures, 53 (91).

[13] EN 1995-1-1 (2010) Design of timber structures - Part 1-1: General - Common rules and rules for buildings. CEN.

[14] EN 384 (2019) Structural Timber - Determination of characteristic values of mechanical properties and density. CEN.

[15] European Assessment Document EAD 130320-00-0304 (2018) Glued laminated timber made of solid hardwood. EOTA.

[16] Lehmann, M; Clerc, G; Lehringer, C; Strahm, T; Volkmer, T (2018) Investigation of the bond quality and the finger joint strength of beech glulam. WCTE, Seoul, Korea.

[17] Ehrhart, T; Fink, G; Steiger, R; Frangi, A (2016) Strength grading of European beech lamellas for the production of GLT and CLT. Paper 49-5-1, INTER - Meeting 49, pp.29-43. Graz, Austria.

[18] Bedelek, E (2019) Caractérisation mécanique du bois de châtaigne. HEIG-VD.

[19] DIN 4074-1 (2012) Strength grading of wood - Part 1 - Coniferous sawn timber. DIN.

[20] EN 408 (2012) Timber structures - Structural timber and glued laminated timber - Determination of some physical and mechanical properties.

[21] EN 13183-1 (2002) Moisture content of a piece of sawn timber - Part 1: Determination by oven dry method. CEN.

[22] Schaffrath, J (2015) Untersuchungen zu Feuchtetransportvorgängen und feuchteinduzierten Verformungen sowie Spannungen bei Betrachtung verschiedener Holzarten und unterschiedlicher klimatischer Randbedingungen. TU Munich.

[23] Benthien, JT; Riegler, M; Engehausen, N; Nopens, M (2020) Specific dimensional change behavior of laminated beech veneer lumber (BauBuche) in terms of moisture absorption and desorption. Fibers, 8 (7).

[24] EN 14358 (2016) Timber structures - Calculation and verification of characteristic values. CEN.

[25] SIA 265 (2021) Holzbau. Schweizerischer Ingenieur- und Architektenverein. Zurich, Switzerland.

[26] EMPA-Bericht Nr. 183 (1955): Über den Einfluss von Wassergehalt, Raumgewicht, Faserstellung und Jahrringstellung auf die Festigkeit und Verformbarkeit schweiz. Fichten-, Tannen-, Lärchen-, Rotbuchen und Eichenholzes.

[27] Dubas, P (1981) Einführung in die Norm SIA 164 Holzbau.

[28] Frese, M; Enders-Comberg, M; Blass, HJ; Glos, P (2012) Compressive strength of spruce glulam. European Journal of Wood and Wood Products 70:801-809.

DISCUSSION

The papers was presented by T Ehrhart

P Dietsch agreed to differentiate K_{mod} between bending and compression from a scientific point of view but stressed that this issue should also be viewed from a design perspective point of view, think of e.g. members under combined loads. He asked how to ensure not having moisture distribution within the cross section. T Ehrhart said this was not checked but the specimens were conditioned in a constant climate chamber until weight change was acceptable.

R Brandner agreed about differentiating K_{mod}. He commented that wood drying/wetting has hysteresis behaviour. Since the study focused in the absorption phase there might be a 2 to 3% difference from the desorption phase. T Ehrhart said the hardwood product was typically glued at 9% MC, the product would always start from the absorption phase and change in MC would be slow; therefore, desorption would be unlikely. R Brandner said in bridges application absorption followed by desorption might happen. All agreed that there is no solution now.

T Reynolds and T Ehrhart discussed using oven dried method and climate chamber method to achieve target moisture.

C Sigrist commented that there is a lot of work needed for EN408 with the introduction of these new products. The third draft of the standard will be released soon and he encouraged comments and suggestions from the colleagues.

S Aicher agreed different K_{mod} for SC1 and SC2. He commented that there are some European technical documents on downgrading compression strength of hardwood (oak, chestnut etc.) with a single factor due to moisture effect. T Ehrhart will look into these documents.

Imperfections of slender glulam beams

Prof. Dr.-Ing. Ulrike Kuhlmann, Head of Institute

Janusch Töpler, M.Sc., Scientific Researcher

Institute of Structural Design, University of Stuttgart

Keywords: Imperfections, lateral torsional buckling, glulam beams, on-site measurements, assembly tolerances, numerical modelling

1   Introduction

Imperfection assumptions are essential for the design verification of imperfection-sensitive (slender) timber members and adjacent structural elements, including roof bracings and fork bearings (Larsen (1977)), (Kuhlmann & Hofmann (2016)). However only few imperfection measurements concerning timber buildings exist (Brüninghoff (1973)), (Dietsch & Henke (2010)), (Ehlbeck & Blaß (1987)), (Kessel & Kühl & Hall (2015)), yet there is a lack of sufficient data regarding slender roof girders. Furthermore, the equivalent imperfections in EN 1995-1-1 (2004), on which the verifications of in-plane buckling and lateral torsional buckling are based, are inconsistent (e.g. initial bow imperfections for glulam included in the effective length method in-plane buckling (k_c-method): $e_y \approx L/1100$ and lateral torsional buckling (k_{crit}-method): $e_y \approx L/288$ to $L/577$) (Ehlbeck & Blaß (1987)), (Heimeshoff (1986)). Consequently, due to the possibility of conservative assumptions of imperfections, load-bearing capacity reserves may be expected in the verification of timber members at risk of lateral torsional buckling, when using the effective length method or design verification according to second order theory. Also, in achieving a more economical design of fork bearings, there is a lack of know-

Figure 1.1. On-site imperfection measurement with a laser scanner Leica ScanStation P20 (building 2020-KW34).

ledge referring to the assembly tolerances of long-spanning roof structures (KUHLMANN & HOFMANN (2013)).

Within a DIBt research project (KUHLMANN & TÖPLER (2021 b)), measurements of the assembly tolerances of timber building structures were carried out by the Institute of Structural Design from 2020 to 2021 (Figure 1.1), in order to create a database of geometric imperfections of slender glulam beams and to develop consistent proposals for equivalent imperfections. These should contribute to the current revision of EN 1995-1-1 (2004) and the preparation of the new European standard "Execution of Timber Structures".

This paper presents the results of imperfection measurements on 139 slender glulam beams in 13 timber buildings using a laser scanner (Figure 1.1) conducted in 2020. Using numerical methods, equivalent imperfections and torsional moments at the fork bearings are determined. The results are compared with current design rules.

2 Imperfection measurements

2.1 General

As part of the DIBt research project DIBt - ZP 52-5-13.194, assembly tolerances of approximately 25 timber buildings shortly after assembly have been determined with a laser scanner from 2020 to 2021. Buildings with glulam beams made of softwood and beam-columns made of beech LVL were surveyed. The measurements were carried out in cooperation with the Institute for Photogrammetry at the University of Stuttgart. This paper reports on the measurement results of the glulam beams.

Detailed explanations can be found in the interim report of the research project (KUHLMANN & TÖPLER (2021 b)).
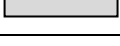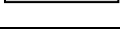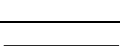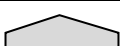
2.2 Measurement programme, setup and execution

2.2.1 Measurement programme

Table 2.1 lists the 13 buildings with 139 slender glulam beams reported. To ensure the representativeness of the sample of timber buildings, typical beam geometries (span L, cross-sectional dimensions H and W and beam shape) and material grades commonly used in construction practice in the DACH (Germany, Austria, Switzerland) region were covered. The timber buildings' elements were fabricated und erected by different manufacturers and assembly companies.

All buildings were single-storey industrial halls with roof constructions made of slender glulam beams (see e.g. Figure 1.1). The beam span of the evaluated members ranged between 6.9 m and 42.4 m, cross-sectional height between 0.69 m and 2.68 m and cross-sectional width between 0.14 m and 0.26 m. Material grades of the beams were GL 24h and GL 28c and roof bracings were realised by means of steel/timber diagonals, glulam roof panels or fixed columns.

Table 2.1. Measured buildings with slender glulam beams.

Building	Beam shape	Span [m]	Cross-sectional height/width	Material	Bracing system	Location (in Germany)
2020-KW23		14.5	5.1	GL 28c	Steel diagonals	73278 Schlierbach
2020-KW27		29.6	12.2	GL 24h	Timber diagonals	84359 Simbach a. Inn
2020-KW32		23.6	9.0	GL 28c	Timber diagonals	74595 Langenburg
2020-KW33		17.9	8.8	GL 28c	Steel diagonals	84577 Tüßling
2020-KW34		13.1 - 17.5	6.5 - 12.6	GL 24h	Timber diagonals + fixed columns	89616 Rottenacker
2020-KW38_1.1		17.4	5.0	GL 28c	Glulam roof panel	68199 Mannheim
2020-KW38_1.2		9.9	3.6	GL 24h	Glulam roof panel	68199 Mannheim
2020-KW38_1.3		10.0	3.8	GL 24h	Glulam roof panel	68199 Mannheim
2020-KW38_1.4		6.9	2.9 + 4.8	GL 24h	Glulam roof panel	68199 Mannheim
2020-KW38_2		42.4	10.6	GL 28c	Timber diagonals	86199 Augsburg
2020-KW45_1.1		23.5	9.2	GL 28c	Steel diagonals	67112 Mutterstadt
2020-KW45_1.2		26.5	9.3	GL 28c	Steel diagonals	67112 Mutterstadt
2020-KW47		20.8	6.8	GL 24h	Timber diagonals	91320 Ebermannstadt

The measurements were taken directly after assembly and alignment of the timber structures. In some cases, the structures were loaded by roofing and wall cladding in addition to their self-weight. The influence of wind actions during the measurement can be neglected, as the estimated Beaufort number describing the wind speed was always ≤ 5 (fresh breeze).

The measured geometry of the structures thus particularly includes influences from assembly, transport and production. Influences from the loading, the long-term behaviour and slip within the connections, which might occur at the first significant loading of the roof structures, are not included in the measurement results (or only included to a negligible extent).

2.2.2 Measurement setup and execution

The measurements were carried out with a Leica ScanStation P20 laser scanner (Figure 1.1), which records measurement points in a grid of 3.1 mm x 3.1 mm when assuming a distance of 10 m (Leica Geosystems AG (2013)). Using several measurement locations per building, a 3D point cloud of the entire structure was generated from the

ground surface (Figure 2.1). The total measurement time per building was between 1.5 and 5 hours.

In addition, the air temperature and humidity and, if possible, the wood moisture content were determined in at least three structural elements per building with a Trotec T2000 multifunctional measuring device. Furthermore, information was collected concerning the building structure, material, manufacture, transport, assembly process, weathering, surface quality and any damage to the timber members.

2.3 Measurement results

2.3.1 *Evaluation*

The measurement error of a measurement point at a distance of the laser scanner to the object of approx. 15 m is specified in the laser scanner manual as approx. 1 mm in the x, y and z directions (position accuracy and range noise) (LEICA GEOSYSTEMS AG (2013)). This coincides with observed deviations when evaluating the measurement results of individual point coordinates. Therefore, in the evaluation, average values of the point coordinates of 200 to 1000 measuring points were always calculated, whereby the accuracy of the averaged point coordinates could be increased to less than 0.1 mm (at a confidence level of 90 % according to (FISCHER (2003)) in the x, y and z directions. Since this is a random error, with expected horizontal bow imperfections e_y of the beams of approx. L/1000 = 6.9 mm (Table 2.1, min L = 6.9 m), the measuring accuracy of the laser scanner is sufficient.

The point clouds (Figure 2.1) were automatically evaluated using Matlab software. The coordinate system used is shown in Figure 2.2. The results of the evaluation are the y and z coordinates of the beam axis over the beam length (bow imperfections e_y) and the torsion of the cross-section around the x-axis (twist imperfections e_ϑ). Figure 2.3 shows examples of measured horizontal bow imperfections e_y and Figure 2.5 displays the twist imperfections e_ϑ over the beam length (x direction). e_ϑ describes the twist of a cross-section around the x-axis without units (gradient of a straight line to the vertical).
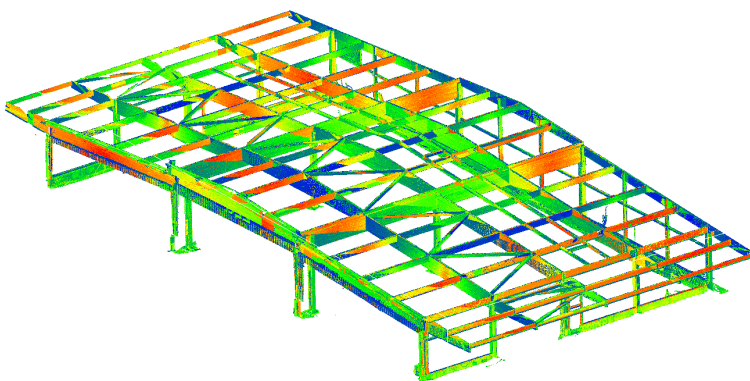

Figure 2.1. Point cloud from laser scan measurements (building 2020-KW34), the colour represents the intensity of the laser signal and has no further meaning.
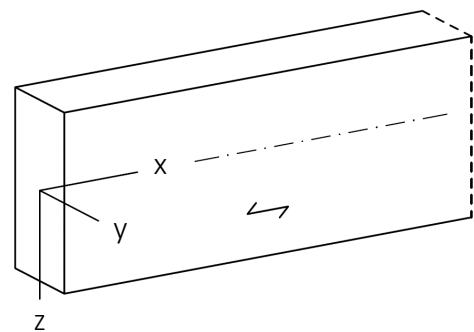
Figure 2.2. Generally used coordinate system.

2.3.2 Results

Figure 2.3 shows typical curves of the measured **horizontal bow imperfections e_y** of the beam axis over the beam length (x direction). The ideal planned beam position with the two supports " x " is shown as a dash line " - - ". Essential observations when assessing the bow imperfection curves are:

- The shape of the bow imperfection over the beam length usually (122 of 139 beams) corresponded approximately to a sinusoidal or parabolic curve (Figure 2.3 (b) and (d)). In some cases (11 of 139 beams) a bump shape occurred (Figure 2.3 (a)). However, in a few cases (6 of 139 beams) a change in the sign of the bow imperfections e_y was observed at a point of application of a compression purlin (Figure 2.3 (c)). In general, the bow imperfection curves could be represented by a sinusoidal half-wave (Kuhlmann & Töpler (2021 b)).

- Over the beam length, discontinuity points / outliers of individual y coordinates were sometimes observed, which were attributed to local defects (e.g. knotholes) or connected members such as purlins. These were neglected in the evaluation.

Figure 2.4 shows the maximum values of the measured horizontal bow imperfections e_y of 139 glulam beams, separated by buildings (see also Table 2.1). Additionally the results of measurements on 7 beams of (DIETSCH & HENKE (2010)) are added in the diagram. The x-axis displays the beam span (distance between the supports of the structural system) and the y-axis exhibits the bow imperfections e_y. Each data point represents the maximum measured horizontal bow imperfection (not necessarily at midspan, Figure 2.3) of a beam. In addition, the equivalent bow imperfection for calculations according to second order theory (EN 1995-1-1 (2004)) with L/400, and the value

(a) Building 2020-KW32 - Beam axis 7

(b) Building 2020-KW33 - Beam axis 4

(c) Building 2020-KW38_2 - Beam axis 25
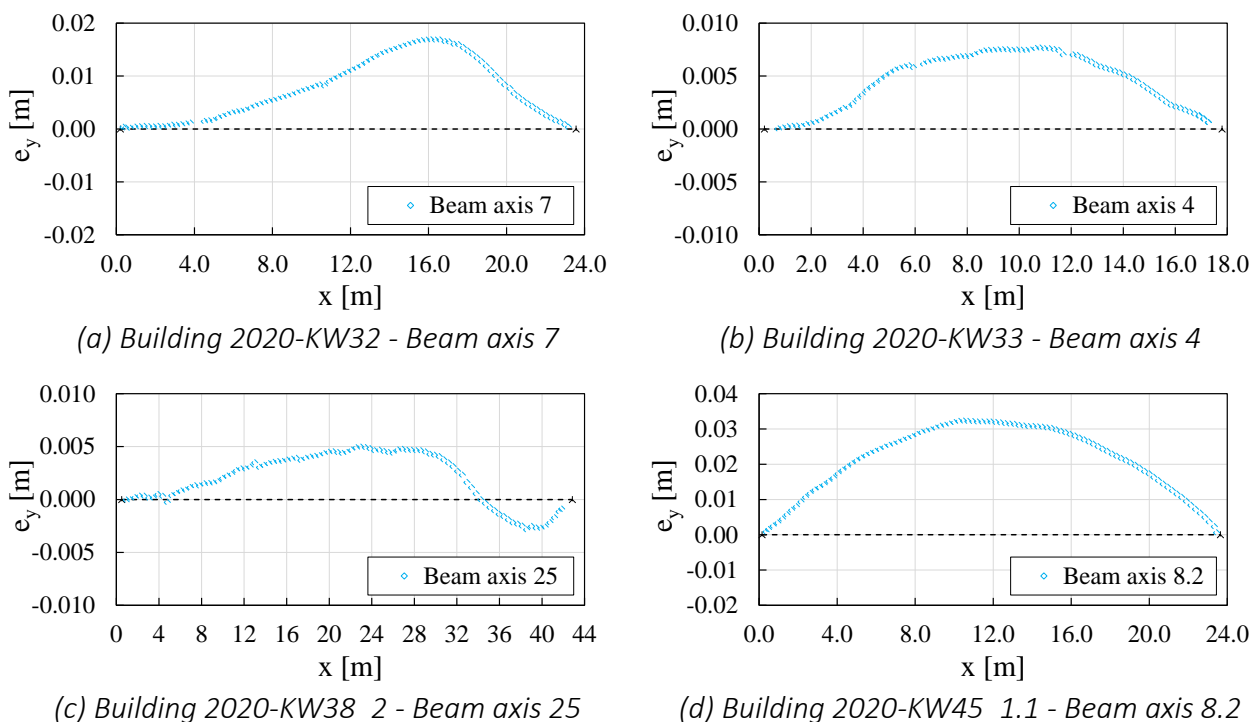
(d) Building 2020-KW45_1.1 - Beam axis 8.2

Figure 2.3. Typical curves of the measured horizontal bow imperfections e_y, or elevated top view of the beams, with x-axis as longitudinal axis.

L/1000 are displayed. All measured bow imperfections e_y were below L/400. A maximum bow imperfection e_y of L/1000 was exceeded by 18 of the 139 glulam beams (13 %). For buildings with beams with measured e_y > L/1000, assembly difficulties were reported due to small tolerances of connectors (2020-KW27), one of two roof bracings was not aligned according to generally accepted standards (2020-KW45_1.1), or the beams were braced by glulam roof panels and therefore could not be aligned horizontally during assembly (2020-KW38_1.1). When looking at the scatter band, the linear relationship between bow imperfection e_y and beam span assumed in EN 1995-1-1 (2004) is generally confirmed. A significant influence of the horizontal beam stiffness on the measured bow imperfections e_y could not be found.

The measurement results (DIETSCH & HENKE (2010)) are somewhat less favourable (Figure 2.4), which could be due to the fact that the 7 measured beams were not only loaded by their self-weight and were partly already subjected to long-term influences.

Figure 2.5 shows typical curves of the measured **twist imperfections e_ϑ** around the x-axis over the beam length (x direction). A positive twist e_ϑ means that the measured y coordinate of the upper edge of the beam is greater than that of the lower edge of the beam (see Figure 2.6). The ideal planned beam position with the two supports " x " is shown as a dash line " - - ". Essential observations when assessing the twist imperfection curves are:

- Unlike the bow imperfection curves, the shape of the twist imperfections over the beam length cannot be assigned to a generally valid curve shape.

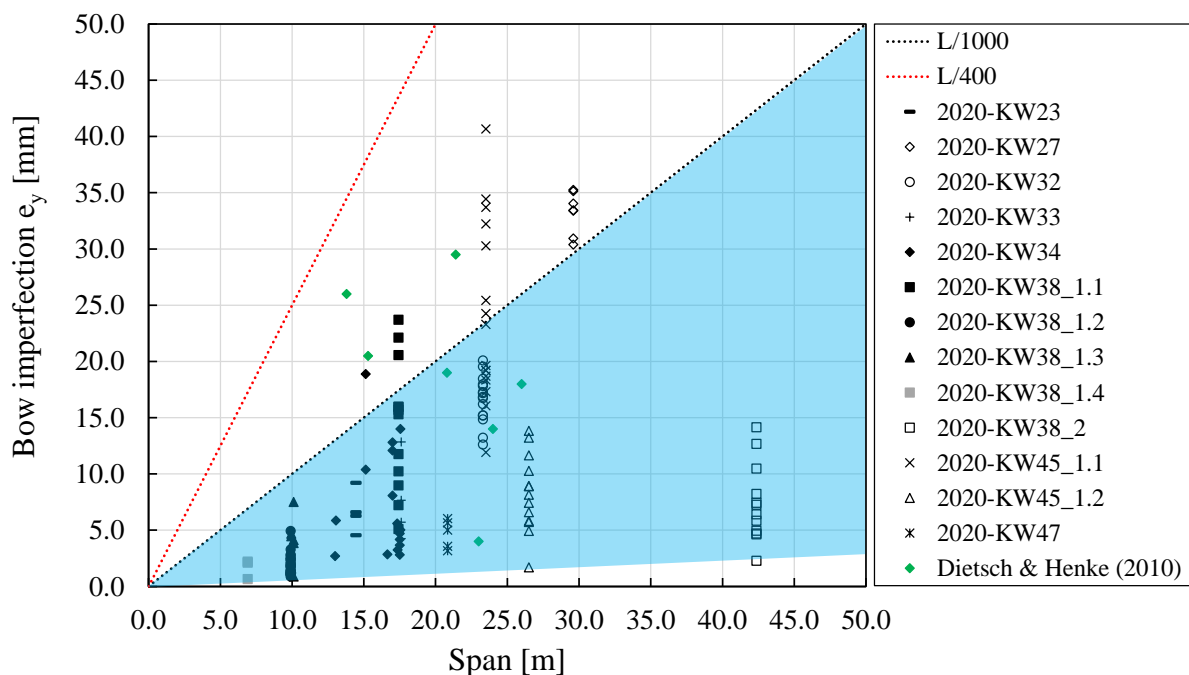- The maximum twist imperfection often occurred at supports (104 of 139 beams),

Figure 2.4. Maximum measured horizontal bow imperfections of 139 glulam beams with scatter band (blue) plotted for 87 % of the measured values, measurement results of 7 beams of (DIETSCH & HENKE (2010)) added, span shown on the x-axis and bow imperfections on the y-axis, each data point representing one beam.

especially if the fork bearings were designed as a reinforced concrete pockets.

- The shape of the twist imperfections along the beam length was in some cases (23 of 139 beams) approximately sinusoidal or parabolic (Figure 2.5 (a)). But in general, the maximum e_ϑ was either at one support (43 beams, Figure 2.5 (b)), at both supports with the same sign (44 beams, Figure 2.5 (c)), or at both supports with opposite signs (17 beams, Figure 2.5 (d)). Not all of the beams could clearly be assigned to one of these cases.

Figure 2.6 shows the maximum values of e_ϑ x H (differences of the measured horizontal displacements of the top edge to the bottom edge of the beam) of the 139 glulam beams, separated by buildings (see also Table 2.1). Additionally the results of measurements on 6 beams of (DIETSCH & HENKE (2010)) are added in the diagram. The x-axis displays the beam span (distance between the supports of the structural system) and the y-axis exhibits e_ϑ x H (twist imperfection x beam height). Each data point represents the absolute maximum value (not necessarily at midspan, Figure 2.5) of a beam. The measured values show increasing horizontal differential deformations e_ϑ x H between the top and bottom edge of the beam as the span increases. This relationship is also shown by the regression line e_ϑ x H = 0.0005 x L, which results from the evaluation of the data. The measurement results (DIETSCH & HENKE (2010)) fit well into the overall picture of the own measurement results.

The correlation e_ϑ = 0.05 x Width / Height found by (LARSEN (1977)) on solid wood test specimens cannot be confirmed by the measurement results.

In Figure 2.6 measured values of beams with fork bearings not made of reinforced concrete pockets (e.g. fork bearing by means of lateral timber plates), are marked in blue.

(a) Building 2020-KW23 - Beam axis 2

(b) Building 2020-KW32 - Beam axis 5

(c) Building 2020-KW33 - Beam axis 3
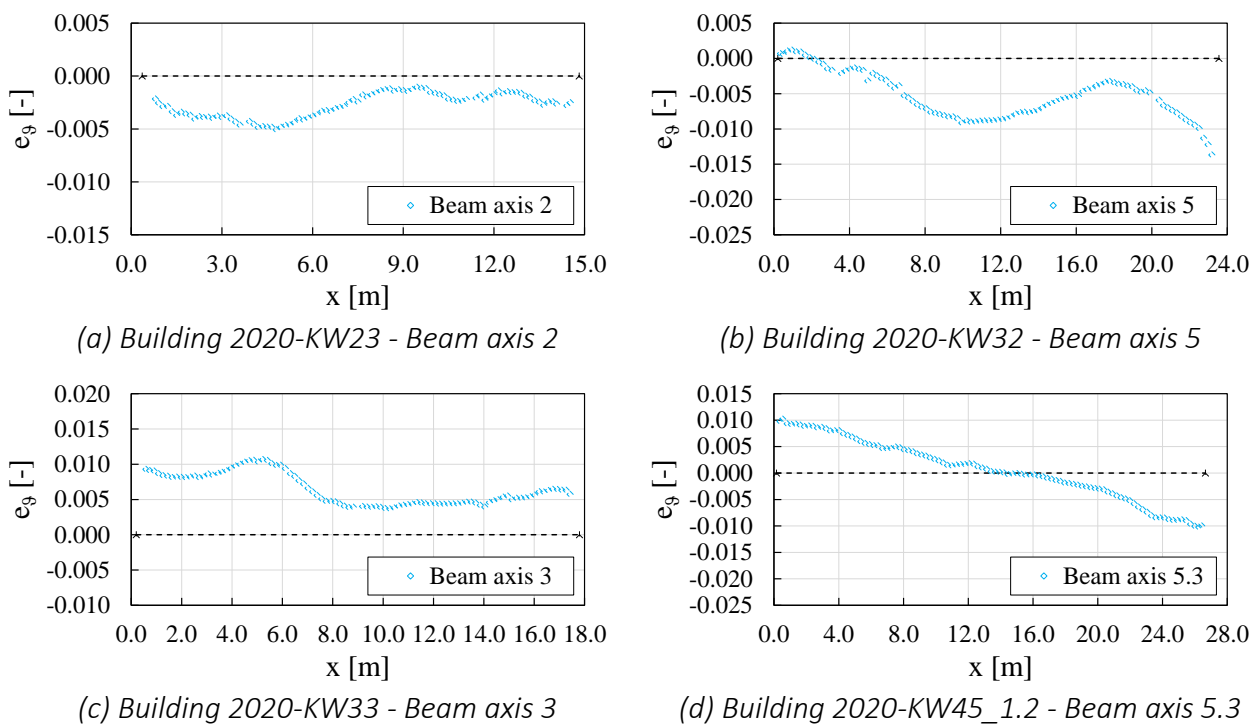

(d) Building 2020-KW45_1.2 - Beam axis 5.3

Figure 2.5. Typical curves of the measured twist imperfections e_ϑ around the x-axis, with x-axis as longitudinal axis.

Such a design seems to favour smaller assembly tolerances with regard to the twist imperfections.

3 Numerical simulations

3.1 General

The numerical calculations were executed with a FE-model in Abaqus/CAE 2018. The aim being to investigate the stability behaviour of the measured beams and to determine equivalent imperfections, as well as to examine the torsional moments at the supports. For each measured beam, calculations of eigenvalues (model 1), computations with measured imperfections (model 2) and with equivalent imperfections (model 3) have been carried out.

3.2 Numerical modelling and calculation procedure

In Figure 3.1 the numerical model of the building 2020-KW23 is displayed. The beam was modelled according to the ideal planned geometry. The horizontal stabilising influence of the roof bracing was taken into account by an equivalent beam, where the stiffness was determined based on (KESSEL & SIEDER & KREUZINGER (2020)). The stiffness of the purlins was mapped by equivalent springs acting only in y direction. For the glulam beam, 20-node quadratic brick elements with a mesh fineness of 100 elements in length, 10 elements in height and 8 elements in width were chosen. An orthotropic material model with mean material properties according to EN 14080 (2013), Poisson's ratios according to (NEUHAUS (1981)), bilinear elasto-plastic material behaviour under compression along the grain and linear elastic material behaviour under tension along
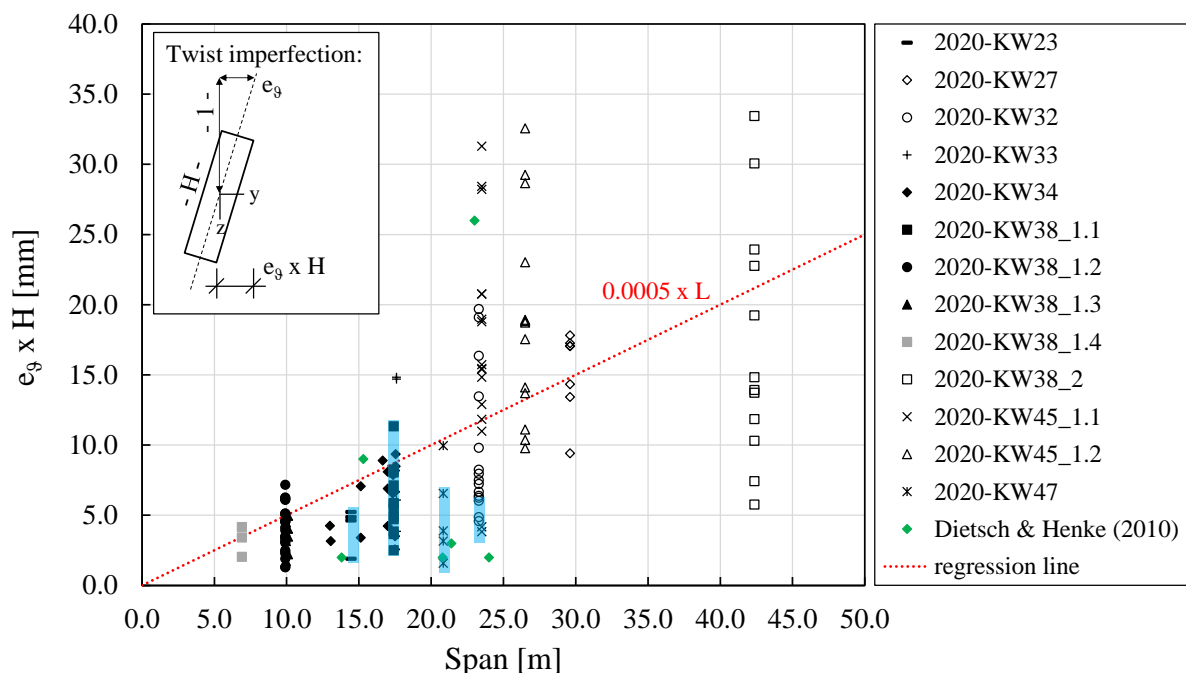

Figure 2.6. Maximum measured twist imperfections around the x-axis of 139 glulam beams, measurement results of 6 beams of (DIETSCH & HENKE (2010)) added, span shown on the x-axis and e_ϑ x H on the y-axis, each data point representing one beam, blue marked are measured values of beams with fork bearings not made of reinforced concrete pockets.
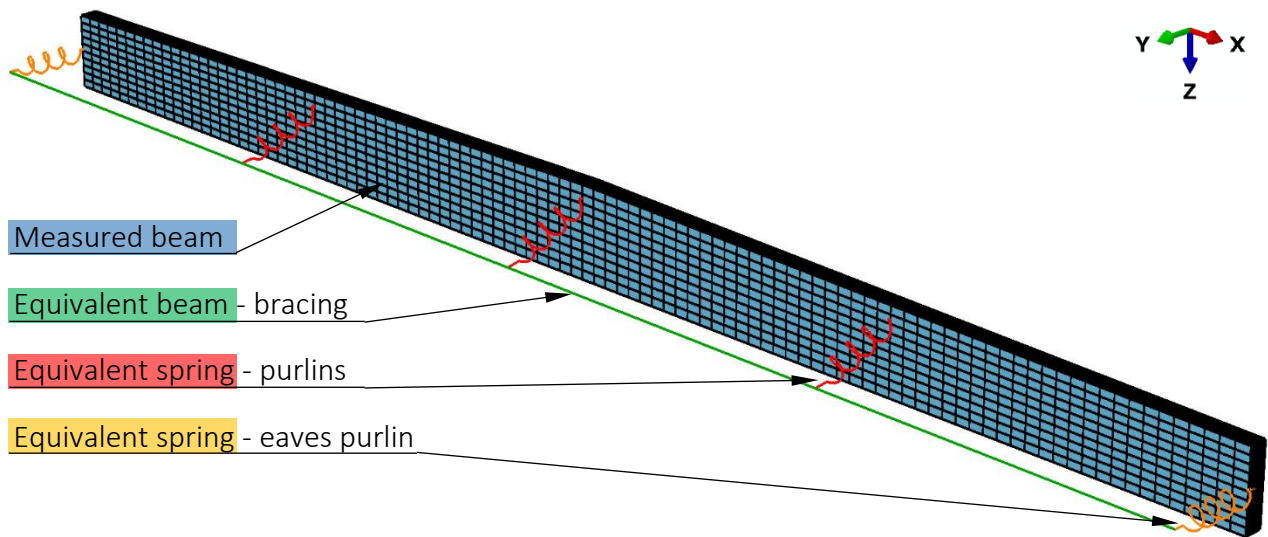
Figure 3.1. Numerical model of the double-tapered beams in building 2020-KW23.

the grain was used. The grain direction was chosen parallel to the bottom edge of the beam, also for curved beams. The load was applied by means of a line load at the upper edge of the beam. The calculations on model 2 and 3 were performed as geometrically and materially non-linear analysis with imperfections (GMNIA, prEN 1993-1-14 (2021)). The verification of the numerical models was achieved according to prEN 1993-1-14 (2021) (see also (KUHLMANN & TÖPLER (2021 a)).

In model 1 no imperfections and purely elastic behaviour were considered. Using model 1, the eigenvalues and eigenmodes of a beam were determined and the relative slenderness ratio $\lambda_{rel,m}$ and resulting $l_{ef,m}$ were evaluated (EN 1995-1-1 (2004)).

In model 2 the measured imperfections were assumed. By means of model 2, the maximum load-bearing capacity and associated line load q_{max} of a beam, at which the tensile stress σ_x reaches the characteristic bending strength $f_{m,k}$ (EN 14080 (2013)), was computed.

In model 3 the equivalent imperfections were applied. Due to the possible eigenmodes, both global equivalent imperfections (wavelength / 2 = beam span), local equivalent imperfections (wavelength / 2 = distance between purlins) and a superposition of both imperfections were included in preliminary investigations (Figure 3.2). While model 2 obtained the line load q_{max} which was then applied in model 3. The corresponding bending stresses and the ratio σ_x / $f_{m,k}$ (= utilization μ_x), which indicates
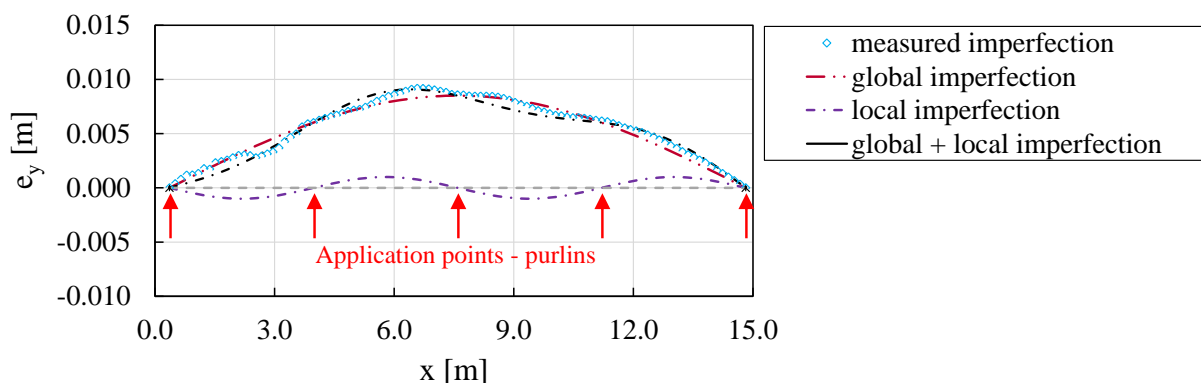

Figure 3.2. Bow imperfections for the numerical modelling, beam axis 2 in building 2020-KW23.

to what extend the approach of the equivalent imperfections is suitable to represent the real beam behaviour (with measured imperfections), were determined.

This procedure was carried out for all 139 beams. Additionally the torsional moments at the supports M_x were derived for all of the beams based on model 2 and 3.

3.3 Results and evaluation

3.3.1 General

The horizontal stiffness of the roof bracing on the measured buildings proved to be substantial, so that for the bending stress verification the governing eigenmode corresponded to a superposition of global and local imperfections (multiwave over the beam length; $0.69 \leq l_{ef,m} / a_{purlins}$ = effective length / distance between purlins ≤ 1.61).

In consultation with structural engineers, the assumption of combined global and local equivalent imperfections similar to Figure 3.2 seems to be too complex for design calculations. Therefore, for the calculations with equivalent imperfections (model 3), only global equivalent bow and twist imperfections (no local ones) were assumed (Figure 3.2). The differences in the load-bearing behaviour between model 2 and model 3 thus also include the influence of local imperfections between the application points of the purlins. The amplitudes of the global equivalent imperfections were chosen so that the area integral of the equivalent imperfections over the beam length corresponded to the area integral of the measured imperfections.

3.3.2 Equivalent imperfections

Table 3.1 illustrates the summarised results of the numerical calculations of the 139 beams. It can be demonstrated that with the chosen approach for the equivalent imperfections (model 3), almost identical utilisations $\mu_x = \sigma_x / f_{m,k}$ have been determined with computations considering measured imperfections (model 2). The mean utilisation $\mu_{x,Mz}$ (caused by bending moments around the weak axis M_z) is approximately 15 % smaller in model 3 than in model 2, which is due to the neglect of local imperfections. However, since the share of utilisation $\mu_{x,Mz}$ in the total utilisation μ_x is a maximum of 26 %, this is not significant. In general, the assumed equivalent imperfections are well suited to represent the load-bearing behaviour of the measured beams for bending.

Table 3.1. Numerically for 139 beams determined mean, min, max and COV values of the relative slenderness ratio $\lambda_{rel,m}$ and the maximum utilisation of the bending stress in x-direction μ_x, utilisation separated for the contributions of M_y and M_z.

	$\lambda_{rel,m}$	Model 2			Model 3		
		$\mu_x = \sigma_x / f_m$	$\mu_{x,My}$	$\mu_{x,Mz}$	$\mu_x = \sigma_x / f_m$	$\mu_{x,My}$	$\mu_{x,Mz}$
Mean	0.79	1.00	0.94	0.06	0.99	0.94	0.05
Minimum	0.52	1.00	0.77	0.01	0.90	0.77	0.01
Maximum	1.01	1.00	0.99	0.23	1.05	0.99	0.26
COV	0.16	0.00	0.05	0.84	0.02	0.05	0.94
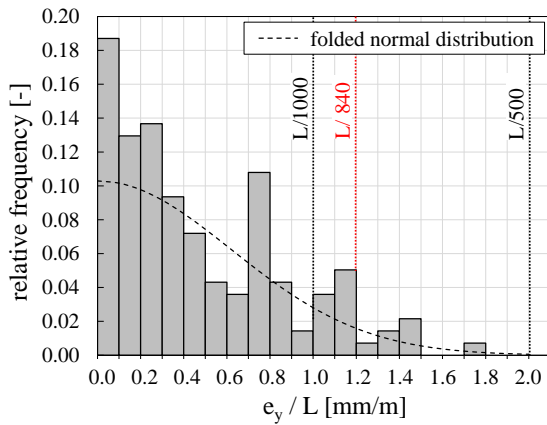
Figure 3.3. Frequency distribution of the computed equivalent bow imperfections e_y in relation to the beam span L of 139 glulam beams.
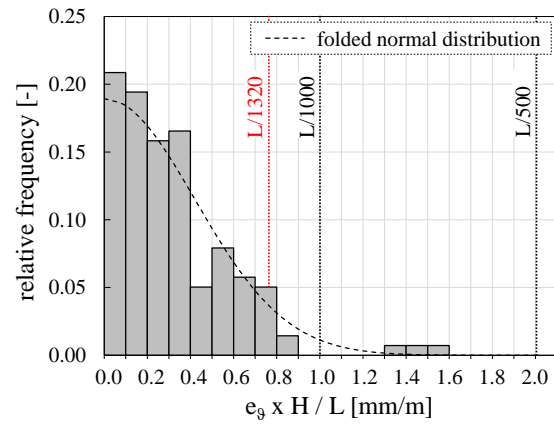
Figure 3.4. Frequency distribution of the computed equivalent twist imperfections e_ϑ x H (beam height) in relation to the beam span L of 139 glulam beams.

Figure 3.3 and Figure 3.4 display the frequency distributions of the absolute values of the equivalent bow and twist imperfections e_y / L and e_ϑ x H / L. A folded normal distribution represents a good approximation of the density functions. The 95 % quantile values of the equivalent imperfections are:

95 % quantile: e_y / L   = 1.19 mm/m ≙ L / 840   (bow imperfections)

                  e_ϑ x H / L   = 0.76 mm/m ≙ L / 1320   (twist imperfections)

3.3.3   Torsional moment at the supports

Figure 3.5 presents the maximum torsional moments M_x at the supports per building determined using model 2 ($M_{x,measured}$) and model 3 ($M_{x,equivalent}$) with measured or equivalent imperfections. In addition, the diagram contains calculation results accord-
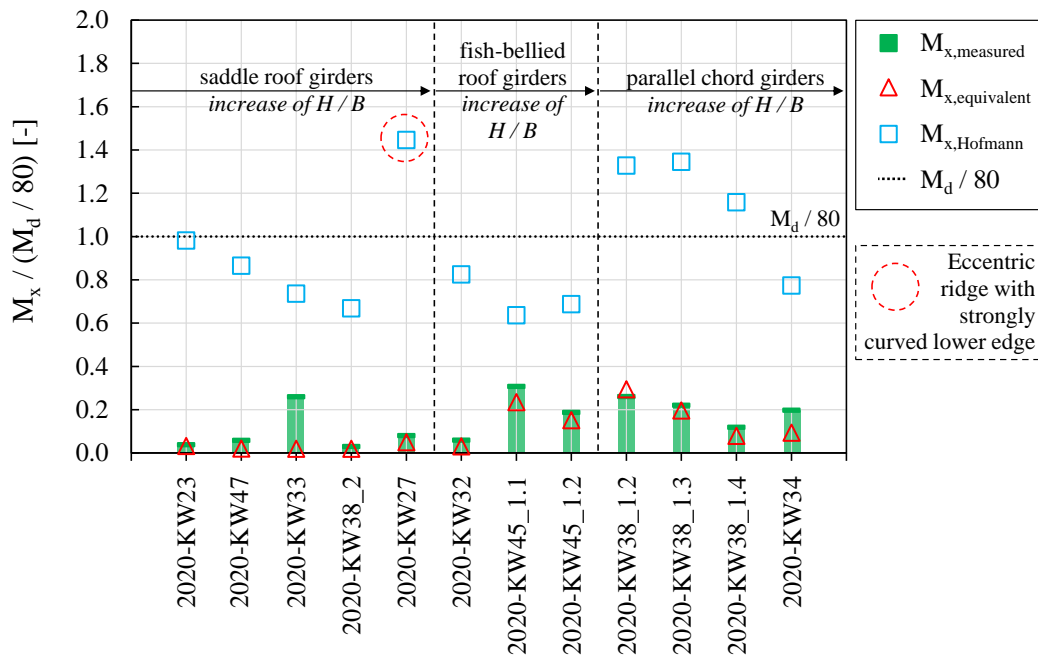
Figure 3.5. Numerically, according to DIN EN 1995-1-1/NA (2013) and (KUHLMANN & HOFMANN (2016)) determined maximum torsional moments M_x at the supports, per building, normalised to M_d / 80.

ing to the design approach in DIN EN 1995-1-1/NA (2013) with $M_x = M_d / 80$ and the results of the approaches ($M_{x,Hofmann}$) proposed by (KUHLMANN & HOFMANN (2016)). The data in Figure 3.5 are sorted by the beam shape and the ratio of beam height to width H / B and for comparability normalised to $M_d / 80$.

The major differences between $M_{x,measured/equivalent}$ and $M_{x,Hofmann}$ result from the different imperfection assumptions. According to EN 1995-1-1 (2004), bow imperfections of $e_y = L/400 + L/500$ were assumed in (KUHLMANN & HOFMANN (2016)), whereas the maximum measured bow imperfection was $e_y = L/578$ (2020-KW45_1.1). This is also reflected in the difference at building 2020-KW45_1.1 between $M_{x,measured}$ and $M_{x,Hofmann}$, which is approximately a factor of 2.

Compared to $M_d / 80$, the more accurate approaches of (KUHLMANN & HOFMANN (2016)) and the numerical calculations presented here take into account the influence of the beam shape and the cross-sectional ratio H / B.

It is evident that the imperfection assumptions in the current approaches for M_x are conservative. A revision of the design rules based on the generated database of measured imperfections and the more accurate approaches of (KUHLMANN & HOFMANN (2016)) is recommended.

4   Summary and outlook

The assembly tolerances have a decisive influence on the design of roof structures with slender glulam beams, yet there is a lack of sufficient data regarding these structures.

Chapter 2 reports on the results of imperfection measurements on 13 roof structures with 139 glulam beams as part of the research project DIBt - ZP 52-5-13.194 (KUHLMANN & TÖPLER (2021 b)). The measured horizontal bow imperfections e_y of the beams were always smaller than L/400 assumed in EN 1995-1-1 (2004) and in 87 % of the cases smaller than L/1000. Likewise significant twist imperfections e_ϑ around the longitudinal axis could be determined for most of the beams. The horizontal displacement from the upper edge to the lower edge of a beam was on average e_ϑ x H = 0.0005 x L. Twist imperfections e_ϑ of beams with fork bearings designed as reinforced concrete pockets were generally larger than with fork bearings made of timber.

It is demonstrated in Chapter 3 by numerical calculations on the 139 measured glulam beams that, assuming sinusoidal equivalent imperfections where the area integral corresponds to the one of the measured imperfections, very similar load-bearing capacities can be determined numerically, compared to calculations with measured imperfections. This may form the basis of recommended values for the new Eurocode 5. Additionally, it should be emphasised that the stiffness of the horizontal bracing of the girders, as well as the fork bearings, have a decisive influence on the load-bearing behaviour (KUHLMANN & HOFMANN (2016)).

The evaluation of the measurement results will continue. In addition to the completion of the evaluation shown in this paper, other possibly systematic effects such as the

assembly procedure, the bracing system, the beam shape, a group effect of several parallel girders, the long-term behaviour and material scatter will be investigated. Possible recommendations will also concern the reduction of tolerances in execution.

5   Acknowledgements

6   References

Brüninghoff, H. (1973): Spannungen und Stabilität bei quergestützten Brettschichtholzträgern (in German). Dissertation, University of Karlsruhe.

DIN EN 1995-1-1/NA (2013): Nationaler Anhang – National festgelegte Parameter – Eurocode 5: Bemessung und Konstruktion von Holzbauten – Teil 1-1: Allgemeines – Allgemeine Regeln und Regeln für den Hochbau. German Institute of Standardization (DIN), Berlin.

Dietsch, P. & Henke, K. (2010): Verformungsmessungen an weitgespannten Brettschichtholzträgern zur Ermittlung horizontaler Verformungen (in German). Research report, Technical University of Munich.

Ehlbeck, J. & Blaß, H. J. (1987): Zuverlässigkeit von Holzdruckstäben (in German). Research report, University Fridericiana Karlsruhe.

EN 1995-1-1 (2004): Eurocode 5: Design of timber structures – Part 1-1: General – Common rules and rules for buildings. European Committee for Standardization (CEN), Brussels, with corrections and amendments + AC:2006 and A1:2008.

EN 14080 (2013): Timber structures - Glued laminated timber and glued solid timber - Requirements. European Committee for Standardization (CEN), Brussels.

Fischer, L. (2003): Charakteristische Werte - ihre Bedeutung und Berechnung (in German). Bauingenieur, 78, p. 179–187.

Heimeshoff, B. (1986): Berechnung und Ausführung von Holzbauwerken (in German). Ingenieur-Holzbau 86 - Fachtagung für Bauingenieure, Stuttgart, Germany.

Kessel, M. H. & Kühl, A. & Hall, C. (2015): Überprüfung und Ergänzung der Imperfektionsannahmen und Montageregeln der DIN EN 1995-1-1 für Nagelplattenkonstruktionen zur Steigerung ihrer Sicherheit und Wirtschaftlichkeit (in German). Research report, Fraunhofer IRB Verlag.

Kessel, M. H. & Sieder, M. & Kreuzinger, H. (2020): Personal contribution by Martin H. Kessel, Mike Sieder and H. Kreuzinger (DE): Bracing of the main girder of a pedestrian bridge. CEN/TC 250/SC 5/WG 3 N 153.

Kuhlmann, U. & Hofmann, R. (2013): Vereinfachte Bemessung von Brettschichtholzträgern variabler Höhe für das Torsionsmoment aus Kippstabilisierung (in German). IGF research project No. 17398 N (Aif/iVTH), Institute of Structural Design, University of Stuttgart.

Kuhlmann, U. & Hofmann, R. (2016): Simplified method to determine the torsional moment due to lateral torsional buckling. INTER, 49-10-2, Graz, Institute of Structural Design, University of Stuttgart.

Kuhlmann, U. & Töpler, J. (2021 a): Analytical and numerical investigations on imperfection-sensitive timber members subjected to combined bending and axial compression. WCTE 2021, Institute of Structural Design, University of Stuttgart.

Kuhlmann, U. & Töpler, J. (2021 b): Imperfektionsmessungen an stabilitätsgefährdeten Holzbauteilen - Zwischenbericht (in German). Research report, DIBt P 52-5- 13.194-2048/19, Institute of Structural Design, University of Stuttgart.

Kuhlmann, U. & Töpler, J. & Gauß, J. & Buchholz, L. (2021): Integrated approach of testing and numerical verifications (IATN). Research project RP 7, DFG Cluster of Excellence "Integrative Computational Design and Construction for Architecture" (IntCDC), EXC 2120/1 − 390831618, Institute of Structural Design, University of Stuttgart, ongoing.

Larsen, H. J. (1977): Laterally Loaded Timber Columns, Tests and Theory. CIB-W18, 8-15-1, Brussels, Belgium.

Leica Geosystems AG (2013): Leica ScanStation P20. User Manual.

Neuhaus, F.-H. (1981): Elastizitätszahlen von Fichtenholz in Abhängigkeit der Holzfeuchtigkeit (in German). Dissertation, Ruhr University Bochum.

prEN 1993-1-14 (14 April 2021): Eurocode 3: Design of steel structures − Part 1-14: Design assisted by finite element analysis (draft version). CEN/TC 250/SC 3/WG 22 N 32.

DISCUSSION

The papers was presented by J Töpler

P Dietsch commented that the differences to other studies on the topic could be due to the consideration of members in finished buildings (i.e. including dead weight). He said imperfection depends on construction quality, which could vary due to different level of experience, and pondered whether and how to take this into account in future version EC5. J Töpler agreed that the assembly process has the highest influence. It would be an important topic for the next generation of EC5 to provide guidance.

E Ussher asked whether the model was calibrated prior to application. J Töpler said the model was calibrated and verified and the information was presented in WCTE 2021.

G Hochreiner stated that imperfections should be defined independent of the structural model. J Töpler replied this is a topic for discussion in term of approaches. G Hochreiner received clarification that the stiffness of the brace elements was based on values from cited paper. They discussed the influence of local and global effects where global effects might be more dominant.

S Aicher also commented that imperfection also depended on the stiffness in the minor axis. J Töpler said there did not seem to be a big difference in the horizontal axis and this might be the case for the unbraced system.

H Danielsson received clarification on the numerical modeling of the compression behaviour as nonlinearly ideal elastoplastic.

Probabilistic description of the mechanical properties of glued laminated timber made from softwood

Stephan Schilling[1], Pedro Palma[2], René Steiger[2], Andrea Frangi[1]

[1] ETH Zürich, Institute of Structural Engineering, Switzerland

[2] Empa – Swiss Federal Laboratories for Materials Science and Technology, Structural Engineering Research Laboratory, Dübendorf, Switzerland

Keywords: Probabilistic modelling, JCSS, Probabilistic Model Code, mechanical properties, glued-laminated timber (GLT), size effects

1 Introduction

1.1 Background

The study presented in this paper stems from a wider project on the reliability of timber trusses, for which a full probabilistic description of relevant timber properties had to be developed. Therefore, the presented statistical inference aims at an overall best fit of available experimental data. Other aspects were also considered, such as choosing distribution functions that are defined only in the positive domain. These objectives and assumptions might not be appropriate for other applications, which focus on, e.g., having a better fitting in the lower tail of the distribution, or deriving characteristic values from test data in a simple way.

1.2 Overview

The two most important aspects in probabilistic modelling of glued laminated timber (GLT) are: i) the significant variability of the mechanical properties, even though some homogenisation results from production; and ii) a marked influence of the size of the structural member on certain strength and stiffness properties. The current version of the Joint Committee on Structural Safety (JCSS) Probabilistic Model Code (PMC): Part 3.5 *Properties of Timber* (2006) provides only prior probabilistic models for the mechanical properties of GLT (Table 1, left). This can only serve as a general guideline, because part of the given values are indicative (Köhler et al. 2007).

New types of probability density functions (PDF) and coefficients of variation (CoV) for a probabilistic description of the mechanical properties of GLT made of softwood were derived in a study which is presented in this paper (Table 1, right) based on an extensive literature review and on the analysis of part of the results of research by Frese (2016), Frese & Blaß (2016) and Frese et al. (2017). In case the available data allowed, size effects were included in the probabilistic models, i.e. correction factors based on the member size in relation to reference dimensions were directly applied to the parameters of the PDF. Since the different parameters are typically linked to the mean (or a specific quantile) and to the CoV, this approach allowed describing the influence of the member size on both, the *location* and the *scale* of the distributions. The proposed correction factors are provided in a format based on Weibull's weakest link theory (Weibull 1939, Gustafsson 2014 and Zok 2017), i.e. power functions in which the base is normalised to a reference size. When the data did not allow for a direct application of the correction factors to the parameters of the PDF, the proposed PDF can be multiplied by global correction factors to account for size effects (i.e. only the *location* of the distribution function is modified). Nevertheless, the use of global correction factors is a valid approach, since it was applied only to brittle failure modes (for perfectly brittle failure modes, the variability is a material constant).

Table 1: Probabilistic models for mechanical properties of GLT.

Property	JCSS PMC (2006)		Proposed	
	Distribution	CoV	Distribution	CoV
Bending strength	Lognormal	0.15	Lognormal, small beams; 2-p Weibull, medium-large beams	0.15
MOE ‖	Lognormal	0.13	Lognormal	0.05
Tensile strength ‖	Lognormal	-	Lognormal, small beams; 2-p Weibull, medium-large beams	0.11
Compressive strength ‖	Lognormal	-	Lognormal	0.04
Shear strength	Lognormal	-	2-p Weibull	0.14
Shear modulus	Lognormal	-	Lognormal	0.05
Tensile strength ⊥	2-p Weibull	-	2-p Weibull	0.30
Compressive strength ⊥	Normal	-	Lognormal	0.10
MOE ⊥	Lognormal	-	Lognormal	0.11
Density	Normal	0.10	Normal / Lognormal	0.05

2 Probabilistic models for GLT properties

2.1 General

In this Section, the background literature on the properties in Table 1 are analysed and PDF, namely Lognormal, Gamma, Beta, two-parameter (2-p) Weibull and three-parameter (3-p) Weibull, are fitted to the available datasets by means of maximum likelihood estimations (e.g. Scholz 2006). The Beta and 3-p Weibull PDF were used by Frese & Blaß (2016) and Frese et al. (2017). Both PDF were shown to describe the individual datasets well, but in the context of reliability analyses both PDF have to be treated carefully, since one or both tails of the distribution functions can show a behaviour, that is not physically plausible. The limitations in adequately describing the left tail (lower bound corresponds to negative infinity) is also the reason why the Normal distribution was excluded in this study *a priori* in most cases. The Gamma distribution mostly shows a behaviour similar to the Lognormal. For these reasons and also due to the observations made during the process of statistical inference (visual comparison of different PDF and QQ-plots and by means of the Bayesian information criterion (BIC)), it was recognised that most properties can be well described with either a Lognormal or a 2-p Weibull distribution – mostly depending on the skewness of the individual datasets.

Although some of the values provided in EN 14080:2013 might have been chosen with specific intentions (e.g. historical reasons, exclusion of certain failure modes), they are shown and – if necessary – discussed in this section. It seems relevant to the authors of this study to be aware of the extent of the deviations from results of pure data analysis and provisions in standards. Only in cases where not sufficient information could be found, values specified in EN 14080:2013 were used.

2.2 Bending strength

For the *bending strength* $f_{m,}$, Fink (2014) reported a certain influence of the strength-grading procedures on the coefficient of variation (CoV). However, the study by Brandner and Schickhofer (2008) and the evaluation of data made available by Frese (2016) shows that the CoV is almost independent of the strength grading procedure of single laminations and hence, as proposed in the JCSS PMC (2006), assuming a constant value of CoV of 15% seems to be appropriate for the reference size.

Regarding size effects, own investigations on Frese & Blaß's (2016) data sets on GLT beams with a length-to-height ratio of 18:1 and heights between 300 and 3'000 mm show that beams with heights smaller than the reference height of 0.60 m are best described by a Lognormal distribution, whereas beams with medium and large heights are best described with a 2-p Weibull distribution. Nevertheless, the errors of adopting 2-p Weibull distributions for all beam sizes is in an acceptable range, where vice versa using the Lognormal PDF for medium and large beams would lead to an overestimation in the lower tail domain.

Since the characteristic values of bending strength represent the indicative values of the different strength classes, these values are used as a starting point for the

probabilistic models. This assumption together with a uniform CoV of 15% for the reference size of all strength classes and a 2-p Weibull distribution leads to the statistics and Weibull parameters a and b in Table 2. The parameter a corresponds to the 63.2% quantile and b has a one-to-one, but inverse relation to the CoV (Gustafsson 2014).

Table 2: Statistical parameters for the bending strength for a reference height h = 0.60 m

	GL 20h	GL 22h	GL 24h	GL 26h	GL 28h	GL 30h	GL 32h
$f_{m,mean}$ [N/mm²]	27.4	30.1	32.9	35.6	38.4	41.1	43.9
$f_{m,k}$ [N/mm²]	20	22	24	26	28	30	32
CoV [%]	15	15	15	15	15	15	15
Parameter a [N/mm²]	29.1	32	34.9	37.9	40.8	43.7	46.6
Parameter b [-]	7.91	7.91	7.91	7.91	7.91	7.91	7.91

The correction factors $k_{m,y,h,a}$ and $k_{m,y,h,b}$ of the two Weibull parameters (Formulae 1 and 2, adjusted to the reference height of 0.60 m) clearly show that both the *scale* and the *shape* of the Weibull distribution change considerably with the beam height (the Weibull parameters a and b are to be multiplied by the correction factors):

$$k_{m,y,h,a} = \left(\frac{0.60}{h}\right)^{0.18} \tag{1}$$

$$k_{m,y,h,b} = \left(\frac{0.60}{h}\right)^{-0.36} \tag{2}$$

where h is the beam height in m.

Modification factors related to other aspects of the behaviour of timber members, e.g. influence of moisture or load-duration effects, were not considered in this study, neither the best way to implement them in the probabilistic description.

2.3 Modulus of elasticity (MOE) parallel to the grain

The JCSS PMC (2006) proposes a Lognormal distribution with a CoV of 13% for the *bending MOE E_m*, which is the same value that is specified for structural timber, even though a lower value could be expected due to homogenisation. Fink (2014) also discussed this issue and reports CoV between 4% and 7.5% based on experimental investigations from literature. Fink's own numerical simulations resulted in CoV of 3% to 4% and the Lognormal PDF describing his data well. Using the mean and characteristic values from EN 14080:2013, with the relationship $E_{0,k} = 5/6 \cdot E_{0,mean}$, and a Lognormal distribution, leads to a CoV of about 11% for all strength classes.

The data provided by Frese (2016) allows for an evaluation and a comparison between the *MOE in tension $E_{t,0}$, compression $E_{c,0}$, and bending E_m*. For all cases, the Lognormal PDF is appropriate. The mean values are highest in tension and lowest in compression, and the CoV are smallest for compression and highest for bending. In design in

practice, one single value for the MOE parallel to the grain is used usually. Since the bending MOE has a mean value between the others and the highest CoV, taking the bending MOE is a good starting point. The statistical parameters for the bending MOE of GLT are presented in Table 3. The given mean values and the CoVs are based on empirical statistics. The first Lognormal PDF parameter λ is related to the mean value and the second parameter ζ to the CoV.

Table 3: Statistical parameters for the bending MOE of GLT for the reference height h = 0.60 m, based on the data made available by Frese (2016)

	GL 24h	GL 28h	GL 32h
$E_{m,mean}$ [kN/mm^2]	12.8	14.0	16.5
$E_{m,k}$ [kN/mm^2]	11.8[*]; 11.8[**]	12.8[*]; 12.9[**]	15.8[*]; 15.7[**]
CoV [%]	5.15	4.87	2.82
λ [-]	2.55	2.63	2.80
ζ [-]	0.0513	0.0487	0.0281

[*] empirical value, i.e. the 50th value of a sorted list of 1'000 values.
[**] 5% quantile of the fitted Lognormal PDF.

The evaluation of the data provided by Frese & Blaß (2016) showed that Lognormal PDF are an appropriate model for all beam sizes. The height effect can be directly considered in the distribution parameters. The parameter λ is only slightly dependent on the member size. Hence, no correction factor is proposed. For the parameter ζ, the correction factor according to Formula 3 is proposed to account for size effects (adjusted to the reference height of 0.60 m) for all strength classes (the parameter ζ is to be multiplied by the correction factor):

$$k_{E,h,\zeta} = \left(\frac{0.60}{h}\right)^{0.78} \tag{3}$$

To account for size effects, Brandner et al. (2007) and Brandner et al. (2008) proposed two models in which the characteristic value is a function of the mean value and of the number of laminations n (up to 15 laminations, which corresponds to a beam height of 0.60 m for a laminations thickness of 40 mm).

$$E_k = E_{mean} \cdot \min\left[\frac{1}{60}(n-1) + 0.67; 0.9\right]. \tag{4}$$

$$E_k = E_{mean} \cdot \min\left[1 - 1.645\frac{0.20}{\sqrt{n}}; 0.9\right]. \tag{5}$$

Figure 1 shows a comparison of the resulting parameter ζ (in this range describing the CoV well) between the linear (Formula 4) and the non-linear model (Formula 5) by Brandner et al. (2007 & 2008) and the proposed non-linear model (Formula 3).

Although the proposed model was fitted to beams with heights between 0.30 to 3.0 m, it seems to be applicable also for beams with smaller heights.
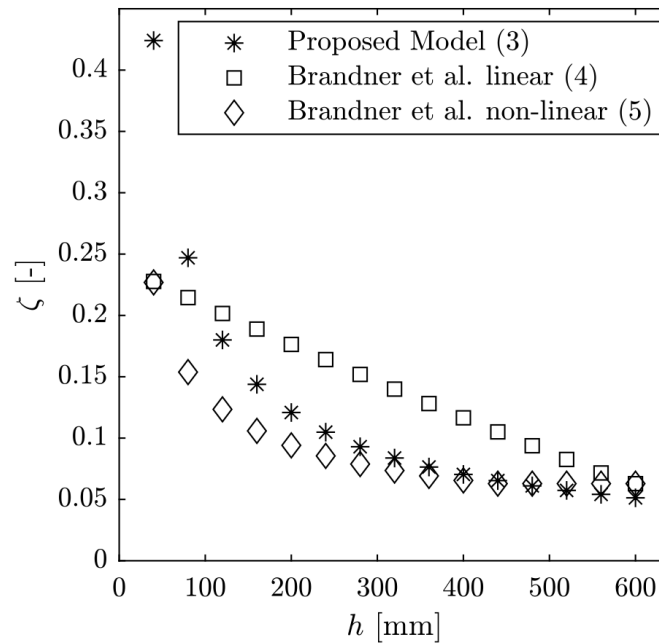
Figure 1: Comparison of height dependent models for the parameter ζ of the MOE ∥

2.4 Tensile strength parallel to the grain

For the *tensile strength parallel to the grain* $f_{t,0}$ the JCSS PMC (2006) proposes a Lognormal distribution, but no CoV. EN 14080:2013 only provides the characteristic values of tensile strength $f_{t,0,k}$, which are assumed to be 80% of the characteristic values of bending strength $f_{m,k}$. By means of numerical simulations (reference beam heights of 0.60 m and lengths of 5.40 m) Frese (2016) determined characteristic values of tensile strength of about 88% of the characteristic values of bending strength, independently of the strength grade of GLT.

Heavy left tails and negative skewness of the datasets made available by Frese (2016) let conclude that the 2-p Weibull is an appropriate PDF. Even though the CoV shows a slight decrease in higher GLT grades, it still seems reasonable to use a constant CoV of 11% for all GLT grades for the reference size (length l = 5.40 m and height h = 0.60 m).

The statistical parameters of the tensile strength for the reference configuration presented in Table 4 are based on three assumptions: (i) the characteristic value of tensile strength is 88% of the characteristic value of bending strength; (ii) there is a constant CoV of 11% for the reference size in all strength classes; and (iii) it is assumed that the 2-p Weibull distribution is valid for all beam sizes, when used with the corresponding size effect models described by Formulae 6 - 9.

Table 4: Statistical parameters for the tensile strength for a reference length l = 5.40 m and a reference height h = 0.60 m

	GL 20h	GL 22h	GL 24h	GL 26h	GL 28h	GL 30h	GL 32h
$f_{t,mean}$ [N/mm²]	22.0	24.2	26.4	28.6	30.8	33.0	35.2
$f_{t,k}$ [N/mm²]	17.6	19.4	21.1	22.9	24.6	26.4	28.2
CoV [%]	11	11	11	11	11	11	11
Parameter a [N/mm²]	23.1	25.4	27.7	30.0	32.3	34.6	36.9
Parameter b [-]	11.0	11.0	11.0	11.0	11.0	11.0	11.0

Regarding size effects, Frese et al. (2017) conducted a parametric numerical study for GLT members (produced according to two grading procedures for GLT grades GL 23h and GL 33h) with lengths between 0.150 and 108 m and heights between 120 mm and 600 mm. Own investigations on the influence of the member length *l* and height on the tensile strength were conducted using this data, but neglecting members with lengths smaller than 1.35 m, and considering heights of 120, 360 and 600 mm only. It could be concluded that beams of short length and small height can be described with a Lognormal distribution, whereas the strength of medium-sized and large beams are clearly following a 2-p Weibull PDF. To describe the size effect, a nested model was applied, i.e. height-correction factors (Formulae 7 and 9) are used within the length-correction factors (Formulae 6 and 8) which then are multiplied by the parameters *a* and *b* of the PDF:

$$k_{t,0,l,a} = \left(\frac{5.4}{l}\right)^{\frac{1}{k_{t,0,h,a}*11.2}} \tag{6}$$

$$k_{t,0,h,a} = \left(\frac{0.60}{h}\right)^{\frac{-1}{6.56}} \tag{7}$$

and

$$k_{t,0,l,b} = \left(\frac{5.4}{h}\right)^{\frac{-1}{k_{t,0,h,b}*12.9}} \tag{8}$$

$$k_{t,0,h,b} = \left(\frac{0.60}{h}\right)^{\frac{-1}{2.24}} \tag{9}$$

Lam (2000) developed a Weibull-weakest-link model for the tensile strength of truss chord members of Canadian solid timber products. The principle of this adjustment factor to account for the effect of member length on the tensile strength could be applied also to GLT, but the exponent of the Weibull-weakest-link model is yet to be determined.

2.5 Compressive strength parallel to the grain

The JCSS PMC (2006) proposes a Lognormal PDF but no CoV for the *compressive strength parallel to the grain* $f_{c,0}$. EN 14080:2013 provides only the characteristic values, which are assumed equal the characteristic values of bending strengths. Frese (2016) found about 1.5 times higher values (Table 5) by means of stochastic simulations of stocky specimens (heights and lengths of 0.60 m).

The own analysis of the data made available by Frese (2016) showed that a Lognormal PDF is appropriate for the description of the compressive strength parallel to the grain. The mean values and CoV in Table 5 have been determined empirically.

Table 5: Statistical parameters for the compressive strength parallel to the grain of GLT, based on the data made available by Frese (2016)

	GL 24h	GL 28h	GL 32h
$f_{c,0,mean}$ [kN/mm²]	40.4	43.7	50.2
$f_{c,0,k}$ [kN/mm²]	37.5[*]; 37.7[**]	40.9[*]; 41.1[**]	48.0[*]; 48.0[**]
CoV [%]	4.16	3.72	2.76
λ [-]	3.70	3.78	3.92
ζ [-]	0.0416	0.0373	0.0277

[*] empirical value, i.e. the 50th value of a sorted list of 1'000 values.
[**] 5% quantile of the fitted Lognormal PDF.

Since the load-carrying capacity of longer compression members is anyway governed by buckling (and hence, by the MOE rather than the strength), size effects are not considered for the compressive strength parallel to the grain. Further, for buckling-restrained members loaded in compression along the grain, the failure mode is ductile, why no size effect is expected.

2.6 Shear strength

The JCSS PMC (2006) proposes a Lognormal PDF but no CoV for the *shear strength f_v*. EN 14080:2013 provides only one characteristic value of shear strength of 3.5 MPa, which is independent of the GLT grade, to ensure that shear is not the governing failure mode for most design situations. Schickhofer (2001) tested 80 I-shaped GLT beams produced from visual and machine-graded lamellas. Even though a slightly negative correlation between the strength classes and the shear strength was observed, a characteristic shear strength value of 3.5 MPa for all strength classes was proposed for design purposes.

The statistical analysis of the data by Schickhofer (2001) revealed that the 2-p Weibull distribution is appropriate to describe shear strength data. The empirical 5% quantile value is 3.24 MPa and, based on the analysis of the right-censored data set (20% of the tested beams failed in failure modes other than shear) with a 2-p Weibull distribution with a 95% significance level for the confidence intervals, the 5% quantile is 3.38 MPa and the CoV is 10.4%. Klöck (2005) conducted 30 shear tests on combined GLT beams,

where the outer lamellas consisted of a higher strength class to avoid bending failures, obtaining shear failures in 60% of the cases. Based on the data published by Klöck, the empirically determined 5% quantile value is 3.64 MPa and, based on the analysis accounting for the right censored data set with a 95% significance level and a 2-p Weibull distribution, the 5% quantile revealed 4.03 MPa with a CoV of 11.1%.

For the tests by Schickhofer (2001), in the study presented in this paper, the stressed volume has been determined as twice the free length between the loading and support plates times the cross-section area of the web of the I-shaped GLT beams (Figure 2, left) and for the test configuration applied by Klöck (2005) twice the free length between the loading and support plates times the width times 60% of the height was used (Figure 2, right). The assumption of basing the calculation of the stressed volume on a value of 60% of the beam height was taken from Ehrhart (2019). Foschi & Barrett (1980) determined a global volume effect model for the longitudinal shear strength of uncracked beams and recommended a species-independent value of 1/6 for the exponent (Formula 10). The study by Foschi & Barrett was performed on solid timber. Due to a lack of further investigations, the model according to Formula 10 herein is proposed to be applied to GLT as well.
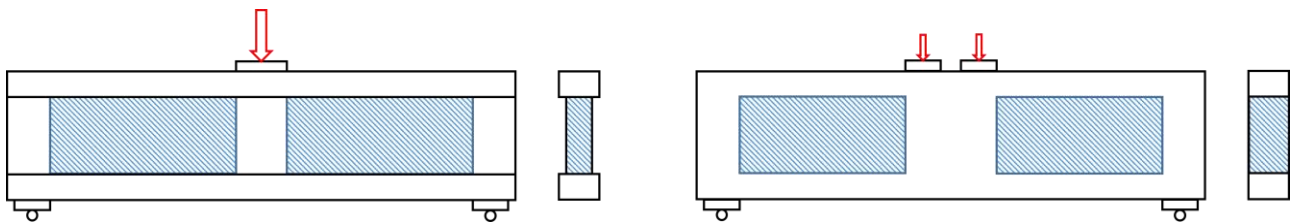
Figure 2: Schematic representation of the determination of the stressed volumes of the I-shaped GLT beams from Schickhofer (2001) on the left and of the combined GLT beams from Klöck (2005) with an assumed stressed height of 60% of the beam height on the right

Steiger & Gehri (2011) compared the shear stress distribution in a test configuration similar to the one applied by Schickhofer (2001) and Klöck (2005), but using glued-in steel rods for the load application to avoid the lateral dispersion of compressive stresses into the shear zone (Figure 3). They report a significant reduction of the volume under pure shear if glued-in rods are not used. However, due to the lack of information on the level of compressive stresses on the shear fields in the tests by Schickhofer (2001) and Klöck (2005), the stressed volume shown in Figure 2 was assumed, even though it very likely is smaller and should be updated in future revisions

of the proposed modification factor, according to the results presented in Steiger & Gehri (2011).
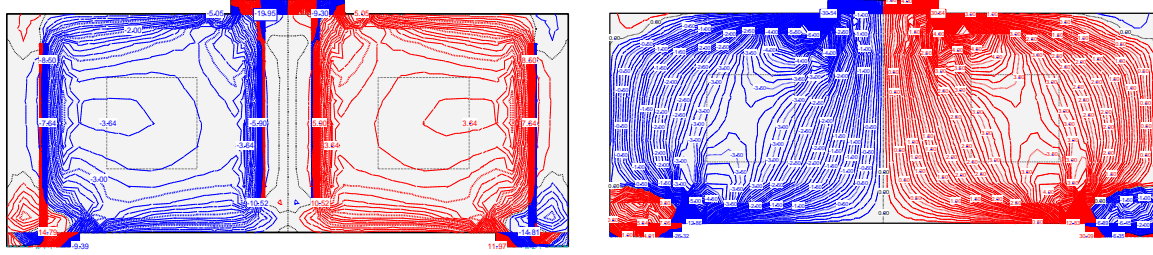

Figure 3: When transferring the loads into the specimen by means of glued-in steel rods, up to the elastic limit fields with uniform shear stress distribution of sufficient size occur (left), whereas they do not when directly transferring the loads to the timber beam (right). Steiger & Gehri (2011)

The datasets published by Schickhofer (2001) and Klöck (2005) were combined and a right-censored 2-p Weibull PDF was fitted to the merged data set. Since from the study by Schickhofer (2001) more data could be extracted, the calculation was performed with the sizes of those beams as reference and hence, the values taken from Klöck (2005) were divided by the volume correction factor according to Formula 10. The obtained PDF parameters for the stressed volume of 0.082 m^3 are $a = 4.63$ and $b = 8.31$. This corresponds to a 5% quantile value of 3.24 MPa and a CoV of 14.3%.

$$k_{\mathrm{v}} = \left(\frac{0.082}{\mathrm{V}}\right)^{\frac{1}{6}}$$
(10)

2.7 Shear modulus

In the JCSS PMC (2006) the *shear modulus G* is proposed to be modelled by a Lognormal distribution. EN 14080:2013 specifies a mean value of 650 MPa and a characteristic value of $G_{\mathrm{k}} = 5/6 \cdot G_{\mathrm{mean}} = 540$ MPa, independent of the GLT grade. Assuming a Lognormal PDF, this corresponds to a CoV of 10.9%. Brandner et al. (2007 & 2008) showed that the method applied during testing has a strong influence on the obtained mean values and on the scattering of data. They proposed a mean value of 650 MPa and the same correction formulae to account for the size effect as proposed for the MOE (Formula 4 and 5) for all grades of homogeneous and combined GLT.

Assuming a Lognormal PDF, a mean value of 650 MPa, and a distribution parameter $\zeta = 0.0513$ (based on the value for the bending MOE of GL 24h (Table 3)), a characteristic value $G_{\mathrm{k}} = 590$ MPa and a distribution parameter $\lambda = 6.47$ are obtained. The height correction factor $k_{\mathrm{G,h},\zeta} = k_{\mathrm{E,h},\zeta}$ for the second parameter ζ is assumed to be identical to the one determined for the bending MOE (Formula 3).

2.8 Tensile strength perpendicular to the grain

The *tensile strength perpendicular to the grain* $f_{t,90}$ is the only property for which JCSS PMC (2006) proposes to apply a 2-p Weibull PDF for the probabilistic description, due to the brittle failure modes associated with tension perp. A CoV is not specified. EN 14080:2013 specifies a characteristic value of $f_{t,90}$ = 0.5 MPa independent of the GLT grade. Many different investigations and meta-studies were conducted to describe the *tensile strength perpendicular to the grain* with a coherent size effect: Mistler (1998), Aicher & Dill-Langer (1997), Ranta-Maunus (1998), Aicher et al. (1998), Blaß & Schmid (1999), Aicher et al. (2002) and Mistler (2016). In these publications, valuable discussions on the nature of the size effect can be found. Nevertheless, in the opinion of the authors of this study no accurate probabilistic model was derived. The reasons might stem from the analysed specimens: the variations in the geometric properties (height, length and width) are too unsystematic, why the influence of the single properties cannot be evaluated properly; and the scattering differs drastically between the different test series per geometric layout. The latter comes from different intentions of the single test series: for some the used timber originates from only one growing area and others were gathered from different sawmills from different regions.

Based on the selection of GLT specimens for testing, the number of tests performed and the selection of the different volumes of the specimens, the 2-p Weibull distribution parameters determined by Blaß & Schmid (1999) for a volume of 0.01 m^3 with a = 0.848 and b = 3.688 is proposed to be applied for probabilistic modelling of the tensile strength perpendicular to the grain $f_{t,90}$. The analysis revealed statistical parameters of $f_{t,90,mean}$ = 0.77 MPa, $f_{t,90,k}$ = 0.38 MPa and a CoV of 30%.

To account for the size effect, the pure volume-based, global correction factors with consideration of the duration of load effects according to Aicher & Dill-Langer (1997), Ranta-Maunus (1998) and Aicher et al. (1998) are proposed for probabilistic modelling (the PDF is to be multiplied by the respective correction factor):

$$k_{t,90,0} = \left(\frac{0.01}{V}\right)^{0.3} \tag{11}$$

$$k_{t,90,\infty} = \left(\frac{0.01}{V}\right)^{0.2} \tag{12}$$

2.9 Compressive strength perpendicular to the grain

In the JCSS PMC (2006) a Normal distribution is proposed for the *compressive strength perpendicular to grain* $f_{c,90}$, given its close relationship to density. EN 14080:2013 specifies a characteristic value of 2.5 MPa independent of the GLT grade, most likely to ensure that perpendicular-to-the-grain stresses in actual structures remain at very low levels, therefore avoiding serious issues such as high creep deformations. Damkilde et al. (1998) conducted 120 tests with GLT cut-offs with a height of 200 mm and different widths. The lengths were adjusted to get a constant area of 25'000 mm^2.

The specimens were collected over several production days from one Danish and three Swedish GLT producers. The grade of the GLT represents normal Nordic GLT quality (presumably GL 24). Damkilde et al. used a strain-based failure criterion and reported the following empirically determined statistical parameters: $f_{c,90,mean}$ = 2.87 MPa, $f_{c,90,k}$ = 2.44 MPa, and CoV = 9%. No PDF was fitted to the data.

As mentioned above, a Normal PDF can cause problems in reliability analyses due to possible negative realisations. Hence, a Lognormal PDF is used instead. Own calculations revealed the following distribution parameters based on the abovementioned mean and characteristic values: λ = 1.05 and ζ = 0.0595. For the Lognormal distribution, a CoV of 9.61% is obtained.

There are no studies on size effects available. For many practical design situations the perpendicular-to-the-grain compressive stresses tend to spread in the longitudinal direction and the stressed volume is therefore limited and not related to the height of the member.

2.10 MOE perpendicular to the grain

In the JCSS PMC (2006) the Lognormal distribution but no CoV is proposed for the *tensile MOE perpendicular to the grain* $E_{t,90}$. EN 14080:2013 specifies a mean value of $E_{90,mean}$ = 300 MPa and a characteristic value $E_{90,k}$ = 5/6·$E_{90,mean}$ = 250 MPa, independent of the strength class. This is to ensure that perpendicular-to-the-grain stresses in actual structures remain at very low levels, therefore avoiding serious issues such as excessive deformations perp to grain, which due to creep would even be enlarged on a long-term perspective. The tests to assess the *compression* perp properties performed by Damkilde et al. (1998) revealed a mean value of $E_{c,90,mean}$ = 320 MPa. Aicher & Dill-Langer (1997) found higher values in their *tensile* perp. to grain tests on specimens of grades GL 32h and GL 36h, i.e. for the reference volume of 0.01 m³: $E_{t.90,mean}$ = 446 MPa; $E_{t.90,k}$ = 398 MPa; and CoV = 6.8%. For the volume of 0.03 m³: $E_{t.90,mean}$ = 419 MPa; $E_{t.90,k}$ = 375 MPa; and CoV = 6.5%.

Starting from the mean and characteristic values specified in EN 14080:2013 and a Lognormal distribution, the following parameters were obtained by own calculations: CoV = 10.8%, λ = 5.70 and ζ = 0.107.

2.11 Density

For the density ρ the JCSS PMC (2006) proposes a Normal distribution together with a CoV of 10%. This is the same value as specified for structural timber, but due to homogenisation during production, the CoV for GLT is expected to be lower though. A Normal distribution seems to be an intuitive choice for the natural occurrence and simple piling of laminations, but, as explained above, it can be problematic for reliability analyses. Therefore, a Lognormal distribution is proposed.

Assuming a Normal distribution and the mean and characteristic values of the GLT classes GL 20h to GL 32h in EN 14080:2013, gives CoVs between 5% and 6% without a clear trend. Damkilde et al. (1998) report a CoV of 4.8% for normal Nordic GLT quality

(presumably GL 24), which supports the CoV values calculated from the properties specified in EN 14080:2013. The resulting statistical parameters including the Lognormal parameters can be found in Table 6.

Table 6: Statistical parameters for the density of GLT according to EN 14080:2013

	GL 20h	GL 22h	GL 24h	GL 26h	GL 28h	GL 30h	GL 32h
ρ_{mean} [kg/m³]	370	410	420	445	460	480	490
ρ_k [kg/m³]	340	370	385	405	425	430	440
CoV [%]	4.9	5.9	5.1	5.5	4.6	6.3	6.2
λ [-]	5.91	6.01	6.04	6.10	6.13	6.17	6.19
ζ [-]	0.0506	0.0613	0.0521	0.0563	0.0474	0.0656	0.0642

3 Open issues

When, e.g. in the course of assessment or calculations of structural reliability, introducing the probabilistic description of properties of GLT members into probabilistic modelling, the correlations between these properties should be taken into account. This is why the *coefficients of correlation* should be specified in the JCSS PMC at least qualitatively (e.g. low, medium, high).

It is well known that the characteristic values of properties for GLT members subjected to edgewise loading underlie considerable system effects (Brandner & Schickhofer 2006). Therefore, a study to get the full *probabilistic description of properties for GLT subjected to edgewise-loading* should be conducted.

Some of the statistics of the GLT properties discussed in this paper are based on only few available studies or on the specifications in EN 14080:2013. *Complementary studies should be conducted* to satisfy the requirements accounting for the variability of properties due to growth characteristics, the validity of numerically derived values and to review code provisions in design codes (factors to account for size effects) and product standards (characteristic values) and respective *data should be made available to the research community*.

4 Conclusions

The specifications for the probabilistic description of mechanical properties of GLT members in the JCSS PMC (2006) are quite limited and should be attempted to be amended. The present paper, covering the most relevant mechanical properties and strength classes of GLT including size effects, contains respective proposals and may initiate the discussion on the development of the GLT related clauses in the JCSS PMC. The proposed models can be used for reliability analysis of structures consisting of GLT members or for code calibration.

5   Acknowledgements

6   References

Aicher, S; Dill-Langer, G (1997): DOL effect in tension perpendicular to the grain of glulam depending on service classes and volume; Paper CIB-W18/30-9-1. CIB-W18 Meeting 30. Vancouver, Canada.

Aicher, S; Dill-Langer, G; Ranta-Maunus, A (1998): Duration of load effect in tension perpendicular to the grain of glulam in different climates. Holz als Roh- und Werkstoff, 56:295-305.

Aicher, S; Dill-Langer, G, Klöck, W (2002): Evaluation of different size effect models for tension perpendicular to grain design; Paper CIB-W18/35-6-1. CIB-W18 Meeting 35. Kyoto, Japan.

Blaß, HJ; Schmid, M (1999): Tensile strength perpendicular to grain of glued laminated timber; Paper CIB-W18/32-6-4. CIB-W18 Meeting 32. Graz, Austria.

Brandner, R; Schickhofer, G (2006): System effects of structural elements - determined for bending and tension. 9th World Conference on Timber Engineering. Portland, Oregon, USA.

Brandner, R; Gehri, E; Bogensperger, T; Schickhofer, G (2007): Determination of modulus of shear and elasticity of glued laminated timber and related examinations; Paper CIB-W18/40-12-2. CIB-W18 Meeting 40. Bled, Slovenia.

Brandner, R; Freytag, B; Schickhofer, G (2008): Determination of shear modulus by means of standardized four-point bending tests; Paper CIB-W18/41-21-1. CIB-W18 Meeting 41. St. Andrews, Canada.

Brandner, R; Schickhofer, G (2008): Glued laminated timber in bending: new aspects concerning modelling. Wood Science and Technology, 42(5):401-425.

Damkilde, L; Hoffmeyer, P; Pedersen, TN (1998): Compression strength perpendicular to grain of structural timber and glulam; Paper CIB-W18/31-6-4. CIB-W18 Meeting 31. Savonlinna, Finland.

Ehrhart, T (2019): European Beech Glued Laminated Timber. Doctoral Thesis, ETH Zürich. Zurich, Switzerland.

EN 14080 (2013): Timber structures - Glued laminated timber and glued solid timber – Requirements. CEN, Brussels.

Fink, G (2014): Influence of varying material properties on the load-bearing capacity of glued laminated timber. Doctoral Thesis. ETH Zürich. Zurich, Switzerland.

Frese, M (2016): Computergestützte Verfahren zur pragmatischen Beurteilung der Tragwiderstände von Brettschichtholz: Zusammenfassung exemplarischer Simulationsstudien. Habilitation Thesis. KIT. Karlsruhe, Germany.

Frese, M; Blaß, HJ (2016): Reliability of large glulam members Part 1: Data for the assessment of partial safety factors for the bending strength. Paper INTER/49-17-1. INTER Meeting 49. Graz, Austria.

Frese, M; Egner, S; Blaß, HJ (2017): Reliability of large glulam members Part 2: Data for the assessment of partial safety factors for the tensile strength. Paper INTER/50-17-1. INTER Meeting 50. Kyoto, Japan.

Foschi, RO; Barrett, JD (1980): Consideration of size effects in longitudinal shear strength for uncracked beams. Paper CIB-W18/13-6-2. CIB-W18 Meeting 13. Otaniemi, Finland.

Gustafsson, PJ (2014): Lecture notes on some probabilistic strength calculation models. Division of Structural Mechanics, Lund University, Report Nr. TVSM-7161. Lund, Sweden.

JCSS Probabilistic Model Code (2006): Part 3 - Resistance Models; 3.5 Properties of Timber. Joint Committee of Structural Safety (JCSS).

Klöck, W (2005): Statistical analysis of the shear strength of glued laminated timber based on full-size flexure tests. Otto-Graf-Journal, 16:225-244.

Köhler, J; Sørensen, JD; Faber, MH (2007): Probabilistic modeling of timber structures. Structural Safety, 29(4): 255-267.

Lam, F (2000). Length effect on the tensile strength of truss chord members. Canadian Journal of Civil Engineering, 27(3):481-489.

Mistler, HL (1998): Querzug-Bemessung von BSH-Trägern nach EC 5 - Ein Vergleich mit Forschungsergebnissen. Holz als Roh- und Werkstoff, 56:51-59.

Mistler, HL (2016): Design of glulam beams according to EN 1995 with regard to perpendicular-to-grain tensile strength: comparison with research results. European Journal of Wood and Wood Products, 74(2):169-175.

Ranta-Maunus, A (1998): Duration of load effects in tension perpendicular to grain in curved glulam; Paper CIB-W18/31-6-2. CIB-W18 Meeting 31. Savonlinna, Finland.

Schickhofer, G (2001): Determination of shear strength values for GLT using visual and machine graded spruce laminations. Paper CIB-W18/34-12-6. CIB-W18 Meeting 34. Venice, Italy.

Scholz, FW (2006): Maximum likelihood estimation. Encyclopedia of statistical sciences. American Cancer Society. John Wiley & Sons, Inc.

Steiger, R; Gehri, E (2011): Interaction of shear stresses and stresses perpendicular to the grain; Paper CIB-W18/44-6-2. CIB-W18 Meeting 44, Alghero, Italy.

Weibull, W (1939): A statistical theory of the strength of materials. Royal Swedish Institute for Engineering Research, Technical University, Report Nr. 151. Stockholm, Sweden.

Zok, FW (2017): On weakest link theory and Weibull statistics. Journal of the American Ceramic Society, 100(4):1265-1268.

DISCUSSION

The papers was presented by S Schilling

C Tapia commented that he is not convinced with size effect consideration of parameters within the Weibull distribution. Only the scale parameter could be modified and the shape parameter related to COV should not be modified. C Tapia also noted that the power law is also related to the Weibull distribution. S Schilling responded that for perfectly brittle material COV would be a material constant. As wood is not a perfectly brittle material changing COV would be okay.

C Tapia stated that modelling compressive strength with normal distribution might be more appropriate compared to lognormal distribution. Also truncation can be used to avoid possible encountering of negative strengths. S Schilling agreed.

R Brandner commented that lognormal distribution for compressive strength perpendicular to grain might be better. Also power law in general can be used and it is not necessarily tied to Weibull theory.

R Brandner asked about the possible physic of material properties with changes in length. S Schilling said accumulation of weak zone might be the issue. R Brandner said lognormal distributions fit better than Weibull distribution in many cases and assuming Weibull distribution might affect results of reliability analysis. He also commented that parameter distribution model by size is messy.

F Lam agreed with most of the comments of C Tapia and R Brandner. He commented he is uncomfortable with having distribution parameters on distribution parameters especially for shape parameter when working with size dependent properties. Canadian test data on glulam beams showed that variability of bending strength did not seem to be size dependent. He said estimation of reliability index (beta) is influenced by the choice of probability distribution but fitting to the lower tails of the strength properties distributions is most important. Also Beta is a relative not absolute value and we just need to be consistent with the approach.

Load-bearing Capacity and Fracture Behaviour of Notched Cross Laminated Timber Plates

Alen Malagic [1], Manfred Augustin [1], Gregor Silly [1], Alexandra Thiel [1], Gerhard Schickhofer [1,2]

[1] holz.bau forschungs gmbh, Competence Centre of Timber Engineering and Wood Technology, Graz, Austria

[2] Institute of Timber Engineering and Wood Technology, Faculty of Civil Engineering, Graz University of Technology, Graz, Austria

1 Introduction

Abrupt changes in the geometry of load-bearing members (e.g., notches, holes), also referred as geometric discontinuities, induce high stress concentrations and high stress gradients in localised area of members. In a good engineering practice one should aim towards avoiding such discontinues in a first place. Nonetheless due to numerous constraints during planning and construction process this is not always possible. In buildings with Cross Laminated Timber (CLT) such examples occur e.g. in connections of slab-slab and wall-slab systems (Figure 1).
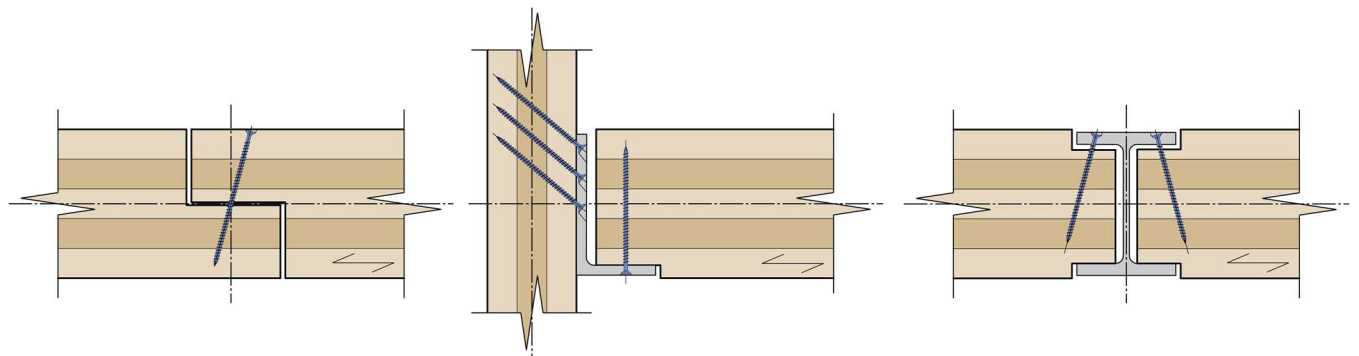

Figure 1   Various types of notches in CLT plates; a) Connection of two CLT plates. b) Connection of a CLT plate with a steel L-profile. c) Connection of CLT plates with a steel I-profile.

When loaded up to a certain level, a crack will be induced at the notch tip due to the combined local stress concentrations in tension perpendicular to grain and shear, latter, depending upon layer orientation result in longitudinal or rolling shear stresses. The crack propagates fast and in an unstable manner leading to the delamination of the member and to its failure, if the residual strength of the member above the crack isn't sufficient. The failure of the notch is therefore regarded as brittle.

The aim of this work is to provide a new analytical approach for unreinforced CLT notches based on Beam on Elastic Foundation (BEF). The analytical approaches are verified with an extensive base of test results. Moreover, the aim is to verify the analytical model referred as Structural Element Model developed by Serrano (2019, 2020) with additional test results. At the end, conclusions and suggestions for the design and calculation of CLT notches as well as their reinforcements are given.

2 State of the art

The models in this chapter and in section 4.2 are developed in a scope of linear elastic fracture mechanics (LEFM) and energy balance method. In this method the failure load at the crack tip is obtained according to the breakthrough work in fracture mechanics, i.e. work of Griffith (1921). The condition for crack growth of an initial crack at the notch according to LEFM is fulfilled, when the difference between the potential energy U_e and the strain energy U_i is equal to the energy dissipated by the crack during an infinitesimal increase in crack area. In scope of LEFM this energy is denoted as G and defined as

$$G = \frac{1}{B}\left(\frac{dU_e}{da} - \frac{dU_i}{da}\right).$$

$$(1)$$

Failure occurs when the energy release rate is equal to the energy crack resistance, also known as fracture energy G_f, which is a material property obtained from experiments. In scope of LEFM it is assumed that $G_f = G_c$. Further, in this paper it is implied that the crack grows only due to the crack opening in Mode I, leading to $G_f = G_{cI}$. With further development of Eq. (1) considering the substitution of $C = \delta/P$ the failure load according to LEFM is obtained as

$$V_f = \sqrt{\frac{2BG_c}{\dfrac{dC}{dA}}},$$

$$(2)$$

where C denotes the compliance of the structure, B the width of the member and V_f the failure load at the support, while the vertical displacement at the loading point is represented by δ.

Through the history the design equations for timber notches have improved from empirical to analytical approaches derived from fracture mechanics. Development culminated with the analytical solution from Gustafsson (1988), later implemented in Eurocode 5 (EC5) for notches in solid timber, laminated veneer lumber (LVL) and

glulam. The approach is based on the energy balance of the end notched beam at the crack tip derived from (LEFM) and the Timoshenko beam theory. The design expression in Eq. (3) represents the solution given in EC5 (Eurocode 5, 2004); for a detailed derivation of Eq. (3) refer to Serrano (2019).

$$\tau_d = \frac{1.5 V_f}{B \alpha h} \leq k_v f_{v,d} \, , \tag{3}$$

where k_v is the strength reduction factor given by

$$k_v = \min \left\{ \begin{array}{c} 1 \\ \dfrac{k_n \left(1 + \dfrac{1.1 i^{1.5}}{\sqrt{h}} \right)}{\sqrt{h} \left(\sqrt{\alpha - \alpha^2} + 0.8 \beta \sqrt{\dfrac{1}{\alpha} - \alpha^2} \right)} \end{array} \right. , \quad k_n = \left\{ \begin{array}{ll} 4.5 & \text{for LVL} \\ 5.0 & \text{for solid timber} \\ 6.5 & \text{for glulam} \end{array} \right. \tag{4}$$

i is the slope of the taper and k_n being the material parameter depending upon fracture energy defined as

$$k_n = 1.5 \frac{\sqrt{\dfrac{G_c G_0}{0.6}}}{f_v} \, . \tag{5}$$

The geometric parameters of the notch α and β are explained in Figure 2b.

2.1 Current design of notched CLT plates

Current design equations for notches in CLT are given in ETA-06/0138 (2017) and Wallner-Novak et al. (2013) based on Eq. (3), but modified with $f_{v,r,d}$ instead of $f_{v,d}$. Approaches for CLT differ one from other in different definition of the effective height h_{ef} as shown in Figure 2a, subsequently leading to different material factors k_n as follows:

$$k_n = \left\{ \begin{array}{ll} 4.5 & \text{for Wallner - Novak} \quad (\text{WN}) \\ 4.7 & \text{for ETA - 06 / 0138} \quad (\text{ETA}) \end{array} \right.$$
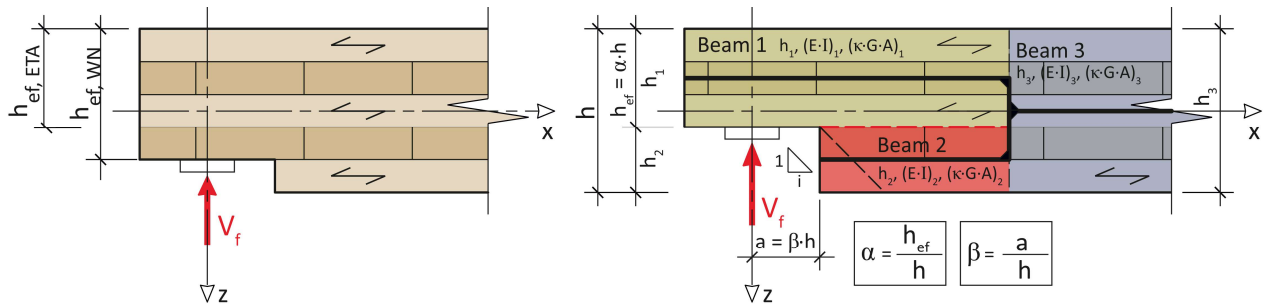

Figure 2   *a) Different definitions of the effective notch height h_{ef}. b) Notch in a CLT plate*

The major drawback of the mentioned approaches is the assumption that Gustafsson´s model can be modified by calibrating the material parameter k_n for CLT, following the

example for k_n in EC5. However, such assumption in EC5 is only valid as calibrations are made for beams which in general provide homogenous response in addition to constant ratios of material properties ($E_0/G_{0,90}$) and constant fracture properties of the material along the height of the member h_{ef}. For CLT the mentioned ratios derived as constant in Eq. (4) change with notch height h_{ef} depending on the position of longitudinal and transversal layers, the layup and number of layers in the member. These parameters of notched CLT elements result in a fundamentally different load-bearing capacity and fracture behaviour. As reported in Serrano (2019) the approach for the fitting parameter k_n can only be applied on a limited number of layups. Consequently, a new and theoretically consistent approach is needed.

2.1.1 Structural element model

The Structural Element Model was developed by Serrano (2019) for this design situation and is represented by two Timoshenko beam elements connected with an elastic spring and a dummy rigid rod (see Figure 3). Calculating the energy release rate according to Eq. (2) and assuming that elastic spring k_φ approaches infinity, the failure load is obtained as

$$V_f = \sqrt{\frac{2BG_c}{\left(\dfrac{1}{(\kappa GA)_1} - \dfrac{1}{(\kappa GA)_3}\right) + (\beta h + \Delta a)^2 \left(\dfrac{1}{(EI)_1} - \dfrac{1}{(EI)_3}\right)}} \ , \tag{6}$$

where $(kGA)_1$, $(kGA)_3$ are the shear stiffnesses and $(EI)_1$, $(EI)_3$ are the bending stiffnesses. Beam 1 represents the part of the member above the crack, while beam 3 is the full uncracked cross section of the CLT member in front of the crack.

The compliance C for this system takes into account the bending and shear part of the deformation calculated according to Timoshenko's theory.
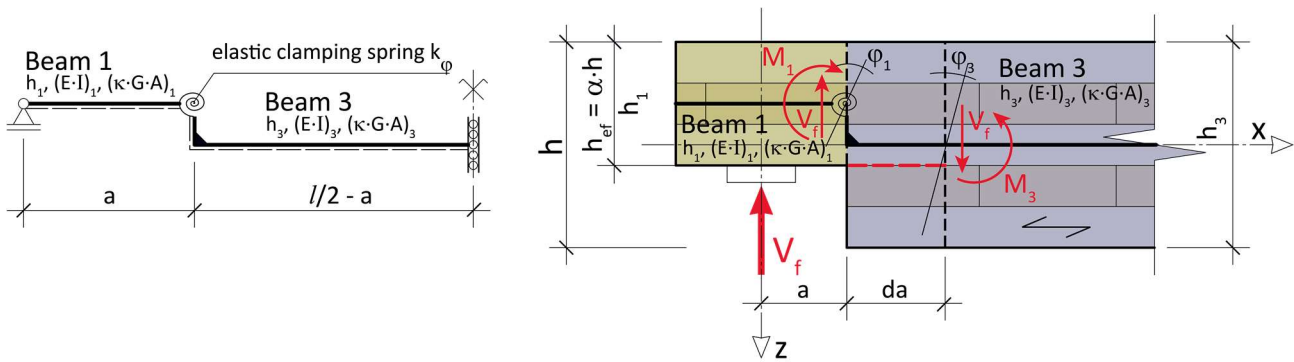
Figure 3   Structural Element Model developed by Serrano (2019, 2020)

The elastic spring k_φ simulates the additional rotation of the cross section at the crack tip due to the abrupt change in the cross section resulting in additional deformation and compliance. The elastic constant k_φ can be derived from numerical investigations as was done in Gustafsson (1988) for homogenous beams; for more details see Serrano (2019). An alternative approach would be to increase the crack length in order to

correctly represent the higher compliance. Modifying the crack length is appropriate for engineering practice as the closed form solution is simplified.

In the Structural Element Model the additional rotation is considered with an increased fictitious crack length. Initial crack length βh is increased by the value $\Delta a = (1-\alpha)h$. The parameter Δa is determined as best fit to the test results from Friberg (2017), Serrano (2020) and numerical investigations based on LEFM. It is noted again that the fitting factor in Serrano (2019) is developed and verified only on a limited number of layups and notch parameters. Therefore further experimental investigations are presented in chapter 3 and compared with predictions of the model in section 5.1 with an objective to check the robustness of the current fitting parameter. In addition, an analytical model is presented taking into account the rotation at the crack tip in section 4.2.1 in order to verify the value of Δa.

3 Experimental program

3.1 General

The layered structure of CLT causes additional difficulties on keeping analytical approaches simple for engineering use and reliable in domain of significant parameters. In order to keep the design simple, it is inevitable to fit the necessary parameters by means of experimental results.

The currently available experimental results regarding notches in CLT are scarce. As known to the authors only Friberg (2017) and Serrano (2020) published results of tests on 5-layered CLT beams with different geometry parameters (α, β) (from which they derived the fitting parameter Δa in Eq. (6)). To overcome this lack of data and in order to get a more extensive view on the behaviour of CLT with notches an extensive test program, described in the next section, varying a broad range of key parameters was conducted.

3.2 Test program, methods and results

In total 182 CLT specimens without glued edge bonding, split up into 23 series with unreinforced notches and 7 series with reinforced notches were tested. To quantify the reduction of the load bearing capacity of notches in comparison to CLT plates without notches reference tests (in total 6 series referred in Table 1 with REF) were carried out. All the 33 specimens of these series failed in rolling shear. The reduction of the mean load bearing capacity referenced to the mean rolling shear capacity of the reference series (without notches) will be denoted in Table 2 and Table 3 as $V_{f, mean} / V_{f, ref}$. An overview about the different series, their layup and their heights is given in Table 1.

Table 1. Overview of test series

	Series	Layup[a)]	h [mm]	B [mm]
3S	REF, 3A	40-<u>40</u>-40	120	
5S	REF, 5A, 5B, 5C, 5D, 5E, 5F, 5A-R1, 5A-R2, 5A-R3, 5C-R1, 5C-R2	30-<u>30</u>-30-<u>30</u>-30	150	
	REF, 5G	<u>30</u>-30-<u>30</u>-30-<u>30</u>	150	600
	REF, 5H, 5I, 5J, 5K, 5L	40-<u>20</u>-40-<u>20</u>-40	160	
7S	REF, 7A, 7B, 7A-R	30-<u>30</u>-30-<u>30</u>-30-<u>30</u>-30	210	
	REF, 7C, 7D, 7B-R	30-30-<u>30</u>-30-<u>30</u>-30-30	210	

a) underline refers to cross layer

All tests were done using a 4-point bending configuration (Figure 4) under controlled displacement. The specimens were notched on both ends in order to reduce material usage. The crack propagation was limited to the point of the first load introduction from the notch (3h), using self-tapping screws with the aim to preserve an intact cross section in the areas relevant for testing the notch on the opposite side of the specimen. The same test configuration depicted in Figure 4 was used for all series.
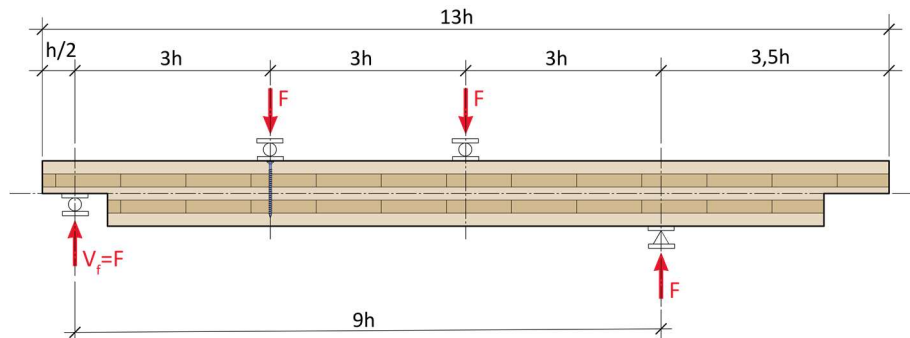
Figure 4   Test configuration for unreinforced and reinforced notches

In order to deduct a suitable test configuration, in a first step the influence of the specimen width B on the statistical parameters was investigated on 150 mm and 600 mm wide CLT members. From the statistical analysis it was found that the coefficient of variation was 18 % for the former and 7 % for the latter. Thus it was concluded that the width of 600 mm was optimal for the main testing program.

All tests were monitored by means of a digital image correlation system (DIC) with its help the correct crack lengths can be determined at the failure. In addition it was used to determine the strain distributions in vicinity of the notch. In particular the influence of grain patterns and stiffness in the radial and tangential direction of the cross layer could be tracked. This was important for the correct depiction of failure and crack propagation there. However, it should be mentioned that the influence of the free surface potentially can cause faulty representation of the real stress states and crack lengths thus limiting the reliability of measurements with the DIC.

3.3   Test results

3.3.1   Test results on unreinforced notches

In Table 2 the results of the test series with unreinforced notches are listed.

Table 2. Detailed results of tests on unreinforced notches

Series	Company	Num. of tests	β	α	$V_{f, mean}$ [kN]	CoV [%]	$V_{f, 005}$ [kN]	MIN/MAX [kN]	$V_{f, mean}$ / $V_{f, ref}$ [%]
REF	1	6	-	-	67.0	6.39	58.7	63.0/75.3	100
3A		10	0.40	0.75	67.0	13.4	50.2	53.0/82.6	100
REF	2	6	-	-	106	4.45	96.4	101/111	100
5A		10	0.40	0.50	48.1	13.2	36.3	37.5/60.5	45.6
5B		10	0.20	0.60	73.9	7.77	63.1	61.5/83.5	70.0
5C		10	0.40	0.60	70.7	8.51	59.5	64.0/82.5	67.1
5D*		9	0.40	0.60	71.4	5.53	64.0	66.0/79.5	67.7
5E		6	0.40	0.80	76.7	8.14	64.6	67.5/84.5	72.7
5F		7	0.40	0.90	114	3.96	114	84.5/121	108
REF	2	5	-	-	74.5	4.54	68.0	69.5/79.0	100
5G		10	0.40	0.5	25.1	7.96	21.4	21.7/28.8	25.1
REF	3	4	-	-	133	1.73	128	130/135	100
5H		10	0.80	0.63	58.2	16.6	40.1	46.0/75.0	43.7
5I		8	0.40	0.63	58.8	10.6	46.9	51.3/70.0	44.2
5J		10	0.40	0.81	105	9.63	85.8	88.0/126	78.7
5K	4	6	0.40	0.63	83.5	7.00	72.5	72.7/90.9	62.8
5L		6	0.40	0.53	53.0	10.0	42.0	92.2/120	39.8
REF	5	6	-	-	113	8.47	94.2	95.5/125	100
7A		6	0.40	0.62	75.1	4.74	68.2	72.0/82.5	66.5
7B		6	0.40	0.71	95.8	5.07	86.4	87.0/103	84.8
REF	6	6	-	-	144	2.98	136	137/150	100
7C		6	0.40	0.57	72.9	7.59	62.0	63.0/79.5	64.5
7D		6	0.40	0.76	109	4.33	99.7	101/117	96.3

*Notch is tapered with i = 1.0, for definition of parameter *i* see Figure 2b)

3.3.1.1   Results

In series 5I, 5K the geometrically equivalent configurations showed high difference in the failure loads. The failure load in series 5K was 1.4 times higher than in 5I, possible cause is lower fracture energy of series 5I. This conclusion is derived from comparison of the test results with analytical and numerical results in section 5.1.

The influence of the notch length as well as the notch taper was investigated in series 5B, 5C, 5D*. As can be seen a notch tapered at 45° (i = 1.0) had only minor influence on the increase of load-bearing capacity. Analysing the test results with the formulation provided in EC5 for the influence of the notch taper on increase of load bearing capacity $(1+1.1i^{1.5}/\sqrt{h})$ an increase of 9 % can be computed. It can be concluded from the tests, that tapering the notches with slopes $i < 1.0$ is not sufficient for an increasement of the load-bearing capacity. Further tests on more tapered specimens ($i > 1.0$) should be conducted and can be recommended in other to create

a basis for the calibration of the load bearing capacity compared to notches without taper. The current formulation from EC5 Eq. (4) seems to be a solid basis for this further development.

A similar diminishing return on the increase of the failure load could be recognised varying the notch parameter β. For series 5B ($\beta = 0.2$), the failure load is increased by only 4 % compared to 5C ($\beta = 0.4$). For comparison the analytical approaches lead to around 5 % increase. A similar behaviour was recognised in series 5H and 5I, however it should be noted that the results in series 5I are influenced by the lower fracture energy.

3.3.1.2   Fracture behaviour of unreinforced notches

A consistent fracture behaviour of the specimens was observed through the experimental program. Two specific failure modes were observed as already reported in Serrano (2019, 2020):

- **Fracture along the grain**, if the notch was placed in a longitudinal layer or at the bottom of a longitudinal layer at the interface. The crack propagation can deviate due to the local grain angle deviations, however the propagation to neighbouring transversal layer due to local grain deviations was not observed. Such behaviour occurred in cases when the notch was placed in the longitudinal layer but close to an interface (e. g. for series 7C, 7D). In some tests, due to the grain deviations, the crack kinked into the transversal layer. However, such behaviour took place after the crack propagated for several centimetres and during the unstable crack propagation, thus not influencing the load bearing capacity.

- **Fracture in the transversal layer**, if the notch is placed in a transversal layer or at the bottom of a transversal layer at the interface. In general the crack propagation can be assumed at an angle of 45° to the horizontal. Nevertheless, in the transversal layer the crack propagation was heavily influenced by the grain pattern, and the location of the notch within the transversal layer. This behaviour can be explained by the heterogenous ratios of the layers E_{90R}/E_{90T} and G_{90R}/G_{90T}. Several failure patterns were recognised from the tests regarding the crack propagation depending on the grain pattern at the notch tip in the transversal layer (Figure 5, middle). Different crack patterns were observed for series 5E, while for series 5G almost all failures occurred at an angle of 45° and some in a zig-zag manner as shown in Figure 5, middle.

- At some specimens a **debonding of the glued interface** was observed, pointing out that the fracture energy of the glued interface plays an important role in the area of the interface.

In series with notch in transversal layer (series 5G, 5E) no significant increase of the load bearing capacity was observed. This implies once more the restricted influence of transversal layers on the load bearing capacity.

For the series 5F and 3A rolling shear before notch failures occurred. Implying that in CLT if only part of the first layer, e.g. 80 % is notched with $\beta < 0.5$, the rolling shear failure is the dominant mode of failure. This hypothesis should be nevertheless further evaluated.
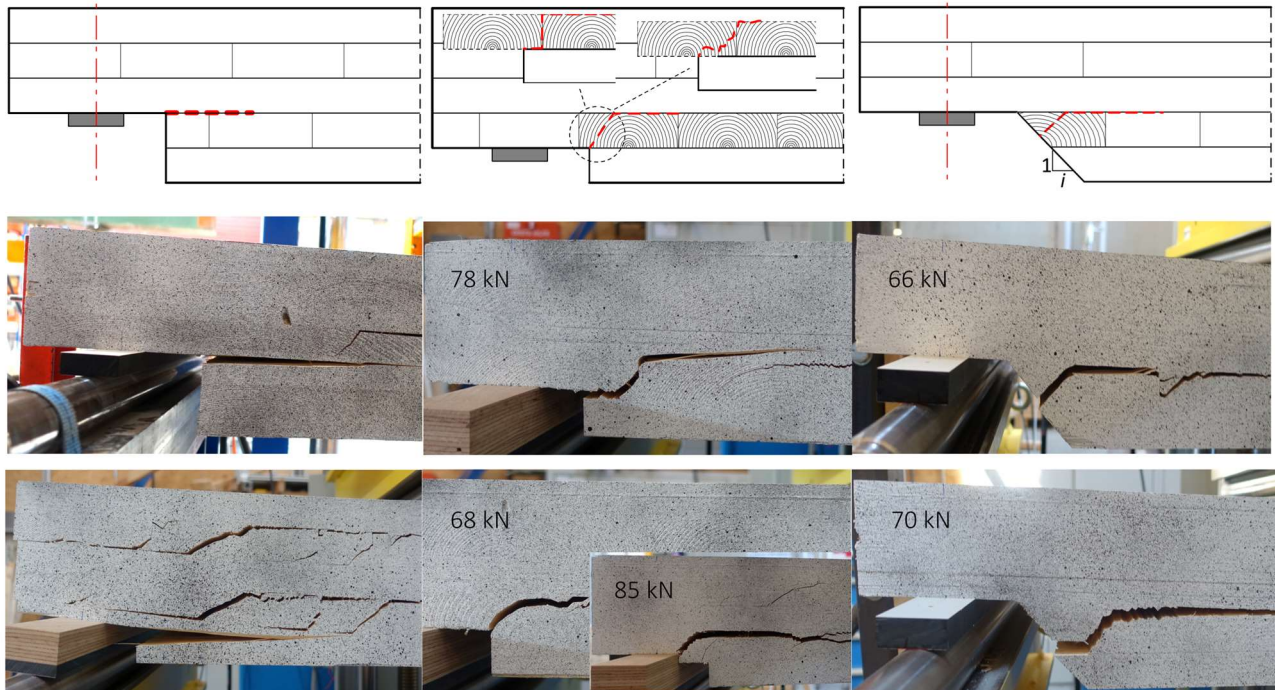
Figure 5   Left: Failure mode in longitudinal layer and failure due to the rolling shear failure in series 5F at bottom left; Middle: Different failure modes in transversal layer for series 5E; Right: Different failure modes in tapered notch series 5D*

3.3.2   Tests on reinforced notches

3.3.2.1   General

The reinforcement consisted for all reinforced series of self-tapping screws with a diameter d = 8 mm and was placed at a distance of 2.5d from the notch tip in order to increase on hand the effectiveness of the reinforcement as reported in Augustin (2016), and on the other to avoid a splitting of the member at the end face. The number of screws, all applied in a row, was varied depending on the expected load carrying capacity and ranged from 2 to 4 equally spaced screws.

In Table 3 for series 5A-R2, 5A-R3, 5C-R1, 5C-R2 the number of screws or side from which screws were applied was varied. In order to reduce the influence of material parameters these variations were made on each specimen, e.g. one side of the specimen was tested with two screws and other side with four.

3.3.2.2 Test results

In Table 3 the results of the test series with reinforced notches are listed.

Table 3. Detailed results of tests on reinforced notches

	Series	5A-R1	5A-R2	5A-R3[a]	5C-R1		5C-R2[a]		7A-R	7C-R
	n_{screw}	3		4	2	4	2	4	3	3
Screw	$F_{,axial}$ [kN]	25.5	23.2	23.2	12.2	24.4	8.5	17.1	24.4	27.5
	d [mm]					8.0				
	Screw angle φ	45		90		90			90	90
	β		0.40			0.40			0.40	0.40
	α		0.50			0.60			0.62	0.57
	$V_{f, r, mean}$ [kN]	84.0	78.0	79.8	80.2	92.6	80.3	88.5	105	100
	V_{crack} [kN]	60.0		45.0		60.0			60.0	70.0
	Num. of tests	6	5	5	4	5	4	5	6	6
	CoV [%]	5.64	1.83	5.77	5.48	4.92	5.94	5.37	5.05	7.10
	$V_{f,05}$ [kN]	37.4	75.2	70.7	71.4	83.6	70.8	79.4	94.7	86.6
MIN	[kN]	78.0	76.0	73.5	77.5	87.5	74.6	79.9	99.0	92.0
MAX		91.5	80.0	87.5	87.8	100	85.0	94.2	115	112
$V_{f, r, mean}/V_{f, ref}$ [b] [%]		79.2	73.6	75.3	75.7	87.4	75.8	83.5	92.9	69.4
$V_{f, r, mean} / V_{f, mean}$ [c] [%]		175	162	166	113	131	114	125	140	133

a) Screws applied from the top side of the plate

b) Reference failure load is referred to rolling shear failure of "REF" series

c) mean failure load of the unreinforced notch of the same notch parameters

3.3.2.3 Fracture behaviour of the reinforced notches

During the tests on the reinforced specimen a significant increase of the failure load could be observed in comparison to the reference tests with unreinforced notches. The load at crack initiation was however similar to the unreinforced notches, implying that the reinforcement contributes to load bearing capacity and crack growth stability only after the initial crack growth. A Similar behaviour is reported in Jockwer (2014) and Augustin (2016). The explanation for this behaviour can be found in the singular behaviour of stresses around the notch tip and the small deformation in the vicinity of reinforcement prior to the crack initiation. This assumption was confirmed by the DIC measurements.

It has to be noted that, although the load bearing capacity significantly increased with the reinforcement, the full load bearing capacity of the unnotched reference specimen, failing in rolling shear, could not be achieved.

The failure mode of the reinforced notched CLT elements was identified as screw withdrawal failure, accompanied by a subsequently instable crack growth. This implies that for the tested notch and screw parameters the withdrawal strength of the screws is the critical property.

The reinforced CLT notches showed a steady crack growth after crack initiation leading to a stable behaviour of the specimens. The crack length at failure, determined by the DIC software, was around 90 mm. Compared with the steady crack growth length in the unreinforced notches of around 20 mm, this is significant higher.

An interesting conclusion can be drawn when comparing the failure loads of the unreinforced and the reinforced notches. In general an empirically load bearing capacity of the notch can be determined as

$$V_{f\,reinforced} = V_{f\,unreinforced} + (1.0\ to\ 1.3)\,n_{screws}F_{ax}\,,$$

where F_{ax} is the (minimum) withdrawal strength of the screw above and below the crack line. The determined empirical regression can be used as a first rough estimate for the load carrying capacity of reinforced notched CLT members. A more detailed analysis and derivation of a detailed analytical model was not done within the scope of this paper and will be made in the future.

4   Analytical and Numerical models

The following calculations of analytical and numerical models were performed with the material properties given in Table 4. It is noted that these properties, especially the fracture energies, are not calibrated because no fracture energy tests on small specimen were carried out. No distinctions between radial and tangential directions were made regarding stiffness and fracture properties.

Table 4. Used material properties for the analytical and numerical models

Parameter	Value	Description
E_0 ; E_{90}	11000 ; 390	MOE longitudinal; transversal [MPa]
$G_{0,\,90}$; $G_{90,\,90}$	690 ; 69.0	Shear modulus, longitudinal; transversal [MPa]
$f_{t,\,90}$	2.00	Strength in tension, perp to grain [MPa]
$f_{v,\,0}$, $f_{v,\,r}$	4.00 ; 2.00	Shear strength, along the grain ; rolling shear [MPa]
$G_{c,\,I}$; $G_{c,\,II}$	0.30 ; 1.20	Critical energy release rate, Mode I ; Mode 2 [mJ/mm^2]
$v_{,\,LR}$; $v_{,\,RT}$	0.56 ; 0.03	Possion ratios [-]

4.1   Numerical investigations

The unreinforced notch configurations from Table 2 were analysed with the FEM analysis software package "Ansys Mechanical 2020R2". Two different numerical approaches were performed using the built in software code for fracture mechanics:

- 2D Plane Stress model based on linear elastic Virtual Crack Closing Technique (VCCT)
- 2D Plane Stress nonlinear contact debonding tool using Cohesive Zone modelling (CZM).

The used numerical model is presented in Figure 6. A mesh convergence study was performed around the notch in order to optimize the mesh size for the computation. The mesh refinement around the notch was made with elements of 0.2 mm in size. In parts of the CLT element not influenced by the stress concentrations at the notch the mesh size is determined depending on height of the intact beam. Only half of the specimen was considered in the analysis using symmetry boundary conditions in order to reduce computation time. The supports were modelled as a non sliding contact between the steel plate support and CLT element. The steel plate is restrained with roller support (u_x = Free, u_y = 0, φ_z = Free). The different contacts between the steel plate and timber were utilised to investigate the influence of support restrictions on the result, however no influence on results was found. The considered numerical fracture models require a predefined crack tip and crack path. For notches in the longitudinal layer a crack path parallel to the grain was implied, while for a notch in the transversal layer the crack was assumed to propagate at 45° through the transversal layer until the next interface is reached. Afterwards it propagates along the interface (see Figure 5, middle). The assumption of 45° angle is reasonable as no distinctions were made between radial and tangential directions in the material properties.
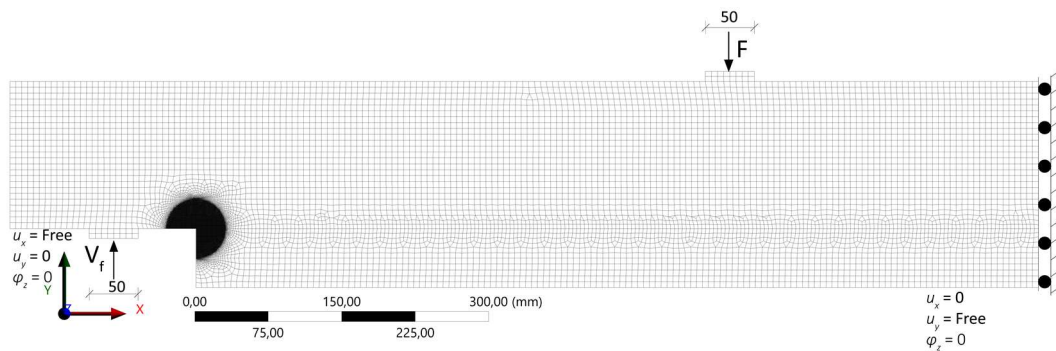
Figure 6   Numerical model used in both numerical analysis with coresponding boundary conditions

Both models were investigated using mixed mode conditions with the objective to determine the influence of mode II on fracture. The failure load is computed using failure criteria for mixed mode delamination. Due to limitations of the used software to consider contact debonding a linear elastic failure criterion was used (Eq. (7)).

$$\left(\frac{G_I}{G_{c,I}}\right) + \left(\frac{G_{II}}{G_{c,II}}\right) = 1 \qquad (7)$$

Although for VCCT several mixed mode fracture criteria are available (e.g. exponential criteria) the linear criteria was applied in both approaches in order to compare two numerical analysis.

The considered models showed, overall, different results: The VCCT model overestimates the failure load of the test specimen by a factor of 1.2 to 1.3. An explanation for this behaviour can be found in the fact, that the fracture process zone is not fully considered in VCCT, in particular in cases when the crack length is equal to

the notch length. Furthermore, VCCT in general overestimates the results as infinite strength of material is assumed ($f_{t,\,90} = \infty$). The overestimation of the load carrying capacity is even more pronounced for larger α and smaller β, where for series 5F the failure is 1.8 times higher. Since the specimen of series 5F and 3A failed in rolling shear, i.e. a different failure mode, such extreme values are of no concern. A better correspondence with the test results can be achieved by increasing the crack length for the length of the process zone. A similar approach was used in Serrano (2019, 2020) from which it can be seen that without a modification of the crack length the failure loads for some notch configurations are overestimated.

The modelling using the contact debonding analysis showed, in general, a good correspondence with the test results, illustrating the influence of process zone in timber.

The results from the numerical analysis will be presented in section 5.1.

4.2 Analytical models

The comparison of results from Eq. (6) with previous test campaigns given in Serrano (2019, 2020) give promising implications regarding the applicability of Eq. (6) as a design equation. However, if the fitting parameter Δa is not considered, the failure loads in general are overestimated, and for a certain domain of α and material properties even unphysical results showing higher failure loads or complex solutions, are possible (Figure 10 right). Due to these reasons the fitting parameter can't be omitted from the analysis and it needs to be investigated in detail over all relevant parameter domain in order to implement it in the next generation of codes. Experimental and numerical testing on numerous layups and different notch parameters becomes exponentially difficult due to the heterogeneity of CLT, therefore in this paper an analytical solution is presented for the evaluation of the fitting parameter Δa. This approach describes the additional rotation of the cross section at the crack tip, in literature deduced as beam root rotation.

4.2.1 Elastic interface-semirigid model

The analytical solution is based on the work of Qiao and Wang (2004) and it represents a solution according to the energy balance method of LEFM on two shear deformable bi-layer beams coupled at the interface considering appropriate kinematic conditions, (see Figure 7). Depending on these conditions at the interface three different levels of solutions, each rising in complexity, can be obtained.

The main kinematic conditions at the interface of the two beams can be expressed as

$$\varphi_1 = \varphi_2 \ \text{ and } \ u_1 + \varphi_1 \frac{h_1}{2} = u_2 + \varphi_2 \frac{h_2}{2}, \tag{8}$$

where φ_i denotes the rotation of beam 1 above the crack and beam 2 under the crack, u_i stands for the longitudinal displacements along the interface and h_i is equal to the height of the beams.

The mentioned three levels of solution are defined as:

Rigid model: This is the simplest model considering both kinematic conditions of Eq. (8) at the crack tip. This is completely equivalent to the solution of the Structural Element Model in case when k_φ approaches infinity and $\Delta a = 0$.

Semi-rigid model: This model releases the boundary condition $\varphi_1 = \varphi_2$ causing the independent rotation of the coupled beams, but considers the displacement continuity condition.

Flexible model: In this approach both kinematic boundary conditions are modified. The solution is improved by taking into account the deformability of the interface by introducing continuously distributed normal and shear springs at the interface boundary. As a consequence, the normal and shear stresses at the interface are proportional to the interface stiffnesses.
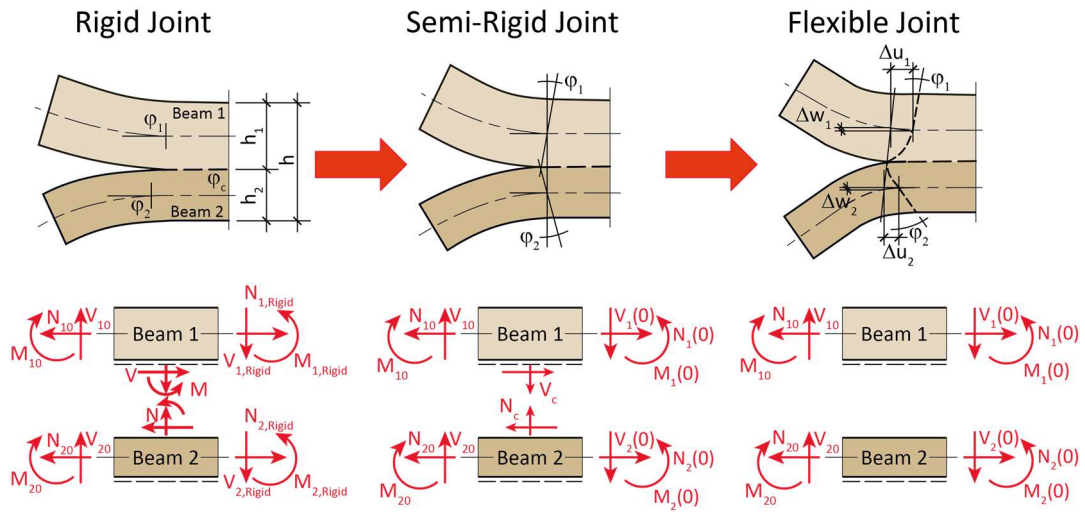
Figure 7   Depiction of crack tip element of joint models in a bi-layer beam system

In the following the crack root rotation in CLT is investigated with the help of the semi-rigid model. This can be interpreted as a good trade-off between complexity and accuracy of the model. Only the main solutions regarding this model will be given in order to keep the paper in a reasonable scale. For a detailed derivation of the mentioned models refer to Qiao and Wang (2004).

By differentiating Eq. (8), taking into account the constitutive equations of the Timoshenko beam theory and considering the equilibrium conditions $\Sigma M = 0$, $\Sigma V = 0$, $\Sigma N = 0$ at the crack tip element (CTE) in Figure 7., the governing equation of the semi-rigid joint model is obtained as

$$\left(\frac{1}{(\kappa GA)_1} + \frac{1}{(\kappa GA)_2}\right)\left(\eta + \frac{\xi h_1}{2}\right)\frac{d^2 N_1(x)}{dx^2} - \left(\left(\frac{1}{(EI)_1} + \frac{1}{(EI)_2}\right)\eta + \frac{(h_1 + h_2)}{2(EI)_2}\xi\right)N_1(x) = -q(x)$$

$$q(x) = \left(\left(\frac{1}{(EI)_1} + \frac{1}{(EI)_2}\right)\frac{h_2}{2(EI)_2} + \frac{\xi}{2(EI)_2}\right)M_{10} + \left(\frac{1}{(EI)_1} + \frac{1}{(EI)_2}\right)\frac{N_{10}}{(EA)_2}, \tag{9}$$

where

$$\xi = \frac{1}{2}\left(\frac{h_1}{(EI)_1} - \frac{h_2}{(EI)_2}\right), \quad \eta = \frac{1}{(EA)_1} + \frac{1}{(EA)_2} + \frac{(h_1 + h_2)}{4(EI)_2} \quad , \quad M_{10} = V_f \beta h, \quad N_{10} = 0$$

The solution of Eq. (9) considering a semi-infinite long beam is

$$N_1(x) = ce^{-kx} + N_{1,RIGID} \quad , \text{ where} \tag{10}$$

$$c = \frac{(2M + h_1 N)\xi}{h_1 \xi + 2\eta}, \quad k = \sqrt{\frac{(\kappa GA)_1 (\kappa GA)_2 \left\{2\left((EI)_1 + (EI)_2\right)\eta + (EI)_1 (h_1 + h_2)\xi\right\}}{(EI)_1 (EI)_2 \left((\kappa GA)_1 + (\kappa GA)_2\right)(2\eta + h_1 \xi)}}$$

M, N form a group of self-equilibrating forces at the CTE describing the deformation of the crack tip obtained by imposing equilibrium conditions on CTE in Figure 7, middle.

At the crack tip the crack root rotation can be computed as

$$\Delta\varphi_1 = \varphi_1(0) - \varphi_{1,\,RIGID}(0) = \int_0^L \frac{M_1}{(EI)_1} dx - \int_0^L \frac{M_{1,\,RIGID}}{(EI)_1} dx . \tag{11}$$

According to the principle of superposition in LEFM the energy release rate of the semi-rigid joint can be obtained from the summation of the compliances of the rigid model, already presented in Eq. (6), and the additional contribution of the crack root rotation (Figure 8). The release rate due to the crack rotation is thus defined as

$$G_{c,\,crack\,rotation} = \frac{V_f^2}{2}\frac{dC_{c,\,crack\,rotation}}{da} = \frac{V_f^2}{4}(\Delta\varphi a + \Delta w) \tag{12}$$

The closed form of the failure load at the support including the contribution of the rigid model and the crack root rotation, leads, after simplification of Eq. (11) and Eq. (12) to

$$V_f = \sqrt{\frac{2BG_c}{\left(\left(\frac{1-\psi}{4(EI)_3} - \frac{1-\rho}{4(\kappa GA)_3}\right) + \frac{1}{4}\left(\frac{(h_1 a_N + 2(1-\psi))}{h_1 \xi + 2\eta}\right) \cdot \left(\frac{2\eta a}{(EI)_1 k} + \frac{\eta}{(EI)_1 k^2} - \frac{1}{(\kappa GA)_1}\left(\eta + \frac{h_1}{2\xi}\right)\right)\right)}} \tag{13}$$

where $\psi = \frac{(EI)_1}{(EI)_3}$ and $\rho = \frac{(\kappa GA)_1}{(\kappa GA)_3}$,

Remark: The closed form solution can be used in future for a parametric analysis and a verification of fitting parameter developed in Serrano (2019).
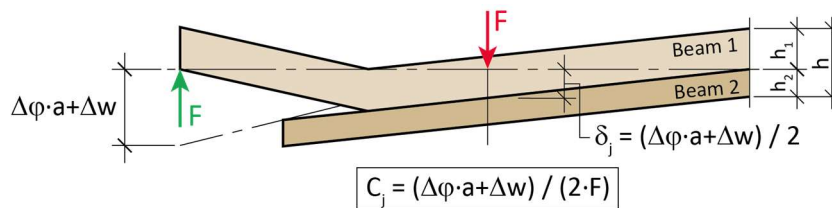

Figure 8   Ilustration of the crack root tip rotation and the subsequent change in compliances

4.2.2 Beam on elastic foundation

An alternative approach to the Structural Element Model can be deduced based on a Timoshenko beam on elastic foundation (BEF) taking into account an adaption for the case of an unreinforced notched CLT plate (Figure 9).
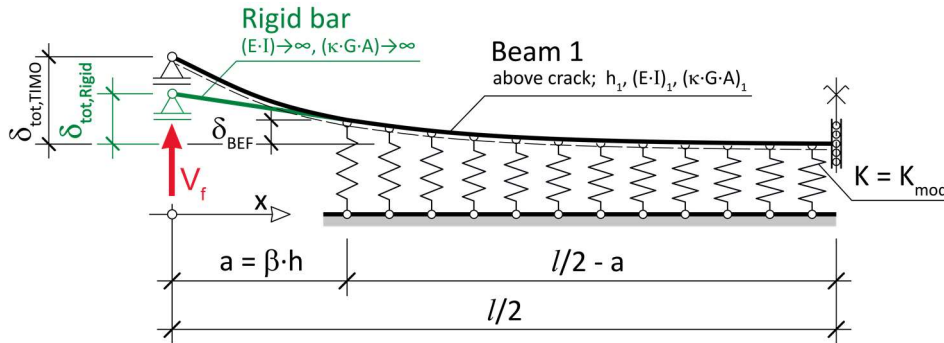

Figure 9   Timoshenko beam on elastic foundation

The model consists of two beams: Beam 1 in the BEF is denoted as part of the CLT beam above the crack. The springs with the spring constant K simulate the elastic delamination of the interface at the crack tip and along the delamination plane. The fracture layer is assumed to be coupled with a stiff foundation. For Beam 2 under the crack, a crude assumption is made, where the deformation and interaction of beam 2 with beam 1 at the interface is ignored due to the assumption of indefinite stiff foundation intrinsic to BEF.

The interface stress at the notch tip according to the BEF can be calculated as

$$\sigma_y(x) = K w_y(x).\tag{14}$$

The general solution of Timoshenko beam on elastic foundation as well as the differential equation are left out in order to reduce the scope of this paper. A detailed derivation can be found in the work of Jorissen (1998).

Solving the differential equation of BEF and introducing the boundary conditions from Figure 9. ($M_1 = V_f \beta h$, $P_1 = V_f$) leads to a solution for the deformation at the end point of BEF, i.e. the crack, expressed as

$$w_y(x) = -\frac{2V_f}{K_{\mathrm{mod}} B}\left(\gamma + \lambda^2 \beta h\right),\tag{15}$$

where

$$\gamma = \sqrt{\lambda^2 + \frac{K_{\mathrm{mod}} B}{4(\kappa GA)_1}} \quad \text{and} \quad \lambda = \sqrt[4]{\frac{K_{\mathrm{mod}} B}{4(EI)_1}}\,.$$

Analogue to the deformation an equation for the rotation at the crack tip can be obtained as

$$\varphi = \varphi_{(0)} = -\frac{V_f}{2EI\lambda^2} - \frac{V_f \beta h}{\gamma}\left(\frac{\lambda^2}{(\kappa GA)_1} + \frac{1}{(EI)_1}\right).\tag{16}$$

The total deformation at the loading point from Timoshenko BEF is then

$$\delta_{total} = \omega_{y(0)} + \beta h \varphi_{(0)} . \tag{17}$$

In this case the deformation at the loading point is assumed to be influenced only by the elastic foundation, i.e. the contribution of the cantilever part of length βh is ignored. This assumption is supported by the poor matching with test result when the compliance of the Timoshenko cantilever beam is considered. This beam section heavily influences the failure load making it over conservative. However, it is noted that the results matched well for $\alpha < 0.3$.

With an increasing notch height the theory underpredicts the failure loads, even with modification of the foundation spring stiffness K_{mod}. Good matching with test results is obtained by assuming a rigid bar instead of the Timoshenko cantilever beam and analysing the contribution from BEF and the rigid bar. In order to take into account the deformation of the ignored cantilever and the influence of beam 2, the modification of foundation spring stiffness may be introduced as

$$K_{mod} = \frac{K}{(1-\alpha)^m}, \text{ where } m = \begin{cases} 1 \ for \ \beta \le 0.3 \\ 3 \ for \ \beta \ge 0.4 \end{cases} . \tag{18}$$

K is the foundation modulus [N/mm^3] and it is derived from the analysis presented in Augustin (2016) leading to $K \approx 2$ [N/mm^3]. The exponent m is developed to take into consideration the length of the notch due to the assumption of rigid bar cantilever.

Combining Eq. (15 to 17), deriving the expression with respect to the crack length βh and solving the equation with help of Eq. (2) the failure load can be obtained as

$$V_f = \sqrt{\frac{2BG_c}{2\dfrac{\beta h}{\gamma}\left(\dfrac{\lambda^2}{(\kappa GA)_1} + \dfrac{1}{(EI)_1}\right) + \dfrac{1}{(EI)_1 \lambda^2}}} . \tag{19}$$

5 Model comparisons with experimental results

5.1 Comparison of analytical and numerical results of unreinforced notches

The following comparison of analytical and numerical results with test results on unreinforced CLT notches is conducted on the basis of mean values.

The distribution of the failure load at the support for different analytical models is illustrated in Figure 10, left. The distribution is shown for the 30-30-30-30-30 layup.

The comparison of the experimental test with the mentioned analytical and numerical methods is depicted in Figure 11.
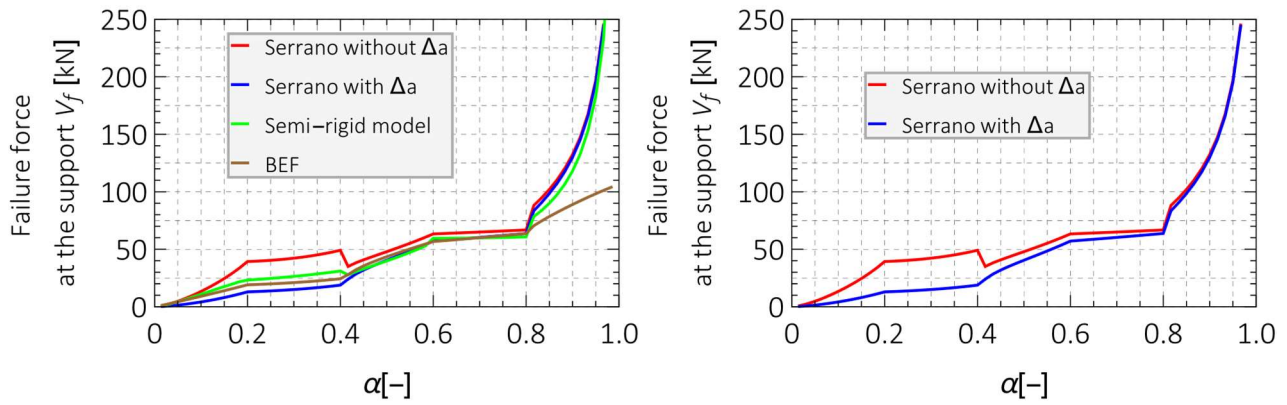
Figure 10   *Left: Distribtuon of failure loads at the support depending on the parameter α for various developed analytical models; Right: Comparison of the Structural Element Model with and without fitting parameter*
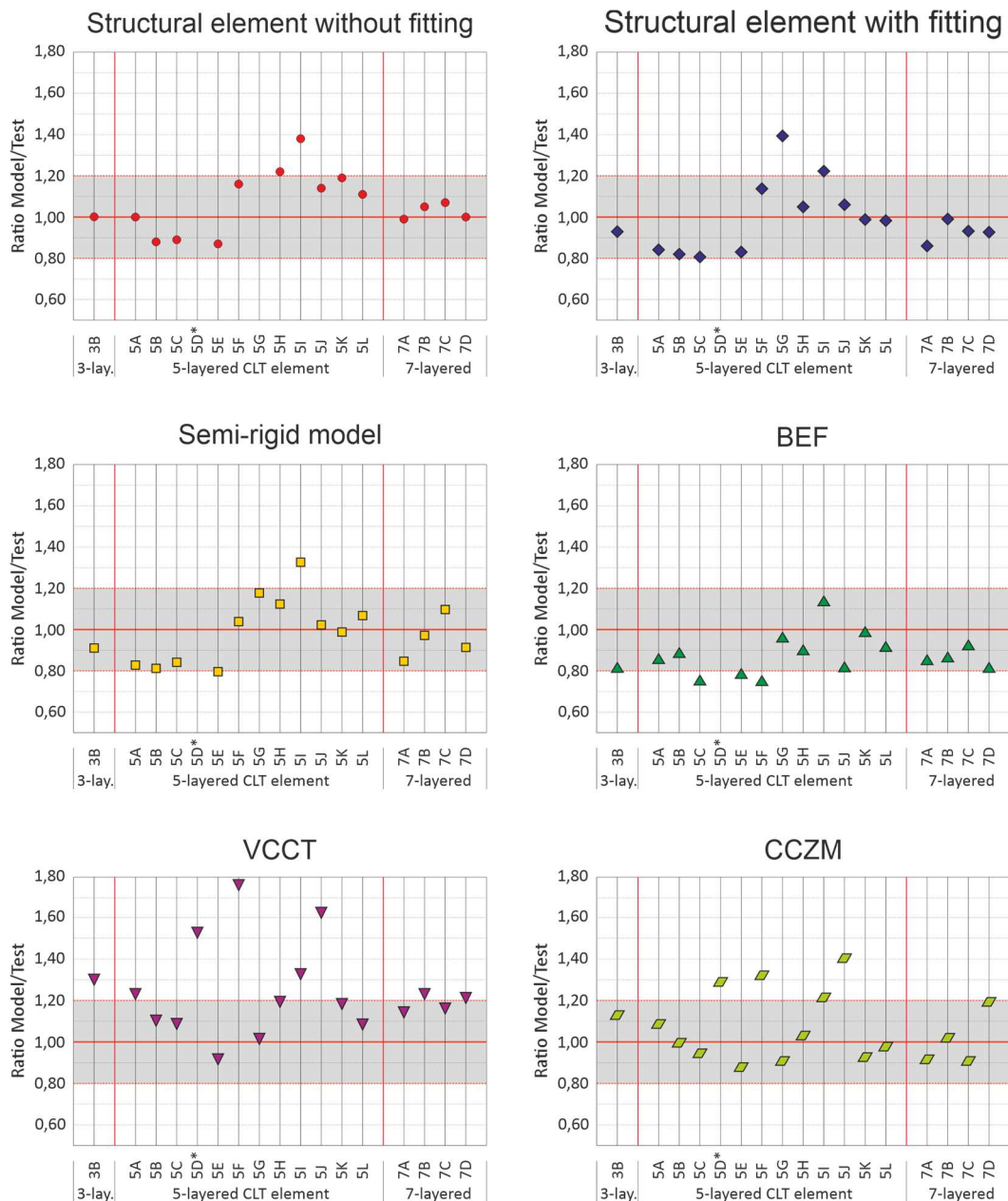
Figure 11   *Comparison of results from the developed models with the conducted experimental tests. Ratio V_{f_Model}/ V_{f_Test} is shown, if ratio > 1 the failure load is overpredicted by the model results, i.e. on the unsafe side*

Before coming to the comparison of results, it should be emphasised that no calibration of material properties was made. As a general statement it could be determined from the comparison that the developed models match good with the experimental tests. The results are for most of the series positioned on the conservative side, excluding series 5I and 5H. It is evident that all the mentioned series were delivered from the same producer. Thus it can be suspected, that these series consisted of a different material with weaker properties, i.e. smaller fracture energy. All the specimen of series 5F, 3A, failed in rolling shear, consequently making a direct comparison of the failure loads at the notch unclear. All other series failed by delamination at the notch making the comparison valid.

The Structural Element Model without fitting (rigid model) presented unsafe results for 7-layer members, while this model considering the fitting parameter provided better results proving applicability of developed Δa also for this domain of tested parameters in addition to the tests in Serrano (2020).

In comparison the semi rigid model and Structural Element Model with fitting factor provided in general the same behaviour in the domain of considered layups and notch parameters.

The BEF model provided more conservative results of failure loads mainly due to the crude assumption of a rigid bar. It seems that the considered modification of the foundation stiffness isn't enough to overcome the used assumption, in particular that of the stiff foundation. Better results can be obtained, if one considers Vlaslov beam on elastic foundation due to the included rotational springs (Yoshida 2018). It is further noted that, the solution of BEF seems to be applicable only if $\beta < 0.6$ due to the made assumptions. For solutions out of this domain results on the conservative side are obtained when comparing to other mentioned models.

The numerical model according to VCCT overestimate the fracture loads in almost all series by a significant factor. Considering the additional length of process zone yields to better result. The additional crack length of 15 mm is chosen for series 5A and failure load was only overestimated for factor 1,05 in comparison to 1,3 when no modification is considered. The crack length is evaluated based on nonlinear fracture mechanics. It should be noted that on results of VCCT the assumption of linear mixed mode fracture criteria plays a role.

The CZM model showed good matching with test results in domain of notches not influenced by rolling shear failure.

The assumption of $Gc = Gc,_I$ showed a good approximation as the mixed mode failures computed in numerical analyses didn´t show significant influence of mode II on failure loads. The mode mixity in CLT notches can also be calculated in an analytical way with the help of semi-rigid model.

6 Conclusion and recommendations for design and further work

The following conclusion can be drawn from the present work:

- The Structural Element Model in general gives good matching with test results over different layups, proving the robustness of the fitting parameter Δa.
- A fitting parameter can be verified through the parametric analysis utilizing model developed in this work.
- The VCCT approach overestimates the load bearing capacity. An additional crack length should be considered for this model.
- The current models given in ETA-06/1038 and Wallner-Novak are not appropriate due to wrong theoretical assumptions. A fitting of the factor k_n would work only on a limited number of layups.
- The current provisions in ETA-06/1038 regarding limit values of geometrical notch parameters seem inadequate for layered structure of CLT. In that direction the following recommendations for limiting values could be:
  - for 3 layered plates: up to 2/3 of first (bottom) layer may be notched; $\beta \leq 0.6$; in case of a deeper notch reinforcement shall be used.
  - for 5 layered plates: $\alpha \geq 0.5$; $\beta \leq 0.6$; if the first (bottom) layer is transversal layer reinforcement shall be used.
  - for 7 layered plates: $\alpha \geq 0.5$; $\beta \leq 0.6$ or maximum notch depth of 4 full layers, otherwise apply a reinforcement.
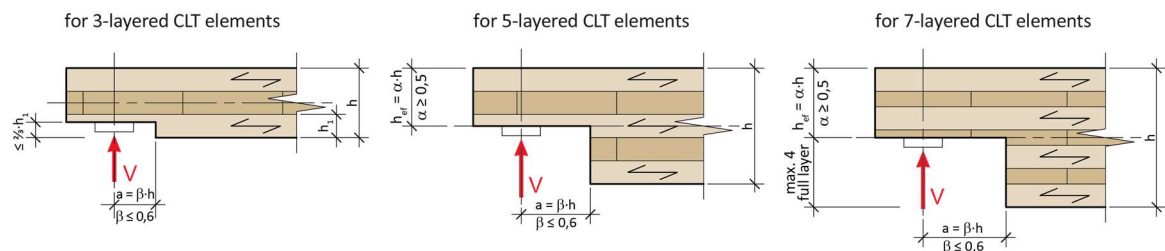
Figure 12   Proposal for limit values of geometric parameters of different lay-ups of CLT elements

- Preliminary test results on tapered notches show a similar behaviour to already developed models for homogenous tapered notches. Nonetheless this can't be concluded only on the basis of one configuration; thus further tests are needed.

Further research should gravitate towards the following topics in CLT notches:

- Calibration of fracture properties in order to further verify the models
- Parametric analysis fitting factor Δa with help of a semi-rigid model
- Further development of analytical and numerical approaches for the determination of the load-bearing capacity of reinforced notches and force in the reinforcement, applying the mentioned models.

- Investigation of the Duration-of-Load (DOL) behaviour as well as the influence of variation of the moisture content on the load-bearing capacity of notches in natural and varying climates.

7 Acknowledgment

8 References

Augustin M., et al. (2016): A Contribution to the Design of Ribbed Plates, World Conference on Timber Engineering, Vienna, Austria

ETA-06/0138 (2017): European Technical Assessment, 20.2.2017

Eurocode 5 (2004): Design of timber structures - Part 1-1: General and rules for buildings. CEN. (EN 1995-1-1).

Friberg, A. (2017): Bärförmåga för KL-trä med urtag–Provning och beräkningsmetoder (in Swedish). (Load-bearing capacity of CLT with notches –Testing and calculation methods). Bachelor thesis, Report THID-5526, Division of Structural Mechanics, Lund University, Sweden

Griffith, A. A. (1921): The phenomena of rupture and flow in solids. Philosophical Transactions of the Royal Society of London, A. 221 (582-593): 163-198

Gustafsson, P. J. (1988): A study of strength of notched beams. In: Proceedings CIB-W18 Meeting 21, Paper CIB-W18/21-10-1, Parksville, Canada.

Jensen, L.J., Gustafsson P.J. (2004): Shear strength of beam splice joints with glued-in rods, J Wood Sci (2004) 50:123–129, Japan, DOI: 10.1007/s10086-003-0538-6

Jockwer, R. (2014): Structural Behaviour of Glued Laminated Timber Beams with Unreinforced and Reinforced Notches, Dissertation, ETH Zurich

Jorissen, A.J.M. (1998): Double shear timber connections with dowel type fasteners, Delft University Press, Delft, Netherlands

Qiao, P., Wang J. (2005): Novel joint deformation models and their application to delamination fracture analysis, Composites Science and Technology 65 (2005) 1826–1839

Serrano, E., Danielsson, H. (2020): Fracture Mechanics Based Design of CLT plates– Notches at Supports and Half and-Half Joints. In: International Network on Timber Engineering Research – Proceedings Meeting 53, Paper INTER/53-12-2, Online.

Serrano, E., Gustafsson, P. J. and Danielsson, H. (2019): Prediction of load-bearing capacity of notched cross laminated timber plates. In: International Network on Timber Engineering Research – Proceedings Meeting 52, Paper INTER/52-12-2, Tacoma, USA.

Wallner-Novak, M., Koppelhuber, J. & Pock, K. (2013): Brettsperrholz Bemessung – Grundlagen für Statik und Konstruktion nach Eurocode (in German). ProHolz Austria, Vienna, Austria.

Yoshida, K., Takahira, A. (2018): Beam on elastic foundation analysis of sandwich SCB specimen for debond fracture characterization, Composite Structures Volume 195, 1 July 2018, Pages 83-92, DOI: https://doi.org/10.1016/j.compstruct.2018.04.032

DISCUSSION

The papers was presented by M Malagic

P Dietsch received clarification that in the paper it is possible to have a linear interpolation of the proposed K_{mod} as a function of m so that K_{mod} is not discontinuous. The use of the term K_{mod} should be reconsidered to avoid misinterpretation. P Dietsch commented that tension strength perpendicular to grain and rolling shear strength seemed too high. A Malagic responded that analysis assumed volume dependency of these strength properties hence higher values.

H Blass asked about the use of notch beam support K_n= 4,5. He said this value is for LVL beams loaded edgewise and asked for justification for their use for CLT as a plate. A Malagic said this is the state of the art in design consideration. H Blass disagreed and commented that this factor cannot be used for CLT.

E Serrano and A Malagic discussed the similarity of the semi rigid approach to a previous paper with different choice of coupling. E Serrano received clarification that comparison of different capacity in units of k_n was based on width of the member used in the experimental program of 600 mm. E Serrano commented that assumed semi infinite length as being a possible severe assumption. A Malagic responded that the transition zone was small and therefore not a limiting factor.

CHARACTERIZATION OF ROLLING AND LONGITUDINAL SHEAR CREEPS FOR CROSS LAMINATED TIMBER PANELS

Charlotte Allemand, Centre Scientifique et Technique du Bâtiment (CSTB), Champs-sur-Marne and Laboratoire Navier, UMR 8205, Ecole des Ponts ParisTech, Univ Gustave Eiffel, CNRS, Marne-la-vallée, France (charlotte.allemand@enpc.fr)

Arthur Lebée, Laboratoire Navier, UMR 8205, Ecole des Ponts ParisTech, Univ Gustave Eiffel, CNRS, Marne-la-vallée, France

Manuel Manthey, Centre Scientifique et Technique du Bâtiment (CSTB), Champs-sur-Marne, France

Gilles Forêt, Laboratoire Navier, UMR 8205, Ecole des Ponts ParisTech, Univ Gustave Eiffel, CNRS, Marne-la-vallée, France

Keywords: rolling-shear , creep , cross laminated timber , long-term behavior , longitudinal shear

1   Introduction

Everywhere around the world, high timber buildings are rising. The construction of these new buildings is possible thanks to the mainstreaming of some engineering products such as cross-laminated timber panels (CLT) and glued laminated timber (GLT). Those panels gained in popularity for several reasons. First, they are a more sustainable solution than concrete designs. Second, the prefabrication process makes them easy to assemble on site. CLT panels also have a high dimensional stability under variation of moisture content compared to other timber products. Because of all those advantages, high buildings up to 80-meters, such as the Mjøsa tower in Norway, are being erected. CLT panels are used both as walls and floors in those constructions.

Rolling and longitudinal shear deformations are involved in the mechanical response of those panels. Shear failure can occure for CLT panels loaded out-of-plane but also when they are under in-plane shear stresses (*Brandner et al.*, 2016). The value of the longitudinal shear modulus $G^0_{l,mean}$ for short-term lies between 440 and 880 MPa depending

on the strength class of the wood (*Eurocode-5*, 2004). In the rolling-shear direction, the short-term modulus $G^0_{r,mean}$ for short-term lies between 50 and 200 MPa (*Ehrhart and Brandner*, 2018; *Franzoni, Lebée, Lyon, et al.*, 2016; *Zhou et al.*, 2014; *Perret et al.*, 2018). Large differences between the studies are due to the difficulty to obtain a pure shear stress and to represent the behaviour of cross layers. Additionally, the sawing pattern and aspect ratio of the board are of importance for CLT (*Krabbe*, 1960; *Aicher and Dill-Langer*, 2000; *Ehrhart and Brandner*, 2018; *Perret et al.*, 2019).

Wood is a material subject to creep and this phenomenon must be investigate to correctly design timber builings as it amplifies the short-term deflections. The first study of creep in CLT is recent (*Park et al.*, 2006) and there are very few attempts to characterize the behaviour of rolling shear creep (*Pirvu and Karacabeyli*, 2014; *Colling*, 2014). In these works, bending tests of CLT panels are achieved and an overall creep factor is derived. It appears clearly that creep is larger with CLT than with GLT. A possible explanation may be a faster creep behaviour coming from rolling shear strains in cross layers.

This paper presents an experimental protocol to measure directly shear stiffness and creep in CLT panels. The methodology originally presented by *Perret et al.* (2018) is used to measure separately those characteristics in the rolling and the longitudinal direction. The paper is organized as follows. In Section 2, the sandwich-beam theory is recalled and the experimental set-up is introduced. In the following section, the short-term characterization of the rolling-shear stiffness modulus and the estimation of the Eurocode coefficient k_{def} (*Eurocode-5*, 2004) by means of a power law are presented. This experiment is referred as Experiment 1 and was conducted during eight months (13/03/2020 - 28/10/2020). Finally, the results of Experiment 2 (11/12/2020- 11/06/2021) are presented in Section 5 and the longitudinal shear stiffness modulus for short and long time are determined.

2 Sandwich beam theory

The rolling shear modulus $G_{r,mean}$ and the longitudinal shear $G_{l,mean}$ are characterized by means of a four-point bending test on sandwich beams constituted of a wooden core glued between two steel skins (Figure 1). The beam is simply supported on a span $d = 602$ mm and two loads $P/2$ are applied at a distance $d_0/2$ from the mid-span, with $d_0 = 200$ mm. The beam is under pure bending between these loads leading to a constant curvature. It is assumed that steel does not creep in time. The full methodology is detailed in *Perret et al.* (2018).

The sandwich beam model (*Lebée and Sab*, 2012) requires a contrast between the stiffness and the thickness of the core and skins, respectively (E_a, e_a) and (E_b, e_b) so that : $e_b \gg e_a$ and $E_a e_a \gg E_b e_b$. Because of this contrast, the bending stiffness D and the shear force stiffness F are (*Allen*, 1969):
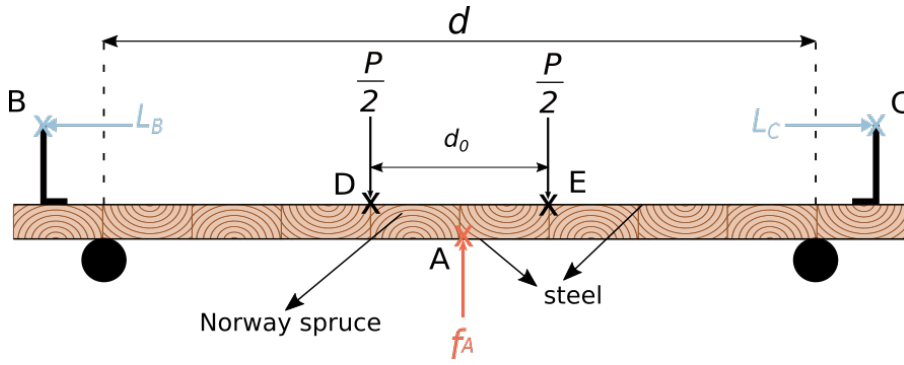
Figure 1. Four-point bending configuration on a sandwich beam, for the rolling shear configuration (experiment 1)

$$D = b\left[\frac{h^3 - e_b^3}{12}E_a + E_b\frac{e_b^3}{12}\right] \qquad (1) \quad \text{and} \quad F = \frac{b(e_b + e_a)^2}{e_b}G_{r,mean} \qquad (2)$$

In this paper, two shear directions are investigated. The rolling shear, or perpendicular to the grain is tested in Experiment 1. In this experiment the wooden core orientation is pictured in Figure 2. The longitudinal shear, or parallel to the grain is tested in Experiment 2. The wooden core is then rotated as pictured in Figure 1.

Whereas for Experiment 1, the contribution of the wooden core to the bending stiffness may be neglected. This is not the case for Experiment 2. Indeed, when measuring the rolling shear (Experiment 1), the contrast assumption is satisfied with E_a = 210 GPa and E_b = 0.43 GPa (litterature values). Equation 1 can be written as $D = E_a I_a + E_b I_b$. The contribution of the steel is calculated with h = (33.5 ± 0.4) mm the total thickness, e_b = (3.9 ± 0.4) mm the wood thickness, and the width of the beam b = (41.1 ± 0.6) mm. This gives $E_a I_a$ = (5.06 ± 0.68) kN m^2 and the contribution of the wooden core is $E_b I_b$ = (44 ± 11) N m^2. From those values, the contribution of the main core to the bending stiffness can be neglected as it contributes to less than 1%. Equation 1 can be rewritten as:

$$D = \frac{b(h^3 - e_b^3)}{12}E_a \qquad (3)$$

This equation can be used in Experiment 1 to calculate the bending stiffness using the litterature value of E_a and the measured dimensions of the beam. The shear force stiffness F can be expressed as a function of the mid-span deflection f_A and the bending stiffness D:

$$\frac{1}{F} = \frac{4f_A}{P(d - d_0)} - \frac{1}{8D}\left(d^2 - \frac{1}{3}(d - d_0)^2\right) \qquad (4)$$

The measurement of f_A gives the evolution of the rolling shear modulus $G_{r,mean}$ in time.

In Experiment 2, the contrast stiffness is not fullfilled but Equation 2 is still valid. The contributions of the steel and the wood are calculated with h = (31.8 ± 0.2) mm, e_b = (29.6 ± 0.2) mm, and b = (40.6 ± 0.2) mm. This gives $E_a I_a$ = (4.48 ± 0.49) kN m^2 and with E_b = 10 GPa ; $E_b I_b$ = (0.88 ± 0.21) kN m^2. The contribution of the wooden core to the bending stiffness is about 16% which can not be neglected. The bending stiffness must be precisely measured, it can be estimated from the absolute rotations at B and C (respectively φ_B and φ_C) as follows:

$$D = \frac{P(d^2 - d_0^2)}{8\Delta\varphi} \tag{5}$$

where $\Delta\varphi$ = $\varphi_B + \varphi_C$. Equations 2 and 4 can still be used to measure the evolution of the longitudinal shear modulus $G_{l,mean}$ in time. For Experiment 2, an accurate measurement of D is necessary in order to calculate the longitudinal shear modulus and to correctly estimate its creep.

3   Methods

3.1   Specimen fabrication

Norway Spruce (*Picea abies*) boards were used to make the specimens. The layer thickness of CLT-boards in Europe are 20 mm, 30 mm and 40 mm according to *Brandner* (2013). It was chosen to use a 30 mm thick layer.

In Experiment 1, eighteen boards were glued together on their narrow edges with a wood glue (Titebond Ultimate 141/5). Glued narrow edges are not not a common practice in the industry but sometimes it is used to reduce the width of the gaps. It will allow here to reduce the stress concentration in the specimens. This wooden plate was then planarized to a thickness of e_b = 30 mm. Then, 800 mm long specimens with a width b = 40 mm and a thickness e_b = 30 mm were cut in this plate. They were cut so that wood fibres are oriented in the transverse direction. They were conditioned at a moisture content of u = (10.6 ± 0.3) % and visually graded C24. Their density was measured to be ρ =(495 ± 32) kg m^{-3}. The boards were oriented so that the pith is alternatively at the bottom or at the top which average their effect on the global behaviour (see Figure 2).

For Experiment 2 the boards used were conditioned at a moisture content of u = (10.2 ± 2.5) % and their density was measured to be ρ = (393 ± 53) kg m^{-3}. Norway Spruce board of 30 × 60 mm were planarized to be 30 × 40 mm and cut to be 800 mm long oriented in the longitudinal direction.

Carbon steel XC75 sheets of Young modulus E_a =210 GPa were used. They are 800 mm

long, b = 40 mm wide and e_a = 1.1 mm thick. They were sanded and glued on the top and bottom faces of the wood with a two components glue including a thixotropic epoxy based impregnating resin and adhesive (Sikadur® 300). The thickness of the glue layer is about 0.5 mm.
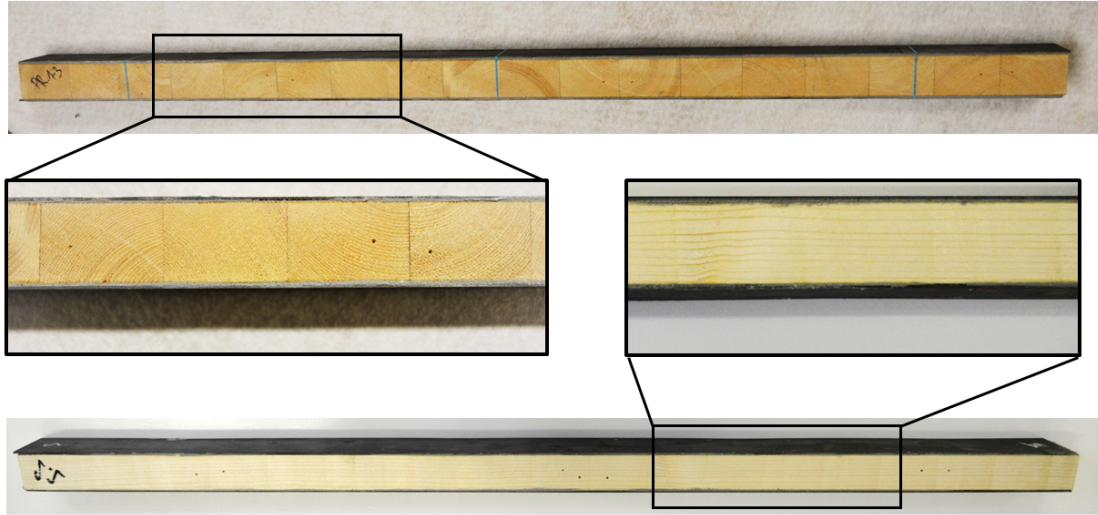
Figure 2. View of the specimens (above : Experiment 1, below : Experiment 2)

For Experiment 1, five specimens (A-E) were fabricated and six specimen (M-R) for Experiment 2. One example of each can be seen in Figure 2.

3.2   Experimental set-up

Figure 3 shows the schematic representation of the frame (0). The specimens (1) are supported on two cylinders (2) of radius R = 23 mm with a span d = 602 mm. They are loaded vertically and symmetrically by two loading fixtures (3) spaced of a length d_0 = 200 mm. The contact between the loading fixtures and the beam is made with a steel ball of diameter d_b = 1.2 mm (10). The rotation of the motor (6) drags a metal thread (9) that ascends and descends the loads (5) and the lever arms (4).

Several sensors are positioned to measure the different variables:

- Three Orbit® linear variable differential transformers (DP20S) are placed on each span of the frame (8). Two of them measure the horizontal displacement of the steel flat angles. They are represented Figure 3 as arrows L_B and L_C. The last linear variable differential transformer (LVDT) measures the vertical deflection of the beam at mid-span (f_A: arrow L_A). They have an expanded measurement uncertainty U = 16 × 10^{-3} mm.

- Two AEP transducers ® S-type load cell (TS) (7) are placed in the loading fixture (3). They measure the load on points D and E. Their expanded measurement uncertainty is U = 4.8 N.

- Two Sensel Measurement® single axis inclinometers (SM-NA) are placed on both sides of the specimen (11). They measure the rotations φ_B and φ_C and have an expanded measurement uncertainty $U = 5 \times 10^{-3}$ rad.
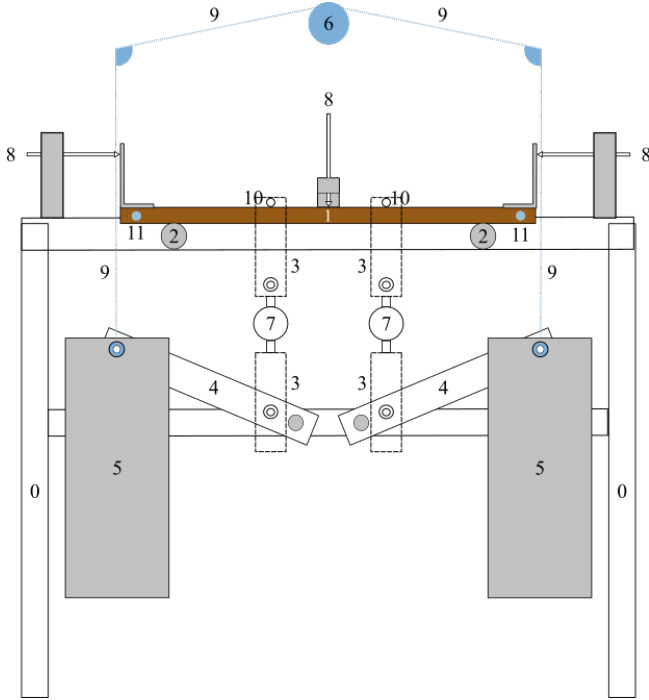
Figure 3. Framework design for the tests

In Experiment 2 the measure of the bending stiffness D is crucial to determine the instantaneous and the long term modulus. Since the inclinometers are not specifically designed for long term experiment, the LVDT sensors will be used to measure the long term displacement.

3.3 Test method

The viscoelastic limit has been well studied in the longitudinal direction (*Hoyle et al.*, 1985; *Nakai and Grossman*, 1983; *Foudjet and Bremond*, 1989; *Hayashi et al.*, 1993; *Bhatnager*, 1964; *King*, 1961) and observed to be between 40% to 50%. It is a priori not the same for the rolling-shear stiffness.

Therefore, Specimens A-E were tested under different load conditions ranging from 27 to 52 % of the characteristic shear strength $f_{r,mean}$ = 1.88 MPa (*Ehrhart and Brandner*, 2018). These stress levels are approximate since the shear strength varies from one board to another. The specimens M-R loaded between 11 and 14% of the characteristic shear strength $f_{l,mean}$ = 7.8 MPa (*Wood-Handbook*, 2010).

Under the viscoelastic limit, *D. G. Hunt* (1999) proposed to separate creep into three different components: pure viscoelastic (time dependent creep), mechano-sorptive creep and pseudo-creep followed by a recovery phenomenon. These components are independent but coupling effects may appear. The present experiment will be achieved such that the pure viscoelastic behaviour is isolated. Therefore, the tests were performed in

a climate-controlled room with constant temperature of $(19 \pm 1)\,°C$ and a relative humidity in the air of $(58 \pm 8)\,\%$ in the first experiment. In the second experiment the temperature was $(20 \pm 1)\,°C$ and the relative humidity in the air of $(54 \pm 6)\,\%$. Both times the specimens were conditioned at least one week in this room before the tests.

4 Rolling shear results

4.1 Short term

Results are plotted for beam C but are similar for all the specimens. In Figure 4 the load P is plotted as a function of the deflection f_A for the first two minutes of the experiment. A linear regression on the linear part of this curve gives an estimation of the modulus $G^0_{r,mean}$ using Equations 2 and 4 and the value of the bending stiffness calculated section 2. Table 1 summarizes the identified moduli.

Table 1. Instantaneous values

Name	$G^0_{r,mean}$(MPa)
A	98.4
B	120
C	99.9
D	115
E	110
Moyenne	109
CoV*(%)	8.6

* Coefficient of Variation
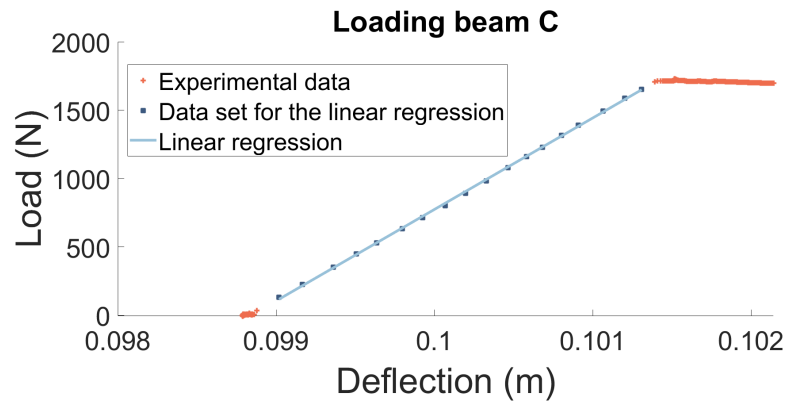
Figure 4. Applied force as a function of the mid-span deflection f_A

The cross-layer shear modulus $G^0_{r,mean}$ = 109 MPa with a coefficient of variation of 8.6% is consistent with the literature values given in Table 2. A rather high value is consistent with the sawing pattern presented in Figure 2. The coefficient of variation found is very low compared to the literature and comparable to the one already found by *Perret et al.* (2018). Indeed, the four-points bending test averages the rolling-shear stiffness on several boards.

Table 2. Short term rolling shear modulus from other experiments

Reference	MC[1](%)	$G^0_{r,mean}$ (MPa)	CoV[2](%)
Aicher and Dill-Langer (2000)	12	50	20
Keunecke et al. (2007)	12	53	
Franzoni, Lebée, Lyon, et al. (2017)		110	27
Perret et al. (2018)	10-13	124	6.7

[1] Moisture Content
[2] Coefficient of Variation

4.2 Long term

The mid-span deflections can be separated in two contributions; the bending and the shear deflection. The total mid-span deflection varies from (1.2848 ± 0.0033) mm dur-

ing the experiment. The symmetric part of the rotations varies from $(1.3 \pm 1.7) \times 10^{-3}$ rad. This variation falls within the accuracy of the LVDT. Hence, we can neglect the variations of the rotations in this experiment and calculate D.

The measured relative creep of the specimens during this experiment are plotted Figure 5 for the rolling-shear modulus $G_{r,mean}^{\infty}$. It can be observed that those curves are close to linear in a log-log scale at long time, therefore the creep can be modelled with a power law:

$$\frac{J(t)}{J_0} - 1 = mt^n \tag{6}$$

where n, m and J_0 are experimental parameters and t the time in seconds. They are independent from the load as long as it is in the linear viscoelastic domain. Indeed, wood creep has been modelled with empirical and mechanical models. Mechanical models come from the thermodynamics (*Schapery*, 1966). They are systems composed of Kelvin and Maxwell elements. Those models are useful to differentiate the several creep components: elastic, viscous and viscoelastic. They are mostly used to model creep occurring with climate changes (*Varnier*, 2019; *Mukudai*, 1983; *D. Hunt and Gril*, 1994). Empirical models are power or logarithmic functions and they fit and predict well those phenomena. *Youngs* (1957) was the first to model wood creep from a 3-days experiment as a power law similar to the Equation 6. *Clouser* (1959) and *Gressel* (1984) used this same equation to fit their 10-year creep tests. It has been widely used since then to fit and predict creep wood behaviour (*Sugiyama*, 1957; *Schniewind*, 1966; *Hayashi et al.*, 1993).

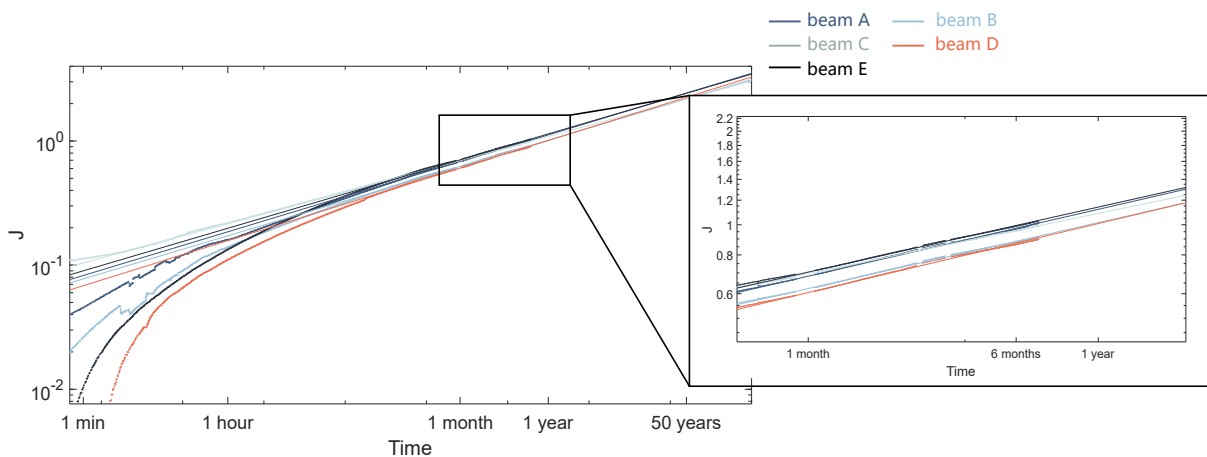*Figure 5. Rolling-shear relative creep curves and power law fittings*

In international standards the design of buildings has to be estimated for 50-years. Therefore, a prediction model is required to extrapolate a value of the deflection of wood at such time period. In the Eurocode, this is taken into account by means of the coefficient k_{def} which corresponds to the relative creep at 50-years. Considering exclu-

sively rolling shear deformations, we define k_{def}^{GR} as:

$$G_{r,mean}^{\infty} = \frac{G_{r,mean}^0}{1 + k_{def}^{GR}} \qquad (7)$$

with $G_{r,mean}^0$ the short-term rolling shear modulus and $G_{r,mean}^{\infty}$ the secant rolling-shear modulus in 50 years. A linear regression was done on the logarithmic values. The k_{def}^{GR} values found are summarized in Table 3 with a mean value of 2.43 and a coefficient of variation equal to 6.18 % which corresponds approximately to the coefficient of variation of the instantaneous modulus. The stress level does not seem to have a significant influence on k_{def}^{GR} which comforts the assumption of linear visco-elasticity.

Table 3. Values of k_{def}^{GR}

Name	k_{def}^{GR}
A	2.59
B	2.44
C	2.22
D	2.34
E	2.54
Mean	2.43
CoV*(%)	6.18

* Coefficient of Variation

Table 4. Fitting coefficients values

Name	J_0	n	m
A	92.8	0.210	0.0302
B	113	0.212	0.0274
C	88.9	0.217	0.0224
D	107	0.211	0.0266
E	106	0.194	0.0422

The values found for the coefficient of Equation 6 are shown in Table 4. They fall into the range of coefficients found in the literature and summarized in (*Tong et al.*, 2020).

5 Longitudinal results

5.1 Short term

The value of the instantaneous bending stiffness is measured with the inclinometers during the loading of each specimen. The load is plotted against the symmetric part of the rotations during the loading Figure 6. Results are plotted for beam *N* and are similar for all specimens. A linear regression on the linear part of this curve allows to determine the bending stiffness *D*. The results are summerized Table 5. They are in the scope of the calculus that was presented in Section 2.

Using Equations 2 and 4 the value of the instantaneous longitudinal shear modulus can be calculated. It is deduced from the slope of the function between the load *P* and the mid-span deflecion f_A. The values found are summarized in Table 5 and, except for beam *O*, the results are consistent. The coefficient of variation found for the longitudi-
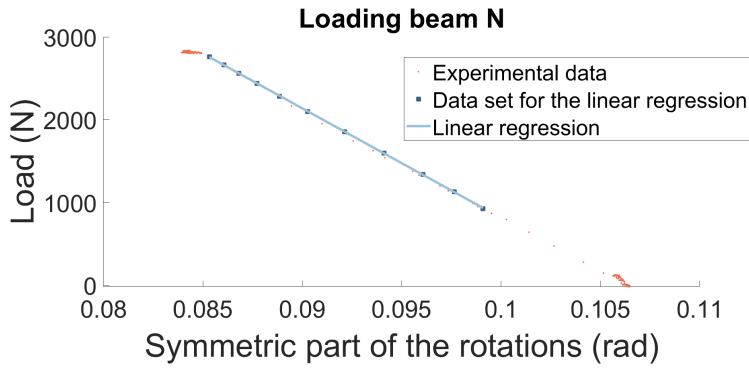
Figure 6. Load P function of the symmetric part of the rotation $\Delta\varphi$, beam N

nal shear is in the scope of the variation of the wood which is about 20%.

Table 5. Instantaneous values for longitudinal shear

Name	M	N	O	P	Q	R	Mean	CoV*(%)
$D^0(\text{kN m}^2)$	5.71	5.26	5.81	5.13	5.21	4.98	5.35	6.2
$G^0_{l,mean}(\text{MPa})$	425	385	229	359	384	355	356	19

* Coefficient of Variation

5.2   Long term

The long term part of the long term mid-span deflection is (0.2959 ± 0.0033) mm while it was (1.2848 ± 0.0033) mm for the rolling-shear. It is much smaller than in the previous experiment and therefore require a more precise analysis. The bending and shear contribution to the mid-span bending can be separated as:

$$f_A = \frac{k_1}{F} + \frac{k_2}{D} \tag{8}$$

where k_1 and k_2 are two coefficients that can be determined with Equation 4 and are constant during the whole experiment.

The long term symmetric part of the rotations is $(1.4 \pm 1.7) \times 10^{-3}$ rad. This variation falls into the uncertainty of the sensors and could be neglected. If this variation is not neglected the bending contribution on the mid-span creep deflection is then about 45%. This contribution may be associated to the creep of the wood Young modulus E_b in the longitudinal direction with Equation 1.

Hence, two estimations of k^{GL}_{def} are proposed here ; one considering that only the shear contributes to the creep of the long term mid-span deflection f_A and one considering that there is a bending creep as well. In the first case, D is assumed constant in Equation 8, while in the second case, D is taken from the long term measurement. In both cases, considering the deformations in the longitudinal direction, we define a creep coefficient k^{GL}_{def} as :

$$G_{l,mean}^{\infty} = \frac{G_{l,mean}^{0}}{1 + k_{def}^{GL}} \qquad (9)$$

with $G_{l,mean}^{0}$ the short-term longitudinal shear modulus, $G_{l,mean}^{\infty}$ the longitudinal shear modulus in 50 years.

Using the power law Equation 6, a linear regression was fitted on the logarithmic values. Figure 7 shows the fitting of the data when assuming that there is no bending creep (D is constant). The cycles visible corresponds to those of the air conditioning that regulated the temperature of the room during the experiment. Those variations correspond to the sensitivity of the LVDT sensors to temperature. They exist in Experiment 1 but are not visible in Figure 5 as the creep deflection is 4 times larger. The values of k_{def}^{GL} are summerized Table 6 with a mean value of 1.1 (CoV = 15%).
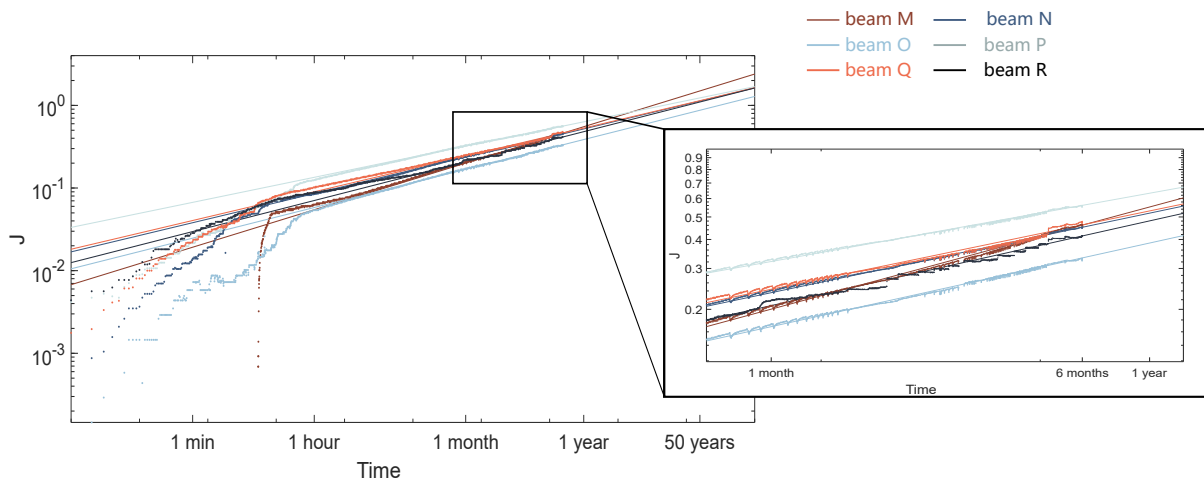
Figure 7. Fitted data, longitudinal creep of $G_{l,mean}$ considering that there is only a shear creep

A similar fitting was done when considering that the bending contributes to the creep of the mid-span. There was a power outage the second month of the experiment and the measure of the rotation of the beam M was lost. Therefore no creep results are presented for this specimen in this case. The results are in Table 6 and k_{def}^{GL} is calculated with a mean value of 0.6 (CoV = 26%).

Table 6. Values of k_{def}^{GL}

Name	M	N	O	P	Q	R	Mean	CoV*(%)
k_{def}^{GL}	–	0.84	0.52	0.68	0.46	0.51	0.60	26
k_{def}^{GL} (without bending creep)	1.4	1.1	0.88	1.2	1.1	1.1	1.1	15

* Coefficient of Variation

In both estimations, the stress level seems not to not have any influence on the creep which validates the hypothesis of linear visco-elasticity. Experiments are still going on to better understand those results and obtain a more precise value of k_{def}^{GL}.

6   Conclusions

The value found in the current version of the Eurocode of the creep coefficient k_{def} is 0.6. This value is the same for all orthotropic elastic moduli (*Eurocode-5*, 2004). The value of the rolling shear coefficient k_{def}^{GR} identified in the present experiment is 2.43 while the value of the longitudinal shear coefficient k_{def}^{GL} is between 0.60 and 1.1. This gives an approximated range of k_{def}^{GL} but seems to indicates that this creep is comparable to the creep of the bending stiffness in the longitudinal direction E_b. The rather large value of the rolling-shear coefficient is not inconsistent and was expected considering previous attempts to estimate k_{def} for CLT panels (*Pirvu and Karacabeyli*, 2014; *Colling*, 2014). Indeed, the deflection of a CLT panel is the superposition of the bending and the shear deflection. The shear contribution in the global creep depends on the slenderness of the panel and varies from 30% of the total deflection for thick panels to few percent for slender panels. Hence, a distinction between the different deformation types might be necessary to have a better estimation of the long term deflection in CLT panels. Indeed, the present results clearly indicates that rolling shear creeps faster than longitudinal shear. More experimental campaigns need to be performed to obtain statistically significant results. If the present value is confirmed it could have consequences for the design of CLT and other timber products. For instance, this may lead to more accurate design guidelines either for serviceability limit state (SLS) or long-term buckling strength of CLT walls, which completes recent recommendations for more accurate modelling (*Franzoni, Lebée, Lyon, et al.*, 2017; *Franzoni, Lebée, Forêt, et al.*, 2015; *Perret et al.*, 2018).

7   References

Aicher, S. and G. Dill-Langer (2000). "Basic considerations to rolling shear modulus in wooden boards." en. In: 11, p. 10.

Allen, H. (Oct. 1969). *Analysis and Design of Structural Sandwich Panels: The Commonwealth and International Library: Structures and Solid Body Mechanics Division*. en. Elsevier.

Bhatnager (1964). "Creep in wood in tension parallel to grain." In: *Holz als Rol-und Werkstoff*.

Brandner, R. (2013). "Production and Technology of Cross Laminated Timber (CLT): A state-of-the-art Report." en. In: p. 33.

Brandner, R., G. Flatscher, A. Ringhofer, G. Schickhofer, and A. Thiel (May 2016). "Cross laminated timber (CLT): overview and development." en. In: *European Journal of Wood and Wood Products* 74.3, pp. 331–351.

Clouser, W. S. (1959). "Creep of small wood beams under constant bending load." en. In.

Colling, F. (2014). "Creep behavior of cross laminated timber in service class 2." en. In: *Technical Report*. Hochschule Augsburg, University of Applied Science, p. 10.

Ehrhart, T. and R. Brandner (2018). "Rolling shear: Test configurations and properties of some European soft- and hardwood species." en. In: *Engineering Structures* 172, pp. 554–572. DOI: `10.1016/j.engstruct.2018.05.118`.

Eurocode-5 (2004). *Design of timber structures*.

Foudjet, A. and C. Bremond (1989). "Creep of four tropical hardwoods from Cameroon." en. In: *Wood Science and Technology* 23.4, pp. 335–341. DOI: `10.1007/BF00353249`.

Franzoni, L., A. Lebée, G. Forêt, and F. Lyon (Aug. 2015). "Advanced modelling for design helping of heterogeneous CLT panels in bending." In: *International Network on Timber Engineering Research*. Sibenik, Croatia.

Franzoni, L., A. Lebée, F. Lyon, and G. Forêt (Sept. 2016). "Influence of orientation and number of layers on the elastic response and failure modes on CLT floors: modeling and parameter studies." en. In: *European Journal of Wood and Wood Products* 74.5, pp. 671–684. DOI: `10.1007/s00107-016-1038-x`.

– (June 2017). "Elastic behavior of Cross Laminated Timber and timber panels with regular gaps: Thick-plate modeling and experimental validation." en. In: *Engineering Structures* 141, pp. 402–416. DOI: `10.1016/j.engstruct.2017.03.010`.

Gressel, P (1984). "Zur Vorhersage des langfristigen Form inderungsverhaltens aus Kurz-Kriechversuchen." de. In: p. 9.

Hayashi, K., B. Felix, and C. Le Govic (1993). "Wood viscoelastic compliance determination with special attention to measurement problems." en. In: *Materials and Structures* 26.6, pp. 370–376. DOI: `10.1007/BF02472963`.

Hoyle, R., M. Grzfith, and R. Itani (1985). "Primary Creep in Douglas-fir beams of commercial size and quality." en. In: *Wood and Fiber Science* 17.3, pp. 300–314.

Hunt, D and Joseph Gril (1994). "Possible contribution of fibre slippage to the longitudinal creep of wood." In.

Hunt, D. G. (1999). "A unified approach to creep of wood." en. In: *Proceedings of the Royal Society of London. Series A: Mathematical, Physical and Engineering Sciences* 455.1991, pp. 4077–4095. DOI: `10.1098/rspa.1999.0491`.

Keunecke, D., W. Sonderegger, K. Pereteanu, T. Lüthi, and P. Niemz (Apr. 2007). "Determination of Young's and shear moduli of common yew and Norway spruce by means of ultrasonic waves." en. In: *Wood Science and Technology* 41.4, pp. 309–327.

King, E G (1961). "Time-Dependent Strain Behavior of Wood." en. In: *Forest Products Journal*, p. 5.

Krabbe, E (1960). "Messungen von Gleit- und Dehnungszahlen an Holzsta¨bchen mit rechteckigen Querschnitten." allemand. PhD thesis. Hannover.

Lebée, A. and K. Sab (Apr. 2012). "Homogenization of cellular sandwich panels." en. In: *Comptes Rendus Mécanique* 340.4-5, pp. 320–337.

Mukudai, J. (1983). "Evaluation on non-linear viscoelastic bending deflection of wood." en. In: *Wood Science and Technology* 17.1, pp. 39–54. DOI: `10.1007/BF00351831`.

Nakai, T and P. U. A. Grossman (1983). "Deflection of wood under intermittent loading." en. In: *Wood Science and Technology* 17, pp. 55–67.

Park, H., M. Fushitani, K. Sato, T. Kubo, and H. Byeon (June 2006). "Bending creep performances of three-ply cross-laminated woods made with five species." en. In: *Journal of Wood Science* 52.3, pp. 220–229. DOI: 10.1007/s10086-005-0750-7.

Perret, O., A. Lebée, C. Douthe, and K. Sab (Oct. 2018). "Experimental determination of the equivalent-layer shear stiffness of CLT through four-point bending of sandwich beams." en. In: *Construction and Building Materials* 186, pp. 1132–1143.

— (May 2019). "Equivalent stiffness of timber used in CLT: closed-form estimates and numerical validation." en. In: *European Journal of Wood and Wood Products* 77.3, pp. 367–379. DOI: 10.1007/s00107-019-01395-x.

Pirvu, Ciprian and Erol Karacabeyli (2014). "Time-dependent behaviour of CLT." en. In: p. 2.

Schapery, R.A. (1966). "An engineering theory of nonlinear viscoelasticity with applications." en. In: *International Journal of Solids and Structures* 2.3, pp. 407–425.

Schniewind, Arno P. (1966). "On the influence of moisture content changes on the creep of beech wood perpendicular to the grain including the effects of temperature and temperature changes." de. In: *Holz als Roh- und Werkstoff* 24.3, pp. 87–98.

Sugiyama, H. (1957). "The creep deflection of wood subjected to bending under constant loading." en. In: *Transactions of the Architectural Institute of Japan* 55.0, pp. 60–70.

Tong, D., S. Brown, D. Corr, and G. Cusatis (2020). "Wood creep data collection and unbiased parameter identification of compliance functions." en. In: *Holzforschung* 0.0.

Varnier, Maximin (2019). "Comportement thermo-hygro-mécanique différé des feuillus." fr. PhD thesis.

Wood-Handbook (2010). *Wood Handbook, Wood as an Engineering Material*. en. U.S. Dept.of Agriculture, Forest Service, Forest Products Laboratory.

Youngs, Robert L (1957). "The Perpendicular-to-grain mechanical properties of red oak as realated to temperature, moisture content and time." en. PhD thesis.

Zhou, Q., M. Gong, Y. Chui, and M. Mohammad (Aug. 2014). "Measurement of rolling shear modulus and strength of cross laminated timber fabricated with black spruce." en. In: *Construction and Building Materials* 64, pp. 379–386.

DISCUSSION

The papers was presented by C Allemand

T Tannert commented that in a CLT the rolling shear having low stiffness would attract lower loads and questioned the level of load considered in the experiment. C Allemand responded that in the rolling shear direction similar load level was guided by the load level for the longitudinal shear direction which was around 40%, based on past research. T Tannert said different load levels should be considered for rolling shear creep studies.

M Schweigler asked about sealing the specimens and possible influence to deflection measurements. C Allemand replied that sealing did not have any mechanical influence and did not affect the deflection measurements.

P Dietsch asked if there were comparisons with known test configurations to check the proposed test setup. C Allemand replied that other configurations were not tried. P Dietsch said that test configuration in EN789 or EN408 could be tried.

M Fragiacomo questioned about the environmental conditions and asked if the experiment focused on pure shear. C Allemand said there was no consideration of mechano-sorptive effects. M Fragiacomo commented that k_{def} in the Eurocode is referenced with some kind of mechano-sorptive consideration and not sure direct comparisons can be made.

G Hochreiner questioned whether the shear load level would lead to stable or unstable creep. C Allemand provided information on the load level and not sure whether the creep is stable or unstable as the load period is only 8 months. G Hochreiner commented that creep test standards for wood based panels exist for N. America and Europe and asked why they were considered. C Allemand said that she will check these out. P Dietsch commented that load level seemed to be high and could lead to exponential creep.

A proposal for capacity-based design of multi-storey CLT buildings

Daniele Casagrande, Institute of Bioeconomy, National Research Council of Italy

Ghasan Doudak, University of Ottawa (Canada)

Mohammad Masroor, University of Ottawa (Canada)

1. Introduction and Background

The energy dissipation in timber buildings, subjected to seismic loading, is typically achieved through a combination of yielding in dowel-type connections, accompanied by some wood crushing, while ensuring that brittle failure modes do not govern the design. Whether at the connection level or more globally at the assembly or building levels, brittle failure modes are avoided by employing the concept of capacity-based design (CD), where dissipative elements are identified and designed to absorb the energy imparted on the system, while non-dissipative elements are overdesigned, considering the resistance of the dissipative zones, typically by means of over-strength factors. The development of such factors needs to consider the variability that exists in the energy dissipative elements, such that the dissipative elements are able to reach the desired levels of strength and displacement without excessively overdesigning the non-dissipative elements.

In buildings where cross-laminated timber (CLT) shearwalls comprise the seismic force resisting system (SFRS), either single-panel (i.e. monolithic) or multi-panel walls (Figure 1) are relied upon to resist the seismic force, generally resulting in low-to-moderate or high levels of energy dissipation capabilities, respectively. The reason single-panel CLT shearwalls have limited energy dissipative capabilities is that the energy is typically absorbed in the steel-to-timber connections used to anchor the wall to either the foundation or floor below (i.e. hold-down and angle brackets). In multi-panel CLT shearwalls, the panel-to-panel vertical joints are identified as dissipative components due to the high ductility usually achieved in such joints. In both aforementioned cases, the CLT panels (i.e. floor and wall panels) and all other non-energy dissipative connections are commonly overdesigned in order to remain elastic.

The global behaviour of buildings with CLT shearwalls has been investigated in several research programs that particularly emphasized the importance of employing the capacity-based design procedure (Ceccotti et al. 2013; Pei et al. 2013; Yasumura et al. 2016). At the connection level, Gavric et al. (2013) proposed that failure modes of dowel-type fasteners used as part of dissipative connections be characterized by the formation of at least one plastic hinge while the timber members, steel plates and an-

choring to foundation of hold-downs and angle brackets be capacity protected. Undesirable brittle failure modes were observed in experimental tests carried out on mechanical anchors, when adequate considerations for CD procedures were not employed (Tomasi and Smith 2015; Flatscher et al. 2015). At the wall level, experimental studies aimed at establishing the cyclic behaviour of multi-panel shearwalls showed higher ductility and energy dissipation capacity in shearwalls that exhibited coupled-panel behaviour, where yielding occurred in the vertical joints, compared to monolithic shearwalls (e.g. Gavric et al. 2015a, Popovski et al. 2010). Nolet et al. (2019) analytically investigated the effect of elasto-plastic rocking behaviour of multi-panel shearwalls, which was expanded upon by Masroor et al. (2020) to take into account the bi-directional effect of the angle-brackets.
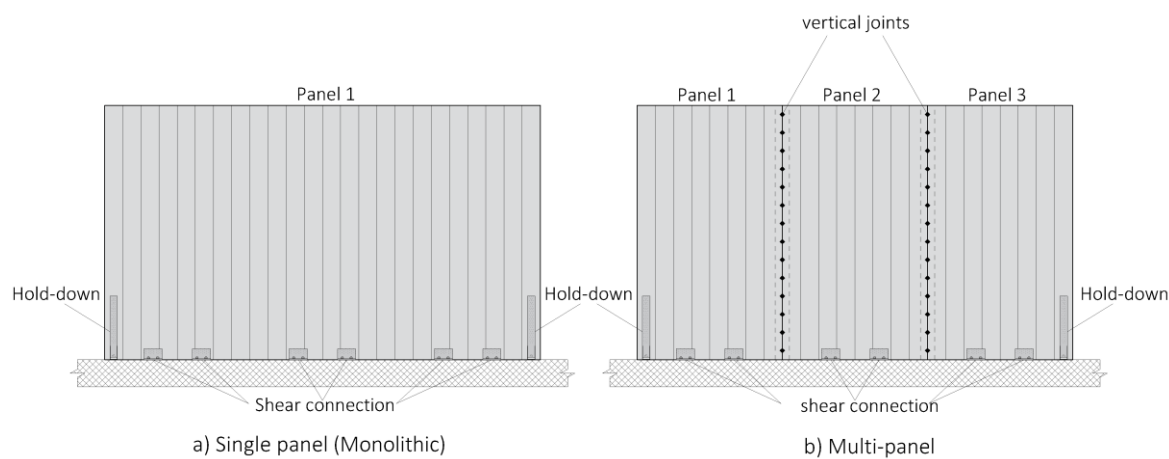
Figure 1: Single- and Multi-panel CLT shearwalls

The applicability of capacity-based design procedure to timber structures was presented by Jorissen and Fragiacomo (2011), where an over-strength factor was proposed. Several studies focused on establishing appropriate values of over-strength factors for different types of connections and mechanical anchors (Fragiacomo et al. 2011; Sustersic et al. 2012; Gavric et al. 2015b; Ottenhaus et al. 2017). Trutalli et al. (2019) discussed a conceptual model for capacity-based design and its applicability at the connection-level both for traditional and innovative connection types used in CLT structures. Shahnewaz et al. (2017) proposed an analytical expression for single-storey single-panel CLT shearwall taking into account the bi-directional behaviour of shear-connections. Casagrande et al. (2019) presented an approach for the applicability of capacity-based design at the wall- and building levels for CLT buildings.

Despite the general agreement that employing the principle of capacity-based design is necessary to ensure a global behaviour involving ductile failure mechanisms, the applicability of such approach to CLT buildings has lacked a clear analytical approach in contemporary international codes (e.g. Eurocode 8 and CSA O86). The current paper aims to contribute to the state of knowledge, particularly to the design provisions in the European and Canadian codes and Standards, by proposing analytical methodologies for the applicability of the capacity-based design approach at wall- and building

levels, addressing the behaviour of single- and multi-panel CLT shearwalls. The proposal follows a general approach, which includes the bi-directional contribution of shear connections in rocking, and is applicable to multi-storey CLT buildings. Specific recommendations, related to the ductility required in the individual connections, the ductility relationship between them as well as the link between the local ductility at the joint level and the global ductility at the building level, are considered outside the scope of this paper.

2. Dissipative zones in CLT structures

2.1 Background

An integral part of establishing capacity-based design provisions is identifying the dissipative zones within the assembly or structure and promoting a failure sequence that would help ensure an overall building behaviour that is consistent with the behavioural factors assumed. Currently, no such requirements are available in the European code for the seismic design of timber structures (i.e. chapter 8 of Eurocode 8). A proposal to include information related to the locations of the dissipative zones, at the wall and building levels, as well as provisions aiming at capacity protecting non-dissipative components, is being developed (Follesa et al. 2018; Fragiacomo et al. 2019). In this proposal, medium ductility class includes CLT shearwalls consisting of either a single-panel or multi-panels connected with relatively stiff vertical joints (relative to the hold-down). Dissipative zones include hold-downs and shear connections used to anchor the shearwall to the foundation or the floor below. CLT structures comprised of multi-panel shearwalls are conversely assumed to possess high ductility, and energy dissipation is assumed to occur in vertical joints, hold-down, as well as the shear connections. For both ductility classes no distinction is made in the kinematic mode being in rocking or sliding.

The Canadian timber design standard (CSA O86) has had general design requirements for buildings containing CLT shearwalls since the 2014 edition (2016 supplement), however it lacks specific analytical provisions related to the applicability of the capacity-based design. Section 11.9.2. of current CSA O86 standard (2019) provides two different values of reduction factors, R_dR_o, representing ductility and over-strength factors (similar in principle to the q-factor used in the Eurocode). CLT structures with limited ductility adopt a value of R_dR_o equal to 1.3, which represents the minimum limit in the National Building Code of Canada (NBC, 2020) for systems with nominal level of overstrength. This includes shearwalls that are constructed with wall panels consisting of aspect ratios (height-to-length) smaller than 2:1 or act in sliding. A value of R_dR_o equal to 3.0 is assumed for CLT structures comprised of shearwall segments with aspect ratios between 2:1 and 4:1 and that dissipate energy in rocking motion through yielding of connections. Dissipative zones are required to include panel-to-panel vertical joints and shear connections, used to anchor the shearwall to the foundation or floor below, in uplift only. Discrete hold-down anchors are required to be designed to attain a factored resistance that is at least 20% greater than the force acting in them

when the panel-to-panel vertical joints achieve their nominal resistance. It is unclear from the current provisions, however, whether the discrete hold-down is allowed to yield and thereby contribute to the energy-dissipation or if it is assumed to behave elastically. CLT panels and non-dissipative connections are required to be capacity protected and remain elastic when the panel-to-panel vertical joints reach 95th percentile of their resistance. This approach is used as an alternative to the application of an over-strength factor. Another requirement in the CSA O86 standard that is noteworthy to highlight is the provision requiring the application of capacity-based design even for CLT structures with limited ductility (i.e. R_dR_o = 1.3). This approach seems overly restrictive since it represents considerations for hierarchy of failure in a design condition that is effectively elastic.

2.2 A proposal for the dissipative zones in CLT structures

Following the review of the existing and proposed design provisions, the current proposed capacity-based design procedure is based on three different levels of ductility classes. The proposal includes the protection of non-dissipative components through an established hierarchy of resistance between non-dissipative and dissipative elements, similar to what has been introduced previously in the literature. In addition, the proposed procedure introduces an original methodology that establishes a hierarchy of yielding amongst dissipative connections as well as between dissipative connections and connections with limited ductility, such that a specific failure behaviour and sequence are attained. In order to achieve rocking behaviour and limit sliding, hold-down and vertical joints are required to be energy dissipative while shear connections are designated as limited ductility connections. Three different over-strength factors are defined: γ_{Rd}, which is used to protect non-dissipative components when dissipative connections yield; an over-strength factor, γ_{Rx}, which ensures a sequence of yielding amongst dissipative connections; and an over-strength factor, γ_{Ry}, used to protect shear-connections and limit sliding failure.

Although developing specific values for the over-strength factors is outside the scope of this paper, a general concept is proposed to help evaluate such values. Regarding the over-strength factor associated with non-dissipative elements, γ_{Rd}, a general expression involving the 95th percentile of the strength capacity of dissipative connection could be adopted, similar to that included in the Canadian timber design standard (CSA O86). Such stringent requirement may not be necessary for establishing the yielding sequence between dissipative connections as well as between dissipative and limited ductility connections, and therefore a generalized expression based on the xth and y^{th} percentile (assumed to be less than the 95th), can be considered, as presented in Table 1.

Level 1 ductility class is assigned to CLT structures consisting of either single- or multi-panel shearwalls, which are designed to behave elastically. There are no requirements

for connection yielding, nor is it necessary to define the requirements for the dissipative elements. In other words, the capacity-based design procedure outlined for the two other design levels is not required to be implemented.

Table 1. Proposed framework for the over-strength factors

Category	Over-strength factor	Percentile of primary dissipative connection strength
Other dissipative connections	γ_{Rx}	x^{th}
Limited ductility connections	γ_{Ry}	y^{th}
Non-dissipative	γ_{Rd}	95th

The proposal for Level 2 ductility class consists of shearwalls with single-panel or multiple panels exhibiting a predominantly single-wall (SW) rocking (Figure 2a). Hold-down is assumed to be the primary dissipative element, although in the case of multi-panel shearwalls, vertical joints may be assumed to act either as dissipative or non-dissipative components. When vertical joints are assumed to act as dissipative connections, no specific hierarchy of yielding is required between them and the hold-down. In order to promote rocking behaviour and limit sliding, the category of elements with limited ductility (i.e. shear connections) are required to be over-designed using the over-strength factor γ_{Ry}. The limited ductility designation for the shear connections is meant to ensure that they do not fail in a brittle manner in case of overloading on the structure.

a) Single-Wall (SW) b) Couple-Panel (CP)
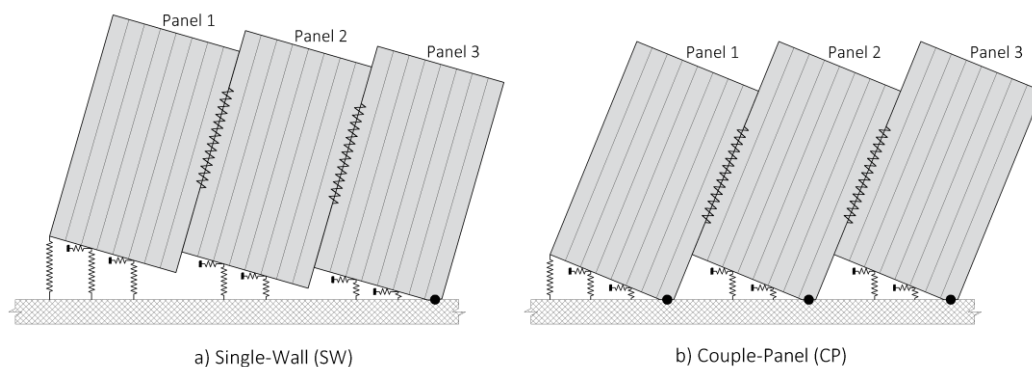
Figure 2: Single-Wall and Coupled-Panel behaviour for multi-panel CLT shearwalls

A level 3 ductility class is proposed for CLT structures consisting of multi-panel shearwalls, where the panels are joined together with connections that can dissipate energy primarily in fastener yielding, leading to a kinematic behaviour of the wall consistent with coupled-panel (CP) rocking behaviour (Figure 2b). Imposing a requirement that hold-down yields after the vertical joints have already yielded ensures that CP, rather than SW, rocking behaviour is attained in the plastic region (Figure 3). Consistently with Level 2 ductility class, ensuring rocking behaviour is achieved by requiring elements with limited ductility (i.e. shear connections) to be over-designed using the over-strength factor γ_{Ry} and to contain a minimum level of ductility capacity. Non-energy dissipative elements are typically characterized by a brittle failure mode and therefore

they are required to remain elastic when the energy dissipative elements reach a desired level of inelastic displacement.

Table 2 summarizes the design requirements for the applicability of the capacity-based design in the current proposed approach.

a) Yielding in the vertical joints   b) Yielding in the Hold-down

Figure 3: Hierarchy of yielding between vertical joints and hold-down in the rocking behaviour of multi-panel CLT shearwalls

Table 2. Design requirements for the capacity-based design in current proposed approach
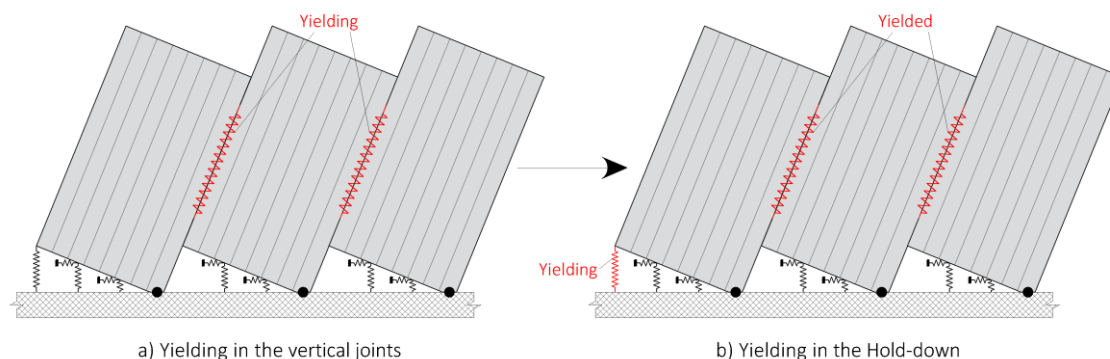
Ductility class	Shearwalls	Required failure modes	Dissipative connections	Hierarchy between dissipative connections	Limited ductility connections	Hierarchy between non-dissipative and dissipative components
Level 3	Multi-panel	Rocking (Coupled-Panel)	vertical joints; hold-down;	I. vertical joints (primary) II. hold-down (other)	shear connections	Yes
Level 2	Single-panel	Rocking	hold-down;	N/A	shear connections	Yes
	Multi-panel	Rocking	hold-down; vertical joints (optional)[1];	No	shear connections	Yes
Level 1	Single- and Multi- panel	N/A	N/A	N/A	N/A	No

[1] vertical joints may be assumed either dissipative or non-dissipative

It should be noted that the procedure outlined herein is mainly applicable to traditional connections currently used in CLT shearwalls. Alternative or proprietary connections may be utilized to dissipate energy in the elastic range (e.g. friction) or in the inelastic range to achieve desired behaviour in the building.

3. Analytical expressions for the proposed approach

3.1 Requirements for Level 1 ductility class

A Level 1 ductility class encompasses CLT structures that are assumed to behave elastically for the entire duration of the seismic event, and as such no specific requirements are needed for capacity-based design, no dissipative zones are required to be defined, and all members and connections are designed not to yield. The strength capacity of members and connections, F_r, is required to be equal to or greater than the design value of the corresponding action, F_f, obtained from the seismic analysis assuming an

almost elastically behaviour of the entire structure (i.e. R_dR_o = 1.3), as presented in Equation 1.

$$F_r \geq F_f \tag{1}$$

1.1 Requirements for Level 2 ductility class

The dissipative connections in this level are designed such that their strength capacity, $F_{r,D}$, is equal to or greater than the design value of the corresponding action, $F_{f,D}$, obtained from seismic analysis assuming plastic behaviour (i.e. $R_dR_o > 1.3$), as presented in Equation 2.

$$F_{r,D} \geq F_{f,D} \tag{2}$$

The capacity-based design procedure establishes a hierarchy of resistance between dissipative and non-dissipative components. This is achieved by requiring that the strength capacity of the non-dissipative components, $F_{r,ND}$, is greater than or equals to the values of actions corresponding to the strength capacity of the weakest storey, as expressed in Equation 3.

$$F_{r,ND} \geq \gamma_{Rd} \cdot \alpha_{\bar{j}} \cdot F_{f,ND} + F_{g,ND} \tag{3}$$

where $F_{f,ND}$ is the value of seismic action on the non-dissipative component obtained from the seismic analysis, γ_{Rd} is defined in Table 1 and $F_{g,ND}$ is the action due to gravity loads on the non-dissipative component. The scale factor, $\alpha_{\bar{j}}$, represents the minimum value of over-capacity coefficient, Ω_j, as defined in Equation 4.

$$\alpha_{\bar{j}} = \min(\Omega_j) \tag{4}$$

where Ω_j is defined, in general terms, as the ratio between the shear strength capacity, $V_{r,j}$, and the cumulative shear load, $V_{f,j}$, at the *j-th* storey, as expressed by Equation 5.

$$\Omega_j = \frac{V_{r,j}}{V_{f,j}} \geq 1 \tag{5}$$

Equation 5 can be expressed in a simplified manner as the ratio between the rocking strength capacity and the rocking moment, since only rocking behaviour is considered, as shown in Equation 6.

$$\Omega_j = \frac{\sum_{i=1}^{N}|M_{r,j,i}|}{\sum_{i=1}^{N}|M_{f,j,i}|} \tag{6}$$

where *N* is the number of CLT shearwalls that are parallel to the seismic action at the *j-th* storey, $M_{r,j,i}$ is the rocking strength capacity of the *i-th* wall, and $M_{f,j,i}$ is the rocking moment on the *i-th* wall.

In order to achieve rocking failure mode and limit sliding, each shear connection of the *i-th* shearwall at the *j-th* storey needs to meet the requirement outlined in Equation 7.

$$F_{r,a,i,j} \geq \gamma_{Ry} \cdot \frac{|M_{r,i,j}|}{|M_{f,i,j}|} \cdot F_{f,a,i,j} \tag{7}$$

where $F_{r,a,i,j}$ is the shear strength capacity of the shear connection of the *i-th* shear-wall at the *j-th* storey and $F_{f,a,i,j}$ is the shear load acting on the shear connection.

This expression is applicable in the case where the shear connections and the hold-down are considered to be only effective along their respective resistance directions (i.e. horizontal shear and vertical tensile resistance, respectively). If bi-directional behaviour of shear-connections is assumed in the analysis, a tensile-shear interacting strength domain should be considered in the calculation of strength capacity of the shearwall (e.g. D'Arenzo et al. 2021; Franco et al. 2021).

For multi-panel shearwalls, and in the case where the vertical joints are assumed to be energy dissipative, the rocking strength capacity of the shearwall, $M_{r,i,j}$, can be calculated as the minimum value of the rocking strength related to either the hold-down or the vertical joints, as presented by Casagrande et al. (2018). Conversely, when vertical joints are considered to be non-dissipative, $M_{r,i,j}$ can be obtained as the rocking strength related to the hold-down only. In this case, the vertical joints are designed to behave elastically in accordance with the requirements outlined in Equation 3.

3.2 Requirements for Level 3 ductility class

In this level, the vertical joints are expected to yield first (see Table 2), and their shear strength capacity, $F_{r,v}$, is required to be equal to or greater than the corresponding action, $F_{f,v}$, obtained from the seismic analysis, using the appropriate R_dR_o value, as outlined in Equation 8.

$$F_{r,v} \geq F_{f,v} \tag{8}$$

The non-dissipative components are designed using the same approach presented for Level 2 ductility class, using the expression presented in Equation 3. Differently from Level 2 ductility class, a coupled-panel rocking behaviour is required in order to optimize the energy dissipation in the building. The over-capacity coefficient for storey *j*, Ω_j, can be calculated according to Equation 6, with the exception that the term associated with the rocking strength is related to the coupled-panel rocking behaviour, where all vertical joints as well as the hold-down are expected to yield using expressions reported in Equation 9 and 10. These equations are developed for a shearwall composed of m panels with length b, covering cases where uni- and bi-directional behaviour of shear connection, respectively, is assumed (Casagrande et al. 2019; Masroor et al. 2022).

$$M_{r,i,j} = b \cdot \left[T_{r,hd} + F_{r,v} \cdot (m-1) \cdot n + \frac{w \cdot b \cdot m}{2} \right] \tag{9}$$

$$M_{r,i,j} = b \cdot \left[T_{r,hd} \cdot (1 + \alpha \cdot \varphi \cdot m) + F_{r,v} \cdot (m-1) \cdot n + \frac{w \cdot b \cdot m}{2} \right] \tag{10}$$

where $T_{r,hd}$ is the tensile strength of the hold-down, n is the number of connections in a vertical joint, w is the total gravity load, φ and α account for the angle brackets in each panel, as outlined in Equations 11 and 12:

$$\varphi = \frac{k_{a,z}}{k_{hd}} \tag{11}$$

$$\alpha = \sum_{r=1}^{n_a} \left(\frac{r}{n_a+1}\right)^2 = \frac{n_a \cdot (2 \cdot n_a + 1)}{6 \cdot (n_a + 1)} \tag{12}$$

where, $k_{a,z}$ and k_{hd} are the elastic vertical-tensile stiffnesses of the shear connection and the hold-down, and n_a is the number of shear connections in each panel, as shown in Figure 4.
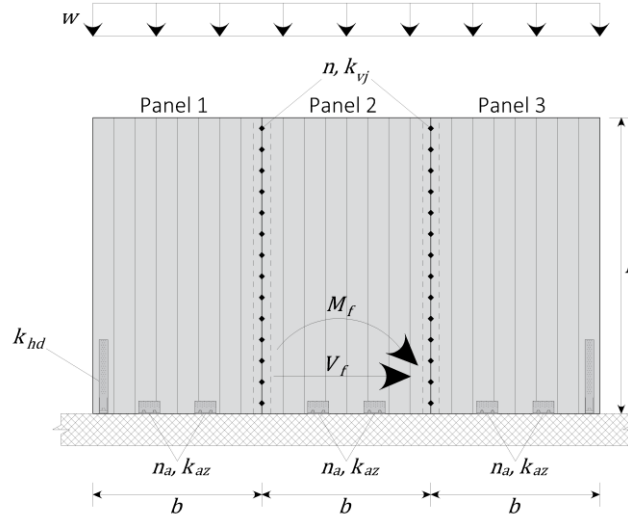

Figure 4: Geometrical dimensions and stiffness of connections of multi-panel CLT shearwall model

In order to ensure a uniform energy dissipation throughout the entire height of the building for a Level 3 ductility class, the ratio between the over-capacity coefficient at storey j (for $j \geq 2$) and that at storey $j - 1$ should be limited to a range, defined by values of ε_1 and ε_2, as outlined in Equation 13. This approach extends the requirement found in the Canadian design standard (CSA O86) for light-frame wood shearwalls, which is limited to first and second storey, to include all stories in the building. The range for ε provided in the CSA O86 (2019) is 0.9 to 1.2.

$$\varepsilon_1 \leq \frac{\Omega_j}{\Omega_{j-1}} \leq \varepsilon_2 \tag{13}$$

Ensuring rocking behaviour in the plastic region and promoting rocking over sliding behaviour are paramount in this ductility level. When a uni-directional behaviour of shear connections is assumed, the same approach adopted for the Level 2 ductility class can be used, as outlined in Equation 7, where $M_{r,i,j}$ is calculated according to Equation 9. In the case where bi-direction behaviour of shear connections is considered, the tensile-shear interaction of shear connection has to be taken into account. As an alternative to Equation 7, the expression presented by Masroor et al. (2022) and reported in Equation 14 can be used to prioritize rocking behaviour over sliding.

$$\left(\frac{\frac{n_a}{n_a+1} \cdot \varphi \cdot \gamma_{Ry} \cdot T_{r,hd}}{F_{r,a,z}}\right)^2 + \left(\frac{M_{r,i,j}}{M_{f,i,j}} \cdot \frac{F_{f,a,i,j}}{F_{r,a,x}}\right)^2 \leq 1 \tag{14}$$

where $F_{r,a,x}$ and $F_{r,a,z}$ are the horizontal shear and vertical tensile strength of each shear connection, respectively, $F_{f,a,i,j}$ is the horizontal shear load acting on the shear connection at the *j-th* storey obtained from the seismic analysis, and $M_{r,i,j}$ is the respective rocking strength calculated according to Equation 10, taking into account the contribution of shear connections to the rocking strength capacity.

In order to achieve coupled-panel behaviour in the plastic region, where all vertical joints yield before the hold-down, a hierarchy of yielding is established between the hold-down and the vertical joints. When shear connections are assumed not to contribute to the rocking strength of the shearwall (i.e. uni-directional behaviour), the requirement presented by Casagrande et al. (2019) for a multi-panel shearwall is reported in Equation 15.

$$T_{r,hd} \geq \gamma_{Rx} \cdot F_{r,v} \cdot \frac{k_{hd}}{k_{vj}} \qquad if \ k_{hd} \geq n \cdot k_{vj}$$

$$T_{r,hd} \geq \max \left(\gamma_{Rx} \cdot F_{r,v} \cdot \frac{k_{hd}}{k_{vj}} ; \gamma_{Rx} \cdot n \cdot F_{r,v} - w \cdot b \right) \ if \ k_{hd} < n \cdot k_{vj} \qquad (15)$$

where k_{vj} is the elastic stiffness of a single connection in the vertical joints.

When bi-directional behaviour of shear-connections is assumed, the conditions to ensure that all vertical joints yield before the hold-down are reported in Equations 16 and 17, according to Masroor et al. (2022).

$$\frac{k_{hd}}{n \cdot k_{vj}} \geq \frac{1 - \frac{\widetilde{M} \cdot (3 \cdot m - 2)}{m^2}}{(1 + \varphi \cdot \rho_a) - \frac{\widetilde{M} \cdot [m \cdot (1 + \varphi \cdot \rho_a) - 2 \cdot (1 + \alpha \cdot \varphi \cdot m)]}{m^2}} \qquad (16)$$

$$T_{r,hd} \geq \gamma_{Rx} \cdot F_{r,v} \cdot \frac{k_{hd}}{k_{vj}} \qquad (17)$$

Where

$$\rho_a = \sum_{r=1}^{n_a} \frac{r}{n_a + 1} = \frac{n_a}{2} \qquad (18)$$

$$\widetilde{M} = \frac{w \cdot m^2 \cdot b^2}{M_{f,i,j}} \qquad (19)$$

3.3

Adopting the proposed procedure to the CSA O86 Standard

An alternative method to the over-strength factor, γ_{Rd}, is currently included in the Canadian CSAO86 Standard, where the non-dissipative elements are required to remain elastic when the dissipative elements reach the 95th percentile of their strength distribution, $F_{r,95th,D}$. Equation 20 outlines the fundamental relationship between non-dissipative and dissipative elements, and relates the procedure using the over-strength factor to that using the 95th percentile the strength distribution of dissipative elements.

$$F_{r,ND} \geq \gamma_{Rd} \cdot F_{r,D} = F_{r,95th,D} \qquad (20)$$

To ensure consistency with the approach adopted in CSAO86, the methodology involving the over-strength factors (γ_{Rd}, γ_{Rx}, γ_{Ry}) is replaced with those containing values related to the 95th, x^{th} or y^{th} percentile strength of the dissipative connections.

The shear and rocking strength of the *i-th* shearwall at the *j-th* storey associated with the 95th percentile strength of primary dissipative connection are defined as $V_{r,95^{th},j}$ and $M_{r,95^{th},i,j}$, respectively. Similarly, $M_{r,y^{th},i,j}$ is defined as the rocking strength associated with the yth percentile strength of primary dissipative connections. The governing equations provided in the previous subsections are presented in Table 3 in a manner that is consistent with the Canadian design approach.

Table 3. Expressions rewritten to be consistent with the Canadian approach

European approach	Canadian approach
Equation 3	$F_{r,ND} \geq \alpha_j \cdot F_{f,ND} + F_{g,ND}$
Equation 5	$\Omega_j = \dfrac{V_{r,95^{th},j}}{V_{f,j}} \geq 1$
Equation 6	$\Omega_j = \dfrac{\sum_{i=1}^{N}\left|M_{r,95^{th},i,j}\right|}{\sum_{i=1}^{N}\left|M_{f,i,j}\right|}$
Equation 7	$F_{r,a,i,j} \geq \dfrac{\left|M_{r,y^{th},i,j}\right|}{\left|M_{f,i,j}\right|} \cdot F_{f,a,i,j}$
Equation 9	$M_{r,95^{th},i,j} = b \cdot \left[T_{r,x^{th},hd} + F_{r,95^{th},v} \cdot (m-1) \cdot n + \dfrac{w \cdot b \cdot m}{2}\right]$ $M_{r,y^{th},i,j} = b \cdot \left[T_{r,x^{th},hd} + F_{r,y^{th},v} \cdot (m-1) \cdot n + \dfrac{w \cdot b \cdot m}{2}\right]$
Equation 10	$M_{r,95^{th},i,j} = b \cdot \left[T_{r,x^{th},hd} \cdot (1 + \alpha \cdot \varphi \cdot m) + F_{r,95^{th},v} \cdot (m-1) \cdot n + \dfrac{w \cdot b \cdot m}{2}\right]$ $M_{r,y^{th},i,j} = b \cdot \left[T_{r,x^{th},hd} \cdot (1 + \alpha \cdot \varphi \cdot m) + F_{r,y^{th},v} \cdot (m-1) \cdot n + \dfrac{w \cdot b \cdot m}{2}\right]$
Equation 14	$\left(\dfrac{\frac{n_a}{n_a+1} \cdot \varphi \cdot T_{r,y^{th},hd}}{F_{r,a,z}}\right)^2 + \left(\dfrac{M_{r,i,j}}{M_{f,i,j}} \cdot \dfrac{F_{f,a,i,j}}{F_{r,a,x}}\right)^2 \leq 1$
Equation 15	$T_{r,hd} \geq F_{r,x^{th},v} \cdot \dfrac{k_{hd}}{k_{vj}} \quad if\ k_{hd} \geq n \cdot k_{vj}$ $T_{r,hd} \geq \max\left(F_{r,x^{th},v} \cdot \dfrac{k_{hd}}{k_{vj}}; n \cdot F_{r,x^{th},v} - w \cdot b\right)\ if\ k_{hd} < n \cdot k_{vj}$
Equation 17	$T_{r,hd} \geq F_{r,x^{th},v} \cdot \dfrac{k_{hd}}{k_{vj}}$

4. Conclusions

It has long been recognized that the principle of capacity-based design can be adequately used to promote ductile failure mechanisms and to prevent brittle failure modes. A methodology involving a proposed analytical procedure for the applicability of the capacity-based design approach at wall- and building levels is proposed. The proposal is applicable to multi-storey CLT buildings and includes the bi-directional contribution of angle brackets in rocking.

Based on a thorough review of existing and proposed design provisions, the proposed procedure defines three different levels of ductility classes, including expressions ensuring the protection of non-dissipative components as well as a methodology that

establishes a hierarchy of yielding amongst dissipative connections as well as between dissipative connections and connections with limited ductility. In essence the proposal ensures that rocking behaviour is attained and sliding is limited by designating hold-down and vertical joints as energy dissipative while assigning shear-connections as limited ductility connections. Three different over-strength factors are proposed to protect non-dissipative components, ensure a sequence of yielding amongst dissipative connections, and protect shear-connections while limiting sliding failure. A general concept is proposed to help evaluate the values the over-strength factors.

5. References

Casagrande D, Doudak G, Mauro L, Polastri A (2018) Analytical approach to establish the elastic behaviour of multipanel CLT shear-walls subjected to lateral loads. J Struct Eng, Volume 144 Issue 2

Casagrande D, Doudak G, Polastri, A (2019). A proposal for the capacity-design at wall- and building-level in light-frame and cross-laminated timber buildings. Bulletin of Earthquake Engineering, 17, 3139-3167.

Ceccotti A, Sandhaas C, Okabe M, Yasumura M, Minowa C, Kawai N (2013) SOFIE project– 3D shaking table test on a seven-storey full-scale cross-laminated building. Earth Eng Struct Dyn 2013;42(13):2003–21.

D'Arenzo G, Casagrande D, Polastri A, Fossetti M, Fragiacomo M, Seim W (2021), CLT shearwalls anchored with shear-tension angle brackets: experimental tests and finite element modelling, J. Struct. Eng. ASCE 147 (7) (2021) 04021089,

CSA O86-14 (2019) Engineering design in wood. CSA Group, Mississauga

EN 1998-1 (2013) Eurocode 8—design of structures for earthquake resistance part 1: general rules, seismic actions and rules for buildings. CEN, European Committee for Standardization, Brussels.

Flatscher G, Schickhofer G (2016) Displacement-based determination of laterally loaded Cross Laminated Timber (CLT) wall systems. INTER 2016 Meeting, Graz, Austria, Paper 49-12-1; 2016.

Follesa M, Fragiacomo M, Casagrande D, Tomasi R, Piazza M, Vassallo D, Canetti D, Rossi S (2018) The new provisions for the seismic design of timber buildings in Europe. Eng Struct 168:736–747.

Fragiacomo M, Dujic B, Sustersic I (2011) Elastic and ductile design of multistorey crosslam massive wooden buildings under seismic actions. Eng Struct 33(11):3043–3053.

Fragiacomo, M., Follesa, M., Casagrande, D., & Piazza, M. (2019). The revision of the timber chapter of the Eurocode 8. 5th International Conference on Structural Health Assessement of Timber Structures. Guimaraes, Portugal.

Franco L, Pozza L, Saetta A, Talledo D (2021) Enhanced N-V interaction domains for the design of CLT shear wall based on coupled connections models. Engineering Structures, 2021, 231, 111607

Gavric I, Fragiacomo M, Ceccotti A (2013) Capacity seismic design of x-lam wall systems based on connection mechanical properties. In: CIB-W18/46-15-2, Vancouver, Canada

Gavric I, Fragiacomo M, Ceccotti A (2015a) Cyclic behavior of CLT wall systems: experimental tests and analytical prediction models. J Struct Eng 2015;141(11):04015034.

Gavric I, Fragiacomo M, Ceccotti A (2015b) Cyclic behavior of typical screwed connections for cross-laminated (CLT) structures. Eur J Wood Wood Prod 73(2):179–191.

Jorissen A, Fragiacomo M (2011) General notes on ductility in timber structures. Eng Struct 33(11):2987– 2997.

Masroor M, Doudak G, Casagrande D (2020). The effect of bi-axial behaviour of mechanical anchors on the lateral response of multi-panel CLT shearwalls. Engineering Structures, 224- 610 111202.

Masroor M, Doudak G, Casagrande D (2022). Design of multi-panel CLT shearwalls with bi-directional mechanical anchors following capacity-based design principle. Submitted to Journal of Performance of Constructed Facilities, ASCE. Unpublished results.

Nolet V, Casagrande D, Doudak G (2019) Multipanel CLT shearwalls: an analytical methodology to predict the elastic–plastic behavior. Eng Struct 179:640–665.

Ottenhaus LM, Li M, Smith T, Quenneville P (2017) Overstrength of dowelled CLT connections under monotonic and cyclic loading. Bull Earthq Eng 1:1–21.

Pei S, Van de Lindt JW, Popovski M (2013) Approximate R-factor for Cross-Laminated Timber walls in multistory buildings. J Archit Eng 2013;19(4):245–55.

Popovski M, Schneider J, Schweinsteiger M (2010) Lateral load resistance of cross-laminated wood panels. In: World conference on timber engineering (WCTE), Riva del Garda.

Shahnewaz M, Tannert T, Alam M, Popovski M (2017) Capacity-based design for cross-laminated timber buildings. In: Structures congress 2017: business, professional practice, education, research, and disaster management—selected papers from the structures Congress 2017, pp 400–410

Sustersic I, Fragiacomo M, Dujic B (2012) Infuence of connection properties on the ductility and seismic resistance of multi-storey cross-lam buildings. In: WCTE 2012, July 15, 2012–July 19, 2012

Tomasi R, Smith I (2015) Experimental characterization of monotonic and cyclic loading responses of CLT panel-to-foundation angle bracket connections. J Mater Civ Eng 2015;27(6):04014189.

Trutalli D, Pozza L (2018) Seismic design of foor-wall joints of multi-storey CLT buildings to comply with regularity in elevation. Bull Earthq Eng 16(1):183–201.

Yasumura M, Kobayashi K, Okabe M, Miyake T, Matsumoto K (2016) Full-scale tests and numerical analysis of low-rise CLT structures under lateral loading. J Struct Eng 2016;142(4):E4015007.

Appendix - Summary of the analytical procedure

Level 2 Ductility Class

Single-panel shearwall

Step		Equation
#1	Design hold-down	(2)
#2	Design shear connections	(7)
#3	Calculate rocking strength $M_{r,i,j}$*	From literature
#4	Calculate the over-capacity coefficient Ω_j at all storeys	(6)
#5	Calculate the scale factor α_j	(4)
#6	Design non-dissipative components	(3)

*contribution of shear-connection may be taken into account

Multi-panel shearwall
Vertical joints are assumed to be dissipative

Step		Equation
#1	Design dissipative connections (i.e. hold-down and vertical joints)	(2)
#2	Design shear-connections	(7)
#3	Calculate rocking strength $M_{r,i,j}{}^*$ of each shearwall	From literature
#4	Calculate the over-capacity coefficient Ω_j at all storeys	(6)
#5	Calculate the scale factor α_j	(4)
#6	Design of non-dissipative components	(3)

* The rocking strength is calculated as the minimum value of the rocking strength where the weakest component is either hold-down or vertical joints (Casagrande et al., 2018)

Vertical joints are assumed to be non-dissipative

Step		Equation
#1	Design dissipative connections (i.e. hold-down)	(2)
#2	Design shear connections	(7)
#3	Calculate rocking strength $M_{r,i,j}{}^*$ of each shearwall	From literature
#4	Calculate the over-capacity coefficient Ω_j at all storeys	(6)
#5	Calculate the scale factor α_j	(4)
#6	Design vertical joints	(3)
#7	Design non-dissipative components	(3)

* The rocking strength is calculated as the value of the rocking strength where the weakest components is the hold-down (Casagrande et al., 2018)

Level 3 Ductility Class

Multi-panel shearwall
Uni-directional behavior of shear-connections

Step		Equation
#1	Design vertical joints	(8)
#2	Design hold-down	(15)
#3	Calculate rocking strength $M_{r,i,j}$ (CP behavior) of each shearwall	(9)
#4	Design of shear-connections	(7)
#5	Calculate the over-capacity coefficient Ω_j at all storeys	(6)
#6	Check the ratios between the over-capacity coefficients Ω_j along the height of the building	(13)
#7	Calculate the scale factor α_j	(4)
#8	Design non-dissipative components	(3)

Bi-directional behavior of shear-connections

Step		Equation
#1	Design vertical joints	(8)
#2	Design hold-down	(16) and (17)
#3	Calculate rocking strength $M_{r,i,j}$ (CP behavior) of each shearwall	(10)
#4	Design of shear-connections	(14)
#5	Calculate the over-capacity coefficient at all storeys	(6)
#6	Check the ratios between the over-capacity coefficients along the height of the building	(13)
#7	Calculate the scale factor, α_j,	(4)
#8	Design of non-dissipative components	(3)

DISCUSSION

The papers was presented by D Casagrande

J Brown commented that considering building level and hierarchy of ductility class, overstrength of connection might be overly penalizing. He asked if one would put in an overstrength factor cap. D Casagrande replied that a cap is considered for ductility level 2 and the cap for ductility level 3 should not be applied.

J Brown asked about diaphragm and whether it would be considered as the capacity of whole system. D Casagrande replied that it is important and should be considered. How to provide a simple equation is difficult. G Doudak commented that the influence of the diaphragm was not incorporated in the model. The behaviour of the diaphragm was lumped as non-dissipative element in the paper.

T Tannert asked if the vertical joint resistance needs overstrength factors. D Casagrande replied no as vertical joints should be as close as possible to the design limit. T Tannert asked about the coupled uplift and shear resistance of shear connectors and the uplift resistance might limit the rocking action when overstrength factors are adopted. D Casagrande said that their contribution into the rocking strength of the system was accounted for with the assumption that the shear connectors did not yield.T Tannert commented that if all the connectors were assumed to have similar yielding mechanism, would this approach work with using different types of connectors having different yield mechanism in a building. D Casagrande replied that this approach should be applied to traditional connection systems and should use similar connections in a building.

R Jockwer asked how to choose overstrength factor percentile for other dissipative connections and limited ductility connections. D Casagrande replied that these should be less than the 95 percentile for the non-dissipative case but these cases are left open for now for further consideration. Running probabilistic analysis on the failure of buildings is needed.O Sisman asked how to consider joint of perpendicular walls and would they be considered as dissipative or non-dissipative cases. He commented that introduction of level 2 and level 3 might be difficult for young practicing engineers to learn. He suggested that combining levels 2 and 3 into a single level would be easier and should be considered. D Casagrande said combining levels 2 and 3 into a single level could be considered. D Casagrande also replied that the connection of perpendicular wall should be considered as non-dissipative connection. More studies on brittle failure mode vs more ductile failure mode should be considered.

M Fragiacomo commented that the proposal would go into the evaluation process soon so receiving timely feedback and suggestions would be important. Eurocode sets the three ductility classes and they cannot be changed. Properties of steel and its scatter would be a concern for overstrength factor. One might need to provide upper limit to their yield strength in future standard.

Temperature-dependent thermal properties for cross-laminated timber exposed to standard fire

Miriam Kleinhenz, Institute of Structural Engineering, ETH Zurich

Alar Just, Tallinn University of Technology

Andrea Frangi, Institute of Structural Engineering, ETH Zurich

1   Introduction

In the draft of the Eurocode 5-1-2 revision (2020), the charred depth of cross-laminated timber (CLT) is modelled using a simplified model, which takes into account two different scenarios: linear charring when the bond line integrity is maintained and stepwise bilinear charring when the bond line integrity is not maintained. It means that fall-off of charred CLT layers is considered when the bond line integrity is not maintained during fire exposure. Numerical simulations based on Finite Element (FE) heat transfer models are usually conducted based on the temperature-dependent thermal properties for wood and the char layer according to the current Eurocode 5-1-2 (2004). König & Walleij (1999, 2000) proposed thermal properties for initially unprotected and protected timber members. In combination with ENV 1995-1-2 (1997), they formed the basis for the thermal properties of the current Eurocode 5-1-2 (2004). However, it is questionable if these can be used for CLT plates showing multiple fall-offs of charred layers.

In the frame of an ongoing research project, the fire behaviour and fire resistance of CLT rib panels is studied with experimental and numerical analyses. The floor system consists of CLT plates rigidly bonded to glued-laminated timber ribs by means of screw-press gluing. Two different types of cross-section are studied as shown in Figure 1. The experimental results of a series of full-scale fire tests showed more than 90 and 120 min of fire resistance and confirmed the assumption of fall-off of single or multiple charred CLT layers.
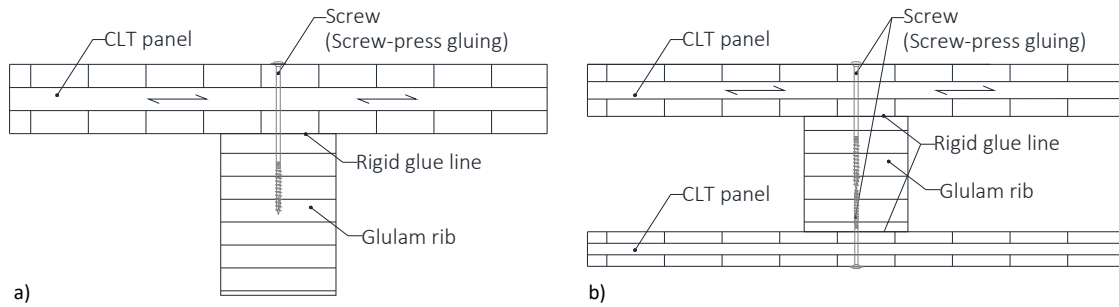
Figure 1. Cross-section types of CLT rib panel: a) T-section; b) box-section.

This paper focuses on the numerical FE simulations of the charring behaviour of the CLT plates exposed to ISO-standard fire on one side, taking into account multiple fall-offs of charred CLT layers. First, numerical simulations of the four tested cross-sections are compared to the experimental results. The temperature-dependent thermal properties are used according to Eurocode 5-1-2 (2004) and a fall-off temperature of 300°C is defined. The thermal simulations predict a significantly earlier fall-off of the charred CLT layers compared to the experimental results. Next, a new set of thermal properties for CLT is presented valid after the first fall-off. The set was calibrated to the experimental result of one tested cross-section. The validation is made by the other three tested cross-sections. At the end, thermal simulations of further experimental results of CLT plates are compared to numerical results using the thermal properties according to Eurocode 5-1-2 (2004) as well as in combination with the new set of thermal properties, defined as revision.

2 Investigations within the framework of the project 'CLT rib panels'

2.1 Experimental investigations

Four full-scale fire resistance tests on CLT rib panel cross-sections were performed as presented in Figure 2 (A, B, C, and D). Of each cross-section type, one has been designed as initially protected cross-section. The tests were performed according to EN 1363-1 (2012) and EN 1365-2 (2014). The horizontal furnace had a length of 5.20 m and a width of 3.00 m. The specimens were simply supported and had three ribs with a flange width per rib of 0.933 m. In the test setup, a constant statical load was applied uniformly via evenly distributed loading points, whereby the moment in the middle of the span corresponded to the target bending moment of the design.

The furnace was controlled with plate thermometers to follow the ISO standard time-temperature curve according to ISO 834-1 (1999). According to Fahrni et al. (2018), inlaid thermocouples of type K-w-e-0.5/2.2/in-pa measured temperatures parallel to the isotherms, between and on top of gypsum plasterboards and CLT layers. They were inserted at quarter points over the length during the production and assembly of the CLT rib panels.
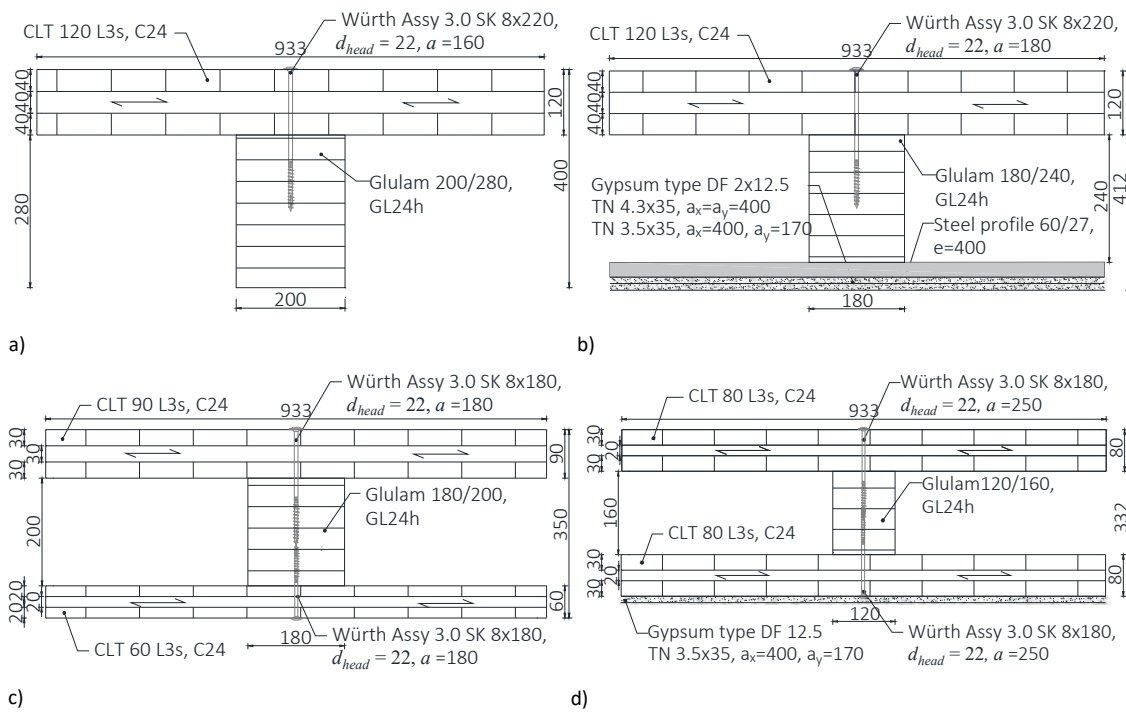
Figure 2. CLT rib panel cross-sections, in [mm]: a) T-section (A); b) T-section initially protected (B); c) Box-section (C); d) Box-section initially protected (D).

Failure times of the fire protection systems $t_{f,test}$ were defined as the first local fall-offs of gypsum plasterboards parts. In the case of initially protected test specimens B and D, the start time of charring $t_{ch,test}$ was defined when the average temperature on the fire-exposed side of the CLT plate reached 300°C. Sudden increases of the temperature measurements to the furnace temperature indicated fall-offs of charred CLT layers. The fall-off times of charred CLT layers $t_{300°C}$ were defined as the average temperature of 300°C between the CLT layers. After termination of the test, the test specimens were lifted from the furnace and extinguished. However, duration of the process lasted around 25 min.

2.2   Numerical investigations

Advanced design methods were applied for the discussion of the development and distribution of the temperatures within the cross-sections. For this objective, heat transfer analyses using 2D FE models were performed as so-called thermal simulations modelling the cross-section of a T-section or box-section. The vertical symmetry in the middle of the cross section was exploited by modelling it as an adiabatic surface. Convective and radiative thermal interactions were defined for the outer timber surfaces with the coefficient of convection taken as 25 W/(m²K) on heated surfaces and 4 W/(m²K) on un-heated surfaces and emissivity as 0.8 for timber and gypsum plasterboards (EN 1991-1-2). The standard fire exposure was applied at the bottom edge. The top edge was exposed to a constant temperature of 20°C. The simulated sections were discretised into rectangular elements. The sizes of the elements varied between 4x4 mm² and 5x5 mm². The time steps were kept at maximum 5 seconds.

The Python programming language (Python Software Foundation 2015) was used to generate the FE heat transfer models based on general properties of the cross-section (layup of CLT, dimension and clear distance of ribs as well as thickness and amount of gypsum plasterboards). The thermal simulations were conducted using SAFIR®, a nonlinear FE software for modelling structures in fire (Franssen & Gernay 2017). As criterion for fall-off of gypsum plasterboards, the fall-off times observed in the fire tests $t_{f,test}$ were used to remove the elements defined as gypsum plasterboards in the FE model. Fall-offs of charred CLT layers were defined as time steps of the thermal simulation when the average temperature between CLT layers exceeded 300°C. In a further simulation step, the FE model was re-created without the fallen-off layer and the calculation was continued until the next CLT layer has fallen off.

The heat transfer analyses depend on temperature-dependent thermal properties (thermal conductivity, specific heat capacity and density) defined for CLT, glulam and gypsum plasterboards. The thermal properties were used for CLT and glulam according to Eurocode 5-1-2 (2004) and for gypsum plasterboards according to FSITB (2010). The moisture content of CLT plates and glulam ribs was measured as 10%. The mean density of the CLT plates was assumed as 465 kg/m^3 according to Stora Enso production. The mean density of the ribs certificated as quality of GL 24h was assumed as 420 kg/m^3 according to EN 14080 (2013). For the gypsum plasterboards, the mean density was chosen as 800 kg/m^3 according to EN 520 (2009).

The heat transfer is influenced by the void cavities. For radiation inside the void cavity, the emissivity of the materials enclosing the void was considered. For convection inside the void cavity, the coefficient of convection on unexposed surfaces was used, regardless of the temperature of the air in the void. Air movement within the cavity was not considered (Franssen & Gernay 2019).

The screw heads ability to conduct heat was a concern in the case of box-sections. The fire tests showed that the higher heat conduction through the screw head remained local and did not extend to the screw tip. The fire behaviour of the cross-section itself remained unaffected. As a result, the screw influence was neglected in the thermal simulations.

2.3 Comparison of experimental and numerical results based on Eurocode 5

Figure 3 shows the measured temperatures per cross-section as single and mean values of the thermocouples between the layers until test termination. Furthermore, the mean temperatures over the length of the CLT and gypsum plasterboard layers were taken from the numerical simulations based on the current Eurocode 5-1-2 (2004). The thermal simulations predict a significantly earlier fall-off of the charred CLT layers compared to the experimental results. The error increases with the number of fall-offs of both gypsum plasterboard and of charred CLT layers. The number of fall-offs would have been overestimated by up to three CLT layers.

Table 1 provides the experimental, analytical and numerical charring rates of the CLT plates until the last experimental fall-off of charred CLT layers before test termination. The analytical results were calculated according to Eurocode 5-1-2 revision (2020). The charred depths of the CLT plates were estimated according to the simplified design method including fall-off of charred CLT layers. After fall-off of gypsum plasterboard or of a charred CLT layer, the charring rate β_0 for solid wood of 0.65 mm/min is doubled to 1.30 mm/min until the charred layer reaches a thickness of 25 mm. Then, the charring rate decreases again to the basic value of the charring rate β_0. In the case of initial protection, encapsulated phases (no charring) and protected charring phases (decreased charring rate) were defined by the estimated start times of charring $t_{ch,EC5}$ and the estimated fall-off times of gypsum plasterboards $t_{f,EC5}$.

The fall-offs of gypsum plasterboards are well predicted according to Eurocode 5-1-2 revision (2020). The simplified design method including fall-off of charred CLT layers leads to safe results for the charring rate in the CLT plates. However, the numerical charring rates are not only higher than the experimental but also higher than the analytical charring rates, giving an incorrect prediction of the fire behaviour of the CLT plates. As advanced design method, the thermal simulations should lead to less conservative predictions than the simplified design method and should be able to predict the actual behaviour. The exception is the initially unprotected cross-section A with only one fall-off of a charred CLT layer, showing a charring rate close to the charring rate β_0 for solid wood of 0.65 mm/min.

Table 1. Start times of charring t_{ch}, failure times of the fire protection system t_f, and charring rates of the CLT plates $\beta_{CLT} = d_{char}/(t_{300°C}-t_{ch})$ of experimental, analytical and numerical results.

Test specimen	Type of cross-section	$t_{ch,test}$ [min]	$t_{f,test}$ [min]	$t_{ch,EC5}$ [min]	$t_{f,EC5}$ [min]	$t_{ch,sim}$ [min]	$t_{f,sim}$ [min]	Charring progress until fall-off of	$\beta_{CLT,test}$ [mm/min]	$\beta_{CLT,EC5}$ [mm/min]	$\beta_{CLT,sim}$ [mm/min]
A	T-section			Initially unprotected				1st layer	0.63	0.65	0.64
B	T-section	55	55	49	58	55	55	1st layer	0.67	0.82	1.16
C	Box-section			Initially unprotected				4th layer	0.84	1.02	1.23
D	Box-section	20	30	24	28	20	30	3rd layer	0.89	1.07	1.42

3 New set of temperature-dependent thermal properties

3.1 Calibration and validation

The fall-off temperature of the charred CLT layers was defined as 300°C for the thermal simulations. The definition agreed well with the experimental results, where the temperatures started to increase between 200 and 300°C. As a result, the definition of the fall-off temperature was not used for adjustment in the calibration.
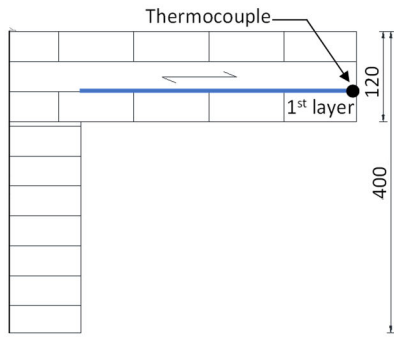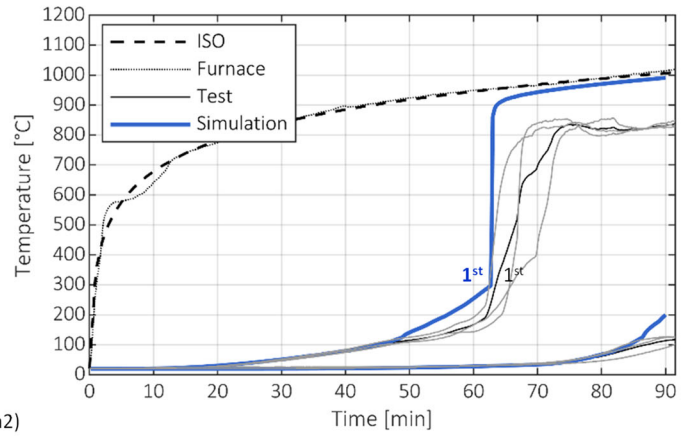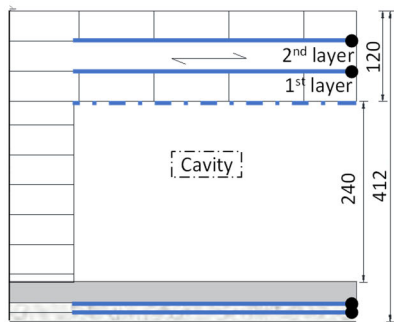
Figure 3. Experimental and numerical temperatures based on the current Eurocode 5-1-2 (2004) (until test termination): a) A; b) B; c) C; d) D.

König & Walleij (1999) have proposed temperature-dependent thermal properties for initially unprotected and protected timber members as basis for the current Eurocode 5-1-2 (2004). The thermal properties were calibrated to test results of initially unprotected linear timber members. Calibrated thermal properties 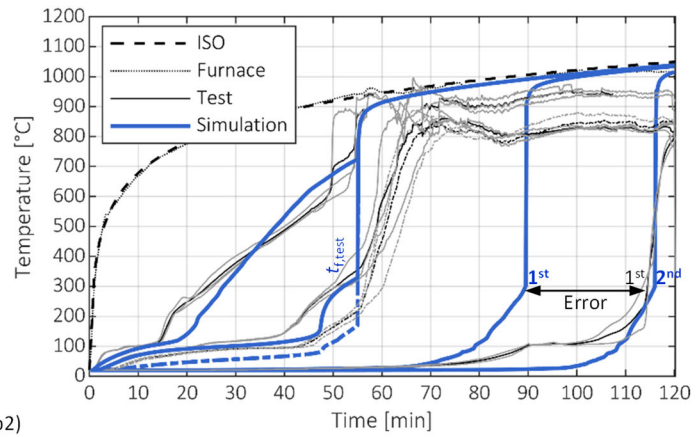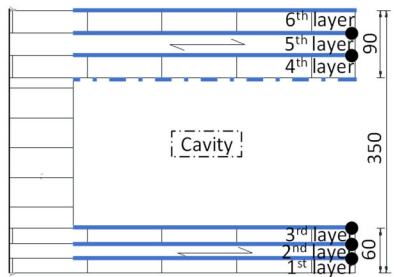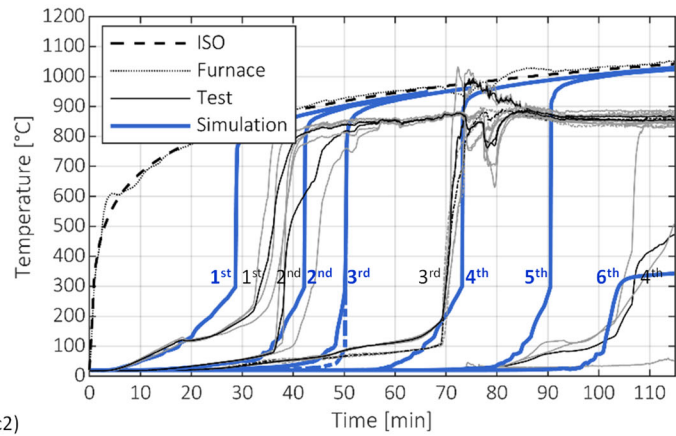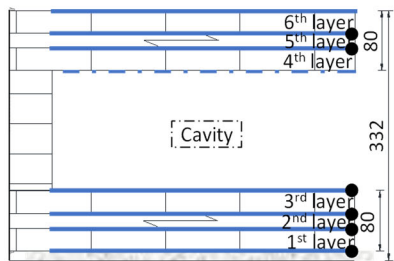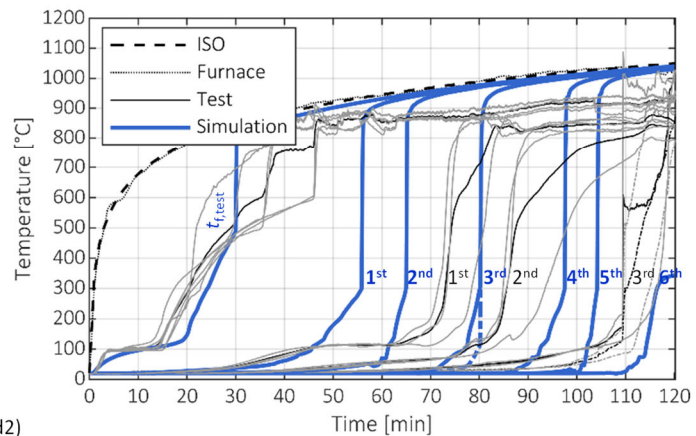were called "effective". To fit the test results of initially protected members, they had to adjust the thermal simulations. In this paper, these thermal properties were re-calibrated to take into account the post-fall-off behaviour of timber. After removing fallen-off layers in the FE model, the time-temperature dependence of the thermal properties must be different, since the relationship between time and temperature differs compared to the ISO-standard time-temperature curve. It was aimed at reducing the conductive heat transfer after fall-off of both - the fire protection system or a charred CLT layer - by revising the thermal properties of the current Eurocode 5-1-2 (2004). This should be achieved by an evolution of the given Eurocode 5-1-2 values rather than a revolution. A conventional calibration was conducted minimizing the error of the fall-off time of the first charred CLT layer in the case of cross-section B between experimental result $t_{300°C,test}$ and numerical result $t_{300°C,sim}$ (see Figure 3).

The best fit is presented in Figure 4 and Table 2. Changes in the given Eurocode 5-1-2 (2004) values were based on literature and physical knowledge. The new set of thermal properties is based on two changes:

- An endothermic reaction heat was included during pyrolysis.
- The effect of thermal insulation by the char layer was increased.

In the literature, a controversial discussion was found whether the pyrolysis can be considered as endothermic or exothermic (Fredlund 1988, Roberts 1971, Mehaffey et al. 1994). König & Walleij (1999) concluded after their calibration that the reaction heat during pyrolysis could be neglected. In this paper, an endothermic reaction heat was included between 200 and 350°C as triangular distribution for the specific heat capacity following Frangi (2001) and Schleifer (2009). For the activation of the pyrolysis, an endothermic reaction heat q_{pyr} of 370 kJ/kg was considered according to Roberts (1971). This reaction heat corresponds to the triangular area under the curve of the specific heat capacity between 200 and 350°C.

As second step, the thermal insulation of the char layer was increased. The literature was searched for lower thermal conductivities for temperatures above 350°C. After comparison of Janssens (1994), Mehaffey et al. (1994) and Thomas (1997), the distribution of the thermal conductivity was adapted between 350°C and 1200°C according to the value of 0.18 W/(mK) at 800°C of Janssens (1994).

3.2   Comparison of experimental and numerical results based on the revision

Thermal simulations of all cross-sections were performed using the new set of thermal properties for CLT after fall-off of the fire protection system (cross-sections B and D) or fall-off of the first charred CLT layer (cross-sections A and C).
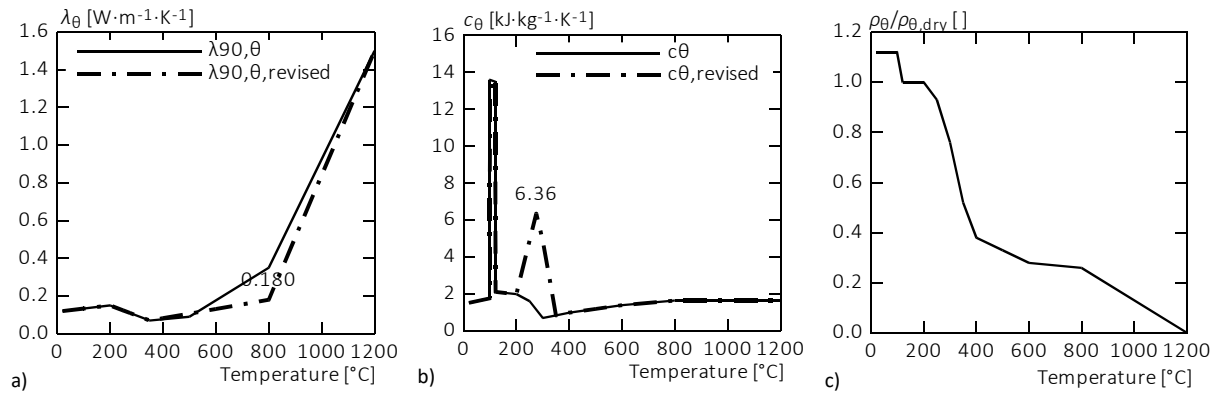
Figure 4. New set of thermal properties for CLT valid after the first fall-off: a) Thermal conductivity; b) Specific heat capacity; c) Density to dry density ratio.

Table 2. New set of thermal properties for CLT valid after the first fall-off: Specific heat capacity; Thermal conductivity; Density to dry density ration (revised values are highlighted in bold).

Temperature	Thermal conductivity	Specific heat capacity	Density to dry density ratio
θ	$\lambda_{90,\theta,revised}$	$c_{\theta,revised}$	ρ_θ/ρ_{dry}
[°C]	[W·m-1·K-1]	[kJ·kg-1·K-1]	[-]
20	0.120	1.53	1.10
99	0.133	1.77	1.10
100	0.133	13.60	1.10
120	0.137	13.50	1.00
121	0.137	2.12	1.00
200	0.150	2.00	1.00
250	0.123	**4.91**	0.93
275	0.110	**6.36**	0.85
300	0.097	**4.91**	0.76
350	0.07	0.85	0.52
400	**0.082**	1.00	0.38
500	**0.107**	1.20	0.33
600	**0.131**	1.40	0.28
800	**0.180**	1.65	0.26
1200	1.50	1.65	0.00

In this paper, this combination of thermal properties of the current Eurocode 5-1-2 (2004) and the new set is called the revision. Figure 6 compares on the right side the experimental temperatures between the layers per cross-section with the numerical temperatures based on the revision. It shows graphically the reduced or even eliminated error between experimental and numerical results. The number of fall-offs would not have been overestimated. Figure 6 illustrates on the left side the charred depths in the CLT plates from start time of charring until test termination. Table 3 provides the experimental, analytical and numerical charring rates of the CLT plates

until last experimental fall-off of charred CLT layers. The experimental and analytical results remain unchanged compared to Table 1. The numerical charring rates are now in a reasonable range, giving a safe prediction of the charring behaviour of the CLT plates without being overly conservative.

Table 3. Start times of charring t_{ch}, failure times of the fire protection system t_f, and charring rates of the CLT plates $\beta_{CLT} = d_{char}/(t_{300°C}-t_{ch})$ of experimental, analytical and numerical results (values based on the revision are highlighted in bold).

Test specimen	Type of cross-section	$t_{ch,test}$ [min]	$t_{f,test}$ [min]	$t_{ch,EC5}$ [min]	$t_{f,EC5}$ [min]	$t_{ch,sim}$ [min]	$t_{f,sim}$ [min]	Charring progress in CLT	$\beta_{CLT,test}$ [mm/ min]	$\beta_{CLT,EC5}$ [mm/ min]	$\beta_{CLT,sim}$ [mm/ min]
A	T-section			Initially	unprotected			1st layer	0.63	0.65	**0.64**
B	T-section	55	55	49	58	55	55	1st layer	0.67	0.82	**0.69**
C	Box-section			Initially	unprotected			4th layer	0.84	1.02	**0.90**
D	Box-section	20	30	24	28	20	30	3rd layer	0.89	1.07	**0.93**

Figure 5 shows the errors per CLT layer of each cross-section. The error between experimental and numerical results of cross-section B could thus be corrected from 25 to 3 min. The error of cross-section A remained unchanged, as there was no further fall-off of charred CLT layers. Likewise, the error of the first layer of cross-section C remained unchanged, since the revised properties apply only after the first fall-off. However, the errors of the following layers of cross-sections C and D were reduced significantly or could even be eliminated. The error of the second layer of cross-section C is still comparatively high. Here, fall-off occurred in the test at very low temperatures (< 100°C) and the charring progressed in a relatively short time (see Figure 6), which is difficult to interpret.
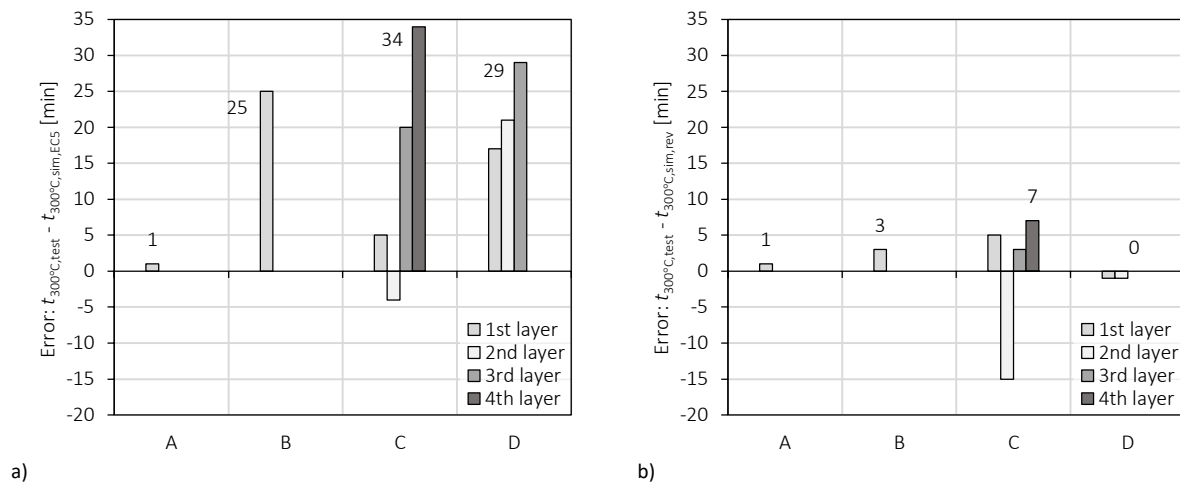
Figure 5. Error between experimental and numerical fall-off times of charred layers per cross-section (until test termination) comparing : a) Based on Eurocode 5-1-2 (2004); b) Based on the revision.
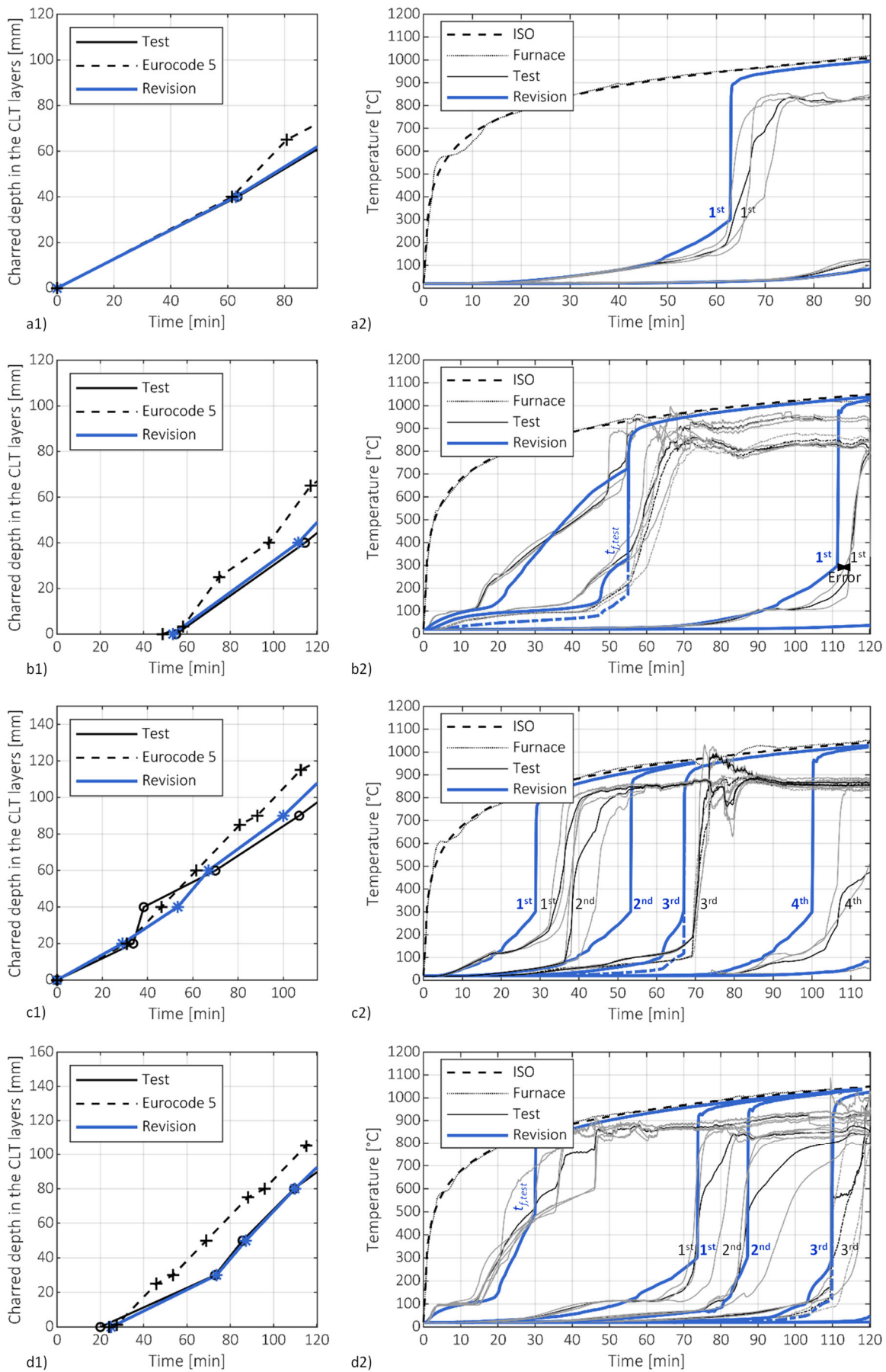
Figure 6. Experimental and numerical temperatures based on the revision and the corresponding charred depths in the CLT plates incl. analytical results based on the current Eurocode 5-1-2 (2004) (until test termination): a) A; b) B; c) C; d) D.

4 Comparison of experimental with numerical results of a database

Further experimental results of initially unprotected CLT slabs were collected into a database. They were exposed to standard fire and showed more than one fall-off. Table 4 summarizes the 20 fire tests of the database. Thermal simulations were conducted using the thermal properties according to Eurocode 5-1-2 (2004) as well as the revision. The sizes of the elements were defined as 1x1 mm^2 with a CLT width of 10 mm. The time steps were kept at 1 second.
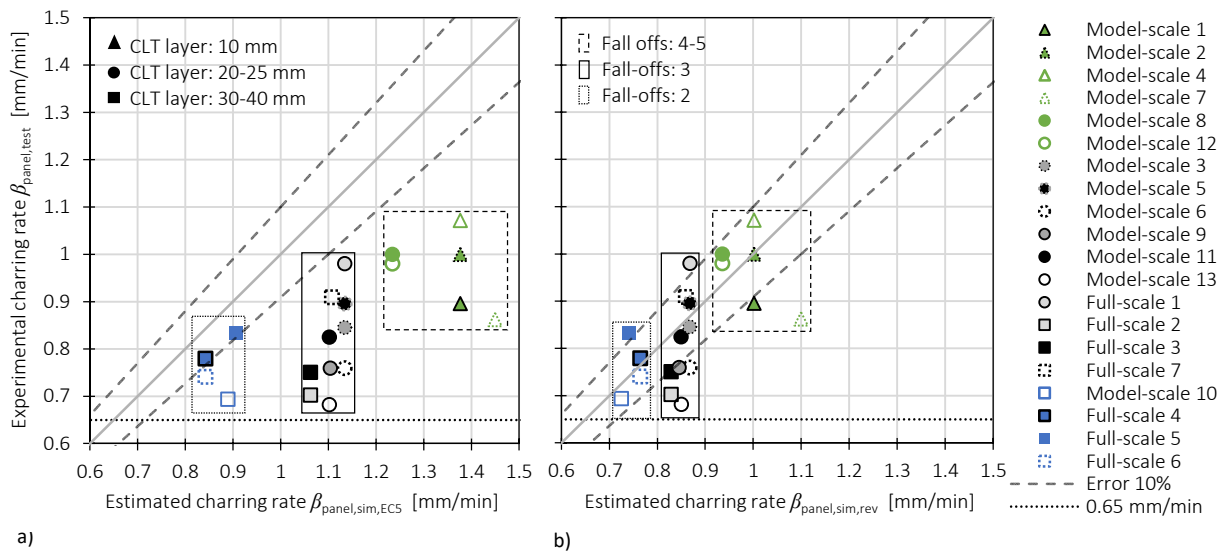
Figure 7. Comparison of experimental and numerical charring rates of the database:
 a) Based on Eurocode 5-1-2 (2004); b) Based on the revision.

Figure 7 presents the numerical results of the charring rates of the single CLT plates in comparison with the experimental charring rates. The difference between numerical and experimental charring rates is expressed by the root mean square error (RMSE). The revision fits three times better the experimental data (RMSE = 0.09 mm/min) than the current Eurocode 5-1-2 (2004) (RMSE = 0.31 mm/min). The comparison based on the revision shows a relationship between experimental and numerical charring rates on the safe side or within an error corridor of 10%. Figure 7 distinguishes between different layer thicknesses (10 – 40 mm) and number of fall-offs of charred CLT layers (2 – 5 fall-offs). The latter can also be associated with longer fire exposure times. Bigger layer thicknesses and less fall-offs lead to results close to the charring rate β_0 for solid wood of 0.65 mm/min. Smaller layer thicknesses and multiple fall-offs result in higher charring rates up to 1.1 mm/min.

5 Conclusion

The temperature-dependent thermal properties according to the current Eurocode 5-1-2 (2004) were not calibrated to model the post-fall-off behaviour of timber. This paper proposes a new set of thermal properties for CLT exposed to standard fire

from one side to take into account the post-fall-off behaviour. It is valid after the first fall-off of the fire protection system or a charred CLT layer. The combination of Eurocode 5-1-2 (2004) and the new set is called the revision. The revision was validated for CLT layers of thicknesses between 10 and 40 mm. The authors propose to consider the introduction of the new set of thermal properties into the Eurocode 5 revision.

6   Acknowledgement

7   References

Bühlmann, A (2014): Brandverhalten von stirnseitig verklebten Brettsperrholzplatten (in German). ETH Zurich, Zurich (Master thesis).

EN 1363-1 (2012): Fire resistance tests - Part 1: General requirements. European Committee for Standardization (CEN), Brussels.

EN 1365-2 (2014): Fire resistance tests for loadbearing elements - Part 2: Floors and roofs. European Committee for Standardization (CEN), Brussels.

EN 14080 (2013): Timber structures - Glued laminated timber and glued solid timber - Requirements. European Committee for Standardization (CEN), Brussels.

EN 520 (2009): Gypsum plasterboards - Definitions, requirements and test methods. European Committee for Standardization (CEN), Brussels.

ENV 1995-1-2 (1997): Eurocode 5. Design of timber structures - Part 1-2: General - Structural fire design. CEN, Brussels.

Eurocode 1-1-2 (2004): Eurocode 1: Actions on structures - Part 1-2: General actions - Actions on structures exposed to fire. CEN, Brussels. (EN 1991-1-2).

Eurocode 5-1-2 (2004): Eurocode 5. Design of timber structures - Part 1-2: General - Structural fire design. CEN, Brussels. (EN 1995-1-2).

Eurocode 5-1-2 revision (2020): SC5.T4 Third draft of prEN 1995-1-2 for commenting. CEN – CENELEC, Brussels. (CEN/TC 250/SC 5 N 1327).

Fahrni, R et al. (2018). Correct temperature measurements in fire exposed wood. World Conference on Timber Engineering (WCTE), Seoul.

Fahrni et al. (2021): Fire safety of cross-laminated timber. ETH Zurich (Report).

Frangi, A (2001): Brandverhalten von Holz-Beton-Verbunddecken (in German). ETH Zurich, Zurich (Doctoral thesis). https://doi.org/10.3929/ethz-a-004228944.

Frangi, A et al. (2009): Experimental analysis of cross-laminated timber panels in fire. Fire Saf. J. 44, 1078–1087. https://doi.org/10.1016/j.firesaf.2009.07.007.

Franssen, J-M & Gernay, T (2017): Modeling structures in fire with SAFIR®: theoretical background and capabilities. Fire Engineering 2017, 8, 300–323. https://doi.org/10.1108/JSFE-07-2016-0010.

Franssen, J-M & Gernay, T (2019): User's manual for SAFIR 2019 – A computer program for analysis of structures subjected to fire. University of Liege, Liege.

Fredlund, B (1988): A model for heat and mass transfer in timber structures during fire - A theoretical, numerical and experimental study. Lund University, Lund (Doctoral thesis).

FSITB (2010): Fire Safety in Timber Buildings – Technical Guideline for Europe. SP Technical Research Institute of Sweden, Stockholm. www.sp.se/FSITB

ISO 834-1 (1999): Fire-resistance tests - Elements of building construction - Part 1: General requirements. International Organization for Standardization (ISO).

Janssens, M (1994): Thermo-physical properties for wood pyrolysis models. Pacific Timber Engineering Conference. Gold Coast, Australia.

König J & Walleij L (1999): One-Dimensional Charring of Timber Exposed to Standard and Parametric Fires in Initially Unprotected and Postprotection Situations. Swedish Inst. for Wood Technology Research, Stockholm.

König J & Walleij L (2000): Timber frame assemblies exposed to standard and parametric fires – Part 2: A design model for standard fire exposure. Swedish Inst. for Wood Technology Research, Stockholm.

Mehaffey, J R et al. (1994): A model for predicting heat transfer through gypsumboard/wood-stud walls exposed to fire. Fire and Materials 18, 297–305. https://doi.org/10.1002/fam.810180505.

Mindeguia, J-C et al. (2020): Thermo-mechanical behaviour of cross-laminated timber slabs under standard and natural fires. Fire and Materials 2020, 1-19. https://doi.org/10.1002/fam.2938.

Python Software Foundation (2015): Python (version 2.7.11) [programming language]. Python Software Foundation. URL: https://www.python.org/.

Roberts, A F (1971): The heat of reaction during the pyrolysis of wood. Combustion and Flame 17, 79–86. https://doi.org/10.1016/S0010-2180(71)80141-4.

Schleifer V (2009): Zum Verhalten von raumabschliessenden mehrschichtigen Holzbauteilen im Brandfall (in German). ETH Zurich, Zurich (Doctoral thesis). https://doi.org/10.3929/ETHZ-A-005771863.

Stora Enso (2021): Loadbearing floor fire tests on CLT elements - carried out at CSI S.p.a. fire laboratory in Bollate, Italy. Unpublished data.

Thomas, G C (1997): Fire Resistance of Light Timber Framed Walls and Floors. University of Canterbury, Christchurch (Fire Engineering Research Report 97/7).

Table 4. Database of this paper: Initially unprotected CLT slabs exposed to ISO-standard fire, crosswise layer orientation, spruce, inlaid thermocouples, multiple fall-off of charred CLT layers.

Reference	Specimen	Adhesive	Layup [mm]	Total thickness [mm]	Layer thickness [mm]	Specimen size [mm²]	Density [kg/m³]	Moisture content [%]	Fire exposure time [min]	Type of fire test	Number of fall-offs [-]
Frangi et al. 2009	Model-scale 1	PU	10/10/10/10/20	60	10	800x1000	405-486	10.0	67	unloaded	5
	Model-scale 2	PU	10/10/10/10/20	60	10	800x1000	405-486	10.0	60	unloaded	5
	Model-scale 3	PU	20/20/20	60	20	800x1000	405-486	10.0	71	unloaded	3
	Model-scale 4	PU	10/10/10/10/20	60	10	800x1000	405-486	10.0	56	unloaded	5
	Model-scale 5	PU	20/20/20	60	20	800x1000	405-486	10.0	67	unloaded	3
	Model-scale 6	PU	20/20/20	60	20	800x1000	405-486	10.0	79	unloaded	3
	Model-scale 7	PU	5x10	80	10	800x1000	463.5	12.0	60	unloaded	5
	Model-scale 8	PU	7x25	175	25	800x1000	447.5	12.0	120	unloaded	4
	Model-scale 9	PU	7x20	140	20	800x1000	471.0	12.0	90	unloaded	3
Fahrni et al. 2021	Model-scale 10	PU	5x35	175	35	800x1000	456.8	12.0	120	unloaded	2
	Model-scale 11	PU	7x25	175	25	800x1000	433.0	12.0	120	unloaded	3
	Model-scale 12	PU	7x25	175	25	800x1000	431.7	12.0	120	unloaded	4
	Model-scale 13	PU	7x25	175	25	800x1000	454.6	12.0	120	unloaded	3
Bühlmann 2014	Full-scale 1	PU	10x20	200	20	2850x5210	450.0*	12.0*	84	loaded	3
Mindeguia et al. 2020	Full-scale 2	PU	5x33	165	33	3900x5600	450.0	12.6	203	loaded	3
	Full-scale 3	PU	5x33	165	33	3900x5600	450.0	11.6	179	loaded	3
	Full-scale 4	PU	40/20/20/20/40	140	40/20	2250x4500	480.0	12.0*	86	loaded	2
Stora Enso 2021	Full-scale 5	PU	40/40/40/40/40	200	40	2340x4500	430.0	12.0*	126	loaded	2
	Full-scale 6	PU	40/20/40/20/4020/40	220	40/20	2250x4500	480.0	12.0*	145	loaded	2
	Full-scale 7	PU	2x30/30/40/30/2x30	220	30	2340x4500	430.0	12.0*	143	loaded	3

* = Assumption made by the authors

DISCUSSION

The papers was presented by M Kleinhenz

S Winter commented the study only looked for the resistance with minimum insulation. He questioned why 300 °C as failure criterion was used and that seemed to be high for PU adhesives. He also asked physical explanations for the thermal properties considered. M Kleinhenz said that in this INTER paper only resistance was considered and not EI and would deal with other issues in future work. The 300 °C was chosen based on previous furnace test results (observation of fall off) and will confirm with own small scale fire tests when equipment becomes available. M Kleinhenz replied about the physical explanation as C having two peaks. The first peak corresponded with water going out. As energy was needed for pyrolysis to turn the timber into charcoal, it makes physical sense to have the second peak. S Winter commented that water wave / moisture movement condensation might be the physical reason.

G Montgomery questioned why one laminar without cross layer was considered in slide 7. M Kleinhenz said the member was assumed to be able to still take a load but this might not be realistic. G Montgomery asked whether this could be seen in the fire test. M Kleinhenz said it was not possible to see this with the flaring up. G Montgomery said it would be more likely to fall off when the second layer fell off.

G Montgomery asked why specimen C with no drywall layer was more variable. M Kleinhenz said more small scale fire tests would be done for these boxes. G Montgomery received confirmation that the loading applied were typical live and dead loads.

G Montgomery asked if Eurocode accounts for the fall off from the glue bond. M Kleinhenz replied that it would be included in future Eurocode with step model.

S Aicher commented on the case of CLT and GLT working as a T Beam with or without insulation. He said the main problem would be the bond between the GLT beam and the CLT plate where temperature dependency of the PU adhesive would play a major role. The 300 °C would not be appropriate for the PU adhesive where 180 °C to 230 °C would be more appropriate. M Kleinhenz agreed about the lower temperature in general but the 300 °C adopted in the project would be correct. The glueline was not considered in design as rigid connections under fire. Image results showed that at 300 °C the glueline would still be intact. S Aicher said that the size of the beam is important here in term of fire performance of the bondline. He also said that ETA of these T Beam products does not allow rigid connection consideration. A Frangi added that the width of the beam was very important here and 300 °C was well established based on falling off observed in tests.

B J Yeh commented that in N. America char layer falling off issues was tightened by adhesive requirements. He asked how to verify assumptions at the moment of char

layer falling off. M Kleinhenz said the model assumed that all elements reaching 300°C were omitted and the model agreed well with results. B J Yeh asked what temperature would be assumed at the fresh layer at the moment of falling off. M Kleinhenz said an instantaneous temperature jump was assumed.

G Ravenhorst received confirmation that there was one test per cross section. He asked about result repeatability with only one test. M Kleinhenz said the model agreed well with results except one case and would like to redo this configuration when equipment becomes available.

Reliability improvements of the fire design for the revision of Eurocode 5-1-2

Reto Fahrni, Institute of Structural Engineering, ETH Zurich

Andrea Frangi, Institute of Structural Engineering, ETH Zurich

Keywords: timber, fire, code calibration, reliability analysis, partial factor, strength, charring rate

1 Introduction

1.1 Background: Calibration of the present Eurocode 5-1-2

The introduction of the Eurocodes in the 1990ies was not only a harmonization of structural design codes[1] in Europe, but also a transition from "allowable stress design" (ASD) to the semi-probabilistic "load and resistance factor design" (LRFD). This meant that "safety" is provided by the application of partial (safety) factors and the use of a fractile value for properties with a significant scatter such as the strength and the loads. It was proposed that for the strength of any material the 5% fractile is applied. At the same time, the code format of Eurocode 5-1-2 should result in comparable designs as the previous timber codes, which was achieved by calibrating the partial factor for the strength. However, as it resulted in a value below one, which subjectively does not imply "safety", it was decided to keep the partial factor at one, like for all other materials' strength in fire. In turn, its fractile was increased from 5% to 20%, which had roughly the same effect (König, 2005). However, this change of the fractile was recently questioned since it deviates from all other materials and shall thus be reconsidered in the current revision of the Eurocodes.

1.2 Relative code calibration

With the choice to calibrate the new code to result in comparable designs as the previous codes, the standardization committee considered the present safety level at

---

[1] "code": the word "code" is understood as synonym to "standard". For consistency with the "*code* calibration" literature and the Euro*code*, the word "code" is used instead of "standard".

that time as sufficient. This safety level can quantitatively be expressed in terms of the mean reliability index of structures designed after the previous code. Such a code calibration is called "relative", since its target is derived in relation to another code (Fahrni et al. 2020). It contrasts "absolute" code calibrations, where the targeted reliability index is derived from cost optimizations and/or taken from a code (e.g. Eurocode (2002) Table B.2).

In contrast to the calibration of the present Eurocode 5-1-2 (2004), the calibrations presented here for the investigation of the 20% fractile are not only relative, but also based on reliability analysis. Thus, they do not only try to match the previous reliability level on average, but also minimize the reliability scatter among the reference structures, which represent the scope of the code format. An absolute calibration on the basis of the target reliability index given in the Eurocode (EN 1990, 2002) would have the drawback that unavoidable biases (Massini, 2019) in the reliability models would significantly bias the calibration results. In a relative code calibration, the target reliability index is calculated using the same (biased) reliability models as are used in the the calibration. Thus, the biases roughly cancel out (Fahrni et al. 2019, Fahrni 2021).

1.3   Outline

The herein presented reliability analyses and code calibrations are done for timber exposed to standard fire. This means a significant bias to the reliability index, because it will not represent the reliability for the real fire situation, but for a certain standard fire exposure. Since the presented calibration is relative, this bias is unproblematic.

A similar code calibration was already presented at INTER 2019 (Fahrni et al., 2019). It has already been shown that lowering the fractile to the typical 5% while maintaining the mean reliability level will significantly increase the reliability scatter among the reference structures. In Fahrni et al. (2019), the effective cross-section method (ECM, e.g. Schmid et al. 2015 (as "reduced cross-section method")) was used as the reliability model for resistance by replacing the strength and the charring rate by probabilistic distributions. By using the same model in the code format and in the reliability model, model biases are not captured in the calibration. For the final calibrations presented herein, the reliability model should be as accurate as possible and consequently be able to capture biases in the ECM.

Finite-element simulations are considered an accurate basis for the subsequent derivation of a reliability model (Chapter 2). The finite-element simulations cannot directly be used as a reliability model due to its computational effort. During one reliability analysis, the reliability model is evaluated several times. Since one code calibration consists of several reliability analysis for each reference structure, a reliability model ideally is just an analytical formula. For this reason, analytical models for the fire resistance of timber beams exposed to standard fire were fitted to the finite-ele-

ment simulations. For beams exposed on the sides and the underside, a new analytical resistance model was developed and fitted: the corner rounding model (CRM) (Chapter 4).

Since the finite-element simulations were done on the basis of the material properties given in Eurocode, it provides the chance to compare the "advanced design method" with the "simplified design method", in particular the ECM (Chapter 3). Based on this comparison, it was decided to increase the zero-strength layer (ZSL) in the final draft of Eurocode 5-1-2 (2021).

The final code calibrations are shown in Chapter 5.

2 Simulations

The finite-element simulations were done with Abaqus Standard 2019, following the requirements and recommendations given in the present Eurocodes 1-1-2 (2002) and 5-1-2 (2004). This included the temperature dependent material properties for the density, heat capacity and conductivity, and the strength and stiffness reduction factors given in the present Eurocode 5-1-2 (2004) (König & Walleij 2000, ENV 1995-1-2 1994). A density of 420 kg/m^3 and a moisture content of 12% were used.

The simulations should cover the full range of reference structures considered in the code calibration. Due to the high effort for finite-element simulations, it was decided to consider only beam structures in the code calibration. Two different exposures were considered: (1) on the underside and the sides and (2) on the underside only. With only the bottom exposed, beam structures have similarities to solid timber panels (STP) and cross-laminated timber (CLT).

Six beam widths (every 50 mm from 100 to 350 mm) with three aspect ratios (width to height) each were simulated with standard fire exposures of 30, 60, 90 and 120 minutes for three-sided exposure. Only structures where the fire situation realistically gets decisive were taken into account, i.e. structures where the section modulus in fire W_{fi} is between 10% and 50% of the section modulus at ambient temperature W_{perm}. In total 31 simulations were considered for three exposed sides (Table 1).

Nine different beam heights (every 25 mm from 50 to 250 mm) for one-sided exposure were simulated. Fire durations of 30, 60, 90 and 120 minutes were analyzed. 16 configurations were within the range of considered resistance ratios (Table 2).

The ultimate bending resistance was simulated in an uncoupled analysis: First, the temperature development in the beams over time was simulated. In the second step, the beams are "tested" in a four point bending setup past the ultimate load (Figure 1). The length of the beams was chosen as six times its height. The loads were applied over the full width and a length of 50 mm at every third of the beam length. The

fire exposure did not consist of the outermost quarters, to allow for a load applica-tion in compression from below. Since the setup is double-symmetrical, only one quarter had to be modeled.
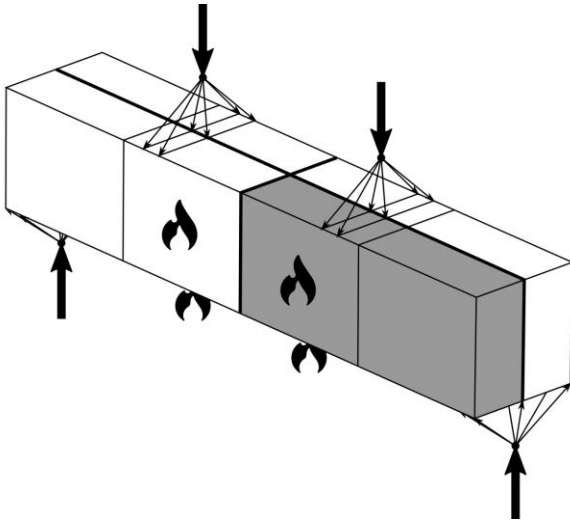
Figure 1: Setup of the 4-point bending simulations. Symmetries (thick lines) were exploited so that only one quarter (shaded) had to be modeled. Sides and the underside exposed to fire in the middle section. Load application and support at every third of the length and distributed over an area.
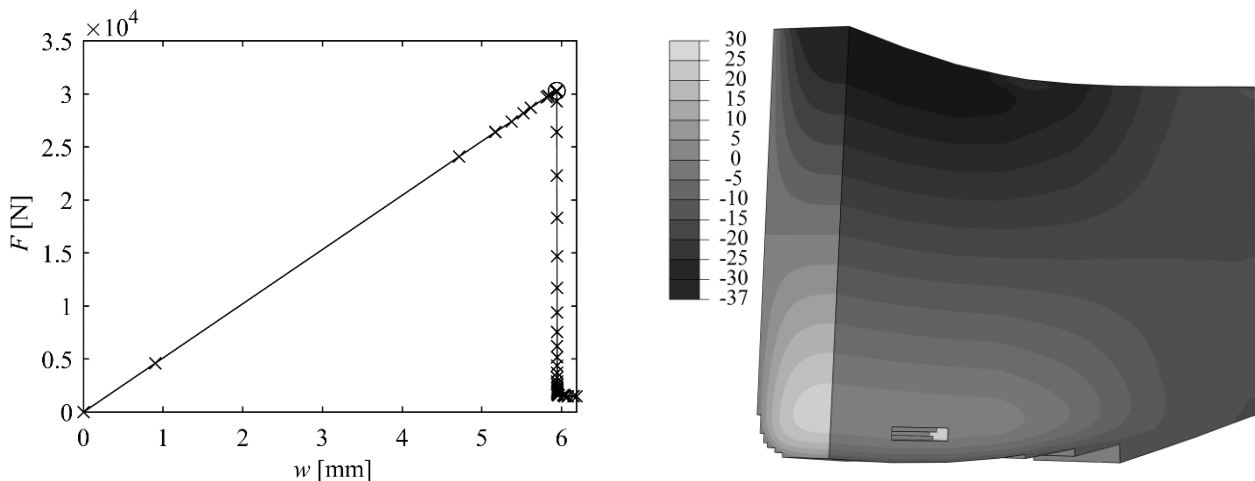
Figure 2: Left: exemplary load displacement curve indicating all increments as crosses. Right: stress state on the symmetry planes at the ultimate load (indicated as a circle on the left). Failed elements were removed.

The material was modeled as linear elastic and perfectly brittle (in tension). In com-pression, neither failure nor plasticity was modeled. If the considered four point bending setup was simulated without the fire exposure, the first element failure in the tension zone would occur when the maximum bending capacity was reached. Considering the elevated temperatures in the tension zone, this is not valid anymore, since the loads of the first failing elements can typically be taken by other, colder, el-ements. In addition, not necessarily the outermost elements fail first (Figure 2), which is a consequence of the difference in the strength and stiffness reduction factor. For this reason, it is important that the finite-element simulation works post the first fail-

ing elements. To avoid convergence problems, a user subroutine (USDFLD) was executed between every increment. It (1) deactivates elements when they were stressed beyond their strength and (2) chooses the next increment wisely, to have large increments where no failure occurs and minimal increments at failure to minimize the overestimation of the ultimate load (Fahrni 2021).

Table 1: Effective section modulus W_{sim} for each simulated beam exposed on the underside and the sides. Additionally, the relative resistance in fire and the deviations of the section modulus according to Eurocode 5-1-2 (2004) and (2021) and the calibrated corner rounding model (CRM) are given.

b	h	t	W_{sim}	$\dfrac{W_{fi}}{W_{perm}}$	dev_{2004}	dev_{2021}	$dev_{CRM,cal}$
[mm]	[mm]	[min]	[10^3 mm^3]				
100	200	30	163	24.5%	-32.9%	-10.8%	-0.2%
100	300	30	428	28.5%	-26.8%	-7.1%	-0.2%
100	400	30	808	30.3%	-25.7%	-6.8%	-1.5%
150	300	30	1076	47.8%	-7.7%	1.3%	4.1%
150	300	60	405	18.0%	-34.7%	-16.3%	-1.5%
150	450	60	1094	21.6%	-27.4%	-11.0%	0.1%
150	600	60	2073	23.0%	-26.9%	-11.1%	-1.3%
200	400	60	1886	35.4%	-11.0%	-2.7%	2.9%
200	400	90	919	17.2%	-18.6%	-4.8%	-0.2%
200	600	60	4610	38.4%	-11.9%	-4.2%	0.4%
200	600	90	2411	20.1%	-16.5%	-3.7%	-1.0%
200	800	60	8508	39.9%	-12.7%	-5.2%	-1.1%
200	800	90	4591	21.5%	-16.1%	-3.6%	-1.9%
250	500	60	4900	47.0%	-5.2%	0.3%	3.7%
250	500	90	3163	30.4%	-7.2%	0.1%	1.7%
250	500	120	1806	17.3%	-5.0%	5.7%	-0.5%
250	750	60	11687	49.9%	-6.5%	-1.4%	1.4%
250	750	90	7867	33.6%	-7.8%	-1.0%	0.0%
250	750	120	4735	20.2%	-3.9%	6.1%	-0.8%
250	1000	90	14628	35.1%	-8.4%	-1.8%	-1.2%
250	1000	120	9018	21.6%	-3.8%	5.9%	-1.3%
300	600	90	7296	40.5%	-2.7%	2.3%	3.1%
300	600	120	5056	28.1%	-0.8%	5.5%	1.4%
300	900	90	17679	43.7%	-3.9%	0.7%	1.2%
300	900	120	12692	31.3%	-1.4%	4.5%	0.2%
300	1200	90	32489	45.1%	-4.8%	-0.3%	0.0%
300	1200	120	23703	32.9%	-2.0%	3.7%	-0.7%
350	700	90	13824	48.4%	-0.5%	3.3%	3.8%
350	700	120	10549	36.9%	1.6%	6.0%	2.9%
350	1050	120	25830	40.2%	0.3%	4.5%	1.3%
350	1400	120	47694	41.7%	-0.6%	3.4%	0.3%

Table 2: Effective section modulus W_{sim} for each simulated beam exposed on the underside. Additionally, the relative resistance in fire and the deviations of the section modulus according to Eurocode 5-1-2 (2004) and (2021) and the calibrated effective cross-section method (ECM) are given.

h	t	W_{sim}	$\dfrac{W_{fi}}{W_{perm}}$	dev_{2004}	dev_{2021}	$dev_{ECM,cal}$
[mm]	[min]	[mm³/mm']				
50	30	60	14.4%	-53.1%	-0.1%	0.3%
75	30	315	33.6%	-24.5%	-2.5%	-2.3%
100	30	816	49.0%	-10.3%	2.8%	2.9%
100	60	363	21.8%	-33.7%	-5.7%	-1.9%
125	60	862	33.1%	-20.6%	-3.0%	-0.5%
150	60	1654	44.1%	-9.0%	3.2%	4.9%
125	90	456	17.5%	-29.5%	1.1%	-4.4%
150	90	1022	27.2%	-16.5%	3.3%	-0.3%
175	90	1809	35.4%	-10.5%	4.2%	1.5%
200	90	2886	43.3%	-4.5%	6.9%	4.8%
225	90	4210	49.9%	-0.7%	8.5%	6.8%
150	120	598	15.9%	-17.8%	12.6%	-3.9%
175	120	1231	24.1%	-9.7%	11.2%	-0.3%

Figure 2 shows an exemplary stress displacement plot and the stress state at the ultimate load. Table 1 and Table 2 present the setups and results of the considered structures. Since the actual moment resistance is linearly dependent on the strength, the results are provided in terms of the effective section modulus W_{sim} instead of the moment.

3   Comparison between simplified and advanced design methods

Since the material model in the finite-element simulations is linear elastic and does not involve plasticity, it is equivalent to the material model applied in resistance calculations on the basis of the ECM. The main difference between the advanced method (FE) and the simplified design method (ECM) is the modelling of the charring and strength/stiffness reduction. The results from FE can be considered more accurate e.g. because they consider the rounded corners due to charring from multiple sides appropriately. Thus, it is interesting to compare the resistance from the analytical model (ECM) $R_{analytical}$ with the accurate resistance R_{sim} from finite-element simulations. It is useful to describe the deviation of the ECM from the finite-element simulation in relative terms. Positive deviations are conservative:

$dev = (R_{sim} - R_{analytical})/R_{sim}$ (1)

Figure 3 (a) shows the relative deviations of the resistances with the ECM implemented in the present Eurocode 5-1-2 ($\beta = 0.65$ mm/min for underside exposed and

$\beta = 0.7$ mm/min for side and underside exposed, $d_0 = 7°$mm) as a function of the fire resistance. All deviations are also presented in Table 1 and Table 2. As can be seen, the fire resistances are overestimated the most for fire durations of 30 min. With increasing fire resistance, the overestimation reduces. The resistance overestimations are up to 53% and thus actually not tolerable. To reduce this time-dependent discrepancy between the simplified and the advanced design methods it is proposed to increase the ZSL d_0 to 10 mm (Eurocode 5-1-2, 2021). Since this affects the shorter fire resistances more than longer ones, the time dependent deviation is significantly reduced (Figure 3 (b)). Additionally, the charring rate of beams exposed only on the underside was increased to $\beta = 0.7$ mm/min, same as for multi-sided exposure.
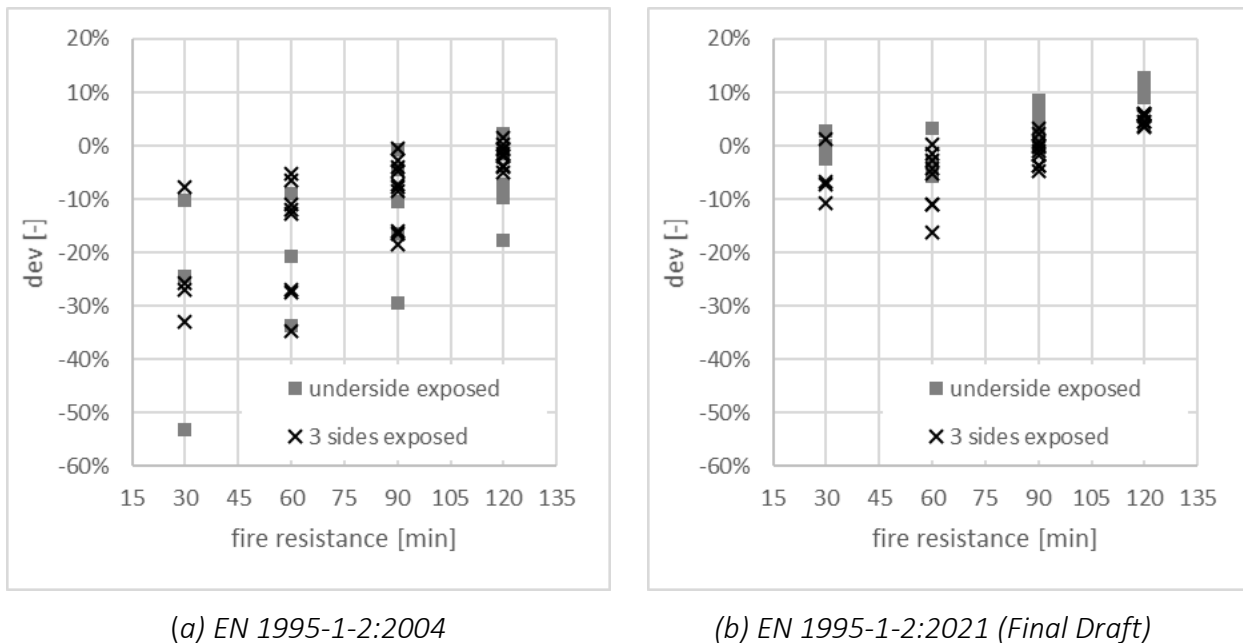
(a) EN 1995-1-2:2004   (b) EN 1995-1-2:2021 (Final Draft)

Figure 3: Comparison between the parametrisations of the ECM in respect of their relative resistance deviations from 3D FE simulations. Negative values indicate overestimations of the resistance of the ECM; see Formula (1).

The discrepancy between the simplified and the advanced method in the present Eurocode 5-1-2 (2004) is likely caused to a significant degree by different temperature dependent reduction factors for strength and stiffness: The properties for the advanced calculation method in Eurocode 5-1-2 are mainly based on König & Walleij (2000), which derived the reduction factors by calibrating them to large-scale standard fire tests. However, the ZSL of 7 mm was chosen based on Schaffer et al. (1986) (actually 0.3 in = 7.6 mm), who derived it applying lower temperature dependent strength reductions. Those reduction factors were derived from small, defect-free samples from various species. However, the main author himself stated that "considerable recent research indicates that temperature and moisture change response of defect-free wood differs significantly from that of lumber and timbers containing knots, checks, and slope-of-grain defects" (Schaffer 1984, p.5). Thus, the proposed

increase of the ZSL can be considered as a harmonization between the simplified and advanced design method on the basis of the most accurate available properties.

The back calculation of the ZSL from tests is delicate since several uncertain properties have to be assumed. Schmid et al. 2014 reviewed many fire resistance tests and back calculated the ZSL as accurate as possible, also giving a qualitative certainty of the result. It could be seen that (1) the scatter among tests is large (from -6 mm to 40 mm) and (2) the average of the most certain results is roughly 12 mm for bending.

A neat test series to derive ZSLs is presented in Lange et al. (2014). They calculated a ZSL of 15 mm based on tests, where the properties used in the back calculation were known more accurately than probably in any other publication.

Considering the test evidence, the proposed increase of the ZSL from 7 mm to 10 mm for bending is not necessarily conservative yet and certainly justified.

4 Analytical resistance models

4.1 Corner rounding model

The analytical resistance model used in the reliability analysis must be able to reproduce the resistance from the finite-element simulations, i.e. the accurate resistance of the beam at a given time. For beams exposed on the underside and the sides, it is essential to consider the rounding of the corners appropriately, which has a more pronounced effect for smaller beams than for larger ones. For this reason, the analytical corner rounding model (CRM) was developed (Fahrni, 2021). In addition to the effective charring depth d_{ef}, which is defined analogous to the ECM in Eurocode 5, it introduces the corner rounding radius. Two phases are differentiated (Figure 4):
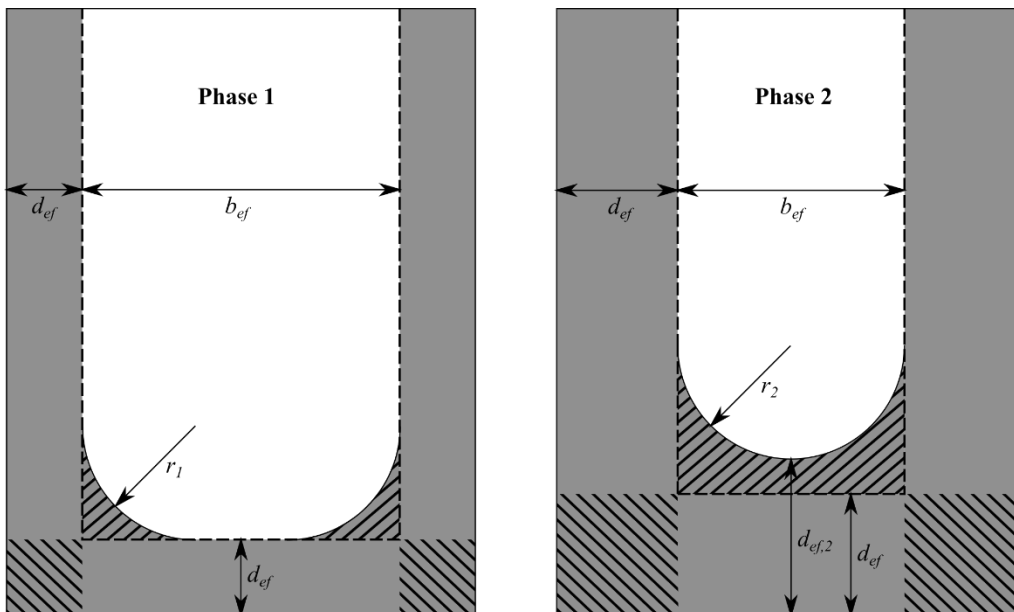

Figure 4: Corner rounding model for charring from three sides (grey). The diagonally shaded areas are in conceptual relation with each other. The dashed line shows the idealistic rectangular remaining cross-section according to the ECM.

In phase 1, the corner radius is given by the multiplication of the effective charring depth with the factor k_r:

$$r_1 = k_r \cdot d_{ef} \tag{2}$$

The area considered as charred due to the corner rounding can be conceptually seen as the compensation for the rectangular corner area, which is "charred from two sides" (Figure 4). A value of $k_r \approx 2.16$ would imply that both areas are identical. However, the calibrated k_r values are significantly lower (see Table 3) and thus the area A_u is uncompensated:

$$A_u = 2 \cdot d_{ef} \left(1 - k_r^2 \left(1 - \frac{\pi}{4}\right)\right) \tag{3}$$

Phase 1 is applicable until the two adjacent quarter-circles touch each other. In the subsequent phase 2, the radius is given by:

$$r_2 = \frac{b_{ef}}{2} \tag{4}$$

To make sure that the uncompensated area continues to follow equation 3, the charring depth $d_{ef,2}$ on the fully rounded side is given by:

$$d_{ef,2} = \frac{r_2^2 \frac{\pi}{2} + b d_{ef} - A_u}{b - 2 \cdot d_{ef}} - r_2 \tag{5}$$

Further details on the corner rounding model and the analytical formula to calculate the section modulus are presented in Fahrni (2021).

The charring rate, the ZSL and the corner rounding factor k_r were calibrated separately for each fire resistance. The charring rates are considered as they result from one-dimensional heat transfer finite-element simulations based on the properties in Eurocode 5-1-2 (Table 3). The 300°C isotherm was considered to represent the charring depth. The ZSL and k_r were then calibrated to represent the section modulus of the simulated beams (Table 1) as close as possible. The deviations between the CRM and the simulations are also shown in Table 1. The standard deviation of the relative error over all four fitted fire resistances is 1.8% (Fahrni 2021). Thus, the CRM is considered to represent the resistance appropriately and the remaining error is covered by the general model error term in the reliability analysis.

Table 3: Charring rate matching the charring depth of the finite-element simulations and calibrated properties of the effective cross-section method (ECM) for underside exposed beams and the corner rounding model (CRM) for beams with three-sided exposure.

		ECM	CRM	
t	β	d_0	k_r	d_0
[min]	[mm/min]	[mm]	[-]	[mm]
30	0.738	8.9	0.61	9
60	0.688	11.6	0.41	11.9
90	0.654	12.7	0.32	13.9
120	0.629	13.5	0.26	15.9

4.2   Effective cross-section method

For beams exposed on the underside only, the analytical resistance model for the reliability analysis bases on the ECM. However, the time-dependent and accurate charring rates (Table 3) are used and the ZSL is calibrated to represent the resistance from the corresponding finite-element simulations. The calibrated ZSL are shown in Table 3 and the deviations from the simulations are presented in Table 2.

The standard deviation of the relative error over all four fitted fire resistances for beams exposed on the underside is 3.7% (Fahrni 2021). The main cause for the slightly larger error compared to the CRM is that only one property is calibrated in the ECM compared to two in the CRM, providing less potential for optimization.

5   Reliability comparison

5.1   Reference structures and reliability models

From a reliability point of view, the present and the proposed code formats should not actually be compared based on resistances (as done in chapter 3), but based on the resulting scatter in the reliability indices of reference structures representing the scope of the code. In the calibrations presented herein, the reference structures consist of beams of varying length (3 to 20 m), aspect ratio (height/width from 2 to 6), fire exposure (one/three-sided), fire resistance (30/60/90/12 min), permanent load (1 to 4 kN/m^2) and variable load (dwelling, office). The reliability indices for the fire design situation and for the permanent design situation were calculated for totally 960 reference structures. 504 structures, where the reliability index in the fire design situation was smaller (i.e. decisive) were then considered in the code calibration.

The following six properties were modelled as random properties in the code calibration: permanent load, variable load, variable load model uncertainty, resistance, resistance model uncertainty, charring rate. The details and the background of all the properties are given in Fahrni (2021).

5.2   Code formats

5.2.1   Introduction

Three different code formats were analysed and/or calibrated: The present Eurocode 5-1-2 (2004), the final draft of Eurocode 5-1-2 (FD, 2021) and a modification of the final draft (FD mod), where the differentiation of the charring rate for one-sided or multi-sided exposure is reintroduced (0.65 mm/min and 0.70 mm/min).

The comparison between the different analysed and calibrated code formats is done in terms of the error term, summing the differences between the mean/target reliability index β_t and the reliability index β_i of each reference structure:

$$E = \sum \frac{(\beta_i - \beta_t)^2}{\beta_t^2} \tag{6}$$

In the calibrations, the error term is minimized by adapting the respective partial factors and eventually the ZSL.

All analysed code formats including the predefined and calibrated properties and the resulting error term are shown in Table 4. A comparison of the resulting reliability scatters is shown in terms of box plots in Figure 6. The detail, i.e. all the single reliability indices separated by the variable load, the exposure and the fire resistance are shown in Figure 5.

Table 4: Setup and results of the analysed code formats based on present Eurocode 5-1-2 (2004), the final draft (FD) and the modified final draft (FD mod). Values in parentheses are not calibrated, but predefined. Mean/target reliability (β_t), fractile of the strength in fire (φ_M), partial factor of the strength in fire (γ_M) and the charring rate (γ_β), zero-strength layer (d_0), error term (E) and the error term relative to the present calibration (E_{rel}).

	Basis	β_t	φ_M	γ_M	γ_β	d_0	E	E_{rel}
1	2004	3.65	(20%)	(1)	(1)	(7)	0.239	(1)
2	2004	3.73	(5%)	(1)	(1)	(7)	0.624	2.61
3	FD	3.76	(20%)	(1)	(1)	(10)	0.402	1.68
4	FD	3.76	(20%) 49%	0.89 (1)	1.04	(10)	0.236	0.99
5	FD	3.76	(20%) 57%	0.86 (1)	1.01	12.4	0.161	0.67
6	FD mod	3.74	(20%)	(1)	(1)	(10)	0.198	0.83
7	FD mod	3.74	(20%) 40%	0.92 (1)	1.03	(10)	0.111	0.46
8	FD mod	3.74	(20%) 46%	0.90 (1)	1.01	11.6	0.084	0.35

5.3   Present Eurocode 5-1-2 (2004)

The code format in the present Eurocode 5-1-2 (2004) uses the 20% fractile and a partial factor equal to one for the strength in fire and has no partial factor applied on the charring rate (equivalent to a factor one, Table 4). The charring rate for one-sided charring is 0.65 mm/min and 0.7 mm/min for multi-sided charring. Applying the code format to the reference structures, the resulting mean reliability is 3.65 and the error term is 0.239 (code format 1, Table 4).

If it were decided to decrease the fractile to 5% (as with all other materials) and keep the rest the same, the mean reliability index would increase to 3.73 (code format 2, Table 4). At the same time, the error term would increase significantly to 0.624.

From Figure 6 it can be seen that dwelling and office structures have comparable reliability indices. With increasing fire resistance, the reliability index increases. Structures only exposed on the underside have a higher reliability than structures exposed on multiple sides.
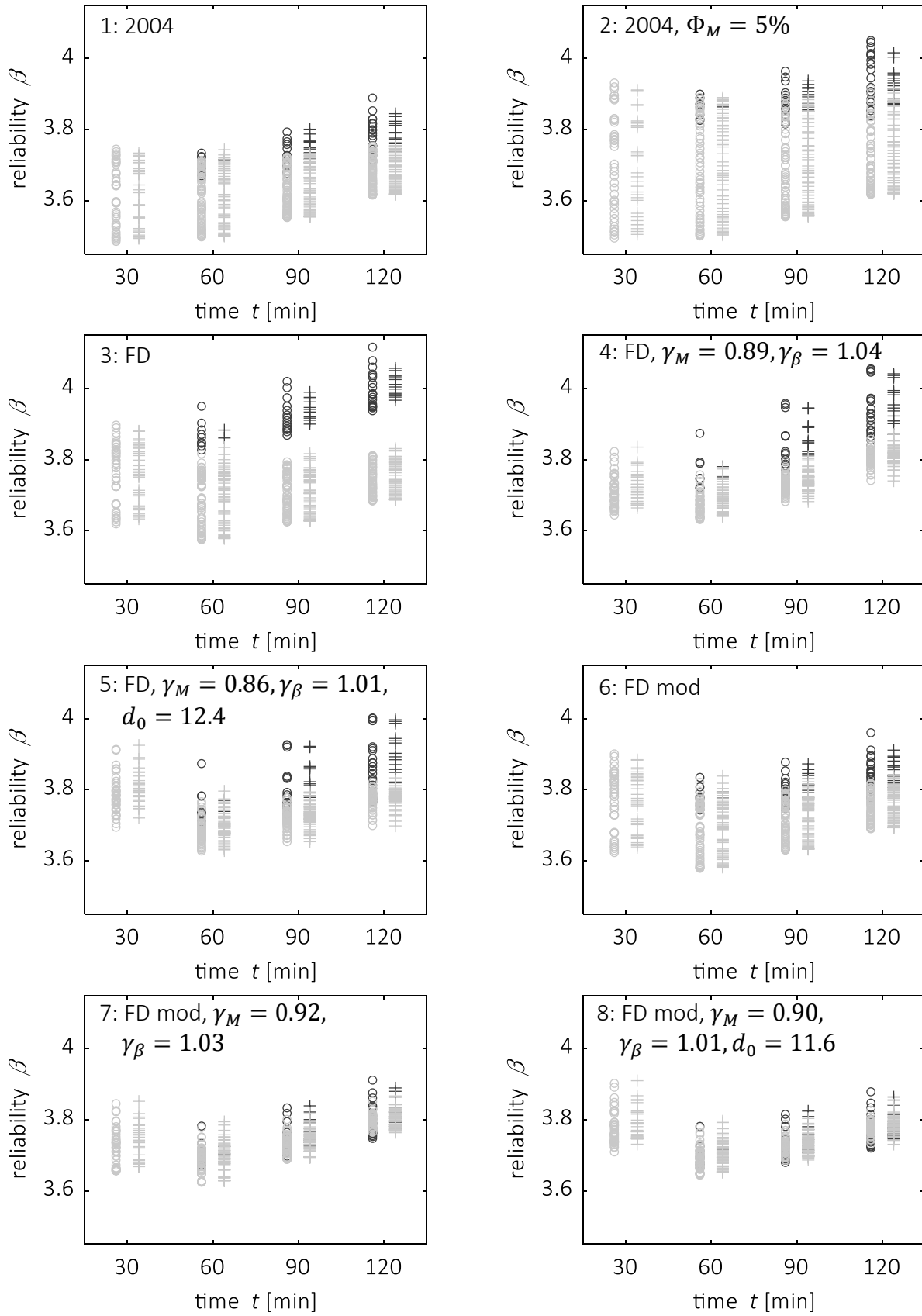
Figure 5: Reliability indices of each reference structure in each analyzed code format, separated by the fire resistance time. Key: black=underside exposed, grey: underside + sides exposed, o=dwellings, +=offices.
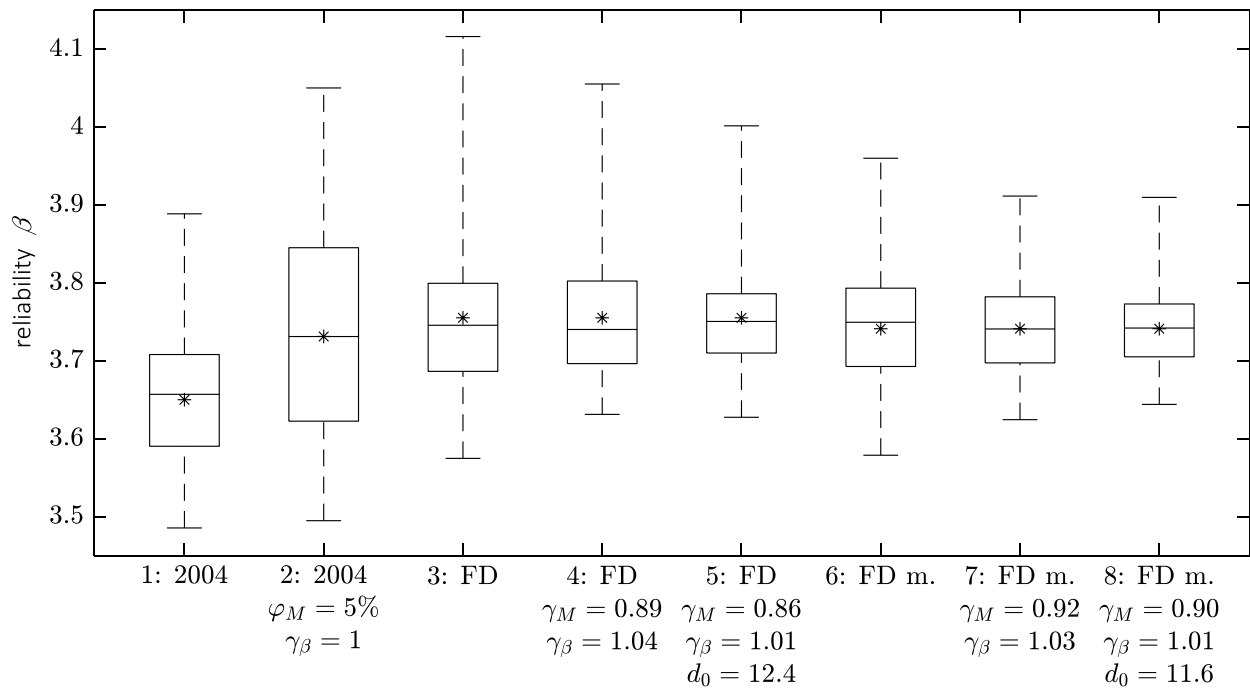
Figure 6: Reliability index box plots of all analyzed code formats (Table 4), indicating the scatter of the reliability index over all considered reference structures. The box represents the reliability indices between the 25% and the 75% quantile, the center line indicates the median, the whiskers indicate the full span (min to max) of the reliability index and the star denotes the mean reliability index.

5.4 Eurocode 5-1-2, final draft (FD)

The code format in the final draft of Eurocode 5-1-2 (2021, code format 3) differs from the present Eurocode 5-1-2 (2004) in terms of the ZSL (10 mm instead of 7 mm) and the charring rate. The latter is given as 0.65*1.08=0.702 mm/min for any kind of exposure. Since the reliability index for structures exposed on the underside only was already higher than for multi-sided exposure in the present code format, the difference increased further (Figure 5, 1 vs 3). This also results in a significantly increased error term of 0.402, which is 68% higher than the present code format (Table 4). The mean reliability index increased to 3.76.

The charring rate implies a significant uncertainty for the reliability of a structure, thus applying a partial factor γ_β (or fractile value) to it would be appropriate. The partial factors on the strength γ_M and on the charring rate γ_β can then be calibrated (code format 4) with the target being the mean reliability index of the final draft (3.76). The resulting error term is minimized to roughly the error term of the present Eurocode 5-1-2 (0.236) with $\gamma_M = 0.89$ and $\gamma_\beta = 1.04$ (Table 4). The partial factor of 0.89 on the strength together with the 20% fractile is equivalent to a partial factor of one with the 49% fractile. It is no surprise that the partial factor on the charring rate increases, since the applied safety (partial factor and fractile) did not yet correspond to the charring rate's contribution to the overall uncertainty. The strength partial fac-

tor in turn must decrease to keep the mean reliability level the same. From the reliability indices of each structure (Figure 5) it can be seen that the difference between the exposures is reduced, which is caused by the fact that, for structures exposed on the underside only, the changed γ_β increases the safety less than the γ_M reduces it. In contrast, for structures exposed on multiple sides, the changed partial factors lead to an overall increase of the reliability index.

If additionally the ZSL is calibrated (code format 5, Table 4), the error term decreases to 0.161. The ZSL is increased to 12.4 mm, while both partial factors decrease a little ($\gamma_M = 0.86$, $\gamma_\beta = 1.01$). This leads to an increased reliability index for structures with 30 min fire resistance and the difference between the two exposures is slightly reduced as well.

5.5 Eurocode 5-1-2, final draft modified (FD mod)

As shown before, the harmonization of the charring rates among the two exposures increases the differences in the reliability indices of both exposures. It would thus be meaningful to revert this change and apply the charring rates as in the present Eurocode 5-1-2 (2004). This was done in the code formats 6-8 (FD mod, Table 4). With partial factors equal to one (code format 6), the mean reliability level is reduced slightly to 3.74, while the error term reduces significantly from 0.402 to 0.198, being 17% below the error term of the present Eurocode 5-1-2 (2004). With this code format, structures exposed on the underside only still have a higher reliability index than structures exposed on three sides.

This is eliminated when both partial factors are calibrated (code format 7, Table 4) keeping the mean reliability on the level of the code format 6: $\gamma_M = 0.92$, $\gamma_\beta = 1.03$. The error term again significantly lowers to 0.111.

The homogeneity of the code format, i.e. the error term, can be further improved by additionally calibrating the ZSL (code format 8, Table 4). As in the code format in the final draft of Eurocode 5-1-2 (2021), the ZSL increases, while both partial factors decrease: $\gamma_M = 0.90$, $\gamma_\beta = 1.01$, $d_0 = 11.6$ mm. The error term is reduced to 0.084.

6 Conclusion

Harmonization between the simplified and advanced design methods makes it necessary that the zero strength layer (ZSL) is increased. From a purely deterministic point of view, i.e. by comparing the resistance between both methods, the proposed ZSL increase from 7 to 10 mm in the final draft of the Eurocode 5-1-2 (2021) is meaningful. Considering the probabilistic code calibrations, it can be seen that a further increase of the ZSL to about 12 mm would result in an even more homogenous reliability level and, thus, a better calibrated code.

Unfortunately, the proposed harmonization of the charring rates to 0.7 mm/min for any exposure (Eurocode 5-1-2, 2021) increases the inhomogeneity of the reliability indices and results in an error term that is 68% higher than the error in the present code format (Eurocode 5-1-2, 2004). It is thus suggested to keep the differentiation of the charring rates for different exposures. Such a code format (0.65 mm/min for underside exposed, 0.7 mm/min for multiple sides exposed, ZSL of 10 mm) would be 13% better in terms of the error term compared to the present Eurocode 5-1-2 (2004).

The increase of the ZSL increases the mean reliability level slightly more than a change from 20% to 5% in the present Eurocode 5-1-2 (2004) would, with and without the harmonized charring model.

A further improvement of the code format would be possible by introducing a partial factor on the charring rate and/or lowering its fractile. Since the present mean reliability level is deemed sufficient, the increase in safety on the charring rate could be compensated by a further increase of the strength fractile. However, such a fundamental change (1) has implications to many formulas in the code apart of the bending resistance, (2) might be difficult to communicate to practitioners and (3) the fractile for the strength would deviate even more from other materials than today. Thus, it is suggested that only the ZSL is changed in the basic resistance model, but neither the strength, nor the charring rates.

7   References

Eurocode 1 (2002): Actions on structures - Part 1-2: General actions - Actions on structures exposed to fire. CEN. (EN 1991-1-2)

Eurocode 5 (1994) Prenorm: Design of timber structures - Part 1-2: General - Structural fire design. CEN. (ENV 1995-1-2)

Eurocode 5 (2004): Design of timber structures - Part 1-2: General - Structural fire design. CEN. (EN 1995-1-2:2004).

Eurocode 5 (2021): Design of timber structures - Part 1-2: Structural fire design. Final Draft. CEN. (EN 1995-1-2:2021).

Fahrni, R., De Sanctis, G., Frangi A. (2019): Code calibration for timber in fire – On the use of 20 % fractiles for the strength. INTER Meeting, 52-16-02, Tacoma WA, USA.

Fahrni, R., De Sanctis, G., Frangi A. (2020): Comparison of reliability- and design-based code calibrations. Structural Safety 88.

Fahrni, R. (2021): Reliability-based code calibration for timber in fire. Dissertation, Institute of Structural Engineering, ETH Zurich.

König, J., Walleij, L. (2000): Timber frame assemblies exposed to standard and parametric fires - Part 2: A design model for standard fire exposure. Rapport. Trätek.

Lange, D., Boström, L., Schmid, J., Albrektsson, J. (2014) Assessment of the influence of parametric fire scenarios on structural timber performance and reliability. SP Swedish Technical Research Institute, SP Report 2014:35, ISBN 978-91-87461-78-1. Boras, Sweden.

Massini, G. (2019) Safety concept of codes: why do fewer structures collapse than codes expect?. Master project thesis. ETH Zurich.

Schaffer, E. L. (1984): Structural Fire Design: Wood. Research Paper FPL 450. Forest Products Laboratory, United States Department of Agriculture.

Schaffer, E. L., Marx, C. M., Bender D. A., Woeste, F. E. (1986) Strength validation and fire endurance of glued-laminated timber beams. Research Paper FPL 468. Forest Products Laboratory, United States Department of Agriculture.

Schmid, J., Klippel, M, Just, A., Frangi, A. (2014) Review and analysis of fire resistance tests of timber members in bending, tension and compression with respect to the Reduced Cross-Section Method. Fire Safety Journal, 68, 81–99.

Schmid, J., Just, A., Klippel, M., Fragiacomo, M. (2015) The Reduced Cross-Section Method for Evaluation of the Fire Resistance of Timber Members: Discussion and Determination of the Zero-Strength Layer. Fire Technology, 51, 1285–1309.

DISCUSSION

The papers was presented by A Frangi

F Lam commented about the calculation of ⌀i for the reliability analysis where the cross sectional geometry of the residual cross section would be used together with the original beam strength distribution to characterize the random resistance. He received confirmation that the parameters needed to establish the residual cross sectional geometry were not considered as stochastic. A Frangi said that it did not matter because this was a code calibration process against a past approach.

P Parma commented that only beam datasets were used for the calibration and asked if the conclusion would change if one considered columns. A Frangi replied that they would not expect any difference with columns as this was a code calibration process. There were discussions that it would be interesting to extend the dataset to other elements and load conditions. Also stability issues could be important.

F Hochreiner and A Frangi discussed the use of zero strength layer as calibration parameter with only one value. G Hochreiner commented that calculation of internal forces was based on original cross section but stress evaluation was based on residual cross section therefore there would be inconsistencies.

4 Peer review of papers for the INTER Proceedings

Experts involved:

The reviews are undertaken by long standing members of the INTER group which is a community of experts in the field of timber engineering.

Procedure of peer review

- Submission of manuscripts: all members of the INTER group attending the meeting receive the manuscripts of the papers at least four weeks before the meeting. Everyone is invited to read and review the manuscripts especially in their respective fields of competence and interest.

- Presentation of the paper during the meeting by the author

- Comments and recommendations of the experts, discussion of the paper

- Comments, discussion and recommendations of the experts are documented in the minutes of the meeting and are printed on the front page of each paper.

- Final acceptance of the paper for the proceedings with

    - no changes
    - minor changes
    - major changes
    - or reject

- Revised papers are to be sent to the editor of the proceedings and the chairman of the INTER group

- Editor and chairman check, whether the requested changes have been carried out.

5 Meetings and list of all CIB W18 and INTER Papers

CIB Meetings:

1	Princes Risborough, England; March 1973
2	Copenhagen, Denmark; October 1973
3	Delft, Netherlands; June 1974
4	Paris, France; February 1975
5	Karlsruhe, Federal Republic of Germany; October 1975
6	Aalborg, Denmark; June 1976
7	Stockholm, Sweden; February/March 1977
8	Brussels, Belgium; October 1977
9	Perth, Scotland; June 1978
10	Vancouver, Canada; August 1978
11	Vienna, Austria; March 1979
12	Bordeaux, France; October 1979
13	Otaniemi, Finland; June 1980
14	Warsaw, Poland; May 1981
15	Karlsruhe, Federal Republic of Germany; June 1982
16	Lillehammer, Norway; May/June 1983
17	Rapperswil, Switzerland; May 1984
18	Beit Oren, Israel; June 1985
19	Florence, Italy; September 1986
20	Dublin, Ireland; September 1987
21	Parksville, Canada; September 1988
22	Berlin, German Democratic Republic; September 1989
23	Lisbon, Portugal; September 1990
24	Oxford, United Kingdom; September 1991
25	Åhus, Sweden; August 1992
26	Athens, USA; August 1993
27	Sydney, Australia; July 1994
28	Copenhagen, Denmark; April 1995
29	Bordeaux, France; August 1996
30	Vancouver, Canada; August 1997
31	Savonlinna, Finland; August 1998
32	Graz, Austria; August 1999

33   Delft, The Netherlands; August 2000

34   Venice, Italy; August 2001

35   Kyoto, Japan; September 2002

36   Colorado, USA; August 2003

37   Edinburgh, Scotland; August 2004

38   Karlsruhe, Germany; August 2005

39   Florence, Italy; August 2006

40   Bled, Slovenia; August 2007

41   St. Andrews, Canada; August 2008

42   Dübendorf, Switzerland; August 2009

43   Nelson, New Zealand; August 2010

44   Alghero, Italy; August 2011

45   Växjö, Sweden; August 2012

46   Vancouver, Canada; August 2013

INTER Meetings:

47   Bath, United Kingdom; August 2014

48   Šibenik, Croatia; August 2015

49   Graz, Austria; August 2016

50   Kyoto, Japan; August 2017

51   Tallinn, Estonia; August 2018

52   Tacoma WA, USA; August 2019

53   Online Meeting; August 2020

54   Online Meeting; August 2021

The titles of the CIB W 18 and INTER papers (starting from 2014) are included in the complete list of CIB/INTER papers: http://holz.vaka.kit.edu/392.php